NASA Conference Publication 2484

Space Electrochemical Research and Technology (SERT)

Proceedings of a conference held at
the NASA Lewis Research Center
Cleveland, Ohio
April 14-16, 1987

NASA

NASA Conference Publication 2484

Space Electrochemical Research and Technology (SERT)

Proceedings of a conference held at
the NASA Lewis Research Center
Cleveland, Ohio
April 14–16, 1987

National Aeronautics
and Space Administration

**Scientific and Technical
Information Office**

1987

FOREWORD

Without electrochemical devices there would be no space program. Though much maligned and not well understood, electrochemistry has shown itself to be an indispensable, if not always a completely reliable, segment of an overall power system. Disposable primary batteries, long-life secondary batteries, and chemically rechargeable fuel cells all play an important role in today's as well as tomorrow's space program. With the wide variety of electrochemical system concepts in various stages of development and the diverse set of future NASA mission requirements, it is necessary to consider what system concepts may best suit the Agency's needs.

The first NASA Space Electrochemical Research and Technology (SERT) Conference was held at the Lewis Research Center on April 14-16, 1987. The conference was conducted on behalf of NASA Headquarter's Power and Propulsion Division (Code RP) of the Office of Advanced Space Technology (OAST). It was designed to identify and assess critical needs and technologies for the NASA electrochemical energy conversion and storage program and was aimed at providing guidance to NASA on the appropriate direction and emphasis of that program. The field of electrochemistry is so broad and varied that the best system for one mission may not be best for another. Advocates, on the other hand, generally view their own favorite technology as ideally suited for almost any mission that presents itself. This conference brought together a proper mix of mission planners, technology advocates, and power system engineers.

The areas of focus at this meeting, were as follows:

(1) Advanced rechargeables
(2) Advanced concepts
(3) Critical physical electrochemical issues
(4) Modeling

A series of related overviews in the areas of NASA advanced mission models (space station, low- and geosynchronous-Earth-orbit missions, planetary missions, and space transportation) as well as perspectives from the American Institute of Aeronautics and Astronautics (AIAA) and the Air Force were presented. The technical sessions that followed consisted of papers grouped into the focus areas. The sessions were chaired by highly respected investigators who are extremely knowledgable in the practical aspects of complete electrochemical system considerations. The chairs assembled their own technical sessions and led the workshops that followed.

This proceedings includes the related overviews, the technical papers, and summaries of the technical workshops.

The next SERT conference is scheduled for the spring of 1989. Prior to that time we will be thinking of ways to improve the usefulness of the meeting as it relates not only to planning the closing years of our electrochemistry program, but also to those whose aim is to stay on the cutting edge of a multifaceted technology.

On behalf of the conference committee and the Lewis Research Center staff, I would like to thank Patricia O'Donnell, my deputy in the Energy Storage Branch, and Jo Ann Charleston, a staff engineer, for their hard work in organizing this conference. Jo Ann also oversaw the publication of the proceedings.

Lawrence H. Thaller
Chief, Energy Storage Branch

CONTENTS

SESSION 2 - ADVANCED CONCEPTS

SESSION 3 - CRITICAL PHYSICAL ELECTROCHEMICAL ISSUES

SESSION 4 - MODELING

WORKSHOP SUMMARIES

STATUS OF SPACE STATION POWER SYSTEM

Cosmo R. Baraona and Dean W. Sheibley
National Aeronautics and Space Administration
Lewis Research Center
Cleveland, Ohio 44135

The manned space station is NASA'S next major program. It presents many challenges to power system designers. The power system in turn is a major driver on the overall configuration. In this paper the major requirements and guidelines that affect the station configuration and the power system are explained. The evolution of the space station power system from the NASA program development-feasibility phase through the current preliminary design phase is described. Several early station concepts are described and linked to the present concept. The recently completed phase B tradeoff study selections of photovoltaic system technologies are described. The present solar dynamic and power management and distribution systems are also summarized for completeness.

BACKGROUND

The space station system is the next major step in the manned space program. The space station will be a multipurpose facility that will enable advancements in science, technology, and space transportation capabilities. It will promote commercialization of space and open new avenues not yet fully realized.

Numerous studies conducted in the 1960's and 1970's (ref. 1) have helped establish a role for a manned space station. Most unmanned satellites launched since the beginning of the space age in 1957 have been powered by photovoltaic systems based on silicon solar cells. A few deep space interplanetary missions and manned spacecraft like Mercury, Gemini, and Apollo are the exceptions. During this era technology has been developed for photovoltaic, solar dynamic, and nuclear systems as well. The primary thrust of these developments has been toward lighter weight, lower volume, higher efficiencies, longer lifetimes, and reliability. These technologies and flight experiences formed the starting point for establishing the feasibility of the current space station and for defining its power system.

FEASIBILITY PHASE

The current Space Station Program can trace its roots back to 1981, when technology steering committees were formed to identify candidate technologies. In early 1982, the Space Station Task Force was formed to determine the feasibility of a space station (phase A in the program development process). The task force analyzed the uses or missions for a manned space station. Specific missions to be performed were determined and studied extensively (ref. 2). These studies showed that the station would serve as an assembly

facility, a storage depot, and a transportation node or way station for payloads intended for higher Earth orbits or for interplanetary missions.

These diverse missions led to the space station concept shown in figure 1. It is composed of a manned core and an unmanned co-orbiting platform, both in a 28.5° orbit. Another platform is in a polar orbit. A system of unmanned vehicles for maneuvering payloads near the station or for transferring them to other orbits is part of the space station system.

The mission analysis studies identified the total requirement for each station element. Power levels were determined as a function of time from the initial operational capability (IOC) through some future power level when the station and the number of missions will have grown. These power requirements have changed as the mission definition has evolved. The current user power levels are shown in table 1. User power means that all system losses for generation, storage, conditioning, and distribution have been taken into account. Note that the IOC station power of 75 kW is about an order of magnitude higher than that used on Skylab. Skylab, the first U.S. manned space station, launched in 1973 is the largest (8-kW user power, 22-kW array power) solar power system flown in space to date. The 75-kW requirement for the planned space station is the most challenging factor facing the power system designer.

Additional challenges arise from programmatic requirements imposed on the power system designer. These additional requirements are management and engineering related. They include cost (both initial and life cycle), schedule, technical development risk, weight, and safety requirements as most large spacecraft projects do. However, the permanent nature of the space station results in some new and unique requirements such as growth capability, maintainability, and commonality of hardware and software across all station elements. Commonality reduces development, qualification, and production costs. It was an important factor in selecting the technologies for use on space station. Replacement and growth of the station systems requires that they be designed so that they can accept changes in technology (i.e., technology transparency) yet still provide the same functions. Other considerations are the station orbital altitude and decay, orbital assembly and buildup, lifetime, logistics and control of spare parts, failure criteria, verification, contingency requirements, load type and location, and interface.

In 1983 the task force took the results from the mission analysis studies and synthesized them into several candidate space station configurations. They also further studied and sharpened technology selection for all the station systems including power.

As a result of the feasibility work NASA received approval to build the space station and have it operational by 1994. The importance of drag area on reboost cost and life-cycle cost coupled with the very large growth power requirements (as high as 450 kW) resulted in the adoption of solar dynamic generators with thermal energy storage in addition to photovoltaic arrays with electrochemical energy storage for detailed study in the definition phase.

Definition Phase

The present space station configuration and the hybrid power system (fig. 2) using both photovoltaic and solar dynamic technologies, were selected

in the definition (or phase B) studies, which began in 1984. Nuclear and other power systems were ruled out on the basis of schedule, cost, risk, and other factors. The size and drag area of the power system were major considerations in selecting the overall space station geometry. This geometry must allow the station and the power system to grow. It must minimize the effect of the power system on viewing angles for experimenters and for communications. The space station and its power system must be controllable and structurally sound. The maximum degree of commonality between the station and platform power systems was necessary to reduce costs. Most importantly, the station must be passively controllable (i.e., gravity gradient stabilized). From these diverse and sometimes contradictory requirements, the power-tower and later the dual-keel configurations were developed and studied by NASA. At the same time the NASA Lewis Research Center, along with its two major phase B contractors, TRW and Rocketdyne, studied numerous power system types. These phase B definition studies are described below.

Definition of Power System Configuration

Early in phase B six power system options were defined for study (fig. 3). The IOC power level of 75 kW and the growth power level of 300 kW were selected. The six cases were established on the basis of IOC power system type (either solar dynamic (SD) or photovoltaic (PV)) and the method of growing from 75 to 300 kW. Case 1 was all PV. Case 6 had minimum PV (12.5 kW) at IOC and all SD at growth. An all-SD system is not feasible because power is needed on the first launch when the accurate Sun tracking required for the SD system is not possible. Cases 2 to 5 had various proportions of SD to PV. Commonality between the station and the platform was considered in these system studies.

The primary selection criterion for these system studies was both IOC and life-cycle cost for the station and the platforms. Development, manufacturing, verification testing, overhead, and launch costs for all the space station system hardware and software were included. An especially important life-cycle cost saving resulted from the reduced aerodynamic drag associated with the SD system. This reduced drag allowed lower orbital altitude and higher shuttle payload capacity.

As a result of these system studies the case 5 hybrid was selected. In this case the PV portion of the power system generates 25 kW with four solar array wings (array power, N57 kW). The station would also use nickel-hydrogen batteries identical to those designed for the platform. This commonality of hardware results in design and development cost savings for the Space Station Program.

The SD portion of the case 5 power system generates about 50 kW. Overall the technologies for the photovoltaic system are low risk and space proven, whereas the solar dynamic technologies offer reduced drag and cost.

Photovoltaic System Technology Studies

Solar array. - Several array concepts were evaluated during the phase B studies. They included planar arrays and concentrators. A planar array with silicon cells was selected. This array design is similar to the NASA Office

of Aeronautics and Space Technology (OAST) flight experiment, OAST 1, launched in August 1984. If fully populated with cells, the array would have a power output of 13 to 14 kW at the wing root. This flight experiment demonstrated that this array type is technology ready and established that space station planners can have a high degree of confidence in it. A more detailed description of the array and the flight experiment results can be found in reference 3.

Energy storage system. - The PV system will store energy electrochemically. This stored energy is needed during the dark portion of the orbit and for contingency purposes when the power system cannot produce or deliver power. The phase B studies showed that the inherent storage capability or residual energy of the electrochemical system was adequate to meet expected contingency requirements. Building in greater contingency capability would be unnecessarily expensive.

Energy storage options studied included nickel-cadmium (NiCd) batteries, regenerative fuel cells (RFC), and nickel-hydrogen (NiH_2) batteries. Although NiCd batteries are established, flight-proven, low-risk devices, their low depth of discharge results in high storage system weight. Space cells in sizes up to 100 A-hr have been produced, so development risk would be low.

RFC's use a fuel cell and an electrolyzer to store energy in the form of hydrogen and oxygen. In the dark portion of the orbit these elements are recombined in the fuel cell to produce water and electricity. During the lighted portion of the orbit excess array power is used to electrolyze the water and "charge" the system with hydrogen and oxygen. The cycle is closed so that the fluids are not consumed. RFC's are lighter than batteries and allows storage of large amounts of contingency power with small changes in tank volume. However, because RFC's are not as efficient as batteries (60 vs 80 percent), the solar arrays must be larger. Also, RFC's are more complex (i.e., contain pumps, valves, etc.) and not as reliable as batteries. RFC's also have higher heat rejection needs. Reliability was a major consideration for the platform, where 3 yr of operation without repair were required. However, commonality between the station and the platform to reduce development, resupply, and the cost of controlling spare parts was also considered.

The individual pressure vessel (IPV) type of NiH_2 battery has been used in geosynchronous (GEO) spacecraft (fig. 4). (The bipolar NiH_2 battery has low technology maturity and was screened out by the early tradeoff studies). IPV, 3.5-inch-diameter, 50-A-hr GEO cells are in production. Other sizes and capacities are available by using scaled-up versions of existing components. The uncertainty with the NiH_2 battery stems from its charge-discharge cycle life. GEO spacecraft experience only a fraction of the cycles that a LEO spacecraft experiences. However, the Space Station Advanced Development Program is beginning to test LEO cells with a goal of demonstrating 5-yr lifetimes.

As a result of the phase B tradeoff studies IPV NiH_2 batteries were selected for the platform. Weight, cost, reliability, development risk, and schedule were the primary considerations. Nickel-hydrogen batteries weigh about half as much and cost less than NiCd batteries and are more reliable than RFC's. An identical IPV NiH_2 battery was also selected for the station on the basis of cost and commonality with the platform. IPV NiH_2 was lower in IOC cost and only slightly higher in life-cycle cost for the station.

The recent evolution of space station energy storage system selection is shown in table II. The selection was strongly influenced by power level, commonality, weight, and cost.

Solar Dynamic Technology Studies

The solar dynamic system consists of an offset parabolic concentrator mirror and a receiver. The mirror focuses the Sun's heat into the receiver. The receiver stores the heat in a salt (e.g., lithium hydroxide) and also transfers it to a working fluid (e.g., toluene or helium-xenon gas). The heated fluid drives a turbine that spins an alternator to generate electric energy. The turbine also drives a pump that recirculates the working fluid. Excess heat is rejected to space by a radiator.

In the tradeoff studies the two conversion cycles considered were closed Brayton cycle (CBC) and organic Rankine cycle (ORC). These systems have not been used in space, but a technology data base for the heat engines has resulted from terrestrial and aircraft applications. Estimating costs, schedules, and other factors during the phase B tradeoff studies therefore involved higher risk for these systems than for the PV system.

Design considerations for the SD system studied in phase B and being worked on in the Advanced Development Program include low-gravity effects for two-phase (gas-liquid) flow, heat flow and distribution in the receiver, lifetime for thermal energy storage (salt) capsules, weight and optical quality of the concentrator, pointing accuracy (0.1°) for the mirror gimbals, atomic oxygen protection, launch packaging, and on-orbit assembly. At the time of this writing both the CBC and the ORC systems are still being considered. More detailed study is required because cost and performance are nearly identical.

Power Management and Distribution Studies

The power management and distribution (PMAD) system must cope with unknown load types and sizes as the station users change and increase in number. Therefore the PMAD system must be user friendly and adaptable to change and growth. The PMAD system for the space station must resemble a terrestrial utility power system rather than the PMAD system of previous spacecraft. Distribution voltages higher than the 28 V previously used are mandatory to reduce losses.

During phase B distribution frequencies of dc, 400-Hz ac, and 20-kHz ac were studied. Component efficiency, size, and weight as well as technology readiness, availability of space components, acoustic noise, electromagnetic interference, and plasma coupling were all considerations. After much deliberation, 20 kHz was selected for the PMAD distribution frequency.

The overall PMAD architecture selected is a dual-ring system with multikilowatt buses supplying power to load areas on the upper and lower keels and the transverse boom. Buses supplying the manned modules are rated at 30 kW. The PMAD system contains numerous switching and control assemblies as well as a control system for sensing and commanding the loads. Isolators and power controllers will sense faults and protect the system.

CONCLUDING REMARKS

The present Space Station Program traces it roots back to 1981. The station configuration and the power system for the present program have been studied extensively in the feasibility and definition phases.

The hybrid power system selected will meet the station and platform requirements initially and into the future. The 25-kW photovoltaic system (57-kW array power) will be larger than any system flown to date. The solar dynamic system will facilitate economics and growth for the power system and the station. The PMAD system enables a growable, balanced utility type of power system approach for maximum friendliness for the station users.

The technologies selected for the photovoltaic, solar dynamic, and power management and distribution systems result in the lowest initial-operating-system and life-cycle costs with acceptable development and schedule risk. This hybrid system also meets programmatic and technical considerations driving the power system definition. The space station power system may set the standard for future spacecraft power systems.

REFERENCES

1. Hook, W. R.: Space Stations - Historical Review and Current Plans. ASME Winter Meeting, Phoenix, AZ, Nov. 14-19, 1982.

2. Space Station Mission Synthesis Workshop. NASA Proceedings, Hampton, VA Mar. 5-8, 1984.

3. Solar Array Flight Experiment, Final Report. Lockheed Missiles and Space Co., LMSC-F087173, Apr. 1986.

TABLE I. - SPACE STATION SYSTEM POWER REQUIREMENTS

Element	Average	Peak
	User power, kW	
Manned core:		
IOC station	75	100
Growth station	300	350
Polar platforms:		
IOC station	8	16
Growth station	15	24
Co-orbiting platforms:		
IOC station	6	6
Growth station	23	23

TABLE II. - EVOLUTION OF SPACE STATION ELECTROCHEMICAL ENERGY STORAGE SYSTEM

Date	Station solar dynamic system	Station photo-voltaic system	Polar platform		Co-orbiting platform	Station	Platform	Comments
			Average	Peak		Electrochemical storage		
	Power level, kW							
Oct. 1985	0	75	8	18	6	H_2O_2 RFC	NiCd	Lacks commonality
Jan. 1986	37.5	37.5	8	18	6	H_2O_2 RFC	NiH_2	Platform weight reliability
Mar. 1986	50	25	8	18	6	NiH_2	↓	65 A-hr; 3.5-in. diameter
Oct. 1986	50	37.5	3.8	3.8	2	NiH_2	↓	40 A-hr; minimum weight
							↓	62 A-hr; minimum cost
Mar. 1987	(a)	(a)	(a)	(a)	(a)	NiH_2	↓	65 A-hr; 23 cells/pack (28 V); 2 packs/platform; 4 packs/station
								Commonality with orbital manuevering vehicle, flight telerobotic services, and mobile support center

[a]To be determined.

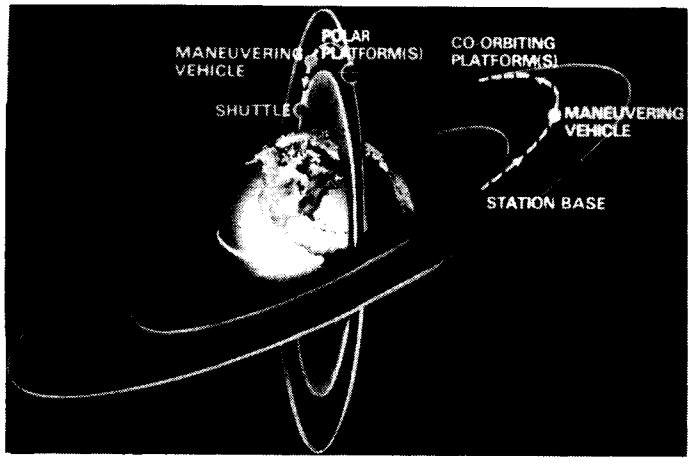

FIGURE 1. - SPACE STATION COMPLEX, EARLY 1990's.

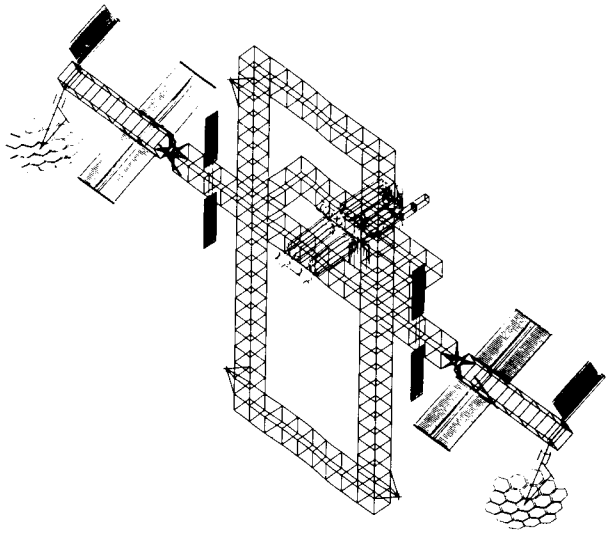

FIGURE 2. - SPACE STATION DUAL KEEL CONFIGURATION 1986.

CASE	INITIAL OPERATIONAL CAPABILITY, IOC	PHOTOVOLTAIC (PV) AND SOLAR DYNAMIC (SD) CAPABILITIES, KWE	GROWTH
1	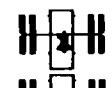	IOC PV GROWTH PV	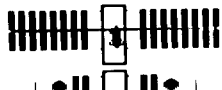
2		IOC PV GROWTH SD	
3		IOC 50 PV-25 SD GROWTH SD	
4		IOC 37.5 PV-37.5 SD GROWTH SD	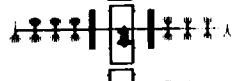
5	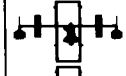	IOC 25 PV-50 SD GROWTH SD	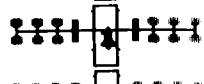
6	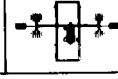	IOC 12.5 PV-75 SD GROWTH SD	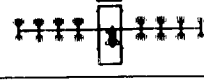

FIGURE 3. - CASES EVALUATED FOR SPACE STATION POWER SYSTEM.

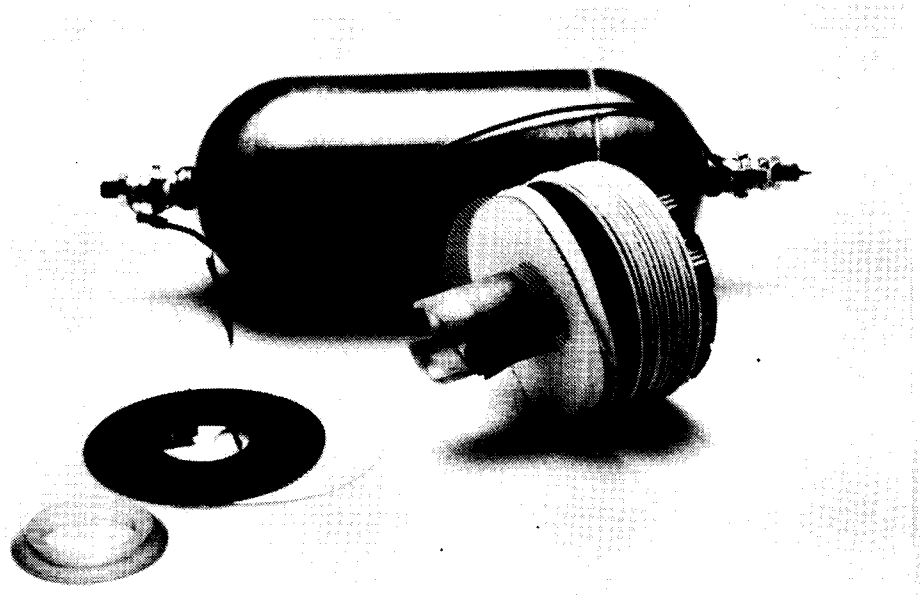

C-85-6445

FIGURE 4. - TYPICAL NICKEL-HYDROGEN CELL.

LEO AND GEO MISSIONS

Enrico Mercanti
National Aeronautics and Space Administration
Goddard Space Flight Center
Greenbelt, Maryland 20771

The Challenger disaster in early 1986 occurred about the same time that a Presidential commission known as the National Commission on Space (NCOS) was finishing its work. The NCOS vision of our Nation's future in space included recommendation that NASA's long-range plans for a world-leadership space program be developed and accelerated. The Challenger disaster, however, almost stopped our space program in its tracks. We could not even make effective use of our ability and experience in the use of expendable launch vehicles (ELV). As a result, plans already established had to be drastically revised and new plans had to be made. For example, Cobe was complete redesigned to fly on an ELV after having been designed and built for the shuttle. Meanwhile NASA created the Space Leadership Planning Group (SLPG) to formulate space mission plans covering a 50-year period based on Agency goals and objectives responsive to NCOS recommendations. This paper presents an interim view of the status of SLPG plans for low-altitude and geosynchronous (LEO, GEO) missions.

For transportation from ground to low Earth orbits and orbits between LEO and GEO, the missions utilize the shuttle and its successors, heavy-lift unmanned cargo vehicles, expendable launch vehicles, manned and unmanned orbital vehicles (OMV, OTV), and a dedicated class of passenger-carrying vehicles. In space, the mission model payloads are accommodated on LEO and (later) GEO space stations, unmanned co-orbiting and polar-orbiting platforms in LEO, GEO platforms, GEO shack, the spaceport, and free-flying satellites. In-orbit servicing is expected to be made available initially in LEO by using the space station, and later in GEO. This capability will permit repairs, equipment changes, and pickup and delivery of supplies or manufactured goods. Activities in both domains can support missions to the Moon, Mars, and interplanetary space.

Mission timelines are based on an annual budget growth of about 2.4 percent and the accompanying translation of research and technology into the transportation and infrastructure base. Specific LEO and GEO missions are shown chronologically up to the year 2035 together with mass-launched and cost estimates. Broad mission and program categories include families of telescopes, electromagnetic and wavelength instruments, the Explorer series, micro- and variable-gravity facilities, radio astronomy, Earth observations, meteorology (weather and climate), magnetic fields, spacelab, bioplatforms, materials processing, and communications. The technology research and development missions in LEO and GEO relate to power, propulsion, robotics servicing and assembly, shielding, environmental effects, docking, waste processing, bioregenerative life support, and medical facilities.

SCIENCE

- EARTH, SOLAR SYSTEM, UNIVERSE

HUMAN PRESENCE

- EXPLORATORY MISSION, BASES, SETTLEMENTS, COLONIES (MOON, MARS)

ENTERPRISE

- DEVELOP SPACE TECHNOLOGY
- TECHNOLOGY APPLICATIONS (U.S., INT'L, COMM'L)
- COMMERCIAL INVOLVEMENT & INVESTMENT
- SPACE TOURISM/UNIVERSITY
- EDUCATIONAL INITIATIVES

Figure 1. - NASA general program goals.

- DATA BASES
  - TO 1985 LANGLEY DATA BASE (TO 2010)
  - TO 1986 CIVIL NEEDS DATA BASE (TO 2035)

- NASA
  - 1985-87 ADVANCED MISSIONS WORKING GROUP (2035, I. BEKEY)
  - 1986-87 SPACE LEADERSHIP PLANNING GROUP (2035, I. BEKEY)
  - 1986-87 CIVIL SPACE LEADERSHIP INITIATIVES (1995 ERA) (S. RIDE)
  - 1986-87 MIXED FLEET STUDY (NASA/HQ)

- OTHER
  - 1986 NATIONAL COMMISSION ON SPACE
    NASA ADVISORY COMMITTEE
    NATIONAL ACADEMY OF SCIENCES
    PROFESSIONAL SOCIETIES (E.G., AIAA)

Figure 2. - NASA and related planning activities.

- DATA BASES
- PROGRAM OPTIONS, WHEN, THRUSTS, EMPHASES
- TRANSPORTATION
- INFRASTRUCTURE
- TECHNOLOGY DEVELOPMENT
- EXTERNAL EFFECTS: NATIONAL, INTERNATIONAL, COMMERCIAL
- EDUCATION, TOURISM

Figure 3. - Scope of planning activities.

- MARS: ROBOTIC, HUMAN
- LUNAR: BASES
- CORE PROGRAM
- COMMON ELEMENTS - ALL THRUSTS:
  - SPACE STATION
  - SHUTTLE, SHUTTLE DERIVED VEHICLES (SDV)
  - EXPENDABLE LAUNCH VEHICLES (ELV)
  - SPACE STAION (GEO & LEO)
  - PLATFORMS (LEO CO-ORBITING & POLAR, GEO)
  - ORBITAL MANEUVERING & TRANSFER VEHICLES (GROUND & SPACE STATION BASED OMV'S & OTV'S)

Figure 4. - Candidates for space thrust.

- UNIVERSE
  - NATURE, ORIGIN, EVOLUTION
- SOLAR SYSTEM
  - NATURE, ORIGIN, EVOLUTION (MOON, MARS)
- EARTH
  - LAND, OCEANS, ATMOSPHERE, BIOSPHERE
- SUN-EARTH
  - ENVIRONMENTAL IMPACT, SOLAR PROCESSES
- ORIGIN OF LIFE
  - SETI
- SPACE ENVIRONMENT EFFECTS (ON HUMANS, PROCESSES)
- TECHNOLOGY
  - DEVELOPMENT, APPLICATIONS, COMMERCIALIZATION
- BASES
  - LEO, GEO, MOON, MARS, INTERPLANETARY SPACE

Figure 5. - LEO and GEO objectives.

- TRANSPORTATION:

  EARTH TO LEO OR GEO
  WITHIN LEO OR GEO DOMAINS
  LEO TO GEO OR OTHER PLANETS & DEEP SPACE

- INFRASTRUCTURE:

  SPACE STATION
  FREE FLYERS
  PLATFORMS

- SERVICING:

  ASSEMBLY, MANUFACTURING, RETRIEVAL

- COMMUNICATIONS:

  COMMAND, CONTROL

- OPERATIONS:

  EARTH & SPACE SCIENCE, METEOROLOGY, EDUCATION

Figure 6. - NASA activities in LEO and GEO.

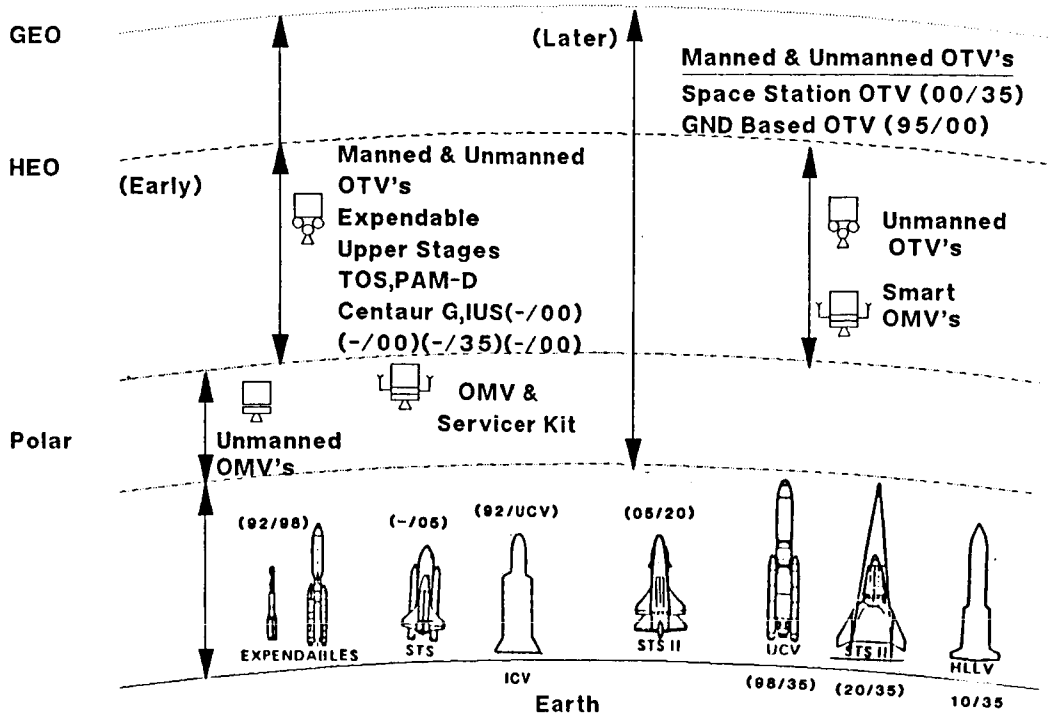

Figure 7. - NASA LEO and GEO transportation.

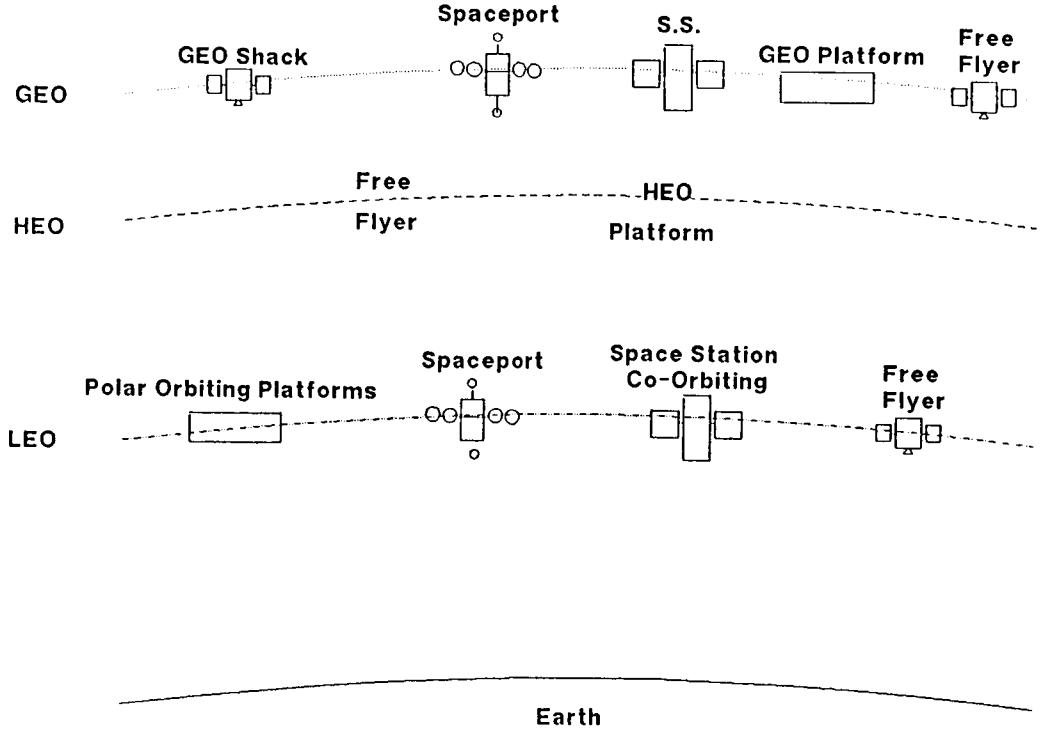

Figure 8. - NASA LEO and GEO infrastructure.

- SATELLITES, OBSERVATORIES, PLATFORMS
  - TELESCOPE: E.G., IR, OPTICAL, IMAGING, SOLAR & OTHER TARGETS
  - EXPLORERS: RAYS, MAGNETICS (MFE) GRAVITY (GRM), ATMOSPHERE, FIELDS & PARTICLES
  - OBSERVATORIES: EARTH OBSERVATIONS, SPACE SCIENCE, ATMOSPHERE
  - COMMUNICATION: ANTENNAS IN GEO
  - TETHERED SYSTEMS
- LEO SS: MATERIAL PROCESSING, SPARTAN, POWER, HEAT TRANSFER
- GEO SS: LIFE SCIENCE, VARIABLE-G, CENTRIFUGE
- GEO SHACK: (NOT PERMANENT PRESENCE)
- SHUTTLE: SPARTAN, HITCHHIKER, SPACELAB, GAS

Figure 9. - NASA LEO and GEO missions.

	1990 - 2010	2010 - 2035
MASS/YR (10^6 LB)		
TOTAL	0.30 - 5.60	3.0 - 7.0
PAYLOAD	0.15 - 1.20	1.0 - 2.2
PAYLOADS INTO ORBIT		
PER YR	15 - 74	40 - 130
TOTAL 0 - 2,500 LB	184	194
2,500 - 10,000 LB	286	248
10,000 - 30,000 LB	187	620
30,000 LB	171	608
	828	1670

Figure 10. - Mission model comparison.

JPL FUTURE MISSIONS AND ENERGY STORAGE TECHNOLOGY IMPLICATIONS

Eugene V. Pawlik
Jet Propulsion Laboratory
California Institute Of Technology
Pasadena, California 91109

The mission model for JPL future programs is presented. This model identifies mission areas where JPL is expected to have a major role and/or participate in a significant manner. These missions are focused, of course, on space science and applications missions, but they also include some participation in space station activities. The mission model is described in detail followed by a discussion on the needs for energy storage technology required to support these future activities.

Potential users of spacecraft technology are to be found primarily in the space science and applications missions such as planetary exploration, astrophysics, earth science, and communications. Future spacecraft will be sent on missions to make observations of comets and asteroids, to return samples from the surface of Mars, and from a comet. These spacecraft will also record the processes of the creation of stars and galaxies, provide a continuous multispectral inventory of earth processes, and will maintain a national preeminence in space communications.

The space station represents an additional area of potential technology needs that is important to the future of JPL. The space station will enable missions involving space science, space technology, commercial ventures, staging, and servicing operations. Mission accomodations will be required as part of space station operations to provide cost-effective resource and engineering interface between primary space station subsystems, such as the truss structure, and the mission payloads. In addition, a related more general objective of the space station program is to advance automation and robotics technologies. The development and operation of a highly automated telerobotic device (the Flight Telerobotic Servicer) is envisioned in order to carry out a variety of manipulative EVA tasks at the space station and elsewhere via the STS RMS and the OMV. Another important area is the utilization of the unique environment of space including the microgravity environment for science and commercial purposes.

A significant increase (factor of 2 to 4) in energy storage capability and/or reduction in mass and extended life of batteries is required to meet the varied missions of the 90's and beyond. They are necessary to meet the large number and types of equipment applications being planned. Lithium and other electrochemical systems are theoretically capable of increasing the energy density capability of primary and rechargeable systems by a factor of 3 to 5. To develop these systems requires a fundamental understanding of the chemistry and processes used to make these systems practical.

A VIEW FROM THE AIAA: INTRODUCTION OF NEW ENERGY STORAGE TECHNOLOGY INTO ORBITAL PROGRAMS

Charles Badcock
The Aerospace Corporation
Los Angeles, California 90009

The development of new energy storage technology must be heavily weighted toward the application. The requirements for transitioning low risk technology into operational space vehicles must remain the central theme even at the preliminary development stages by the development of efforts to define operational issues and verify the reliability of the system. Failure to follow a complete plan that results in a flight qualified unit may lead to an orphan technology. Development efforts must be directed toward a stable development where changes in design are evolutionary and end items are equivalent to flight units so that life and qualification testing can be used as a vehicle to demonstrate the acceptability of the technology.

INTRODUCTION

The American Institute of Aeronautics and Astronautics promotes the development and application of aircraft and aerospace technologies. We participate in the formation of space policy by commenting on national plans and budgets through our national umbrella technical committees. The technical committees of the AIAA are the organizational units that deal with individual disciplines within the overall structure. The Aerospace Power Systems Technical Committee (APSTC) promotes space power interests through publications, policy support, and the support of the Intersociety Energy Conversion Engineering Conference and other conferences. The level of interaction with electrochemistry is at the user level in the area of space power. While efforts at a more fundamental level are of interest, it is at the lowest individual unit, e.g. the battery cell, solar cell, etc., that our interests become well defined. It is the intent of this paper to describe some of the requirements for the deployment of energy storage technology into operational (non-experimental) power systems.

Even the most advantageous developments in energy storage technology are not assured of adoption for use in space vehicles. Few space programs will adopt new technology in the utility subsystems of a space vehicle unless the risks are well defined and acceptably small, and the actual mission of the program is either enabled by the use of the technology or the penalties in using older, established technologies are severe. Clearly, "better" is insufficient for the adoption of new technology. The success of space efforts when coupled with the conservatism brought on by the tremendous costs of most space operations more often leads to acceptance of reduced performance rather than accepting the risks associated with new technology in the power subsystem. Furthermore, the high reliability and longevity available from current technology sets the standards for future developments.

The environment for the adoption of new technology is unlikely to change when the penalties for failure are severe. Any technology effort must therefore respond to the conditions and requirements laid down by potential users if it is to be successful. The requirements for adoption can then become a guide to assist in directing research, development, testing, and transition to space applications. These requirements also provide data for estimating the total cost and funding profiles.

The typical energy storage portion of an electrical power system, EPS, for a space vehicle has a reliability requirement, i.e., an estimate of the probability that it will provide for the specified performance of the mission for the specified duration, greater than 0.97. After the reliabilities of necessary auxiliary hardware such as cell interconnects, connectors, thermal control features, and mounting fixtures in batteries, and, additionally, pumps, plumbing, and reactant storage in fuel cells are deducted, the reliability requirement for an individual cell unit can exceed 0.9999. Cell reliability requirements can be reduced somewhat if the cell failure mode is a short, or bypass devices protect against open circuit failure without reducing the system reliability; the EPS must also be able to accept lowered and varied delivery voltages from energy storage. Furthermore, the power system and the space vehicle designers really expect more than a specified probability of success. If failure or wear-out is to occur, the event should be predictable and non-catastrophic. Failures should be soft so that operation can continue at less than specified levels of performance after a component failure. These requirements define both the quantity and quality of the information that must be provided for any space-qualified energy storage device.

The topic of discussion below is the minimum unit development for secondary (rechargeable) battery systems and regenerative fuel cells. This comprises the cell in batteries, but might represent a cell stack in a fuel cell. While these comments also might apply to primary (not recharged) cells, the long life requirements of rechargeable or regenerable units makes development of flight acceptable items both long-term and expensive. It is assumed here that a parallel effort to design and develop the additional requirements for the "integrable" assembly, the battery or the fuel cell unit including tankage, has been performed.

DISCUSSION

The basic, non-directed research aspects of the development of an energy storage device constitute the smallest portion of the work necessary to bring the technology to fruition. Once a concept is defined and subjected to analysis, a decision to proceed with development can be based on properties that include cost, energy density, electrical characteristics, projected lifetime, development of supporting devices and materials, environmental requirements, safety, and development time. Comparison of new technology with the actual performance of current state-of-the-art cells, as opposed to performance requirements in specifications, will provide an indication of the value of proceeding with the development. Since the real article is being compared with a "projected" technology, truly significant improvements need to be projected. For instance, energy density improvements of fifty percent can rapidly become insignificant as development proceeds. Actual devices are hardly ever as good as projected for a new technology and the state-of-the-art moves forward.

Once a concept has passed muster and proceeds into the various phases of development, it is imperative that preliminary failure modes and effects analyses

(FMEA), and reliability analyses be performed. Key elements that impact reliability and longevity should be defined. This is a development tool, not an advertising tool, to demonstrate the level of progress that has been made. The objective is to develop a program to properly define and understand the weak points in the technology. Research programs can then be designed to define the problems and suggest corrective actions as well as the limits of the technology. Often those problems that have the better defined solution receive the most attention while more subtle, long term problems are shunted aside. Directed research on the technology that emphasizes the more subtle and longer term issues should be a continuing effort that extends well into the final, life testing phase of the development.

Periodic reviews of the technology to assess its current status in terms of both development and directed research are critical. One must be assured that no practically unsolvable show-stoppers are imbedded in the technology and that the real advantages of the new technology over the state-of-the-art are verified at an early stage. Updating technology comparisons is particularly important because the performance of state-of-the-art technology generally improves while the projections of performance for new technology generally decrease as development moves toward a deliverable product. A realization that the new devices will only be competitive or slightly better than the current state-of-the-art would indicate that the ultimate development will be fruitless and should be cancelled.

Development prototype units permit the validation of the design and confirmation of the FMEA. They should be subjected to straw man qualification testing and abusive environments in order to define the limits of the design(s) and the response of the technology to extrema. These units should be used as guides and not as advertising tools. The intentional or unintentional abusive testing and the need to establish a learning curve for construction and operation of the units limit the value of the operational data acquired from the first units. It is questioned whether preliminary development units should be placed in the data base to establish flight-worthiness. Similarly, poor results at this stage should not bring about cancellation of the program unless the technology is found to be fundamentally flawed. Any difficulties with these cells skews the database with early failures and slows the establishment of adequate reliability estimates. Similarly, the premature testing of any unit in a way that implies that the results are representative of the end item can be very detrimental.

The flight prototype manufacture occurs in the final stages of development and signals the production of a qualified end item. Building on the design, manufacturing, and performance experience, design changes should by now have become an evolutionary rather than a revolutionary process. Future changes should be readily correlated with the data base established with cells produced earlier. The documentation of the manufacturing and testing must be converted from development to production. This generally involves increased definition of requirements, quality monitoring, and a higher level of traceability. An end item FMEA must be generated using the data from both development and research to establish the operational constraints and inherent failure modes of the unit. A detailed performance description should be prepared that describes the performance limits of the item in terms of projected lifetime, electrical capabilities, and environmental constraints. A reliability analysis should be performed to provide assurance that the components have an adequate reliability. However, energy storage devices are limited in reliability by complex chemical and physical interactions within the device and not, typically, by individual component reliability. The reliability and long term performance must be demonstrated before it will be accepted for operational vehicles.

This is a time consuming and expensive process that requires planning and commitment at the onset of the development program.

The construction and testing of a complete integrable assembly and life testing in some form are required to demonstrate reliability and long term performance. The verification of the integrable unit, the battery or fuel cell assembly, can be by either a ground test or flight test. Environmental testing and proper simulation during life testing generally suffice to demonstrate operation in space for the individual cells. The cell unit is sealed and a space environment should not change the operation of the unit appreciably. Operation cannot depend on gravity or atmospheric pressure; this should have been demonstrated during the preliminary development and design phases. Battery or fuel cell assemblies require experience in integration into spacecraft and demonstration that the new assembly will operate compatibly with its own and other subsystems. Flight testing provides a "warm feeling" but the integration and testing activity is the most valuable portion. Typically, performance data from flight experiments are poorer in quality and limited in range than that acquired on the ground and it is certainly the more expensive to acquire. An additional problem with demonstration flight testing in the future is the trend toward increasing sizes of energy storage flight units. A flight test of a unit sized to provide 5 kW or more is impractical on most test flights and few programs will risk an entire mission on an unproven energy storage unit. The option then is to flight test a scale model, e.g. 250 to 500 W, or to perform ground tests only.

The requirements of the life testing are to provide long term performance and reliability data, to verify acceptable means of controlling charge and discharge of the units, and to demonstrate an acceptable environmental range for operation. In order to provide statistically significant data, a large number of units must be tested under conditions that adequately simulate actual use. A sufficient number should be subjected to representative qualification level environmental testing to provide assurance that no long term effect exists. The number of units that should be life tested depends on the variations in design and the range of conditions desired. The number of test units can also be traded with the duration of the test; fewer units can be tested for a longer period to demonstrate an arbitrary reliability and confidence level for a specified mission duration. A generic life test of new technology should provide a <u>data base</u> that supports reliability estimates and conditions of operation for appropriate applications. The actual reliability estimates for a specific application will also require mission-specific life testing. Thus a generic life test must have as a goal providing a sufficient data base that will result in establishing an acceptable reliability and confidence level when it is combined with all other available data.

Life testing must be performed within an assured performance envelope. New technology must demonstrate significant performance improvements over existing technology. However, testing new technology at levels near extremities of performance can result in failure of the units and severe delays in the adoption of the technology. A life test should demonstrate the superiority of the technology, but should not risk failure by overtesting. In addition to demonstrating the advantages of the new technology and establishing a data base, another important aspect of a life testing is the promotion of the technology. It should not explore performance limits.

If the technology were to be adopted for a mission at the beginning of the life testing, the probability of success should be quite high, even if relatively undefined. The life test objective is to demonstrate that the existing design(s) are

highly reliable and acceptable for routine use. The risk in acting on this presumption prior to verification is that long term performance problems will only surface later in the mission. Additionally, the management of the assembly on orbit (charge, discharge, and maintenance) may not have been adequately evaluated. These risks are greatest when the new technology is similar to the existing state-of-the-art because the tendency is to assume that the same techniques and procedures can be used on both technologies. A more subtle problem with premature use of the technology is that it will be applied at levels significantly less than its capability in order to mitigate the risk. This then creates a baseline for use that will only slowly change with time (mission experience uber alles) where the technology shows only modest apparent gains over previous technology rather than the level of performance demonstrated in life testing.

As the life testing proceeds successfully and the continuing research further defines the limits of operation and application, the technology can be applied at levels that are nearer the operational limits. Development is then complete and the technology can be used whenever it is required.

AIR FORCE ELECTROCHEMICAL POWER RESEARCH AND TECHNOLOGY PROGRAM FOR SPACE APPLICATIONS

Douglas Allen
Air Force Wright Aeronautical Laboratories
Wright Patterson Air Force Base, Ohio

An overview is presented of the existing Air Force electrochemical power, battery, and fuel cell programs for space applications. Present thrusts are described along with anticipated technology availability dates. Critical problems to be solved before system applications occur are highlighted. Areas of needed performance improvement of batteries and fuel cells presently used for flight applications are presented. Long range plans and performance goals are outlined including target dates for key demonstrations of advanced technology. Anticipated performance and current schedules for present technology programs are reviewed.

Programs that support conventional military satellite power systems and special high power applications are reviewed. Battery types include bipolar lead-acid, nickel-cadmium, silver-zinc, nickel-hydrogen, sodium-sulfur, and some candidate advanced couples. Fuel cells for pulsed and transportation power applications are discussed as are some candidate advanced regenerative concepts.

TIMELY DELIVERY OF ELECTROCHEMICAL POWER

TECHNOLOGY TO MEET THE REQUIREMENTS OF FUTURE

MILITARY SPACE SYSTEMS

Figure 1. - Program objectives.

- PERFORMANCE LIKE NON-MILITARY SYSTEMS
- AUTONOMY
- SURVIVABILITY

Figure 2. - Program requirements.

* CONVENTIONAL POWER SYSTEMS

- TRANSITION IPV Ni-H_2 TO USERS
- DEVELOP AND DEMONSTRATE FLIGHT QUALITY Na-S CELLS AND BATTERIES
- RESEARCH NEXT GENERATION BATTERY BEYOND Na-S

* SPECIAL POWER SYSTEMS

- HIGH POWER CONCEPTS

Figure 3. - Program emphasis.

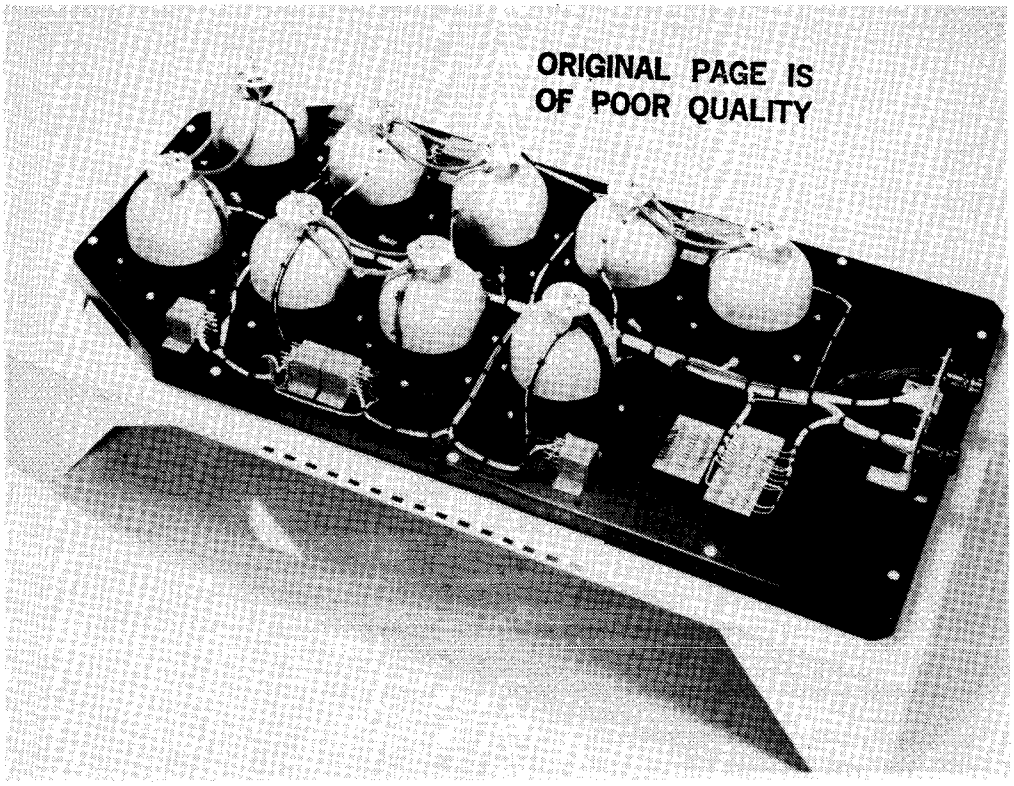

Figure 4. - Nickel-hydrogen battery cell pack.

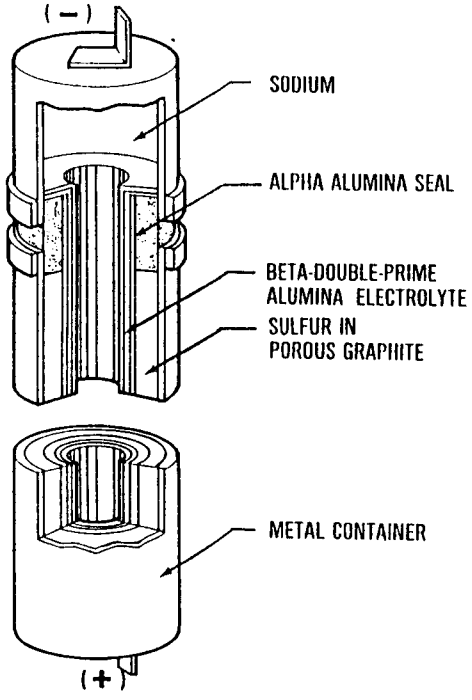

Figure 5. - Sodium-sulfur battery cell. Operating temperature, 350 to 400 °C.

- CONTINUED Ni-Cd USE
- Ni-H_2 USE INCREASING 1980's
- Na-S AVAILABLE- mid 1990's
- ADVANCED SYSTEM AVAILABLE- AFTER 2000

Figure 6. - Timetable.

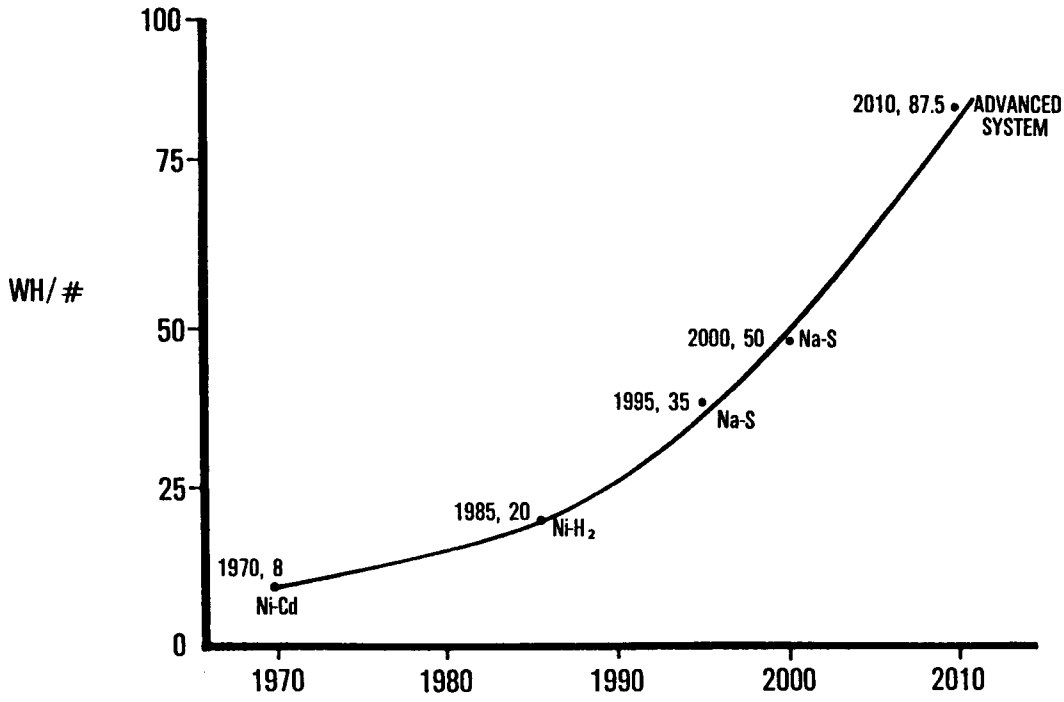

Figure 7. - Specific energy.

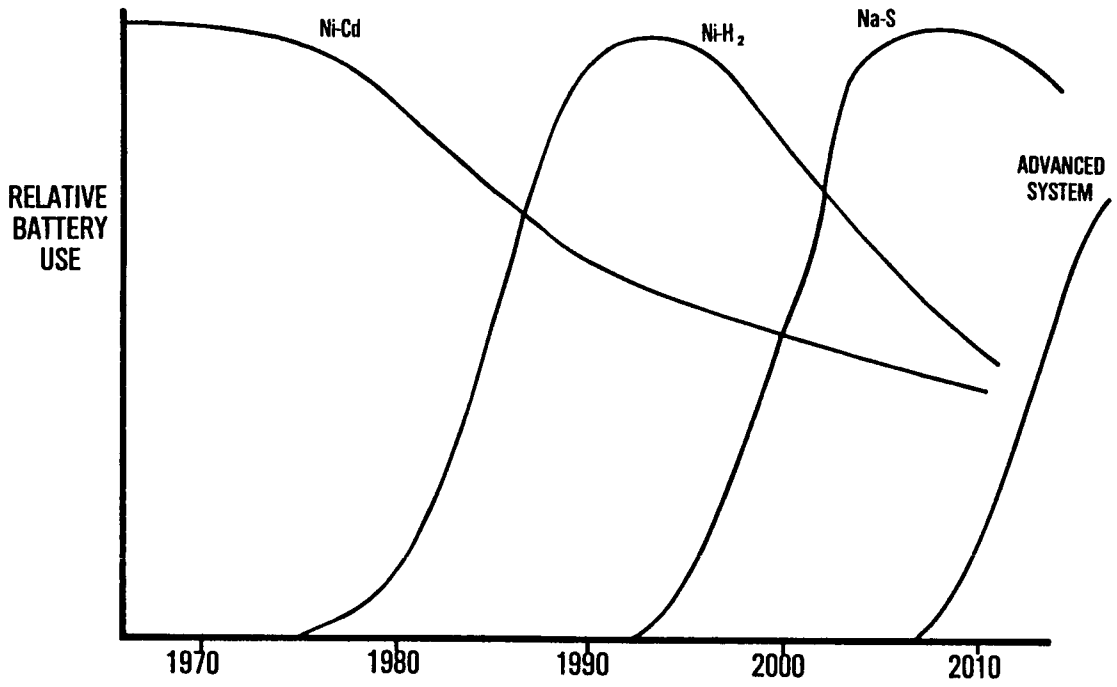

Figure 8. - Use profile.

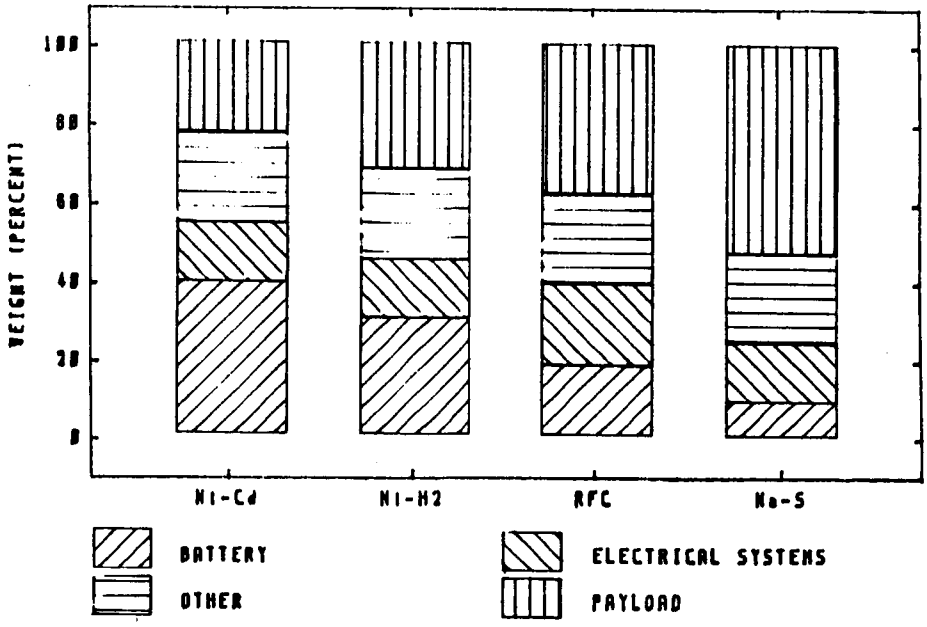

Figure 9. - Radar satellite weight summary.

100 WH/# BATTERY, USEABLE PER CYCLE

5 WH/IN ^{3}

HIGH CELL VOLTAGE, > 3.5 V/CELL

ALL ORBIT CAPABILITY

80% ENERGY EFFICIENCY, 100% COULOMBIC

STATE OF CHARGE

TIGHT VOLTAGE REGULATION

OPERATING TEMP COMPATIBLE WITH EFFECTIVE THERMAL CONTROL

15 YR CALENDAR LIFE; 6000 ONE HR DISCHG, 23 HR CHG CYCLES;
30000, 0.5 HR DISCHG, ONE HR CHG CYCLES

SURVIVABLE

EASILY MODELED, PREDICTABLE BEHAVIOR

100 THERMAL CYCLES

AFFORDABLE, $50K/KWH

NORMAL MECHANICAL AND ENVIRONMENTAL SPECS

Figure 10. - Requirements of advanced systems.

EML PROJECTILE BATTERY (KKV)

HIGH RATE LITHIUM BATTERY

HIGH POWER DENSITY FUEL CELL

BIPOLAR LEAD-ACID BATTERY

BIPOLAR SILVER-ZINC BATTERY

ALKALINE BATTERY

NATIONAL SPACE TRANSPORTATION SYSTEM FUEL CELL

SODIUM-SULFUR BATTERY

Figure 11. - SDI battery and fuel cell technology programs.

KOH CONCENTRATION EFFECT ON CYCLE LIFE OF NICKEL-HYDROGEN CELLS

H.S. Lim and S.A. Verzwyvelt
Hughes Research Laboratories
Malibu, California 90265

A cycle life test of Ni/H_2 cells containing electrolytes of various KOH concentrations and a sintered-type nickel electrode was carried out at 23°C using a 45-min accelerated low earth orbit (LEO) cycle regime at 80% depth of discharge. One of three cells containing 26% KOH has achieved over 28,000 cycles, and the other two 19,000 cycles, without a sign of failure in this accelerated cycle life test, which is still in progress. Two other cells containing 31% KOH electrolyte, which is the concentration presently used in aerospace cells, failed after 2,979 and 3,620 cycles in the same test. This result indicates that the cycle life of the present type of Ni/H_2 cells may be extended by a factor of 5 to 10 simply by lowering the KOH concentration from 31% to 26%.

Long cycle life of a Ni/H_2 battery at high depth-of-discharge operation is desired, particularly for an LEO spacecraft application. Typically, battery life of about 30,000 cycles is required for a five-year mission in an LEO. Such a cycle life with presently available cells can be assured only at a very low depth-of-discharge (below 40%) operation** (ref. 1). Previously, in an effort to develop a long life nickel electrode for Ni/H_2 cells, we studied various design parameters of the electrode. Those studies included evaluation of the effects of plaque pore size, mechanical strength, and active material loading level on the cycle life of the electrode (ref. 2 to 4). Although the variations in these parameters significantly affected the cycle life, improvement over the present aerospace standard electrodes was relatively small. In a continuing effort, we began to investigate effects of KOH concentration in the electrolyte on the cycle life (ref. 5). This paper is a progress report of this study: results already show that the cycle life of an Ni/H_2 cell is tremendously improved simply by using an electrolyte of lower KOH concentration (26%) than a state-of-the-art value of 31%.

TEST CELLS AND LIFE TEST CYCLING REGIME

The average theoretical capacity of the test cells was 7.3 Ah, as calculated from the amount of active material without correcting for

*This study is supported by NASA-Lewis Research Center (Contract NAS 3-22238; Project Manager: John Smithrick).
**Thaller, L. H. and Lim, H. S.: A Prediction Model of Depth-of-Discharge Effects on Cycle Life of a Storage Cell. Submitted for Publication in Proc. 22nd IECEC, Aug. 1987.

the amount of cobalt additive. Each cell capacity was rated at 6.24 Ah. Therefore, C rate for these cells equals 6.24 A.

The cycle life test was carried out at 23°C by continuous cycling to 80% depth-of-discharge of the rated capacity in a 45-min cycle regime. This cycle regime was a 2.74 C rate discharge for 17.5 min, and a 27.5-min charge at 1.92 C rate for 110% recharge. The life tests of cells BP1 to BP6 began ten months earlier than cells BP7 to BP10. The cycling test was interrupted periodically for capacity measurements – at approximately every 1500 cycles. The end-of-charge voltages (EOCV) and pressures (EOCP), and end-of-discharge voltages (EODV) and pressures (EODP) of each cell were measured daily (every 32 cycles). This cycling test was continued to the failure point, at which the value of the EODV dropped to 0.5 V.

Two different failure criteria, EODV values of 0.9 and 0.5 V, were used to define the cycle life of the cell. The value 0.9 V represents the utilization of only the main discharge voltage-plateau, while 0.5 V represents the utilization of the total cell capacity, including that of the second voltage-plateau, which occurred at about 0.8 V. (This second discharge voltage-plateau will be discussed later.) The KOH concentration of the electrolyte of individual test cells and the cumulative life test status of the test cells are shown in table I. Further details of the test cell design and life test conditions were reported earlier (ref. 5).

LIFE TEST RESULTS

The cumulative EODVs of the cells are plotted against the number of life cycles in figures 1 and 2. The cell with 36% KOH failed by the 0.9 V criteria after 1268 cycles, while two cells with 31% KOH cycled for 2979 and 3620 cycles. However, all three cells containing 26% KOH electrolyte (BP2, 8, and 9) are still being cycled without a sign of failure, accumulating over 19,000 and up to 28,000 cycles. (One of the four 26% KOH cells (BP3) had a mechanical defect in tab-welding on one of the hydrogen electrodes.) These results indicate that the cycle life of an Ni/H_2 cell is greatly increased as the KOH concentration is reduced in each 5% step (36% to 31% and 31% to 26%). The improvement in cycle life with the concentration change in the latter step is especially remarkable.

The cycle life change, however, appears to be complicated when the KOH concentration is further decreased below 26%: the value of the EODV of BP10 (23.5% KOH) decreased below 0.9 V after 4800 cycles. The value remained at about 0.8 V for several thousand cycles before it began to rebound after about 10,000 cycles. The BP10 cell recovered its initial EODV value after about 15,000 cycles, indicating that the capacity was increased rather than being decreased with cycling, as shown in figure 2. BP1, which contained 21% KOH, had cycled 5049 times when its EODV went below 0.9 V, and BP1 has presently accumulated over 28,000 cycles. The EODV of this cell was unstable during the test, although values became more or less stable at about 0.8 V after 20,000 cycles, as shown in figure 1. The changes

of EOCV, EOCP, and EODP of these cells were discussed previously (ref. 5).

Duplicate or triplicate interim capacity measurements of all test cells were made out after roughly every 1500 cycles by charging the cells at C rate for 80 min and then discharging them at 1.37 C rate to 1.0 V. The capacity values of the first measurements after the cycle interruptions were slightly different from (usually larger than) those of subsequent measurements, while the second and the third usually agreed with each other. The differences are probably due to the cycling history at a higher rate than that at which the capacity is measured. The values of the cell capacity from the second measurement are plotted against the cycle number in figure 3. These changes in capacity are generally consistent with the EODV changes, as expected from the nature of their interrelationship. All the cells with 26% KOH electrolyte showed consistently higher capacity than those with the lower KOH concentrations. The discharge voltage curves of these interim capacity measurements are shown in figures 4 and 5.

The main voltage-plateau capacity (to 1.0 V) of BP1 decreased with cycling, as shown in figures 3 and 4, while the second voltage-plateau capacity (about 0.8 V) increased. Total capacity, including the second voltage-plateau capacity (to 0.5 V), remained almost unchanged, as shown in figure 4. The stable low EODV of this cell over the last several thousand cycles recorded in figure 1 is due to this second plateau capacity. The main voltage-plateau capacity of BP2 remained almost constant after an initial decrease over the first several thousand cycles (figure 3), while the second voltage-plateau capacity increased steadily with cycling in a rate similar to that of BP1, as shown in figure 6. The overall capacity of this cell increased with cycling. This increase is probably caused by gradual plaque corrosion, which creates additional active material.

Another noticeable aspect of the discharge voltage curves is that the discharge voltage of the main plateau increased gradually with cycling as shown in figures 4 and 5. This voltage shift and the second plateau phenomena are not fully understood at the present time, and studies of these phenomena are planned as part of the failure analyses.

CONCLUDING REMARKS

The cycle life of an Ni/H_2 cell in the accelerated test increased greatly as the KOH concentration in the electrolyte was decreased from 36% to 26%. The cycle life improvement from using 26% KOH instead of the present aerospace standard of 31% is tremendous, as shown in figure 7. This cycle life improvement should not be discounted on the basis that the initial capacity of the cell decreases slightly with the decrease in KOH concentration, as reported earlier (ref. 5), because all the test cells in this study were rated at the same capacity value (6.24 Ah) independent of the KOH concentration used. However, the cycle life effects in further reducing KOH concentration below 26% are not clear, because of observed erratic behavior at concentrations of 23.5% and 21%.

REFERENCES

1. Levy, E.: Life Test Data and Flight Predictions for Nickel-Hydrogen Batteries. Proc. 17th IECEC, Los Angeles, CA, Aug. 1982, pp. 774-779.

2. Lim, H. S.; Verzwyvelt, S. A.; Bleser, C.; and Keener, K. M.: Long Life Nickel Electrodes for a Nickel-Hydrogen Cell: I. Initial Performance. Proc. 18th IECEC, Orlando, Florida, Aug. 1983, pp. 1543-1557.

3. Lim, H. S. and Verzwyvelt, S. A.: Long Life Nickel Electrodes for a Nickel-Hydrogen Cell: Cycle Life Test. Proc. 31st Power Sources Symposium, Electrochemical Socity, Inc. June 1984, Cherry Hill, NJ, pp. 157-170.

4. Lim, H. S., and Verzwyvelt, S. A.: Long Life Nickel Electrodes for a Nickel-Hydrogen Cell: Results of an Accelerated Test and Failure Analyses. Proc. 19th IECEC, San Francisco, CA, Aug. 1984, pp. 312-318.

5. Lim, H. S. and Verzwyvelt, S. A.: KOH Concentration Effects on the Cycle Life of Nickel-Hydrogen Cells. Proc. 20th IECEC, Miami, Florida, Aug. 1985, pp. 1.165-1.170; Proc. 21st IECEC, San Diego, CA, Aug. 1986, pp. 1601-1606.

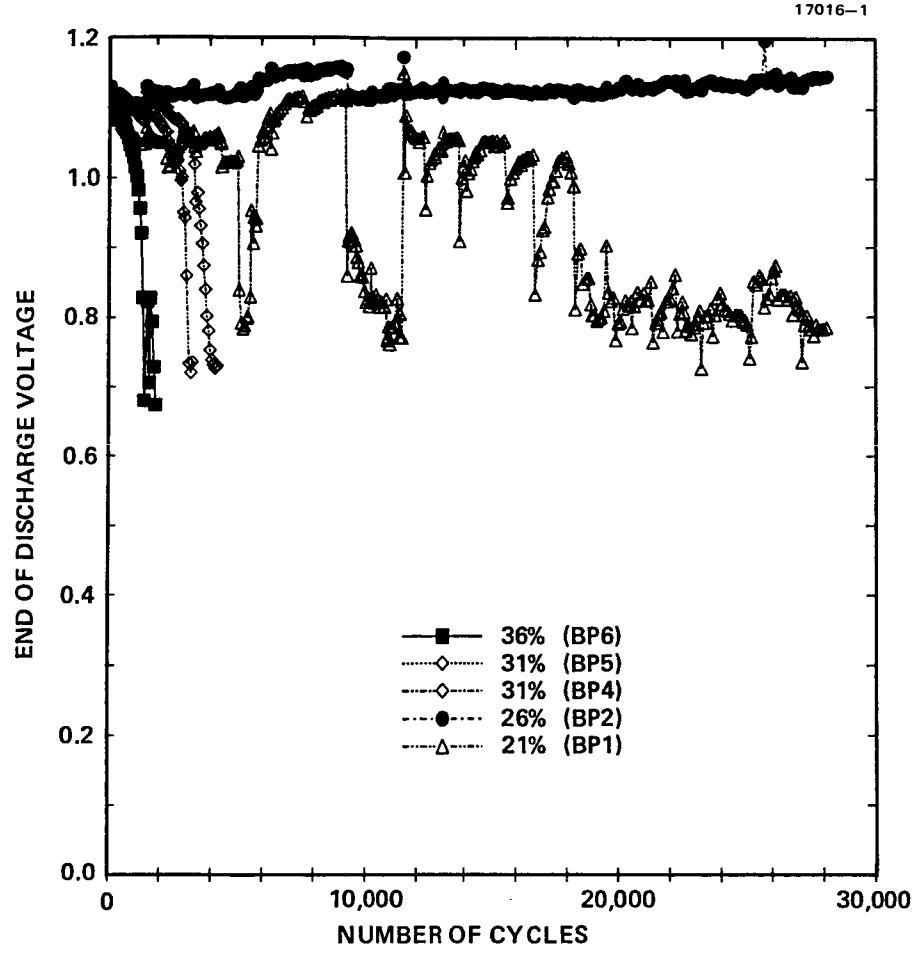

Figure 1. Plots of the EODV vs cycle number for Ni/H_2 cells (BP1 to BP6) with various KOH concentrations. All cells were cycled at 80% depth-of-discharge except for the cycles between 5785 and 9209, when the depth-of-discharge value was 74%.

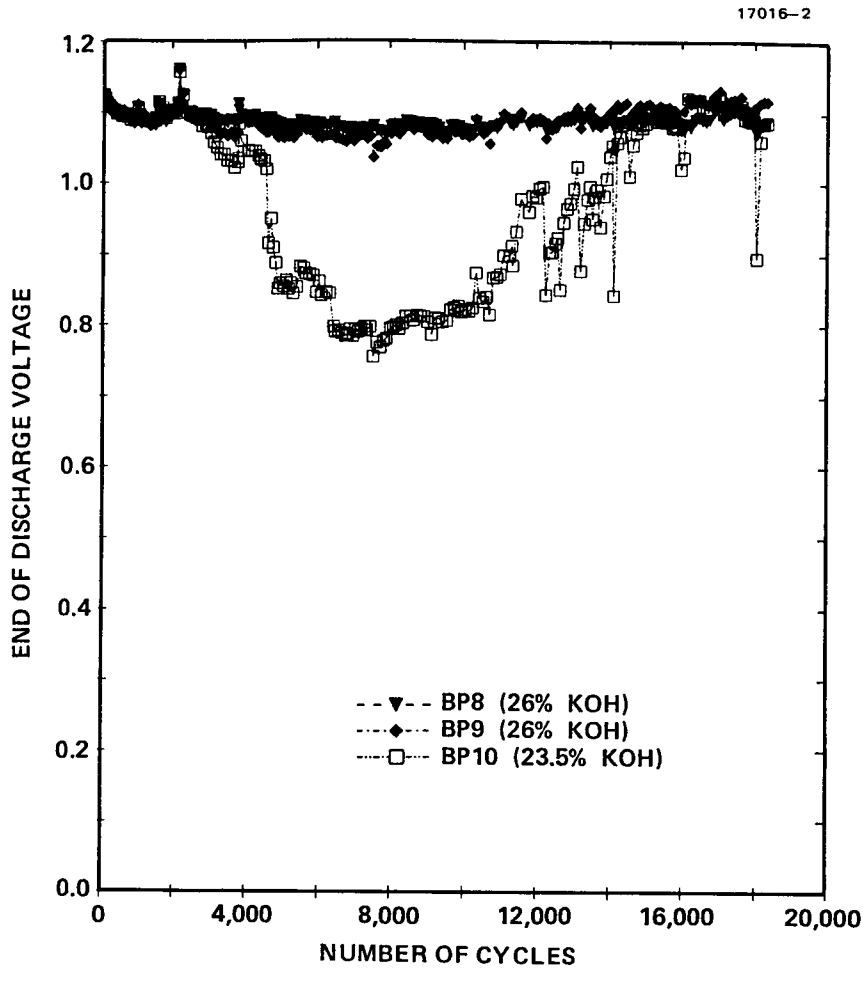

Figure 2. Plots of the EODV at 80% depth-of-discharge vs cycle number for Ni/H_2 cells (BP8 to BP10) with various KOH concentrations.

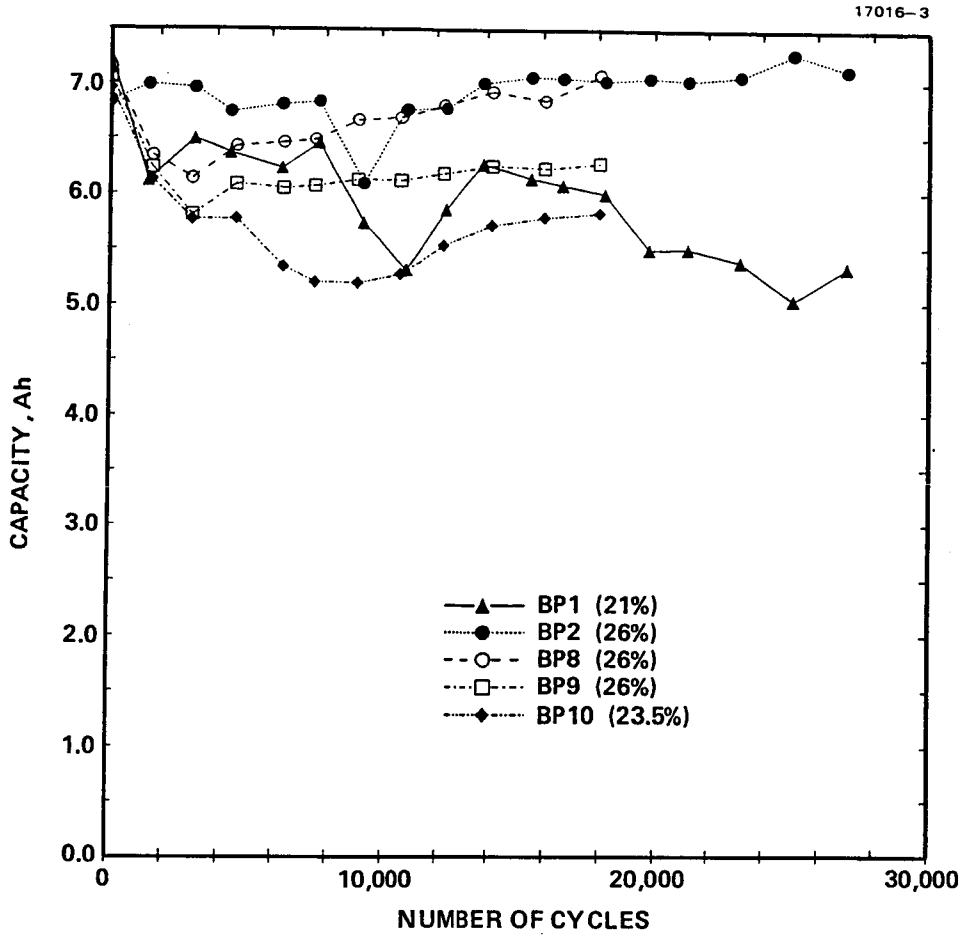

Figure 3. Plots of interim capacity values (second measurement) of Ni/H_2 cells with various KOH concentrations vs cycle number. The capacities were measured by charging the cells at C rate for 80 min and then discharging them to 1.0 V at 1.37 C rate.

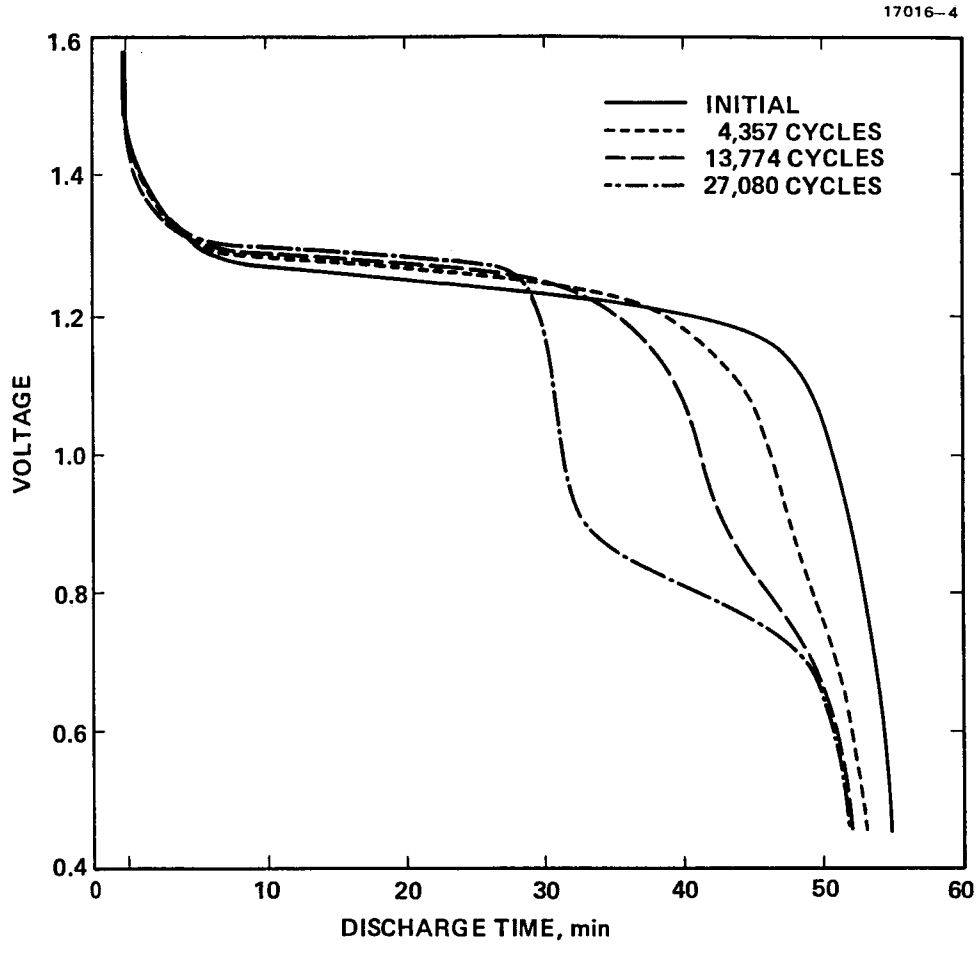

Figure 4. Discharge voltage traces of BP1 during interim capacity measurements at various life cycles.

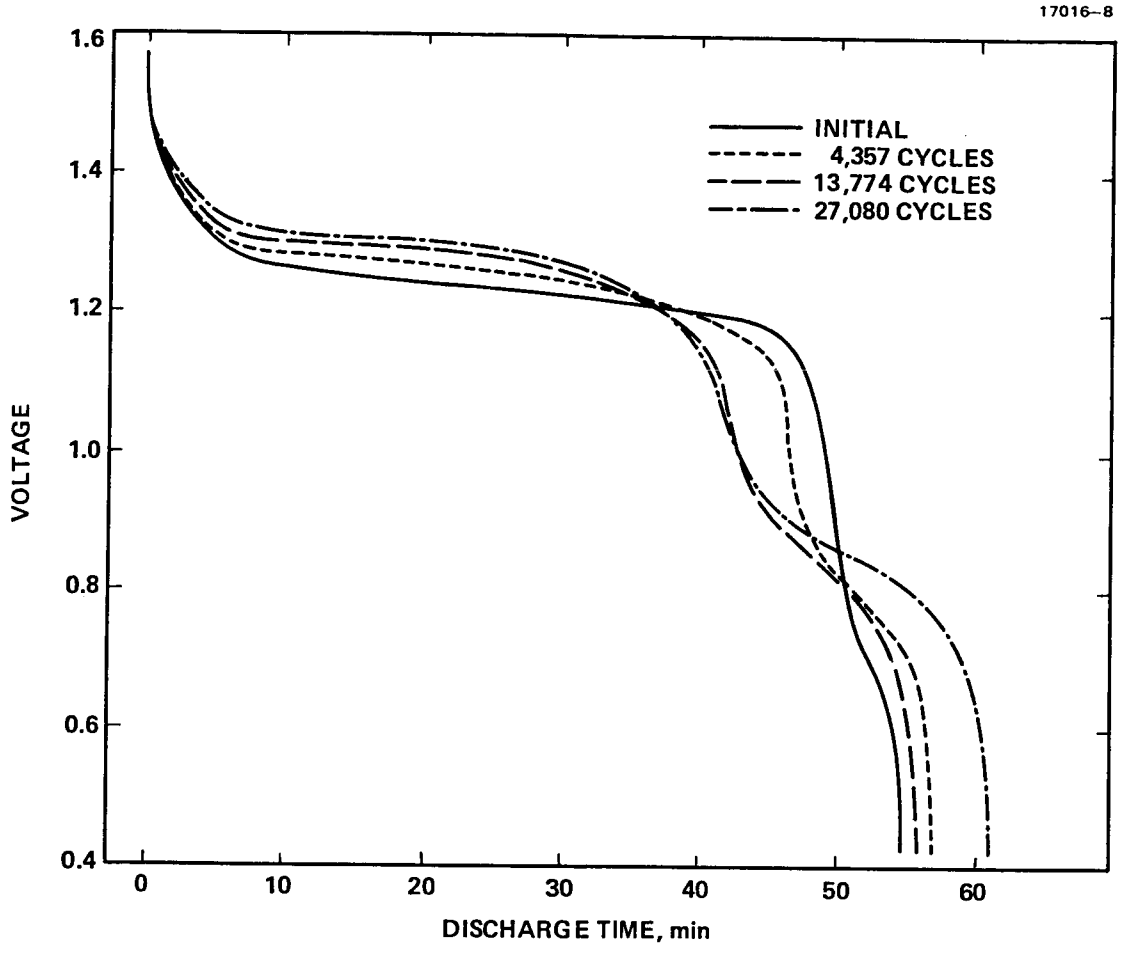

Figure 5. Discharge voltage traces of BP2 during interim capacity measurements at various life cycles.

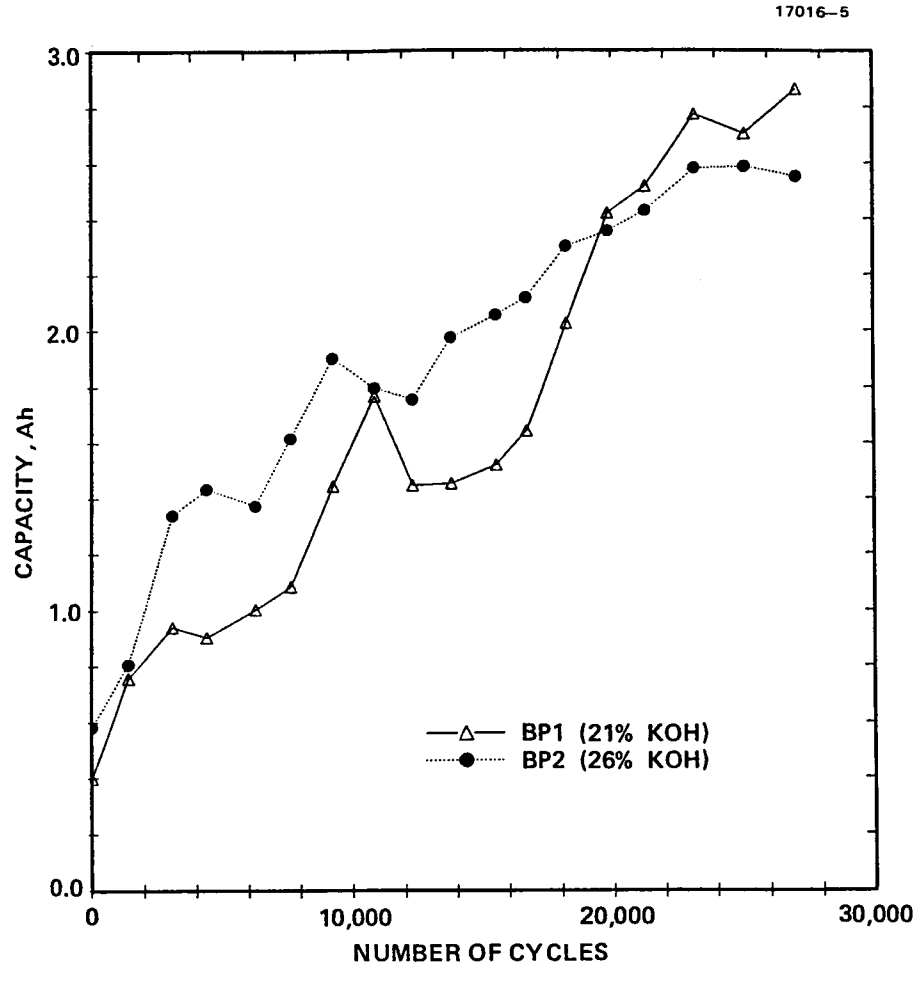

Figure 6. Plots of the second discharge voltage-plateau capacities vs cycle number. These capacities were calculated by the difference between the capacity values to 0.5 V and 1.0 V.

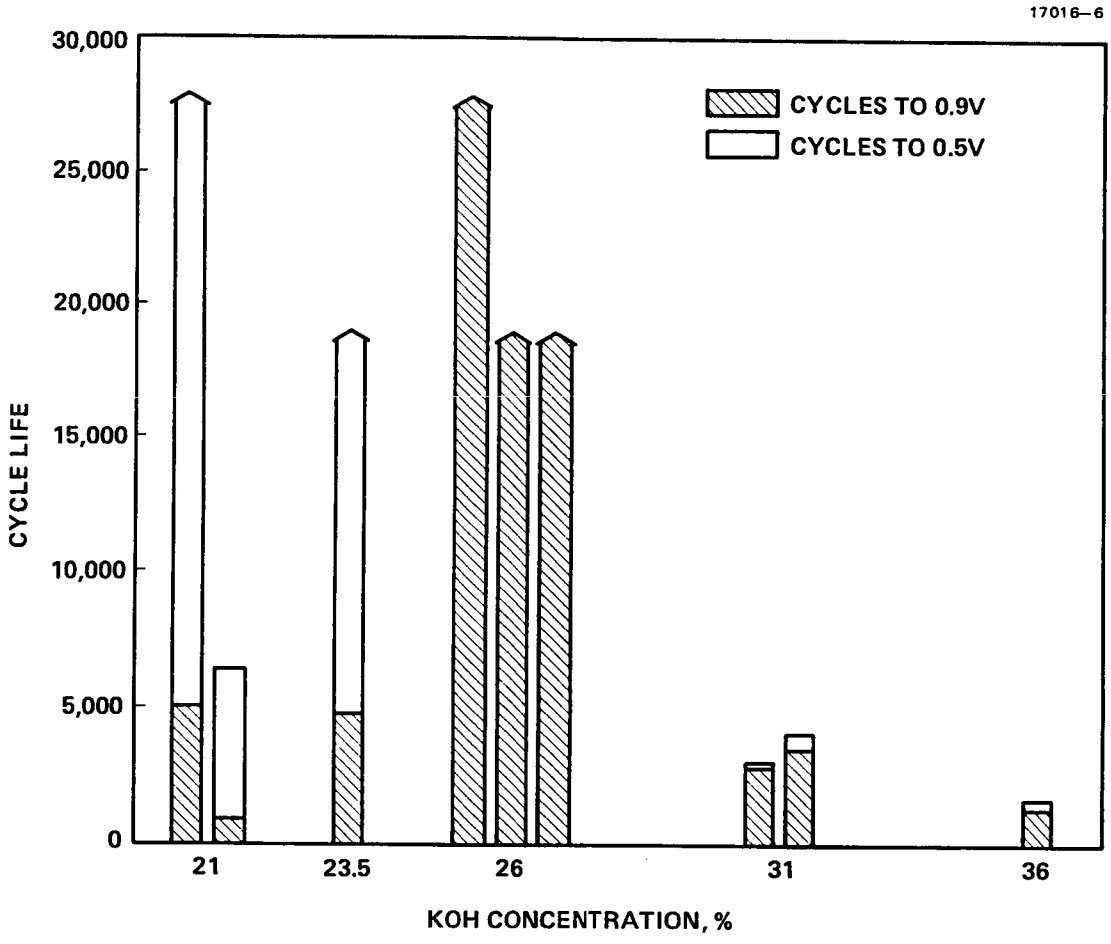

Figure 7. Comparison of cycle life of Ni/H_2 boiler plate cells containing various KOH concentrations.

LONG-TERM STORAGE OF NICKEL-HYDROGEN CELLS*

H. Vaidyanathan
COMSAT Laboratories
Clarksburg, Maryland 20871-9475

Representative samples of nickel-hydrogen cells for the INTELSAT VI program were used to evaluate the effects of prolonged storage under passive conditions such as open-circuit discharged at 0°C, room temperature, and -20°C, and under quasidynamic conditions such as top-off charge and trickle charge. Cell capacity declines when cells are stored open-circuit discharged at room temperature, and a second plateau occurs in the discharge curve. Capacity loss was 47 percent for a cell with hydrogen precharge and 24.5 percent for one with no hydrogen precharge. Capacity recovery was observed following top-off charge storage of cells which had exhibited faded capacity as a result of passive storage at room temperature. Cells stored either at -20°C or on trickle charge maintained their capacity. At 0°C storage, the capacity of all three cells under test was greater than 55 Ah (which exceeds the required minimum of 44 Ah) after 7 months.

INTRODUCTION

Long-term storage of nickel-hydrogen batteries has become an important issue since the storage requirements for the INTELSAT VI battery have been increased from 28 to 60 months as a result of launch delays. The capacity maintenance characteristics of INTELSAT VI nickel-hydrogen cells were discussed in 1986 (ref. 1). This present paper continues that work by elaborating on the capacity variations observed in these cells after extended storage under various conditions.

The nickel-hydrogen cells discussed here are of the U.S. Air Force/Hughes design, containing 40 sets of positive and negative plates, with zircar as the separator, in a recirculating stack configuration. There are two types of cells, positive- and negative-limited, which are defined based on differences in the amount of hydrogen precharge. Positive-limited cells use about 150 psi of hydrogen gas as precharge; negative-limited cells use no hydrogen precharge. A cell capacity of 44 Ah is considered sufficient to meet the load requirements of the INTELSAT VI satellites (ref. 2).

STORAGE MODE STUDY APPROACH

A storage mode investigation was begun using selected nickel-hydrogen cells. First, the initial capacity of the cells was determined at 10°C. The cells were then divided into groups and stored under a variety of conditions, as follows:

- -20°C open-circuit discharged
- 0°C open-circuit discharged
- room temperature open-circuit discharged

*This paper is based on work performed at COMSAT Laboratories under the sponsorship of the International Telecommunications Satellite Organization (INTELSAT). Views expressed are not necessarily those of INTELSAT.

- trickle charge at room temperature
- top charge

Several points must kept in mind when discussing the results of this study. Cells are oriented vertically while in storage. Cells stored at -20°C, 0°C, and room temperature are in the fully discharged state, which is achieved by power discharge at 23.5 A to 0.1 V, followed by draining through 1 Ω for 18 to 24 hours and shorting for 4 hours. Top-charge and trickle-charge cells are charged at 4.8 A for 18 hours at 10°C prior to storage. All capacity determinations are performed at a C/2 rate (23.5 A) at 10°C.

EFFECT OF ROOM TEMPERATURE STORAGE

Five cells were stored at room temperature, and their resulting capacity variation is shown in figure 1. (Cells with negative precharge are denoted by the letter N, and those with positive precharge by the letter P.) In this storage mode, the cells showed capacity loss of as much as 47 percent for a cell with hydrogen precharge and 24.5 percent for one with no hydrogen precharge. The capacity loss appears to level off after 94 days. One result of room temperature storage is the occurrence of a second plateau in the discharge curves, as depicted in figure 2. The capacity below 1 V (not all in the plateau region) increases with time in storage, as shown in figure 3. The occurrence of the second plateau is of major concern, since it is not known whether the plateau can be eliminated by any recovery procedure. The capacity of the cells after almost 1 year of storage at room temperature falls short of the amount required to fully support the spacecraft load.

STORAGE AT 0°C

Three cells were tested after storage at 0°C, and their capacity variation with storage time is shown in figure 4. Two of the cells are maintaining capacity, and the third shows only a negligible decline in capacity. There was no second plateau in the discharge profiles of these cells. After 8 months of storage at 0°C, cell capacity is above the required minimum of 44 Ah. These results appear encouraging.

TOP CHARGE AT ROOM TEMPERATURE

Four cells were used in this experiment in which the cells are recharged for 10 hours at 4.8 A every 7 days. Figure 5 shows the capacity variation of the cells for two periods of top charge. One of the cells showed capacity loss in the first period. In the second period, all the cells exhibited increased capacity. Two of the cells showed remarkable recovery, from capacities in the 30's at the beginning to high 50's at the end of the second period.

Figure 6 gives EMF profiles of the four cells, which are of particular interest in regard to the second plateau. Two of the cells show a capacity of about 8 Ah below 1 V, which is much less than for cells stored at room temperature. In addition, the capacity that was in the second plateau at the beginning of the top-charge experiment has moved to the major plateau, as illustrated by the two profiles for cell 8-1127P.

TRICKLE CHARGE

The trickle-charge storage mode closely resembles that of the battery in orbit during non-eclipse periods. Three cells were used in this experiment. One, which had a lower capacity, was trickle charged at 0.65 A for 64 days at 10°C. The cell gained 5 Ah, as shown in figure 7. This cell, along with the other two, was then trickle charged at the same rate but at room temperature. After 184 days, capacity determination revealed almost the same capacity as at the beginning, with negligible capacity below 1 V. These results show that capacity recovery initially occurs when a faded cell is trickle charged, and capacity is maintained thereafter.

-20°C STORAGE

A group of four cells, three with hydrogen precharge and one without, were stored at -20°C and their capacity was determined at intervals. Table 1 presents the resulting capacity variations. Two of the cells gained capacity and the other two maintained capacity. Thus, passive storage at -20°C appears to be an excellent storage method. However, some misgivings exist regarding the stability of the seal at this temperature, although no cell leakage was observed in the four cells tested.

CELL PRESSURE

Pressure variation was monitored for the cells, which were instrumented with strain gauges. Table 2 illustrates the end-of-charge and end-of-discharge (to 1 V) pressure of the cells. As expected, cells with hydrogen precharge show higher pressures than those with positive precharge. The end-of-discharge pressure is abnormally high for the cell stored at room temperature, which indicates that some positive active material is not dischargeable at the C/2 rate.

The pressure of the cell stored in the top-charge mode is higher than expected for a positive precharge cell. The end-of-charge pressure for this cell increased from 740 psi at the beginning of the experiment to 781 psi at the end of the first period and 824 psi at the end of the second period. The increase in end-of-charge pressure corresponded with the increase in capacity. It is unclear whether the present selection of 10 hours at C/10 is appropriate in view of this pressure increase. Additional experiments which use less than 10 hours of recharge are needed. Nevertheless, recharge every 7 days appears to be a successful and practical method for recovering and maintaining cell capacity.

CONCLUSIONS

INTELSAT VI nickel-hydrogen cells exhibit capacity fading when stored passively at room temperature for extended periods. This loss in capacity is accompanied by a gradual growth in capacity in the second plateau. In contrast, capacity is maintained when cells are stored at -20°C and at 0°C in the open-circuit discharged condition.

Top-charge and trickle-charge storage modes also maintain cell capacity. Preliminary results have shown a capacity recovery in the top-charge mode. The second plateau is absent in cells stored in the trickle-charge mode at room temperature. The common denominator in the top-charge and trickle-charge storage modes is the overcharge, which is perpetuated continuously in one procedure and at regular intervals in the other.

REFERENCES

1. Vaidyanathan, H., and Dunlop, J. D., "Capacity Maintenance for INTELSAT VI Nickel-Hydrogen Cells," 22nd Intersociety Energy Conversion Engineering Conference, American Chemical Society, Washington, D.C., 1986, Proc., Vol. 3, pp. 1560-1564.

2. Wong, D. W., Herrin, J., and Stadnick, S. J., " INTELSAT VI Nickel-Hydrogen Battery," 22nd Intersociety Energy Conversion Engineering Conference, American Chemical Society, Washington, D.C., 1986, Proc., Vol. 3, pp. 1541-1546.

Table 1. Capacity Variation at -20°C

Cell No.	Precharge	Initial Capacity (to 1 V) (Ah)	Storage Period (days)	Final Capacity (to 1 V) (Ah)
4-1104N	H_2	63.6	270	66.0
5-1116N	H_2	60.7	270	67.2
13-1382P	None	66.7	112	66.3
1-1081N	H_2	59.9	112	60.3

Table 2. Cell Pressure Variation

Cell No.	Precharge	Storage Mode	End-of-Charge Pressure (psi)	End-of-Discharge Pressure (to 1 V) (psi)	Cell Capacity (Ah)
15-1110P	Positive	Trickle charge	742	125	61.9
8-1127P	Positive	Top-off charge	824	264	54.5
4-1104N	H_2	0°C	847	219	59.5
3-1033N	H_2	Room temperature	766	432	31.0

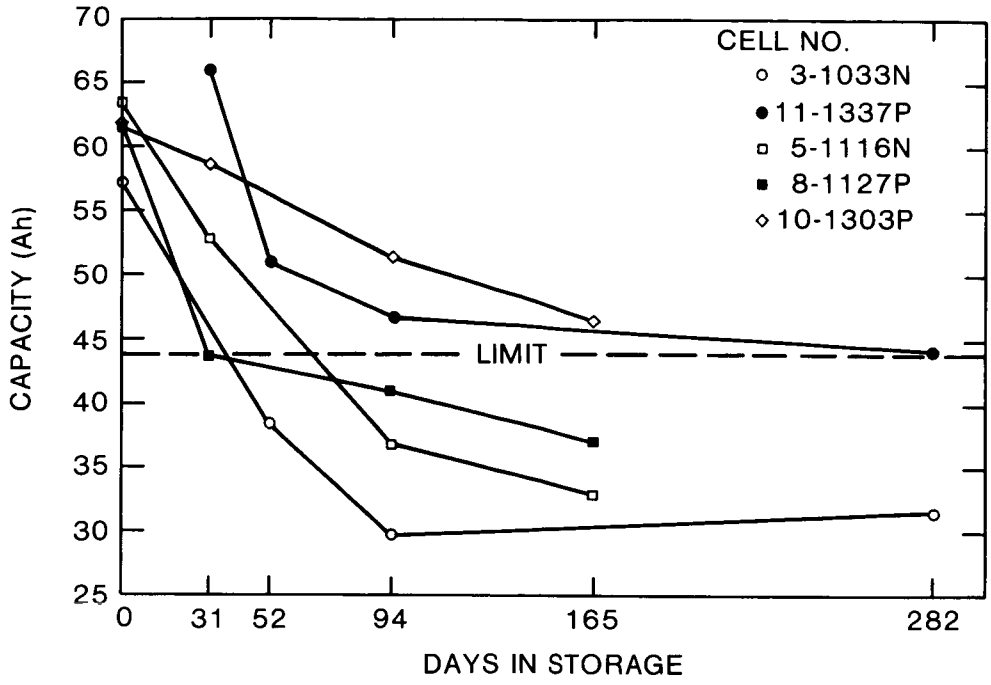

Figure 1. Capacity (to 1 V) Variation for Cells Stored at Room Temperature

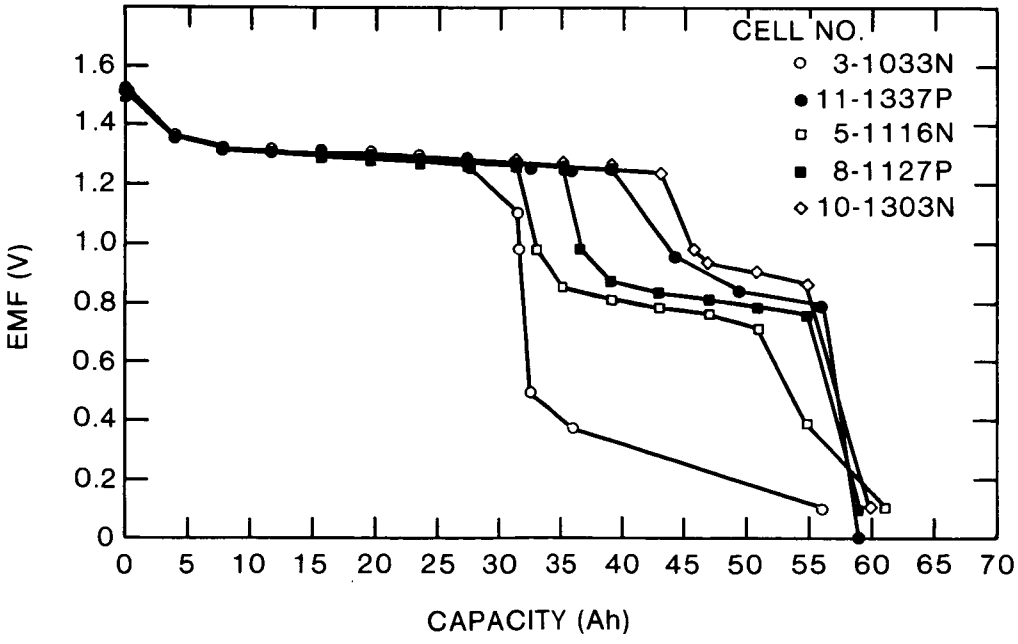

Figure 2. EMF Profile of Cells Stored at Room Temperature at 23.5-A Discharge Rate

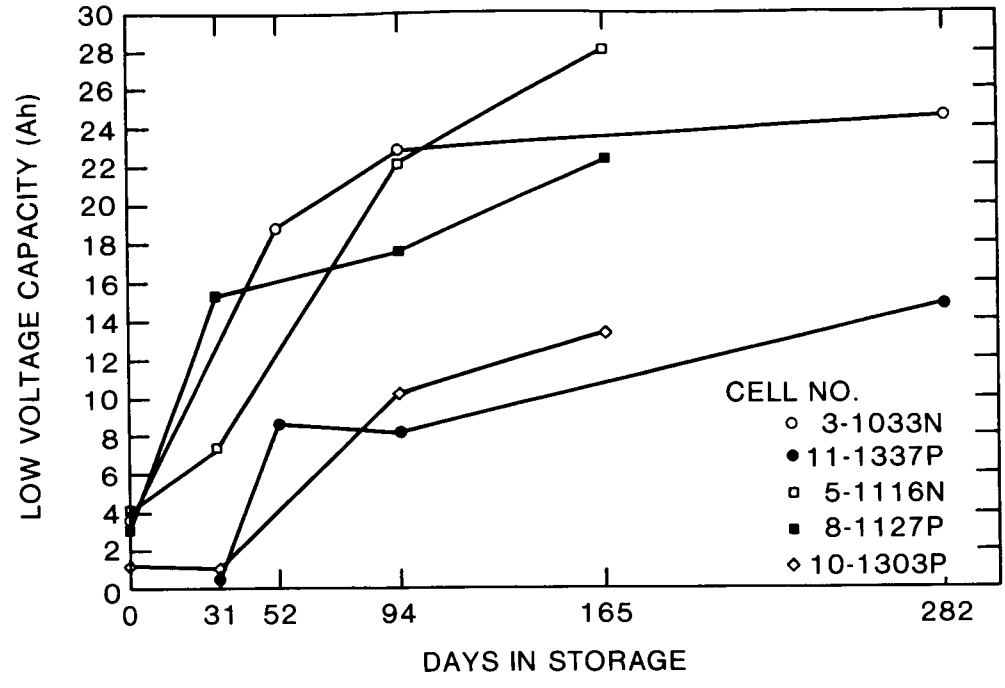

Figure 3. Variation of Additional Capacity at Low Voltages With Storage Time at Room Temperature

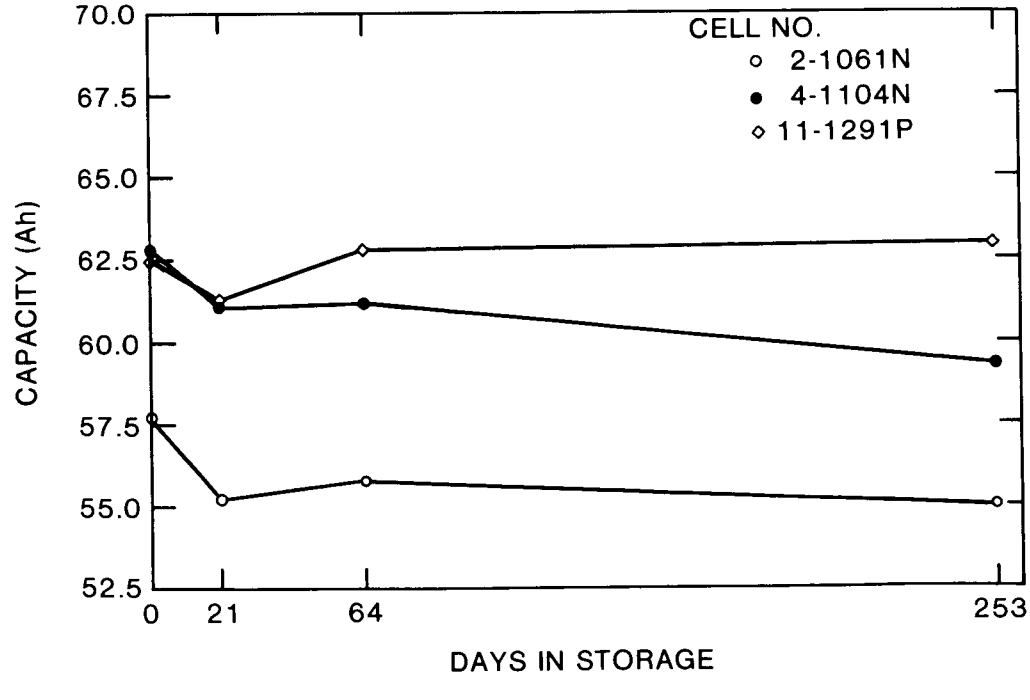

Figure 4. Capacity (to 1 V) Maintenance for Cells Stored at 0°C

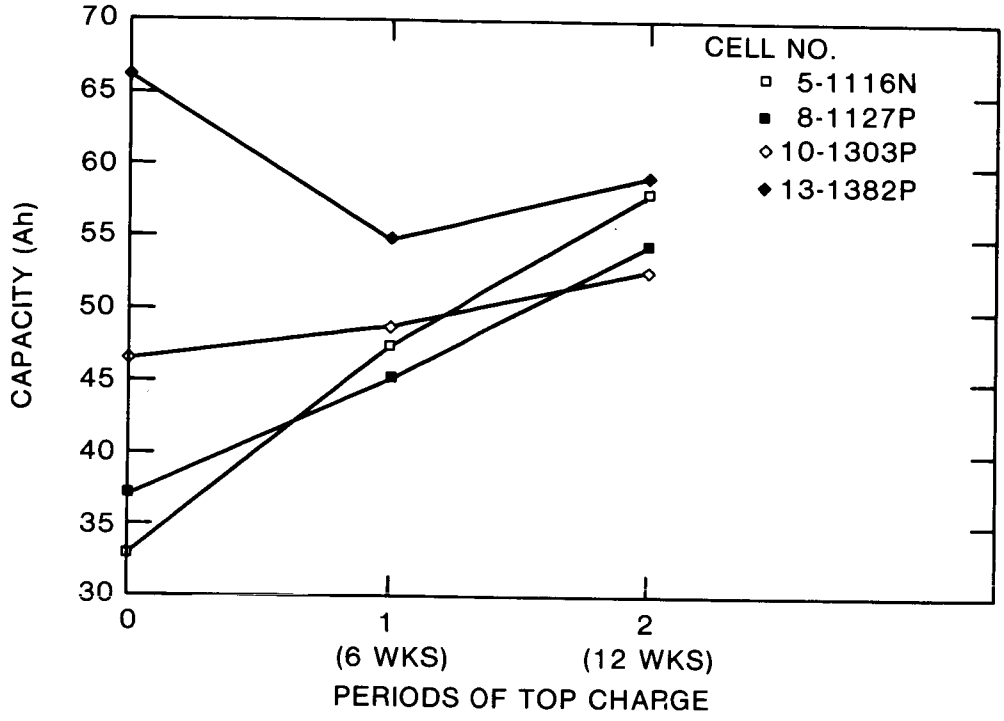

Figure 5. Capacity (to 1 V) Variation in the Top-Off Charge Storage Mode

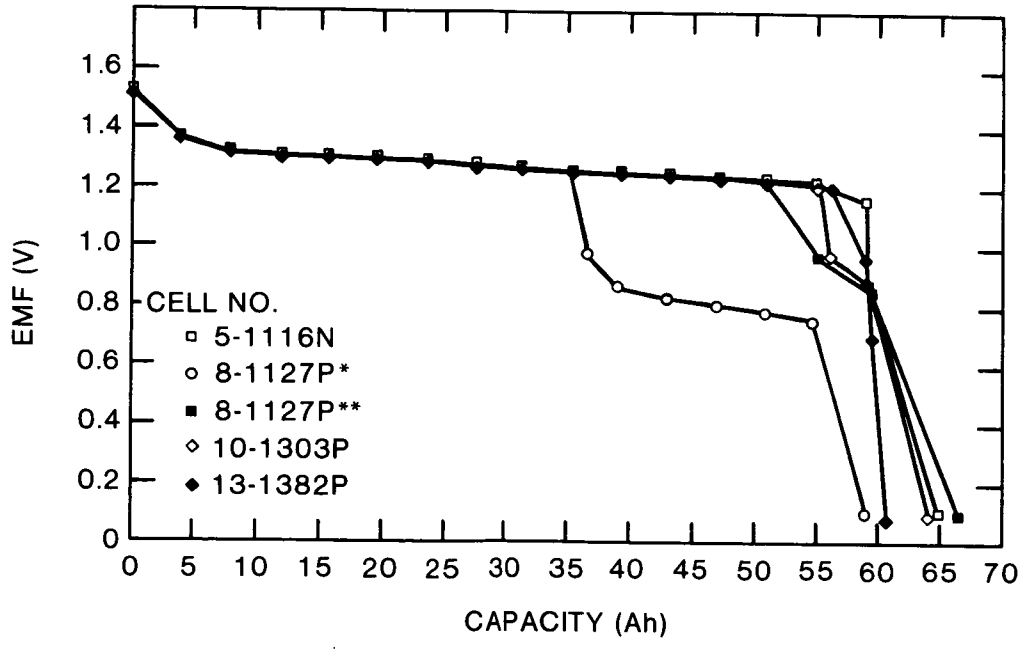

*BEFORE TOP CHARGE
**AFTER TOP CHARGE

Figure 6. EMF Profile of Cells at 23.5-A Discharge Rate After Two 6-Week Periods of Top-Off Charge

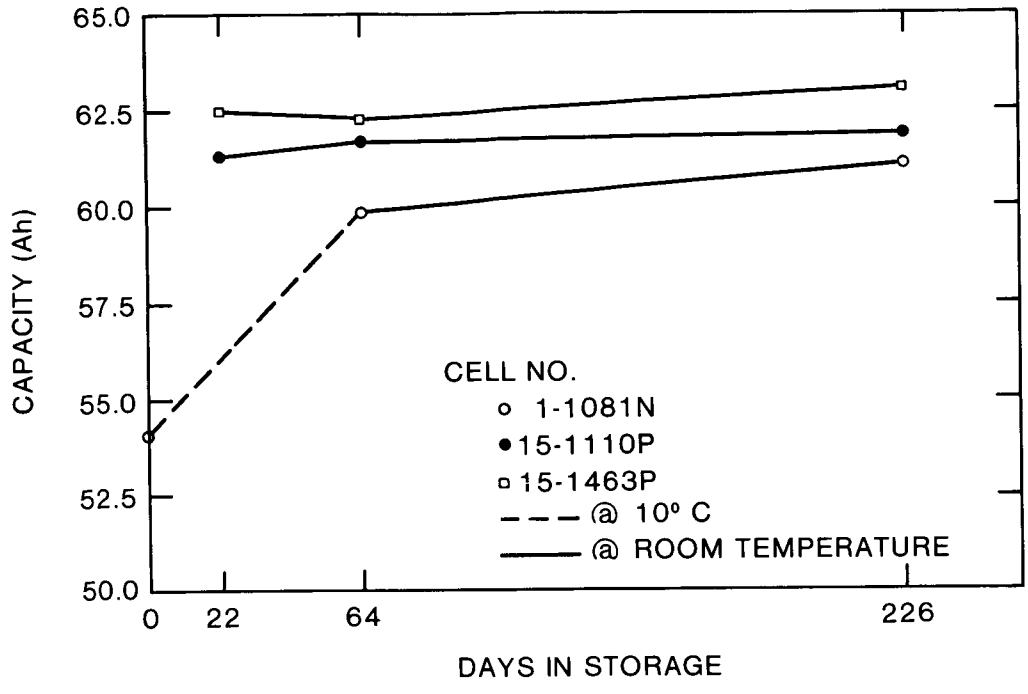

Figure 7. Variation of Capacity (to 1 V) for Cells in the Trickle-Charge Storage Mode

COST REDUCTIONS IN NICKEL-HYDROGEN BATTERY

Richard L. Beauchamp and Jack F. Sindorf
Johnson Controls, Inc.
Milwaukee, Wisconsin 53201

For the past several years, Johnson Controls, Inc. has been working with COMSAT Laboratories and Sandia National Laboratories on the development of the nickel hydrogen battery for terrestrial applications. We feel that some of the results are sufficiently interesting that consideration of them for aerospace applications is warranted.

The major emphasis of the program was on reduction of the manufacturing cost of the aerospace cell. The intent of the developmental effort was to re-design and re-develop the battery for terrestrial applications where first-cost and life-cycle were important considerations but with only minimal changes in the performance characteristics.

The approach was to adapt JCI's experience in the high-volume production of lead acid automotive batteries to the manufacture of the nickel hydrogen battery. The battery would consist of a number of individual, prismatic cells in a common pressure vessel. The prismatic cells prepared in this developmental effort consisted of a multiple of cell-modules in a back-to-back configuration and were housed in monolithic polypropylene cases. JCI battery manufacturing experience was drawn on to make the batteries and experimental cells.

A significant reduction in cost was achieved through several technical developments, compound changes, and process improvements. Two technical developments led to the majority of the reduction. The first was the development of an energy-efficient 70-mil thick positive electrode. The second was a negative electrode utilizing a platinum-on-carbon catalyst. The thicker positive electrodes permitted a one-third reduction in the number of cell components usually used. A second benefit of the thicker positives was a 45% increase in the cell's ampere-hour capacity. The cost of the platinum-on-carbon catalyst is only 10% of the platinum-black used with aerospace cells. No significant degradation in the performance of the batteries resulted from the use of this catalyst although it was necessary to develop an incoming electrochemical inspection procedure to qualify the catalyst.

As an integral part of the program, the details of the manufacturing costs were carefully studied. One purpose was to highlight those raw material and assembly costs which were most responsible for the high cost of the battery and to provide guidance as to the areas where further development effort would, as above, have the greatest impact. Another purpose of the cost-study was to determine if the ambitious programmatic cost goal of $375 per kilowatt-hour could be met. The study showed that even at the low production rate of a pilot plant (approximately one Megawatt-hour of batteries per year), the selling price of the re-developed nickel hydrogen battery would be only $1,451 per kilowatt-hour. The study also pointed out several areas for further research and

development which if successful, when coupled with a higher but reasonable production rate, would make the goal achievable.

INTRODUCTION

The use of nickel hydrogen cells and batteries for storage of photovoltaic energy in aerospace applications was pioneered by COMSAT Laboratories (ref. 1). It is recognized that this battery system has many attributes that make it very useful for similar terrestrial applications. It's clean, with an absence of noxious fumes; it requires practically no maintenance; it has excellent energy efficiency; it has a long calendar life and a long cycle life; and it's highly reliable. Furthermore, the state-of-charge is readily determined as it is directly proportional to the pressure. Unfortunately, the batteries used in aerospace applications have one characteristic that make them unsuitable for terrestrial applications: a very high first cost (ref. 2).

Johnson Controls has been working with COMSAT Laboratories on a program for the Department of Energy under the sponsorship of Sandia National Laboratories for the "Design and Development of 100 AH Hydrogen/Nickel Oxide Batteries". The objective was the development of a nickel hydrogen battery which would be cost competitive with other technologies, including lead acid, for use in terrestrial applications such as the storage of electric power from autonomous photovoltaic installations. The program involves design, development, assembly and testing of cells and batteries, and the preparation of a comprehensive COST-STUDY.

The configuration of the cells and batteries developed for terrestrial applications in this program was a departure from that used in aerospace. The terrestrial cells are prismatic, and the batteries contain a multiple of these cells in a common pressure vessel (see figure 1). High volume manufacturing practices, several of which are identical to those used in the assembly of automotive lead acid batteries, were used to produce the nickel hydrogen cells and batteries. The Battery Division's engineering pilot shop, located near JCI's corporate headquarters in Milwaukee, is equipped with a line of automatic equipment for the assembly of experimental lead acid batteries. This equipment was used in the assembly of nickel hydrogen batteries for processes such as completing the inter-cell connections by resistance welding and for heat-sealing the covers on the battery cases. A flow chart of the processes employed to produce a terrestrial nickel hydrogen battery is shown in figure 2. The similarity between the assembly processes of this battery and lead acid batteries can be seen, and one of the effects of this similarity is a lowering of costs (ref. 3).

The modular building block of JCI's prismatic cell is the cell-module, displayed in figure 3. A cell-module consists of two electrode pairs and separators, bound together by the diffusion screens. Figure 4 shows the arrangement of the components. The positive electrodes are located in the center of the cell-module and are back-to-back. Cell stacking consists of merely bringing the appropriate number of cell-modules together so as to completely fill the cell case. The ease of stacking cells in this manner contributed to the cost reduction achieved. Cells containing from seven through eleven cell-modules have been tested. The theoretical capacities for these cells ranged from 100 AH to 190 AH in cell cases either 3.8 or 5.1 cms thick.

The cell cases are portions of lead acid battery cases and are shown in figure 5.

Testing of experimental cells in boiler plate pressure vessels was done using automatic cell cyclers and a computerized data acquisition system.

Several batteries were assembled and tested during this project. They consisted of either a multiple of individual cells, or a 6-cell monoblock, in common pressure vessels. The cost of the very first battery, assembled by hand in the lab for this project, was determined to be $5900/kWh. It was also determined from this costing exercise which areas warranted additional research and development to further reduce the cost. The $5900/kWh cost, although too high for terrestrial applications, was much less than the cost for an aerospace battery. It is realized that this lower cost was due in part to the overall requirements for preparing a terrestrial battery being less stringent than for preparing an aerospace system. A major factor in bringing the cost down to $5900/kwh was the use of a 10% platinum-on-carbon catalyst in the negative electrode (in place of the pure platinum black used in aerospace cells). Still, the study indicated that the catalyst remained a relatively high-cost item.

Areas, other than the catalyst, seen as significant contributors to the $5900/kWh price were the:

a) positive electrode
b) negative substrate
c) diffusion screen
d) battery container/hardware.
e) KOH usage.

Reducing the costs of the items other than the positive electrodes was fairly straightforward. But a substantial developmental effort was required to effect a cost reduction in the area of the positive. This effort resulted in a 70-mil thick electrode. Going from 32-mil thick electrodes to 70-mil thick electrodes allowed the use of one-third fewer electrodes, separators, and screens. In addition, a 45% increase in AH capacity is now available from the same size cell stack. The "fewer-components" and "capacity-increase" were a two-fold cost-reduction effect by the change of a single component.

POSITIVE ELECTRODE DEVELOPMENT

The quality of the slurry type nickel plaque had been optimized during the developmental effort on the Zn/NiO battery at JCI to the point where it was difficult to distinguish between the JCI slurry plaque and dry powder plaque, including by microscopic examinations. This effort was concentrated on 32-mil thick plaque material. Table 1 reveals minimal differences in physical characteristics between 32-mil slurry and dry-powder plaque. As was mentioned above, the battery costing exercise indicated the need for a thicker electrode; 70-mils was selected as the thickness to develop in order to optimally fill out the cell case.

The problems of sagging slurry, inherent in the thicker applications required for the 70-mil nickel plaque, were overcome through innovative process control. Plaque material, with very a uniform distribution of nickel throughout the thickness, was developed. The good physical characteristics of the 32-mil plaque material were retained; observe also in table 1 that there is very little difference in the physical characteristics between the 70-mil and the 32-mil slurry plaque.

Electrochemical impregnation of the 32-mil plaque had been developed during the Zn/NiO effort. But the impregnation of the 70-mil plaque material required additional developmental effort. The initial thick electrodes did not meet performance expectations, neither in flooded cell tests, nor in actual nickel hydrogen cells. Backscattered electron (BSE) image analysis showed the active material to be concentrated midway between the plane of the grid wires and the electrode surface (ref. 4). Being concentrated, the active material could not be properly utilized, and lower cell voltage and lower AH capacity resulted. An intensive study was undertaken to evaluate the impregnation process. The goals of the developmental effort were to move the zone of precipitation of the nickel hydroxide uniformly throughout the plaque thickness during impregnation, and to shorten the time of impregnation in order to minimize corrosion of the nickel sinter in the hot nickel nitrate solution. The current-time relationships were adjusted to accomplish these objectives. The effort resulted in a much improved distribution of active material with a correspondingly improved utilization. The AH capacity of cells with the new 70-mil electrodes increased by 33%. A comparison of the discharge performances of cells with 32-mil and 70-mil thick electrodes is shown in figure 6. It should be noted that the same size cell stacks were used for both tests.

NEGATIVE ELECTRODE DEVELOPMENT

The goal of this developmental effort was to use the least quantity of platinum while still retaining acceptable levels of cell performance.

A commercially available catalyst (10% platinum-on carbon) was evaluated in polarization tests and in actual H2/NiO test cells as an alternative to pure platinum black. This catalyst (about 1/10th the cost of the fuel cell grade platinum) was incorporated in a multi-layer composite electrode developed by COMSAT Laboratories. The electrode was made by first roll-compacting Teflon together with the electro-catalyst powder to form one of the layers. This layer was then laminated to one side of a current collecting grid member, with a porous Teflon layer laminated to the other side. Pressing, sintering, and cutting to size completed the fabrication process. Two full-size cells were tested to compare the in-cell performances of the 10% Pt/carbon with the pure Pt catalyst. The discharge capacities of both cells to 1.0 volt were about 103 AH with the mid-discharge voltages of both about 1.25 volts. The discharge capacities are displayed in figure 7. This test demonstrated that, at the discharge rates normally used in terrestrial photovoltaic applications, there is no discernible difference in the performances of electrodes with the 10% Pt/carbon (at .45 mg Pt/cm2) and the pure Pt (at 8 mg Pt/cm2) catalysts. Additional tests were conducted to determine the acceptability of further reducing the platinum loading. The performances of catalysts prepared with 5% and 2% platinum-on-carbon were compared to the 10% Pt/carbon catalyst. The overvoltage of an electrode with 5% Pt/carbon catalyst (at .24 mg Pt/cm2) is very close to that of an electrode with the 10% catalyst at a current density normally used in photovoltaic applications, whereas the overvoltage of the electrode with the 2% catalyst (at .16 mg Pt/cm2) is about 100 mv higher (see figure 8). The processing expense of the 5% and 2% catalysts is a larger component of the total cost and thus there is not a proportionate cost reduction from the 10% catalyst (ref. 5).

Studies were therefore conducted on reducing the quantity of 10% Pt/carbon catalyst used per electrode. The cost reduction this way would be directly

related to the platinum removed. Electrodes were prepared with 0.8, 0.6, 0.4, 0.2, and 0.1 mg Pt/cm2 by using appropriate quantities of the 10% Pt/carbon catalyst. In these tests, the average polarization resistances were determined for electrodes before and after sintering. It can be concluded from the data in figure 9, that electrodes containing even less than 0.2 mg Pt/cm2 (sintered) give acceptable performance. Life-cycle tests are currently underway to determine whether stable performance can also be obtained using these very low loadings of platinum.

COST STUDY

Studies were performed to determine the cost of manufacturing a 15 kWh H2/NiO battery in order to : 1) provide bench marks from which more detailed and more realistic cost estimates could be determined, 2) identify the best areas for further cost reduction efforts, and 3) determine if the ultimate cost goal of under $500 per kilowatt-hour was obtainable. A 15kWh battery was selected because a battery of this size was being considered as a deliverable to Sandia. An initial study was made in 1984/1985 with a refined cost study prepared in 1986.

Some of the features to be incorporated in the battery and which were included in the refined cost study were:

a) 70-mil positive electrodes
b) Improved formation process for positive electrodes
c) 10% platinum-on-carbon catalyst
d) Electroformed negative grids
e) Elimination of the porous Teflon film on the negative electrodes
f) Polypropylene fabric diffusion screens
g) Low cost intercell connectors and battery terminals.

The impact of both the 70-mil positive electrodes and the 10% Pt/carbon catalyst have been discussed. But just to give an idea of the impact of some of the others:

a) using an electroformed negative grid instead of a special expanded metal grid reduced the cost by $405/kWh.
b) $43/kWh was saved by using a polypropylene diffusion screen instead of woven screen.
c) eliminating the porous Teflon film saved about $92/kWh.

The labor aspect of the cost was considered. Streamlined processes were devised to reduce the labor content to levels normally found in the assembly of lead acid batteries.

Three production levels were studied because production levels have a major impact on the final battery cost. The levels selected coincided with bottleneck manufacturing processes. The nickel plaque sintering furnace, operated one shift per day, would limit production to 72 15kWh batteries per year. If the sintering operation were up-graded, the limiting operation would then be the preparation of the negative electrodes, and 270 battery systems could be produced per year. Investing capital to speed up the preparation of negative electrodes would shift the limiting operation to making the inter-cell connection, and 1024 battery systems could be produced per year. The battery costs at the various production levels are shown in figure 10. The 1984 costs are based on the configuration of the cells and batteries as of July 1984. The

1986 costs reflect continued R&D effort through the first third of 1986 resulting in a price below the $1000/kWh level.

Because the battery we have been developing will be competing with other terrestrial battery systems, the results of the cost study have been used to generate a cost comparison. From the cost comparisons made in table 2, it is clear that the nickel hydrogen battery is economically competitive with these other systems on a cents/kwh-cycle basis.

ADDITIONAL EFFORTS

Efforts are continuing to develop the nickel hydrogen battery into a marketable product. Under sponsorship of Sandia National Laboratories, a 7 kWh battery is to be assembled and delivered to Sandia for testing in a photovoltaic application. There are corporate plans are to assemble similarly sized and larger batteries for testing in the Load Management Facility at Johnson Controls. Cost reduction efforts will continue. Additional cost reductions are anticipated through the use of 90-mil (and thicker) positive electrodes, currently under development. Catalysts, less expensive than platinum-on-carbon, are being evaluated and may prove acceptable. The development of a "production" pressure vessel is underway.

SUMMARY AND CONCLUSIONS

Significant progress has been made toward the development of a commercially marketable nickel hydrogen battery. The costs projected for this battery are remarkably low when one considers where we are on the learning curve for commercialization of this system. Further developmental efforts on this project are warranted as the nickel hydrogen battery is already cost competitive with other battery systems.

REFERENCES

(1) National Materials Advisory Board, Assessment of Research Needs for Advanced Battery Systems, Report of the Committee on Battery Materials Technology, National Academy Press (Washington, 1982)

(2) L. Burant & W. Gentry, "An Interim Cost Study of a Terrestrial Hydrogen/Nickel Oxide Battery", Presented at the 18th IEEE Photovoltaic Specialists Conference, Las Vegas, Nevada, 1985.

(3) J. Sindorf, L. Burant, & J. Dunlop, "Design and Cost Study of a 15kWh Hydrogen/Nickel Oxide Battery for Photovoltaic Applications", Presented at the 20th IECEC, Miami, Florida, 1985.

(4) J. Dunlop, W. Gentry, et. al., Design and Development of a Sealed 100-AH Hydrogen/Nickel Oxide Battery, Final Report, SAND85-7219, Sandia National Laboratories (1985).

(5) H. Vaidyanathan & J. Dunlop, "Performance of Carbon-Based Negative Electrodes in the Nickel-Hydrogen Battery", Presented at the 14th International Power Sources Symposium, 1984, Brighton, England.

Ni PLAQUE PHYSICAL CHARACTERISTICS				
	32 MIL		70 MIL	
	JCI SLURRY	DRY POWDER	JCI SLURRY	DRY POWDER
POROSITY %	83.8	83.6	81.9	83.8
AVE PORE DIA μ	8.26	9.00	9.08	8.82
SURFACE AREA μ	.248	.220	.212	.257

TABLE 1

TABLE 2

THIRTY YEAR, 15-kWh PHOTOVOLTAIC BATTERY SYSTEMS AVAILABLE BETWEEN 1986 AND 1991 (*)

	Hydrogen/Nickel Oxide	Lead/Acid Flooded	Lead/Acid Sealed	Zinc/Bromine	Sodium/Sulfur
Initial Cost ($/kWh)	375 to 930	80 to 120	99 to 160	40 to 120	400 to 1,200
Cycle Life (80% DOD)	15,000 to 5,200	1,600 to 800	1,200 to 600	1,800 to 400	2,000 to 900
Units Required (for 10,000 cycles)	1 to 2	7 to 13	9 to 17	6 to 25	5 to 12
PRESENT VALUE (cents/kWh-cycle)	3.8 to 14.5	3.4 to 9.3	5.3 to 16.2	4.7 to 17.8	13.2 to 84.6
Estimated Maintenance Cost (cents/kWh-cycle)	0.1 to 2	6 to 46	0.5 to 17	7 to 54	0.5 to 20
PRESENT VALUE (cents/kWh-cycle)	0.1 to 1.2	3.5 to 26.4	0.3 to 9.8	4.0 to 31.1	0.3 to 11.5
TOTAL LIFE CYCLE COST (cents/kWh-cycle)	3.9 to 15.7	6.9 to 35.7	5.6 to 26.0	8.7 to 48.0	13.5 to 96.1

(*) Costs are in constant, 1986, dollars. Range is from "optimistic" to "reasonable". Present values are calculated using a 4% real discount rate based on 12.5% current discount and 8.5% inflation rates; see DOE/CE-0072: NATIONAL PHOTOVOLTAICS PROGRAM. FIVE YEAR RESEARCH PLAN. 1984-1988.

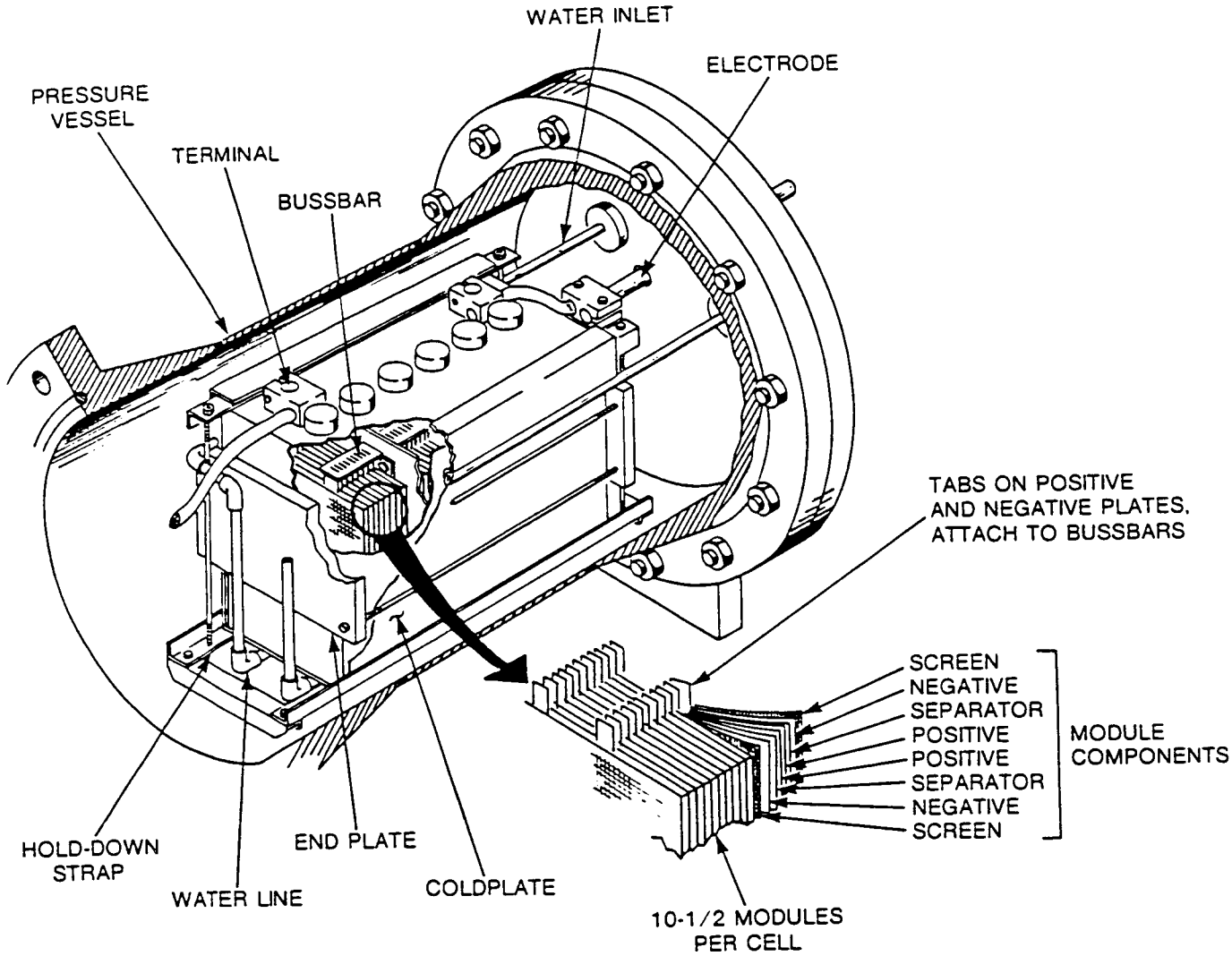

Figure 1 Cross sectional view of a 6-cell hydrogen/nickel oxide battery delivered to Sandia National Labs.

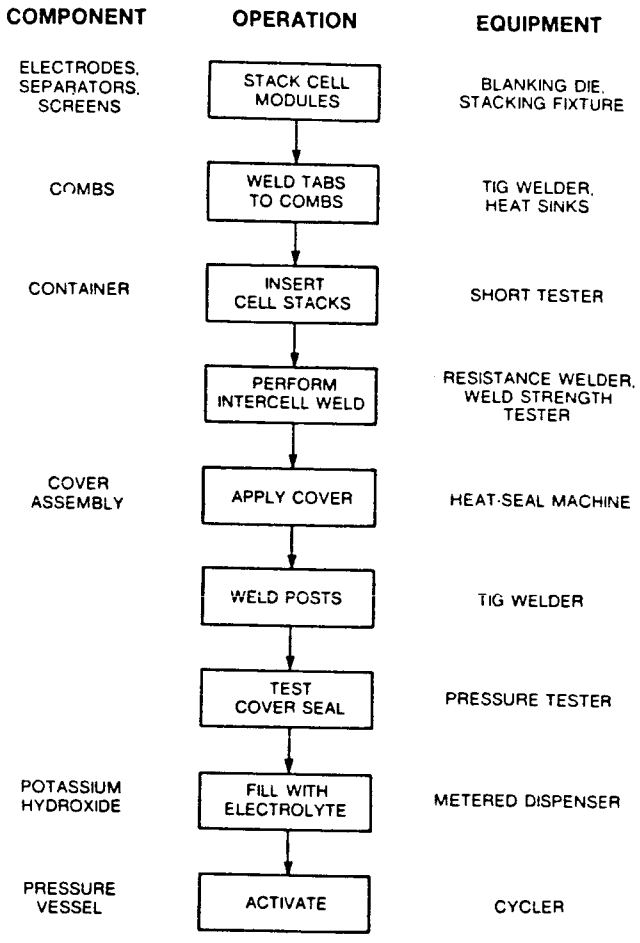

Figure 2 Sequence of operations for assembling the hydrogen/nickel oxide battery including the respective tooling.

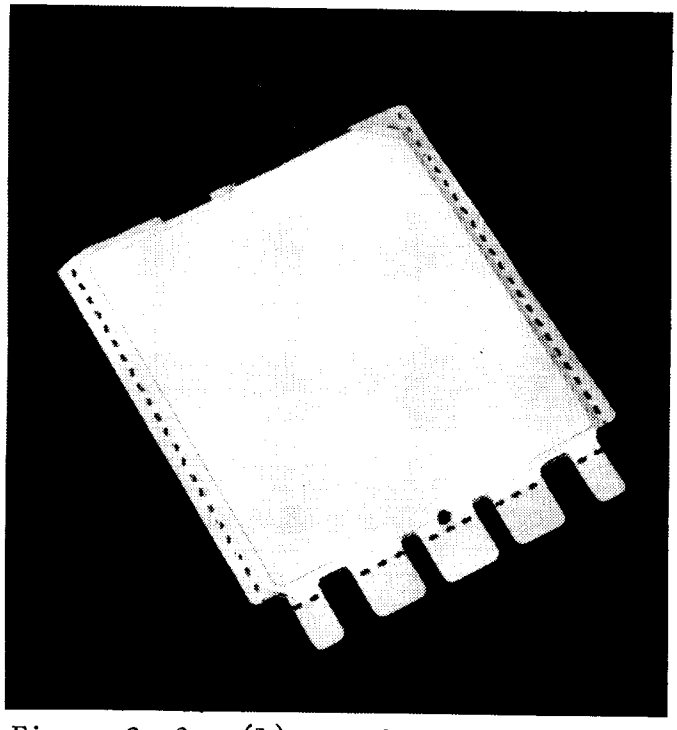

Figure 3 One (1) assembled and sealed cell-module.

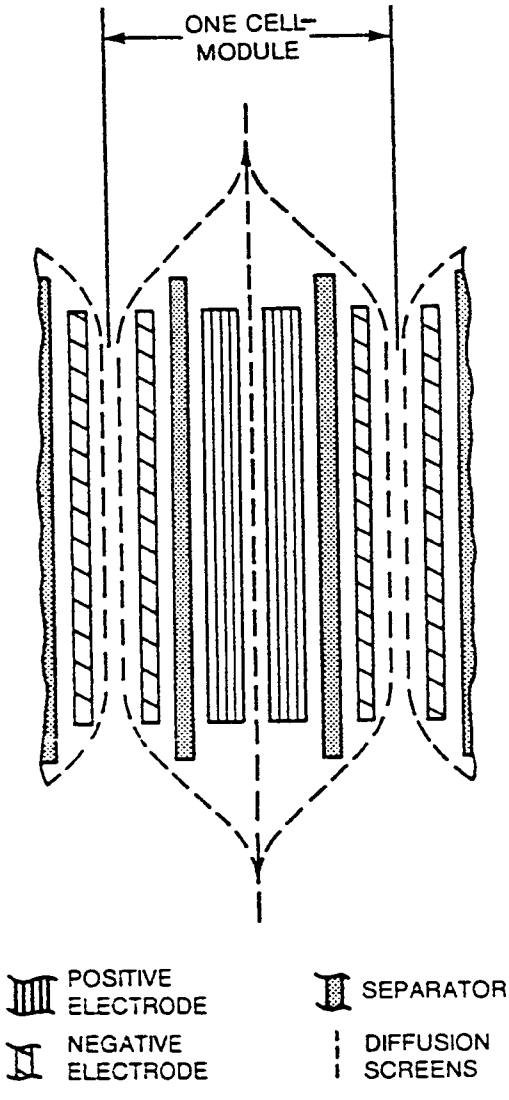

Figure 4 Component stacking arrangement of the cell-module illustrating the diffusion/binding functions of the screen.

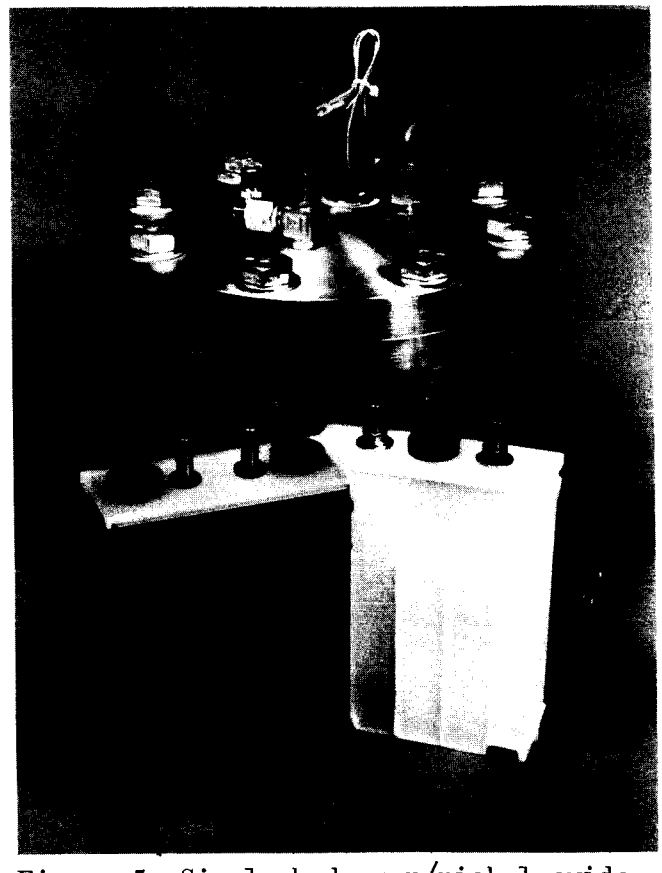

Figure 5 Single hydrogen/nickel oxide cells (3.8 & 5.1 cms thick) and boiler-plate pressure vessel in which lab tests were conducted.

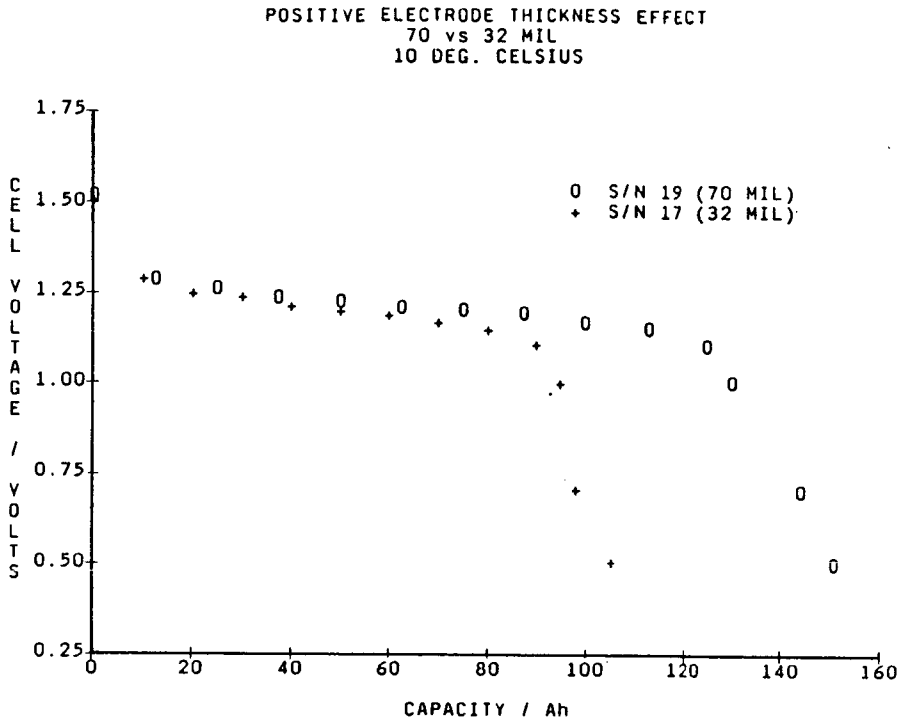

Figure 6 Discharge curves of prismatic cells containing 32-mil and 70-mil thick positive electrodes.

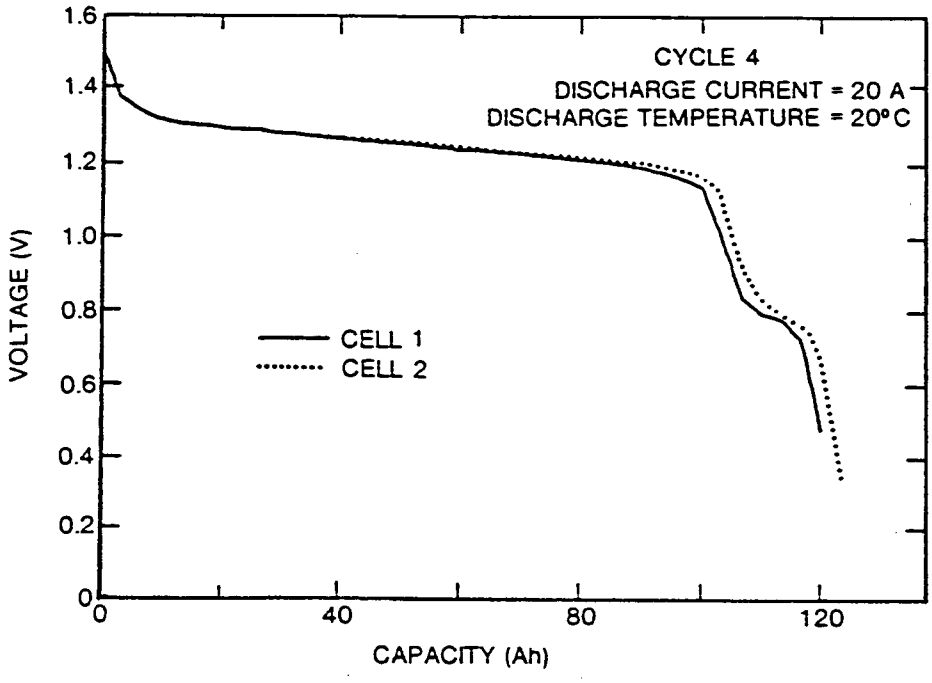

Figure 7 Discharge curves of prismatic cells comparing performances of negative electrodes containing 0.45 mg Pt/cm2 (cell 2) with 8 mg Pt/cm2 (cell 1).

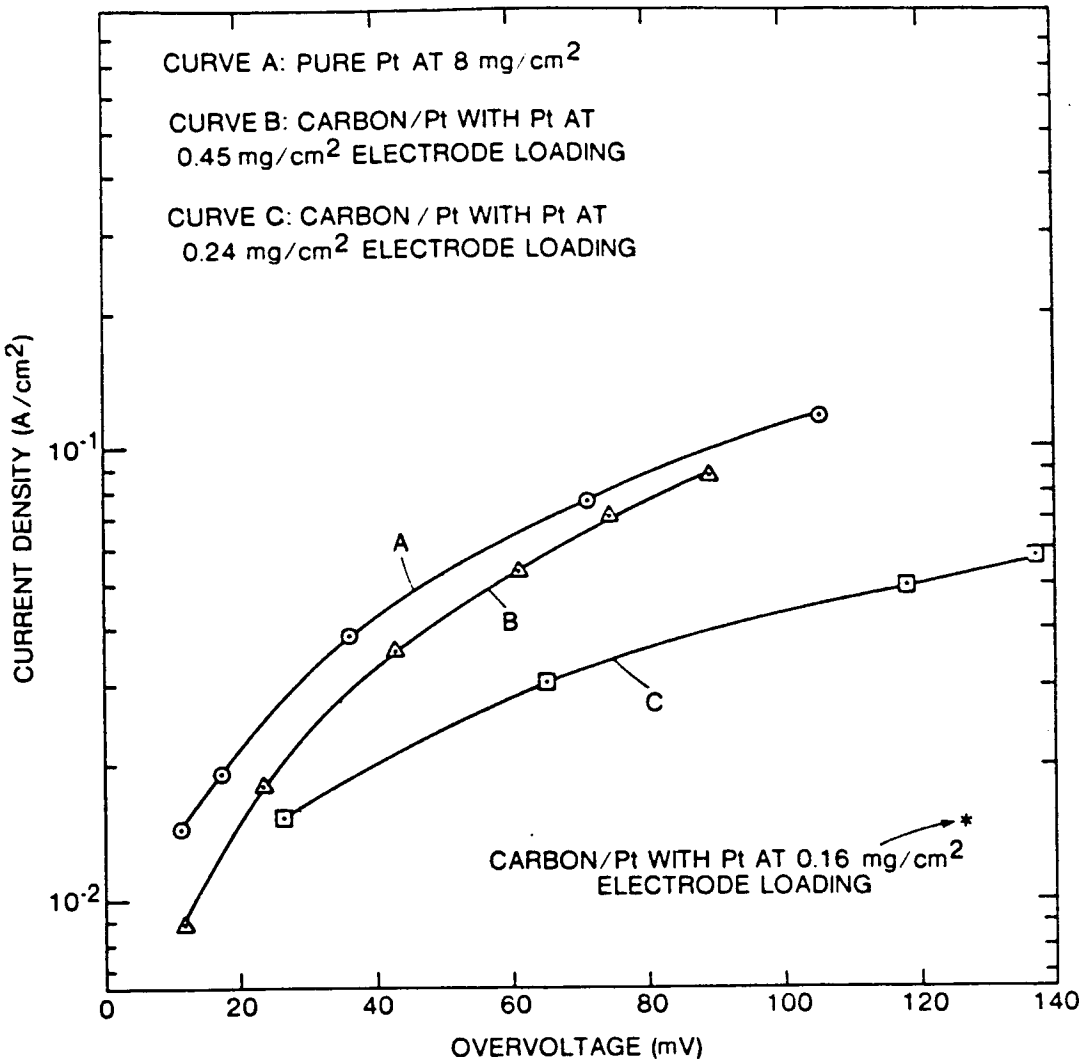

Figure 8 Variation of potential with current density.

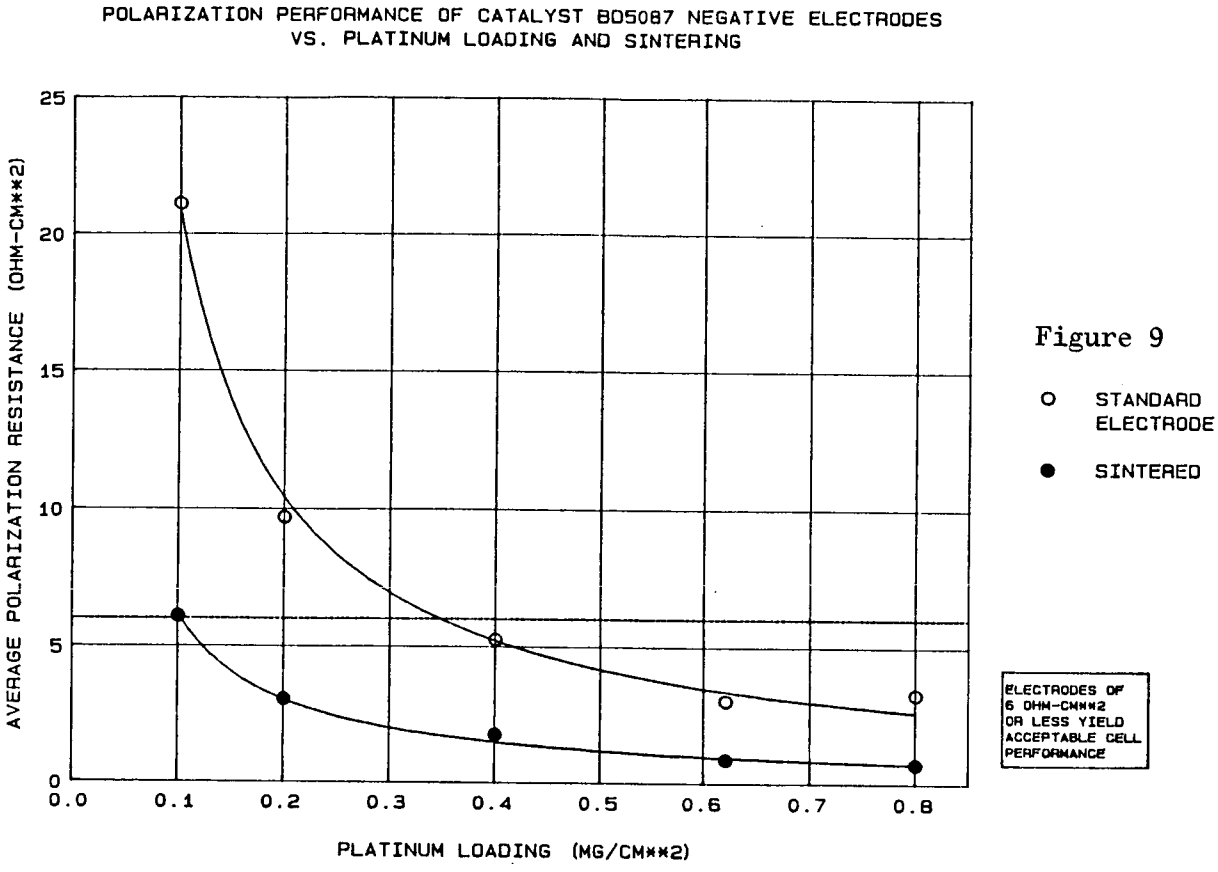

Figure 9

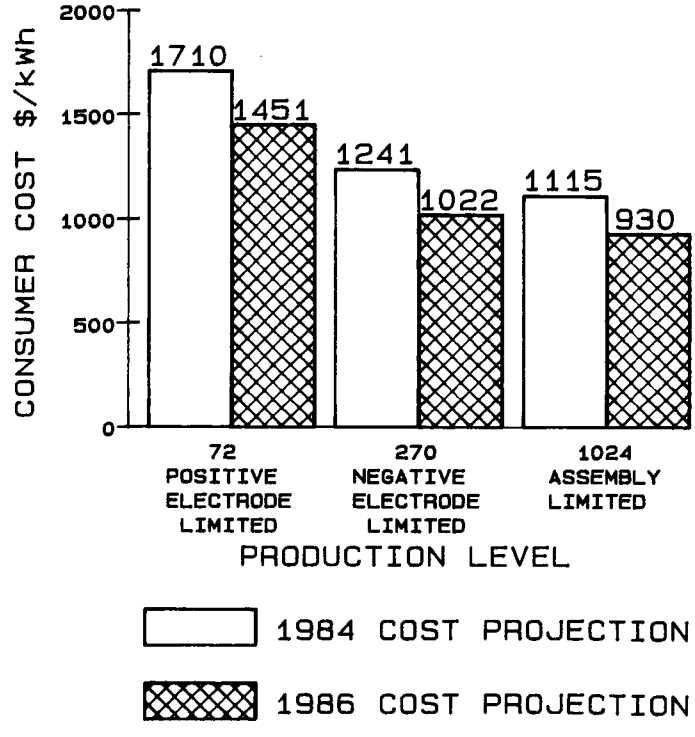

Figure 10 Reduction in cost of a 15 kWh hydrogen/nickel oxide battery as a function of production levels and continued cost reduction efforts.

ADVANCED NICKEL-CADMIUM BATTERIES FOR GEOSYNCHRONOUS SPACECRAFT

David F. Pickett, Hong S. Lim,
Stanley J. Krause, and Scott A. Verzwyvelt
Hughes Aircraft Company
Los Angeles, California 90009

A nickel-cadmium battery has been developed that can be operated at 80% depth of discharge in excess of 10 (possibly 15) years in a geosynchronous orbit application, and has about a 30% weight savings per spacecraft over state-of-the-art nickel-cadmium batteries when used with a 1000 watts eclipse load. The approach used in the development was to replace nylon separators with inert polymer impregnated zirconia, use electrochemically deposited plates in place of conventional chemically precipitated ones, and use an additive to extend negative plate lifetime. The design has undergone extensive testing using both engineering and protoflight cell configurations.

HUGHES GEOSYNCHRONOUS BATTERY BACKGROUND

The Nickel-Cadmium Evolution

Since the late 1960s the design of nickel-cadmium battery cells used by Hughes, for its geosynchronous spacecraft, has undergone a series of evolutionary developments. Each of these generations of battery cells, starting with Generation 1 in 1968 through today's Generation 4, has a number of major cell design factors which show a continued progression toward optimum values that have enhanced performance and reliability with concomitant improvements in useable energy density. The design factors selected for each new generation have been built on the data base collected from laboratory life tests, as well as continued observation of actual in-orbit performance of a large number of spacecraft over the years. Table 1 shows a summary of some of the more important nickel-cadmium cell design features for the four generations of cells utilized by Hughes over the past 18 years. In addition, Figures 1-3 show graphical representations, by generation, of the values for some of these parameters. These graphs clearly show the evolutionary trends of these parametric changes which supported the improved performance from those early satellite days. These parametric values, incidentally, are intended to be nominal in nature and are in implementation represented by a range of values about the nominal. The various generations of nickel-cadmium cells were flown or will be flown on the programs listed below. Not all programs and applications are listed, but representative ones are shown, along with the approximate calendar period for the design and applications activities.

- oGeneration 1 Ni-Cd Cells--ANIK A, INTELSAT 4--1968-1972
- oGeneration 2 Ni-Cd Cells--WESTAR 1-3, INTELSAT 4A, PALAPA, COMSTAR--1973-1977

oGeneration 3 Ni-Cd Cells--GOES, LEASAT, HS376 Series--1978-Present

oNickel-Hydrogen Cells--Military Applications, HS-393 Series, Future--1979-Present

oGeneration 4 Ni-Cd Cells--Future HS-376, Low Power DBS and Special Applications--1987-Future

Generation 4 Nickel-Cadmium Cells

Since nickel-hydrogen technology became available for flight applications soon after the third generation of nickel-cadmium cells, as noted in the timeline data above, why develop a fourth generation nickel-cadmium cell? A number of system-level trade studies had shown that a high performance nickel-cadmium cell would continue to show favorable weight and cost advantages over nickel-hydrogen cells when used in low power or small satellite applications. A nickel-cadmium cell which could equal nickel-hydrogen performance for 10 year synchronous missions, i.e., operate at or near 80% depth-of-discharge (DOD), would show such advantages at power levels below 1500 watts (W).

A further study was made in 1982 to determine the best approach to providing an aerospace-quality sealed nickel-cadmium cell. It was decided that incorporation of some nickel-hydrogen technology could benefit the performance of a new generation nickel-cadmium cell. Specific areas for improvement would focus on the positive electrode and the separators. An internally funded program was initiated to develop the new nickel-cadmium cell design that would meet the goals of 10-15 years in geosynchronous orbit at 80% DOD.

DEVELOPMENT OF GENERATION 4 NICKEL-CADMIUM CELLS

Initial Evaluations with Nickel-Hydrogen Type Separators

In our initial investigations with nickel-hydrogen cells we found that a yttria-stabilized zirconia cloth made by the Zircar Corporation was well suited to the alkaline and oxidizing environments within the cell, but some difficulty was encountered in handling the brittle material. In order to alleviate the handling problem, as well as reduce direct flow of oxygen through the highly porous material from the positive to negative plate, techniques were developed to impregnate this Zircar material (ref. 1) with polymers compatible with the harsh cell environment. Although one of these polymers had a tendency to poison catalytic activity of the hydrogen electrode, it appeared to function quite well in a nickel-cadmium cell(ref. 2). Encouraged by these results, we began a series of electrochemical and physical measurements on the separators and constructed Ni-Cd engineering (boilerplate) and protoflight cells to further evaluate lifetimes in both low earth orbit (LEO) and geosynchronous orbit (GEO) regimes. These tests were performed at our Malibu Research Laboratories (HRL) and Space and Communications Group (S&CG) test facilities.

Accelerated Testing Techniques

In order to evaluate our new separator materials (as well as other components and additives), in a timely manner, it was necessary to devise accelerated cycle life tests which could closely simulate real time battery performance in orbit. This was especially true for the higher GEO orbits since only 1000 cycles are accumulated over a ten year period in real time. Even in the lower 90 minute orbits, if cycling occurs at a low DOD, one may wait three to four years to observe a cell failure under real time conditions. As the results below will show, this time can be reduced by at least 50%, with reasonable confidence in the data, by using an accelerated test. Other results will show that an extraordinarily large number of cycles at a high rate will not guarantee long lifetime in a GEO situation.

In order to simulate real time GEO conditions as accurately as possible we used three different accelerated testing techniques. One of these techniques was a four-day cycle regime (Regime I) which included a 16-cycle period. It has been described previously (ref. 3). This regime was applied to all boilerplate cell testing and to some flight type cells. The regime included cycles of various DODs in 10% steps: 10, 20, 30, ..., 70, 80, 80, 70, ..., 20, 10% DOD, respectively. A charge/discharge ratio of 1.2 at a temperature of 10 to 15 deg. C. was used. A nine minute trickle charge at 0.02C rate followed the recharge at the 0.1C rate. Discharge was at the 0.5C rate. Test cells were reconditioned typically every third eclipse period by discharging them at the 0.5C rate for one hour followed by discharge across a 10 ohm resistor for 77 hours then constant current charge at 0.1C for 18 hours. This technique was extremely valuable in evaluating GEO cycling capability of a boilerplate cell with new additive and negative electrode components. If the cell would not perform under this cycling regime, it would not perform under real time conditions.

Another accelerated regime (Regime II) used in this study was that in which only the solstice period is accelerated by an elevated temperature. The eclipse portion of the regime was performed using 46 day real time GEO cycling at 10 deg. C. The accelerated continuous sunlight period consisted of trickle charge at C/36 for 21.25 days at 50 deg. C. Test cells were reconditioned after each eclipse season as described in reference 3. This test regime was probably more severe than a real time regime since state-of-the-art cells, which had lasted over 10 years in a real time test regime, lasted only ten seasons in this one.

In order to compare our data to that of accelerated testing being performed on our flight programs, a third GEO regime (Regime III) was used. This regime was similar to Regime II except that temperature was not elevated during the continuous sunlight (solstice) period. Time between eclipse seasons was 14 days with C/60 trickle charge. Reconditioning was performed prior to each eclipse season.

In our initial LEO testing of boilerplate cells in an accelerated regime, a cycle regime (Regime IV) was used which allowed us to perform testing in about one-half the time normally used to perform testing for a 90 minute orbit (ref. 2).

S&CG Protoflight Design Cell Tests

The 12 ampere-hour (AH) cells used in this test were constructed using new electrochemically deposited (ED) electrodes and various separator combinations. Cells having Pellon 2505 nylon material were used as controls. Preliminary results of the tests have been described in an earlier publication (ref. 3). In summary, separators used in the test were polysufone impregnated Zircar (PS-Z), polybenzimadazole impregnated Zircar (PBI-Z), polybenzimadazole impregnated polypropylene (PBI-PP) and Pellon 2505. Two different test regimes were used to evaluate the above configurations, a real time test closely simulating possible flight conditions in GEO and Regime II. Cells were constructed as close to flight configuration as possible at the General Electric Battery Business Department, Gainesville, FL. Prior to being placed on cycle life testing, the cells were subjected to the Hughes standard flight acceptance tests.

Results of the life testing on the PBI-Z and PBI-PP configurations are illustrated in Figure 4. As reported earlier (ref. 3), cells with Pellon 2505 failed after 10 seasons in the accelerated test due to high charge voltages which resulted in hydrogen gassing. (The 50 deg. C. temperature acceleration was apparently too severe causing accelerated nylon hydrolysis which resulted in loss of overcharge protection.) The PS-Z cells were removed from test since they were slightly damaged during initial construction. Other details of the testing will be given later in this paper. Since results of this testing were accumulated over a long time period, they did not influence the course of this development program, initially, as did other results such as those from the LEO tests.

LEO Testing of Boiler Plate Cells

Prior to fabrication of the 12 AH flight cells described above, we had performed studies on a series of boilerplate Ni-Cd cells which contained the chemically stable, polymer reinforced, Zircar separators. In this case conventional electrodes having chemically deposited active material were used. An accelerated cycle life test (Regime IV) was carried out at various temperatures (25, 40 and 50 deg. C.) in a cycle regime similar to a LEO regime rather than a GEO regime (ref. 2). Cycle life (to 0.5V) of those cells containing polysulfone impregnated Zircar (PS-Z) is compared with that of aerospace Ni-Cd cells containing Pellon 2505 nylon separators (ref. 5) in Figure 5. These results showed that the cycle life of a nickel-cadmium cell is remarkably (roughly three times) improved with this new separator. Cycle life up to 43,000 cycles was observed at 25 deg. C. at 40% DOD. The results at various temperatures showed that Arrhenius activation energy for the cycle life was 11 kcal/mole as shown in Figure 6. These extremely encouraging results allowed us to initiate the development of the Generation 4 advanced Ni-Cd battery for GEO applications with an ambitious goal of over 10 years operation at 80% DOD operation.

Capacity Fading and Storage Problems

Although cells with the new separators and CD electrodes showed excellent cycle life in a LEO type regime, they showed a rapid capacity fading in GEO cycling (ref. 3). The cells usually failed within 10 eclipse periods in Regime I (80% DOD). This capacity fading was identified to be due to the

fading of cadmium electrode capacity at low rate (0.1 C) charging which is normally required on a GEO spacecraft. This fading was believed to be due to formation of large cadmium crystals during low rate charge (ref. 6).

In order to eliminate this problem, which is usually observed with low rate charging, a high rate pulse charging scheme (HGEO regime) was successfully developed (ref. 3). This scheme involves sequential charging of individual battery sub-packs one at a time at a 0.4 C rate or higher. Seven out of eight boiler plate cells in a test series completed over 120 eclipse periods of Regime I cycling using this method of charge. Failure was defined as end-of discharge-voltage (EODV) falling below 1.0 volt. This cycle life corresponds to a 20 year equivalent number of cycles in GEO indicating that not further improvement might be needed for the goal performance, if the HGEO charging could be implemented in the spacecraft. Spacecraft systems level studies indicated that a conventional low rate charging scheme would be more desireable due to weight and cost considerations. Therefore, our subsequent efforts were directed toward development of a cell design which did not depend on a HGEO charging regime.

In attempts to test a second series of protoflight cells in which CD negative electrodes and ED positive electrodes were present, we experienced a loss in capacity on storage which accompanied the capacity loss associated with low rate charging. This storage capacity loss was attributed to the ED positive electrode since it was not observed in cells with CD positive electrodes. This type of capacity loss was eliminated with a modification in the processing of the ED positive electrodes. Test results confirming a stable storage capacity are given later in the paper.

Investigation and Formulation of Permanent Solutions to Capacity Losses

In our search to find a solution to negative capacity fading other than HGEO charging, it became rather obvious that the first 12 AH protoflight cells which we had on test had not experienced capacity fading that was present in the boilerplate cells and the second series of protoflight cells. The 12 AH cells had the unique feature of ED negative electrodes. Thus an investigation into the capacity stability of ED cadmium electrode was initiated. At the same time an investigation into the various "expanders" that were used for cadmium electrodes was pursued. As test results below indicate, we were successful in finding an additive which serves as an expander, and were able to demonstrate that use of an ED cadmium electrode will eliminate capacity fading associated with low rate charging.

In the course of this study over 40 different design variations were evaluated using cycle Regime I. Our investigations included examination of: variation in active material impregnation procedure (CD or ED) and loading levels of both cadmium and nickel electrodes, various additives to the electrolyte or the cadmium electrode, variation of polymers for the impregnation of the zirconia separator, variations in electrode spacing, and variation of activation (or preconditioning) procedures.

EVALUATION AND TESTING

Storage Evaluation Tests/ Boilerplate Cells

Storage evaluation tests were performed on four different test cells using three different storage modes in sequence. The initial storage mode was

an open circuit storage at room ambient temperature (about 22 deg. C.) after discharging test cells to 0.5 V. at the C/2 rate from a fully charged state. The second storage mode was another open circuit storage at ambient temperature after shorting the cells across a 1.0 ohm resistor for 70 hours. The last storage mode was a shorted storage with a 1 ohm resistor across the terminals at ambient temperature after discharging the cells.

Results of the boilerplate cell storage tests are shown in Figure 7. The capacities of cells containing ED nickel electrodes showed no decrease during open storage up to 77 days, while a gradual minor decrease was observed during subsequent shorted storage for additional 160 days (Fig. 7A and 7B). The cells containing CD nickel electrodes showed a slight decrease after initial 18-day open circuit storage, but no further decrease was observed on additional storage in the same storage mode (Fig. 7C and 7D), while the capacity improved during the second mode of open circuit storage. This improved capacity did not decrease significantly during the subsequent shorted storage. Overall, no significant storage problem is expected with any of these designs. However, for a long term storage (ca. 100 days), an open circuit mode appears to be preferred for the advanced Ni-Cd cell which contains ED nickel electrodes.

Storage Evaluation Tests / Protoflight Cells

Results of this test are summarized in Table 2. Data support results from boilerplate cell tests and clearly indicate that shorted storage for periods less than 71 days does not result in capacity loss. We thus have eliminated the gross capacity fading which was present in earlier cell designs with ED plates.

Cycle Life Testing / Boilerplate Cells

In the course of arriving at our advanced design we have fabricated approximately 120 boilerplate test cells and performed accelerated cycle life tests on more than 100 cells. These tests were divided into seven different iterative series screening out less desirable designs in each iterative step. In the final test series design variables were narrowed down to the use of mostly polybenzimidazole impregnated zirconia (Zircar) separators (PBI-Z), a Hughes proprietary additive, and mostly ED electrodes. Some of these cells have been cycled over 190 eclipse periods in cycle Regime I at 80% DOD without a deterioration of their voltage performance as shown in Figure 8. This cycle life is equivalent to about 30 years of cycling in a GEO regime. We believe that these cells will have lifetimes of over 10 years or probably over 15 years at 80% DOD operation in GEO. The final recommended designs included a combination of ED nickel and cadmium electrodes, PBI-Z separators and an additive.

Effectiveness or stability of the additive has been demonstrated after four calendar years of continuous cycling. Results are shown in Figure 9. Although it is not a demonstration in a real time regime, it is an extremely encouraging indication for the long term effectiveness of the additive. In addition, no harmful effect of this additive for long life has been identified.

Cycle Life Testing / Protoflight Cells

Over the past eight years some 45 flight configuration (protoflight) cells with various separators, electrode and additive combinations have been cycle life tested in order to verify boilerplate cell tests which are described above. We have described preliminary results of 12 AH first iteration cells in a previous publication (ref. 3) and have summarized the results in Figure 4. Test conditions were described earlier in this paper. Results of this testing have been quite encouraging, but it has taken some time to accumulate the data.

Shortly after placing the 12 AH cells on test, a second 20 AH design iteration, containing CD cadmium electrodes, was purchased from the same vendor and subjected to the same tests as the 12 AH cells. The cells exhibited a voltage decrease to below 1.0 V per cell after a couple of seasons (80% DOD max.) of cycling in Regime II. Shortly after obtaining these results we began the extensive testing with various boilerplate combinations.

After our boilerplate cell tests had indicated that the CD cadmium electrode had a tendency to fade in capacity at GEO charge rates in the absence of an additive at 80% DOD, it was decided that a third iteration of flight configuration cells should be fabricated and tested in order to verify the boilerplate cell test results. Some 30 of these cells were purchased from one vendor and another 10 from a second vendor and placed on test using GEO Regimes I and III. Control cells without additive and with CD cadmium electrodes were included in the group. Results to date have been quite encouraging with more than 25 years equivalent of cycling in Regime I and over 5 years equivalent in Regime III to date. Some typical voltage at maximum DOD versus eclipse season plots are shown in Figure 10.

Tear Down Analyses

Tear down analyses were carried out on both Ni-Cd boilerplate cells, which were heavily cycled in an accelerated LEO type regime, and 12 AH protoflight cells, which had undergone 9 seasons of real time GEO cycling.

Results of the analyses on GEO cells are summarized in Table 3. Original plate thicknesses were 0.029+/-0.001 inches. Specified capacities were 12 AH and initial negative/positive ratios were set at 1.7. These results show amazingly little swelling of the electrodes, good capacity and remarkably little cadmium migration.

Analyses on the LEO boilerplate cells consisted of visual inspection, microscopic and SEM studies of cycled electrodes, measurements of electrode thicknesses, flooded electrode capacities, BET surface area, and pore distribution by mercury intrusion porosimetry.

Results of some of these analyses are summarized in Table 4. The CD(chemically deposited or chemically precipitated) electrodes from cells 31 and 32 expanded several times more than those of ED electrodes from other cells indicating an advantage of ED electrodes over CD electrodes. General morphology of electrodes under SEM was similar in nature to those described earlier (ref. 7). The predominant mode of failure in this LEO test was the gradual capacity degradation of the nickel electrode and development of shorts

by cadmium migration. Although the separator dryout looked severe, it did not appear to be the direct cause of cycle failure. We believe that there is sufficient amount of micropores in the zirconia separator for retaining the electrolyte and providing the minimum required conductivity across the separator for cell operation.

ESTABLISHMENT OF FINAL DESIGN FOR FLIGHT QUALIFICATION

A fourth design iteration has recently been implemented which is simply an optimized version of the best performing design from the third iteration. Cells of the fourth iteration design are just now beginning characterization and environmental testing. This design will be used on our next flight in place of conventional nickel-cadmium cells. Figure 11 shows how batteries using this new cell design will compare to conventional ones in terms of power versus weight.

CONCLUSIONS AND SUMMARY

The decision to initiate a program for the improvement of nickel-cadmium cell performance to levels similar to nickel-hydrogen cells was a difficult one. There was no evidence at that time that such an effort was even feasible or that the performance objectives were achievable with even moderate risk. Further, considerable industry-wide effort and resources were being spent on nickel-hydrogen technology, the new generation aerospace battery, with very little attention paid to nickel-cadmium technology improvement. However, our studies continued to show that considerable cost and weight benefits could be derived from nickel-cadmium cells that performed as well as nickel-hydrogen cells, when such cells were used in low power, generally below 1500 watts, low earth orbit and synchronous orbit applications.

A four year development effort was initiated, with a team from the Hughes Space and Communications Group and the Hughes Research Laboratory. The program has progressed to the point where several candidate designs have been assembled to Hughes specifications into flight configuration, flight quality cells at Gates Energy Products (fomerly General Electric in Gainesville, Florida) and are awaiting the start of final characterization/qualification testing in readiness for their first flight program application in the near-future. This milestone is the culmination of an extensive and detailed design/development/test program which probably surpasses any previously implemented for aerospace nickel-cadmium cells.

The program is continuing, extending the cycle and calendar life data base. Eight years of real time testing on protoflight and boilerplate cells at 60-80% DOD has now been achieved. Over 4000 80% DOD accelerated GEO cycles on boilerplate cells have been recorded to date. Other data has shown that this advanced cell design, even in several variations, exceeds the cycle life of conventional aerospace nickel-cadmium cells by threefold. In all test programs, at any DOD, temperature, and cycle test regime, over any calendar period, the advanced design always demonstrated three times the cycle life of state-of-the-art nickel-cadmium cells. One group of test cells has exceeded 43,000 accelerated cycles at 40% DOD at room temperature with no failures. Other life test cell groups have exceeded 2000 geosynchronous simulated cycles (accelerated calendar time) at 80% DOD at 10 deg. C.

Significant component improvements to achieve such performance in this advanced design include the non-degradable impregnated zirconia separator, electrochemically impregnated nickel and cadmium electrodes, modified interelectorde spacing and plate compression, and an additive which prevents the formation of large cadmium crystals on the negative electrode. Test data has shown that cadmium migration in this cell is reduced by a factor of 5 to 10 below that of conventional cells.

In conclusion, the advanced nickel-cadmium cell should easily make a 10 year, and likely 15 years, mission in geosynchronous orbit operating at 80% DOD, based on the data generated thus far.

REFERENCES

1. H. S. Lim, S. A. Verzwyvelt, A. E. Schmitz, J. D. Margerum, and R. C. Knechtli, " New Separators for Nickel-Cadmium Cells", Proc. of the 16th Intersociety Energy Conversion Engineering Conference (IECEC), Atlanta, GA, Vol. 1, p. 182, Aug. 9 - 14, 1981.

2. H. S. Lim, S. A. Verzwyvelt, J. D. Margerum, and R. C. Knechtli, "Long Life Ni-Cd Cells with Zirconia Separators: Accelerated Cycle Tests", Proc. of the 17th IECEC, Los Angeles, CA, August 8-12, 1982, p. 716.

3. H. S. Lim, S. A. Verzwyvelt, D. F. Pickett, J. D. Margerum, R. C. Knechtli, and H. H. Rogers, "Long life and Low Weight Ni-Cd Cells for Spacecraft", Proc. of the 19th IECEC, San Francisco, CA, August 1984, p. 609.

4. H. S. Lim, J. D. Margerum, S. A. Verzwyvelt, and A. M. Lackner, "Studies on the Stability of Nylon Separator Material", 27th Annual Proceedings of the Power Sources Conference, June 1976, p.83.

5. "Accelerated Test Program", Interim Report, 3 May, 1979, prepared for Jet Propulsion Laboratory by NWSC, Crame, IN.

6. J. P. Harivel, B. Morignat, and J. Migeon, "Investigation on the Negative Eelectrode of Nickel-Cadmium Cells with Sintered Plates," 4th International Power Sources Symposium, Brighton, September 1964, p. 107.

7. H. S. Lim and S. A. Verzwyvelt, "Long Life Nickel Electrodes for a Nickel-Hydrogen Cell: Results of an Accelerated Test and Failure Analyses", Proc. 19th IECEC, August 1984, p. 312.

TABLE 1. Ni-Cd CELL DESIGN SUMMARY

PARAMETER	GENERATION			
	1	2	3	4
POSITIVE PLATE LOADING, gm/dm 2	14	12	10	9
NEGATIVE PLATE LOADING, gm/dm 2	16	14	12	12
POSITIVE PLATE THICKNESS, IN.	0.028	0.028	0.024	0.028
INTERELECTRODE SPACE, IN.	0.004	0.006	0.007	HUGHES PROPRIETARY
TERMINAL INSULATOR	CERAMASEAL	GE	GE	GE
FILL TUBE JOINT	TIG WELD	Ni-Au BRAZE	Ni-Au BRAZE	Ni-Au BRAZE
SEPARATOR	PELLON 2505	PELLON 2505	PELLON 2505	PBI-Z
ELECTROLYTE CENTRATION, % KOH	34	31	31	31
FILL LEVEL, cc/Ah	2.5	3	4	4.5
CASE CONSTRUCTION	WELDED SEAMS	1 PIECE	1 PIECE	1 PIECE, CORRUG .

TABLE 2. ADVANCED Ni-Cd PROTOFLIGHT CELL STORAGE MODE TEST RESULTS[a]

CELL DESIGNATION, 1 CELL EACH[b]	INITIAL CAPACITY	74 DAY OC[a]	ADDITIONAL 26 DAYS OC	ADDITIONAL 49 DAYS SHORTED	ADDITIONAL 71 DAYS SHORTED
ED (+)/PBI-Z/ED (−)	21.08	21.43	21.32	21.12	21.45
CD (+)/PBI-Z/CD (−)	23.46	23.71	23.47	23.44	23.65

a - CAPACITIES MEASURED BY 0.1C CHARGE FOR 18 HOURS WITH DISCHARGE AT 0.5C RATE (10.0 A) AFTER CONDITIONING CYCLE OF C/20 CHARGE FOR 40 HR FOLLOWED BY C/2 DISCHARGE TO 1.0 V. ALL CAPACITIES MEASURED TO 1.0 V

b - ED (−) = ELECTROCHEMICALLY DEPOSITED, POSITIVE
PBI-Z = POLYBENZIMADAZOLE IMPREGNATED ZIRCAR, SEPARATOR
ED (−) = ELECTROCHEMICALLY DEPOSITED, NEGATIVE
CD = CHEMICALLY DEPOSITED

TABLE 3. ANALYSIS SUMMARY FOR 12 AH CELLS (AFTER 9 REAL TIME SEASONS)

GE PART NO.	ECO1	ECO2	ECO4	ECO5
FILL DATE	21 NOV 78	21 NOV 78	21 NOV 78	21 NOV 78
SEPARATOR	POLYPROPYLENE/ PBI	ZIRCAR/ PBI	POLYPROPYLENE/ PBI	ZIRCAR/ PBI
POS THICKNESS (AVERAGE), IN.	0.032	0.031	0.31	0.031
FLOODED CAP				
POSITIVE, AH	16.30	16.50	16.59	15.59
NEGATIVE, AH	22.80	21.50	24.30	22.00
Cd/Sep, G	0.0016	0.0032	0.0022	0.0026
Cd IN, G/CELL*	0.021	0.042	0.029	0.033

* - 0.1 GM TO 0.4 GM/CELL SEEN IN MARISAT CELL TESTS

TABLE 4. TEARDOWN ANALYSES DATA OF HEAVILY CYCLED NI-Cd BOILER PLATE CELL IN AN ACCELERATED LEO TYPE CYLCE REGIME

CELL NO.	CELL TYPE	NO. OF CYCLES	CYCLING CONDITIONS % DOD/°C	Ni ELECTR EXPANSION, %	FLOODED CAPACITY*, Ah
31	CD/Z-PS/CD≠	43,113^{V}	40/25	36.4	1.27 (2.18)
32	CD/Z-PS/CD	43,113^{V}	40/25	42.7	1.18 (2.18)
42	ED/Z-PS/CD	8,276^{V}	60/40	6.7	1.45 (1.69)
43	ED/Z-PS/CD	5,838^{S}	60/40	7.1	1.78 (1.69)
44	ED/Z-PBI/CD	5,051^{S}	60/40	5.2	1.87 (1.69)
45	ED/Z-PBI/CD	5,139^{S}	60/40	7.1	1.72 (1.69)
46	ED/Z-PS/CD	9,447^{V}	80/25	6.0	1.41 (1.69
47	ED/Z-PBI/CD	6,255^{S}	80/25	3.6	1.65 (1.69)

*: VALUES IN PARENTHESES ARE RATED CAPACITY OF THE ELECTRODE IN Ah
v: CYCLE FAILURE BY A GRADUAL VOLTAGE DROP TO BELOW 0.5 V
s: FAILURE BY AN ABRUPT VOLTAGE DROP DURING CYCLING PROBABLY DUE TO AN INTERNAL SHORT FORMATION
≠ Z-PS= POLYSULFONE INPREGNATED ,SEPARATOR
Z-PBI= PBI-Z
SEE TABLE 2 FOR OTHER DESIGNATIONS

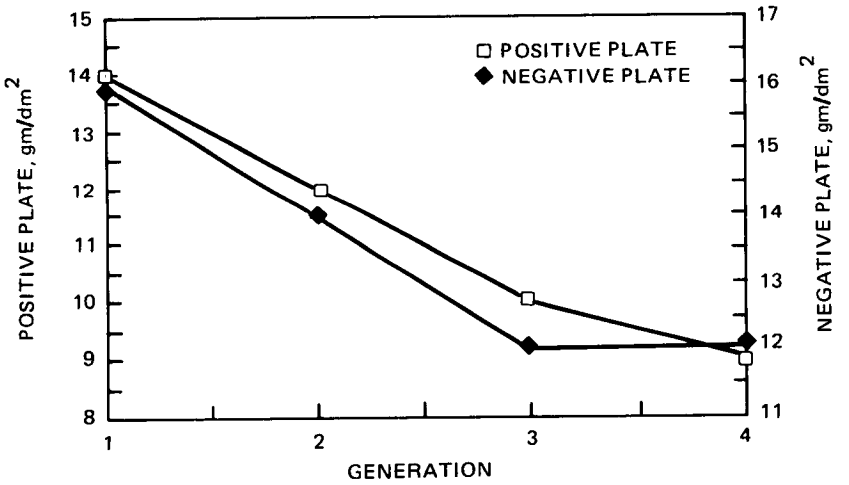

FIGURE 1. PLATE LOADING EVOLUTION Ni-Cd CELLS

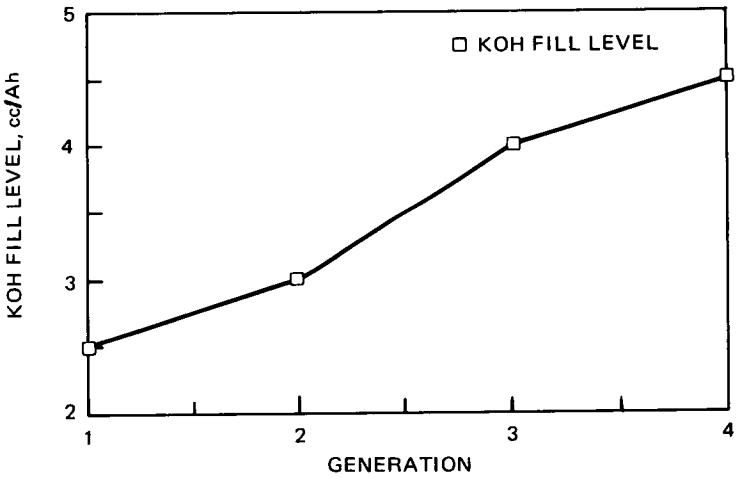

FIGURE 2. ELECTROLYTE FILL LEVEL EVOLUTION

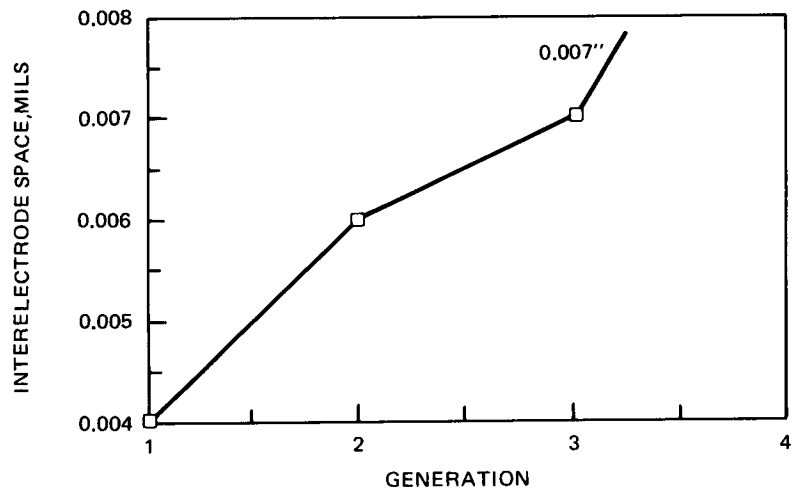

FIGURE 3. EVOLUTION OF INTERELECTRODE SPACING

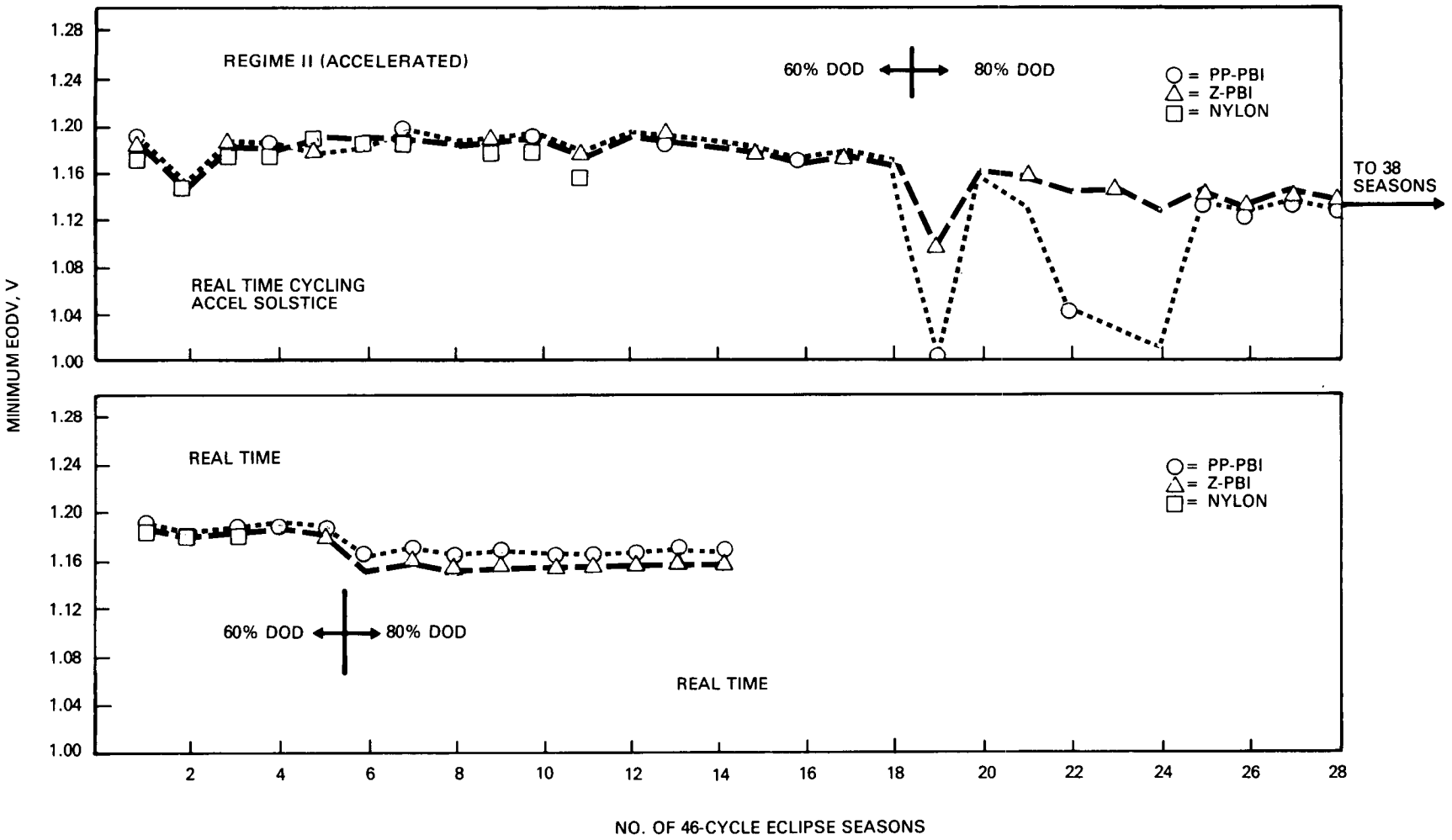

FIGURE 4. PERFORMANCE OF 12 AH PROTOFLIGHT CELLS IN REAL TIME AND ACCELERATED GEO REGIMES

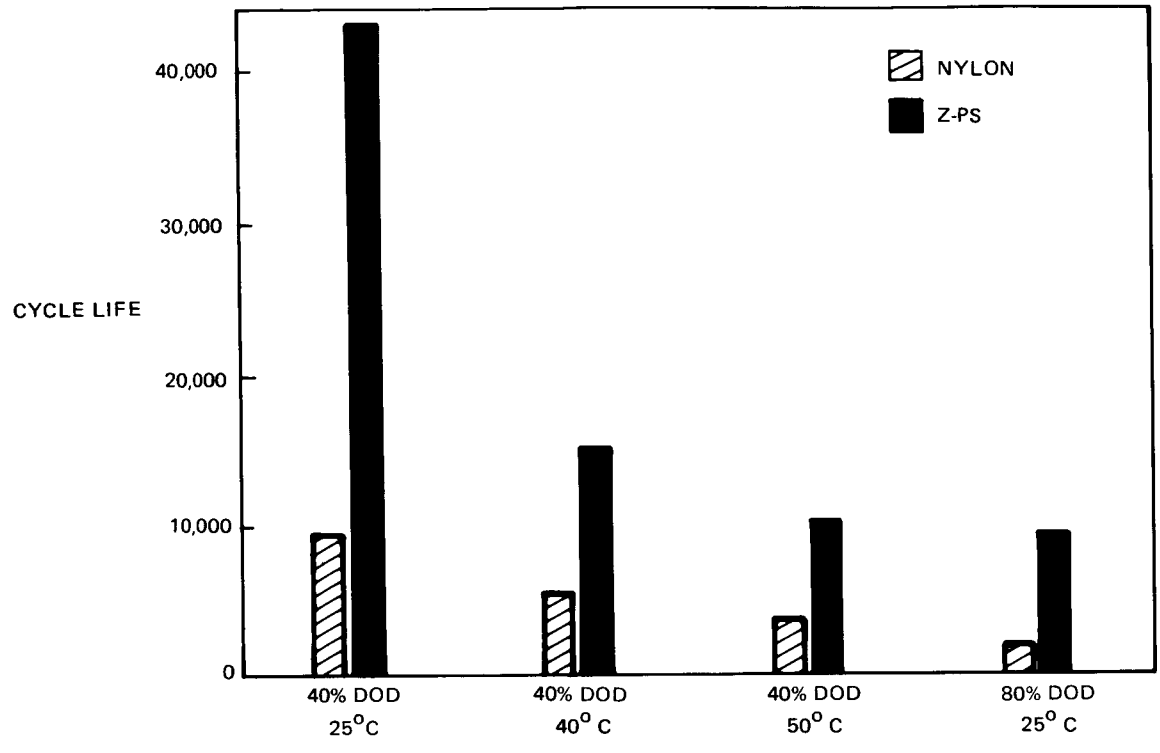

FIGURE 5. CYCLE LIFE COMPARISON OF Ni-Cd CELLS CONTAINING Z-PS SEPARATORS WITH CELLS CONTAINING NYLON SEPARATORS

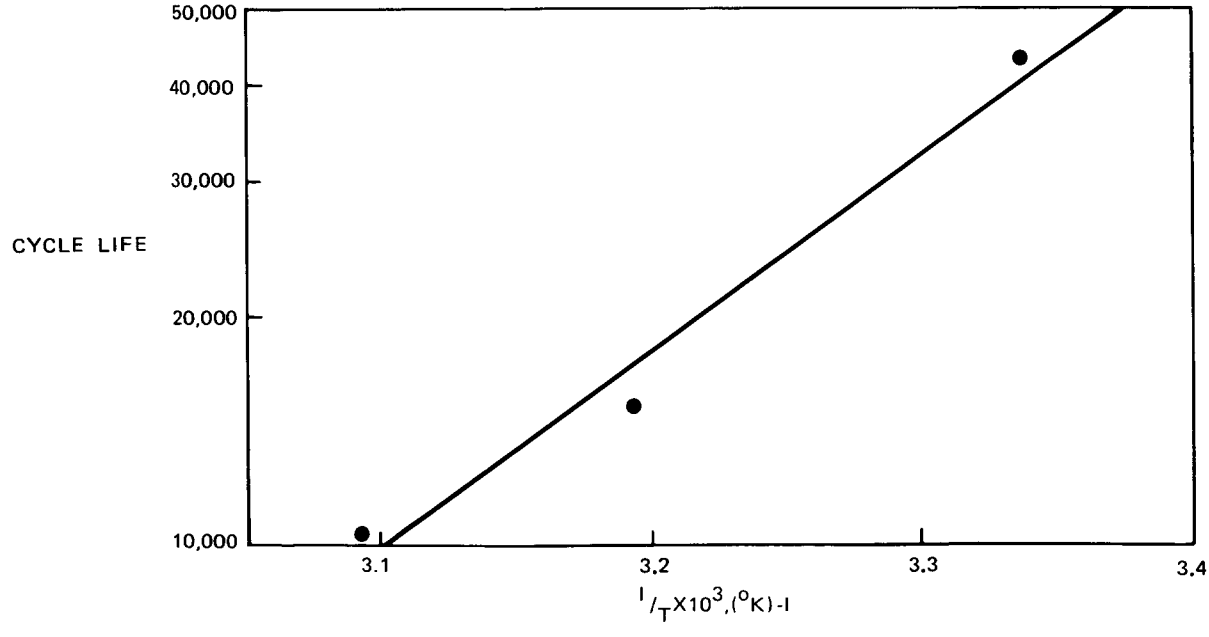

FIGURE 6. CYCLE LIFE OF Ni-Cd CELLS CONTAING Z-PS SEPARATORS AT 40% DOD VS 1/T

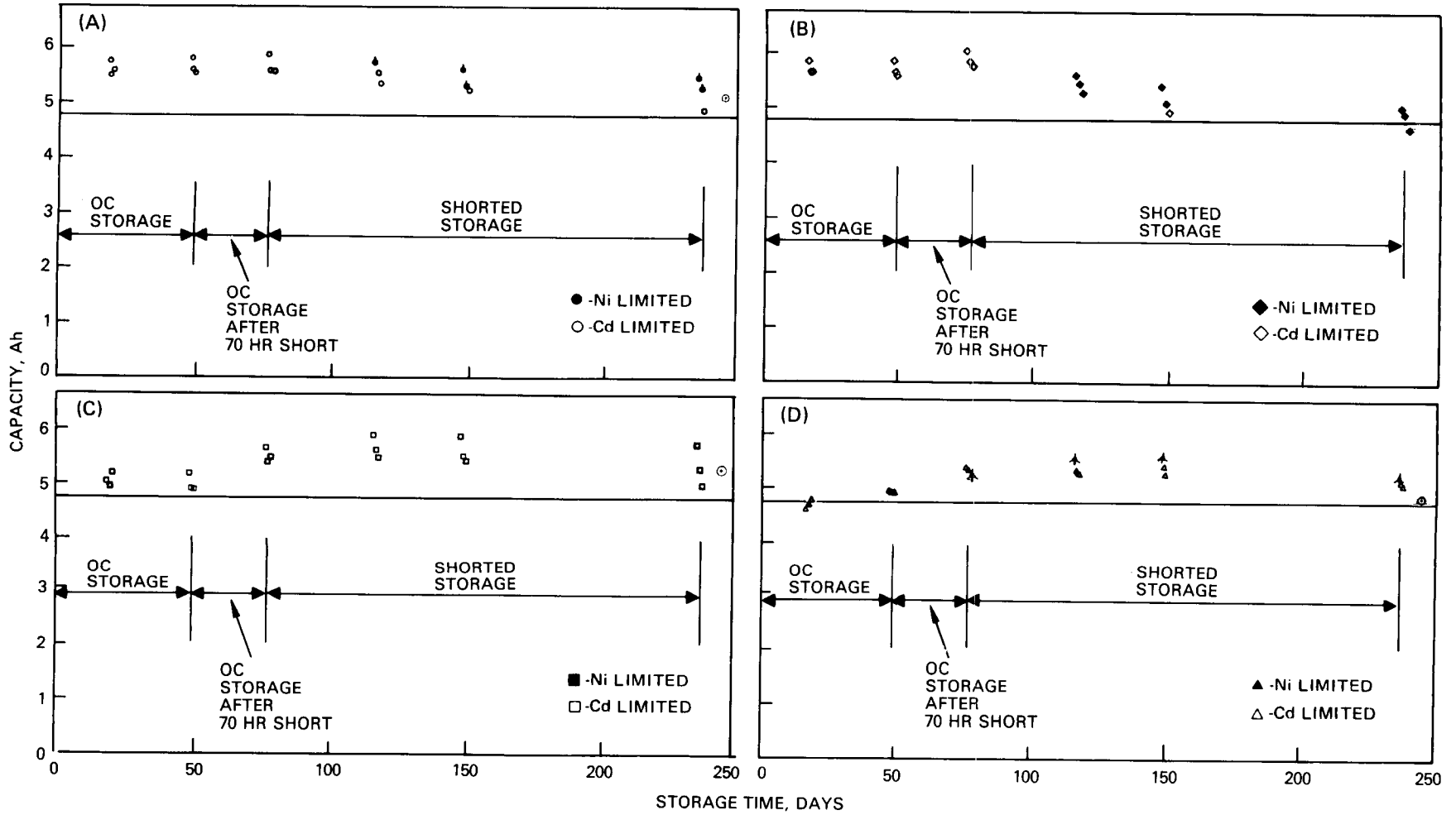

FIGURE 7. CAPACITY OF TEST CELLS VS STORAGE TIME AT VARIOUS STORAGE MODES. ALL CAPACITIES WERE MEASURED BY C/2 RATE DISCHARGE TO 1.0 V. A. A BOILER PLATE CELL CONTAINING ED NICKEL AND ED CADMIUM ELECTRODES WITHOUT THE ADDITIVE. B. SIMILAR CELL TO A WITH THE ADDITIVE. C. A BOILER PLATE CELL CONTAINING CD NICKEL AND ED CADMIUM ELECTRODES WITHOUT THE ADDITIVE. D. A BOILER PLATE CELL CONTAINING CD NICKEL AND CD CADMIUM ELECTRODES WITH THE ADDITIVE. FILLED SYMBOLS REPRESENT NICKEL ELECTRODE LIMITED CAPACITY AND OPEN CYMBOLS REPRESENT CADMIUM ELECTRODE LIMITED CAPACITY. THE LAST CAPACITY VALUE REPRESENTED BY A CIRCLE WITH A DOT INSIDE WAS MEASURED AFTER C/20 RATE CHARGE FOR 40 H.

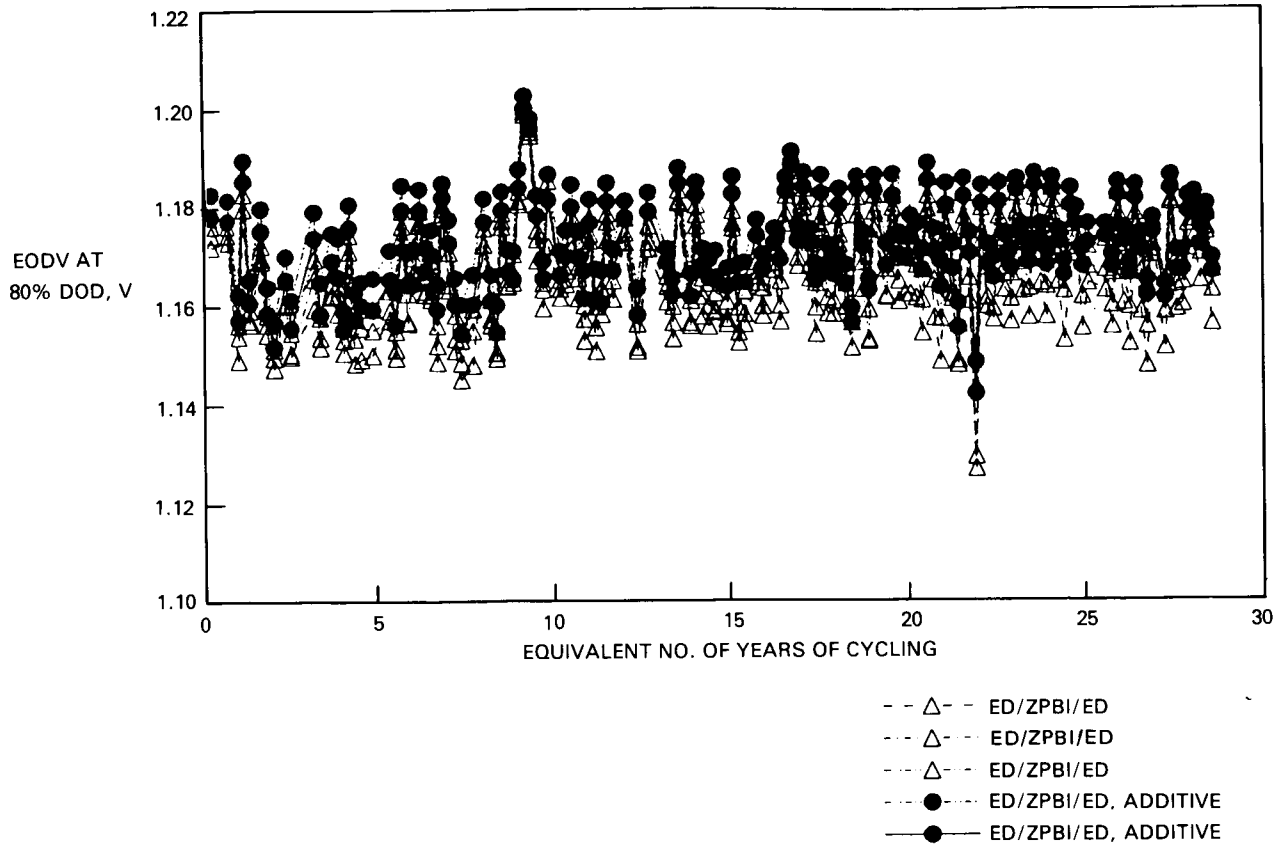

FIGURE 8. EODVs AT 80% DOD IN REGIME I VS CYCLE LIFE FOR THE ADVANCED Ni-Cd CELLS OF TWO DIFFERENT DESIGNS (FILLED CIRCLES AND OPEN TRIANGLES)

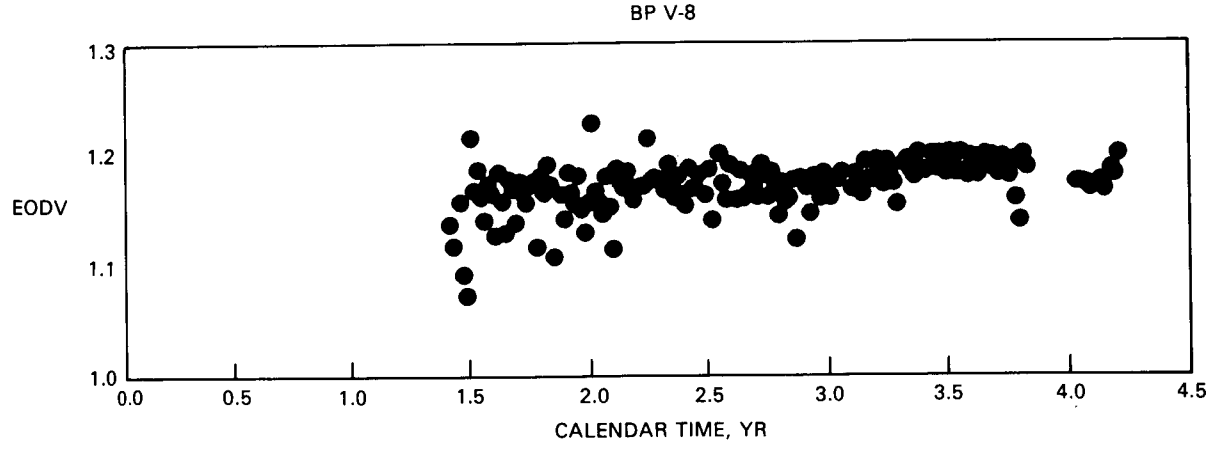

FIGURE 9. EODVs OF A TEST CELL WITH CD NICKEL AND CADMIUM ELECTRODES WITH THE ADDITIVE IN REGIME I VS CALENDAR TIME

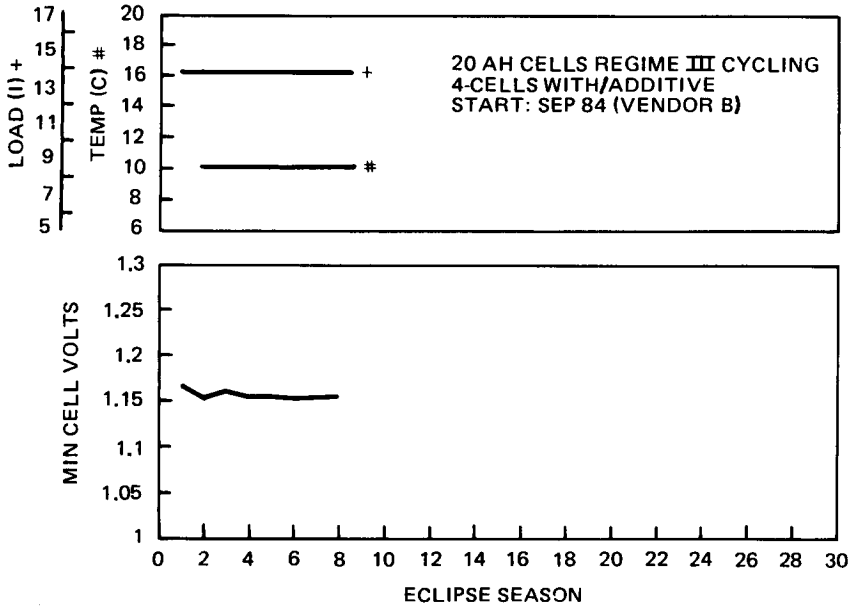

FIGURE 10A. ACCELERATED GEOCYCLE PERFORMANCE OF THIRD INTERATION PROTOFLIGHT CELLS

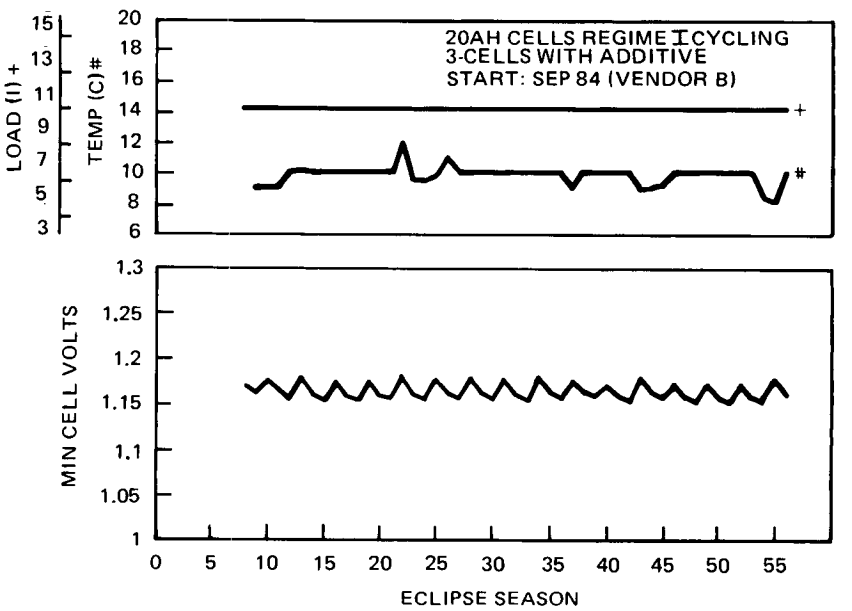

FIGURE 10B. ACCELERATED GEOCYCLE PERFORMANCE OF THIRD INTERATION PROTOFLIGHT CELLS

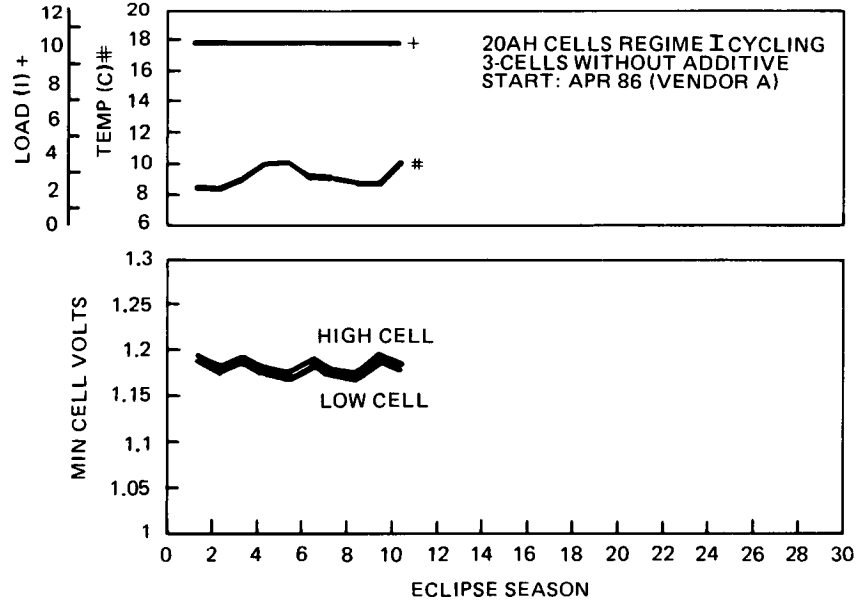

FIGURE 10C. ACCELERATED GEOCYCLE PERFORMANCE OF THIRD INTERATION PROTOFLIGHT CELLS

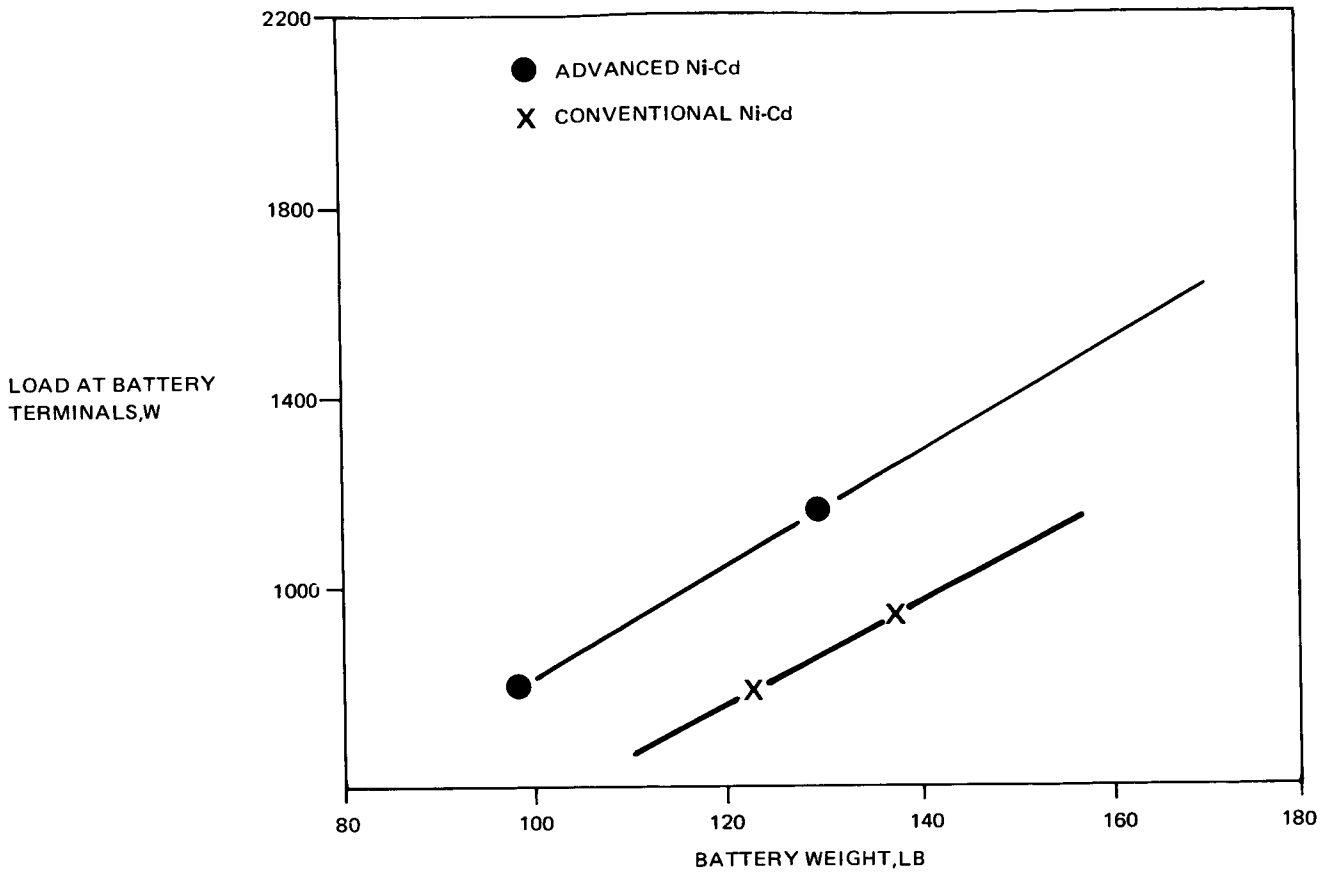

FIGURE 11. BATTERY WEIGHT VS SPACECRAFT POWER COMPARISON FOR ADVANCED AND CONVENTIONAL Ni-Cd

ALUMINUM-OXYGEN BATTERIES FOR SPACE APPLICATIONS

Marilyn J. Niksa and Douglas J. Wheeler
Eltech Systems Corporation
Fairport Harbor, Ohio 44077

An aluminum-oxygen fuel cell is under development at Eltech Systems Corporation. Several highly efficient cell designs have been constructed and tested. Air cathodes catalyzed with cobalt tetramethoxy porphorin have demonstrated more than 2000 cycles in intermittant use conditions. Aluminum alloys have operated at 4.2 kWH/kg at 200 mA/cm^2. A novel separator device, an impeller fluidizer has been coupled with the battery to remove the solid hydrargillite discharge product. A 60-kW, 720-kWH battery system is projected to weigh about 2200 lbs., for an energy density of 327 WH-lb.

INTRODUCTION

Existing secondary batteries suffer from high life cycle costs, short range and acceleration, as well as long recharge times. Eltech Systems Corporation has operated research programs on aluminum-air or oxygen batteries and components since 1980. The ultimate goal of this endeavor is the development of a battery for electric vehicles which will overcome these limitations. The high specific energy density of aluminum-air (300+ WH/lb Al) and power density (26 - 30 W/lb peak) as well as the feature of mechanical rechargeability has made its application to an electric automobile viable and attractive. The battery is returned to its fully charged state by replacement of aluminum into the cell stack, replenishment of the oxygen supply (if necessary), addition of water, and removal of the aluminate discharge product.

The aluminum-oxygen battery releases electric energy by the dissolution of aluminum at the anode and reduction of oxygen at the cathode:

Cathode: $3/4\ O_2 + 3/2\ H_2O + 3e^- \longrightarrow 3\ OH^-$

Anode : $Al + KOH + 3OH- \longrightarrow KAl(OH)_4 + 3e^-$

The electrolyte can be either saline or alkaline, such as potassium or sodium hydroxide. The use of saline electrolyte dramatically limits the power output of the battery due to its low electrical conductivity and the tendency of the electrolyte to become gelatinous with cell discharge. The Eltech system uses an aqueous 5 - 10 molar solution of potassium or sodium hydroxide. As the aluminum discharges it dissolves until a level of saturation is reached. The aluminum then precipitates as hydrargillite:

properly designed electrolyte management system, electrolyte conductivity can be maintained at a high level and the power output of the battery system is not compromised. The reaction product (granular hydrargillite) is then continually discharged or stored and removed periodically.

OXYGEN CATHODES

The heart of the aluminum-air battery is the air cathode. Cathode research at ELTECH has resulted in dramatic improvement of lifetime and performance (Figure 1). This is due to improvements in structure, catalyst, and catalyst support. A major break-through in catalyst stability and life under intermittent use conditions was the development of cobalt tetramethoxy porphorin (CoTMPP) as a replacement for platinum. Extension of cathode life is also due to the development of a two-layer electrode structure. A strong, hydrophobic, conductive wetproof layer of carbon is pressed into a screen current collector. Next, a catalyzed active carbon layer is added. This structure has virtually eliminated loss of mechanical integrity and flooding as modes of electrode failure. In addition to the two-layer structure, air cathodes have been custom fabricated to meet specific performance targets.

ANODE DEVELOPMENT

Commercially available aluminum is not adequate for this application due to its very high corrosion rate in the alkaline electrolyte. Much work has been devoted to the optimization of aluminum alloys (1-5). ELTECH has developed and/or tested a variety of proprietary alloys which have demonstrated very high power densities and energy yields (Figure 2). It can be seen that one alloy, BDW has a specific energy of 4.2 kWH/kg at 200 mA/cm^2 and a power density of 0.6 W/cm^2. In lieu of adding the alloying agents in situ, corrosion inhibitors and potential boosters are effective when added directly to the electrolyte. It was found that addition of small amounts of $In(OH)^3$ and Ga_2O_3 directly to the electrolyte reduced corrosion and polarization of a five nines pure aluminum anode.

CELL DESIGN AND TESTING

With anode and cathode performance characteristics well within range of target values, the integration of these into a functioning aluminum-air prototype cell progressed rapidly. The first testing was done on the "wedge" type cell (Figure 3). This prototype has operated routinely at a peak power of 440 watts and 1.15 volts per cell module. A 10 cell stack or 4.4-kW unit has recently been installed in a small vehicle and successfully operated as the main traction power source.

Several new battery designs are now in the prototype stage. Unlike the wedge cell these units are insensitive to changes in orientation, are sealed against electrolyte leakage, and can be

manufactured by mass-production methods. Both designs are bipolar and have substantially reduced weight and volume. Multi-stack testing is expected to commence in several months.

SYSTEM INTEGRATION

The process system for the aluminum-air battery is shown in Figure 4. Air or oxygen is provided to the cell in cryogenic or compressed form. The caustic electrolyte is recirculated to provide for optimum battery output and thermal management. Circulation and separation of the aluminate discharge product is provided by a novel device, an impeller fluidizer. This device (Figure 5) separates, contacts, and pumps the solid/liquid electrolyte. A locally confined fluidized bed of fine particles is dynamically held within the vessel by the interaction of centrifugal force and convection, both produced by an impeller-driven swirling flow. Clear electrolyte stripped of solid discharge product is returned to the battery stack while a highly concentrated solids containing stream is stored for removal at a later date.

The importance of solids removal from the electrolyte which is returned to the battery stack is shown in Figure 6. As solids build up in the stream, the electrolyte conductivity is compromised and the battery voltage is reduced.

BATTERY PERFORMANCE PROJECTIONS

Projections of cell performance can be made based on polarization and electrolyte conductivity generated at ELTECH. A high performance air cathode coupled with an RX808 anode using a stannate inhibitor in a 5 M KOH electrolyte at 60 deg. centigrade is shown in Figure 7. As can be seen, the cell voltage is in excess of one volt even at current densities of 1.2 A/cm^2.

Projections of size and weight of a battery system can be made based on pilot cell testing. The following gives an estimate of the size and weight of a 60 kW battery operated continuously for 12 hours:

Reactants	Weight (lbs)	FT3
Aluminum	600	3.6
Oxygen	600	*
H_2O	600	9.5
Process equipment	400	10.0
TOTAL	2200	23.1 *
WATT-HOURS/ POUND:	**327**	

* Oxygen form not specified

The power density of the aluminum-oxygen system is sensitive to the requisite power rating and larger battery systems have higher energy and power densities (Figure 8).

CONCLUSIONS

The aluminum-oxygen battery system is in the prototype stage at ELTECH Systems Corporation. Cell performance projections indicate that cell voltages in excess of one volt can be obtained at a current density of 1.2 amps/cm^2.

Figure 1

AIR CATHODE IMPROVEMENTS

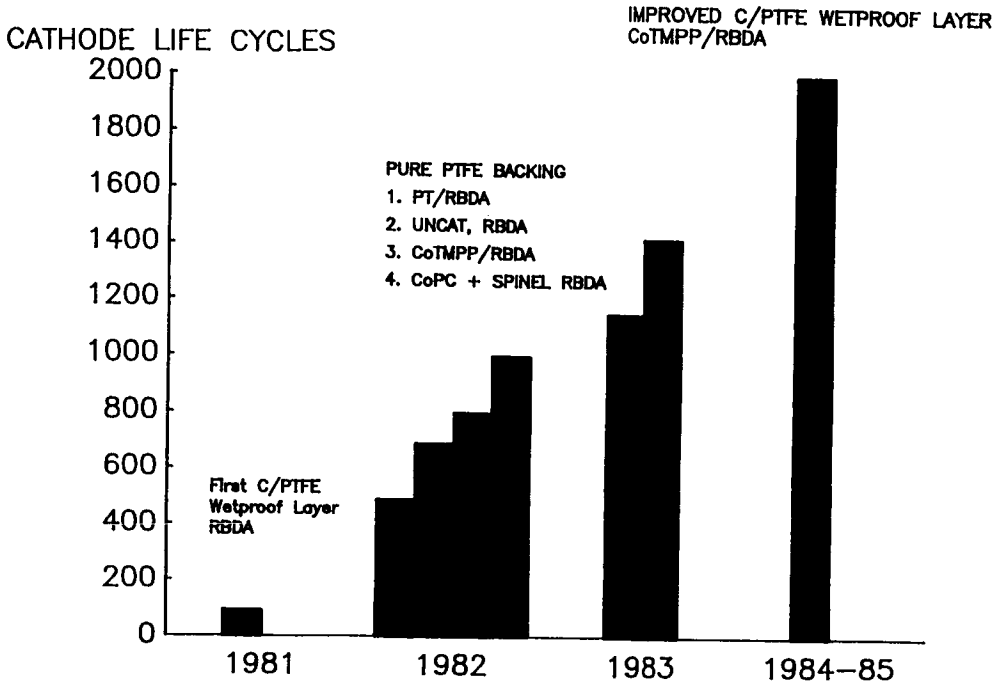

Figure 2

ENERGY YIELD vs. C.D.

AL ALLOYS

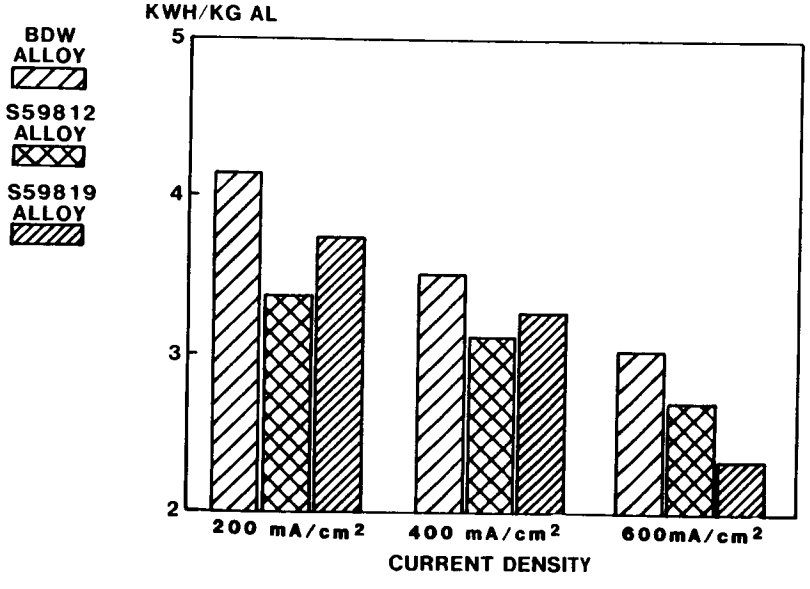

C-2

Figure 3
WEDGE CELL
5-CELL STACK

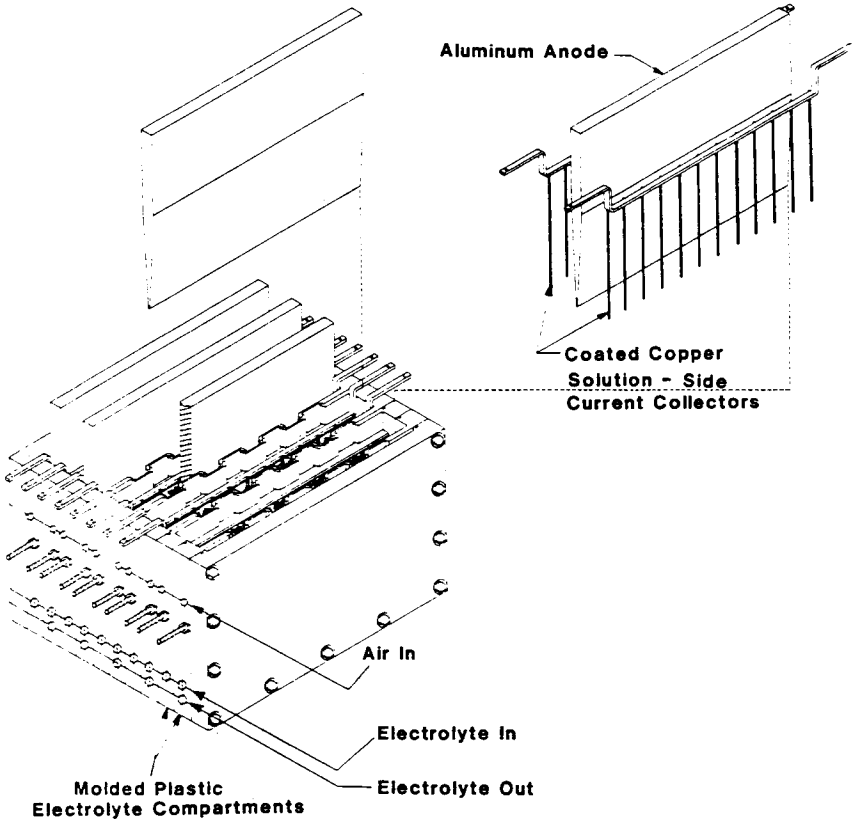

Figure 4
Al/Air Battery System

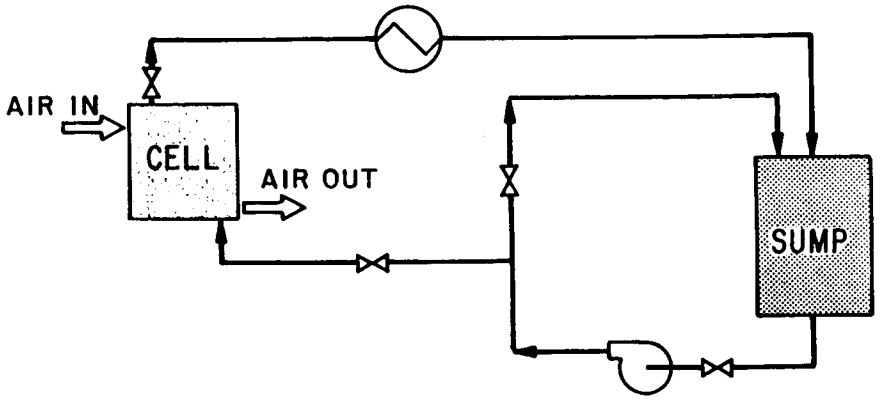

Figure 5
Helipump Impeller Fluidizer

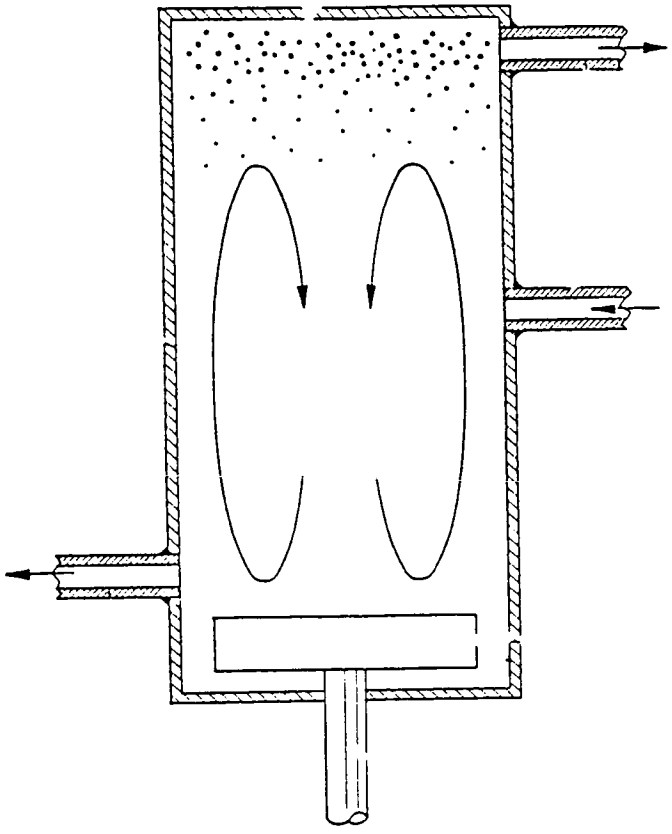

Figure 6

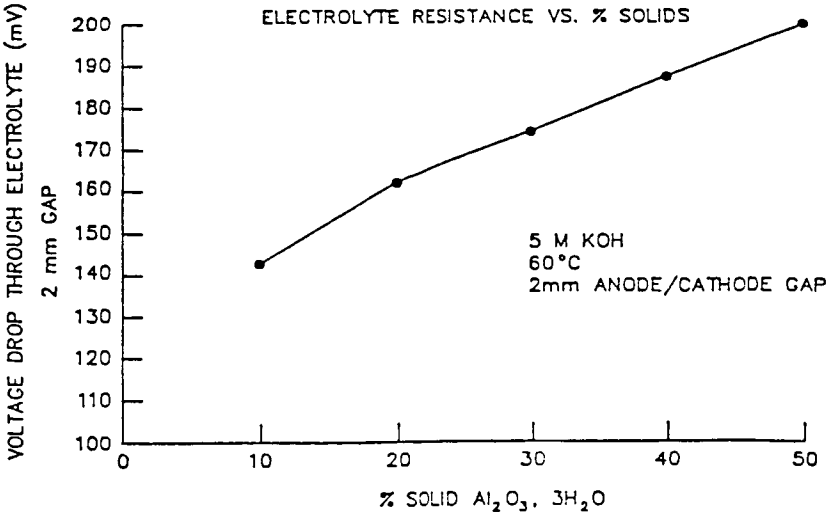

Figure 7

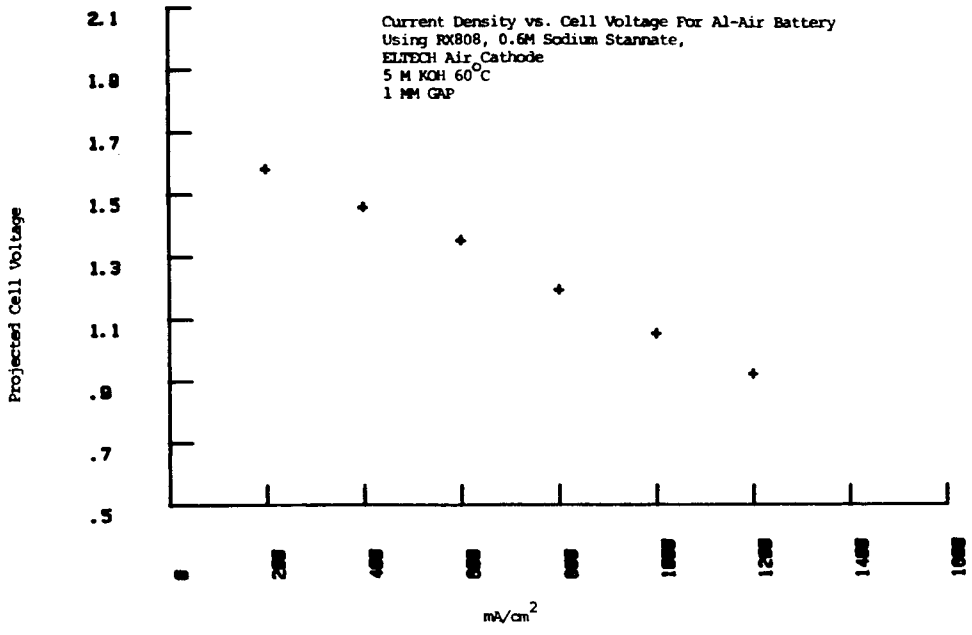

Figure 8

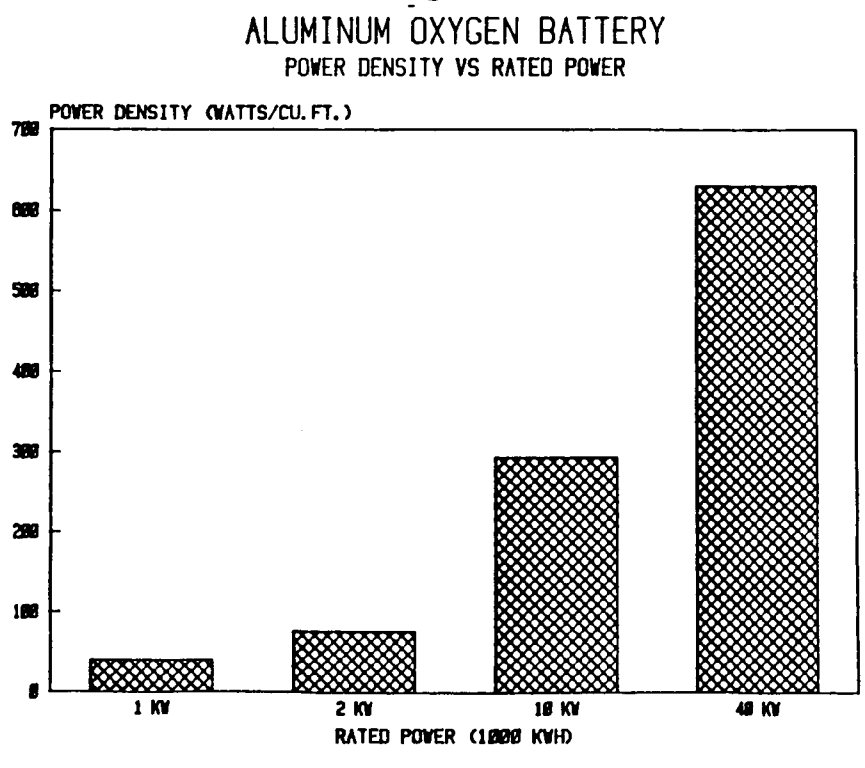

DEVELOPMENT OF AMBIENT TEMPERATURE SECONDARY LITHIUM CELLS

S. Subbarao, D.H. Shen, S. Dawson, F. Deligiannis,
J. Taraszkiewicz, and G. Halpert
Jet Propulsion Laboratory
California Institute of Technology
Pasadena, California 91109

Under a NASA-OAST sponsored program, JPL is developing ambient temperature secondary lithium cells for future spacecraft applications. Prior studies on experimental laboratory type Li-TiS_2 cells yielded promising results in terms of cycle life and rate capability. To further assess the performance of this cell, 5Ah engineering model cells were developed. Initially baseline cells were designed and fabricated. Each cell had 15 cathodes and 16 anodes and the ratio of anode to cathode capacity is 6:1. A solution of 1.5 molar $LiAsF_6$ in 2Me-THF was used as the electrolyte. Cells were evaluated for their cycle life at C/2 and C/5 discharge rates and 100 percent depth of discharge. The cells were cycled between voltage limits 1.7 and 2.8 volts. The rate of charge in all cases is C/10. The results obtained indicate that cells can operate at C/10 to C/2 discharge rates and have an initial energy density of 70 Wh/kg. Cells delivered more than 100 cycles at C/2 discharge rate. This paper describes the details of cell design, the test program, and the results obtained.

INTRODUCTION

Under a NASA OAST sponsored program, Jet Propulsion Laboratory is developing ambient temperature secondary lithium batteries for future space applications. These lithium batteries have a number of intrinsic and potential advantages such as higher energy density, longer active shelf life, lower self discharge etc. over conventional Ni-Cd, Pb-acid and Ag-Zn batteries. The main objective of the program is to demonstrate the feasibility of developing cells with greater than 100 Wh/kg specific energy while delivering 1,000 cycles at moderate depths of discharge (60-70%). The program pay-offs are 2-3 fold increase in energy storage capability and a longer active shelf life over Ni-Cd and Ni-H_2. Some of the projected applications of these batteries are for Mars Rover, planetary space craft/probes, astronaut equipment, and GEO spacecraft. To achieve these ambitious goals, we have examined the performance potential of Li-TiS_2, Li-MOS_3 and Li-V_6O_{13} systems in detail. Among these three, the Li-TiS_2 system has shown the longest cycle life and highest rate capability. Experimental five cell Li-TiS_2 batteries (10.5V, 0.4Ah), developed in-house, have completed twelve simulated and accelerated GEO seasons successfully (1). These encouraging results prompted us to assess the performance capability of the Li-TiS_2 system in engineering model 5Ah cells. This study will serve as an intermediate step before

building prototype flight 20-35Ah cells. Development of 5Ah cells is proposed to be completed by 1989. In this paper we report the results of our preliminary work done on the development of baseline SOA 5Ah cells.

CELL DESIGN

The computer program, developed earlier (2) for the design trade-off studies of 35Ah Li-TiS_2 cells was used in the selection of a design for the 5Ah baseline engineering model cells. Some of the important design features of the cell are given in Table 1. The TiS_2 cathode is the limiting electrode and ratio of anode to cathode capacity is 6:1. This high anode to cathode capacity was chosen to accommodate the degradation of Li electrode and achieve maximum cycle life. Results of the design trade-off analysis indicate that the capacity ratio has minimal effect on specific energy of the cells (Table 1). The operating current density of the cell at C/2 discharge rate was 2 mA/cm^2. Operation at current densities higher than 2 mA/cm^2 is limited by the poor conductivity of the electrolyte. The cell contains 15 TiS_2 cathodes and 16 Li anodes. Celgard 2400, a porous polypropylene film, was chosen as the separator material. The composition of the electrolyte is 1.5M $LiAsF_6$/2Me-THF and each cell is activated with 40 cc of electrolyte. This electrolyte quantity is designed to fill the internal void volume of the electrodes, and separator, and other minor cell void spaces. The cell weighs approximately 230 grams, and the weight budget is given in Figure 1. It may be noted that the cell can is the major contributor to cell weight. Among the active materials, Li contributes the least to the overall weight. The collector grids contribute more to the weight than does lithium alone. The use of titanium cases and aluminum grids will reduce cell weight considerably.

TiS2 CATHODE DEVELOPMENT

The suitability of various processing methods such as brushing, pressing, and rolling have been examined in the fabrication of TiS_2 cathodes with EPDM binder. The brushing method even though simple, was not found suitable for making large electrodes. Considerable problems were encountered in making electrodes by the pressing method due to poor flow characteristics of the electrode active material. The rolling method on the other hand, offered many advantages such as amenability to scale-up, uniform loading, incorporation of integral tabs, etc.

The TiS_2 electrodes required for 5Ah baseline cells were fabricated by the rolling method and the details of processing are given in Figure 2. TiS_2, the active material of the cathodes, was processed in-house by a vapor transport method involving a chemical reaction between titanium and sulphur. This material had a stoichiometry of $Ti_{1\pm0.1}S_2$. The approximate composition of electrode material is 86% TiS_2, 10% conducting diluent and 4% binder. Shawinigan black was chosen as the conducting diluent in view of it's chain-like structure, high conductivity and purity (3). EPDM was used as the binder material. The binder was dissolved in cyclohexane (1%) and added to TiS_2 and carbon mix. Excess solvent was removed by vacuum extraction. The resulting material was ground to a fine powder and applied onto a nickel exmet screen by rolling. Electrode active material preparation was carried out in an argon atmosphere chamber. The electrode processing was done in a dry room (humidity less that 0.5%).

Master electrodes (6" x 6" x 0.02") were fabricated and cut into required dimensions. The porosity of the electrodes is about 35 to 40% and the active material loading is 75± 5mg/cm^2. The surface area of the electrodes is about 12M^2/gm. These electrodes have exhibited more than 90% faradic utilization initially in experimental cells (150mAh) and yielded more than 200 cycles (100% DOD) with only 20% loss in capacity.

RESULTS AND DISCUSSION

Baseline engineering model cells were evaluated for their charge/discharge characteristics, rate capability, and cycle life. Cells were charged by constant current method at C/10 rate to 2.7V. Cells were discharged at different rates to a cutoff voltage of1.7V. Charge discharge characteristics of the cell at C/10 rate are given in Figure 3. The cell exhibits sloping charge/discharge curves which are typical for the intercalation cathodes. Discharge characteristics of the cell at C/10, C/5, and C/2 rates are given in Figure 4. At the C/10 rate cells delivered approximately 7.8Ah which is roughly equivalent to 100% capacity. Energy density of the cells at this rate is found to be about 75 wh/kg. At C/2 discharge rate, cells have exhibited approximately a capacity of 6Ah. Cells were evaluated for their cycle life characteristics at C/5 & C/2 discharge rates to 100% DOD. The capacity of the cells as a function of cycle number is given in Figure 5. The cells were found to lose capacity upon cycling. The impedance of cells was also found to increase on cycling. The cells cycling at C/2 lost approximately 0.05Ah/cycle and by the end of 100th cycle cells delivered only about 3Ah. Surprisingly the cells cycling at C/5 discharge rate failed at about 60 cycles. Probably, the cells developed "soft-shorts" as revealed by longer charge periods. Similar problems were encountered (soft shorts) while testing commercial secondary Li cells at low discharge rates (4). The low cycle life performance of the 5Ah baseline cells may be due to electrolyte degradation, starved electrolyte condition, processing of cells in the dry room, non-optimized cell design, or charge methodology. We are in the process of evaluating and optimizing these parameters. Cells with optimized design will be built and tested for their performance and safety and we are anticipating to complete this work by the end of 1989.

FUTURE DIRECTIONS

A number of areas are under investigation to improve the energy density and the cycle life performance of secondary Li cells. Some of the major areas are high energy density cathode materials, high performance electrode structures, stable electrolytes, design optimization, and improved charge methodology. Among various cathode materials, $NbSe_3$ appears promising and its performance potential is being assessed in experimental cells. The limited cycle life capability of rechargeable lithium cells is mainly due to the high reactivity of lithium with the electrolyte. A number of mixed solvent electrolytes are currently being evaluated for conductivity, viscosity, stability towards lithium and lithium cycling efficiency. Pulse charging and modified constant current charging methods will be examined to improve cell performance. We are planning to complete these activities by 1992 and build prototype cells for flight qualification.

ACKNOWLEDGEMENTS

This work represents one phase of research performed by the Jet Propulsion Laboratory, California Institute of Technology sponsored by the National Aeronautics and Space Administration under contract NAS-7-918.

REFERENCES

1 B. Otzinger, 1984 GSFC Battery Workshop, NASA Conference Publication 2382, 1985, pg. 95.

2 D.H. Shen, S. Subbarao, S.P.S. Yen and R.B. Somoano, Journal of Power Sources, 18 (1986) 127-131.

3 D.H. Shen, S. Subbarao, S.P.S. Yen, B.J. Carter and R.B. Somoano, ECS Extended Abstracts, 84-2, 1984, pg.190.

TABLE I. - INFLUENCE OF ELECTRODE CAPACITY RATIO ON SPECIFIC ENERGY

ANODE TO CATHODE CAPACITY RATIO	SPECIFIC ENERGY (Wh/Kg)
5.5	58.2
5.0	58.4
4.0	58.8
3.0	59.3
2.0	59.8
1.0	60.3

TABLE II. - OUTLINE OF 5-Ah Li-TiS_2 CELL DESIGN

1)	THEO. ANODE CAPACITY (Ah)	= 38.5
2)	THEO. CATHODE CAPACITY (Ah)	= 6.6
3)	ELECTRODE CAPACITY RATIO	= 5.8:1
4)	NO OF ANODES (2.75"*2.5"*.014")	= 15
5)	NO OF CATHODES (2.75"*2.5"*.025")	= 14
6)	CURRENT DENSITY (mA/cm2)	= 2.0
7)	ELECTROLYTE (1.5M LiAsF6/2Me-THF)	= 40
8)	CELL WEIGHT (g)	= 230
9)	CELL DIMENSIONS (in)	= 2.78*4*.98

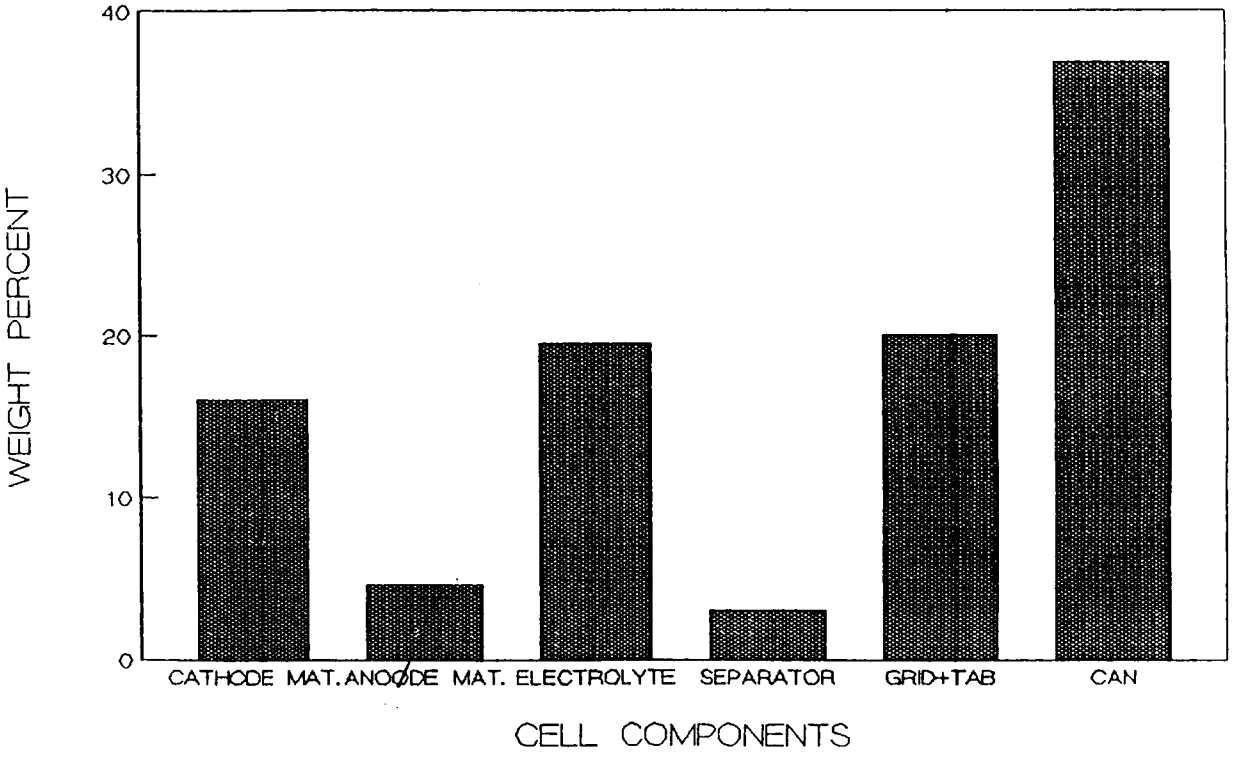

Figure 1. - 5-Ah Li-TiS_2 cell weight budget.

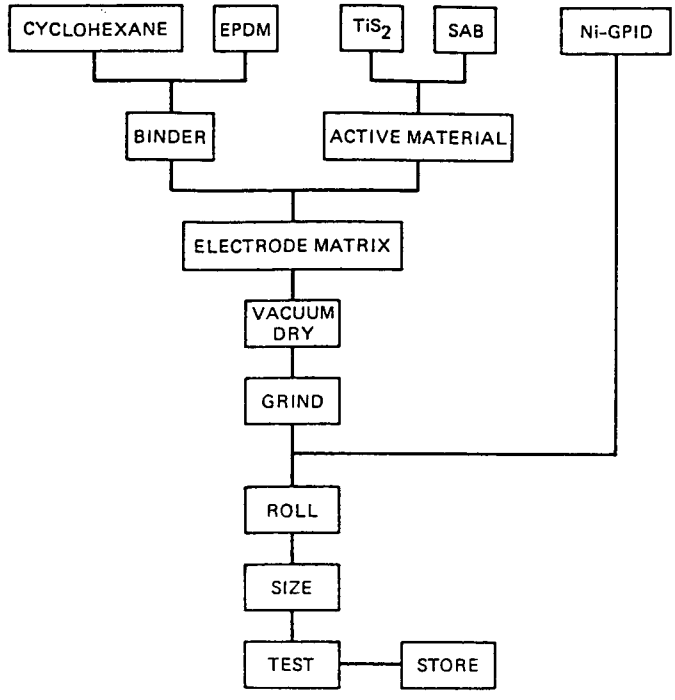

Figure 2. - TiS_2 electrode process.

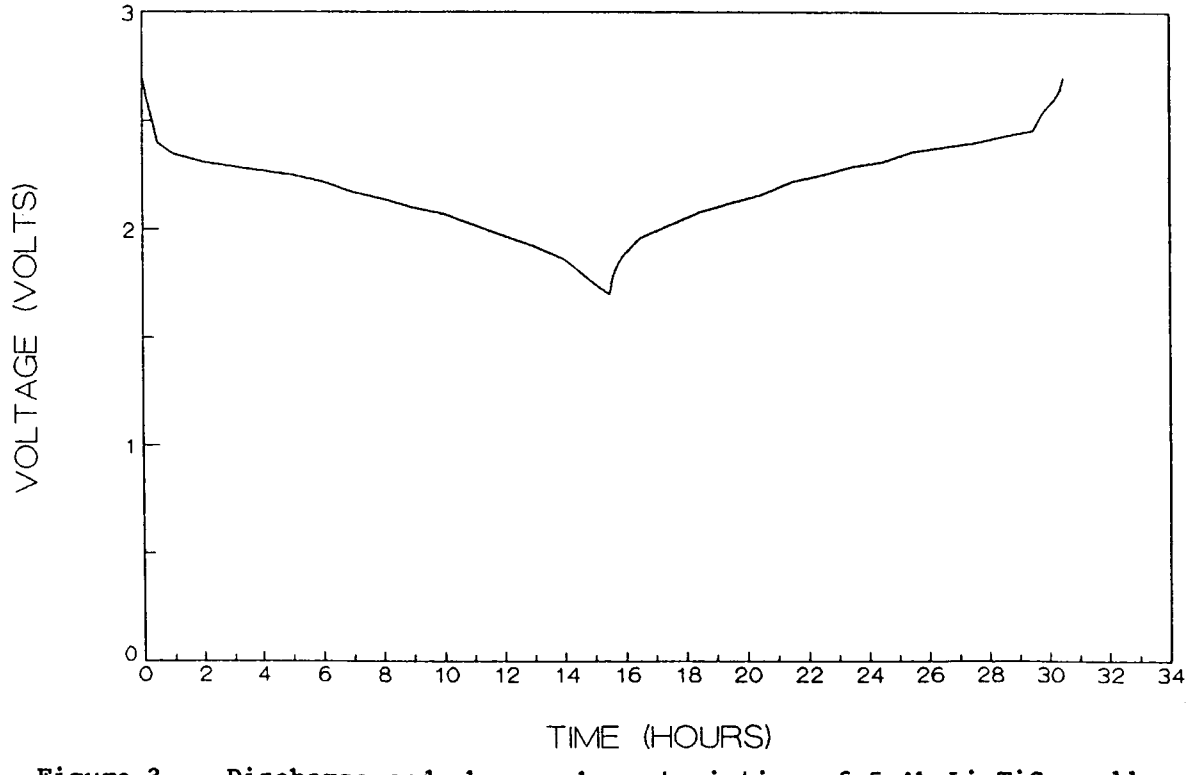

Figure 3. - Discharge and charge characteristics of 5-Ah Li-TiS_2 cells.

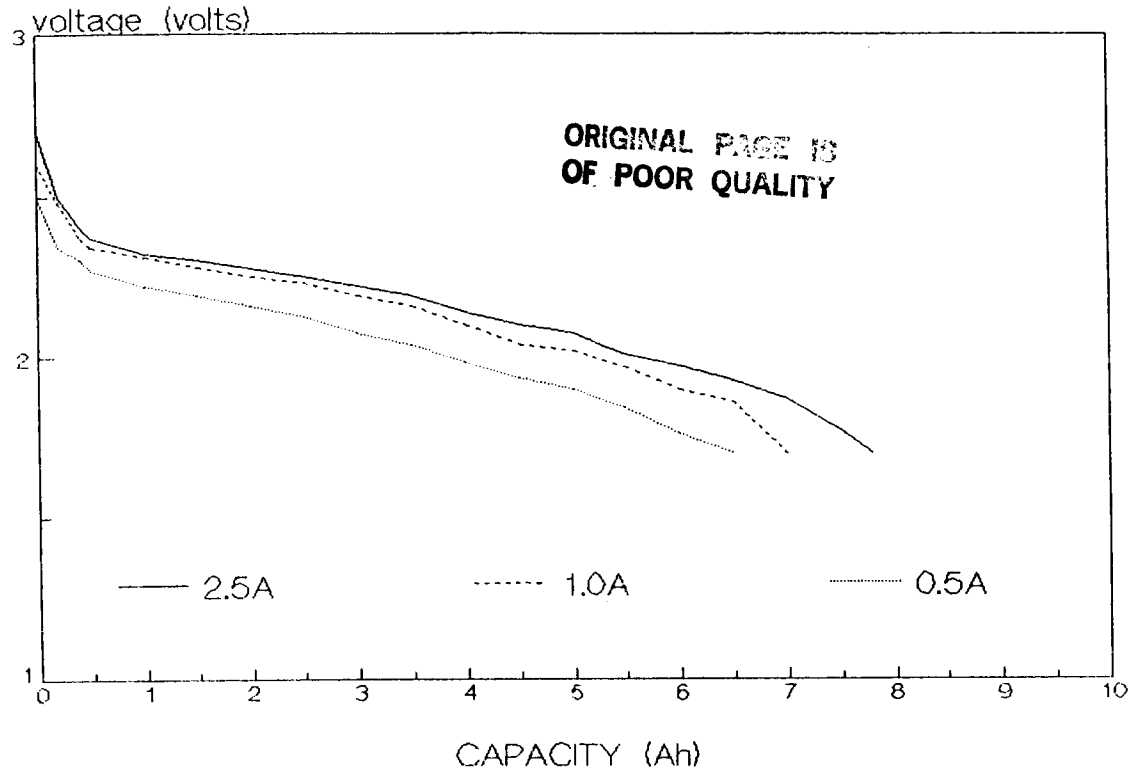

Figure 4. - Discharge characteristics of 5-Ah Li-TiS_2 cells.

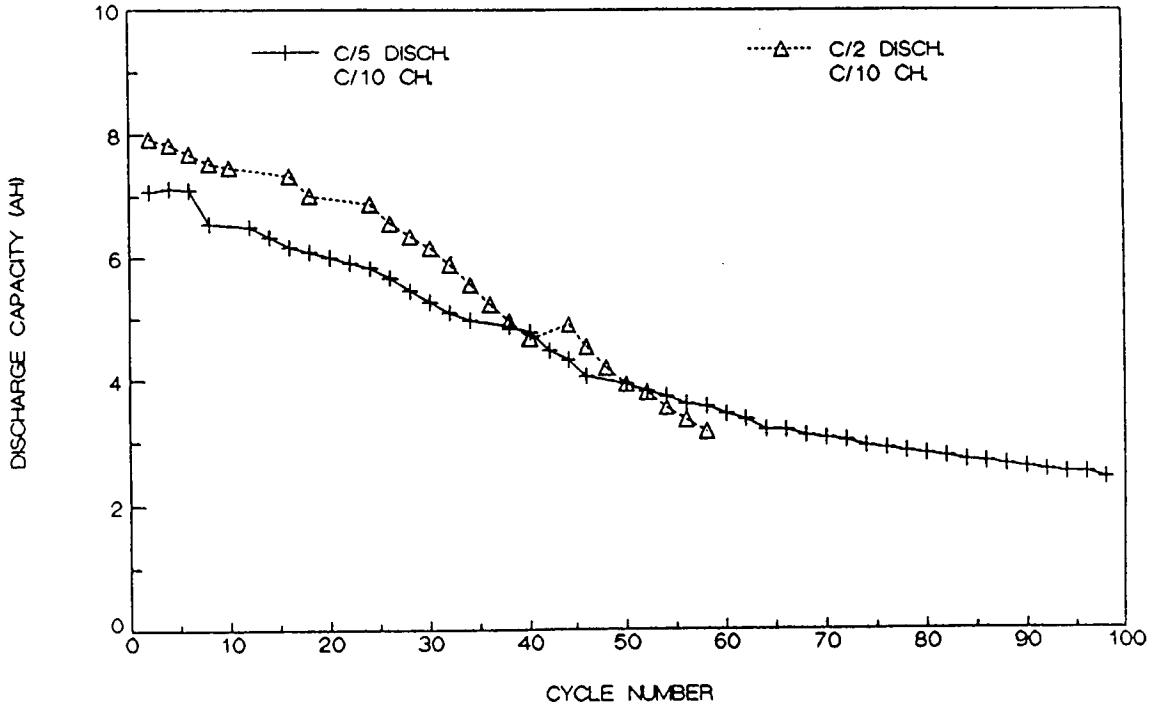

Figure 5. - Cycling characteristics of JPL 5-Ah Li-TiS_2 cells.

DEVELOPMENT OF LITHIUM-THIONYL CHLORIDE BATTERIES FOR CENTAUR

Gerald Halpert, Harvey Frank, and Ralph Lutwack
Jet Propulsion Laboratory
California Institute of Technology
Pasadena, California 91109

Lithium-thionyl chloride ($Li-SOCl_2$) primary cells and batteries have received considerable attention over the last several years because of their high theoretical specific energy and energy density. The development of the technology has been supported by the NASA Hq., Office of Aeronautics and Space Technology at the Jet Propulsion Laboratory for the past several years. The objective is to develop a 300 wh/kg cell capable of safe operation at C/2 rate and active storage life for 5 to 10 years. This technology would replace other primary cell technologies in NASA applications mainly the silver-zinc (Ag-Zn) batteries presently in use. The $Li-SOCl_2$ system exceeds the capabilities of the Ag-Zn in terms of specific energy of 300 wh/kg (compared with 100 wh/kg for Ag-Zn), active storage life of 10-20 times the 3-6 months active storage and has a significantly lower projected cost.

During the course of the NASA development effort, the Air Force/Space Division (AF/SD), was struggling with a significant weight problem for its CENTAUR vehicle. The progress in the JPL development, in which cells produced in-house exceeded the goals listed above, was noticed by the AF/SD. A back of the envelope calculation projected a weight savings for the CENTAUR of more than 250 lbs. (100 Kgs) for the batteries required to meet CENTAUR mission goals. The result was a 3 year AF/SD contract with JPL to develop $Li-SOCl_2$ 150Ah and 250Ah cells and batteries for this application. The effort was to be a cooperative effort between JPL and cell/battery manufactures to meet the AF requirements. This paper will describe the present activities and status of the program with some of the findings to date.

In introducing the subject, it is interesting to note that there are a number of applications in space activities for primary batteries. Among these are space transportation systems; including astronaut backpacks, portable equipment and deployable instruments, transportation vehicles; Centaur, crew escape vehicle, or orbit transfer vehicle and IUS, and most importantly for planetary deep space, probes penetrators balloons and landers. The common denominator, is high specific energy, high volume energy density, long activated shelf life and high discharge rate capability.

The history of the $LI-SOCl_2$ development program at JPL is given in Figure 1. Although some work was done prior, the serious cell design activities started in the early 80's. The result as can be seen is the demonstration of cylindrical and prismatic cell designs resulting in the demo of a 330 wh/kg "D" size cell operated at the 5 amp (C/2) discharge rate. A prismatic 20Ah cell was assembled and tested, achieving 280 wh/kg at the C/4 rate narrowly missing the design goals.

The objectives of the A.F./S.D. effort are given in Figure 2. The program involves a coordinated contractor/JPL effort to produce prototype 150 & 250AH cells and batteries hardware and a design package described as a Manufacturing Control Document (MCD) available for procurement. The in-house work at JPL would involve analysis, cathode enhancement, and quality.

Figures 3 and 4 from General Dynamics provide a schematic view of the CENTAUR and the battery location. There are 6-8 batteries necessary for the power requirements: Figure 5 is a comparison of the present Ag-Zn battery and the projected LI-$SOCl_2$ battery. The weight savings of more than 50% is indicated. The volume savings is also substantial. The LI-$SOCl_2$ battery will have to occupy the same footprint and therefore be lower in height. The difference is due to the lower number of cells 9 vs. 19 cells because of the cell voltage of 3.4 V compared to silver-zinc of 1.5 V/cell. It is also due to the difference in specific energy.

Figure 6 includes a power usage scenario projected to the mission. The 80 amps pulse at a 40A average required for the battery are consistent with the 150 Ah and 250 Ah requirements.

One of the areas of interest is the cathode structure. JPL LI-$SOCl_2$ "D" cells have exceeded the performance at high rates of existing LI-$SOCl_2$ cell. We believe the basis is the high performance cathode. The baseline cathode data is given in Figure 7. The range of current density required in this application is 1-5 ma/cm^2. This indicates that 1.5 Ah/gm utilization of the cathode is required. The behavior of voltage at this rate must be minimized in order to reduce heat dissipation problems. We have shown that the projected voltage is 3.3 $\pm$1 volts which is quite satisfactory. Projected improvements in cathode design could result in a specific energy of 40 wh/kg at the 100% utilization level shown in Figure 8.

The electrode thickness is being modeled also to optimize specific energy, minimize polarization and capacity. Figure 9 gives the relationship between plate thickness and specific energy. The indication is there is a maximum at 30 mils if the grid design and thickness is constant. Obviously, if the plate thickness was reduced the grid would also have to be modified thus altering the shape of this curve.

The initial internal cell design is given in Figure 9, in which the materials and component size and weight are given. The projected overall mass for a 150Ah cell based on the JPL 20 Ah prismatic cell is given in this figure. The battery mass utilizing 9 of these cells is given in figure 10. The resultant design including a 1.2 factor for battery mass indicates a 55% weight savings.

In summary, the task initiated in October 1987, is a coordinated contractor (probably 2)/JPL effort to develop 150 & 250 Ah cells and batteries to reduce the CENTAUR battery weight by 50%. The contract effort is expected to start in early May. The result will be a design package with drawings and QA/QC to produce batteries for the CENTAUR application.

The authors acknowledge the support of Steve Dawson, Jack Rowlette and David Shen in this effort.

FIGURE 1

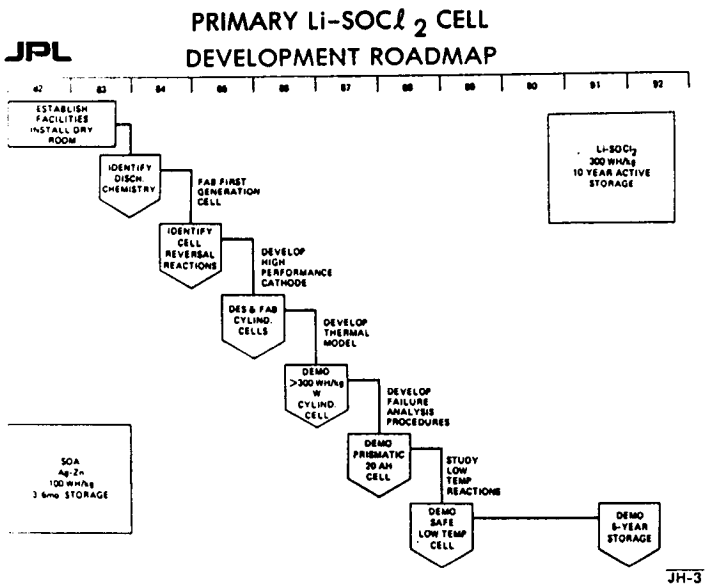

FIGURE 3 SCHEMATIC OF CENTAUR

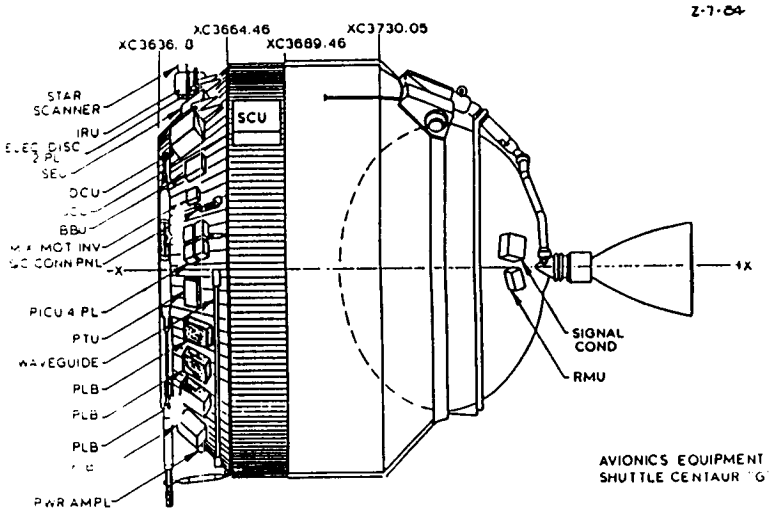

FIGURE 2

JPL

CENTAUR Li-SOCl$_2$ BATTERY TASK
OBJECTIVE/APPROACH

- OBJECTIVE
  - DEVELOP PROTOTYPE 150AH AND 250AH Li-SOCl$_2$ BATTERIES FOR CENTAUR WITH DOCUMENTATION WITHIN 3 YEARS
  - A PRINT PACKAGE READY TO FABRICATE
  - MUST BE SAFE
  - WEIGHT GOAL IS 50% OF EXISTING Zn-AgO BATTERY WEIGHT
- APPROACH
  - CO-ORDINATED JPL-CONTRACTOR EFFORTS
  - CONTRACTOR DEVELOP HARDWARE UNDER JPL DIRECTION
  - JPL CONDUCT INDEPENDENT DESIGN AND ANALYSES TO CRITIQUE, SUPPORT, AND ENHANCE CONTRACTOR DESIGN AND R & QA
  - JPL ALSO CONDUCT VERIFICATION AND SAFETY TESTS ON COMPONENTS AND CELLS
  - SOME CATHODE DEVELOPMENT AT JPL AND CONTRACTOR CENTAUR Li-SOCl$_2$ BATTERY TASK

FIGURE 4 CROSS SECTIONAL VIEW OF CENTAUR

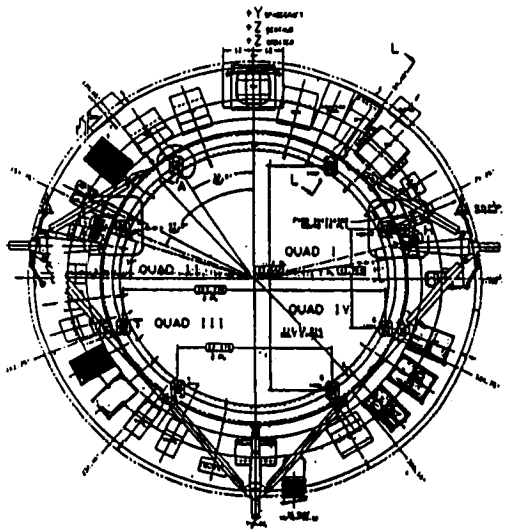

CENTAUR 'G', FWD ADAPTER PRELIM EQUIP ARRGMT

FIGURE 5 COMPARISON OF Ag-Zn AND Li-$SOCl_2$ BATTERIES

JPL

150AH CENTAUR BATTERY

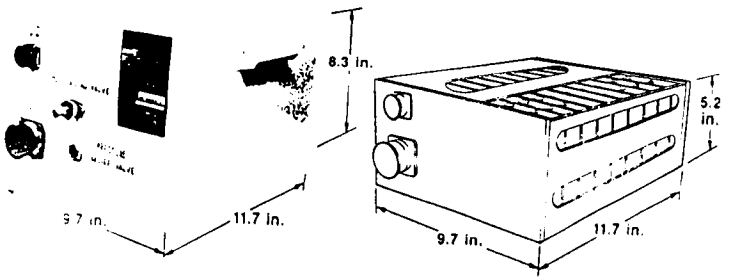

SILVER-ZINC
(STATE-OF-THE-ART)

19 CELLS
28 V NOMINAL (1.5 V/cell)
85 lbs

LITHIUM THIONYL CHLORIDE
(JPL TECHNOLOGY)

9 CELLS
28 V NOMINAL (3.4 V/cell)
< 40 lbs

FIGURE 6 POWER SCENARIO FOR CENTAUR LAUNCH

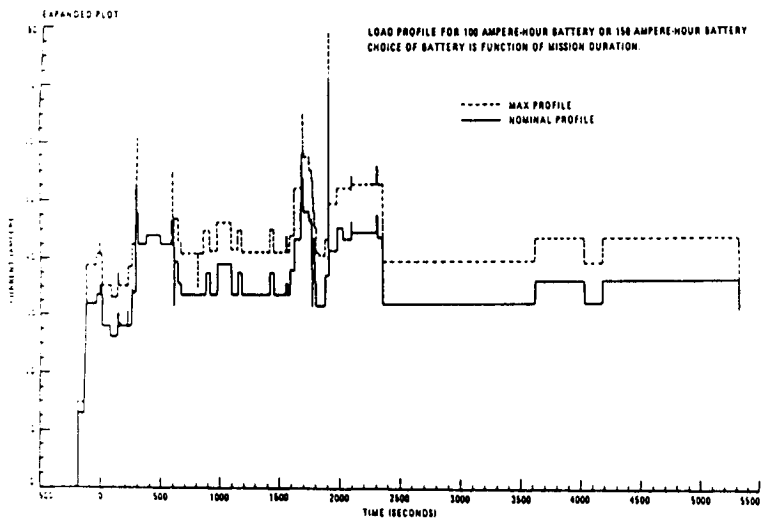

FIGURE 7

JPL

CENTAUR Li-$SOCl_2$ BATTERY TASK BASELINE CATHODE DATA

CURRENT DENSITY (mA/cm^2)

	0.1	1	10	100
CAPACITY (AH/G)	3.1	2.2	1.3	0.5
MID POINT POTENTIAL (VOLTS)	3.50	3.30	3.04	1.50

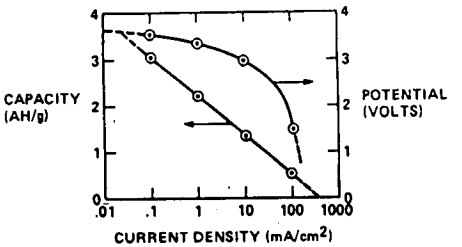

FIGURE 8

DEPENDANCE OF SPECIFIC ENERGY ON CATHODE UTILIZATION

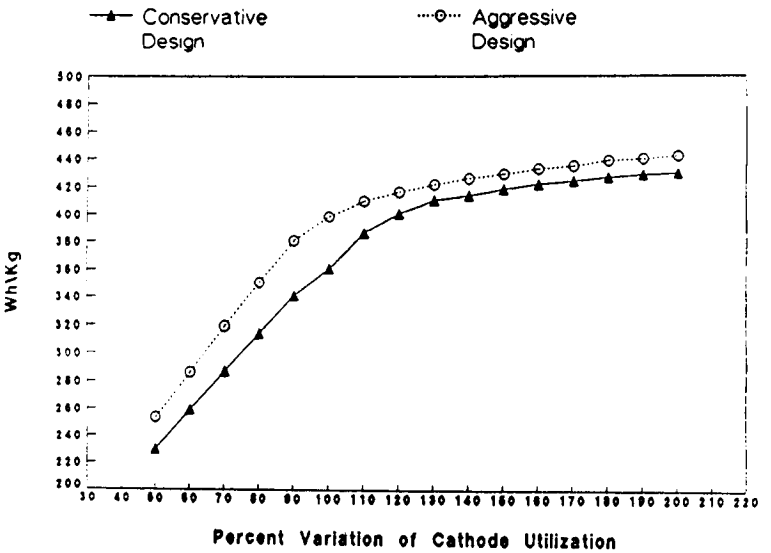

FIGURE 9

JPL

LITHIUM - THIONYL CHLORIDE BATTERIES FOR CENTAUR

OPTIMIZED BATTERY PROJECTION

- CELL WEIGHT ..... 1.68 KG (3.69 LBS)
- NO. OF CELLS /BATTERY 9
- WEIGHT FOR 9 CELLS..... 15.1 KG (33.2 LBS)
- ESTIMATED PACKAGING WEIGHT..... 3 KG (6.6LBS)
- PROJECTED BATTERY WEIGHT..... 18.1 KG (39.8 LBS)
- EXISTING AG-ZN BATTERY WEIGHT..... 38.6 KG (85 LBS)
- PROJECTED WEIGHT REDUCTION..... 53 %

FIGURE 10

JPL

CENTAUR Li-$SOCl_2$ BATTERY TASK
POINT DESIGN FOR A 150 AH CENTAUR CELL
BASED ON JPL 20 AH CELL

ITEM	MATERIAL	L,cm.	W,cm.	t,cm.	#	Wt,gm
Anode	1) Li	11.80	12.00	0.10	29	61.3
	2) Ni,Exp.	11.80	12.00	0.02	29	101.8
	3) Tab			0.02		7.4
Cathode	1) C,80% Por	11.80	12.00	0.10	30	128.2
	2) Teflon Binder					14.1
	3) Ni, Exp	11.80	12.00	0.02	30	105.0
	4) Tab			0.02		7.4
Separator	Glass Mat	11.80	12.50	0.0076		41.2
Electro-lyte	$SOCl_2$					788.2
Case (out-side)	SS,304L	13.80	13.10	5.05*		402.4
Cover	SS,304L					20.0
						1677.0

* Outside Dimension, can wall thickness = 0.078 cm

FIGURE 11

DEPENDANCE OF SPECIFIC ENERGY ON CATHODE THICKNESS

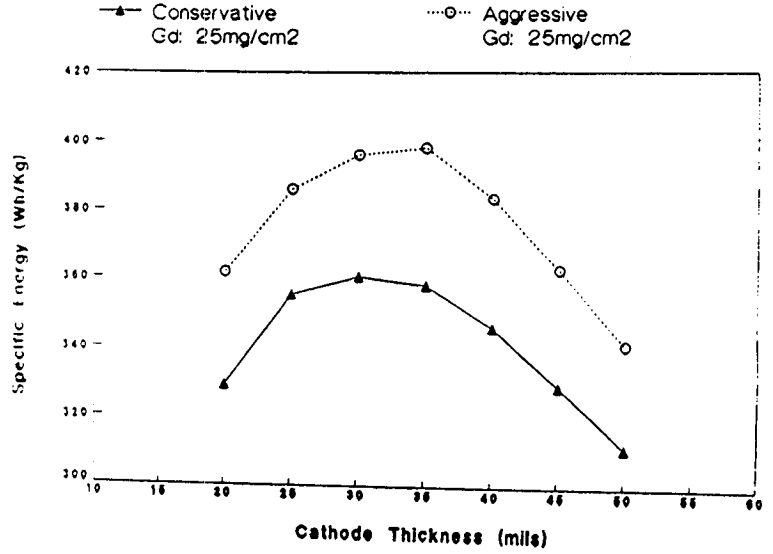

Na/BETA"-ALUMINA/$NaAlCl_4$, Cl_2/C CIRCULATING CELL

Jing-Yih Cherng and Douglas N. Bennion
Brigham Young University
Provo, Utah 84602

A study has been made of a high specific energy battery based on a sodium negative electrode and a chlorine positive electrode with molten $AlCl_3$-NaCl electrolyte and a solid beta"-alumina separator (open circuit potential = 3.8 V, theoretical energy density = 1740 Wh/kg). The basic performance of a Na/beta"-alumina/$NaAlCl_4$, Cl_2/C circulating cell at 200 °C has been demonstrated. This cell can be started at 150 °C. The use of melting sodium chloroaluminate electrolyte overcomes some of the material problems associated with the high working temperatures of present molten salt systems, such as Na/S and Li-Al/FeS, and retains the advantages of high energy density and relatively efficient electrode processes. Preliminary investigations were conducted on a sodium-chlorine static cell, material compatibility, electrode design, wetting, and theoretical calculations to assure a better chance of success before assembling a Na/Cl_2 circulating cell.

In the sodium-chlorine static cell experiment, an open circuit potential of the sodium-chlorine couple in the range of 3.78-3.81 V was measured. A current density of 10 mA/cm^2 at steady state discharge could be obtained at a 3.0-V cell potential. Causes of the polarization losses were identified as poor wetting of sodium on the surface of beta"-alumina tubes and slow chlorine mass transfer rate to the chlorine electrode.

The materials and corrosion tests reveal that nickel and monel are corrosion resistant in the molten $NaAlCl_4$. Carbon cloth and vitreous carbon are the best materials for the chlorine electrode. Grafoil^R and Teflon^R were useful as seal and gasket material. In general, the materials used performed well; however, the Monel pump shaft and parts contacting stagnant electrolyte showed a noticeable corrosion rate. The products of corrosion such as $CuCl_2$ and $NiCl_2$ affect the performance of the chlorine electrode to some extent.

Diffusivity and solubility of chlorine in $NaAlCl_4$, needed in the mathematical models, were measured as functions of temperature. The low solubility and diffusivity of chlorine in the neutral $NaAlCl_4$ melt (about 10^{-6} $mole/cm^3$ and 10^{-5} cm^2/s, respectively) confirm a low chlorine mass transfer rate to the carbon electrode. It was found that the addition of acetylene carbon black in the molten sodium improved the wetting of molten sodium on the surface of beta"-alumina tubes.

Different designs of the chlorine electrodes were tested and modeled theoretically. Limiting current density can be as high as 200 mA/cm^2 and an operating current density can be 180 mA/cm^2 at a -0.7-V chlorine electrode overpotential by using a bubble-through chlorine electrode.

A Na/beta"-alumina/$NaAlCl_4$, Cl_2/C circulating cell compared to the usual static cell design has indefinite capacity which depends on the size of the reservoirs. The theoretical specific energy is approached as the reservoirs

become large compared to the cell itself. The power is limited by the mass transfer rate of chlorine to the carbon electrode. It can be used as either a sodium-chlorine secondary battery or a sodium-chlorine fuel cell. Its measured open circuit voltage is between 3.78-4.13 V. After the problem of contact between molten sodium and beta"-alumina was partly solved, an output at 37.5 mA/cm^2 and 3.2 V was demonstrated.

Mathematical models provide a theoretical explanation for the performance of the Na/Cl_2 battery. The results of mathematical models match the experimental results very well. According to the result of the mathematical modeling, an output at 180 mA/cm^2 and 3.2 V can be obtained with optimized cell design.

DEVELOPMENT OF NEW SEALED BIPOLAR LEAD-ACID BATTERY

A.I. Attia and J.J. Rowlette
Jet Propulsion Laboratory
California Institute of Technology
Pasadena, California 91109

New light weight composite bipolar plates which can withstand the corrosive environment of the lead-acid battery have made possible the construction of a sealed bipolar lead-acid battery that promises to achieve very high specific power levels and substantially higher energy densities than conventional lead-acid batteries. Performance projections based on preliminary experimental results show that the peak specific power of the battery can be as high as 90 kW/kg, and that a specific power of 5 kW/kg can be sustained over several thousand pulses.

I. INTRODUCTION

A program for the development of a 50-kW sealed bipolar lead-acid battery is currently underway at JPL, under the sponsorship of the Air Force Wright Aeronautical Laboratories. This three year program which started in July 1987 is in competition with three other programs using other electrochemical couples, all aiming at the development of 50-kW batteries by the end of 1989. At that time a single system will be selected for the construction of a 100 Megawatt battery.

II. BACKGROUND

Two distinct designs of the sealed bipolar lead-acid battery are under development. One of the designs is based on a bipolar battery developed by TRW for the Environmental Protection Agency (EPA) in 1972 [Ref. 1]. That battery utilizes bipolar plates made of a polymeric matrix filled with vitreous carbon and bonded to a thin lead sheet; our contractor for that system is Gates Corp. The other design which is the subject of this paper grew out of several years of JPL's involvement in the Electric & Hybrid Vehicle Project of the Department of Energy; the key elements of this new bipolar design are sealed construction, a light-weight composite bipolar plate made of conductive glass and carbon fibers embedded in a polymeric matrix, and the addition of tin dioxide coated glass fibers to the positive active material. A contract for the development of this new battery has been awarded to ENSCI, Inc. in Chatsworth, California.

III. DESCRIPTION OF SYSTEM

a. System Design

This new lead-acid battery designed for high power applications is unusual in that it is a bipolar battery with sealed design. Figures 1 and 2 show diagrams of the bipolar stack and the sealed battery respectively. The requirement of maximum specific power dictates a bipolar construction in order to eliminate resistance through the grid and the active mass. For any application either terrestrial or space, such a battery needs to be sealed, as watering would be impractical because of the large number of very thin cells required.

b. New 2-Layer Light-Weight Plastic Composite Bipolar Plate

Lead has been the commonly used material for the bipolar plate in previous lead-acid batteries [Ref. 2], but the weight of lead is unacceptable in minimum practical thicknesses. The battery described here uses a plastic composite for the bipolar plate, in which the conductors embedded in the plastic matrix are tin dioxide coated glass fibers on the positive side of the biplate and carbon fibers on the negative side. This light weight composite biplate is currently being manufactured by ENSCI, under a contract with JPL. Table 1 shows recent results obtained by ENSCI for several biplates; the most recent versions of the bipolar plate have a thickness of 20 mils, a volume resistivity of 2 ohm-cm and an area density less than 0.1 g/cm^2. With the use of thermoset resins for the polymeric matrix the open porosity of the bipolar plate is essentially eliminated.

The bipolar plate is manufactured using conventional polymeric composite technology. Both thermoset and thermoplastic resins have been used with equal success, but better results are obtained for very thin bipolar plates with the thermoset resins. The carbon fibers are commercially available, whereas no commercial source of tin dioxide coated glass fibers is available at the present time. Currently, the thin conductive stannic oxide films on the glass fibers are produced by spraying a solution of tin tetrachloride in the presence of air on a heated glass fiber mat. This process, known as spray pyrolysis [Ref. 3], has long been a production method for applying transparent SnOx conductive thin films to glass. Figures 3 and 4 show photomicrographs of glass fibers of 10 micron diameter, coated with 1 micron of conductive tin dioxide. At the present time, the process variables are well under control, but the production rate is low.

Corrosion tests indicate that while SnO2 is thermodynamically stable with respect to oxidation and thermodynamically stable with respect to reduction at the positive electrode in normal operation, it is subject to reduction during reversal of that electrode [Ref. 4]. The material will never be life-limiting when used in the positive plate environment, providing only that care

be taken to prevent reversal of the positive plates.

c. Conductive Glass Fibers in Positive Active Material.

In this new battery design, the conductivity of the positive active material (PAM) is enhanced by the addition of the stannic-oxide coated glass fibers. The use of these conductive fibers in the PAM is especially important as the state of charge of the battery declines. Figure 5 shows the per cent positive active material utilization as a function of discharge rate with and without the addition of the fibers. A 75 % increase in utilization at the 1-hour rate of discharge is observed in cells with the fibers.

IV. ADVANTAGES

a. High Specific Power

The fundamental advantage of the lead-acid couple for high power applications is due to three characteristics: high open circuit voltage, low electrolyte resistivity, and discharge with an increase in entropy. Very few couples can match the ratio of the square of the open circuit voltage to electrolyte resistivity of the lead-acid couple and most couples discharge exothermically (see Table 2). For the lead-acid battery, the change in entropy makes the reversible component of heating negative on discharge. This heating must therefore be positive on charge but charge rates are very low compared to discharge rates. Furthermore, the sealed bipolar lead acid battery described above has the advantages of very light weight construction and a thermodynamically stable conductor in the bipolar plate.

The specific power, in kW/Kg, can be factored into two parts: the surface power density, in W/cm^2, and the specific area, in cm^2/Kg. Batteries very often do well on one of these factors but fail to show a high specific power because of doing poorly on the other.

The maximum surface power density, Psmax, of an electrochemical cell is given by

$$Psmax = \frac{Pmax}{A} = \frac{(E'oc)^2}{4RA} \qquad (1)$$

where Pmax is the maximum total power, A is the plate area, E'oc is the battery open circuit potential extrapolated to zero current from the polarization curve, and R is the total internal resistance. If the electrolyte resistance dominates the battery resistance, and l is the thickness of the electrolyte between the plates (separator thickness) then

$$Psmax = \frac{(E'oc)^2}{4rl} \qquad (2)$$

where r is the electrolyte resistivity. For comparison purposes Psmax for an electrochemical cell can be expressed as a figure of merit (M) as given by

$$M = \frac{(E'oc)^2}{r} \qquad (3)$$

which allows a comparison to be made among various battery couples to predict the ones most capable of having the highest surface power densities. The figure of merit, M, is calculated for nine different couples in Table 2. The values of E'oc (except for Na-S and Li-FeS) were extrapolated from E-I curves in the literature and those for r were from the battery literature. The lead-acid system based on the intrinsic properties of the couple alone has 3 times the Ag-Zn and more than 4 times the Ni-H2 and Ni-Cd surface power density.

Table 2 also shows the calculated quantity Q/E which is the ratio of thermal to electrical energy when discharging at 2/3 E'oc. The values for the Q/E ratio are consistent with those projected from thermodynamic considerations. The lead-acid system appears to be optimum.

The specific area of this new battery is also high due to the multistack bipolar construction, the lightweight composite plastic bipolar plate (0.1 g/cm^2), and the lack of need for auxiliary equipment such as pumps, cooling loops, and heavy storage containers required by the other systems.

b. The use of conducting tin oxide coated glass fibers in the positive active material (PAM) is another distinguishing feature of this battery. Lead dioxide makes an unusualy low resistance contact with the stannic oxide and the contact resistance appears to be unchanging with time or state of charge. The benefit for a very high pulse power requirement is that these conductive fibers will enhance conduction in the positive plate and that this conduction will reduce the usual power decline with decreasing state of charge. Additional benefits expected from the presence of a stable conductor within a few microns of all parts of the PAM are : longer cycle life because of reduced morphological degradation, rapid and total formation in all cases, and very high utilization of the positive electrode. This last effect was repeatedly demonstrated by scientists at ENSCI who consistently measured utilization efficiencies in excess of 40% at the 1 hour discharge rate (see Figure 5).

V. PERFORMANCE PROJECTIONS

Performance estimates for the sealed bipolar lead-acid battery have been made for a number of different discharge modes. These include constant current discharges to depletion of capacity of 1, 5, 10, and 100 seconds and pulse discharges of 5 msec per pulse at 5 Hz for 1000 seconds. The estimates based on

preliminary information on the physical charateristics of the bipolar plate are shown in Figure 6. A full description of the design and operational variables for the battery will be the subject of a paper currently in preparation, to be presented at the 22nd IECEC meeting in Philadelphia, August, 1987.

A battery of specified power output would have a size dependent upon the time allotted for its complete discharge. The size and shape of the battery would also be determined in part by its voltage. Based upon the characteristics known about the battery at this time it is calculated that a 50 KW battery of a nominal 100 Volts would have approximately the characteristics shown in Table 3.

VI. PERFORMANCE CHARACTERISTICS OF TEST CELL

A test cell consisting of the two end electrodes of a bipolar battery was recently assembled and tested at JPL. In this cell, the end electrodes, approximately 15 mils thick, are pasted onto a 1/4 inch thick pure lead disk, 2 inches in diameter, which acts as a current collector. The cell has an active electrode area of 5 cm^2 and a theoretical capacity of 200 mAh assuming 100% utilization.

The cell was tested at various rates of discharge ranging from 1 second to 15 minutes. Figure 7 shows the ampere-hour capacity and the PAM utilization to a 1-Volt cutoff at 25 C for these high rate discharges. The cell limiting current was measured at 3.25 A/cm^ 2.

Constant current polarization curves were also obtained, as shown in Figure 8. Each of the data points in Figure 8 represents the cell voltage for a constant current discharge, measured after a fixed time interval from the start of the discharge. Four such intervals are shown for eight constant current discharges. For the given time intervals, the area resistivities range from .48 to .68 ohm-cm^2, or roughly twice the values assumed for our calculations of projected performance. Improvements in actual performance are expected upon optimization of the cell design.

VII POTENTIAL PROBLEMS

The sealed bipolar lead acid battery shares an important problem with other sealed batteries. It must be carefully designed in order to prevent gas leaks to the outside. Special attention must also be paid to preventing electrolyte leaks from cell to cell.

Another problem which may be unique to this design is that the light weight bipolar plates are not good heat conductors; the mean specific heat of this battery, however, will be considerably

higher than other lead-acid batteries, and likely higher than other batteries in general because of its high fraction of aqueous electrolyte and the fact that much of the lead is replaced by a plastic.

ACKNOWLEDGEMENT

The work described in this paper was carried out by the Jet Propulsion laboratory, California Institute of Technology, and was sponsored by the Air Force Wright Aeronautical Laboratories through an agreement with the National Aeronautics and Space Administration.

REFERENCES

[2] "Development of High Charge and Discharge Rate Lead-Acid Battery Technology", TRW, Inc., Final Report prepared for Environmental Protection Agency, Contract No. 68-04-0028, April, 1972.

[2] J. E. Clifford, "Study of Bipolar Batteries", Prepared by Sandia National Laboratory for the Department of Energy under contract DE-AC04-76DP00789, 1985

[3] J. B. Mooney and S. B. Radding, "Spray Pyrolysis Processing", Ann. Rev. Mater. Sci., vol. 12, 1982, pp. 81-101.

[4] J. J. Rowlette, S. A. Alkaitis, N. Pinsky and J. Y. Josefowicz, Proceedings of 21st Intersociety Energy Conversion Engineering Conference, San Diego, California, August 1986.

TABLE 1

PHYSICAL CHARACTERISTICS OF 2-LAYER BIPOLAR PLATES

Sample #	Weight (g/cm^2)	Thickness (mils)	Volume Resistivity (ohm-cm^2)
D-411-1	0.116	32	9.6
P1700-1	0.137	32	4.6
K-720-1	0.072	18	1.2
K-720-2	0.074	18	1.1
K-730-2	0.108	22	2.1
K-730-2	0.110	23	5.3
K-730-3	0.112	26	8.3
K-460-2	0.109	22	2.1
K-460-3	0.120	29	6.4
P1700-2	0.078	21	2.8
P1700-3	0.083	24	4.7
D-470-1	0.071	19	4.1

TABLE 2

COMPARATIVE CHARACTERISTICS OF ELECTROCHEMICAL COUPLES

Couple	E'oc (Volt)	r (ohm-cm)	M*** (Watts/cm)	Q/E (@2/3 E'oc)
Lead-Acid	2.10	1.12 (1)	3.93	0.45
Li(Al)-FeS	1.33	0.64 (2)	2.76	0.55
H2-O2	1.05*	0.50 (3)	2.20	1.11
Ni-Zn	1.72*	1.84 (4)	1.61	0.54
Ag-Zn	1.59*	1.84	1.37	0.75
Ni-H2	1.32*	1.84	0.95	0.80
Ni-Cd	1.30*	1.84	0.92	0.58
Na-S	2.08*	4.7 (5)	0.92	0.55
LiSOCl2	3.32	47.6 (6)	0.28	0.68

Q/E is the ratio of thermal to electrical power at 2/3E'oc.

(1) Value at 30 C
(2) Value at 450 C
(3) Value at 100 C
(4) Value at 18 C
(5) Value at 300 C
(6) Value at 50 C

* Extrapolation from E - I curves
** Open circuit voltage used because of low activation polarization.
*** M = Figure of merit = (E'oc)^2/r

TABLE 3

PROJECTED 50 KW BATTERY CHARACTERISTICS

	Constant Current Discharge			
	1 sec*	5 sec*	10 sec	100 sec
No. of Cells	50	50	50	50
Cell Voltage Under Load	1.84	1.75	1.74	1.91
Cell Current, Amps	543	571	575	524
Case Dimensions				
Height	1.75"	2.0"	2.35"	3.55"
Width	9.7"	9.9"	10.0"	17.8"
Length	9.7"	9.9"	10.0"	17.8"
Battery Weight, Kg	2.5	3.6	5.4	33.3
Mean Specific Power kW/kg	20	14	9.3	1.5

* Current limited to 1.0 A/cm^2

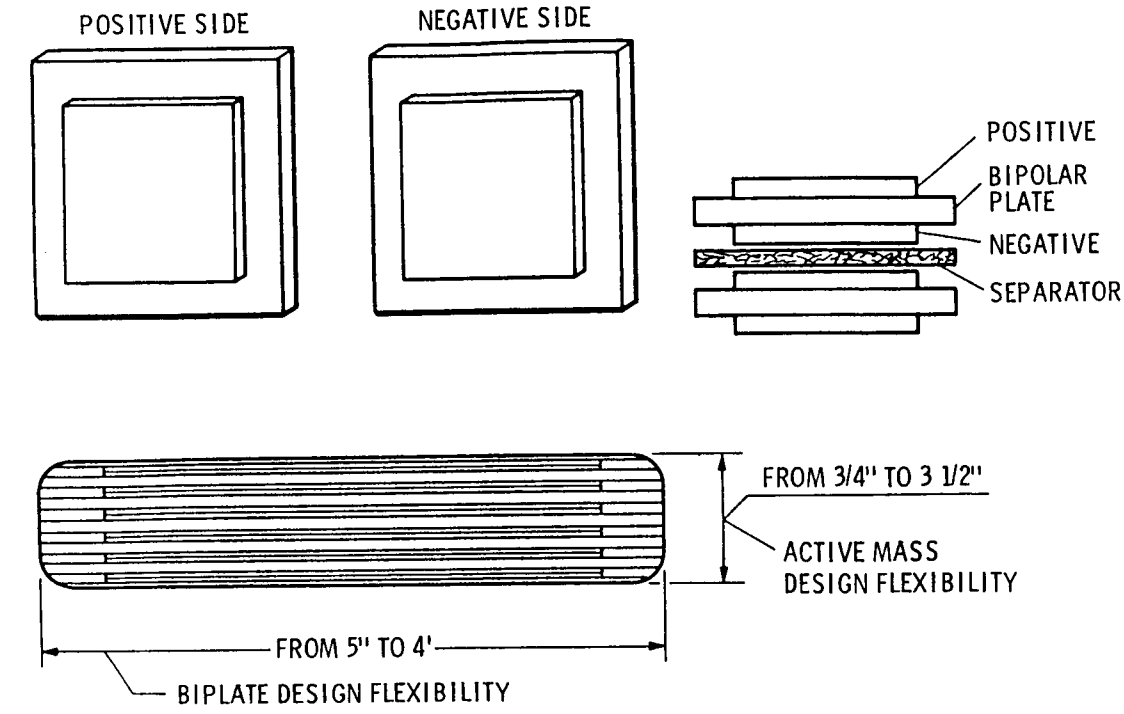

Figure 1. - Bipolar lead-acid battery.

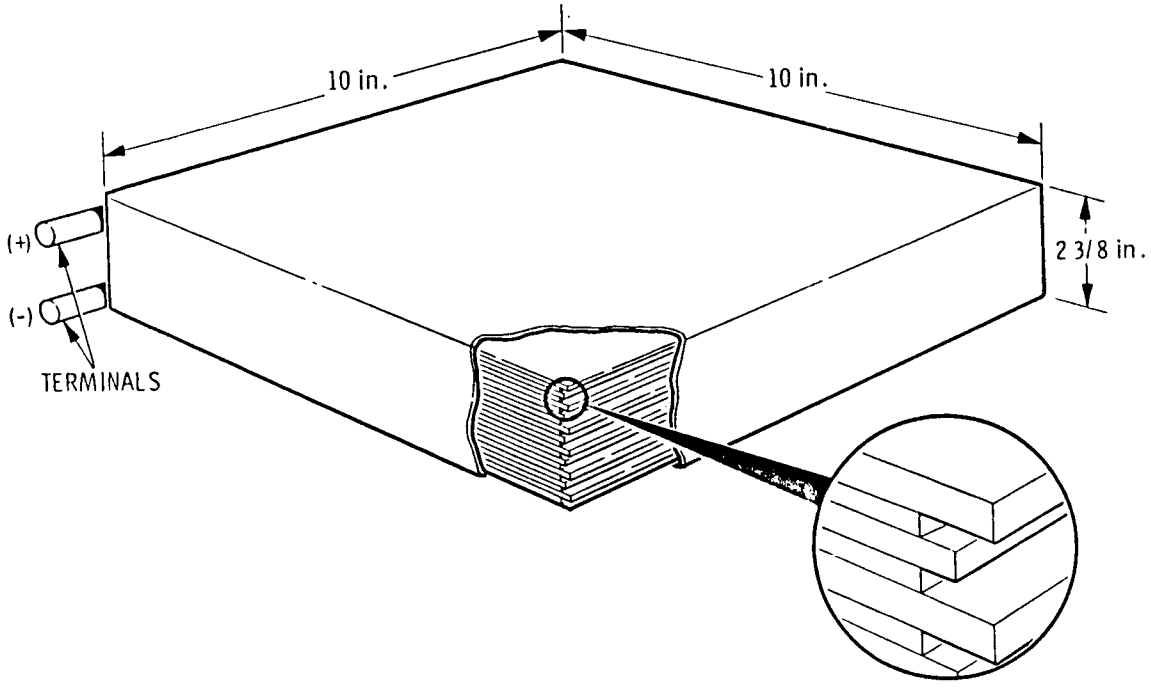

Figure 2. - 50-KW, 50-cell bipolar lead-acid battery. Discharge, 10 sec; weight, 12 lb.

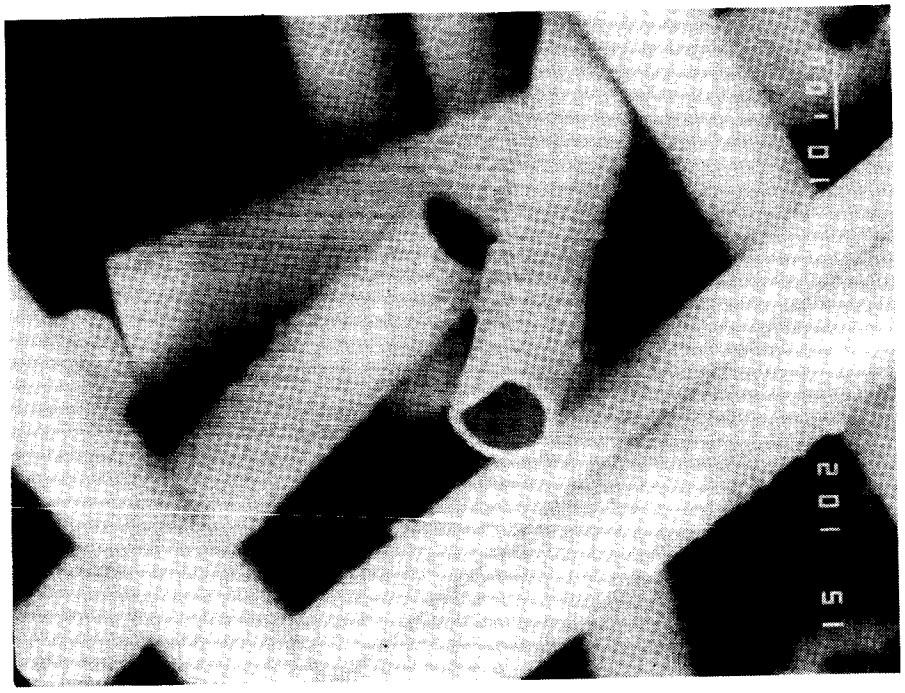

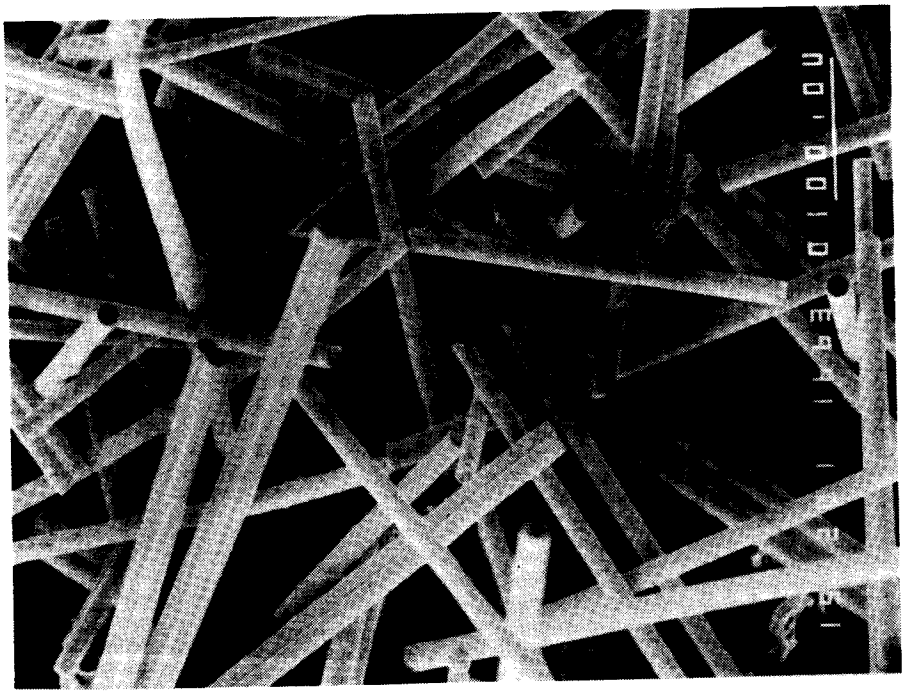

Figure 3. - SnO_2-coated glass fibers.

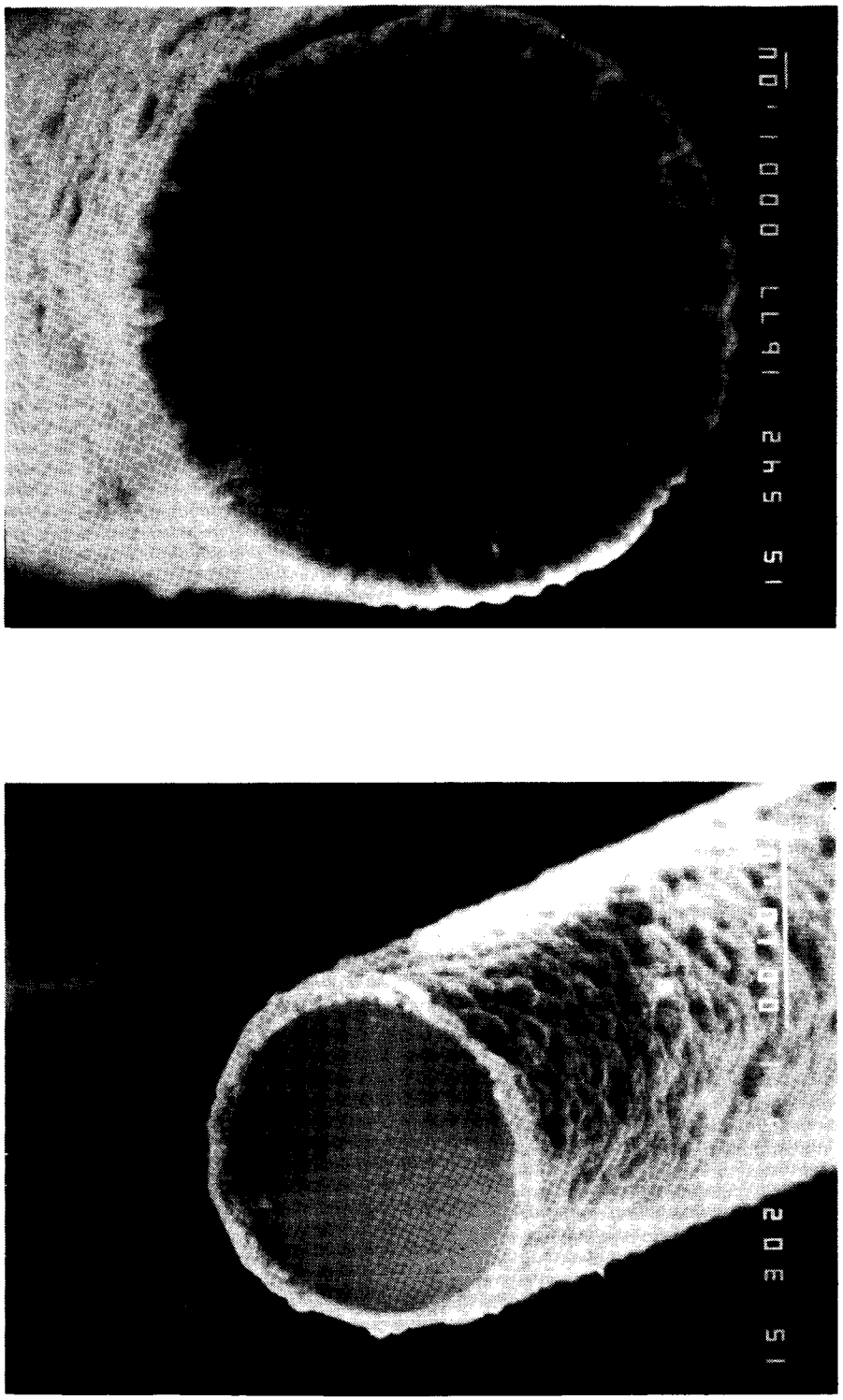

Figure 4. - SnO_2-coated glass fibers.

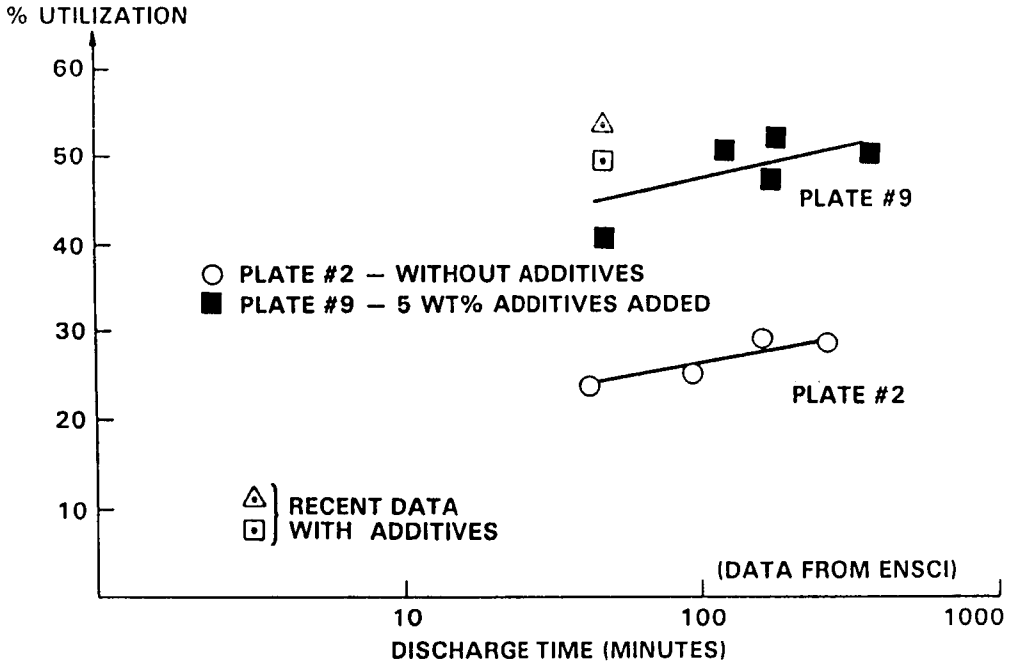

Figure 5. - Utilization efficiency of positive active material.

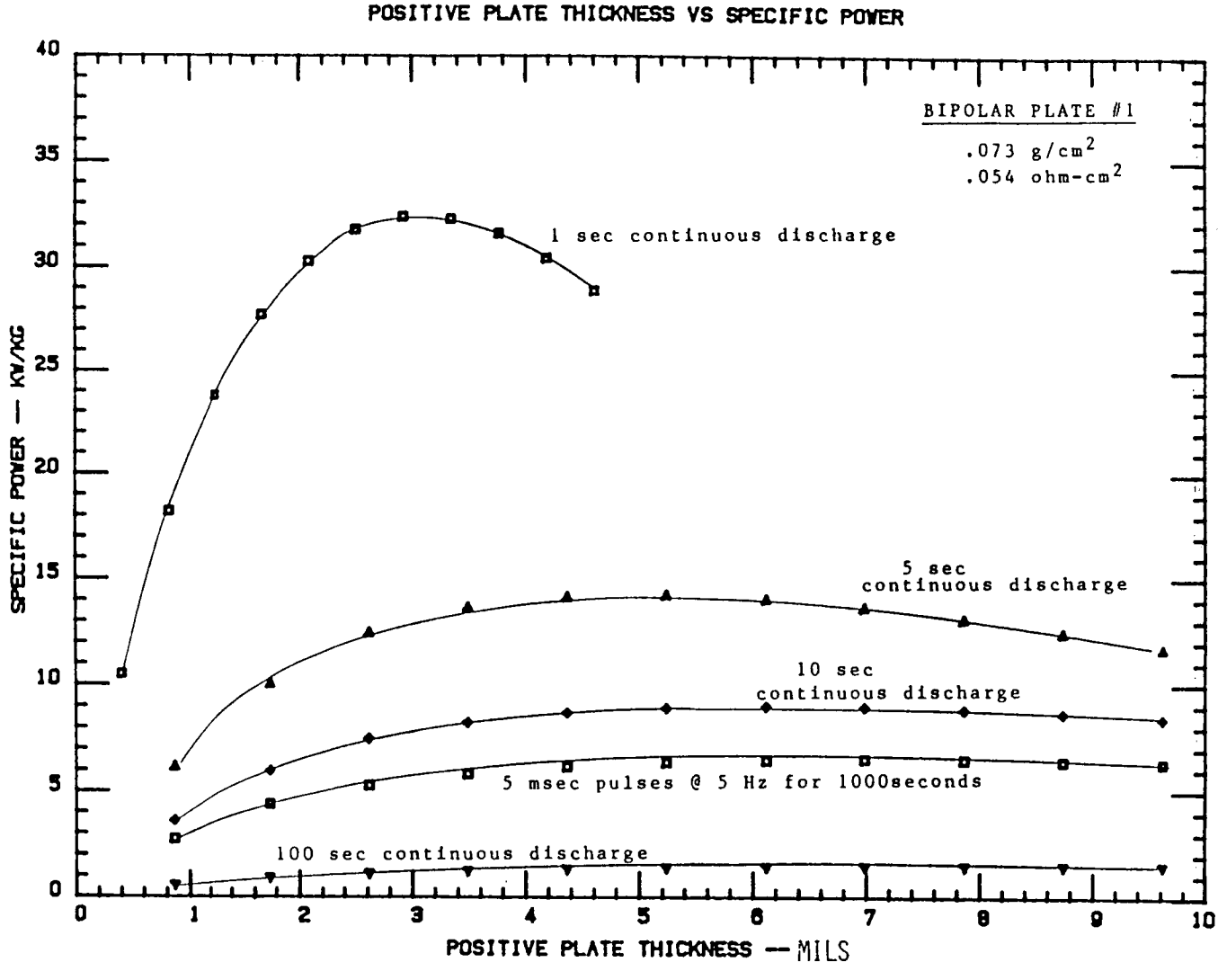

Figure 6. - Positive plate thickness vs specific power.

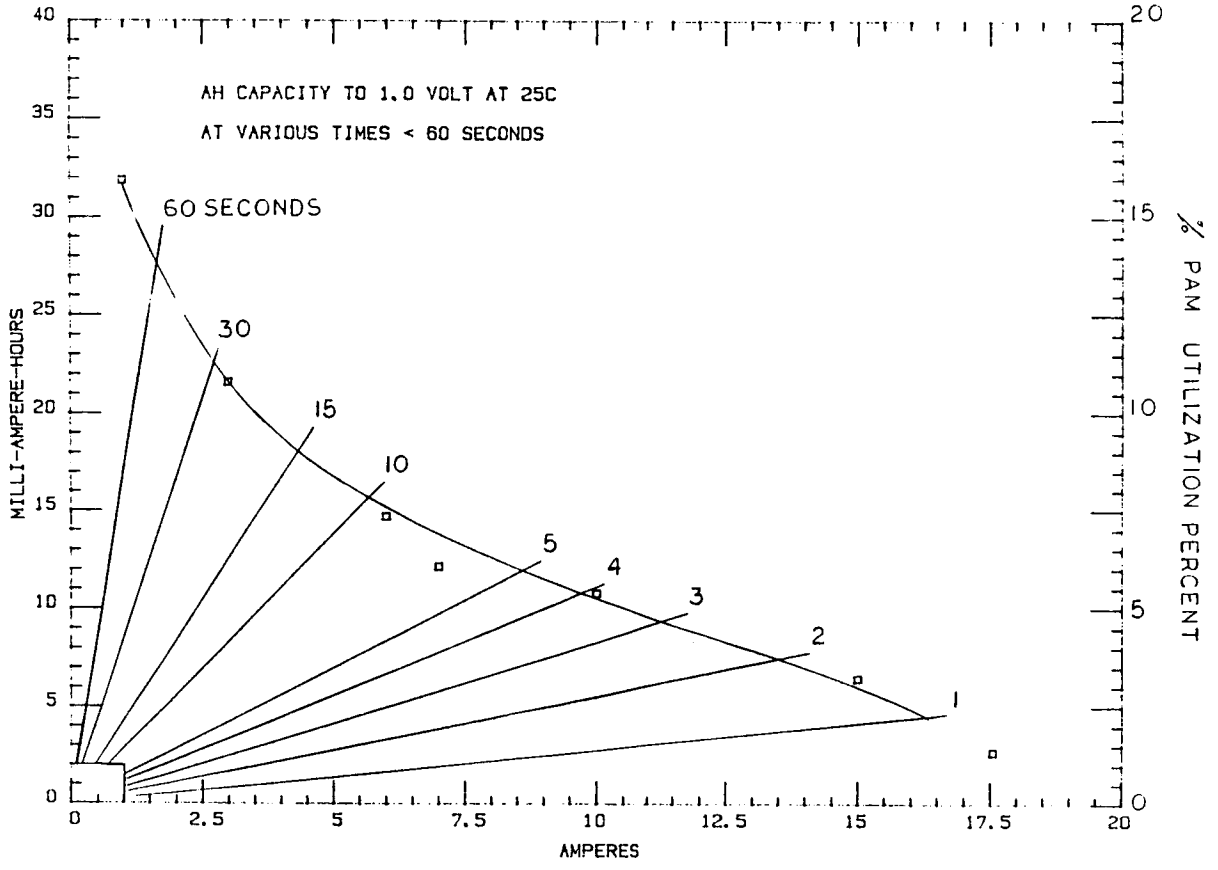

Figure 7. - Testing of monopolar cell with bipolar geometry.

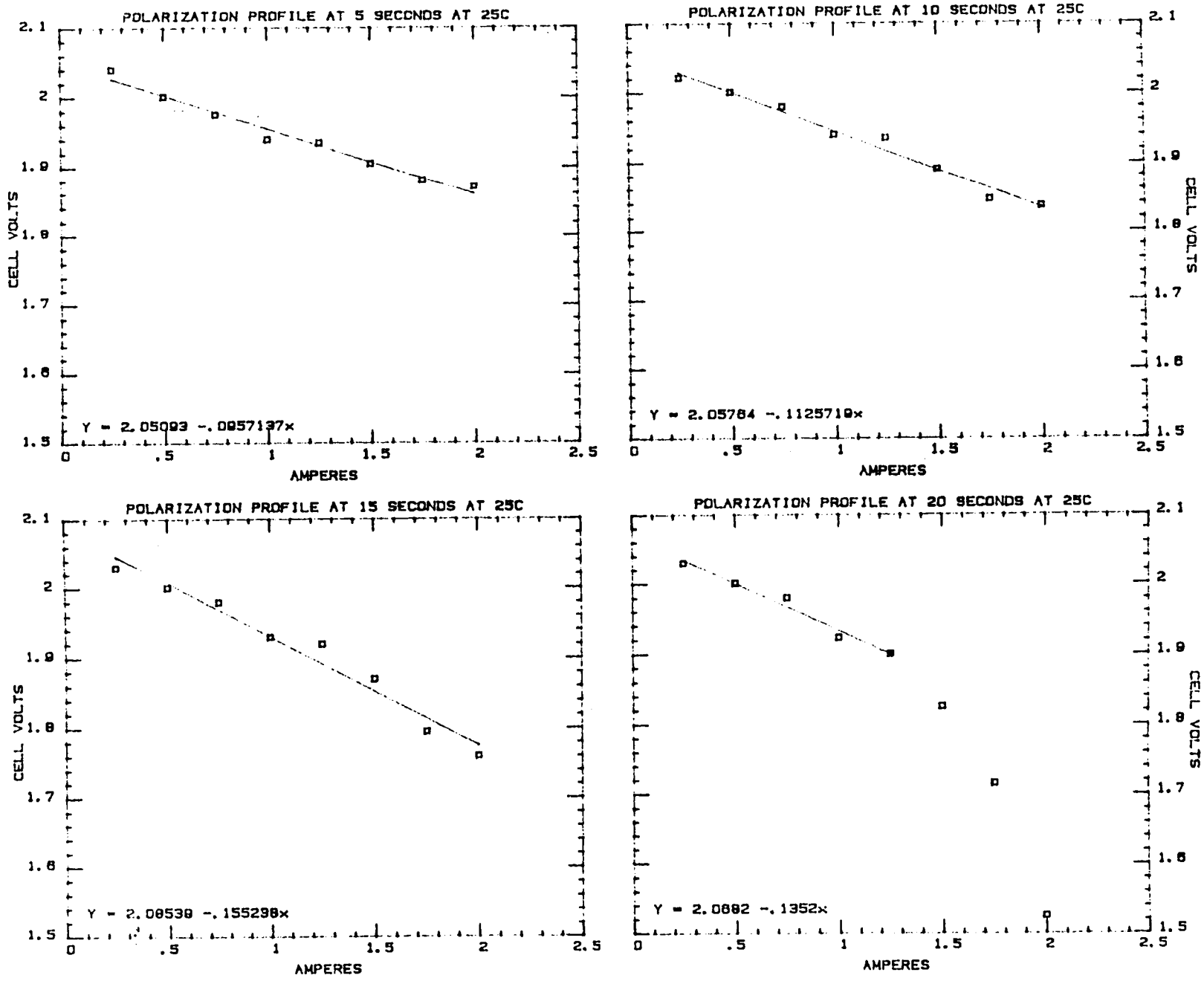

Figure 8. - Polarization curves for monopolar cell with bipolar geometry.

ELECTROCHEMICAL GENERATION OF USEFUL CHEMICAL SPECIES FROM LUNAR MATERIALS

Anthony F. Sammells and Krystyna W. Semkow
Eltron Research, Inc.
Aurora, Illinois 60504

This work is directed towards the electrochemical characterization of a high temperature electrolytic cell which simultaneously generates oxygen at the anode and liquid alkali metals at the cathode. The electrolytic technology being investigated utilizes the oxygen vacancy conducting solid electrolyte, yttria-stabilized zirconia, which effectively separates the oxygen evolving (at $La_{0.89}Sr_{0.10}MnO_3$) and alkali metal (Li, Na) reducing (from a molten salt at either Pt or $FeSi_2$) half-cell reactions. In the finally engineered cell liquid alkali metal would be continuously removed from the cathode compartment and used as an effective reductant for the direct thermochemical refining of lunar ores to their metallic state with simultaneous oxidation of the alkali metal to its oxide. The alkali metal oxide would then be reintroduced into the electrolytic cell to complete the overall system cycle.

RESULTS AND DISCUSSION

There are clear incentives to identify new technical strategies for the generation of useful chemical species from lunar materials directly on the Moon's surface. This is a consequence of the obvious high costs associated with the transportation of necessary materials from the Earth. The eventual development of a permanent manned base on the Moon's surface leading to eventual colonization by people will require a plentiful supply of both oxygen for breathing and refined metals for the assembly of permanent structures. In order to accomplish this, technologies must be characterized now for the extraction of oxygen from lunar ores and for their reduction to metal species by appropriately identified reducing agents, which might themselves be regenerated under lunar conditions.

Analysis of lunar soils and rocks collected during the highly successful Apollo program have shown conclusively the presence of pyroxene type minerals (iron magnesium calcium silicates), plagioclase feldspars (calcium aluminum silicates) and ilmenite (iron titanium oxides). Additionally, the presence of iron-nickel alloys was found, presumably of meteoric origin[1,2]. Thus, the major elements contained in such lunar "ores," from the random samples returned to Earth during the Apollo program, would appear to be oxygen, silicon, aluminum, calcium, iron, magnesium, titanium and nickel. Previous workers have suggested that oxygen might be extracted from ilmenite ($FeTiO_3$) via its initial chemical reduction by hydrogen initially transported from the Earth[3-5]. Other strategies suggested for the reduction of lunar metal ores[6,7] have included carbothermic reduction to give the desired metal species.

Initial work on the high temperature electrochemistry of simulated lunar materials was performed on a number of metal silicate melts using platinum electrodes. Electrolysis of such melts has been shown to result in the simultaneous evolution of oxygen at the anode[8-12] and the deposition of a reduced metal silicon alloy slag at the cathode[13-16]. This preliminary work by others clearly demonstrated the feasibility of high temperature molten salt electrochemical techniques as a strategy for the simultaneous generation of oxygen and reduced metal species from lunar type materials. The following technical limitations have however presented themselves in the direct electrorefining of molten salt lunar materials:

- Oxygen generated at the anode of a molten silicate electrolytic cell ($CaMgSi_2O_6$ containing Fe^{3+}, Co^{2+} or Ni^{2+}) can become partly trapped within the electrolyte, creating a localized foam in the proximity of the anode. This can create problems associated both with the efficient removal of oxygen from the cell and in making such oxygen more susceptible to its electrochemical reduction at the cathode.
- Molten salt cells operated at temperatures (>1300°C) where many chemical and electrochemical materials problems would be introduced limiting overall lifetime.
- Reduced metal or metal silicate species deposited at the cathode of high temperature molten silicate electrolyte cells will be dendritic in nature and will eventually lead to inter-electrode shorting. This is a common problem in both ambient and high temperature electrolytic cells where metals are deposited. No electrochemical technique or strategy has as yet been identified to satisfactorily address this issue for metal deposition.
- The continuous removal of reduced solid metallic species from the cathode would not be practical in such a cell and would consequently be limited to a batch type operation.

Many of the limitations implied by the above comments are currently being addressed by a program directed towards the development of an electrolytic cell which anodically evolves oxygen via an oxygen vacancy conducting solid electrolyte and simultaneously deposits a liquid alkali metal at the cathode. Liquid sodium or lithium deposited at the cathode could be continually removed in the finally engineered cell and used as a valuable reducing agent for the refining of lunar 'ores' via for example the general chemical reaction:

$$2Li(\text{or } Na) + MO \rightarrow Li_2O + M \qquad (1)$$

where MO is a metal oxide ore on the lunar surface. The overall electrolytic cell being developed possesses the general configuration:

⊖	cathode ($FeSi_2$ or Pt)	Li^+ or Na^+ conducting molten oxide salt	O^{2-} conducting yttria stabilized zirconia	O_2 evolving $La_{0.89}Sr_{0.10}MnO_3$ anode	⊕

The anodic reaction in this cell corresponds to

$$O^{2-} \rightarrow \tfrac{1}{2}O_2 + 2e \qquad (2)$$

with the cathodic reaction being

$$2Li^+(Na) + 2e \rightarrow 2Li(Na) \qquad (3)$$

giving the overall reaction

$$Li_2O(Na_2O) \rightarrow 2Li(Na) + \tfrac{1}{2}O_2 \qquad (4)$$

A schematic of the experimental arrangement being developed is shown in Figure 1. Molten salts being evaluated for incorporation into the cathode compartment of this cell include Li_2O(24m/o)-Na_2O, Li_2O(66m/o)B_2O_3, and Li_2O-LiF-LiCl. As can be seen from Figure 1, containment of the alkali oxide containing molten salts is being accomplished by the use of zirconia based solid electrolytes stabilized in the cubic form by the introduction of lower valence metal ions. This introduces oxygen vacancies necessary to produce O^{2-} conductivity at high temperature. Materials which have frequently[17-23] been introduced to promote such conductivity have included CaO, Ce_2O_3, Y_2O_3 and Yb_2O_3. By comparing the oxygen ion vacancy conductivity of the various stabilized zirconias at around 900°C, it appears that highest conductivities (by a factor of 5-10) are realized for the rare earth stabilized materials, compared to those containing calcia. Previous workers[24] have shown that yttria-stabilized zirconia also possesses some resistance to corrosion in high temperature silicate melts. Thus, the presence of trace silicates in alkali metal oxide electrolysis cell should not be a major technical limitation.

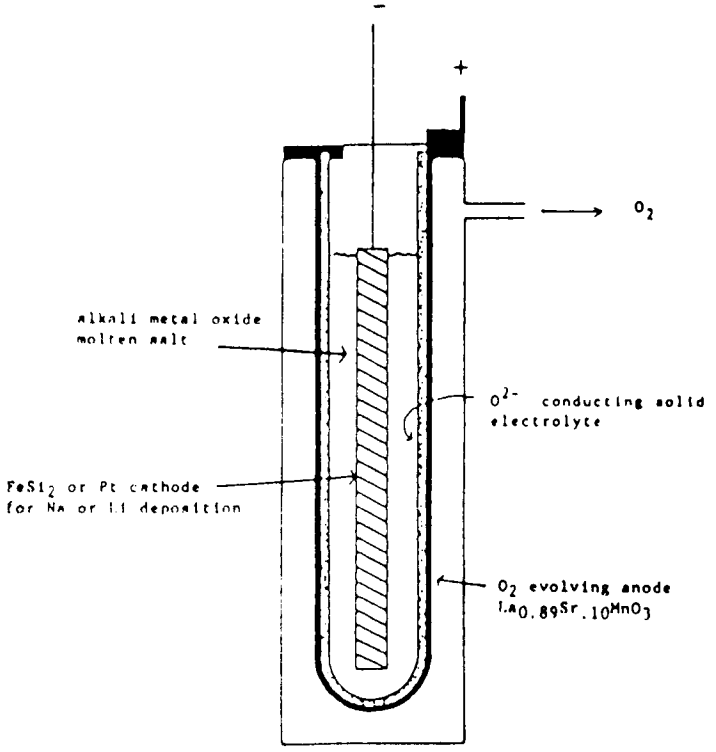

Figure 1. Schematic drawing of yttria stabilized zirconia cell being developed for the electrolytic generation of alkali metals and oxygen from molten alkali metal oxide melts.

Investigation of (24m/o)Li_2O-Na_2O molten oxides at 800°C in a stainless steel container using platinum working and counter electrodes, gave a polarization curve suggesting electrolysis of the melt to form oxygen and alkali metal. Sodium was observed in the cell after its disassembly. This in part could be promoted by the direct thermal decomposition of sodium oxide to sodium at the temperatures used.

Other investigations were directed towards electrolysis of Li_2O in LiCl (70m/o)-LiF melts. The liquidus curve for this ternary melt is shown in Figure 2. Melting points were determined using DC resistance measurements. Ionic conductivity for Li_2O(5-28m/o) in LiCl(70m/o)-LiF were found to be in the range 2-4ohm^{-1}cm^{-1} at 600-700°C as determined using AC impedance measurements. A current overpotential curve for the cell

$$FeSi_2 \left| \begin{matrix} (23.9\text{-}23.6\text{-}52.5)\text{m/o} \\ Li_2O\text{-}LiF\text{-}LiCl \end{matrix} \right| ZrO_2(8\text{w/o } Y_2O_3) \left| La_{0.89}Sr_{0.10}MnO_3 \right| Pt$$

is shown in Figure 3. The cell had an initial open-circuit voltage of 1.43V at 700°C and gave current densities at the $FeSi_2$ electrode of 60mA/cm^2 at 1.0V applied overpotential. Lithium deposition was observed to proceed via the formation of a series of progressively more negative Li_xFeSi_2 voltage plateaus. Oxygen evolution from the anode was found to be Faradaic. The temperature dependency for cell resistance is shown in Figure 4. The activation energy obtained from the slope (23.2kcal/mole) agrees well with the activation energy for oxide ion diffusion through calcia stabilized zirconia[25]. Thus, the overall cell resistance is predominantly due to the solid electrolyte. Thus, zirconia solid electrolyte geometry will be of importance in the finally engineered cell. Also, appropriate provision will be necessary for both the convenient removal of liquid lithium from the cathode compartment and for the reintroduction of Li_2O into the molten salt electrolyte.

The electrochemical results briefly outlined above clearly show the technical viability of this overall strategy for the indirect electrochemical refining of lunar ores to produce reduced metals and oxygen.

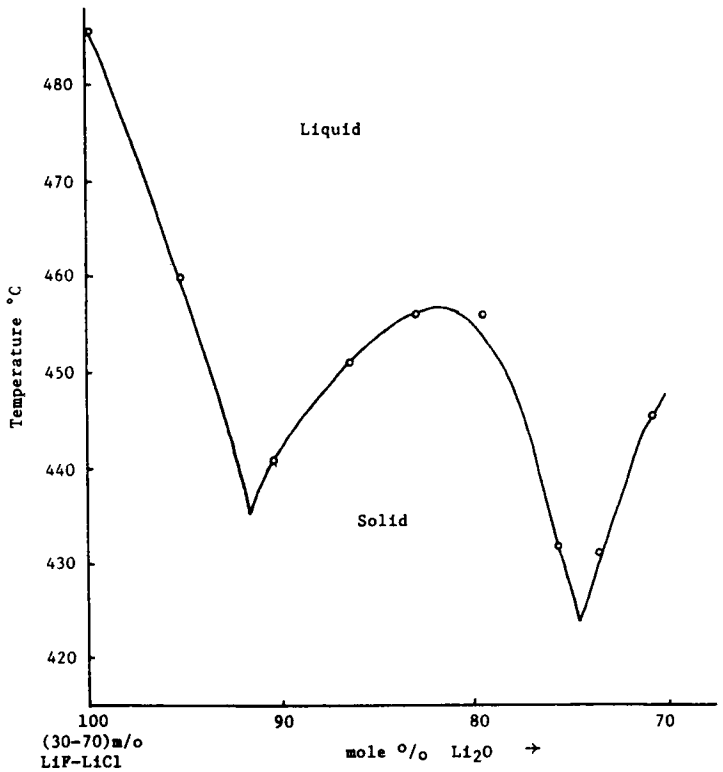

Figure 2. Liquidus curve for the system Li_2O - (30m/o LiF, 70m/o LiCl).

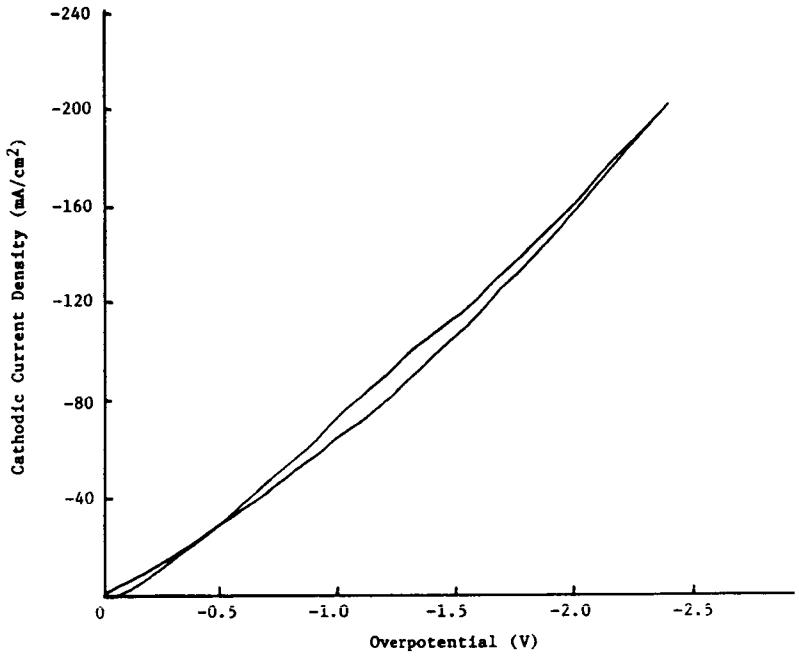

Figure 3. Current-overpotential curve for the cell $FeSi_2/Li_2O(23.9m/o)$-$LiF(23.6m/o)$-$LiCl(52.5m/o)/ZrO_2(8w/o\ Y_2O_3)/La_{0.89}Sr_{0.10}MnO_3/Pt$. Open-circuit voltage 1.43V. Temperature 700°C. Voltage scan rate 0.1V/sec.

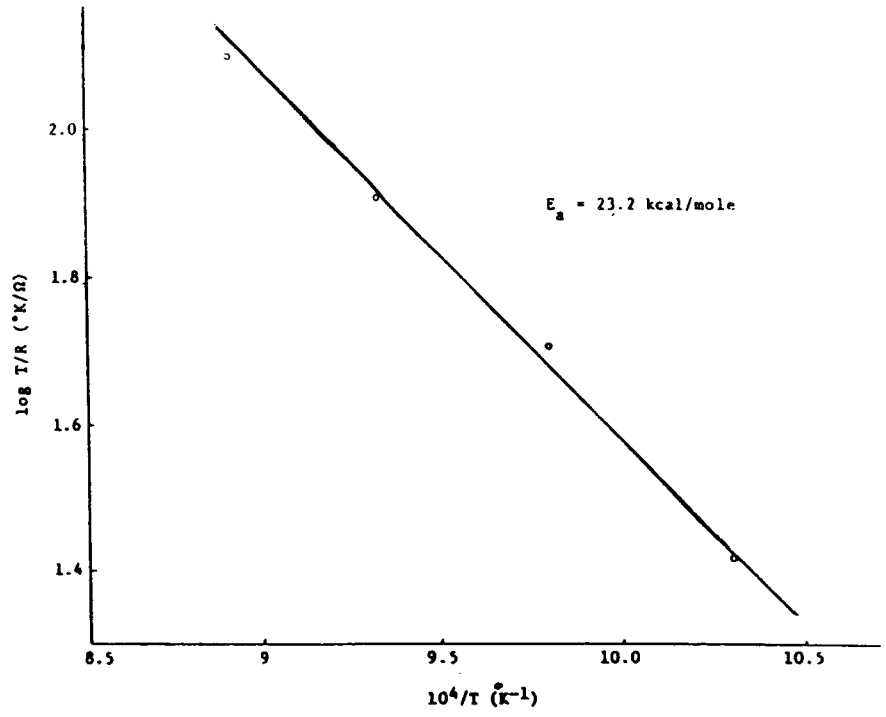

Figure 4. Temperature dependence for the resistance of the cell Pt/$La_{0.89}Sr_{0.10}MnO_3/ZrO_2(5w/o\ CaO)/Li_2O(5m/o)$-$LiF(28.5m/o)$-$LiCl(66.5m/o)$/Fe.

ACKNOWLEDGEMENT Support by NASA under the SBIR program (contract #NAS 9-17743) is gratefully acknowledged.

REFERENCES

1. R. D. Waldron and D. R. Criswell, Princeton Conf. on Space Manufacturing Facilities, Report 79-1379, Princeton, New Jersey, (1979).
2. R. J. Williams and J. J. Jadwick, Handbook of Lunar Materials, NASA, 1980.
3. H. P. Davies, Eagle Engin. Report #EEL 83-63, Houston, (1983).
4. M. A. Gibson and C. W. Knudsen in Lunar Bases and Space Activities of the 21st Century, NASA, 1984, p. 26.
5. E. Kibler, L. W. Taylor and R. J. Williams in Lunar Bases and Space Activities of the 21st Century, NASA, 1984, p. 25.
6. W. C. Phinney, et. al., in Space Based Manufacturing From Nonterrestrial Materials, Amer. Inst. of Aeronautics and Astronautics, New York, 1977.
7. A. H. Cutler in Lunar Bases and Space Activities of the 21st Century, NASA, 1984, p. 22.
8. K. W. Semkow and L. A. Haskin, Geochim. Cosmochim. Acta, 49, 1897 (1985).
9. K. W. Semkow and L. A. Haskin, Abstracts to Lunar Plant Sci., XVI, 1985, p. 761.
10. A. Ghosh and T. B. King, Trans. Metall. Soc., AIME, 245, 145 (1969).
11. J. K. Higgins, Glass Technol., 23, 90 (1982).
12. J. K. Higgins, Glass Technol., 23, 180 (1982).
13. D. S. Kesterke, U.S. Dept. of Interior Bureau of Mines Report of Invest. RI-7587, (1971).
14. D. J. Lindstrom and L. A. Haskin in Space Manufacturing Faciltiies 3, T. Grey and C. Krop, Eds., Amer. Inst. Aeronautics and Astronautics, New York, 1979.
15. W. F. Carroll, Jet Propulsion Laboratory Report 83-36, (1983).
16. R. H. Lewis, D. J. Lindstrom and L. A. Haskin, Abstracts to Lunar Planet Sci., XVI, 1985, p. 489.
17. H. S. Spacil and C. S. Tedmon, Jr., J. Electrochem. Soc., 116, 1627 (1969).
18. W. Fisher, H. Kleinschmager, F. J. Rohr, R. Steiner and H. H. Eysel, Chem. Ing. Tech., 44, 726 (1972).
19. R. Bohm and H. Kleinschmager, Z. Naturforsch, 269, 780 (1971).
20. R. Steiner, Energ. Conv., 12, 31 (1972).
21. H. L. Tuller and A. S. Nowick, J. Electrochem. Soc., 122, 255 (1975).
22. T. Kudo and H. Obayashi, J. Electrochem. Socl, 122, 142 (1975).
23. T. H. Etsell and S. N. Flengas, J. Electrochem. Soc., 118, 180 (1971).
24. T. Tran and M. P. Brungs, Phys. Chem. Glasses, 21, 133 (1980).
25. D. K. Hohnke in Fast Ion Transport in Solids, P. Vashishta, J. N. Mundy and G. K. Shenoy, Eds., North-Holland, New York, 1979, p. 669.

ADVANCED FUEL CELL CONCEPTS FOR FUTURE NASA MISSIONS

J.K. Stedman
International Fuel Cell
South Windsor, Connecticut 06074

In-house studies of primary fuel cells for advanced "all-electric" shuttle-type vehicles show an all fuel cell power system with peak power capability of 100's of kW to be potentially lighter and have lower life cycle cost than a hybrid system using advanced H_2-O_2 APU's for peak power and fuel cells for low power on orbit. Fuel cell specific weights of 1-3 lb/kW, a factor of 10 improvement over the orbiter power plant, are projected for the early 1990's. Critical development issues include development of high power density cells with capability for hundreds of missions.

For satellite applications, a 12-month study to identify high performance regenerative hydrogen-oxygen fuel cell concepts for geosynchronous orbit has recently been completed for NASA Lewis Research Center. Emphasis was placed on concepts with the potential for high energy density (Wh/lb) and passive means for water and heat management to maximize system reliability. Both alkaline electrolyte and polymer membrane fuel cells were considered.

An integrated alkaline electrolyte concept utilizing a configuration in which the fuel cell and electrolysis cells are alternately stacked inside a pressure vessel was evaluated. This concept uses completely passive means for product water transfer and thermal control.

The lightest and simplest design concept is a reversible cell configuration, in which each individual cell can operate in both the fuel cell and electrolysis mode, thus eliminating the need for two separate stacks and associated equipment. System energy densities of up to 115 Wh/lb are projected, pointing out the benefits to be gained if a reversible alkaline electrolyte fuel cell can be developed. The critical issue is a reversible oxygen electrode.

Another technology, the solid polymer membrane electrolyte fuel cell, has potential for several NASA missions including the regenerative energy storage applications and hydrogen-air power systems for advanced air vehicles. Improvements in cell operability and water removal have been demonstrated in in-house programs. However, improved cell performance is required to meet mission requirements. Research on reducing membrane ionic and electrode-membrane interface losses is required.

ADVANCED HYDROGEN ELECTRODE FOR HYROGEN-BROMINE BATTERY

J.A. Kosek and A.B. LaConti
Giner, Inc.
Waltham, Massachusetts 02254-9147

Binary platinum alloys are being developed as hydrogen electrocatalysts for use in a hydrogen-bromine battery system. These alloys have been varied in terms of alloy component mole ratio and heat-treatment temperature. Electrocatalyst evaluation, performed in the absence and presence of bromide ion, includes floating half-cell polarization studies, electrochemical surface area measurements, X-ray diffraction analysis, SEM analysis and corrosion measurements. Results obtained to date indicate a platinum-rich alloy has the best tolerance to bromide ion poisoning.

INTRODUCTION

The hydrogen-bromine battery is being developed by NASA as a power source suitable for space applications. This battery could also be used on earth for large-scale energy storage in load-leveling applications [Refs. 1-4]. The system can be independently sized for various energy and power requirements, and reactants and products stored externally to the the electrochemical cell. One proposed configuration of this system utilizes a solid polymer electrolyte membrane, such as Nafion, as the cell separator/electrolyte. A schematic drawing of the regenerative hydrogen-bromine system, showing both the charge and discharge modes, is shown in Figure 1.

The hydrogen-bromine cell has several advantages which make it attractive for use: (a) the system has a high electric-to-electric efficiency because of fast electrochemical reaction kinetics of both the hydrogen and bromine electrodes; (b) the same electrochemical cell can be used for both charge and discharge operations which would lower the power/weight requirements for a space-based power source; (c) it can be operated with shallow discharges and can tolerate both overcharge and overdischarge; (d) the use of a solid polymer electrolyte membrane allows a high differential pressure to be obtained in the cell; (e) the cell has a high coulombic efficiency because of low self-discharge rate; and (f) there are no mass transfer limitations in the cell operation because of the high solubility of bromine in the hydrobromic acid electrolyte.

A major concern of this system which must be resolved is the adsorption of bromide ions on the hydrogen electrode which results in poisoning of the electrode. This problem is caused by the marginal rejection properties of bromine species by presently available commercial solid polymer electrolyte membranes.

Nafion^{R}-type* membranes which are utilized as perselective solid polymer electrolytes, would ideally transport only protons (or cations). Thus, under ideal conditions in a hydrogen-bromine battery, the hydrogen electrocatalyst will only be exposed to gaseous and ionic hydrogen. In reality, Nafion membranes do not completely prevent bromide ions from migrating across the membrane and adsorbing on the hydrogen electrode. Similarly, the membrane does not completely reject other bromine species

* Nafion^{R} is a registered trademark of the E.I. duPont Corporation.

(Br_2), which also migrate across the membrane and poison the hydrogen electrode surface. The state-of-the-art hydrogen electrocatalyst, Pt black, is known to adsorb halide ions, "become poisoned," and render decreased hydrogen oxidation/reduction activity [Refs. 5-7]. Studies have shown that this effect can be minimized by always maintaining the electrode at hydrogen potentials. Also, studies conducted in this laboratory under NASA Contract NAS3-24394 have identified a Pt alloy which has improved tolerance to bromine/bromide ion adsorption, as compared to Pt black.

One of the objectives of a current NASA-funded program (NAS3-24878) is the optimization, in terms of stability and performance, of the hydrogen electrocatalyst. This paper describes some of the results obtained during the optimization.

EXPERIMENTAL

The electrocatalyst was prepared by the co-precipitation of platinum and the base metal using a modification of a procedure originally published by Giner, et al. [Ref. 8]. After filtration and drying, the electrocatalyst was separated into smaller batches and subjected to one hour heat-treatment under an inert atmosphere, with heat-treatment temperatures ranging from 500° to 1100°C; platinum to base metal mole ratios were varied from 90:10 to 25:75.

Gas diffusion electrodes were fabricated from the various heat-treated electrocatalysts, using electrocatalyst loadings of 7.5 mg/cm² plus 5% PTFE binder and sintered at 345°C. Carbon fiber paper was used as a substrate. Initial electrodes were fabricated using 20% PTFE. However, these proved to be too hydrophobic for use in the floating half-cell studies. Subsequent to fabrication of a large electrode (typically 20x20 cm), 1 cm² area buttons were cut out and used for either electrochemical surface area analysis by cyclic voltammetry, or floating half-cell polarization studies.

The apparatus shown in Figure 2 was used for the floating half-cell hydrogen oxidation studies; experiments were performed at room temperature, 23 ± 1°C. Initial experiments were run in 2 M H_2SO_4 electrolyte and subsequently in 2 M H_2SO_4 with increasing amounts of bromide ion added in the form of KBr. The data were corrected for iR polarization by a current interruption technique and are presented as overvoltage from the open circuit voltage. The currents were adjusted manually and steady-state potentials recorded.

The effect of bromide ion adsorption on the electrocatalyst surface was studied by measuring the amount of hydrogen adsorbed on the electrode surface using cyclic voltammetry. Electrode potentials were scanned between 50 and 800 mV vs. a dynamic hydrogen electrode, which was located in a separate compartment but in electrical contact with the sensing electrode by means of a Luggin capillary. Results were not corrected for the effect of a liquid junction potential. Electrochemical surface areas were measured initially in 2 M H_2SO_4, and then with increasing amounts of bromide ion added to the solution.

Corrosion testing was also performed on several of the hydrogen electrocatalysts. In this set of experiments, 50 mg of electrocatalyst was placed in 25 ml of 1M KBr/2M H_2SO_4 in a vial containing about 15 ml of air. After 14-20 days at ambient temperature the color of the solutions was noted and the remaining electrocatalyst washed and weighed.

Electrocatalyst powder (no PTFE present) was also examined by means of scanning electron microscopy (SEM) and X-ray diffraction (XRD) analysis.

RESULTS AND DISCUSSION

Half-cell polarization curves for hydrogen oxidation on non-heat-treated and 500°C heat-treated G86-1-2 electrocatalysts are shown in Figure 3. For clarity, only the data points obtained in 2 M H_2SO_4 and 4.5 M KBr/2 M H_2SO_4 have been plotted; polarization data was also obtained at intermediate concentrations of KBr.

The results indicate that the heat-treated and non-heat-treated electrocatalysts respond similarly to H_2 in the absence of bromide ion, with the heat-treated sample performing slightly better. However, in the presence of bromide ion, the non-heat-treated catalyst electrode exhibited superior performance. Thus, at 400 mA/cm², the addition of 4.5 M KBr caused a 34 mV additional polarization loss with the heat-treated electrocatalyst, whereas there was only an 8 mV loss with the non-heat-treated electrocatalyst at 600, 800, and 1000 mA/cm². Using the heat-treated electrocatalyst the polarization exceeded 180 mV in the presence of 4.5 M KBr (off-scale on Figure 3), but was less than 140 mV for the non-heat-treated electrocatalyst electrode, even at 1000 mA/cm².

Similar results, not shown, were observed for the G86-1-3 electrocatalyst (lower platinum content), with the lowest polarization losses occurring for the non-heat-treated electrocatalyst, and increasing with heat-treatment temperature. Polarization curves in H_2SO_4, only for the non-heat-treated G86-1-2 and G86-1-3 electrocatalysts are very similar. However, the additional polarization loss in the presence of bromide ion was larger for the G86-1-3 electrocatalyst system.

Results obtained from the cyclic voltammetry of all five non-heat-treated electrocatalyst systems tested to date are presented in Figure 4. Here we have plotted a normalized response S/S_o (defined as the ratio of surface area in the presence of bromide ion S, to the surface area in the absence of bromide ion, S_o) as a function of bromide ion concentration. For an electrocatalyst system which was not poisoned by bromide ions, the value of S/S_o would be unity over the entire range of bromide ion concentrations tested.

It has been demonstrated in the literature that bromide ion adsorption on a smooth platinum surface, for bromide ion concentrations in the range $1x10^{-6}$ to $1x10^{-3}$ M will not decrease the area available for hydrogen adsorption [Ref. 6]. These concentrations were not tested here. Instead, bromide ion concentrations from $1x10^{-3}$ up to 4.5 M were evaluated. In Figure 4, S/S_o values greater than 1 have been observed for platinum black. It is suspected that during the cycling of the electrode potential the platinum surface is roughened by a dissolution mechanism, thus increasing the effective surface area of the electrode.

The data in Figure 4 suggest that, as the platinum content of the electrocatalyst decreases, the tolerance to bromide ion adsorption also decreases.

A similar plot of S/S_o was obtained for the G86-1-3 electrocatalyst as a function of heat-treatment temperature. In this set of experiments, plots were obtained for the non-heat-treated, the 500°C and the 700°C heat-treated electrocatalysts. With these results, the best tolerance to bromide ion was found with the non-heat-treated electrocatalyst. Not enough data has been obtained with the other electrocatalyst systems to determine if the trend exists for all systems.

Results of the corrosion test experiments are summarized in Table I. In all cases the non-heat-treated samples dissolved to a much greater extent than the heat-treated samples. Except for the platinum black sample, all the non-heat-treated

samples appear to have liberated bromine in solution, as suggested by the red-to-brown coloration in solution. Heat-treatment, even at 500°C, appears to have changed the stability of the electrocatalyst somewhat, as evidenced by the higher percent recovery of the heat-treated materials. Also, the heat-treated materials do not appear to have liberated bromine as the resulting solutions were either blue or green in color. The most stable materials for a given electrocatalyst system appear to be those heat-treated at 700°C.

The electrocatalyst samples were also examined by means of X-ray diffraction, with results summarized in Table II. X-ray patterns were obtained on electrocatalyst powder directly, using a Norelco X-ray generator type 12045 with a Co radiation source. Lattice parameters, calculated from the position of at least four peaks, are summarized in Table II. Several trends are appearing, but additional data is required. With 500°C heat-treatment, an expansion in lattice parameter was observed. This is not unusual since the size of the base metal is greater than that of platinum. Very little change is noted going from 500 to 900°C, then a drop in parameter occurs with 1100°C heat-treatment. With the non-heat-treated electrocatalyst, a decrease in lattice parameter was noted with a decrease in platinum content.

Finally, scanning electron microscopy was performed on all electrocatalyst samples available at this time. Individual particles were too small to be seen, even at 50 Kx magnification. No significant differences were noted in particle sizes among the non-heat-treated materials. Some sintering was noted with the 900°C heat-treated materials, with a larger amount of sintering occurring with the platinum-rich electrocatalysts.

CONCLUSIONS

Experiments performed previously under NASA Contract NAS3-24394 demonstrated that a non-heat-treated platinum alloy had an improved tolerance to the presence of bromide ion as compared to platinum black. Data obtained to date on the present program and presented here, especially the floating half-cell and cyclic voltammetry results, are also suggesting that a non-heat-treated, or a low-temperature heat-treated platinum-rich electrocatalyst yields the best response and minimum polarization losses in the presence of bromide ion. As demonstrated in Table I, heat-treatment of the platinum alloy improves its resistance to corrosion as evidenced by the higher percent recoveries. Corrosion of the hydrogen electrocatalyst is not expected to be a significan problem, since it can be overcome by maintaining the hdyrogen electrode in a hydrogen environment, or, at the very least, by preventing the electrode from reaching an anodic potential where dissolution could occur.

Although it could not be confirmed visually with SEM analysis except for the 900°C heat-treated samples, for a given electrocatalyst composition, the surface area decreased as the heat-treatment temperature increased, due to sintering of the electrocatalyst particles. The larger particle size appears to have less tolerance to the presence of bromide ion, although the reasons for this are unknown at this time. This loss in surface area is also giving rise to increased polarization losses, even in the absence of bromide ion.

Additional information, especially half-cell and cyclic voltammetry is required prior to making a decision as to the composition and heat-treatment conditions of the hydrogen electrocatalyst; these experiments are currently in progress. Also planned are several experiments changing the composition of the base metal alloying component.

REFERENCES

1. Gileadi, E.; Srinivasan, S.; Salzano, F.J.; Beaufrere, A.; Gottesfeld, S.; Nuttall, L.J.; and LaConti, A.B.: J. Power Sources, vol. 2, 1977, pg.191.

2. Srinivasan, S.; Yeo, R.S.; and Beaufrere, A.: in Proceedings of the Second Information Meeting for Hydrogen Contractors in DOE Hydrogen Energy Program, Airlie, Va.; November 8-9, 1976 (BNL-22164).

3. Beaufrere, A; Yeo, R.S.; Srinivasan, S.; McElroy, J.; and Hart, G: in Proceedings of the 12th Inter-Society Energy Conversion Engineering Conference, Washington, D.C.; August 29-Sept. 2, 1977; Paper No. 779148.

4. Chin, D.T.; Yeo, R.S.; McBreen, J.; and Srinivasan, S.: J. Electrochem. Soc., vol. 126, 1979, pg. 713.

5. Bagotzky, V.S.; Vassilyev, Y.B.; Weber, J.; and Pirtskhalava, J.N.: J. Electroanalytical Chem., vol.27, 1970, pg.31.

6. Breiter, M.W.: Electrochim. Acta, vol. 8, 1963, pg. 925.

7. Frumpkin, A.N.: in Advances in Electrochemistry and Electrochemical Engineering, vol. 3, Interscience Publishers, 1963.

8. Giner, J.; Parry, J.M.; and Smith, S.M.; in Fuel Cell Systems II, ASC Advances in Chemistry Science Series, no. 90, 1969.

TABLE I

CORROSION TESTING EXPERIMENTS (SOLUTION COLOR AND CATALYST RECOVERY)

Catalyst	Untreated	Treatment 500°C	700°C	900°C	1100°C
Pt Black	Lt.Green 64.4%	NT	NT	NT	NT
G86-1-2B	Brown 60.0%	Lt.Green 85.8%	Lt.Blue 90.4%	Lt.Blue 84.8%	Colorless 80.6%
G86-1-3	Reddish-Brown 48.4%	Lt.Blue 91.0%	V.Lt.Blue 92.0%	V.Lt.Blue 88.1%	Colorless 76.0%
G86-1-4	Dk.Brown 69.6%	NT	NT	NT	NT
G86-1-5	Lt.Brown 80.3%	NT	NT	NT	NT

Dk. = Dark
Lt. = Light
V.Lt = Very light
NT = Not Tested

TABLE II

LATTICE PARAMETERS
CALCULATED FROM X-RAY DIFFRACTION DATA

Electrocatalyst	Non-Heat-Treated	500°C	700°C	900°C	1100°C
Pt Black	3.911	NT	NT	NT	NT
G86-1-2	3.908	3.915	3.915	3.914	3.908
G86-1-1	3.903	NT	NT	NT	NT
G86-1-3	3.896	3.909	3.908	3.907	3.889

NT = Not Tested

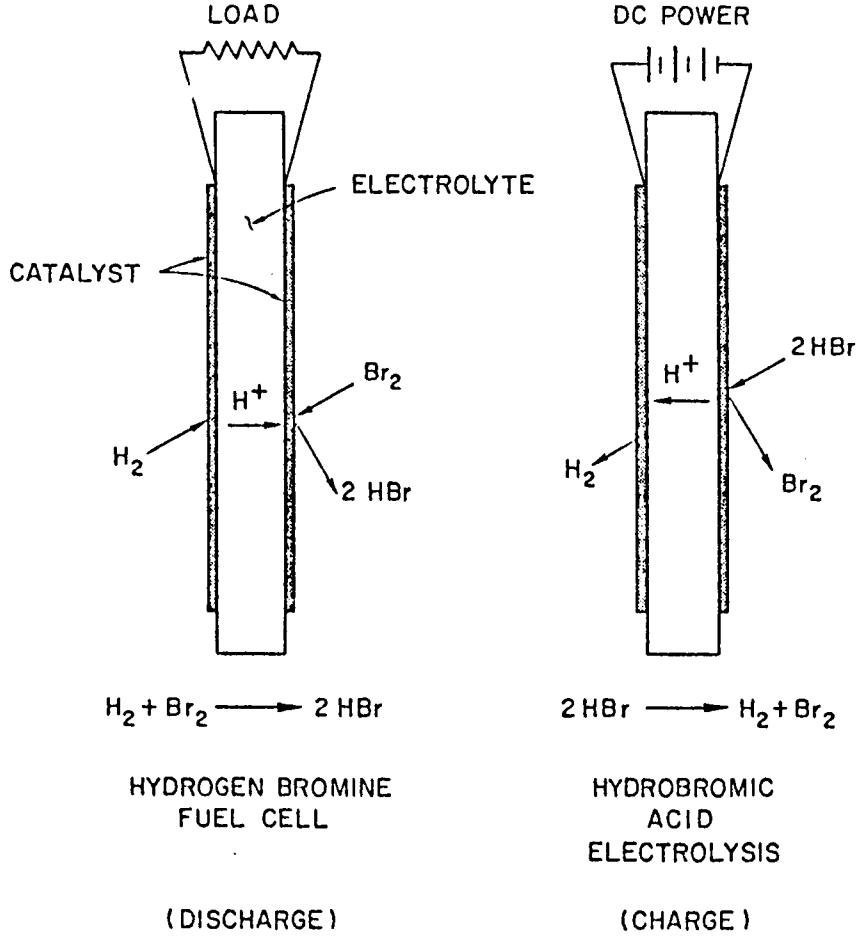

Figure 1: HYDROGEN / BROMINE REGENERATIVE FUEL CELL CYCLE

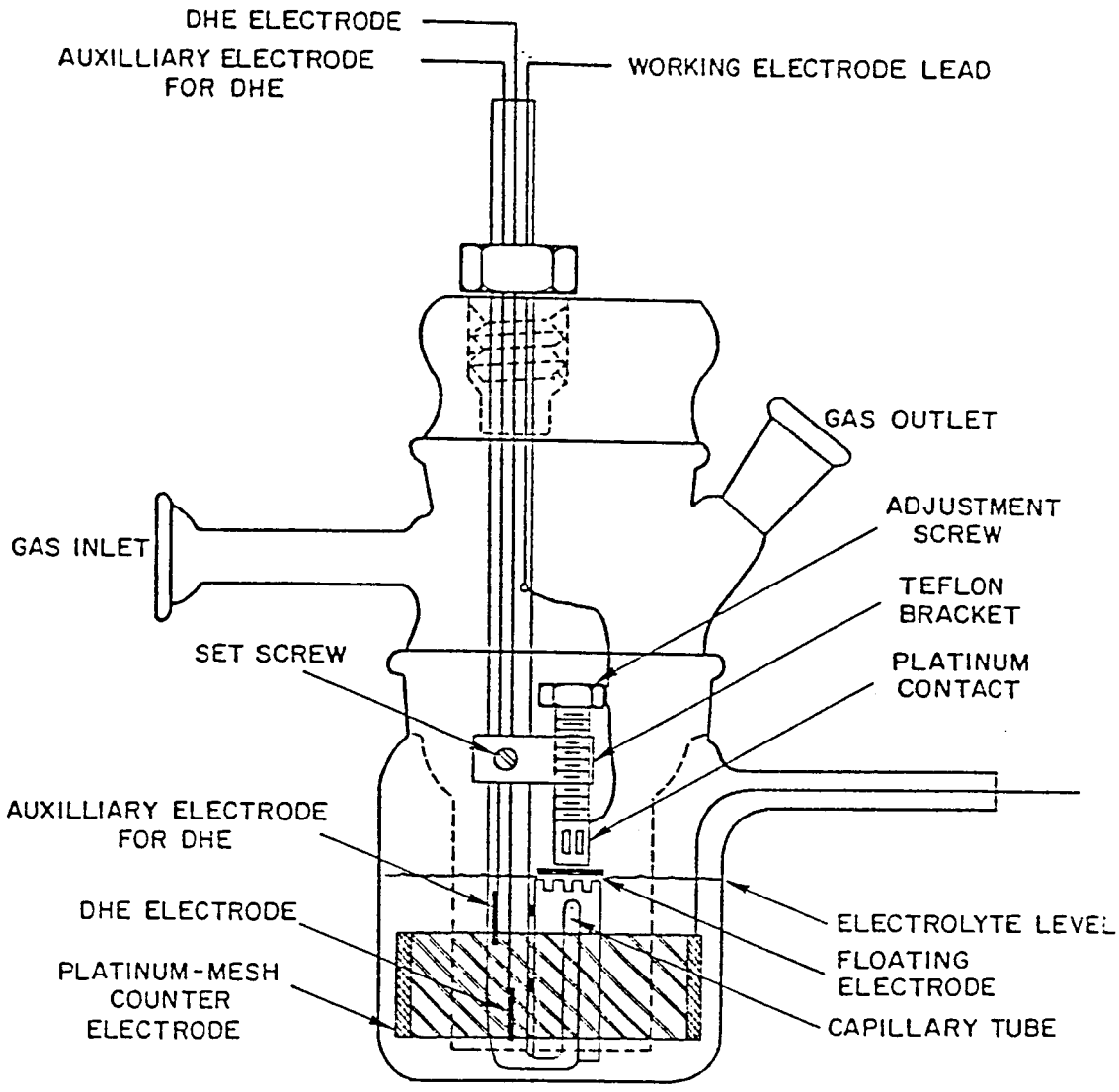

Figure 2: FLOATING ELECTRODE HALF-CELL APPARATUS

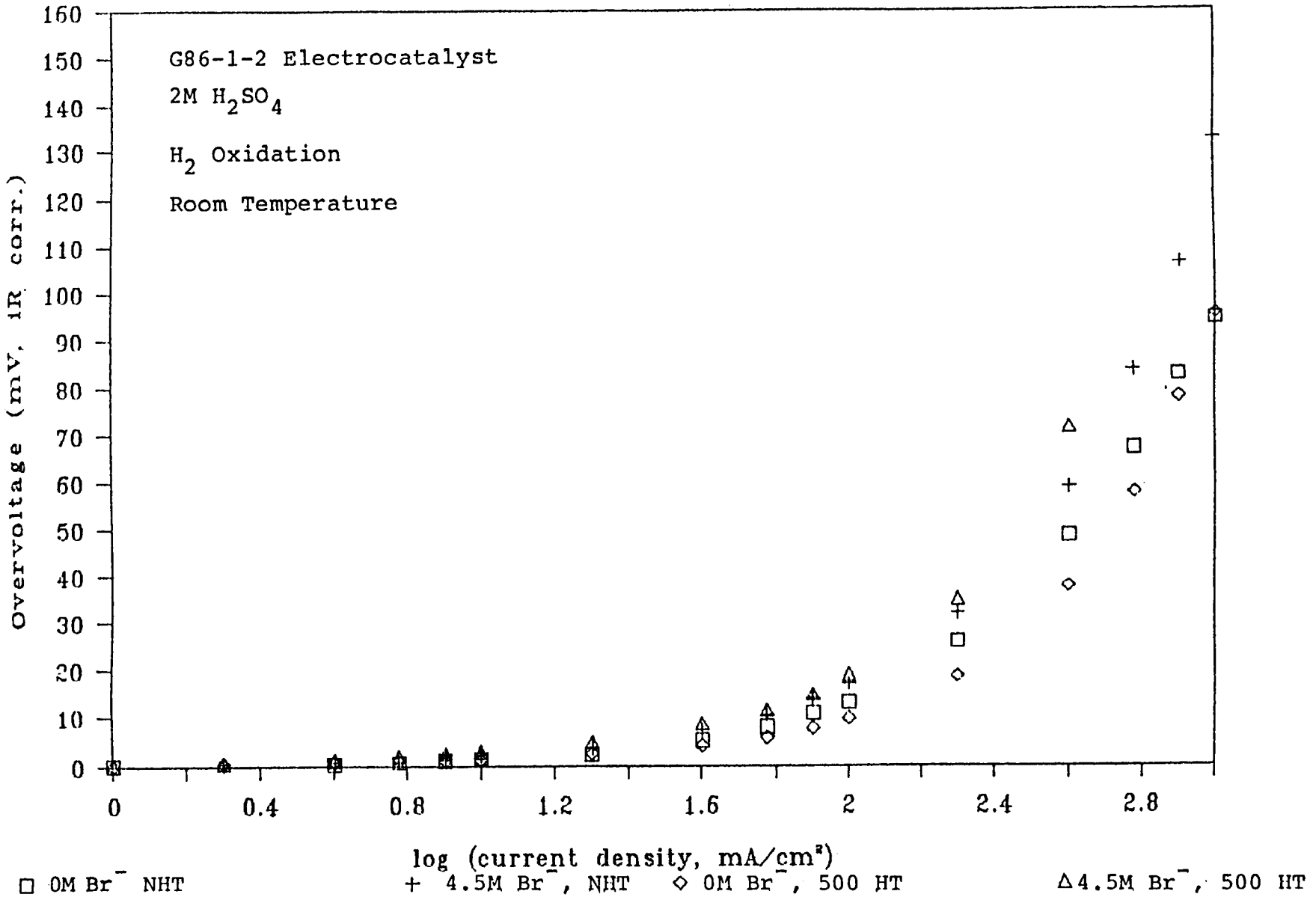

Figure 3: Effect of Bromide Ion and Heat-Treatment Temperature on H_2 Oxidation.

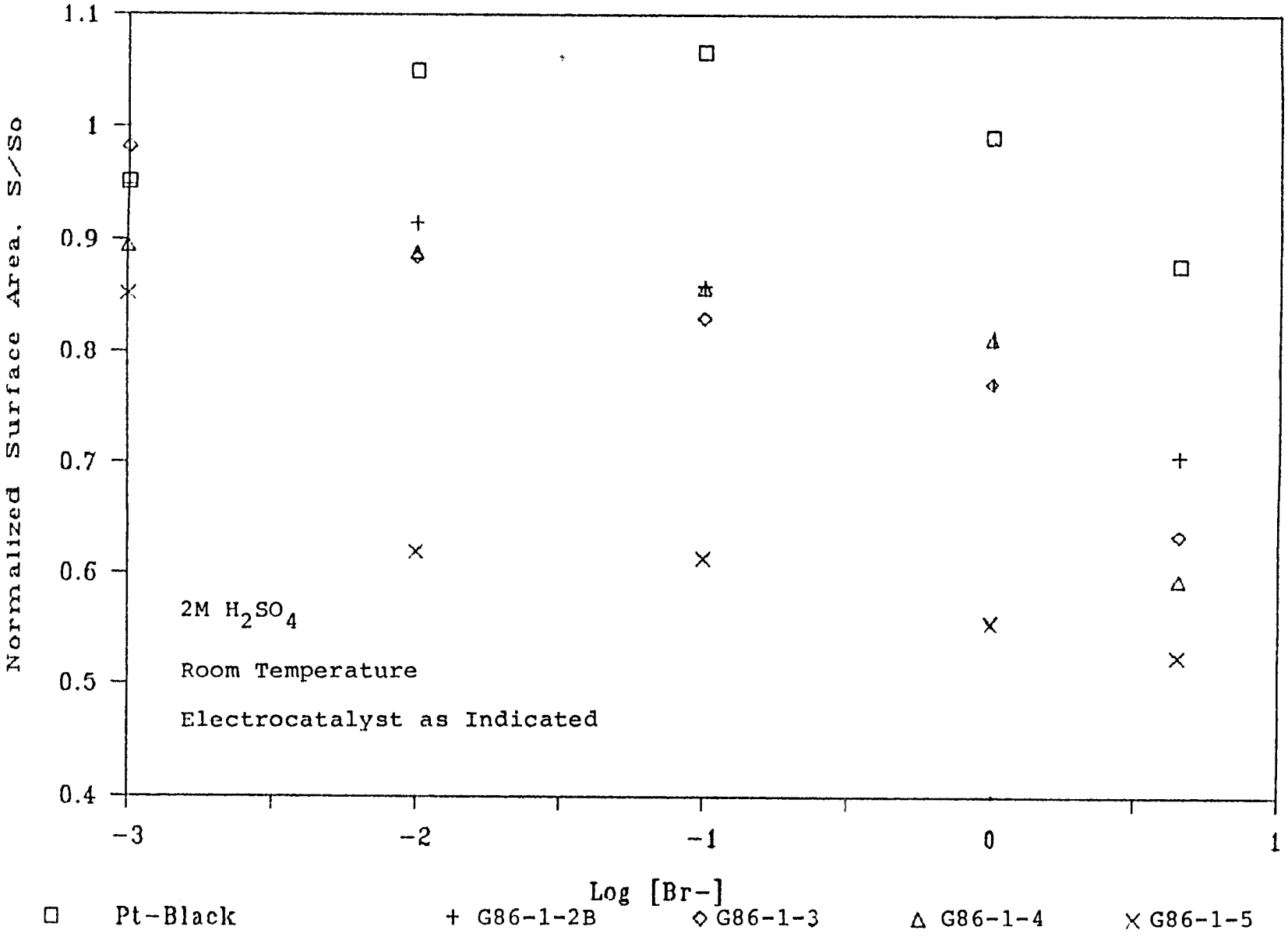

Figure 4: Effect of Bromide Ion Adsorption on Electrocatalyst Surface Area.

SATELLITE POWER USING MAGNETICALLY SUSPENDED FLYWHEEL STACK*

James A. Kirk and Davinder K. Anand
University of Maryland
College Park, Maryland 20742

This paper reports upon research activities with magnetically suspended flywheels, that are being cooperatively conducted by TPI, Inc. and the University of Maryland for GSFC. The purpose of the effort is to critically examine and further the development of all the key technologies which impact the inertial energy storage system.

The results presented in this paper discuss the concept of a magnetically suspended flywheel as it applies to a 500 Watt-hour energy storage system. The proposed system is currently under hardware development and is based upon two "pancake" magnetic bearings arranged in a vertical stack.

INTRODUCTION

To effectively design a 500 WH flywheel energy storage device, several parameters concerned with the specifications, design goals, and applications of the device have to be known apriori. For spacecraft applications, it is important to minimize the mass and size of the device without sacrificing its energy storage capacity. Therefore, one design goal of the system is to maximize the SED (specific energy density). This SED should exceed that of electrochemical systems which is typically 14 WH/kg. A system SED goal for a past 300 WH flywheel design [2-5] has been to exceed a value of 20 WH/kg or 9 WH/lb. This was the design goal used for the 500 WH energy storage system.

The proposed energy storage system is based on a "pancake" magnetic bearing stack as shown in Figure 1. The magnetic bearings used in the stack have been discussed by Kirk and Studer [6,7] and are a required element for a viable and efficient energy storage system. The acceleration of the flywheel or charge cycle (motor mode) must occur during a 60 minute interval when the satellite is exposed to sunlight. The spindown of the flywheel or discharge cycle (generator mode) must occur during a 30 minute interval when the satellite is exposed to darkness. The energy storage system during discharge must supply power at a constant voltage of 150 ±2% volts DC. However, to design a flywheel with suitable size and capacity, operating speeds which are directly proportional to generator output voltages must vary by 50% (the high operating speed being twice as much as the low operating

*A portion of the work reported in this paper was performed under NASA contract NAS5-29272 [Reference 1].

speed). Therefore, some type of power conditioning must be incorporated to maintain the required output voltage. In addition, energy losses in the electronics associated with the charge and discharge cycles must be minimized. For the 300 WH design, an efficiency of 90% for each cycle is desired. This was also assumed for the 500 WH design. Therefore to supply 500 WH, a 550 WH capacity flywheel was sized.

Other design goals of the system include modularity, suitability to withstand outside load disturbances and protection of equipment when failure of flywheel material or suspension occur. An additional design criteria specifies that the rotor remain magnetically suspended under a 2-G radial load. This criteria is used in the 500 WH design. To protect the magnetic bearing, suspension ring and motor/generator when failure of the magnetic suspension occurs, back-up ball bearings are used. The outside portion of the ball bearing (see Fig. 2) is set just beyond the gap operating range of the magnetic bearing (typically ± .01"). The ball bearings support the flywheel when the flywheel deflection due to outside disturbances exceeds this operating range. They protect the magnetic bearing and motor/generator materials from collision. A detailed discussion on magnetic bearing back-up ball bearings is given in a paper by Frommer [2,8]. For protection of satellite equipment if the flywheel material fails under high speeds (burst condition), it is necessary to design the flywheel for separation of the outermost rings from the remainder of the flyweel [as was done in reference 9-14]. Doing this makes the containment of failed flywheels easier.

PROPOSED FLYWHEEL DESIGN

The 500 WH capacity flywheel was analyzed using the FLYANS2/FLYSIZE software developed by UMCP [11-13] and modified by TPI. The computer program FLYANS2 performs a stress analysis on a multi-ring flywheel arrangement given material properties and inner radius ratios (inner radius of ring/outer radius of entire flywheel). Other inputs include the inner radius displacement ratio limit and the ring interference (in assembly) ratio limit. The inner radius displacement ratio input limits the gap growth (between the suspension ring of the flywheel and the magnetic bearing) of the suspension system due to the centrifugal forces generated by the spinning flywheel. Gap growth effects the suspension control system in a detrimental way by reducing the control system active stiffness, K_A. The ring interference limit is the limit on the amount of interference between rings. FLYANS2 performs a stress analysis for both noninterference fitted and interference-fitted rings. For interference fitted rings, it computes ring interface pressures that maximize SED while staying within a prescribed limit (typically 0.6%).

The data from FLYANS2 is used for the FLYSIZE computer program to actually size the flywheel. The FLYSIZE output for the 500 WH flywheel is shown in Table 1 with the upper and lower operating speed ratio, selected as .375 and .75 of the burst speed.

It is assumed that the flywheel has a weight of half the total energy storage system. Therefore its SED must be twice the system SED. Through repeated simulations, it was determined that a flywheel configuration with an inner return ring made of segmented iron and 5 composite (Celion 6000 graphite/epoxy) outer rings, interferenced fitted and having inner radius ratios (inner radius of ring/outer radius of outer ring of flywheel) of .48, .5, .6, .7, .8 and .9, yielded high SEDs that exceeded twice the system SED. The inner radius displacement ratio limit and the

ring interference limit value used was .006. Repeated computer runs for a 500 WH flywheel with a high SED have yielded a flywheel configuration weighing approximately 30 lbs.

The stack bearing consists of 2 magnetic bearings, a motor/generator and 2 back-up ball bearings as shown in Fig. 1.. One requirement for the flywheel is that it must have a large enough height to house the components shown in Figure 1. Based on the sizing of the 300 WH flywheel system, the minimum component heights for the 500 WH system is 4.50 inches (11.4 cm).

Flywheels incorporating 4", 5" and 6" (10.2 cm, 12.7 cm and 15.2 cm) magnetic bearings were analyzed and designed using the FLYANS2, FLYSIZE, and MAGBER computer programs. MAGBER developed at UMCP was used to determine the bearing's axial-load carrying capability. The results of design runs for flywheels using 4", 5" and 6" (10.2 cm, 12.7 cm and 15.2 cm) diameter magnetic bearings is summarized in ref. 1.

As mentioned before, centrifugal forces cause the inner radius of the flywheel to expand at high speeds (called air gap growth). FLYSIZE determines this expansion at the low and high operating speeds of the flywheel and reports these numbers to the user. Through iterative design runs using FLYANS2 and FLYSIZE, one can meet the air gap condition as well as achieve a high SED. The 500 WH design yielded a SED value of 19 WH/LB (42 WH/Kg) and an air gap growth between lower and upper operating speeds of .015 inches (0.381 mm).

MAGNETIC BEARING TECHNOLOGY

The magnetic bearing for a 500 WH energy storage system was designed to support a 2-g axial load without loss of suspension. An additional goal was to achieve a certain permanent magnet radial stiffness, K_x, and current-force sensitivity, K_I. Design values for K_x and K_I were assumed based on maintaining suspension control system performance similar to past UMCP magnetic bearings.

Based on the UMCP 3" (7.6 cm) laboratory model, K_I was taken to be one hundredth the value of K_x in lb/amp. Thus, for the 500 WH design, K_I was chosen to be 56 lb/amp, while the value of K_x was chosen as 5600 lb/in (1002 kg/cm) with a flywheel linear excursion range [around a uniform air gap] of ±.01 inches (±0.254 mm).

Knowing the desired system axial-load carrying capability, K_x, K_I, and minimum current, the following physical and magnetic properties of the bearing are then determined using the MAGBER design program:

> Stator radius, Air gap, Permanent magnet (PM) area, PM thickness, PM operating point, Leakage Permeance, Air gap Permeance, Air gap Flux and flux density, Coil turns, Coil wire size and Axial Drop.

The sizing of the magnetic bearing involved an iterative process via computer simulation using the program MAGBER. Magnetic circuit permeances, fluxes, and flux densities were computed for trial physical dimensions (i.e., pole face thickness, gap distance, axial drop, magnet area, magnet length) and material magnetic properties of the bearing. The operating flux density of the permanent magnets was also derived. K_x, K_I, coil turns (N), and axial-load carrying capability (W_a) could then be determined using the computed magnetic circuit parameters.

Based upon the trial dimensions pole face thickness and air gap distance was increased to avoid saturation in the iron material (which limits the amount of useful flux that crosses the suspension air gap). The flux density within the Fe material should not exceed the value of 1.5 teslas or saturation will occur. The maximum flux density of the iron material was determined by computing the flux density at the thinnest portion of the flux plates - i.e., at the pole faces. MAGDESIGN (a program developed at TPI for this project) was used to determine saturation conditions for various displacements of the flywheel. The object was to remain at an unsaturated condition within the operating gap range of the suspension control system.

SUSPENSION CONTROL SYSTEM DESIGN

The design goal for the suspension control system for the 500 WH energy storage system was to design a control system which would keep the flywheel suspended under static and dynamic loads. To withstand static loads (in this case a 2-G radial load), a system gain was selected which provided a steady state active stiffness sufficient to satisfy the required operating excursion range of the flywheel.

Nearly all of the electronic component values from previous UMCP laboratory suspension control systems were used in the design of the 500 WH control system. A schematic of the control system for the magnetic bearing is shown in Figure 3.

The input reference voltage was determined to be within the range of 0 to +15V, which was the range used in past systems. The maximum operating current was used to size the coil wire and the power amplifiers. To minimize the control current and yet maintain the same steady state active stiffness the current-force sensitivity K_I was increased and the adjustable reference voltage was reduced by the same proportion. By increasing K_I the amount of coil turns needed for design was increased. For a value of R_{17} = 11 kΩ and K_I = 56 lb/amp (25.5 kg/amp), N was computed to have a value of 825 turns/coil with a maximum operating current of 10.12 amps. K_I was then increased by a factor of 2.5 to reduce the coil amperage to 4.05 amps and reduce the variable resistance to 4360 Ω. This resulted in a K_I value of 140 lb/in (25 kg/cm) and a turns/coil value, N, of 2100 turns. The modified values were used for the 500 WH design.

The final parameter that was determined for the suspension control system was the compensation network time constant, T. This parameter influences the damping of the system. For the 500 WH system, it was desirable to maximize the damping so as to limit the flywheel excursions due to mass unbalance. To maximize system damping and minimize dynamic loading effects, an optimum value of T was selected. To optimize T, root locus plots and Bode plots were used and the results are shown in Ref. 1.

For the 500 WH system, a value of T = .0016 sec was chosen to minimize the amplitude of response and maximize damping. This called for a capacitance value of .016 μF in the compensation network of the control system (keeping the resistance the same as previous values of past systems).

Based upon experience gained in designing the control system shown in Figure 3, a modified version of the control system, as shown in Fig. 4, is being currently investigated for use in the 500 WH system.

MOTOR/GENERATOR DESIGN

The motor/generator design for the 500 WH system is based upon a permanent magnet, electronically commutated, 3 phase machine, shown conceptually in Fig. 5. Several improvements in the conceptual design have been incorporated into the 500 WH system, and these are shown in Fig. 6.

The first step in design was to determine power, voltage, and armature current variation during the charge cycle of the motor and the discharge cycle of the generator. It was assumed that the bus of the motor receives a constant power of 650 watts from the solar array at 150V + 2% DC. This happens during the time span of an hour. Since motor voltage is proportional to flywheel speed and flywheel speed was chosen to vary by 50%, a motor voltage profile varying from 70V to 140V was used in the design. (This assumed a voltage drop of 10V during transfer of energy from PV array to flywheel motor).

Armature current variation (per phase) was determined by dividing the time equation of power by the time equation of voltage. At the beginning of the charge cycle, the armature current/phase was computed to be 3.1 amps and at the end it was computed to be 1.4 amps. A proportional discharge cycle was assumed such that over 21 minutes, the generator discharges at a low power of 625 watts and over the remaining nine minutes the generator discharges at a high power of 1875 watts. All together, the generator delivers 1100 watts over 1/2 hour equal to 550 WH. 500 WH actually gets to the satellite power system due to energy losses in the power electronics. (This was a previously mentioned design goal). The voltage variation of the generator is linear from 140V to 70V, but it varies at two different rates due to the change in power delivered. It was determined that the maximum current in the armature per phase is 8.93 amps/phase.

This maximum current (which exceeds that of the motor) is used to design the coils in the armature. In the proposed motor/generator, the rotating ring will be replaced by a stationary ferrite ring glued onto the inside periphery of a stationary ironless armature. The outside rotating ring assembly is made up of PM magnets and is attached to a soft iron backing ring. An 8-pole machine is proposed using a delta-connected winding operating at 4000 Hz maximum frequency. The dimensions of the device are constrained by the size of the flywheel and the magnetic bearing. For the 500 WH design, the outside radius of the soft iron backing ring could not exceed the inner radius of the first composite ring of the flywheel. A 2 in. packaging height was a design goal. The gap distance between PM's and armature coils needed also to exceed the gap distance of the magnetic bearing. Based on these constraints, PM size and armature coil configuration and size were determined.

Of further interest is the determination of energy losses within the armature and also within the power electronics of the device. Armature loss ($3I^2_{max}R$) was computed to be 2.11 watts while the loss due to the ferrite ring was determined to be negligible (less than one watt). Most of the other losses for the 500 WH energy storage system were kept the same as or scaled up from the 300 WH design.

500 WH DESIGN

The proposed design of the 500 WH magnetically suspended flywheel energy storage system is shown in Fig. 7. The specifications of the entire system is summarized in Tables 1 and 2.

Table 1 summarizes flywheel specifications computed using the FLYSIZE/FLYANS2 software. Table 2 gives magnetic bearing specifications which were determined using magnetic circuit theory and the design programs previously discussed.

CONCLUSIONS/RECOMMENDATIONS

Based upon the state-of-the-art review and the proposed design of the 500 WH system, it can be concluded that

- Magnetically suspended flywheel energy storage systems are a viable and superior alternative to batteries
- System issues of attitude control and power transfer are manageable
- The magnetically suspended flywheel system can be designed using current knowledge in modules varying in size from 100 WH to 1000 WH.

Consistent with these conclusions, the following activities are currently underway:

- Construct Prototype 500 WH Energy Storage System using proposed design.
- Bench test prototype to 20,000 RPM.
- Enhance robustness of control electronics based on bench test.
- Design a test program to cycle energy storage wheel through operating range.
- Construct Spin Test Facility for cyclic testing at design speeds.
- Test and evaluate prototype operation under design conditions. Incorporate test results in final design.
- Construct flight hardware experiment.

REFERENCES

1. SBIR Report "Design of a 500 Wh Magnetically Suspended Flywheel Energy Storage System," Contract NAS 5-29272, August 1986.

2. Anand, D.K., Kirk, J.A. and Frommer, D.A., "Design Considerations for a Magnetically Suspended Flywheel System", Proceedings of the 20th Intersociety Energy Conversion Engineering Conference, August 18-23, 1985, Miami Beach, Florida, pgs. 2.449-2.453.

3. Anand, D.K., Kirk, J.A., Zmood, R.B., et al, "System Consideratins for a Magnetically Suspended Flywheel", Proceedings of the 21st Intersociety Energy Conversion Engineering Conference, Aug. 25-29, 1986, San Diego, CA pgs. 1829-1833.

4. Anand, D.K., Kirk, J.A. and Bangham, M.L., "Simulation, Design and Construction of a Flywheel Magnetic Bearing", ASME Paper 86-DET-41, Presented at the Design Engineering Technical Conference, Columbus, Ohio, Oct. 5-8, 1986.

5. Anand, D.K., Kirk, J.A. and Bangham, M.L., "Design, Analysis and Testing of a Magnetic Bearing for Flywheel Energy Storage", ASME Paper 85-WA/DE-8, presented at 1985 ASME Winter Annual Meeting.

6. Kirk, J.A., "Flywheel Energy Storage - Part I, Basic Concepts", International Journal of Mechanical Sciences, Vol. 19, 1977, pp. 223-231.

7. Kirk, J.A. and Studer, P.A., "Flywheel Energy Storage - Part II, Magnetically Suspended Superflywheel", International Journal of Mechanical Sciences, Vol. 19, 1977, pp. 233-245.

8. Frommer, D.A., "Mechanical Design Considerations for a Magnetically Suspended Flywheel", University of Maryland, M.S. Thesis, August 1986.

9. Kirk, J.A., Anand, D.K. and Khan, A.A., "Rotor Stresses in a Magnetically Suspended Flywheel System", Proceedings of the 20th Intersociety Energy Conversion Engineering Conference, August 18-23, 1985, Miami Beach, Florida, pgs. 2.454-2.462.

10. Evans, H.E. and Kirk, J.A., "Inertial Energy Storage Magnetically Levitated Ring-Rotor", Proceedings of the 20th Intersociety Energy Conversion Engineering conference, August 18-23, 1985, Miami Beach, Florida, pgs. 2.372-2.377.

11. Kirk, J.A. and Huntington, R.A., "Stress Analysis and Maximization of Energy Density for a Magnetically Suspended Flywheel", ASME paper 77-WA/DE-24, presented at 1977 ASME Winter Annual Meeting.

12. Kirk, J.A. and Huntington, R.A., "Stress Redistribution for the Multiring Flywheel", ASME paper 77-WA/DE-26, presented at 1977 ASME Winter Annual Meeting.

13. Kirk, J.A. and Huntington, R.A., "Energy Storage - An Interference Assembled Multiring Superflywheel", Proceedings of the 12th IECEC Conference, Washington, D.C., September 2, 1977, pp. 517-524.

14. Kirk, J.A. and Anand, D.K., et al, "Magnetically Suspended Flywheel System Study", NASA Conference Publication 2346, "An Assessment of Integrated Flywheel System Technology", Dec. 1984, pgs. 307-328.

TABLE 1 FLYWHEEL SPECIFICATIONS FOR 500 WH ENERGY STORAGE SYSTEM

Inner Diameter	:	5.760 in. (14.630 cm)
Outer Diameter	:	12.000 in. (30.480 cm)
Thickness	:	5.474 in. (13.904 cm)
Configuration	:	Multiring → 1 seg. iron ring 5 graphite/epoxy rings
Burst Speed	:	70 k rpm
Max. Oper. Speed	:	52 k rpm
Low Oper. Speed	:	26 k rpm
Weight	:	29 lbs. (13.2 kg)
Usable Energy Density	:	18.96 WH/lb. (41.71 WH/kg)
Burst Energy Density	:	44.95 WH/lb. (98.91 WH/kg)
Air Gap Growth @ Burst Speed	:	.0353 in. (0.8966 mm)
Air Gap Growth @ 52 k rpm	:	.0199 in. (0.5055 mm)
Air Gap Growth @ 26 k rpm	:	.0050 in. (0.1270 mm)

TABLE 2 MAGNETIC BEARING SPECIFICATIONS FOR 500 WH ENERGY STORAGE SYSTEM

Radial Stiffness, K_x :	5600 lb/in. (1002 kg/cm)
Current-Force Sensitivity, K_I :	140 lb/in. (25.1 kg/cm)
Turns/Electromagnetic Coil, N :	2100 turns
Maximum Operating Current, i_{max} :	4.05 amps
Gap Operating Range :	± .01 in. (±0.254 mm)
Nominal Gap Distance, g_o :	.038 in. (0.965 mm)
Stator Radius :	2.88 in. (7.32 cm)
Pole Face Thickness :	0.15 in. (0.38 cm)
Magnet Diameter :	1.8 in. (4.57 cm)
Magnet Length:	0.3 in. (0.76 cm)

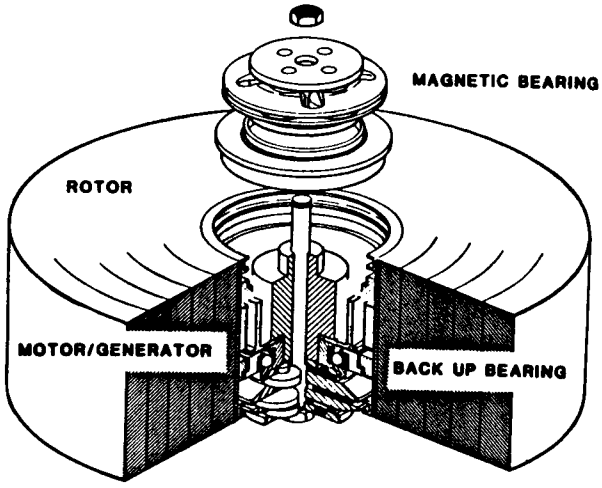

FIGURE 1- MAGNETIC BEARING STACK FOR 500 WH SYSTEM

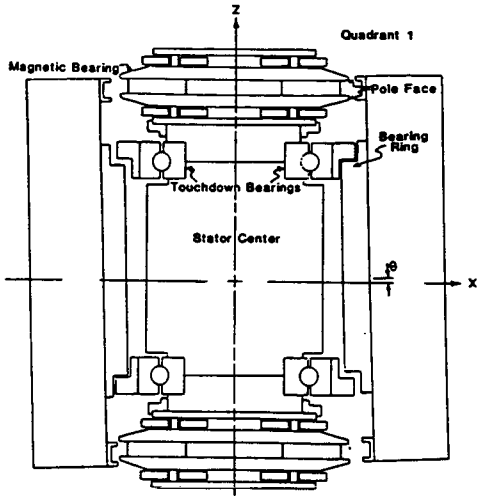

FIGURE 2- FLYWHEEL TOUCHDOWN FOR A DOUBLE MAGNETIC BEARING STACK

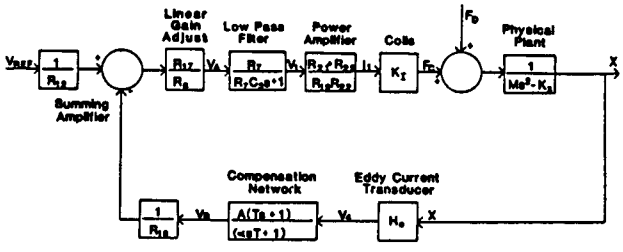

FIGURE 3- CONTROL SYSTEM FOR MAGNETIC SUSPENSION

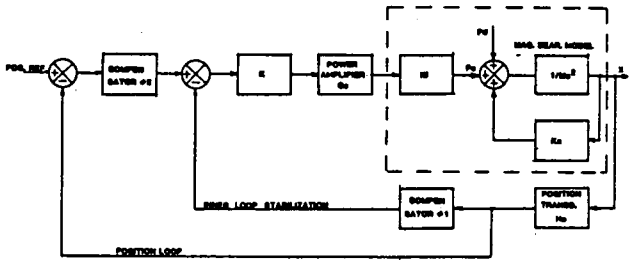

FIGURE 4- CONTROL SYSTEM FOR 500 WH DESIGN

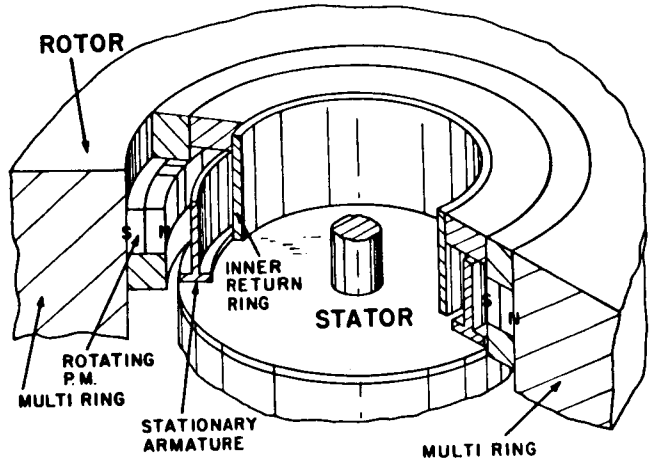

FIGURE 5- LABORATORY MODEL OF PERMANENT MAGNET MOTOR/GENERATOR

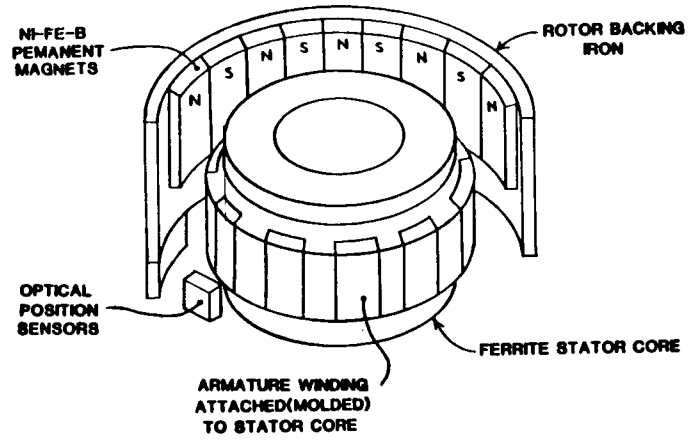

FIGURE 6- MOTOR/GENERATOR DESIGN FOR 500 WH SYSTEM

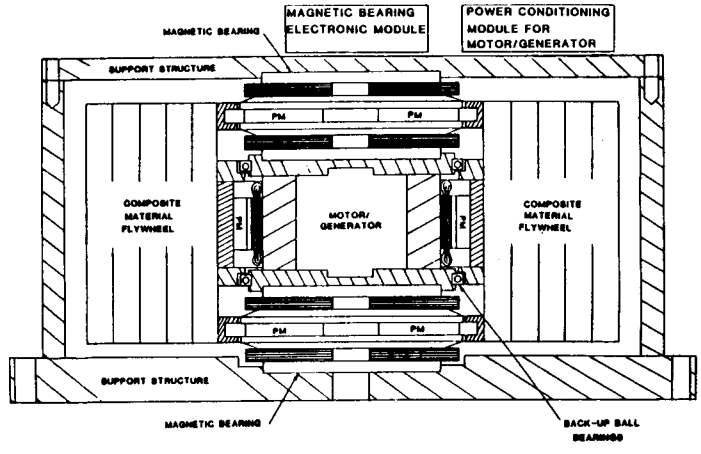

FIGURE 7- CROSS-SECTION OF 500 WH FLYWHEEL ENERGY STORAGE SYSTEM

APPLICATION OF ADVANCED FLYWHEEL TECHNOLOGY FOR ENERGY STORAGE ON SPACE STATION*

M. Olszewski
Oak Ridge National Laboratory
Oak Ridge, Tennessee 37831

In space power applications where solar inputs are the primary thermal source for the power system, energy storage is necessary to provide a continuous power supply during the eclipse portion of the orbit. Because of their potentially high storage density, flywheels have been given consideration for use as the storage system on the proposed orbiting space station.

During the past several years graphite fiber technology has advanced, and this has led to significant gains in flywheel storage density. The tensile strength of current fibers is a factor of two to three higher than previous materials. Use of these improved fibers in experimental flywheel rims has resulted in ultimate storage densities of 878 kJ/kg being achieved.

With these high-strength graphite fibers, operational storage densities for flywheel storage modules applicable to the space station storage need could reach 200 kJ/kg. This module would also be volumetrically efficient occupying only about 1 m^3. Because the size and mass of the flywheel storage module are controlled by the storage density, improvements in fiber strength can have a significant impact on these values. With improvements in fiber strength that are anticipated within the next five years, operational storage densities on the order of 325 kJ/kg may be possible for the flywheel module.

INTRODUCTION

Space power systems using a solar primary energy source, require an energy storage component to maintain operation of the platform during the eclipse portion of the orbit. Flywheels offer a number of advantages that make them attractive for such systems. They possess relatively high energy storage densities; this results in a low storage system mass. Also, the power density of the flywheel is independent of the energy density and is fixed by the output device rather than the flywheel. This results in a storage system whose charging and discharging rates can differ greatly without affecting its performance. In addition, the rotating mass of the flywheel can provide for attitude control of the space platform, while also fulfilling its energy storage role. Because of these valuable operating characteristics, NASA has sponsored several flywheel workshops (refs. 1 and 2) and has investigated a concept

*Research sponsored by the Office of Nuclear Energy under U.S. DOE contract No. DE-AC05-840R21400 with Martin Marietta Energy Systems, Inc.,

that integrates energy storage and attitude control functions (ref. 3) in a single flywheel module.

In this paper, advances in flywheel performance are detailed and potential improvements estimated. A flywheel energy storage module suitable for the needs of the space station is described. Performance of the module, in terms of energy storage density, is estimated using demonstrated flywheel performance. In addition, anticipated improvements in flywheel storage densities are used to determine potential performance increases for the storage module.

FLYWHEEL DEVELOPMENT

Flywheel Rotor Materials

In space power applications, minimization of system mass is a critical design parameter. For the flywheel designer, this translates into a requirement that the storage system possess the highest possible storage density. As shown in Table 1, this necessitates that the flywheel rotor be constructed of composite material.

Early Composite Flywheel Performance

Composite flywheel technology was initially established in the Mechanical Energy Storage Technology (MEST) Program conducted by the Oak Ridge National Laboratory (ref. 4). In the initial stages of the program, a number of rotor designs (configurations and materials) were fabricated and tested. The purpose of these initial tests was to determine the performance limits of the design and verify rotor failure mechanisms. Thus, the testing regime was limited to ultimate speed evaluations. The performance results of these initial ultimate speed tests are given in Table 2. The energy density and stored energy figures represent the rotor's capability at the maximum speed attained in the test. Actual operational values would, of course, be lower. The highest ultimate energy density achieved was 266 kJ/kg with a subcircular Kevlar rim design. Following closely, at 233 kJ/kg, was a disk/ring design made of graphite and S-glass. The highest stored energy, 7.67 MJ, was achieved with a graphite overwrap configuration.

For the second stage of testing in the MEST Program, the field of candidate rotors was narrowed; and the testing regime expanded to include cyclic fatigue tests. Results of these tests are given in Table 3. The disk and disk/rim rotors completed the full 10,000 cycle test. Subsequent ultimate speed tests of these rotors yielded energy densities of 175 and 229 kJ/kg, respectively. The disk/rim results were particularly instructive, because ultimate speed data were obtained for rotors with no cycles and with 10,000 cycles. Comparison of the energy density achieved in the two tests (233 kJ/kg and 229 kJ/kg) indicated that there was no degradation in performance through 10,000 cycles.

Advances in Flywheel Performance

The MEST Program was phased out in 1983, and flywheel technology was essentially frozen at these performance levels. Flywheel development activities resumed at Oak Ridge in 1985, and significant advances in rotor performance were achieved through precision fabrication of carbon fiber/epoxy material (ref. 5). The fibers used were Hercules IM6 and AS6. The Hercules IM6 fiber came to the market in 1985 and represented a significant improvement in fiber strength. Previous graphite fibers had

ultimate tensile strengths on the order of 2640 MPa (383 ksi). The IM6 fiber at 5340 MPa (775 ksi) more than doubled this strength and led to significant advances in flywheel performance.

The focus of this effort was the design, fabrication, and spin testing of carbon/epoxy flywheels using the advanced high-strength fibers. The first series of rims to be tested (the only ones to be tested to date) was designated the Demo 1 series. To construct the rotors, fibers were wet wound and cured on a mandrel to form a thick-walled cylinder. The fabricated cylinder was then sectioned to form the test rims. In this design, the lower-modulus higher-strength material (IM6) was used for the outer portion of the rim and AS6 for the inner portion.

Test results for the Demo 1 series are summarized in Table 4 and compared with the MEST results in Figure 1. Since the purpose of the program was to demonstrate advances in rotor technology, no attempt was made to optimize the web structure. In these tests, the web structures were relatively heavy being about equal to the rim weight. In an optimized system, the web would be much lighter (potentially on the order of 20% of the rim weight). Consequently, the data points for "rim + web" do not reflect a typical design.

The most dramatic result was obtained with Demo 1C. This rotor was intentionally accelerated until failure occurred at a peripheral speed of 1405 m/s. At this speed, the energy density of the rim only was 878 kJ/kg. The total kinetic energy stored by the unit (rim + web) was 7.28 MJ. The 1405 m/s peripheral velocity was an increase of ~40% over previous spin tests. The demonstrated failure speed of 1405 m/s provides firm experimental evidence for a safe flywheel design operating speed in the range of 1100 to 1200 m/s.

SPACE STATION FLYWHEEL STORAGE MODULE

Module Configuration

A schematic for a flywheel energy storage concept applicable to the needs of the space station is shown in Figure 2. This concentric configuration was chosen because it is highly efficient in its volumetric characteristics. The flywheel module would consist of two such flywheels. Energy is stored in the two counter-rotating flywheel rotors, which are aligned on a common axis. This results in the momentum vectors of the two flywheels canceling and the platform experiencing a zero net momentum vector. A highly efficient (on the order of 96%), lightweight (specific power of 5 kW/kg) axial gap permanent magnet motor/generator is used for charging and discharging the flywheel. The suspension system uses magnetic bearings to achieve very low drag and minimize standby losses. This also allows the bearing stiffness to be adjusted during operation of the system.

Estimated System Performance

Mass estimates were prepared for the flywheel storage module illustrated in Figure 2. In performing the analysis, it was assumed that the required module output power was 87.5 kW. The time available for charging (solar time during orbit) was set at 55 minutes, and the discharge time (eclipse portion of the orbit) was assumed to be 36 minutes.

The flywheel operational storage density was governed by several major assump-

tions. The maximum operating speed of the flywheel was limited to 80% of the burst speed. A 2:1 speed ratio was used resulting in a 75% depth of discharge (on an energy basis). For efficiency in material use, a relatively thin rim was used; the ratio of inner to outer radius was set at 0.85.

The flywheel rotor was examined at three technology levels. With currently available fibers, a burst speed of 1405 m/s has been demonstrated. This yields a maximum operating speed of 1125 m/s and an operational storage density of 410 kJ/kg for the rim only. Within the next several years, it is anticipated that fiber strength can increase by about 13%. This would raise the maximum operational speed to 1190 m/s and produce an operational storage density of 460 kJ/kg (rim only). Within the next five years, fibers may be available that would permit operational maximum speeds to reach 1400 m/s. With these fibers the flywheel operational storage density would be 650 kJ/kg (again, rim only).

Previous analysis of flywheel storage modules designed for low power (on the order of 100 kW) applications with charge/discharge time ratios near unity have indicated that the module operational storage density is about half that of the rim only value (ref. 5). Using this relationship results in the flywheel module operational storage densities shown in Table 5. As indicated, the module operational storage density, using current fibers, would be 205 kJ/kg. A modest 10% improvement is anticipated within the next several years resulting in a module storage density of 230 kJ/kg. With fiber technology advances anticipated within the next five years, the module storage density could be raised to 325 kJ/kg.

Since the concentric design has all power components within the bore of the flywheel, the module volume is fixed by the size and shape of the flywheel rotor. In sizing the rotor, it was assumed that the rotor length was equal to the rotor diameter. This criterion was used to determine the volume occupied by the modules designed to meet the storage needs of the space station. As indicated in Table 5, the storage module, using current fibers, would occupy 1.07 m^3. Within two years, advances in fiber technology would result in the volume being reduced to under 1 m^3. With the longer term advances, the module volume could potentially be reduced to 0.67 m^3.

Another measure of the volumetric storage efficiency is given by the volumetric storage density. As shown in Table 5 with present technology levels, the module stores 177 MJ in one cubic meter. This could rise to 199 MJ/m^3 within two years and 282 MJ/m^3 within 5 years, if the anticipated increases in fiber strength are realized.

CONCLUDING REMARKS

The flywheel module appears to be an attractive energy storage option for the space station application. With current fibers, the system operational energy storage density is expected to be 205 kJ/kg. This compares favorably with battery and fuel cell systems, which are anticipated to be in the range of 25 to 75 kJ/kg (refs. 1 and 2). In addition, the flywheel module is volumetrically more efficient than the competing systems. The flywheel volumetric storage density of 177 MJ/m^3 is about an order of magnitude higher than that of battery systems (from ref. 1 the volumetric density of NiCd batteries is about 25 MJ/m^3).

If anticipated increases in fiber strength are realized, the performance of the

flywheel storage module would increase substantially. If fiber strength increases are fully realized, it will be possible to raise the storage density (on a mass basis) to 325 kJ/kg with a volumetric density of 282 MJ/m^3.

REFERENCES

1. Keckler, C.R., et al., "Integrated Flywheel Technology 1983," Proceedings of workshop held at Greenbelt, MD, August 2-3, 1983, NASA Conference Publication 2290.

2. Keckler C. R., et al., "An Assessment of Integrated Flywheel System Technology," Proceedings of Conference held at Huntsville, AL, February 7-9, 1984, NASA Conference Publication 2346.

3. Van Tassel, K. E. and Simon, W. E., "Inertial Energy Storage for Advanced Space Station Applications," Proceedings of 20th Intersociety Energy Conversion Engineering Conference, Miami Beach, FL, August 18-23, 1985.

4. Olszewski, M., "Flywheel Performance: Current State-of-the-Art," Proceedings of 19th Intersociety Energy Conversion Engineering Conference, San Francisco, CA, August 19-24, 1984.

5. Olszewski, M. and O'Kain, D. U., "Advances in Flywheel Technology for Space Applications," Proceedings of 21st Intersociety Energy Conversion Engineering Conference, San Diego, CA, August 25-29, 1986.

Table 1. Characteristics of materials used in flywheels

Material	Ultimate tensile strength (σ) MPa	Density (ρ) g/cm^3	σ/ρ [kJ/kg (Wh/kg)]
Steels			
4340	1517	7.7	197 (54.7)
18 Ni (300)	2070	8.0	259 (71.8)
Composites			
E-glass/epoxy	1379	1.9	726 (201.6)
S-glass/epoxy	2069	1.9	1089 (302.5)
Kevlar[a] epoxy	1930	1.4	1379 (382.9)
Graphite epoxy	1586	1.5	1057 (293.7)
Other			
METGLASS[b]	2627	8.0	328 (91.1)

[a]Kevlar is a trademark of Du Pont.

[b]METGLASS is a registered trademark of the Allied Corporation, Morristown, N.J.

Table 2. Performance results for initial ultimate speed configuration tests

Manufacturer	Wheel type	Material[a]	Energy density at maximum speed (KJ/kg)	Energy stored (MJ)
ORNL	Overwrap	K49	178	2.02
Brobeck	Rim	SG/K49	229	2.55
Garrett/ AiResearch	Rim	K49/K29/SG	266	4.43
Rocketdyne	Overwarp Rim	G	143	7.67
APL-Metglass	Rim	M	81	0.14
Hercules	Disk (Contoured Pierced)	G	135	3.06
AVCO	Disk (Pierced)	SG	158	1.44
LLNL	Disk (Tapered)	C	225	1.12
LLNL	Disk (Flat)	SG	242	0.58
GE	Disk (Solid/ Ring)	SG/G	233	2.37
Owens/Lord	Disk	SMC	63	0.61
	Disk/Ring	SMC/G	90	1.01
		SMC/G	100	1.30
		SMC/G	132	1.44

[a]Material legend is: SG = S-glass; K49 = Kevlar 49; K29 = Kevlar 29; G = Graphite; M = Metglass; SMC = S-glass sheet molding compound.

Table 3. Fatigue and ultimate speed tests results from MEST Program

	Flywheel design			
	Disk	Disk/rim	Subcircular rim	Bidirectional weave
Material	SGL[a]	SGL[a]/G	K49	K49
Completed 10,000 Cycle Test	Yes	Yes	No[b]	-[c]
Ultimate Energy Density (kJ/kg)	175[d]	229[d]	237	134
Total stored energy (MJ)	1.86	2.32	2.24	1.50
Speed at failure (rpm)	40,638	47,058	30,012	27,575

[a]S-glass laminate.

[b]Rotor failed at 2586 cycles.

[c]Rotor was not cycle tested.

[d]Rotor had previously completed cyclic test.

Table 4. Test results for advanced flywheel rotors

1985 date	Demo unit	Velocity m/s	Rim specific energy kJ/kg (Wh/kg)	Result
Oct. 17	1A	1055	495 (138)	Web failure, small crack. No rim damage.
Nov. 8	1B	1173	605 (168)	Stopped for inspection. No damage.
Nov. 12	1C	1221	663 (184)	Stopped for inspection. No damage.
Dec. 9	1C	1405	878 (244)	Intentional failure test.

Table 5. Flywheel energy storage module characteristics

Fiber technology	Operational storage density (kJ/kg)	Volume (m^3)	Volumetric storage density (MJ/m^3)
Demonstrated	205	1.07	177
Within 2 years	230	0.95	199
Within 5 years	325	0.67	282

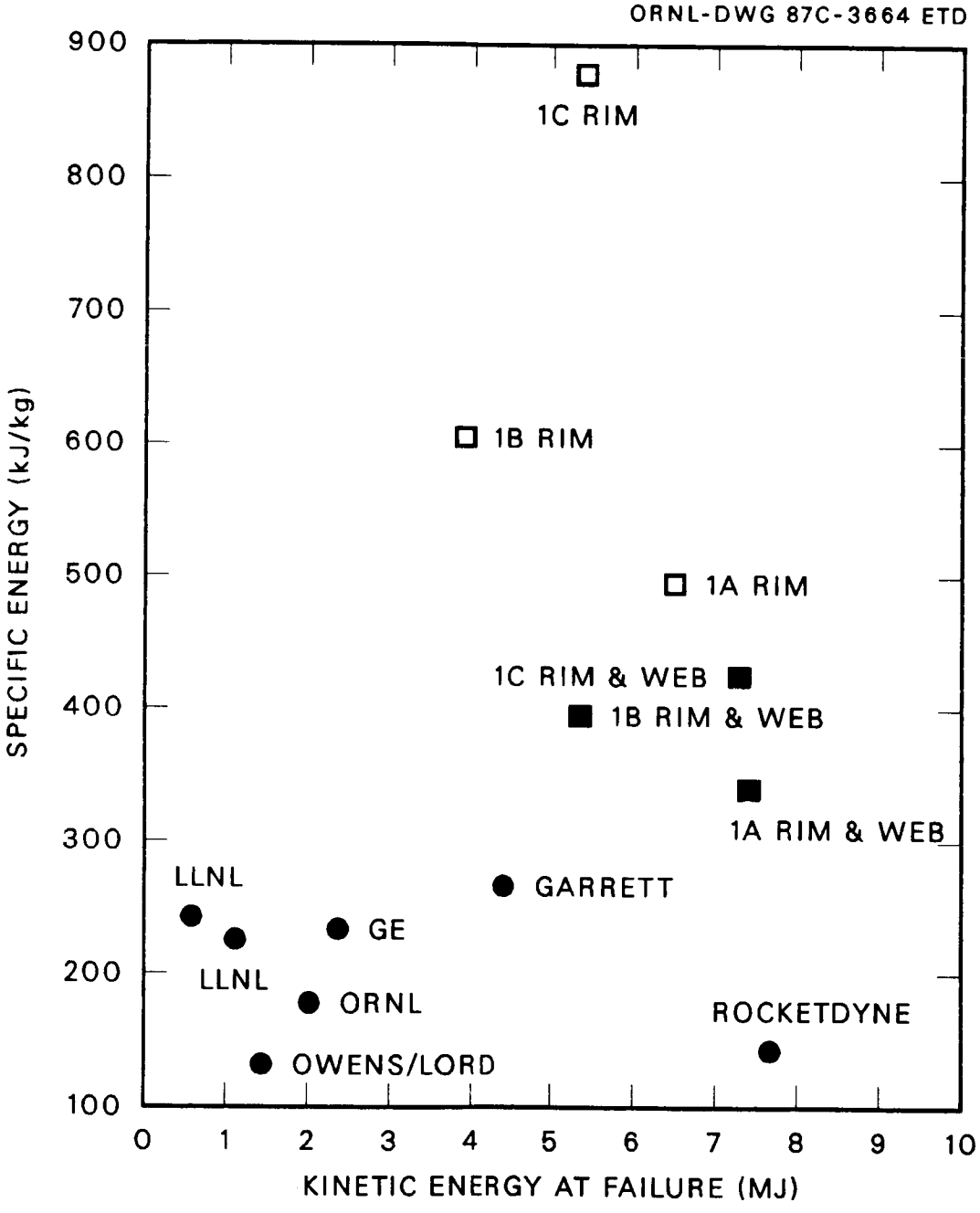

Fig. 1. Comparison of rotor performance.

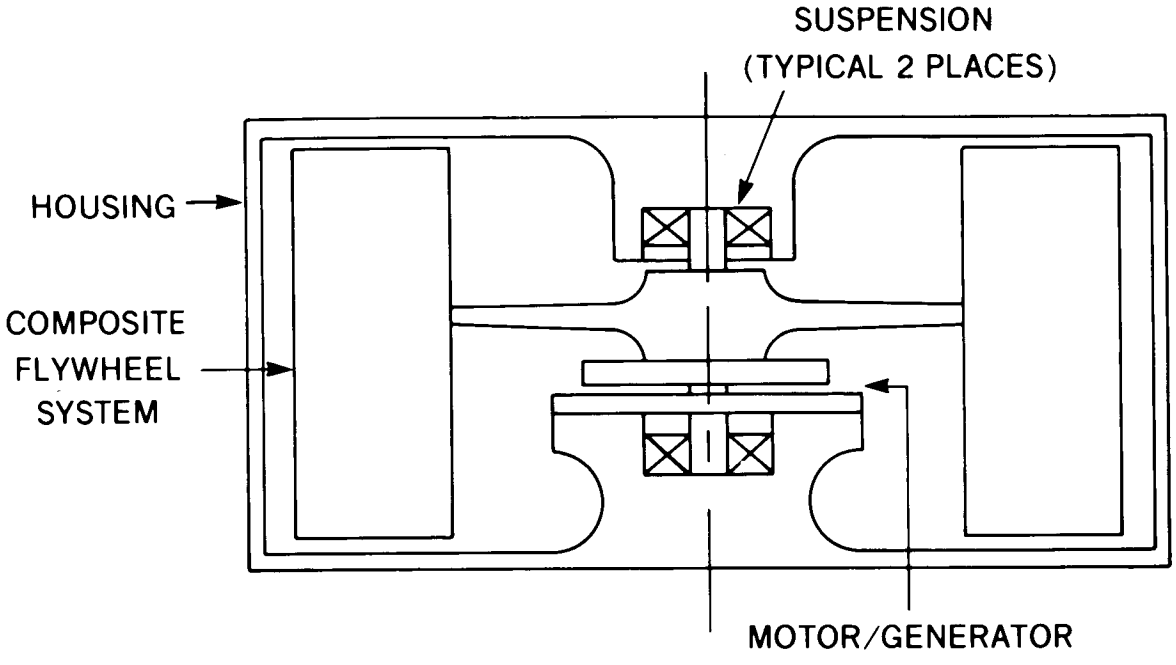

Fig. 2. Schematic of flywheel module for space station application.

EXAFS: NEW TOOL FOR STUDY OF BATTERY AND FUEL CELL MATERIALS

James McBreen and William E. O'Grady
Brookhaven National Laboratory
Upton, New York 11973

Kaumudi I. Pandya
Case Western Reserve University
Cleveland, Ohio 44106

Extended X-ray absorption fine structure (EXAFS) is a powerful technique for probing the local atomic structure of battery and fuel cell materials. The major advantages of EXAFS are that both the probe and the signal are X-rays and the technique is element selective and applicable to all states of matter. This permits in situ studies of electrodes and determination of the structure of single components in composite electrodes, or even complete cells. EXAFS specifically probes short range order and yields coordination numbers, bond distances, and chemical identity of nearest neighbors. Thus, it is ideal for structural studies of ions in solution and the poorly crystallized materials that are often the active materials or catalysts in batteries and fuel cells. This paper uses studies on typical battery and fuel cell components to describe the technique and the capability of EXAFS as a structural tool in these applications. Typical experimental and data analysis procedures are outlined. The advantages and limitations of the technique are discussed. Other techniques, using high intensity synchrotron X-rays are also briefly discussed.

INTRODUCTION

The performance and life of batteries and fuel cells are often determined by subtle aspects of the structure of various components. Examples of these interrelationships are as follows: 1) Lead-acid battery life is determined by the structure of the basic lead sulfates in the cured plates (ref. 1). 2) Zinc-manganese dioxide battery performance strongly depends on the structure of MnO_2 (ref. 2). 3) Swelling of nickel electrodes is related to the structure of $Ni(OH)_2$ (ref. 3). 4) The activity and stability of carbon supported platinum catalysts are dependent on strong carbon platinum interactions (ref. 4). 5) The quality of zinc deposits in flow batteries (ref. 5) and the efficiency of redox systems are related to electrolyte structure (ref. 6-7).

Structural determinations of battery and fuel cell electrode materials are often very difficult. The situation is exacerbated when in situ determinations are attempted. Often these materials are amorphous and exhibit very weak or even no X-ray diffraction patterns. Examples are $Ni(OH)_2$, NiOOH (ref. 8), MnO_2 (ref. 9), and pyrolyzed metal-macrocyclic electrocatalysts (ref. 10). Many battery materials such as NiOOH and the discharge products of MnO_2 are hydrated so meaningful ex situ measurements using various photoelectron spectroscopies are nearly impossible. Some in situ methods are of limited value because they require specular surfaces (reflectance spectroscopy and ellipsometry) or are applicable only to a few elements

(Mossbauer spectroscopy and SERS (surface enhanced Raman spectroscopy)). Interpretation of spectroscopic data (e.g. Raman spectroscopy or photoacoustic spectroscopy (PAS)) from a typical electrode containing additives, conductive diluents, electrolyte and plastic binders is essentially impossible.

Determination of the structure of electrolytes is also a problem. The application of various scattering (e.g. Raman) and absorption (e.g. infrared and nuclear magnetic resonance (NMR)) spectroscopies to electrolyte studies has been critically reviewed (ref. 11). In many cases the lack of a reliable theoretical framework has led to conclusions that are qualitative in character. This is particularly true when the spectroscopies are applied to hydrated ions. For instance the Raman method is not able to yield information about ion-water distances in solution. In the case of neutron scattering, even in concentrated solutions, ion-water contributions to the total scattering pattern are only ~10%. This makes elucidation of the ion-water terms very difficult.

The present paper discusses how EXAFS can help in these structural determinations. The basic principles, the experimental methods, and data analysis for EXAFS will be outlined. This will be done using examples of EXAFS studies on typical battery and fuel cell components.

THE EXAFS TECHNIQUE

Experimental Aspects: An EXAFS experiment is simply the accurate determination of the X-ray absorption coefficient (μ) of a material, as a function of photon energy, in an energy range that is below and above an absorption edge of one of the elements in the material. The most direct method is to do a transmission X-ray absorption experiment. Figure 1 is a schematic representation of the experimental configuration. It consists of an X-ray source, a double-crystal monochromator, a thin sample of the material, detectors for monitoring the X-ray beam before and after it passes through the material, and a data acquisition system. The data acquisition system is used for several purposes. This includes stepping the monochromator to pass the desired photon energies (E), alignment of the sample in the beam and monitoring the signals from the detectors.

The Origin of EXAFS: EXAFS is the result of a photoelectric absorption process. In most cases X-ray absorption involves the interaction of X-rays with the outer shell electrons of elements. This can be described by the simple Lambert equation

$$I = I_o \exp(-\mu x) \qquad (1)$$

where I_o is the intensity of the incident photon beam, I the intensity of the transmitted beam, and x the thickness of the sample. Figure 2 is a X-ray absorption spectrum for a dry plastic bonded nickel oxide electrode. The initial monotonically decreasing part of the curve, where μ is approximately proportional to E^{-3}, can be described by equation (1) and is determined by the chemical composition of the electrode including all the elements in the conductive diluent, the $Co(OH)_2$ additive and the plastic binder. When the X-ray energy (8337 eV) is sufficient to liberate an inner nickel K-shell electron, and excite it to an unoccupied continuum state, an abrupt increase in the absorption is observed. This is called the absorption edge and is unique to the element. For photon energies greater than E_b = 8337 eV, the ejected photoelectron travels as an outgoing spherical wave with a wavelength (λ)

$$\lambda = \frac{2\pi}{k} \tag{2}$$

where k, the photoelectron wave vector

$$k = \left\{\frac{2m}{\hbar^2} (E-E_b)\right\}^{1/2} \tag{3}$$

where $E = \hbar\omega$ is the energy of the incident photons, m is the electron mass, and h is Planck's constant divided by 2. If the nickel atoms had no neighbors (e.g. as in an inert gas) then μ would continue to decrease with a smooth $\sim E^{-3}$ dependence beyond the absorption edge. However, neighbor oxygen and nickel atoms in the β-$Ni(OH)_2$, backscatter a small fraction of the outgoing photoelectron wave. Interference between the outgoing wave and the incoming waves from neighboring atoms, modulates the photoelectron wave function in the nickel core region, and results in the sinusoidal variation of μ versus E. This yields the EXAFS (χ) - the oscillations in the absorption that extend for about 1000 eV above the absorption edge. In energy space, the EXAFS - $\chi(E)$ is defined as

$$\chi(E) = \frac{\mu(E) - \mu_o(E)}{\mu_o(E)} \tag{4}$$

where $\mu(E)$ is X-ray absorption coefficient and $\mu_o(E)$ a hypothetical absorption coefficient of the nickel with no surrounding atoms. The $\chi(E)$ function can be converted to photoelectron wave vector (k) space by the relationship in equation (2). The physical basis for $\chi(k)$ has been worked out (ref. 12) and is given in its simplest form by

$$\chi(k) = \sum_j \frac{N_j}{R_j^2} B_j(k) \exp(-2k^2\sigma^2_j) \exp(-R_j/\lambda(k)) \sin[2kR_j+\phi_j(k)] \tag{5}$$

where N_j refers to the coordination number in a shell of identical atoms, R_j is the respective coordination distance, F_j is the backscattering amplitude of the coordinating atoms, σ_j is the root mean square variation in R_j due to static or thermal disorder (the Debye-Waller factor), $\lambda(k)$ is the mean free path of the photoelectron, and $\phi_j(k)$ is a phase shift due to the photoelectron traversing the distance R_j twice and encountering the potential of the scatter atom once, and that of the absorbing atom twice. The EXAFS is a summation of the effects of different shells of atoms. For a simple case such as a hydrated ion with one coordination shell, the EXAFS is a simple sinusoidal function whose frequency depends on R and the amplitude on the hydration number N. Figure 3 shows the EXAFS for β-$Ni(OH)_2$. It consists of the summation of at least three sinusoidal waves.

This is a rather simplified description of EXAFS. More details are provided in several excellent reviews (ref. 13-15). From this description it is evident that the EXAFS contains a lot of information about the coordination of the excited atom.

Preliminary Data Analysis - The First Fourier Transformation: The aim of data analysis is the determination of the unknown quantities in equation (5). The quantities of most interest to chemists are R_j, N_j, and σ_j. The first step is a Fourier transformation of $\chi(k)$. Equation (5) is the superposition of an unknown

number of coordination shells. Fourier transformation of $\chi(k)$ yields peaks in r space corresponding to individual shells around the absorbing atom. The Fourier transform is given by

$$\theta_n(r) = \frac{1}{(2\pi)^{1/2}} \int_{kmin}^{kmax} k^n \chi(k) \exp(2ikr)\, dk \qquad (6)$$

The function $\theta_n(r)$ is called a radial structure function and it contains a series of peaks whose positions R_j are related to the coordination distances. Figure 4 is a Fourier transform of the data in figure 3. The first peak corresponds to the Ni-O coordination and the second peak to the first Ni-Ni shell in the brucite structure plane. These peaks are shifted to R values that are lower than the actual Ni-O and Ni-Ni distances because of the phase shift $\phi_j(k)$.

Reduction of the raw data in figure 2 to the radial structure function in figure 4 requires several mathematical manipulations. This includes subtraction of the background, normalization of the EXAFS oscillations and the Fourier transformation. Background subtraction includes a fitting of the pre-edge portion in the spectrum in figure 2, to within 50-70 eV of the edge and extrapolation to the energy region where the EXAFS is present. In this way, the contributions of atoms other than nickel are determined. Fitting is terminated below the edge because of pre-edge features that occur, particularly with transition metals. The EXAFS data are removed from the measured data by subtraction of a cubic spline background. A powerful method for checking whether this is done properly is to examine the derivative of the background and by an iterative technique and a smoothing parameter continue the process until the residual EXAFS oscillations are barely visible in the background derivative. The next step is to normalize the EXAFS by dividing by the height of the absorption edge ($\Delta\mu$) which is usually taken at 50 eV above the absorption edge. To reduce termination errors in the Fourier transform the values of k_{min} and k_{max} are chosen to coincide with nodes in the $\chi(k)$ function. It is a relatively simple process to reach this first stage in the data reduction. Often this suffices, particularly if one wants to only "fingerprint" a material in the same way as diffraction patterns are used. An example is given in figure 5 where radial structure functions for cobalt metal foil and pyrolyzed cobalt phthalocyanine on Vulcan XC-72 carbon are shown. The pyrolysis product at 900°C in argon is obviously cobalt.

Final Data Analysis - Determination of R_j, N_j, and σ_j: After the first Fourier transform is obtained the next step is isolation of the contributions of each shell. In cases like β-$Ni(OH)_2$, where the peaks of the Fourier transform do not overlap (figure 4), the contribution from each shell can be isolated by doing an inverse transform of single peaks back to k-space. All other peaks, except the one of interest, are set to zero. Thus, the individual χ_j is isolated. Figure 6 shows an inverse transform of the first peak in figure 4. The result is a simple sinusoidal wave of a single shell scatterer.

Once χ_j is isolated, the next step is a separate analysis of the phase ($\Phi(k)$) and amplitude ($A(k)$) functions in equation (5). These are respectively

$$\Phi(k) = 2kR + \phi(k) \tag{7}$$

and

$$A(k) = \frac{N}{R^2} \; B(k) \; \exp(-2k^2\sigma^2) \; \exp(-R/\lambda(k)) \tag{8}$$

Determination of N, R,and σ depends on knowing B(k), $\phi(k)$ and $\lambda(k)$. The best way of doing this is by comparison with standard compound(s) of known structure, having identical absorbers and backscatters to the unknown (u). In this case the standard compound NiO, which has a rock salt structure and a Ni-O distance of (R_s = 2.08Å), and a coordination number of (N_s = 6). The Debye-Waller factor is given a value σ_s = 0. So the disorder of β-$Ni(OH)_2$ is determined relative to NiO. The quantities of B(k), $\phi(k)$ and $\lambda(k)$ are assumed to be "transferable" from the standard to the unknown. For NiO $\phi_u(k_u)$ can be calculated. Then for β-$Ni(OH)_2$ which is the unknown

$$\phi_u(k_u) = \phi_s(k_s)$$

After minor corrections for the inner potential (ΔE_o) - differences in absorption edge position for β-$Ni(OH)_2$ and NiO - R_u is calculated as 2.067Å from

$$R_u = [\Phi(k) - \phi_s(k_s)]/2k$$

This is the N-O distance in β-$Ni(OH)_2$. Thus, phase analysis yields actual bond lengths which are somewhat higher than R_j in the radial structure function (figure 4).

The value of R_u is then used to do an amplitude analyses for the determination of N_u and σ_u. Since σ_u is in a k-dependent term it can be separated from N_u by a simple ratio method involving the logarithms of the ratio of the single shell amplitudes of the unknown and the standard

$$\ln \frac{A_u(k)}{A_s(k)} = \ln \frac{N_u R_s^2}{N_s R_u^2} - \frac{2(R_u - R_s)}{\lambda(k)} - 2k^2(\sigma_u^2 - \sigma_s^2)$$

The k dependence of λ can be neglected so a plot of $\ln[A_u(k)/A_s(k)]$ vs k^2 yields a straight line of intercept

$$\ln \frac{N_u R_s^2}{N_s R_u^2}$$

and slope

$$2(\sigma_u^2 - \sigma_s^2) = 2\Delta\sigma^2$$

Thus, N_u, R_u, and $\Delta\sigma^2$ can be determined. The term $\Delta\sigma^2$ gives the relative disorder for Ni-O in β-$Ni(OH)_2$. The respective values for N_u, R_u, and $\Delta\sigma^2$ are 5.96, 2.067Å and -0.00124. Data analysis can be done using theoretical values of the phase and amplitude functions (ref. 16).

This data analysis is relatively simple, since the first two shells are well separated and are of widely different atomic numbers (Z). The situation is much more complicated when there are overlapping shells of similar Z value. Examples of these are reported in the literature (ref. 17). A recent book (ref. 18) gives further details of data analysis.

X-ray Sources for EXAFS Studies: The choice of source of X-rays for EXAFS studies are the bremsstrahlung from a rotating anode X-ray tube or synchrotron radiation from electron or positron storage rings. The EXAFS (fig. 2) are only about 5% of total absorption. Signal-to-noise ratios (S/N) of greater than 100 are required to determine the EXAFS accurately. Since S/N is proportional to the square root of the X-ray intensity, a high flux of X-ray photons is required. The intensity of a synchrotron source is about 10^4-10^6 times higher than from a conventional X-ray tube. This reduces measurement time for a typical EXAFS experiment from a week or more to less than half an hour. Synchrotron radiation also permits studies of dilute samples, including additives and the metallic constituents of metal macrocyclics. Figure 7 shows the EXAFS spectra for the cobalt additive in the nickel oxide electrode of figure 2. Even though the additive is dilute, the spectrum is excellent. However, conventional sources are sometimes convenient. A unit with a rotating anode for electrolyte studies has been recently described (ref. 19).

Near Edge Structure - XANES: The X-ray absorption near edge structure (XANES) portion of the spectrum - within 30 eV of the edge - contains chemical information about the absorbing atom. It depends on the oxidation state of the excited atom, the coordination geometry and the type of ligands. There is an excellent review of early work in this area (ref. 20). The absorption edge energy shifts linearly with valence state and follows Kunzl's law (ref. 21). XANES is an area of very active experimental and theoretical work. Further theoretical developments will permit its use for a variety of coordination chemistry studies.

Dispersive EXAFS: At present there are two facilities, one in France (ref. 22), and the other in Japan (ref. 23), for time resolved EXAFS studies. The technique uses a bent triangular crystal to focus and disperse the quasi-parallel polychromatic X-ray beam from a synchrotron. The sample of interest is placed in the focal point of the beam. The transmitted beam then diverges towards a position sensitive detector. The one in France consists of 1024 sensing elements (2500 μ high x 25μ wide). This permits acquisition of high quality XANES and EXAFS spectra in times as short as 16 msec. With the advent of detectors with faster response, even shorter times can be achieved. The technique permits in situ time resolved kinetic studies.

APPLICATIONS OF EXAFS AND DESIGN OF EXPERIMENTS

EXAFS is the preferred technique for in situ structural studies in electrochemical cells, since both the probe and the signal are X-rays. It is often the only suitable technique for amorphous materials or components of composite structures. It is useful for the study of any element with an atomic number of 16 and above. Once EXAFS is chosen, the important experimental design aspects are sample preparation, the choice of suitable standards and the method for detection.

The simplest method of detection is to do transmission EXAFS using the setup shown in figure 1. For these experiments, uniformity of the sample is important. If possible, the sample should be chosen to give an absorption of $\Delta\mu x \sim 1.5$ at the edge of interest. Several methods for preparation of uniform solid samples are described in the literature (ref. 24-26). Most methods used by battery and fuel cell technologists for preparing of electrodes and separators are useful for preparing samples. One method that the authors have used is a vacuum table technique for casting samples (ref. 27, 28). It is important that the samples be pinhole free and free from cracks. If the elemental composition of a sample is known, the mass of material (M) needed to form a specimen with the desired absorption characteristics can be calculated from the equation

$$M = \frac{A \ \ell n(I_o/I)}{\sum_j f_i(\mu/\rho)_i} \qquad (12)$$

where A is the sample area, f_i is the weight fraction of the ith element in the sample, and $(\mu/\rho)_i$ is the mass absorption coefficient of the ith element at the wavelength of interest. Compilations of $(\mu/\rho)_i$ may be found in a report by McMaster (ref. 29). Summary tables are also given in the most recent editions of the CRC Handbook of Chemistry and Physics (ref. 30). A value of $\ell n(I_o/I) = \Delta\mu x \sim 1.5$ usually gives the best results. However, if a sample contains two or more stong absorbers (e.g. $ZnBr_2$) or is inherently very dilute (e.g. carbon supported platinum catalysts) then lower values of $\Delta\mu x$ may have to be used. However, good data can be obtained with $\Delta\mu x$ values as low as 0.05.

In situ transmission EXAFS of carbon supported platinum electrodes has been done in operating phosphoric acid fuel cells (ref. 31), using a slightly modified version of a cell that was previously described (ref. 32). A cell was designed for in situ studies of the charge/discharge processes of plastic bonded nickel oxide electrodes (ref. 28). This is shown in figure 7. Equation (12) can be used in the design of cells of this type. Absorbence of cell components in the X-ray path have to be taken into account. It is important that no inhomogeneity such as current collector wires be in the path of the beam. Carbon current collectors such as Grafoil are best. Bubbles in electrolyte samples and cells should also be avoided.

For liquid samples such as electrolytes, a sample chamber like that shown in figure 9 is suitable. The chamber thickness can be varied depending on electrolyte concentration. The thickness can be calculated using equation (12).

It is important to use good standards which have known excited atom/backscatter coordination. The Fourier transforms for these should have single well separated peaks. Thus, ferrocene is a good Fe-C standard, whereas cobaltocene is not a good Co-C standard. The latter has two Co-C distances and overlapping peaks in the Fourier transform. Metal foil stndards are usually good for M-M standards, except for b.c.c. metals where the first and second shells overlap.

Apart from transmission measurements, other detection schemes are fluorescence measurements and electron detection. These methods are reviewed in the literature (ref. 14, 33). Fluorescence methods are very good for working with dilute samples - down to about 100 ppm. Electron detection schemes are useful for investigating processes occurring within a few hundred Angstroms of a surface. With the fluorescence method, homogeneity of the sample is not as critical as in transmission measurements. With electron detection a smooth sample surface appears to be important.

Several synchrotron sources are now available for EXAFS measurements, their locations and characteristics are given in two recent reviews (ref. 34-35). Several other souces are under construction or are planned (ref. 36). Since the time available at these sources is usually limited, it is very important, particularly in the case of in situ measurements, to have electrodes and cells that are functioning properly before doing the EXAFS measurements.

EXAFS STUDIES OF BATTERY AND FUEL CELL MATERIALS

Even though extensive application of the EXAFS technique is recent, there have been several publications on materials related to batteries and fuel cells. These are briefly reviewed.

Aqueous Electrolytes: Early work on the application of EXAFS to aqueous electrolyte studies has been reviewed (ref. 13). The EXAFS technique is unique in that it can sort out ion-ion and ion-water interactions unambiguously. Lagarde et al. (ref. 37) used EXAFS in a study of $ZnBr_2$ solutions in the concentration range 0.089 - 8.08 M. In going from the lower to the higher concentrations the bromide coordination number increased from 1 to 3.5 and waters of hydration decreased from 7 to 2.5. The Zn-Br bond length was 2.37Å and the Zn-O bond length was 1.94Å. Aliotta et al. (ref. 38) did an EXAFS study of mixed $ZnBr_2$-$CuBr_2$ and mixed $ZnBr_2$-$SrBr_2$ solutions. In both cases it was found that the $CuBr_2$ and $SrBr_2$ acted as bromine donors and that the mean coordination value for bromide ions around zinc increased to four as the bromide to zinc ion ratio increased. Similar increases in the coordination value for bromide ions have been observed on addition of either HBr or $AlBr_3$ to $ZnBr_2$ electrolytes (ref. 39). Other studies of interest to battery researchers are EXAFS investigations of Ni^{2+} ions in concentrated $Ni(NO_3)_2$ solutions (ref. 40), Mn^{2+} ions in $MnCl_2$ solutions (ref. 41), and the Jahn-Teller complexes of $Cu(H_2O)_6^{2+}$ and $Cr(H_2O)_6^{2+}$ (ref. 42).

Polymeric Electrolytes: EXAFS of iron, in iron neutralized Nafion ionomers, has been used to probe ion aggregation in the membrane (ref. 43). This has been done in hydrated and dried membranes.

The poly ethylene oxide (PEO) complexes - $RbSCN(PEO)_4$, $RbSCN(PEO)_4$ and $RbI(PEO)_8$ - have been investigated using EXAFS (ref. 44). These materials are amorphous at room temperature. The results showed that Rb is in well defined sites of four coordination with ether oxygens, with the actual configuraton being anion dependent. In the case of iodide, there are two long and two short Rb-O bonds with the iodide outside the first coordination shell at 3.7Å. The thiocyanate complexes have a single set of oxygen neighbors and the N atom of the thiocyanate group appears to be also located within the first shell.

Linford et. al. (ref. 45) have done Cu EXAFS on electrolyte from the system

$$M\,|\,CuI + \text{sulfonium iodide}\,|\,I_2 - \text{perylene}$$

Measurements were made on a fresly prepared electrolyte (a 5.5:1 CuI-4 methyl-1,4-oxathianium iodide adduct) and an electrolyte from a cell after 2000 h of discharge. These results show that the starting electrolyte consists mainly of γ-CuI. After discharge sulfur appears to be incorporated in the first coordination shell of copper, implying decomposition of the sulfonium cation.

Solid Oxide Electrolytes: There has been one EXAFS study of yttria-stabilized zirconia over the temperature range -120° to 770°C (ref. 46). Both Y and Zr EXAFS were obtained in 18 wt % Y_2O_3-stabilized zirconia. The results indicate that at low temperatures the anion vacancies are preferentially sited closer to the Zr^{4+} ions. This displaces the Zr^{4+} ions from their centrosymmetric sites. Increasing the temperature leads to a random distribution of anion vacancies. Recent results on calcia-stabilized zirconia (ref. 47) indicate that the vacancies are also associated with the Zr^{+4} ions. Similar effects have been observed for 40% Y_2O_3 in Bi_2O_3 (ref. 48).

In Situ Studies in Cells: In situ EXAFS has been done on the ferrocyanide/ferricyanide system in a thin layer spectroelectrochemical cell (ref. 49). The results show that the Fe-C bond length is 0.03Å shorter in the ferricyanide than in the ferrocyanide complex.

In situ EXAFS studies have also been done on plastic bonded nickel oxide electrodes (ref. 26, 50). During oxidation of $Ni(OH)_2$ to NiOOH there is a contraction along the a axis of the $Ni(OH)_2$ brucite structure. The Ni-O distance decreases from 2.04Å to 1.88Å. The first Ni-Ni distance also decreases from 3.16°Å to 2.87Å. On discharge the interatomic distances revert to the original values. During the formation cycles considerable disorder is generated in the $Ni(OH)_2$ structure.

Electrocatalysts: Extensive work has been done using EXAFS to study metal catalysts on non-conductive supports. This work has been reviewed (ref. 51). A good example of the capabilities of the technique are the papers of Koningsberger and his co-workers (ref. 17, 52-54), which includes work on platinum supported on alumina. Other platinum catalysts, including the Adams catalyst have been investigated (ref. 55). The results indicate that it is a disordered form of α-PtO_2. Recently, EXAFS has been used to study metal-carbon interactions in carbon supported platinum catalysts in fuel cell electrodes (ref. 56). The data indicate two types of Pt-C interactions.

There is one report on EXAFS studies of pyrolysed cobalt porphyrin catalyst supported on active carbon (ref. 57). The results have been interpreted on the basis that a CoN_4 group is retained in the heat treated catalyst.

Battery Materials: EXAFS has been used to study several battery materials such as metal chalcogenides (ref. 58) and superionic conductors (ref. 59). Work on other materials of interest to battery research are to be found in several reviews (ref. 13-15, 34, 60, 61).

XANES STUDIES OF BATTERY AND FUEL CELL MATERIALS

XANES has been used recently to investigate several battery and fuel cell related materials. These include an investigation of the cerous/ceric redox system (ref. 62), the interaction of carbon monoxide with ferric tetrasulfophthalocyanine in alkaline solution (ref. 63), a study of vanadium oxides in various oxidation states (ref. 64) and an investigation of high temperature corrosion of Fe-Cr alloys (ref. 65).

In a recent study (ref. 66), XANES spectra were used to detect a SiO_2 like layer at the interface between nickel and a yttria-stabilized zirconia electrolyte. Linford et. al. (ref. 45) also used XANES to identify changes in the copper environment after discharging cells.

An interesting application of XANES is its use as a quantitative technique for the determination of the number of unoccupied d-electron states in platinum catalysts (ref. 67).

SYNCHROTRON RADIATION AND FUNDAMENTAL ELECTROCHEMICAL STUDIES

The application of synchrotron radiation to fundamental studies of the electrode/electrolyte interface has really only begun. Recent results on the adsorption of iodine on platinum (111) show that the technique can be applied to monolayers (ref. 68). It has also been shown that various fluorescence and electron detection schemes can be used (ref. 69). Electron-yield EXAFS data have been successfully obtained from a nickel surface covered with a thin film of water (ref. 70). Recently the X-ray standing wave technique has been used to study iodine and copper layers on platinum (ref. 71). Several other synchrotron radiation techniques have been used for the study of chemisorbed atoms and molecules. These have been reviewed (ref. 72) and some are applicable to electrochemical systems. Another promising technique for fundamental studies is X-ray topography (ref. 73). Many of these techniques, such as X-ray standing wave and X-ray topography, are old but synchrotron radiation greatly reduces data acquisition times.

ADVANTAGES OF EXAFS AND FUTURE APPLICATIONS

Progress in basic and applied electrochemical research has been hampered because of the lack of a technique for *in situ* studies at a molecular level (ref. 74). The small amount of work so far indicates that synchrotron radiation techniques will change this. The EXAFS technique is versatile in that it is element specific and can be applied to most elements in the periodic table. Furthermore, it can be applied to all states of matter, whether they be solids, liquids, gases, or absorbed monolayers. It is an excellent technique for investigations of dilute systems. Together with XANES it yields both chemical and structural information.

Unlike X-ray diffraction of single crystals, EXAFS is not an *ab initio* structural determination technique. However, many battery active materials, electrolytes and electrocatalysts cannot be prepared as single crystals. EXAFS is the best technique for studying these amorphous materials. With a careful choice of standards and exhaustive data analysis for phase and amplitude, unknown coordinating atoms can be determined by EXAFS. The relative merits of EXAFS and diffraction have been recently reviewed (ref. 75).

From a basic point of view, the greatest impact of these X-ray techniques will be new insights into the electrode/electrolyte interface. It will also attract scientists from other disciplines to electrochemistry. In practical applications, it will permit *in situ* studies of active material and catalyst preparation,

including catalyst-support interactions. The investigation of performance limiting and degradation mechanisms can be studied in actual cells at a molecular level. EXAFS is an excellent technique for investigating disordered materials and materials with defects. An example of the latter are transformation toughened ceramics. With the advent of more synchrotron sources (ref. 34-36) and the development of more simplified data analysis packages the technique will find widespread use.

ACKNOWLEDGMENTS

The data reported in the figures in this paper were obtained at Beam Line X-11 of the National Synchrotron Light Source at Brookhaven National Laboratory. The authors thank the Department of Energy, Division of Materials Sciences for operating funds for Beam Line X-11, under Contract DE-AC05-80ER10742.

LIST OF SYMBOLS

A	Sample area
$A(k)$	Amplitude of EXAFS as a function of k
$A_s(k)$	Amplitude of EXAFS for standard excited atom - backscatterer combination
$A_u(k)$	Amplitude of EXAFS for unknown compound
$A_j(k)$	Amplitude of EXAFS for a particular coordination shell j of the same type of atoms at a distance R_j from the excited atom
$B(k)$	The backscattering amplitude of neighbor atoms around the excited atom; the substripts s, u and j have the same meaning as for A(k)
E	Energy of the X-ray photon
E_b	Binding energy of a core electron in the absorber atom
f_i	Weight fraction of an element i in a sample
I	Intensity of transmitted X-ray beam
I_o	Intensity of incident X-ray beam
k	Wave vector of ejected photoelectron
m	Mass of the electron
N_j	Coordination number for a single shell j of backscatterers; the subscripts s and u have the same meaning as for A(k)
R_j	The distance between an absorber atom and a single shell j of backscatterers; the subscripts s and u have the same meaning as for A(k)

x	Sample thickness
$\hbar$	Plancks constant divided by 2
$\theta_n(r)$	Fourier transfer of the EXAFS, called the radial structure function
λ	Wavelength of the photoelectron
$\lambda(k)$	Mean free path length of the photoelectron
μ	X-ray absorption coefficient of a sample
$\mu(E)$	X-ray absorption coefficient of an absorber as a function of photon energy
$\mu_o(E)$	X-ray absorption coefficient of an absorber without any backscatterers
$(\mu/\rho)_i$	Mass absorption coefficient of the element i
σ_j	Deviation in R_j caused by static and thermal disorder of the backscatterer j
$\Delta\sigma_j^2$	Debye-Waller factor - deviation of σ^2 with respect to some standard
$\phi_j(k)$	The phase shift due to a single shell of backscatterers j; the subscripts s and u have the same meaning as for A(k)
Φ	The argument of the Sin term in the EXAFS - equation 5
χ	The EXAFS
ω	Radial frequency of X-ray photon

REFERENCES

1. Biagetti, R. V. and Weeks, M. C. Bell. Syst. Tech. J., 49 (1970) 1305.

2. Brodd, R. J., Kozawa, A. and Kordesch, K. V., J. Electrochem. Soc., 125., (1978) 271c.

3. Pickett, D. F., Martin, U. D., Logsdon, J. W. and Leonard, J. F., Proc. 27th Power Sources Symp., PSC Publications, Red Bank, NJ (1976), pp. 120-3.

4. Ehrburger, P., Mahajan, D. P. and Walker, Jr., P. L., J. Catalysis, 43 (1976) 61.

5. McBreen, J. and Gannon, E., J. Electrochem. Soc., 130 (1983) 1667.

6. Gahn, R. F., Hagedorn, N. H. and Ling, J. S., Proc. Intersoc. Energy Convers. Eng. Conf., 18th (Vol. 4) (1983) 1647-52, CA, 99:161425b.

7. Peter, L. M., Durr, W., Bindra, P. and Gerischer, H., J. Electroanal. Chem., 71 (1976) 31.

8. Barnard, R., Randell, C. F. and Tye, F. L., J. Applied Electrochem., 10 (1980) 109.

9. Brenet, J. P. and Ghosh, S., Electrochim. Acta, 7 (1962) 449.

10. Wiesener, K., Electrochim. Acta, 31 (1986) 1073.

11. Enderby, J. E. and Neilson, G. W., Rep. Prog. Phys., 44 (1981) 593.

12. Sayers, D. E., Stern, E. A. and Lytle, F. W., Adv. X-ray Anal., 13 (1970) 248.

13. Lee, P. A., Citrin, P. H., Eisenberger, P. and Kincaid, B. M., Rev. Mod. Phys., 53 (1981) 769.

14. Stern, E. A. and Heald, S. M. in Koch. E. E. (ed.), Handbook on Synchrotron Radiation, Vol. 1, North-Holland, Amsterdam, 1983, Chapter 10, pp. 955-1014.

15. Hayes, T. M. and Boyce, J. B., Solid State Phys., 37 (1982) 173.

16. Teo, B. K. and Lee, P. A., J. Amer. Chem. Soc., 101 (1979) 2815.

17. Van Zon, J. B. A. D., Koningsberger, D. C., Van't Blick, H. F. J. and Sayers, D. E., J. Chem Phys., 82 (1985) 5742.

18. Teo, B. K., EXAFS Basic Principles and Data Analysis, Springer Verlag, Berlin (1986).

19. Dreier, P. and Rabe, P., Rev. Sci. Instrum., 57 (1986) 214.

20. Srivastava, U. C. and Nigam, H. L., Coordination Chemistry Reviews, 9 (1972) 275.

21. Kunzl, V., Trav. Cjim. Techecolovaquie, 4 (1932) 213.

22. Flank, A. M., Fontaine, A., Jucha, A., Lemonier, M., Raoux, D. and Williams, C., Nucl. Instr. Methods, Phys. Res., 208 (1983) 651.

23. Phizackerley, R. P., Rek, Z. V., Stephenson, G. B., Couradson, S. D., Hodgson, K. O., Matsushita, T. and Onyanayi, M., J. Appl. Cryst., 16 (1983) 220.

24. Eanes, E. D., Costa, J. L., MacKenzie, A. and Warburton, W. K., Rev. Sci. Instrum., 51 (1980) 1579.

25. Lu, K.-Q. and Stern, E. A., Nucl. Instrum. Methods Phys. Res., 212 (1983) 475.

26. Wong, J. Nucl. Instrum. Methods, Phys. Res., A238 (1985) 554.

27. McBreen, J., U.S. Patent 4,000,005, Dec. 28, 1976.

28. McBreen, J., O'Grady, W. E., Pandya, K. I., Hoffman, R. W. and Sayers, D. E., Langmuir, (1987) in press.

29. McMaster, W. H., Kerr Del Grande, N., Mallet, J. H. and Hubbell, J. H., Report UCRL - 50174, Lawrence Radiation Laboratory, University of California, Livermore.

30. CRC Handbook of Chemistry and Physics, Weast, R. C. and Astle, M. J., (eds.), CRC Press, Inc., Boca Raton, Florida (1981) pp. E-139-43.

31. O'Grady, W. E., Sayers, D. E., Budnick, J. I. and Hayes, G. H., Ext. Abst., No. 639, Electrochem. Soc. Proc. Vol. 85-1, 1985, p. 895-6.

32. Olender, H., McBreen, J., O'Grady, W. E., Srinivasan, S. and Kordesch, K. V., J. Electrochem. Soc., 129 (1982) 135.

33. Heald, S. M., in Koningsberger, D. C. and Prins, R., (eds.), Application Techniques of EXAFS, SEXAFS and XANES, John Wiley & Sons, New York (1987).

34. Wong, J., Mat. Sc. Eng., 80 (1986) 107.

35. Catlow, C. R. A. and Greaves, E. N., Chem. Br., 22 (1986) 805.

36. Robinson, A. L., Science, 235 (1987) 841.

37. Lagarde, P., Fontaine, A., Raoux, D., Sadoc, A. and Migliardo, P., J. Chem. Phys., 72 (1980) 3061.

38. Aliotte, F., Galli, G., Maisano, G., Migliardo, P., Vasi, C. and Wanderlingh, Nuovo Cimento, 2D (1983) 103.

39. McBreen, J., O'Grady, W. E., Sayers, D. and Yang, C. Y., Ext. Abst. No. 574, Electrochem. Soc, Proc. Vol. 86-1, 1986, p. 834-5.

40. Licheri, G., Pashcina, G., Piccaluga, G., Pinna, G. and Vlaic, G., Chem. Phys. Lett., 82 (1981) 384.

41. Beagley, B., Gahan, B., Greaves, G. N., McAuliffe, C. A. and White, E. W., J. Chem. Soc. Commun., 1804 (1985).

42. Sham, T. K., Hastings, J. B., Pearlman, M. L., Chem. Phys. Lett., 83 (1981) 391.

43. Pan, H. K., Yarusso, D. J., Knapp, G. S., Pineri, M., Meagher, A., Coey, J. M. D. and Cooper, S. L., J. Chem. Phys., 79 (1983) 4736.

44. Catlow, C. R. A., Chadwick, A. V., Greaves, G. N., Moroney, L. M. and Worboys, M. R., Solid State Ionics, 9 (1983) 1107.

45. Linford, R. G., Hall, P. G., Johnson, C. and Hasnian, S. S., Solid State Ionics, 14 (1984) 199.

46. Catlow, C. R. A., Chadwick, A. V., Greaves, G. N. and Moroney, L. M., J. Am. Ceram. Soc., 69 (1986) 272.

47. Moroney, L. M. and Sayers, D. E., J. Phys., 47 (1986) C8-725.

48. Battle, P. D., Catlow, C. R. A., Chadwick, A. V., Greaves, G. N. and Moroney, L. M., J. Phys., 47 (1986) C8-669.

49. Smith, D. A., Elder, R. C. and Heineman, W. R., Anal. Chem., 57 (1985) 2361.

50. McBreen, J., O'Grady, W. E. and Sayers, D., Ext. Abstr. No. 105, Electrochem. Soc. Proc. Vol. 86-2, 1986, p. 151-2.

51. Joyner, R. W. and Meehan, P., Vacuum, 33 (1983) 691.

52. Koningsberger, D. C., van Zon, J. B. A. D., van't Blik, H. F. J., Visser, G. J., Prins, R., Mansour, A. N., Sayers, D. E., Short, D. R. and Katzer, J. R., J. Phys. Chem., 89 (1985) 4075.

53. Koningsberger, D. C. and Sayers, D. E., Solid State Ionics, 16 (1985) 23.

54. Duivenoorden, F. B. M., Koningsberger, D. C., Uh, Y. S. and Gates, B. C., J. Am. Chem. Soc., 108 (1986) 6254.

55. Mansour, A. N., Sayers, D. E., Cook, Jr., J. W., Short, D. R., Shannon, R. D. and Katzer, J. R., J. Phys. Chem., 88 (1984) 1778.

56. O'Grady, W. E. and Koningsberger, D. C., J. Chem. Phys. (to be published).

57. Joyner, R. W., van Veen, J. A. R. and Sachtler, W. M. H., J. Chem. Soc., Faraday Trans. I, 78 (1982) 1021.

58. Cramer, S. P., Liang, K. S., Jacobsen, A. J., Chang, C. H. and Chianelli, R. R., Inorg. Chem., 23 (1984) 1215.

59. Hayes, T. M., Boyce, J. B. and Beeky, J. L., J. Phys., 11 (1978) 2931.

60. Sandstrom, D. R. and Lytle, F. W., Ann. Rev. Phys. Chem., 30 (1979) 215.

61. Lengeler, B., Z. Phys. B, 61 (1985) 421.

62. Sham, T. K., J. Chem. Phys., 79 (1983) 1116.

63. Linkous, C. A., O'Grady, W. E., Sayers, D. and Yang, C. Y., Inorg. Chem., 25 (1986) 3761.

64. Wong, J., Lytle, F. W., Messner, R. P. and Maylotte, D. H., Phys. Rev. B, 30 (1984) 5596.

65. Long, G. G., Druger, J. and Tanaka, D., J. Electrochem. Soc., 134 (1987) 264.

66. Gozzi, D., Tomellini, M., Bianconi, A. and Fanfoni, M., J. Electroanal. Chem., 198 (1986) 53.

67. Mansour, A. N., Cook, J. W. and Sayers, D. E., J. Phys. Chem., 88 (1984) 2330.

68. Gordon II, J. G., Melroy, O. R., Borges, G. L., Reisner, D. L., Abruna, H. D., Chandrasekhar, P. and Blum, L., J. Electroanal. Chem., 210 (1986) 311.

69. Kordesch, M. E. and Hoffman, R. W., Nucl. Instr. Methods Phys. Res., 222 (1984) 347.

70. Pandya, K. I., Yang, K., Hoffman, R. W., O'Grady, W. E. and Sayers, D. E., J. Phys., 47 (1986) C8-159.

71. Bedzyk, M. J., Bilderback, D., White, J., Abruna, H. D. and Bommarito, M. G., J. Phys. Chem., 90 (1986) 4926.

72. Stohr, J., Z. Phys. B, 61 (1985) 439.

73. Graeff, W., Z. Phys. B, 61 (1985) 469.

74. Yeager, E., Surf. Sci. 101 (1980) 1.

75. Raoux, D., Z. Phys. B, 61 (1985) 397.

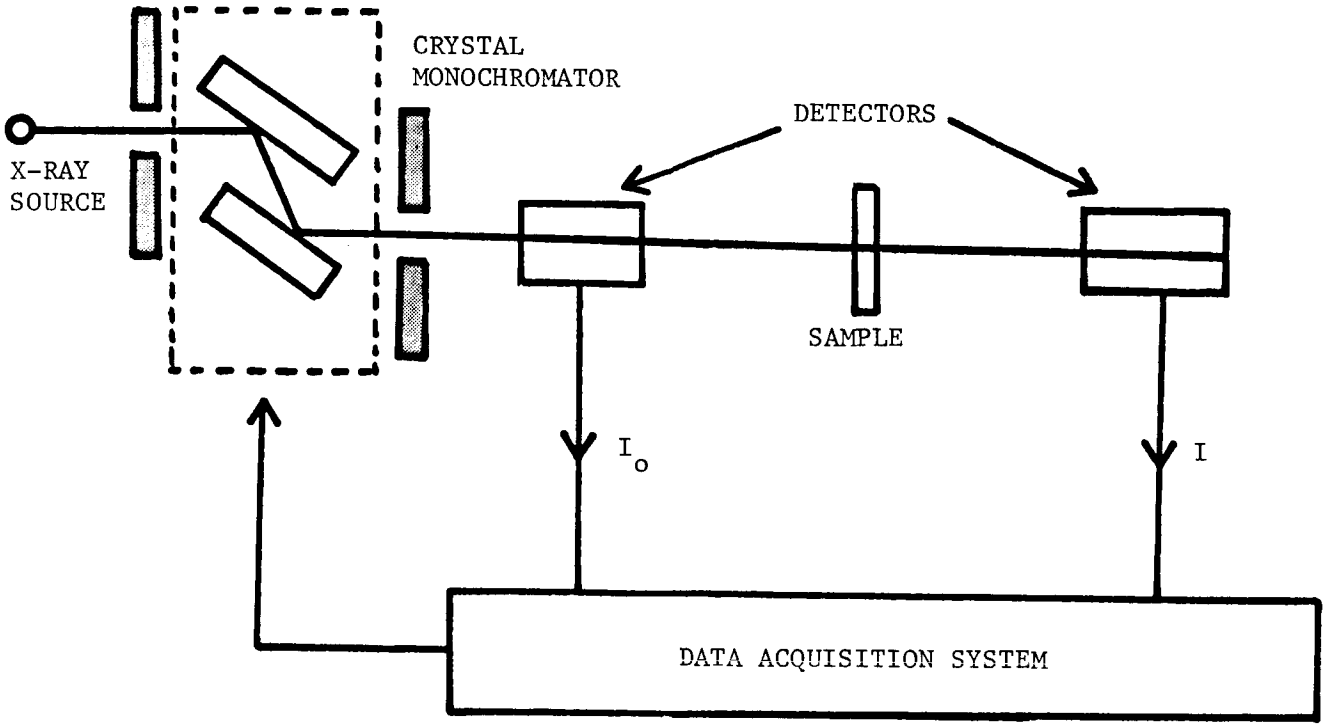

Figure 1. Experimental setup for transmission EXAFS measurements.

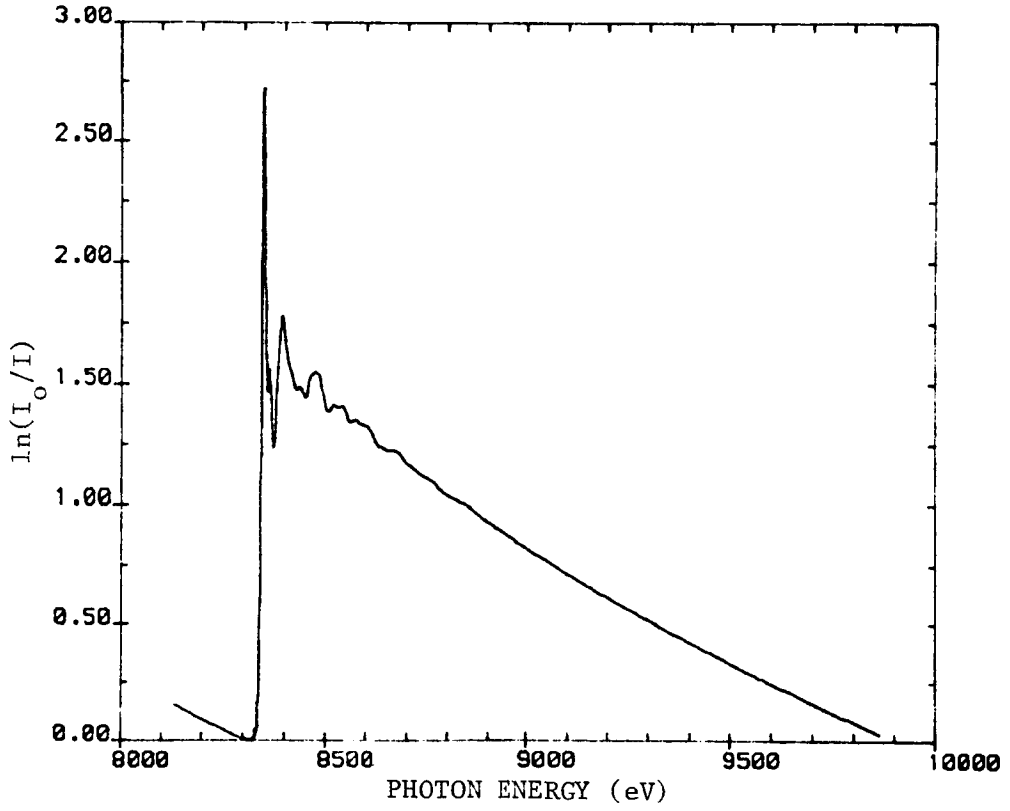

Figure 2. X-ray absorption spectrum for a plastic bonded nickel oxide electrode. The electrode composition was 52.6% $Ni(OH)_2$ + 4.2% $Co(OH)_2$ + 24.7% KS-2 graphite + 8.9% carbon fibers + 9.6% Kynar.

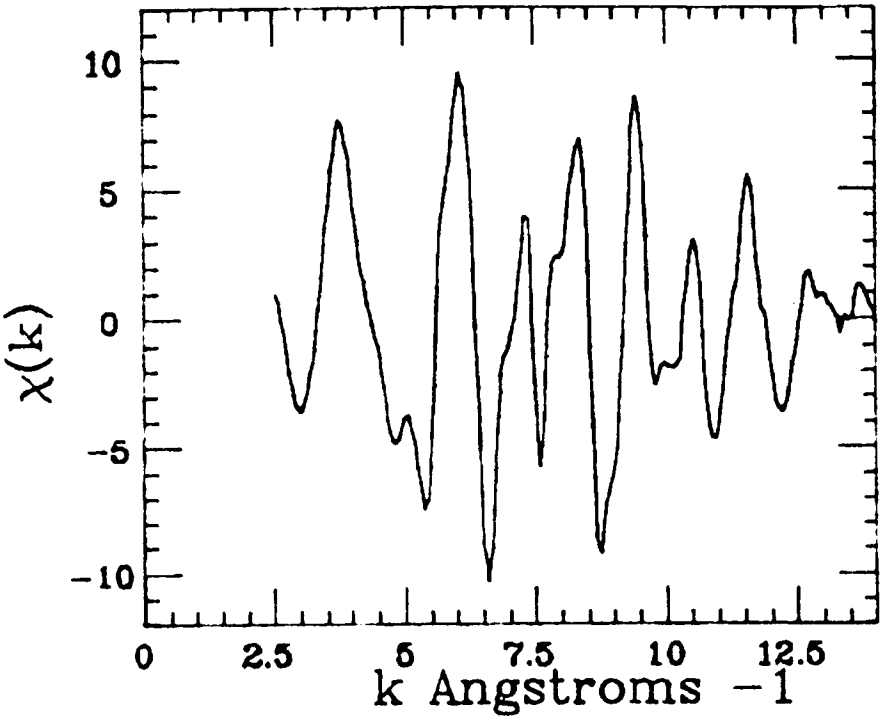

Figure 3. EXAFS from spectrum in Figure 2.

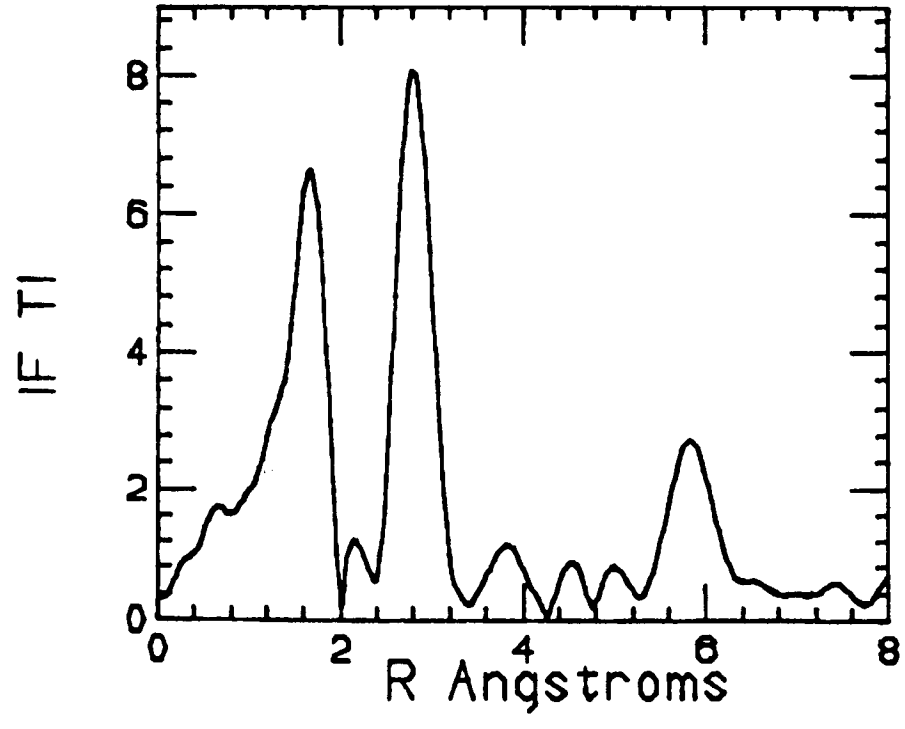

Figure 4. Fourier transform of data in Figure 3.

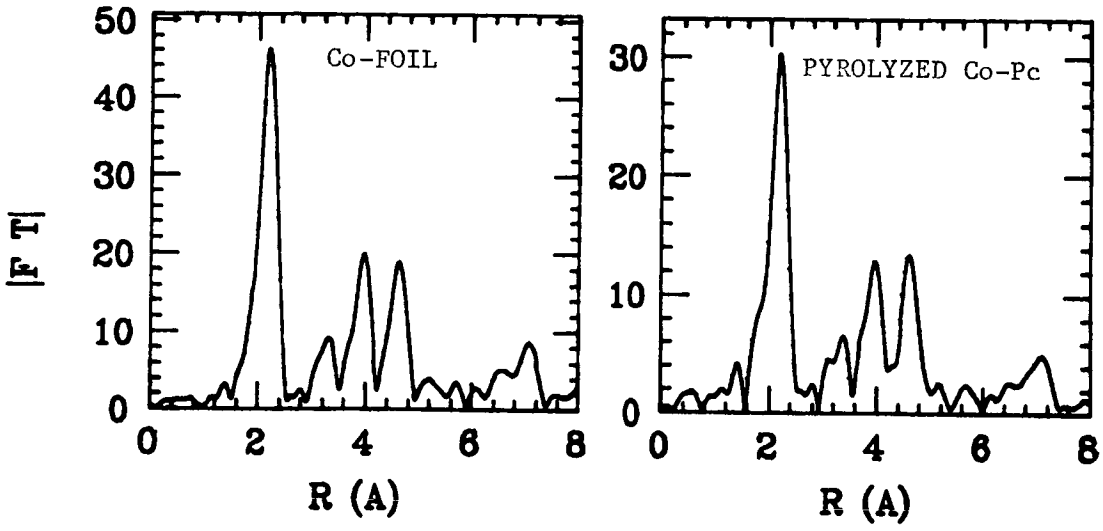

Figure 5. Radial structure functions for cobalt metal foil and cobalt phthalocyanine on Vulcan XC-72 carbon, after pyrolysis at 900°C.

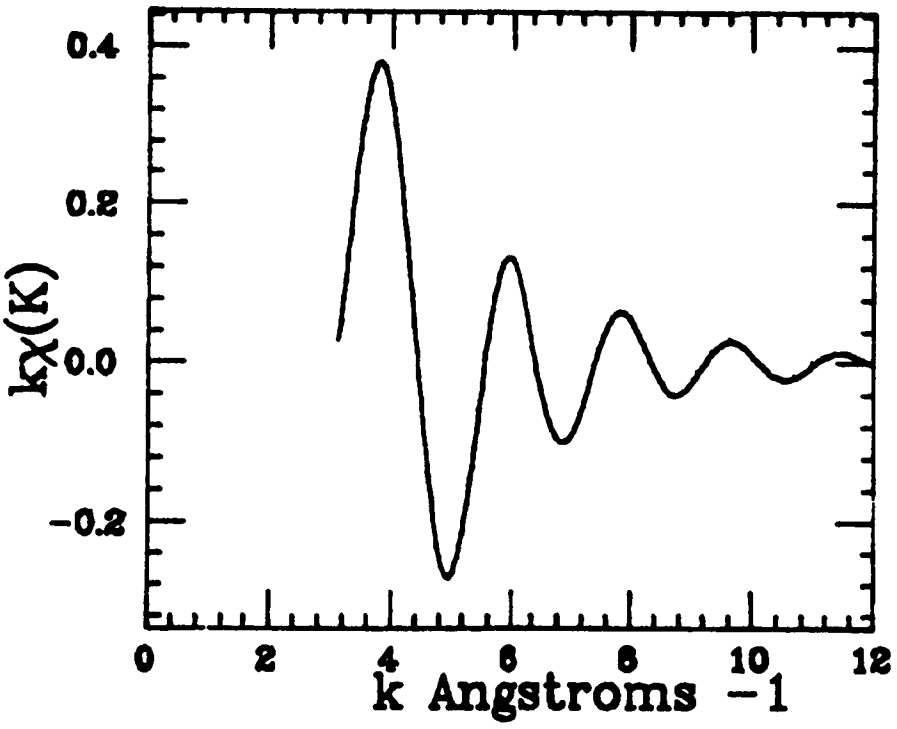

Figure 6. Inverse transform of the first peak of the Fourier transform in figure 4.

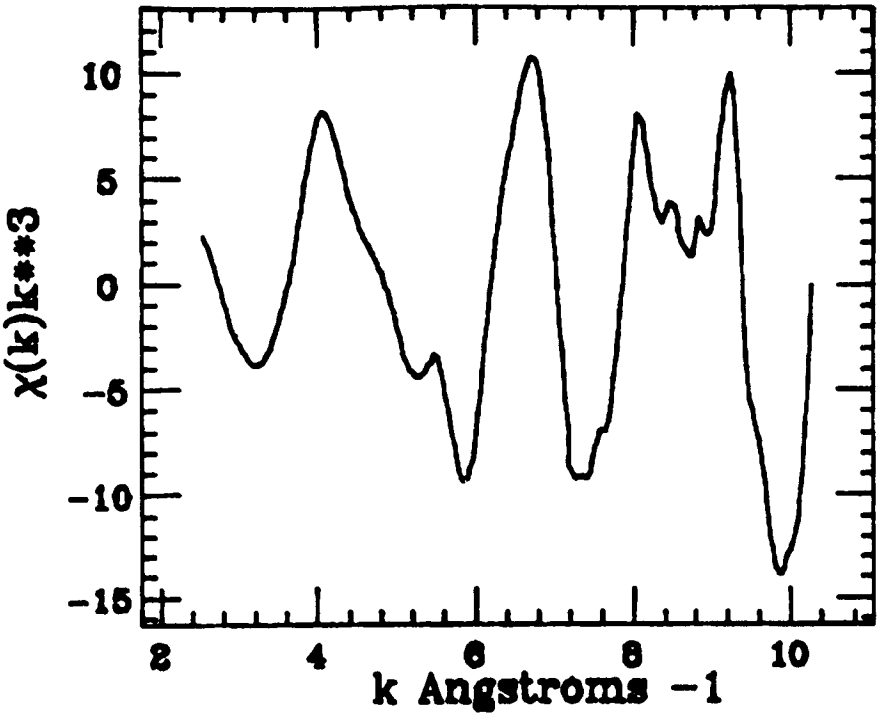

Figure 7. EXAFS for Co in electrode of figure 2.

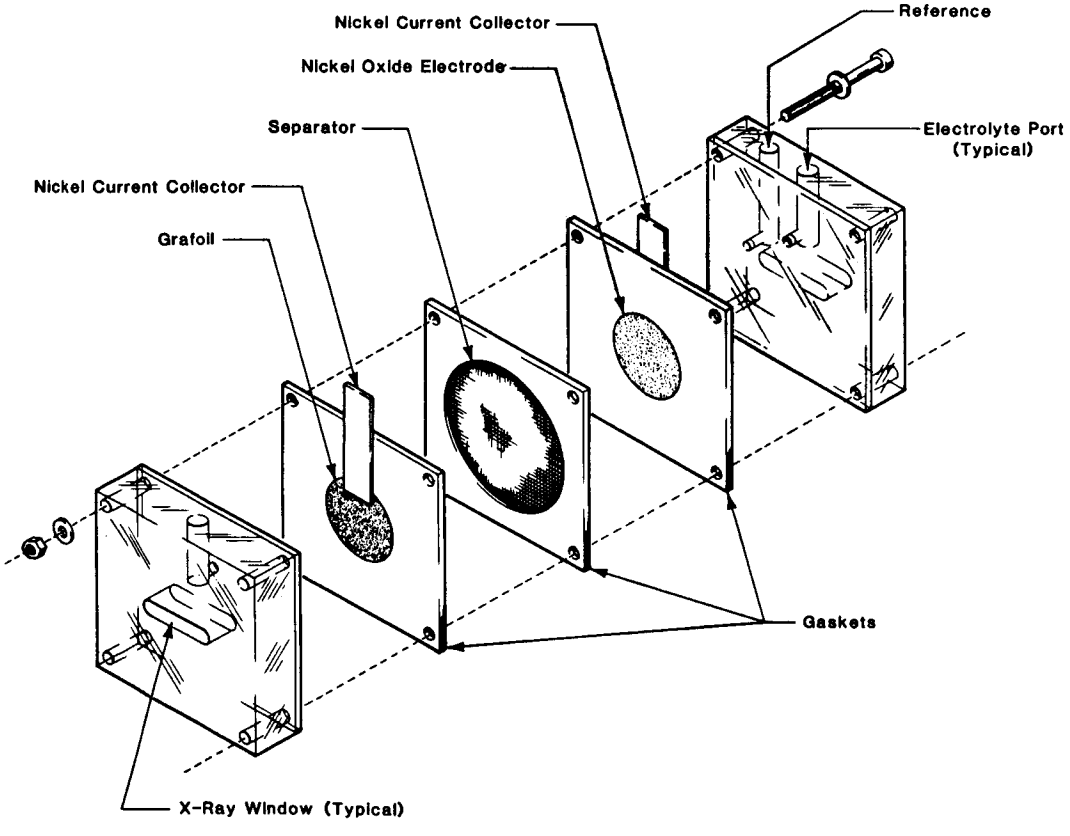

Figure 8. A cell for <u>in situ</u> studies of nickel oxide electrodes.

C-3

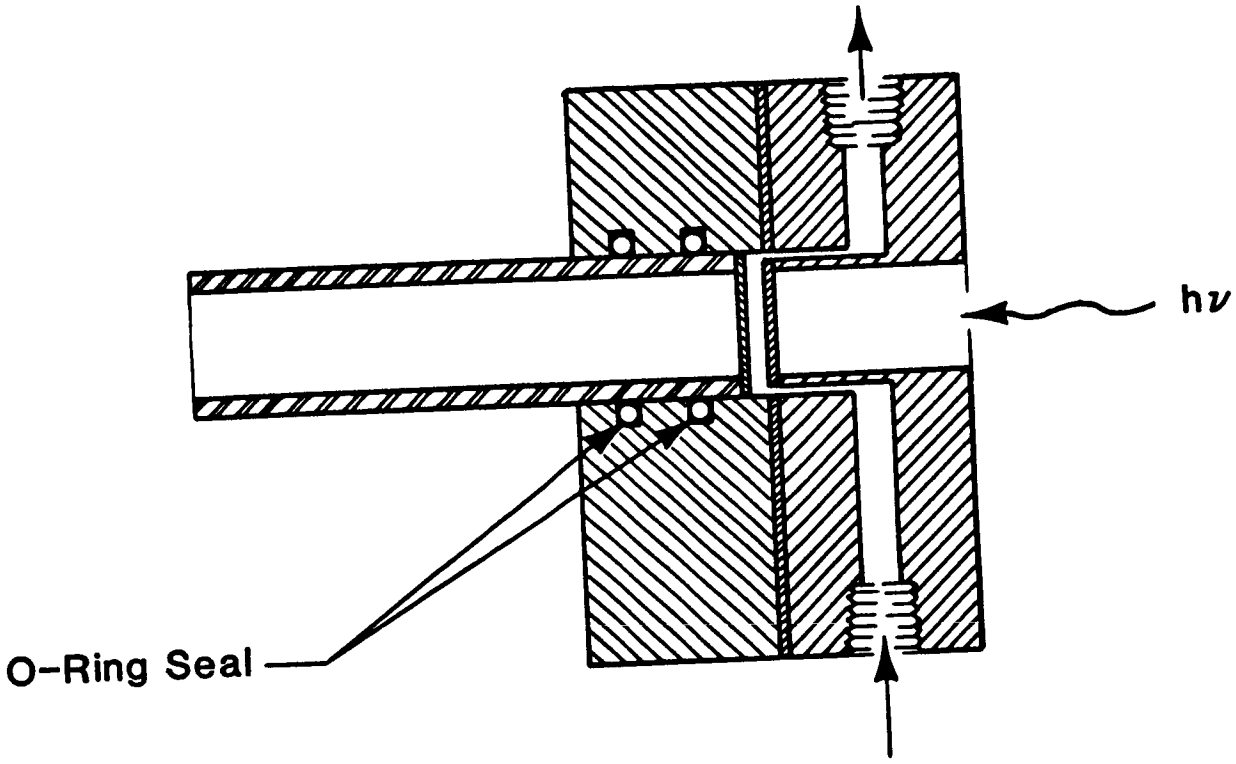

Figure 9. A cell for electrolyte EXAFS studies.

POLYPHASE ALLOYS AS RECHARGEABLE ELECTRODES IN ADVANCED BATTERY SYSTEMS

Robert A. Huggins
Stanford University
Stanford, California 94305

The rechargeability of electrochemical cells is often limited by negative electrode problems. These may include loss of capacity, increased impedance (which may be observed as reduced cell voltage upon discharge, and increased overvoltage upon recharge), macroscopic shape change, dendrite growth, or a tendency for filamentary or whisker growth.

In principle, these problems can be reduced or eliminated by the use of alloys that undergo either displacement or insertion reactions at reactant species activities less than unity, rather than pure elements. On the other hand, this approach always involves some sacrifice of cell voltage and a reduced specific energy.

The fundamental reasons for some of these problems with elemental electrodes, as well as the basic principles involved in the different behavior of alloys, will be briefly discussed.

A considerable amount of information is now available concerning the thermodynamic and kinetic properties of a number of alloys of potential interest for use as electrodes in elevated temperature lithium battery systems. Several of these have been found to have quite rapid kinetics and attractive capacities, with relatively small voltage losses and weight penalties.

In addition, recent results have extended these results down to ambient temperatures, indicating that some such materials may be of interest for use with new low temperature molten salt electrolytes, or with organic solvent electrolytes.

The all-solid mixed-conductor matrix concept will also be reviewed briefly. In this approach, the thermodynamic behavior of two different binary alloy systems can be combined to produce dense all-solid electrodes that have the kinetic properties of fine particle dispersions, as well as potentially attractive microstructural reversibility upon cycling.

INTRODUCTION

The cycling behavior of electrochemical cells, especially at lower temperatures, is often limited by negative electrode problems. These may include gradually increasing impedance, which is observed as increased electrode overvoltage. In some cases, there is macroscopic shape change. If elemental electrodes are used (below their melting points), there may be

dendrite growth, or a tendency for filamentary or whisker growth. This may lead to disconnection and electrical isolation of active material, resulting in loss of capacity. It may also result in electrical shorting between electrodes.

In the absence of a significant nucleation barrier, deposition of a species will tend to occur anywhere at which the electric potential is such that the element's chemical potential is at or above that corresponding to unit activity. This means that electrodeposition may take place upon current collectors and other parts of an electrochemical cell that are at the same potential as the negative electrode, as well as upon the electrode structure where it is actually desired. This was a significant problem during the period in which attempts were being made to use pure (molten) lithium as the negative electrode in high temperature molten salt cells. Another problem was the fact that alkali metals dissolve in their halides at elevated temperatures, leading to electronic conduction and self discharge.

In addition to these problems, the electrodeposition of a pure elemental negative electrode upon recharge can be inherently unstable on a microscopic scale, even in the presence of a chemically clean interface. It has been shown that electrodeposition can lead to an electrochemical analog of the constitutional supercooling that occurs during thermally-driven solidification (ref. 1,2). This will be the case if the current density is such that solute depletion in the electrolyte near the electrode surface causes the local gradient of the element's chemical potential in the electrolyte immediately adjacent to the solid surface to be positive. Under such a condition, there will be a tendency for any protuberance upon the surface to grow at a faster rate than the rest of the interface. This leads to exaggerated surface roughness, and eventually to the formation of stable dendrites. In more extreme cases, it leads to the nucleation of solid particles in the liquid electrolyte ahead of the growing solid interface.

Further, the interface between the negative electrode and the adjacent electrolyte is often not clean. Instead, reaction between the electrode and species in the electrolyte can lead to the formation of reaction product layers. The properties of these layers can have significant effects upon the resultant behavior of the electrode. In some cases they may be useful solid electrolytes, and allow electrodeposition through them. But in many others they are ionically blocking, and thus can greatly increase the interfacial impedance. The presence of such layers, and the local nature of their electrical breakdown, generally related to defects in their structure that lead to spots of locally reduced impedance, often causes the formation of deleterious filamentary growths upon recharge. This is an endemic problem with the use of organic solvent electrolytes with lithium electrodes at ambient temperatures.

These problems can often be alleviated by the use of alloys, instead of elements, as negative electrode reactants. If the diffusion of the depositing species, e.g. Li, in the alloy is sufficiently fast that the activity at the surface remains less than unity, dendrite formation can be avoided. Deposition also occurs preferentially upon the desired electrode structure, rather than at other locations in the cell. In favorable cases, the formation of deleterious surface films may also be avoided.

However, the use of alloys with reduced activities implies reduced cell voltages, as well as increased weight. Therefore, possible increases in reversibility and cycle life of such electrodes are accompanied by reductions in the associated specific energy and energy density of cells in which they are employed.

Another potential problem in the use of alloy electrodes relates to the fact that there may be a significant volume or shape change involved in the electrode reaction. In some cases this will lead to mechanical deterioration of the electrode structure. In other cases, it is negligible.

EXPERIMENTAL RESULTS

A number of investigations have now been completed which have established the theoretical basis for understanding and predicting the potentials and capacities of both binary and ternary lithium alloys. These important practical parameters are directly related to the thermodynamic properties and compositional ranges of the pertinent phases in the respective phase diagrams.

In addition, measurements have been made of the chemical diffusion coefficient, which controls the kinetic behavior, in intermediate phases in a group of lithium alloy systems. Some of these have crystal structures that result in very high rates of lithium diffusion, indicating that they are good candidates for high rate cells.

There are three different types of reactions that can occur in electrodes, formation reactions, displacement reactions, and insertion reactions. In the first two of these, the number of phases present is equal to the number of components (under isothermal and isobaric conditions), so that, according to the Gibbs Phase Rule, all of the intensive parameters are independent of overall composition. This means that the electrode potential, under equilibrium or near-equilibrium conditions, is essentially constant. This leads to generally-desirable plateaus in discharge curves.

The length of these plateaus is determined by the extent of the two-phase regions in the related phase diagrams, in the case of binary alloys. In the ternary case, it is determined by the width of the three-phase constant-potential triangles.

Thermodynamic Data

Whereas, as pointed out above, it is possible to have insertion reactions in alloys, it has been found that these do not generally extend over appreciable compositional ranges in lithium-based alloy systems. For this reason, as well as the fact that such solid solution reactions produce potentials that vary with composition, rather than exhibiting constant - voltage plateaus, the bulk of the work to date has focussed upon materials that undergo displacement reactions.

An experimental arrangement employing the LiCl-KCl eutectic molten salt has been used in our laboratory at temperatures near 400 ^{o}C to study the phase diagrams and thermodynamic properties of alloys in the Li-Al, Li-Si, Li-Sb,

Li-Bi, Li-Sn, Li-Pb, Li-In, Li-Ga and Li-Cd binary systems. The equilibrium potentials, as well as the stoichiometric ranges over which they are found, are presented in Table I.

More recently, attention has been turned to the evaluation of such properties at lower temperatures. This has involved measurements (ref. 3) using $LiNO_3$-KNO_3 molten salts at about 150 °C, as well as experiments with organic solvent-based electrolytes at ambient temperatures (ref.4,5).

Coulometric titration data were obtained over this wide temperature range for two alloy systems, Li-Sb and Li-Bi, each of which have two intermediate phases, in order to illustrate relevant principles. The temperature dependence of the potentials of the two - phase equilibria in the Li-Sb system fell upon two straight lines, corresponding to the reactions 2 Li + $\underline{Sb}$ = Li_2Sb and Li + Li_2Sb = Li_3Sb, where $\underline{Sb}$ indicates the lithium-saturated terminal phase.

In the Li-Bi case, however, where the comparable reactions are Li + $\underline{Bi}$ = LiBi and 2 Li + LiBi = Li_3Bi, the temperature dependence is different. The data for the two reactions converge at high temperatures. Above about 420 °C, the phase LiBi is no longer stable, and there is only a single reaction, 3 Li + $\underline{Bi}$ = Li_3Bi.

In addition, the potentials of the second reaction fall along two straight line segments, depending upon the temperature range. There is a significant change in slope at about 210 °C, resulting in a negligible temperature dependence of the potential at low temperatures, due to the melting of bismuth.

From these temperature dependences, one can obtain values of the molar entropies of these several reactions. They are given in Table II.

In addition to the investigations at elevated temperatures, attention has been given to the ambient temperature properties of several alloy systems. Data on the potentials and stoichiometric ranges of the plateaus in the Li-Sb, Li-Bi, Li-Sn, Li-Pb, Li-Zn and Li-Cd systems at 25 °C are shown in Table III.

The Li-Cd system is especially interesting, for it has a long plateau, spanning about 1.5 Li per mole, at a potential only about 50 mV above pure lithium.

Kinetic Data

As mentioned above, the kinetic properties of alloy electrodes are often determined by the rate at which solid state diffusion can occur through the outer phase of a two-phase microstructure. The pertinent basic parameter here is the chemical diffusion coefficient.

Several techniques have been developed whereby precise and reliable values of the chemical diffusion coefficient can be obtained by the use of molten salt electrochemical cell techniques (ref. 6-10). The physical arrangement can be closely related to that used for the thermodynamic measurements mentioned above.

The principles underlying the application of use of transient or relaxation electrochemical methods for the determination of the chemical diffusion coefficient in solids have been reviewed in a number of the places cited above, and thus will not be discussed here. One of the especially attractive features of this approach, compared to conventional methods, is the relative ease with which one can obtain data of high precision.

In addition to these methods, it was shown a few years ago (ref.10-14) that a steady state ac method can also be used to obtain chemical diffusion data.

By the use of a combination of kinetic measurements and coulometric titration, which provides great compositional resolution, the variation of the diffusion coefficient with composition within phases, even if they have very narrow ranges of composition, can be readily obtained. This is particularly important in understanding the kinetics of polyphase electrode reactions.

As pointed out by Carl Wagner in an important paper (ref.15) in 1953, the chemical diffusion coefficient can be very much greater than the self diffusion coefficient in some materials. It is the latter quantity that has generally been measured in conventional radiotracer studies of diffusion in metals and alloys. This relationship is simply $D_c = D_s \cdot W$, where the quantity W is an enhancement factor, which can be written $W = d \ln a_i / d \ln c_i$, where a_i and c_i are the activity and concentration of electrically neutral species i, respectively. This enhancement factor has been discussed by Wagner (ref.15,16), and was expressed in a somewhat different form by Darken (ref.17), who called it the "thermodynamic factor". A general discussion of this factor, and its evaluation under various conditions relevant to electrochemical systems appeared (ref.6) in 1977. By the use of the coulometric titration technique, the compositional variation of W can be experimentally determined.

These various techniques have been used to investigate chemical diffusion in a number of binary lithium alloys at elevated temperatures, and more recently, at ambient temperatures. Some of these data are included in Table IV. It can be seen that the value of W can be very large in some cases, and that this can lead to unusually high values of the chemical diffusion coefficient. This is indeed a fortunate circumstance, for it permits much faster electrode kinetics than would otherwise be the case.

The Mixed-Conductor Matrix Concept

In order to provide a high reactant surface area, and thus be able to achieve appreciable macroscopic current densities while maintaining low local microscopic charge and particle flux densities, many battery electrodes that are used in conjunction with liquid electrolytes are produced with porous microstructures containing very fine particles of the solid reactant materials. This porous structure is permeated with the electrolyte.

This porous fine-particle approach has several characteristic disadvantages. Among these are difficulties in producing uniform and reproducible microstructures, and limited mechanical strength when highly porous. In addition, they often suffer time-dependent changes in both microstructure and properties during cyclic operation.

A quite different approach was introduced a few years ago (ref. 18-20), in which a dense solid electrode is fabricated which has a composite microstructure in which particles of the reactant phase are finely dispersed within a solid mixed-conducting metallic matrix. This provides a large internal reactant/matrix interfacial area. If the matrix material has a high chemical diffusion rate for the electroactive species it can be rapidly transported through the solid matrix to this interfacial region, where it undergoes the chemical part of the electrode reaction. If the matrix material is also an electronic conductor, it acts as the electrode's current collector, and the electrochemical part of the reaction takes place on the outer surface of the composite electrode.

Upon discharge of such an electrode by deletion of the electroactive species, if a residual reactant particle does not interact with the surrounding matrix, it remains as a relic in the microstructure. This provides a fixed permanent location for the reaction to take place during following cycles. This provides a mechanism for the achievement of true microstructural reversibility.

There are several features of this situation that serve to illustrate and expand upon some of the principles discussed above. There are both thermodynamic and kinetic requirements that must be met.

The matrix and the reactant phase must be thermodynamically stable in contact with each other. One can evaluate this possibility if one has information about the relevant phase diagram - which typically involves a ternary system - as well as the titration curves of the component binary systems. In a ternary system, two materials must lie at the corners of the same constant-potential tie triangle in the isothermal ternary phase diagram in order to not interact. The potential of the tie triangle determines the electrode reaction potential. Therefore, an additional requirement is that the reactant material have two phases present in the tie triangle, but the matrix phase only one. This is another way of saying that the stability window of the matrix phase must span the reaction potential, but that the binary titration curve of the reactant material has a plateau at the tie triangle potential. One can evaluate the possibility that these conditions are met from knowledge of the binary titration curves, without having to do a large number of ternary experiments.

The kinetic requirements for a successful application of these concepts are also understandable. The primary issue is the chemical diffusion rate of the electroactive species in the matrix phase. That can be determined by the various techniques discussed above.

An example has been demonstrated (ref.18-20) that meets all of these requirements, the use of the phase with the nominal composition $Li_{13}Sn_5$ as the matrix, in conjunction with reactant phases in the lithium-silicon system at temperatures near 400 °C. This is an especially favorable case, due to the high chemical diffusion coefficient of lithium in the $Li_{13}Sn_5$ phase. There are surely other examples. We are currently investigating some possible combinations that might be useful at ambient temperatures in lithium systems.

One other obvious requirement is that the microstructure must have the ability to accommodate any volume changes that might result from the reaction

that takes place internally. This can surely be taken care of by clever microstructural design and fabrication techniques.

REFERENCES

1. R. A. Huggins, J. Electrochem. Soc. 122, 90C (1975)

2. R. A. Huggins and D. Elwell, J. Crystal Growth 37, 159 (1977)

3. J. P. Doench and R. A. Huggins, J. Electrochem. Soc. 129, 341C (1982)

4. J. Wang, I. D. Raistrick and R. A. Huggins, J. Electrochem. Soc. 133, 457 (1986)

5. J. Wang, P. King and R. A. Huggins, Solid State Ionics 20, 185 (1986)

6. W. Weppner and R. A. Huggins, J. Electrochem. Soc. 124, 1569 (1977)

7. W. Weppner and R. A. Huggins, Z. f. Physik. Chem. NF 108, 105 (1977)

8. W. Weppner and R. A. Huggins, J. Solid State Chem. 22, 297 (1977)

9. W. Weppner and R. A. Huggins, in Annual Review of Materials Science, Vol 8, ed. by R. A. Huggins, Annual Reviews, Inc. (1978), p. 269

10. C. J. Wen, C. Ho, B. A. Boukamp, I. D. Raistrick, W. Weppner and R. A. Huggins, in International Metals Reviews 5, 253 (1981)

11. R. A. Huggins, in Chemical Metallurgy - A Tribute to Carl Wagner, ed. by N. A. Gokcen, A.I.M.E. (1982), p. 149

12. B. A. Boukamp, I. D. Raistrick and R. A. Huggins, in Fast Ion Transport in Solids, ed. by P. Vashishta, J. N. Mundy and G. K. Shenoy, North-Holland (1979), p. 177

13. C. Ho, I. D. Raistrick and R. A. Huggins, J. Electrochem. Soc. 127, 343 (1980)

14. C. Ho, Ph.D. Dissertation, Stanford University (1980)

15. C. Wagner, J. Chemical Physics 21, 1819 (1953)

16. C. Wagner, in Atom Movements, American Society for Metals (1951), p. 153

17. L. S. Darken, Trans. A.I.M.E. 175, 184 (1948)

18. B. A. Boukamp, G. C. Lesh and R. A. Huggins, J. Electrochem. Soc. 128, 725 (1981)

19. B. A. Boukamp, G. C. Lesh and R. A. Huggins, in Proceedings of the Symposium on Lithium Batteries, ed. by H. V. Venkatasetty, Electrochem. Soc. (1981), p. 467

20. R. A. Huggins and B. A. Boukamp, U. S. Patent 4,436,796 (1984)

21. L. R. McCoy and S. Lai, in Proc. of Symposium and Workshop on Advanced Battery Research and Design, Argonne Nat'l Lab. ANL-76-8 (1976), p. B-167

22. S. Lai, J. Electrochem. Soc. 123, 1196 (1976)

23. R. A. Sharma and R. N. Seefurth, J. Electrochem. Soc. 123, 1763 (1976)

24. C. J. Wen and R. A. Huggins, J. Solid State Chem. 37, 271 (1981)

25. C. J. Wen, Ph.D. Dissertation, Stanford University (1980)

26. C. J. Wen and R. A. Huggins, Mat. Res. Bull. 15, 1225 (1980)

27. M. L. Saboungi, J.J. Marr, K. Anderson and D.R. Vissers, J. Electrochem. Soc. 126, 322C (1979)

28. C. J. Wen and R. A. Huggins, J. Electrochem. Soc. 128, 1636 (1981)

29. C. J. Wen and R. A. Huggins, J. Electrochem. Soc. 128, 1181 (1981)

30. C. J. Wen. B.A. Boukamp, R.A. Huggins and W. Weppner, J. Electrochem. Soc. 126, 2258 (1979)

31. W. Weppner and R.A. Huggins, J. Electrochem. Soc. 125, 7 (1978)

32. W. Weppner and R. A. Huggins, J. Solid State Chem. 22, 297 (1977)

33. C. J. Wen and R. A. Huggins, J. Solid State Chem. 35, 376 (1980)

Table I.
Thermodynamic Data For A Number of Binary Alloys

Voltage vs. Li	System	Range of y	Temp. (°C)	Reference
0.047	Li_ySi	3.25 - 4.4	400	(21-24)
0.058	Li_yCd	1.65 - 2.33	400	(25)
0.080	Li_yIn	2.08 - 2.67	400	(26)
0.089	Li_yPb	3.8 - 4.4	400	(27)
0.091	Li_yGa	1.53 - 1.93	400	(28)
0.122	Li_yGa	1.28 - 1.48	400	(28)
0.145	Li_yIn	1.74 - 1.92	400	(26)
0.156	Li_ySi	2.67 - 3.25	400	(21-24)
0.170	Li_ySn	3.5 - 4.4	400	(29)
0.237	Li_yPb	3.0 - 3.5	400	(27)
0.271	Li_yPb	2.67 - 3.0	400	(27)
0.283	Li_ySi	2 - 2.67	400	(21-24)
0.283	Li_ySn	2.6 - 3.5	400	(29)
0.300	Li_yAl	0.08 - 0.9	400	(30)
0.332	Li_ySi	0 - 2	400	(21-24)
0.373	Li_yCd	0.33 - 0.45	400	(25)
0.375	Li_yPb	1.1 - 2.67	400	(27)
0.387	Li_ySn	2.5 - 2.6	400	(29)
0.430	Li_ySn	2.33 - 2.5	400	(29)
0.455	Li_ySn	1.0 - 2.33	400	(29)
0.495	Li_yIn	1.2 - 0.86	400	(26)
0.507	Li_yPb	0 - 1.0	400	(27)
0.558	Li_yCd	0.12 - 0.21	400	(25)
0.565	Li_yGa	0.15 - 0.82	400	(28)
0.570	Li_ySn	0.57 - 1.0	400	(29)
0.750	Li_yBi	1.0 - 2.82	400	(31)
0.875	Li_ySb	2.0 - 3.0	400	(31)
0.910	Li_ySb	0 - 2.0	400	(31)

Table II.
Thermodynamic Data For The Li-Sb and Li-Bi systems

Reaction	Molar Entropy of reaction (J/K · mol)	Temp. range (°C)
$2Li + Sb \rightarrow Li_2Sb$	-31.9	0 - 500
$Li + Li_2Sb \rightarrow Li_3Sb$	-46.5	0 - 600
$Li + Bi \rightarrow LiBi$	0	0 - 200
$2LI + LiBi \rightarrow Li_3Bi$	-36.4	0 - 400

Table III.

Plateau Potentials And Composition Ranges
in Lithium Alloys at Low Temperatures

Voltage vs. Li	System	Range of y	Temp. (°C)	Reference
0.005	Li_yZn	1 - 1.5	25	(5)
0.055	Li_yCd	1.5 - 2.9	25	(5)
0.157	Li_yZn	0.67 - 1	25	(5)
0.219	Li_yZn	0.5 - 0.67	25	(5)
0.256	Li_yZn	0.4 - 0.5	25	(5)
0.292	Li_yPb	3.2 - 4.5	25	(5)
0.352	Li_yCd	0.3 - 0.6	25	(5)
0.374	Li_yPb	3.0 - 3.2	25	(5)
0.380	Li_ySn	3.5 - 4.4	25	(4)
0.420	Li_ySn	2.6 - 3.5	25	(4)
0.449	Li_yPb	1 - 3.0	25	(5)
0.485	Li_ySn	2.33 - 2.63	25	(4)
0.530	Li_ySn	0.7 - 2.33	25	(4)
0.601	Li_yPb	0 - 1	25	(5)
0.660	Li_ySn	0.4 - 0.7	25	(4)
0.680	Li_yCd	0 - 0.3	25	(5)
0.810	Li_yBi	1 - 3	25	(4)
0.828	Li_yBi	0 - 1	25	(4)
0.948	Li_ySb	2 - 3	25	(4)
0.956	Li_ySb	1 - 2	25	(4)

Table IV
Data On Chemical Diffusion in Lithium Alloy Phases

Nominal Comp.	Range of Composition (% Li)	Max. Value of D_c (cm^2/sec)	Max. Value of W	Temp (^oC)	Reference
LiAl	16.4	1.2×10^{-4}	70	415	10,30
Li_3Sb	0.05	7.0×10^{-5}	70000	360	6
Li_3Bi	1.37	2.0×10^{-4}	370	380	32
$Li_{12}Si_7$	0.54	8.1×10^{-5}	160	415	24
Li_7Si_3	3.0	4.4×10^{-5}	111	415	24
$Li_{13}Si_4$	1.0	9.3×10^{-5}	325	415	24
$Li_{22}Si_5$	0.4	7.2×10^{-5}	232	415	24
LiSn	1.9	4.1×10^{-6}	185	415	33
Li_7Sn_3	0.5	4.1×10^{-5}	110	415	33
Li_5Sn_2	1.0	5.9×10^{-5}	99	415	33
$Li_{13}Sn_5$	0.5	7.6×10^{-4}	1150	415	33
Li_7Sn_2	1.4	7.8×10^{-5}	196	415	33
$Li_{22}Sn_5$	1.2	1.9×10^{-4}	335	415	33
LiGa	22.0	6.8×10^{-5}	56	415	28
LiIn	33.0	4.0×10^{-5}	52	415	26
LiCd	63.0	3.0×10^{-6}	7	415	25
Li_3Sn_4		$6\text{-}8 \times 10^{-8}$		25	4
Li_7Sn_3		$3\text{-}5 \times 10^{-7}$		25	4

STRUCTURAL MODELS FOR NICKEL ELECTRODE ACTIVE MASS*

B.C. Cornilsen, P.J. Karjala, and P.L. Loyselle
Michigan Technological University
Houghton, Michigan 49931

Raman spectroscopic data allow one to distinguish nickel electrode active mass, alpha- and beta-phase materials. Discharged active mass is not isostructural with beta-$Ni(OH)_2$. This is contrary to the generally accepted model for the discharged beta phase of active mass. It is concluded that charged active mass displays a disordered and nonstoichiometric, non-close packed structure of the $R\bar{3}m$, NiOOH structure type. Raman spectral data and x-ray diffraction data are analyzed and shown to be consistent with this structural model.

INTRODUCTION

Raman spectroscopy has proven to be sensitive to subtle structural changes in nickel electrode active mass and related materials. The experimentally observed Raman and IR spectral selection rules provide unique structural information.

Earlier results showed that discharged active mass is not ordered beta-$Ni(OH)_2$ (ref. 1). In contrast, the similar selection rules observed for charged and discharged active mass indicated closely related structures (ref. 2). A structure was proposed for active mass which contains NiO_2 layers in the the $R\bar{3}m$ space group, usually referred to as an oxyhydroxide-type structure. The layer-layer stacking is non-closed packed ABBCCA. The crystal structure, together with empirical formulae, define the site occupancy. Nickel vacancies are induced by the nickel deficit nonstoichiometry. Vacancies may be occupied by alkali cations and/or excess protons. The excess protons need not be incorporated as molecular water in this model. Ionization of the vacant cation sites forms Ni(IV) point defects on Ni(III) lattice sites. The nonstoichiometry and dopants control the average nickel oxidation state, and this model explains the maximum values observed empirically.

The presence of point defects increases the disorder of the structure (ref. 2). The nonstoichiometry and point defect content are expected to strongly influence two properties critical to optimum electrochemical performance, proton mobility and electrical conductivity. The enhanced properties for the alpha/gamma cycle are consistent with both a larger vacancy content (calculated on the basis of the NiOOH lattice) and the observed spectral shifts (ref. 2). Proposed structures must also be consistent with experimental x-ray powder diffraction patterns.

In this paper we first summarize Raman structural data which allow one to uniquely distinguish active mass, alpha-, and beta-phase materials. This is followed by a structural analysis of charged active mass. Two key structural models of charged active mass will be discussed in terms of the experimental Raman spectra and x-ray powder diffraction patterns. These results show the structure of charged active mass is non-close packed with the NiOOH structure.

* This research has been supported by NASA Lewis Research Center.

EXPERIMENTAL

Compounds described in this paper were prepared according to literature methods. Chemical alpha, first precipitate beta-, and recrystallized beta-$Ni(OH)_2$ were made as described by Barnard et al. (ref. 3). Cathodic alpha was prepared as described by MacArthur (ref 4). The discharged alpha-phase was formed by cycling the cathodic alpha to -0.2 V in low KOH electrolyte, 0.2 M, to prevent beta-phase formation (ref. 4). The charged gamma-phase was formed by charging this alpha-phase to +0.51 V, in 0.2 M KOH. The preparation method of Bode et al. was used to prepare the chemically oxidized, gamma-one material (ref. 5). Potentials were measured and reported with respect to a Hg/HgO/0.2 M KOH reference electrode.

RESULTS

Spectra a and b in figure 1 are typical of cycled active mass. Only two lattice modes are exhibited. No O-H stretches are observed above 3000 cm^{-1}. The charged spectrum is similar to that reported by Jackovitz (ref. 6). This discharged spectrum is reported for the first time. The latter spectrum is different than the spectra of the two beta-phases in figures 1c and 1d. Figures 1e and 1f, of alpha-phase materials clearly show that cathodic alpha and chemical alpha differ in structure and that neither is the same as discharged active mass. The spectrum of our discharged phase (fig. 1b) differs from Jackovitz's result (ref. 1). The spectrum he reports is similar to that in figure 1d, although only the 3600 cm^{-1} O-H stretch was shown. The spectrum in fig. 1d is that of a first precipitate beta-phase. It is not a well ordered material as seen by comparison with figure 1c (ref. 3). The latter is of a recrystallized beta-$Ni(OH)_2$. Clearly Jackovitz's spectrum was of a disordered beta, not true beta, and not of discharged active mass.

The Raman (fig. 1a) and IR spectra of the charged active mass and the chemically oxidized material are identical, despite the fact that the x-ray pattern of the former material is extensively broadened. This indicates that these two materials are isostructural.

A powder pattern of chemically oxidized material (isostructural with charged active mass) shows qualitative agreement with gamma-type patterns of Glemser and Einerhand and Bode et al. (table I) (ref. 5 and 7). The experimental d-spacings agree well, whereas the intensities vary considerably. A re-analysis of this data in terms of the Bode et al. Cm model (six nickel sites per unit cell) and the $R\bar{3}m$ (Z=1, one nickel site per unit cell) model has been carried out. The latter model is consistent with Raman and IR data, the former is not. Calculated values for the $R\bar{3}m$ model show better agreement than the Bode et al. unit cell (table 1). Note several lines are predicted by the Bode model which are not observed. No discrepancy between observed and calculated lines occurs for the $R\bar{3}m$ model. More importantly, the agreement between observed and experimental intensities is much improved for the $R\bar{3}m$ model.

THEORETICAL ANALYSIS

Raman spectra for beta-$Ni(OH)_2$ with the brucite ($P\bar{3}m1$ - D_{3d}^3), $Mg(OH)_2$, structure are expected to display three lattice modes (below 700 cm^{-1}) and one O-H stretch above 3000 cm^{-1}. Spectrum 1c of recrystallized beta-$Ni(OH)_2$ agrees with these predictions. These selection rules were first predicted for brucite by Mitra (ref. 8). It is well known that beta-$Ni(OH)_2$ has the brucite structure (ref. 9).

In this structure, the oxygen atoms are hexagonal close packed, ABAB, with nickel atoms in between every other layer.

The second structure of interest is one which exhibits NiO_2 layer stacking that is non-close packed (i.e. BB, CC or AA). The simplest space group with this packing contains one formula unit (Z=1) of NiO_2H_x with ABBCCA stacking (space group $R\bar{3}m$ - D_{3d}^5). A factor group analysis for this model structure predicts only two Raman active lattice modes and no O-H stretching modes for centric H-atoms positioned in the interlamellar space (x can be 1 to 2). The Raman spectra of active mass display selection rules which are consistent with this structure.

DISCUSSION

Figure 1 contains spectra of cycled active mass (charged and discharged), two different beta-phase materials, and two different alpha-phase materials. These six materials each display a different spectrum which is indicative of a different structure. Each of these materials was prepared according to literature methods to represent either active mass or one of the traditional models for active mass.

Spectra a and b in figure 1, typical of active mass, are clearly different than the beta- and alpha-phases, although to various degrees. Discharged active mass (fig. 1a) and the beta-phases (c and d) are therefore not isostructural. Chemical alpha, cathodic alpha, and discharged active mass (figs. 1e, 1f and 1b) also differ in structure. It is apparent that the formation process involves structural transformation from an alpha- or beta-type structure to the active mass structure. Recent in situ spectra are consistent with the ex situ spectra. More detailed structural analyses of the beta- and alpha-materials will appear in forthcoming publications.

An $R\bar{3}m$, ABBCCA structural model has been proposed for charged active mass (ref. 2). This has been based upon the agreement of the observed Raman selection rules with those predicted for this model. This space group was actually first proposed by Glemser and Einerhand and later interpreted in terms of a larger, Cm unit cell by Bode et al. (ref. 5 and 7).

The charged active mass structure can be confirmed by x-ray powder pattern analysis. Table I shows the experimental and calculated powder patterns for a chemically oxidized material which is isostructural with charged active mass based on IR and Raman spectra. The agreement between calculated and observed d-spacings and peak intensities supports this $R\bar{3}m$ model. The poor agreement between calculated and observed peak intensities and the extra, unobserved peaks calculated for the Cm, Bode et al. model, do not compare favorably. This together with the fact that the vibrational selection rules for the large Cm unit cell are not consistent with the observed spectra indicates that the $R\bar{3}m$, NiOOH unit cell is the better structural model.

We refer to this as the "charged active mass structure" because the observed Raman and IR selection rules are identical for both charged gamma (fig. 1a) and charged beta electrochemical materials (ref. 2). The difference between these two materials has been accounted for in terms of this NiOOH lattice and a point defect containing model (ref. 2). The fundamental difference is in the cation vacancy contents.

CONCLUDING REMARKS

The Raman spectral "fingerprints" allow qualitative distinction of several electrode related materials. Structural differences are apparent in the vibrational spectra of nickel electrode active mass and related phases, which were not detected via other techniques such as x-ray diffraction. These differences show that the structures of active mass and those for traditional alpha and beta phases differ. The structural changes which take place during the formation process are mirrored by these differences.

It is concluded that charged active mass is made up of non-close packed NiO_2 layers (ABBCCA). The Raman spectroscopic and x-ray powder diffraction data are completely consistent with an NiOOH, single formula unit cell in the $R\bar{3}m$ - D_{3d}^5 space group. This type of stacking encourages the stacking disorder which broadens x-ray patterns. This disorder is combined with point defects which result from extensive cation nonstoichiometry to form excessively disordered materials with unique electrochemical properties.

REFERENCES

1. Loyselle, P. L.; Luehrs, D. C.; and Cornilsen, B. C.: Nickel Electrode Structures, Extended Abstracts of the 168th Electrochemical Society Meeting, Las Vegas NV, October, 16, 1985.

2. Loyselle, P. L.; Karjala, P. J.; and Cornilsen, B. C.: Proc. Symp. on Electrochemical and Thermal Modeling of Battery, Fuel Cell, and Photoenergy Conversion Systems, J. R. Selman and H. C. Maru eds., Electrochemical Society, Pennington, NJ, 1986, pp. 114-121.

3. Barnard, R.; Randell, C. F.; and Tye, F. L.: Studies Concerning The Ageing of Alpha and Beta $Ni(OH)_2$ in Relation to Nickel-Cadmium Cells. Power Sources 8, J. Thompson, ed., Academic Press, London, 1981, pp. 401-423.

4. MacArthur, D. M.: The Hydrated Nickel Hydroxide Electrode; Potential Sweep Experiments. J. Electrochem. Soc., Vol. 117, 1970, pp. 422-426.

5. Bartl, H.; Bode, H.; Sterr, G.; and Witte, J.: Zur Kenntnis der Nickel hydroxidelektrode IV. Kristallstrukturuntersuchung des Hochoxidierten Gamma-one Nickelhydroxids. Electrochim. Acta, Vol. 16, 1973, pp. 615-621.

6. Jackovitz, J. F.: The Vibrational Spectra of Nickel Hydroxide and Higher Nickel Oxide. Proc. Symp. on the Nickel Electrode, R.G. Gunther and S. Gross, eds., Electrochemical Society, Pennington NJ, 1982, pp. 48-68.

7. Glemser, O. and Einerhand, J.: Die Struktur Hoherer Nickelhydroxyde. Z. Anorg. Allg. Chem., Vol. 261, 1950, pp. 43-51.

8. Mitra, S. S.: Vibration Spectra of Solids. Solid State Physics, F. Seitz and D. Turnbull, eds., Vol. 13, 1962, pp. 1-80.

9. Szytula, A.; Murasik, A.; and Balanda, M.: Neutron Diffraction Study of $Ni(OH)_2$. Phys. Stat. Sol. B., Vol. 43, 1971, pp. 125-128.

TABLE I

Calculated and Experimental Powder Patterns for Chemically Oxidized Material
Peak Intensities and d-Spacings

Experimental Bode et al.*		Experimental This Work		Cm Model Calculation		$R\bar{3}m$ Model Calculation		
d_{hkl}	I	d_{hkl}	I	d_{hkl}	I	d_{hkl}	I	(hkl)
7.06	100	6.997	100	6.983	100	7.002	100	(003)
				4.252	12			
				4.162	2			
				3.632	4			
3.50	100	3.506	22	3.492	20	3.501	15	(006)
				2.981	1			
2.421	60	2.424	7	2.437	17	2.434	13	(101)
2.366	80	2.379	20	2.389	10	2.387	14	(012)
2.204	40	2.219	1	2.223	9	2.221	9	(104)
				2.126	2			
2.120	90	2.111	12	2.117	14	2.117	10	(105)
				2.112	9			
				2.042	1			
				1.967	1			
1.905	60	1.895	1	1.898	6	1.898	5	(107)
				1.895	5			
1.792	80	1.789	6	1.790	4	1.792	5	(018)
1.754	40			1.746	1			(00$\underline{12}$)
1.601	60	1.595	1	1.594	2	1.595	3	(10$\underline{10}$)
				1.591	2			
1.509	60	1.505	1	1.504	3	1.506	2	(10$\underline{11}$)
				1.418	2			
1.410	80	1.411	5	1.415	2	1.415	2	(00$\underline{15}$)/(110)
				1.397	2			
				1.389	1			
1.385	80	1.383	5	1.387	1	1.387	3	(113)

* Joint Committee for Powder Diffraction Standards, Card No. 23-1407. Interplanar spacings, d_{hkl}, are in Angstroms, and Miller indices are given for the $R\bar{3}m$, hexagonal cell.

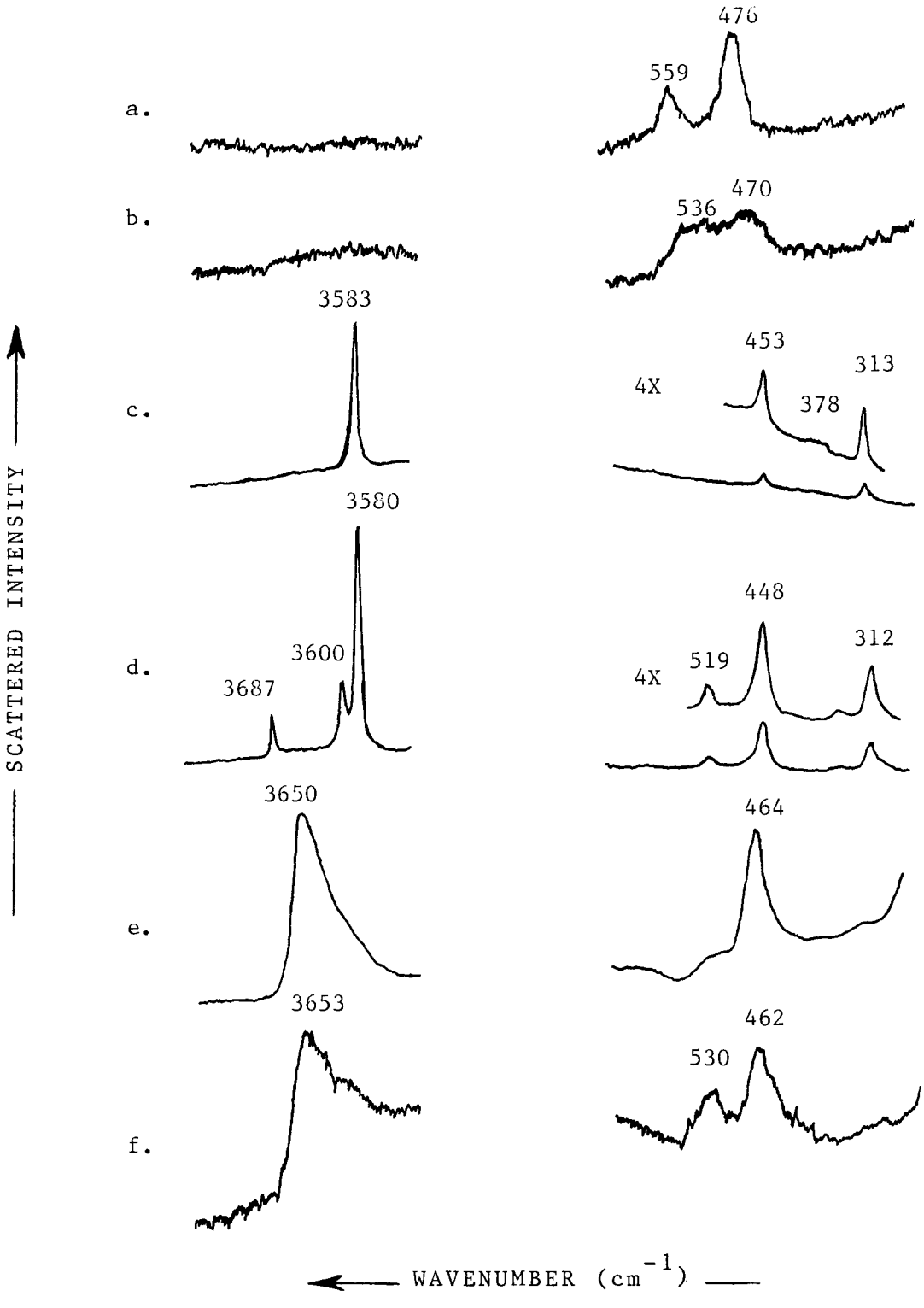

Figure 1. Raman spectra of nickel electrode active mass and model compounds: a) charged gamma active mass, b) discharged alpha active mass, c) recrystallized beta-$Ni(OH)_2$, d) first precipitate beta-phase, e) chemical-alpha, and f) cathodic-alpha.

ADVANCES IN SOLID POLYMER ELECTROLYTE FUEL CELL TECHNOLOGY WITH LOW-PLATINUM-LOADING ELECTRODES*

S. Srinivasan, E.A. Ticianelli, C.R. Derouin, and A. Redondo
Los Alamos National Laboratory
Los Alamos, New Mexico 87545

The Gemini Space program demonstrated the first major application of fuel cell systems. Solid polymer electrolyte fuel cells were used as auxiliary power sources in the spacecraft. There has been considerable progress in this technology since then, particularly with the substitution of Nafion for the polystyrene sulfonate membrane as the electrolyte. Until recently the performance was good only with high platinum loading (4 mg/cm^2) electrodes. This paper presents methods to advance the technology by (i) use of low platinum loading (0.35 mg/cm^2) electrodes; (ii) optimization of anode/membrane/cathode interfaces by hot-pressing; (iii) pressurization of reactant gases, which is most important when air is used as cathodic reactant; and (iv) adequate humidification of reactant gases to overcome the water management problem. The high performance of the fuel cell with the low loading of platinum appears to be due to the extension of the three dimensional reaction zone by introduction of a proton conductor, Nafion. This was confirmed by cyclic voltammetry.

INTRODUCTION

The Solid Polymer Electrolyte Fuel Cell - The First Demonstration of Application of Fuel Cell Systems

Historically, the first major application of fuel cells systems was in the Gemini space flights and for this purpose the solid polymer electrolyte fuel cell system of the General Electric Company was chosen (Ref. 1). The main advantages of fuel cell systems for space applications are the high power and energy densities with respect to weight and volume, high efficiency, few moving parts, minimum noise and vibration, and reliability. The General Electric solid polymer electrolyte fuel cell system, rated at a power level of 1 kw, was used as an auxiliary power source in the space vehicles, and the pure water, the product of the fuel cell reaction, was used for drinking purposes by the astronauts.

Though the fuel cells performed quite well for space missions of 1-2 weeks duration, there were some problems with this technology, such as the power densities attained were still not high enough (<50 mw/cm^2); the polystyrene sulfonate ion exchange membrane was not stable under the electrochemical environments in the cell; and the platinum loading was quite high. It is for

*This work was carried out under the auspices of the U.S. Department of Energy. One of us (E.A.T.) is at Los Alamos on a Brazilian government (CNPq) scholarship. The authors wish to thank Drs. S. Gottesfeld, R. A. Lemons, and I. D. Raistrick, for helpful discussions and suggestions.

these reasons that the alkaline fuel cell system was chosen for the later Apollo program and the space shuttle flights.

Progress in Solid Polymer Electrolyte Fuel Cell Technology Since its Utilization in Gemini Space Flights

The General Electric Company pursued the development of solid polymer electrolyte fuel cells after their use in the Gemini space flights. The major breakthrough was the identification of the perfluorinated sulfonic acid polymer, Nafion produced by DuPont, as the electrolyte. The main advantages of Nafion over polystyrene sulfonic acid membranes are (i) the higher acidity because of the presence of the fluorocarbon rather than hydrocarbon groups (the fluorine atom is electron withdrawing) and (ii) the higher stability of the C-F compared to the C-H bond under the electrochemical environments (Ref. 2). However, progress in this technology was slow due to the "drying out" of the membrane, during operation of the systems.

The General Electric Company made more progress with the solid polymer electrolyte technology for water electrolysis than for fuel cells (Ref. 3). The main reason for this is that the membrane can be maintained wet during electrolytic hydrogen production. Excess water is fed to the anode compartment where oxygen is produced, and a considerable number of water molecules are carried along with the protons to the cathode where hydrogen evolution occurs. Using high surface area unsupported platinum (2-4 mg/cm^2) for the cathode and a ternary mixed oxide (Ru-50%, Ir-25%, Ta-25, total 4 mg/cm^2) for the anode catalyst, the cell performance was 1.00 A/cm^2 at 1.85 V at 80°C. Water electrolyzers with a power input of 50 kw were designed, built, and demonstrated.

The major problem encountered with the General Electric fuel cell was maintaining a wet membrane under operating conditions. Proper humidification of the reactant gases is necessary. The water management in this cell is controlled by (i) transport of water molecules from anode to cathode, (ii) production of pure water at the cathode, and (iii) water loss by evaporation from the membrane. The General Electric Company solved the water management problem by (i) internal humidification of the reactant gases in a separate chamber and (ii) differential pressurization, i.e., using a higher pressure on the cathode side (say 10 atm with air) than on the anode side (say 2 atm with hydrogen). The noble metal loading in the General Electric/Hamilton Standards International Fuel Cells Corporation (GE/HS-IFC)* fuel cell is still high (4 mg/cm^2 Pt on anode as well as on cathode), because unsupported platinum particles are used as electrocatalyst. The unsupported platinum particles are mixed with Teflon particles and hot pressed on to the membrane. A wet-proofed carbon paper is attached to the catalyst layer. The conductive wet-proofed carbon fiber paper prevents flooding of the catalyst layer-gas interface and serves to transport electrons from the current collector plate to the cathode. The support side for the anode is an unattached wet-proofed carbon fiber paper. The carbon fiber paper prevents the membrane from creeping into the current collector grooves and transfers electrons from the catalyst layer to the current collector. Good performances were obtained in this cell with

*The General Electric Company solid polymer electrolyte technology was purchased by Hamilton Standards - International Fuel Cells Corporation.

hydrogen/oxygen as reactants at 105°C with a pressure of 2 atm on the anode side and 10 atmos on the cathode side. Thus a cell potential of 0.825 V at 300 mA/cm^2 was obtained. These cells could generate current densities of 1 A/cm^2 at a cell potential of 0.5 V. The slope of the cell potential versus current density plot in the linear region was 0.3 ohm cm^2.

The performance of the GE/HS-IFC cell was not satisfactory with air as the cathode reactant. In spite of the high pressure, the cells reached a limiting current density at only about 300 mA/cm^2 and 105°C.

Ballard Technologies Corporation in Canada has made significant advances in the solid polymer electrolyte fuel cell technology. The detailed design and assembly of single and multicells have not been published; however, it appears to be quite similar to the GE/HS-IFC fuel cell. Electrodes with a high platinum loading and Teflon are attached to the membrane. The major improvements in performance appear to be due to the utilization of a Dow membrane instead of Nafion as the electrolyte layer. The Dow membrane has about 1/2 to 3/4 the equivalent weight of Nafion; hence, its conductivity and water retention capability are considerably better than Nafion. It has been reported that at about 3 atm pressure and an operating temperature of 80°C, cell potentials of 0.68 V and 0.55 V are attained at current densities of 2 A/cm^2 with H_2/O_2 and H_2/Air, respectively, as reactants. The slopes of the cell potential versus current density plots in the linear region are only 0.1 and 0.2 ohm cm^2, respectively. The thickness of the Dow membranes used in these fuel cells is 75-100μ, whereas the thickness of the Nafion membrane in the GE/HS-IFC fuel cells is 175-200μ. The higher conductivity of the Dow membranes and the smaller thickness account for the lower slope of the linear region in the Ballard fuel cell, as compared with that in the GE/HS-IFC fuel cells (0.3 - 0.4 ohm cm^2).

Siemens in Germany is also using the GE/HS-IFC technology to develop fuel cell systems for submarine power applications. Siemens has, like Ballard Technologies Corporation, reported high-power densities with H_2 and O_2 as reactants under pressure.

One of the critical problem areas in the solid polymer electrolyte fuel cell technology is water management. Ergenics Power Systems, Inc. (EPSI), is using a novel approach to solve this problem. In this fuel cell, the cell construction permits internal transport of water for humidification of the gases and hence, of the membrane. Currently, efforts have focused on atmospheric pressure operation. Single and multicell stacks have been built and tested with this design. The cells are operated at 50 to 60°C and with H_2/air as reactants; at 200mA/cm^2, the cell potential is about 0.65 V. The slopes of the linear region in the cell potential-current density plots are 0.42 and 0.80 ohm cm^2 with H_2/O_2 and H_2/air, respectively, as reactants. EPSI is developing a 200-watt fuel cell system coupled with hydrogen and oxygen storage systems sufficient for 8-12 h. This fuel cell system will be used for power requirements by astronauts during their space flights.

The Dow Chemical Company is developing membranes for utilization in fuel cells and chlor-alkali cells. Membrane and electrode assemblies are being prepared and tested by this organization in GE/HS-IFC fuel cell test stations.

Needed Advances in Technology and Scope of Present Paper

Recently (Ref. 4), it was demonstrated that by incorporation of a proton conductor, Nafion, into the fuel cell electrode structures containing carbon supported platinum electrocatalyst, the same level of performance of the half cell reactions (hydrogen oxidation and oxygen reduction) in fuel cells can be achieved as in the GE/HS-IFC fuel cell, but with only one tenth of the noble metal loading (i.e., 0.35 mg/cm^2 vs 4.0 mg/cm^2). Nafion, rather than platinum, will become the most expensive material in the solid polymer electrolyte fuel cell once the technology is developed for utilizing the low noble metal loading in fuel cell electrodes. Thus, either alternatives for Nafion need to be found (the Dow membrane appears very promising but its price is unknown) or power densities of about 1 watt/cm^2 need to be achieved to reduce the effective cost of the membrane. According to the work at GE/HS-IFC, the water management problem was overcome with differential pressurization. Such a solution has complexities in developing a multicell stack and an alternative approach is needed.

The present work demonstrates improvements in performance of solid polymer electrolyte fuel cells with respect to efficiency, power density, and lifetime by (i) utilization of low platinum loading electrodes impregnated with a proton conductor, (Nafion); (ii) optimization of anode/membrane/cathode interface by hot pressing the electrode on to the solid polymer electrolyte under pressure and at a temperature close to that of the membrane glass transition temperature; (iii) pressurization of reactant gases, which is essential when air is used as the cathodic reactant; and (iv) adequate humidification of the gases to overcome the water management problem.

EXPERIMENTAL

Design and Assembly of Single Cells

Three types of single cells were used in the present work. For most of the experiments, a single cell made with carbon (Union Carbide nuclear grade graphite) end plates was used. The graphite end plates contain gas feed inlets and outlets, ribbed channels for gas flow behind the electrodes, and holes for cartridge heaters and a thermocouple. After positioning the membrane and electrode assembly between the graphite end plates, the latter were clamped between stainless steel plates that were insulated from the cell body with PTFE sheets. The active cell area (geometric) in this cell is 5 cm^2. For the control cell, the GE/HS-IFC membrane and electrode assembly was used. In the test cells, as-received and Nafion-impregnated Prototech electrodes were hot pressed to Nafion membranes at 120°C and 50-60 atm pressure for 30 s. In one experiment, the Nafion-impregnated Prototech electrodes were hot pressed onto a Dow membrane. The reactant gases were externally humidified in this cell.

A new cell with an active electrode area of 10 cm^2 and internal humidification was designed and fabricated. In the new cell, separate humidification chambers for the anodic and cathodic reactants are adjacent to the respective electrodes. In each of these chambers, a Nafion membrane/porous titanium sheet

composite separates the water and gas flow compartments. The water that permeates through the Nafion membrane humidifies the reactant gases. The area for humidification of the gases is four times the electrode area.

The third cell assembly is the one designed and constructed by GE/HS-IFC. The active area of the electrodes in this cell is 50 cm^2. This cell also incorporates a humidification chamber, split into two separate compartments for the humidification of the reactant gases. Platinum particles were deposited within the membrane to serve as a catalyst for the combination of hydrogen and oxygen gases in case cross-mixing occurred. The GE/HS-IFC test station is well equipped for the supply and removal of reactant gases, water for humidification of gases, temperature and pressure control, and electrochemical measurements (cell potential vs current density and life testing). Safety features for turning off the system when there is a cell failure or other emergency are also incorporated in the test station.

Optimization of Humidification of Reactant Gases

The preliminary experiments, carried out in the 5 cm^2 cell with external humidification, proved to be valuable in optimizing the humidification conditions for the reactant gases. The water management in the solid polymer electrolyte is complex because protons that are formed by the oxidation reaction tend to carry 4-6 molecules of water per proton from the anode to the cathode. The situation is made even more complex with the Nafion-impregnated electrodes because the micropores in the active layer tend to dry out. This increases the cell resistance. Another problem is that water formed at the oxygen electrode can cause flooding. Further complication arises when operating the cells at close to 100°C - the desired operating temperatures to obtain better electrocatalysis and minimize carbon monoxide poisoning effects. Under these conditions, the vaporization losses become significant.

However. water management problem is not as serious as it was originally thought for the following reasons: (i) the concentration gradient that is set up in the membrane and electrode assembly due to water drag by protons and production of water at the cathode is sufficiently high to transport water at fast enough rates back from cathode to anode; (ii) vaporization losses can be minimized by operating the cells at higher pressures and temperatures and by adequate humidification; (iii) it is necessary to humidify the gases at temperatures of about 5 to 10°C above the cell temperature to prevent the drying out problem, particularly within the pores of the Nafion-impregnated electrodes.

In the 10 cm^2 and 50 cm^2 cells with internal humidification, the humidification chambers are probably at a slightly higher temperature, but because the water diffuses through the Nafion membrane in a vapor or droplet form, the efficiency of humidification is high.

Measurements of Cell Potential as a Function of Current Density at Different Temperatures and Pressures

Cell potential-current density measurements were made periodically by interrupting the constant current density operation to obtain lifetime performance data. For this purpose the measurements in the 5 and 10 cm^2 cells were made using the PAR Model 173 Potentiostat/Galvanostat. For higher current density measurements, a power supply with a higher current output was used. More recently a Hewlett Packard programmable power supply 6033A and an IBM Micro computer were interfaced with the electrochemical cell to obtain the cell potential vs current density data.

Measurements were made as a function of temperature and pressure. The initial studies were carried out at 25 and 50°C at atmospheric pressure. The more recent experiments were carried out at 50 and 75°C and at pressures of 1 to 5 atmos above atmospheric pressure. The high frequency resistance measurements were made in the cells to obtain ohmic overpotentials. However, this measurement does not yield the ohmic overpotential within the porous electrode structure due to its behavior like a transmission line. An AC impedance spectroscopic method will have to be used to obtain this resistance.

The GE test station is well equipped for obtaining cell potential-current density data in the 50 cm^2 cell. This test station can also be adapted when using the 10 cm^2 cell with internal humidification. A set of experiments was carried out with 50 cm^2 Nafion-impregnated Prototech electrodes hot pressed on to Nafion membranes. In all cases, measurements were made with hydrogen/oxygen and hydrogen/air as reactants.

Lifetime Studies

A few experiments were carried out to determine the long term performance of the electrodes. For this purpose, the cells were maintained at a constant current density (100 to 200 mA/cm^2) and the potentials followed as a function of time. There were periodic interruptions for either making cell potential vs current density measurements or cyclic voltammetric studies.

Cyclic Voltammetry on Electrodes to Ascertain Electrochemically Active Surface Area

This technique proved to be quite valuable to ascertain the electrochemically active surface area of the electrodes. For this purpose, the PAR 173 Potentiostat/PAR 175 Programmer was used. Cyclic voltammograms were generally recorded at 100 mV/s. Argon gas was passed through the test electrode compartment and hydrogen through the counter electrode compartment. Due to the negligible overpotential, the counter electrode also served satisfactorily as the reference electrode.

RESULTS AND DISCUSSION

Analysis of Cell Potential - Current Density Relations

The cell potential-current density data were analyzed using an equation of the form:

$$E = E_o - b \log i - R_i i \qquad (1)$$

The assumption made in this equation is that mass transport limitations are negligible, which is generally the case until the current densities are close to the limiting current density. In Eq. (1), E_o is a constant, and if it is assumed that the hydrogen oxidation reaction is considerably faster than the oxygen reduction reaction:

$$E_o = E_r + 2.303 \frac{RT}{\alpha F} \log i_o \qquad (2)$$

where E_r is the reversible potential for the cell, and i_o and α are the exchange current density and transfer coefficient for the oxygen reduction reaction. In Eq. (1) b is the Tafel slope for the oxygen reduction reaction and R_i is the slope of the linear region in the E vs i plot, the predominant contribution being ohmic overpotential, with smaller ones due to activation and mass transport control. The parameters, E_o, b and R_i were evaluated by non-linear least squares fits to the experimental points. Typical cell potential versus current density plots for (i) the control cell with GE/HS-IFC membrane and electrode assembly; (ii) the test cell with the as-received Prototech electrode hot-pressed onto a Nafion membrane; and (iii) the Nafion-impregnated electrode hot-pressed on to a Nafion membrane are presented in Fig. 1. The solid lines that represent the computer generated plots show excellent agreement with the experimental points. The results obtained in the cell with the 50 cm^2 electrodes with H_2/O_2 and H_2/Air as reactants at 50°C are plotted in a linear manner (E vs. i) in Fig. 2 and in a semilogarithmic manner (E vs logi) in Fig. 3. These figures also confirm the excellent agreement between the computer generated plots and experimental points.

The electrode kinetic parameters for the control cell with the GE/HS-IFC membrane and electrode assembly and for the test cells with the Prototech electrodes (as-received and Nafion-impregnated) hot pressed on to Nafion or Dow membrane, are summarized in Table I. Also shown in this table are the high frequency resistance and the current density at a cell potential of 0.7 V. The following conclusions can be drawn from the results in Table 1. (i) The control cell with the GE/HS-IFC membrane and electrode assembly and the test cells with the Nafion-impregnated electrodes exhibit similar electrode kinetic parameters. (ii) The differential resistance (R_i) of the cell is at least 50% higher for the hydrogen/air fuel cells as compared with hydrogen/oxygen fuel cells. This is not the case in phosphoric acid fuel cells (typical results also given in Table 1). The reason for this anomalous behavior with solid polymer electrolyte fuel cells is probably due to a greater degree of mass transport and ohmic limitations with air instead of oxygen as the cathodic reactant. (iii) The differential resistance in the test cell with as-received Prototech electrodes is at least an order of magnitude higher than in the test cells with Nafion-impregnated Prototech electrodes. The high frequency resistance is nearly the same in all cells. These results correlate well with

the considerably higher electrochemically active surface areas in the electrodes where there is either a higher noble metal loading or an extension of the three dimensional reaction zone. (iv) The high frequency resistances are considerably less than the differential resistances of the cell in all cases except one. This behavior can be interpreted on the basis that the high frequency resistance does not include the resistance within the electrodes due to mass transport and ohmic limitations. (v) The Tafel slope for the cell with the as-received Prototech electrodes is nearly twice that in the other cells. This is because of combined effects of activation and ohmic overpotential in the former and only activation overpotential in the latter.

Significant Effects of Pressure on Performance of Fuel Cells With Hydrogen/Air as Compared With Hydrogen/Oxygen as Reactants

Operation at pressures of at least 3 atm above atmospheric pressure is essential to attain high power density in solid polymer electrolyte fuel cells for at least three reasons. (i) At higher pressures, and temperatures and with adequate humidification water loss from the membrane by evaporation or carry-over with the reactant gases is reduced. (ii) Higher pressures are required for operating the cells at close to 100°C, which is favored from an electrode kinetic point of view, and it also increases the tolerance of the anode to carbon monoxide (which may be at a level of 0.1 to 0.3% in the anode fuel stream). (iii) Higher pressures improve the electrode kinetic performance of the cells.

Two types of pressure effects are observed. A slight increase of pressure (0.1 atm) above 1 atm has a stronger effect on the performance of hydrogen/air than on hydrogen/oxygen fuel cells (Fig. 4). Thereafter, the increase of performance with pressure is nearly the same in both cases.

The pressure and temperature effects in the cell with the 50 cm^2 electrode on the electrode kinetic parameters are presented in Table II and III. Figures 5 and 6 exhibit the effect of pressure on the cell potential versus current density plots at 80°C with hydrogen/oxygen and hydrogen/air as reactants. The increase in cell potential (ΔE) with pressure at a constant current density due to enhanced electrode kinetics should follow the equation:

$$\Delta E = b \log P_2/P_1 \qquad (3)$$

where P_2 is the higher pressure and P_1 is the lower one. One can observe from Figs. 5 and 6, as well as from Tables II and III (the value of E_o), that pressure effects are higher than expected (except for the case when the pressure is increased from 40 to 60 psig with air). The thermodynamic effect of pressure on the reversible potential is small. The higher potentials observed (when compared to equation [3]) can be explained by assuming that higher pressure favors water management, particularly humidification in the fuel cell (i.e., within the electrode and the membrane). A theoretical analysis of the pressure effect is in progress and will be the subject of a future communication.

Stable Long Term Performance

Several cells were subjected to life testing, mostly with hydrogen/air as reactants. Cells were operated under constant load (100, 150 mA/cm^2). The cell that was tested for the longest period was the one with the Nafion-impregnated electrode hot-pressed on to a Dow membrane (Fig. 7). The life testing was interrupted periodically to record cell potential versus current density data or cyclic voltammograms. Life testing on the cell with the 50 cm^2 electrode was also carried out at the three temperatures and three pressures with oxygen as the cathodic reactant; it was possible to maintain stable cell potentials at a constant current density of 500 mA/cm^2. With air as the cathodic reactant, the maximum current density at which the cell potential remained constant for at least an 8 hour period was 200 mA/cm^2. The present work demonstrates that with proper external humidification of the reactant gases (i.e., at a temperature of 5-10°C above the cell temperature), there was hardly any performance variation with time.

Cyclic Voltammetry on Electrodes to Ascertain Electrochemically Active Surface Area

One the of main problems with the use of this technique with supported electrocatalysts is that the carbon features (double layer charging, redox behavior of surface active groups on carbon, for example, quinone/hydroquinone) mask the hydrogen adsorption/desorption characteristics. Also, if the anodic limit is extended beyond 1V/RHE, oxidation of carbon occurs. In spite of these problems, the technique proved to be useful to ascertain the electrochemically active surface of the electrodes. As seen in Fig. 8, the coulombic charge over the entire potential scan is approximately the same for the GE/HS-IFC and the Nafion-impregnated Prototech electrodes, but an order of magnitude less for the as-received Prototech electrodes. This increase in electrochemically active surface area correlates well with the observed cell potential-current density plot (Fig. 1) and also with the values of differential resistances of the cells in the linear regions of these plots. The results clearly demonstrate the extension of the three dimensional reaction zone by incorporation of a proton conductor into the electrode containing a low noble metal loading.

CONCLUSIONS

The emphasis of the work presented in this paper was to attain a high level of performance in solid polymer electrolyte fuel cells with electrodes containing a low platinum loading (0.35 mg/cm^2 as compared with state of the art 4 mg/cm^2). The following conclusions can be drawn from the results obtained.

(1) By impregnation of the Prototech electrodes (0.35 mg/cm^2 Pt) with a proton conductor, there appears to be an extension of the three dimensional reaction zone in the porous electrode structure and a considerable improvement in the fuel cell performance. The fuel cell performance obtained is practically the same as with the state-of-the-art membrane and electrode assembly (4 mg/cm^2 of Pt). Confirmation of the extension of the three dimensional reaction zone

is demonstrated (i) by the analysis of the experimental results using Eq. 1 - the slope of the cell potential-current density curve in the linear region in the cell with the as-received Prototech electrode is an order of magnitude higher than in the cell with the Nafion-impregnated Prototech electrode; and (ii) by ascertaining the electrochemically active surface areas using the cyclic voltammetric technique.

(2) Analysis of the cell potential/current density curves using Eq. 1 shows that the Tafel slope for the oxygen reduction reaction in the cells with the state-of-the-art membrane and electrode assembly and with the Nafion-impregnated electrodes is approximately 0.060 V/decade. In the cell with the 50 cm^2 electrode, the Tafel slope with hydrogen/air as reactants is 0.045 V/decade. This Tafel slope appears to be independent of temperature and pressure. The Tafel slope in the cell with the as-received Prototech electrode is about 0.095 V/decade, and this may be interpreted as being due to the combined effects of activation and ohmic control.

(3) It is essential to hot press the electrodes on to the membrane at a temperature of 120°C (glass transition temperature for Nafion) and under pressure (50 atm) to minimize activation and ohmic overpotential.

(4) There is a significant effect of pressure in the low range (0-2 psig) on the performance of the cells, with hydrogen/air as reactants. Above this pressure, both hydrogen/air and hydrogen/oxygen fuel cells show a linear increase in current density at a constant cell potential, with pressure.

(5) Optimal humidification of the reactant gases (5-10°C above the cell temperature) is necessary to obtain stable long term performances.

REFERENCES

1. Maget, H. J. R.: The Ion Exchange Membrane Fuel Cell. Handbook Fuel Cell Technology, C. Berger, Ed., Prentice-Hall, Englewood Cliffs, NJ, 1967, pp. 425-491.

2. Tilak, B. V., Lu, P. W. T., Coleman, J. E., and Srinivasan, S.: Electrolytic Production of Hydrogen. Chapter 1 in Comprehensive Treatise of Electrochemistry, Vol. 2, Bockris, J. O'M, Conway, B. E., Yeager, E., and White, R. E. Eds., Plenum Press, New York, 1981.

3. Appleby, A. J., and Yeager, E. B.: Solid Polymer Electrolyte Fuel Cells. Assessment of Research Needs for Advanced Fuel Cells, Penner, S. S., Ed., Chapter 4, DOE/ER/30060-T1, NTIS, U.S. Department of Commerce, Springfield, VA, 1985.

4. Raistrick, I. D.: Modified Gas Diffusion Electrodes for Proton Exchange Membrane Fuel Cells. Extended Abstracts of the 169th Meeting of the Electrochemical Society, Boston, Massachusetts, May 4-9, 1986, 86-1, 60, 1986.

TABLE I. - ELECTRODE KINETIC PARAMETERS FOR FUEL CELLS OBTAINED BY METHOD OF LEAST SQUARES FIT OF CELL POTENTIAL - CURRENT DENSITY MEASUREMENTS USING EQUATION $E = E_o - b \log i - R_i i$

Cell # Type	Temperature °C	E_o V	b V	R_i Ohm/cm^2	R_{HF} Ohm/cm^2	Current Density at 0.7 V mA/cm^2
PEM 3[1], H_2/Air	50°	0.924	0.068	1.808	0.88	60
" H_2/O_2	50°	0.950	0.055	1.214	0.88	120
" H_2/Air	25°	0.928	0.049	3.342	-	55
" H_2/O_2	25°	0.957	0.055	1.906	-	80
PEM 5[2], H_2/Air	50°	0.721	0.099	26.250	1.05	1
" H_2/O_2	50°	0.760	0.091	21.600	1.05	2
" H_2/Air	25°	0.757	0.098	31.510	-	1
" H_2/O_2	25°	0.776	0.092	21.960	-	2
PEM 6[3], H_2/Air	50°	0.878	0.052	1.438	0.73	70
" H_2/O_2	50°	0.934	0.049	0.851	0.73	150
" H_2/Air	25°	0.878	0.040	1.976	-	50
" H_2/O_2	25°	0.932	0.066	0.866	-	120
PEM D/120[4] H_2/Air	25°	0.849	0.065	1.469	0.65	40
" H_2/O_2	25°	0.885	0.062	0.877	0.65	80
" H_2/Air	50°	0.883	0.058	1.402	0.43	50
" H_2/O_2	50°	0.914	0.069	0.580	0.43	120
" H_2/Air	75°	0.854	0.057	1.281	-	40
" H_2/O_2	75°	0.890	0.065	0.715	-	100
PA[5], H_2/Air	150°	0.893	0.103	0.656	0.46	40
PA, H_2/O_2	150°	0.962	0.105	0.624	0.46	100

[1]PEM 3: GE/MS-IFC Membrane and Electrode Assembly
[2]PEM 5: Prototech Electrode/Nafion Membrane
[3]PEM 6: Nafion Impregnated Prototech Electrode/Nafion Membrane
[4]PEM D/120: Nafion Impregnated Prototech Electrode/Dow Membrane
[5]PA: Phosphoric Acid Fuel Cell.

TABLE II. - ELECTRODE KINETIC PARAMETERS FOR FUEL CELLS OBTAINED BY METHOD OF LEAST SQUARES FIT OF CELL POTENTIAL - CURRENT DENSITY MEASUREMENTS USING EQUATION $E = E_o - b \log i - R_i i$ CELL WITH 50 cm^2 ELECTRODES, H_2/O_2 REACTANTS

Temperature °C	Pressure Above Atmospheric psig	E_o V	b V	R_i Ohm cm^2	Current/Density At 0.7 V mA/cm^2
50°	0	0.920	0.066	0.509	120
50°	20	0.944	0.067	0.470	180
50°	40	0.956	0.060	0.484	210
50°	60	0.971	0.061	0.465	250
70°	20	0.956	0.063	0.382	240
70°	40	0.972	0.066	0.387	300
70°	60	0.980	0.057	0.376	340
80°	20	0.954	0.066	0.350	240
80°	40	0.972	0.063	0.332	310
80°	60	0.981	0.059	0.333	360

TABLE III. - ELECTRODE KINETIC PARAMETERS FOR FUEL CELLS OBTAINED BY METHOD OF LEAST SQUARES FIT OF CELL POTENTIAL - CURRENT DENSITY MEASUREMENTS USING EQUATION $E = E_o - b \log i - R_i i$ CELL WITH 50 cm^2 ELECTRODES, H_2/AIR REACTANTS

Temperature °C	Pressure Above Atompheric psigs	E_o V	b V	R_i Ohm cm^2	Current/Density At 0.7 V mA/cm^2
50°	0	0.902	0.047	0.898	60
50°	20	0.929	0.046	0.930	120
50°	40	0.945	0.043	1.012	140
50°	60	0.959	0.061	1.035	150
70°	20	0.929	0.053	0.919	120
70°	40	0.940	0.045	0.884	150
70°	60	0.948	0.040	0.944	160
80°	20	0.920	0.046	0.666	120
80°	40	0.940	0.053	0.577	160
80	60	0.949	0.041	0.756	190

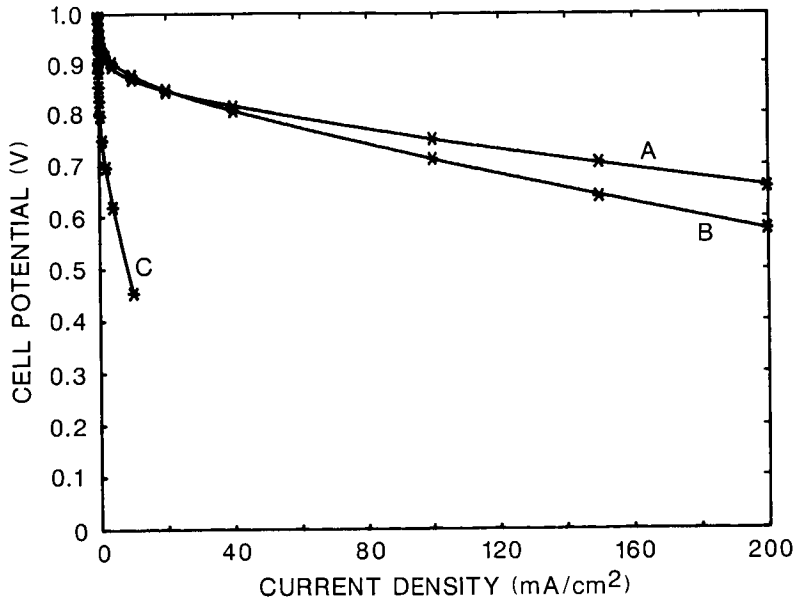

Fig. 1. Cell potential/current density plots for H_2/O_2 fuel cells at 50°C and 1 atm pressure (electrodes 5 cm^2): A and C Nafion-impregnated and as-received Prototech electrodes (0-35 mg/cm^2 Pt) hot-pressed to Nafion membranes; B - GE/HS-IFC membrane and electrode (4 mg/cm^2 Pt). Solid line - computer generated plots; * - experimental points.

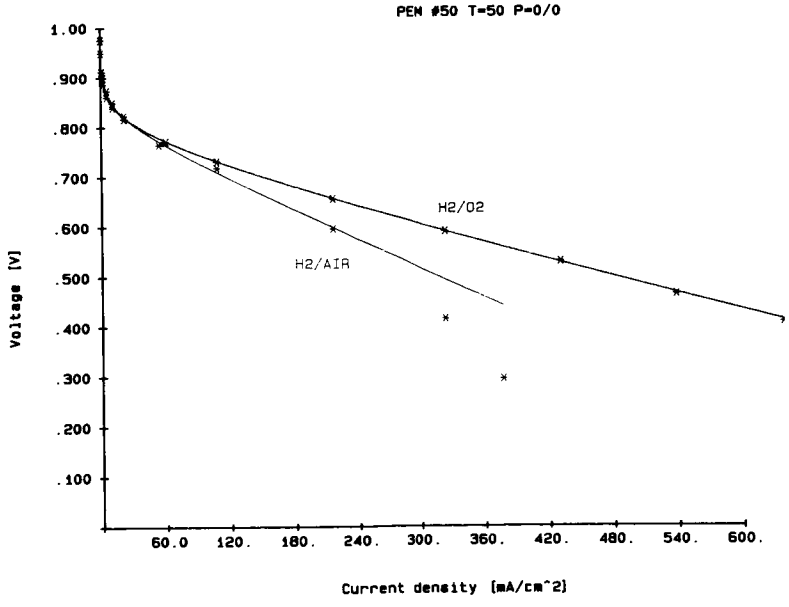

Fig. 2. Cell potential/current density plots for H_2/O_2 and H_2/air fuel cells at 50°C and 1 atm pressure (electrodes 50 cm^2). Nafion-impregnated Prototech electrodes (0.35 mg/cm^2 Pt) hot-pressed to Nafion membrane. Solid lines - computer generated plots; * - experimental points.

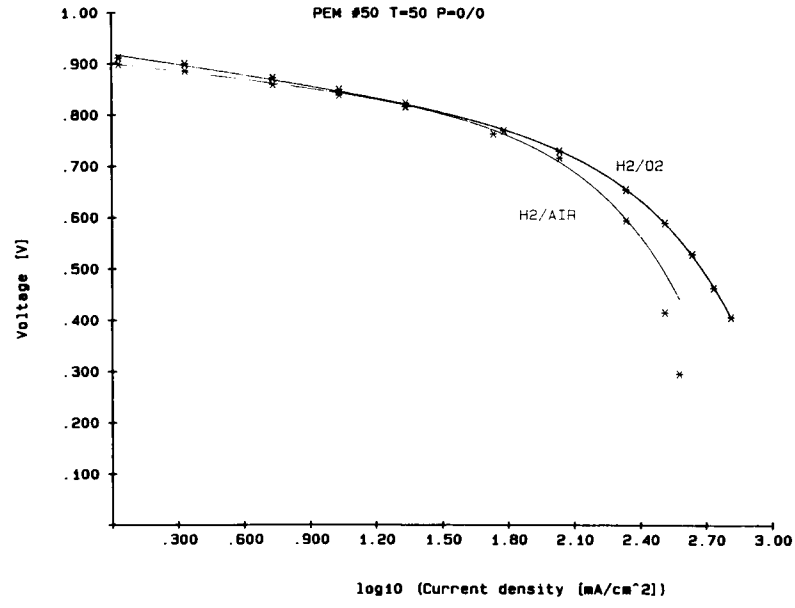

Fig. 3. Cell potential/log current density plots for H_2/O_2 and H_2/air fuel cells at 50°C and 1 atmos pressure (electrodes 50 cm^2). Nafion-impregnated Prototech electrodes hot-pressed to Nafion membrane. Solid lines - computer generated plots; * - experimental points.

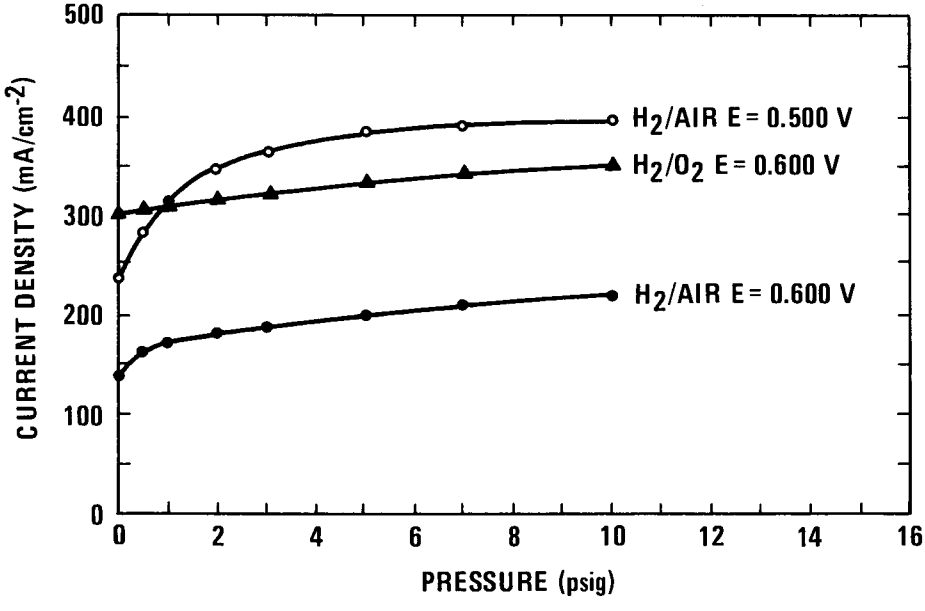

Fig 4. Current density at constant cell potential/pressure plots at 50°C for H_2/O_2 and H_2/air fuel cells (electrodes 50 cm^2). Nafion-impregnated Prototech electrodes (0.35 mg/cm^2 Pt) hot-pressed to Dow membrane.

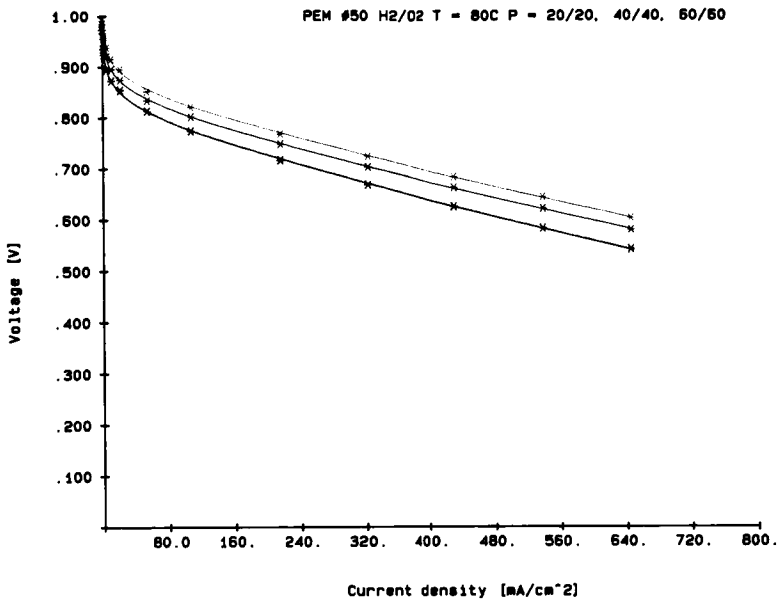

Fig. 5. Cell potential/current density plots for H_2/O_2 fuel cell at 80°C and pressures of 20, 40 and 60 psig (electrodes 50 cm^2). Nafion-impregnated Prototech electrodes (0.35 mg/cm^2) hot-pressed to Nafion membrane. Solid lines - computer generated plots; * - experimental points.

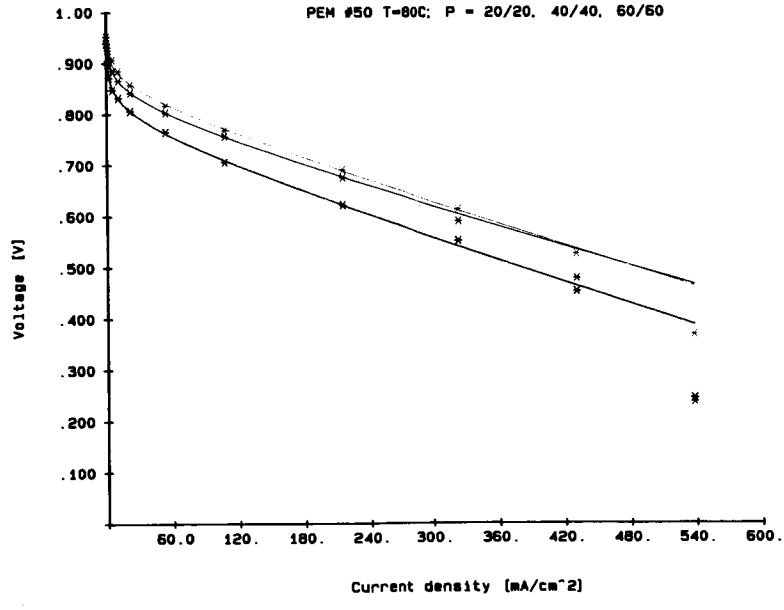

Fig. 6. Cell potential/current density plots for H_2/air fuel cell at 80°C and presures of 20, 40 and 60 psig (electrodes 50 cm^2). Nafion-impregnated electrodes (0.35 mg Pt/cm^2) hot-pressed to Nafion membrane. Solid lines - computer generated plots; * - experimental points.

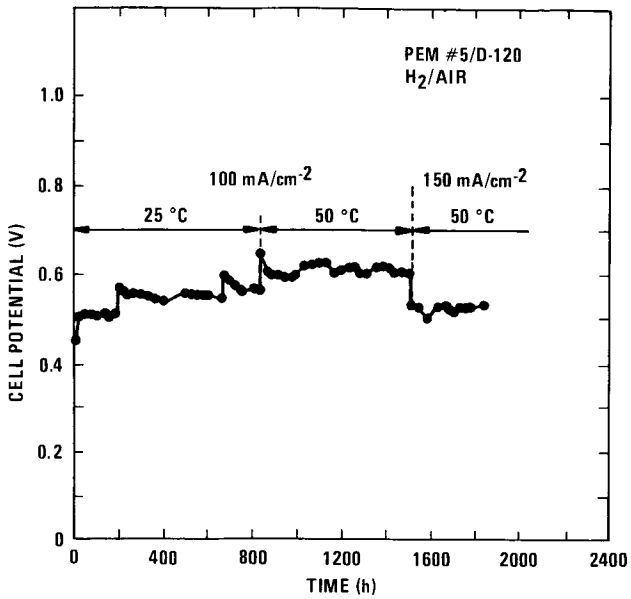

Fig. 7. Life testing of H_2/Air fuel cell (electrodes 5 cm^2). Nafion-impregnated Prototech electrodes hot-pressed to Dow membrane.

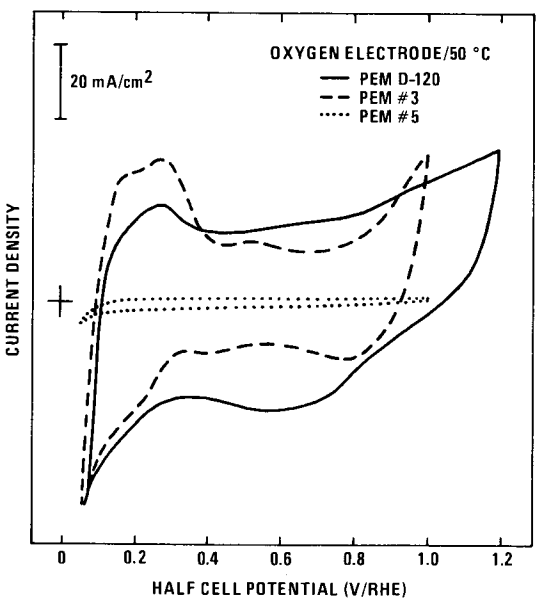

Fig. 8. Cyclic voltammograms on oxygen electrodes in fuel cells (electrodes 5 cm^2). PEM D-120-cell with Nafion-impregnated Prototech electrodes (0.35 mg/cm^2 Pt) hot-pressed to Dow membrane; PEM #3-cell with GE/HS IFC membrane and electrode assembly (4 mg/cm^2 Pt); and PEM #5-cell with as-received Prototech electrodes (0.35 mg/cm^2 Pt) hot-pressed to Nafion membrane.

N87-29938

REGENERATIVE FUEL CELLS FOR SPACE APPLICATIONS

A.J. Appleby
Texas A&M University
College Station, TX 77843

After several years of development of the regenerative fuel cell (RFC) as the electrochemical storage system to be carried by the future space station, the official stance has now been adopted that nickel-hydrogen batteries would be a better system choice. This paper compares RFCs with nickel-hydrogen and other battery systems for space platform applications.

INTRODUCTION

Originally the RFC was conceived as a suitable system for unmanned platforms in low-earth orbit (LEO) and in geosynchronous orbit (GEO), for the permanently manned LEO space station, and for orbital transfer vehicles between LEO and GEO. In addition, it might also be used for various military surveillance, command and weapons applications connected with space platforms of various types. For these applications, primary power would be provided either by deployable photovoltaic (PV) arrays, solar thermal (dynamic solar) systems, or from a small nuclear reactor such as the proposed General Electric SP100 unit, which was originally to be rated at 100 kW, but which may grow (if developed) to 300 kW. At the present time, the potential for safe launching of nuclear units cannot be established, so that PV and solar thermal primary power sources must be looked upon as being the main contenders for these applications. The solar systems would require on-board storage for eclipse periods, and all would need storage for peak-load.

The main technical objectives of the on-board storage power units would be light weight (and compactness) for the given mission, very long cycle life and in-orbit maintainability. It was considered that initial electrochemical storage units would be in the 50-100 kW peak load class or less, and that modularity would be used to build up units of any desired future size.

RFC CONCEPTS

LEO storage was examined from 1979 by NASA's Johnson and Lewis Research Centers. The RFC was at this time recognized as having the capability of meeting a 40,000 life requirement. This system, it was considered, could be ready for deployment by the end of 1986 (ref. 1). It was to consist of fuel cells to supply peaking and eclipse power, with PV cells to supply both power during sunlight periods, when electrolyzer cells would also be operated whose product hydrogen and oxygen would be stored for use in the fuel cell. The

system was to consist of separate fuel cell and electrolyzer packages because these were already available, and this would also avoid the design of special electrodes that could operate in both charge and discharge modes. As we will see below, this is difficult for many systems. Finally such a system using proven components avoids the problems of man-rating of new concepts and allows easy optimization of electrode areas and numbers of active cells in each mode.

Although the overall efficiency of the H_2/O_2 fuel cell electrolyzer combination is only 50-60%, its waste heat can be thermally integrated at 70-95°C to provide a useful source of spacecraft heating during both charge and discharge modes. On this basis, it is superior to competing battery systems operating close to 25°C. Its disadvantage is that it would require a larger PV panel area than batteries, but such a system would probably require additional solar-thermal collector area for spacecraft life-support heating.

A further advantage of the RFC compared with conventional batteries with a proven space ability in the late 1970s was system lifetime for a given weight. As is well known, conventional secondary battery lifetime rapidly diminishes with increasing depth of discharge (DOD), since the active materials must undergo phase and/or crystalline alterations associated with volume changes and some degree of irreversibility. These lead to degradation in electrode structure and in active material utilization, often accompanied by destructive corrosion of the positive due to successive formation and breakdown of oxide films on each charge-discharge cycle.

Thus, in the 1970s, only one proven candidate secondary battery for space applications requiring many years of life was available -- namely nickel-cadmium. Most applications were for GEO communications satellites, for which there are two 45-day eclipse periods per year and one eclipse per eclipse day in a typically-inclined orbit. In a 24-hour orbit the eclipse time might be about 1.2 h. Thus, 900 cycles would be required over a 10-year lifetime. These cycles would vary from medium-discharge (60% DOD) to shallow-discharge, with discharge at the C/2 rate for 1.2 h. Accordingly, such cells are usually tested at 1.8 h charge, C/2 (1.2 h) discharge at 60% DOD to determine lifetime performance capability.

For typical aerospace Ni-Cd cells this exceeds 2000 cycles under these conditions. Hence for GEO use, Ni-Cd cells were adequate. However, under aerospace conditions, when mounted in a battery, they are little better than 20 Wh/kg at 100% DOD at the C/2 rate.

For LEO applications, sunlight is typically 0.9 h in an equatorial orbit, with eclipse for 0.6 h, with one cycle per orbit or 5840 cycles per year.

The calculated system weights for a 100 kw power storage plant with a 10 year orbit life have been quoted as: RFCs: 6,000 kg; Ni-Cd batteries (50% DOD): 7000 kg; Ni-Cd batteries (25% DOD): 16,000 kg (ref. 2), where the orbit lifetime of Ni-Cd cannot be relied on.

As a consequence of the above, a "proof of technology readiness" based on small General Electric SPE fuel cell-electrolyzer components (ref. 3, developed since early 1984 by UTC's Hamilton Standard Division), and on UTC lightweight alkaline fuel cells (AFCs) combined with Life Systems, Inc. alkaline electrolyzers were selected by NASA for demonstrations. Earlier programs supported by the U.S. Navy on submarine life-support systems using Nafion SPE membrane cells (ref. 3) demonstrated 35,000 hours of life at 82°C and indicated a potential electrolysis SPE membrane life in excess of 100,000 h. Similarly, the Life Systems alkaline electrolyzer also has a proven lifetime.

The SPE demonstrator consisted of an 8-cell stack of 1000 cm^2 fuel cells combined with a 22-cell stack 210 cm^2-cell electrolyzer. The fuel cell operated at 112 A, 6.5 V, 71°C. Cell voltages to sustain electrolyzer current densities of 200 and 800 mA/cm^2 have however been reported as 1.59 and 1.78 V (ref. 4). Hydrogen storage was at 880 kPA (8.8 atm) and oxygen at 780 kPA (7.8 atm). This unit was delivered to Johnson Space Center in February 1983, and it completed 3500 hours before being terminated. No measurable degradation was observed. The alkaline system fuel cell consisted of the lightweight version (refs. 5,6) of the space shuttle orbiter fuel cell (ref. 5), with later stack improvements. Stack lifetimes for the space shuttle system for over 10,000 h have been achieved (ref.1). Goals were determined to be 40,000 h life at 110 mA/cm^2 and 3,000 at 0.9 V, 1.1 A/cm^2 for pulsed power application (ref. 7).

The Life Systems electrolyter technology used cells of about 90 cm^2 area, and has been tested over 13,000 h. The alkaline breadboard was delivered to Johnson Space Center in January 1984 and contained a 30-cell electrolysis unit rated at 1.5 kW. Voltages of 1.52 and 1.82 V were attained at 200 and 800 mA/cm^2 respectively (ref. 4). In April 1984, it was replaced by a 6 cell, 930 cm^2 area unit rated at 3 kW to provide a better match with the UTC fuel cell. The system was tested over many LEO cycles, the fuel cell showing less than 1 mV/1000 h voltage degradation.

In May 1986, the program changed, since NASA decided not to consider RFCs for the future space station, presumably as an economy measure. The projected power requirements of the manned space station started to change with its proposed size, and it was to have 25 kW of installed deployable PV together with 50 kW of solar thermal system. The proposed polar orbital platform was was to use nickel-hydrogen batteries as storage units for its PV array. It was felt that the same system could be used for both. Since that time, the space station PV requirement has risen, first to 37.5 kW of PV, and perhaps to 50 kW as specifications change.

COMPARISON BETWEEN Ni-H_2 AND THE RFC

The Ni-H_2 battery grew out of a proposed true RFC (i.e. with one-piece fuel cell and electrolysis cell elements) concept for GEO use in the late 1960s (ref. 7). This consisted of an AFC with high-loading noble metal electrodes in a lightweight pressure vessel internally divided in such a way that hydrogen and oxygen could be stored separately. The system was rapidly abandoned and replaced by various metal-gas battery concepts, such as zinc (or cadmium)-oxygen (ref. 8). Metal-oxygen systems, particularly zinc-oxygen, are in principle attractive since they have lightweight, high energy negatives (zinc has a practical energy density of 0.6 Wh/g when combined with an oxygen electrode, whereas practical nickel positives combined with hydrogen negatives are 0.135 Wh/g, Ref. 9). In addition, oxygen storage requires half the volume of hydrogen storage for the same number of Ah, hence a lighter container. As a result of the above, zinc negative-oxygen positive systems have a 50% higher energy density (on paper) than nickel positive-hydrogen negative systems. However, while their coulombic efficiency is good, they have poor voltage efficiency due to the irreversible characteristics of the oxygen electrode, even on Pt group metals or Au under pressure (overall efficiency 60%).

Finally, the zinc electrode has a poor cycle life capability, and it can react explosively with compressed oxygen if the electrolyte dries out, for example on overcharge at high rates. In consequence, the favored couple is Ni-H_2, which operates at a coulombic efficiency of 75% and a voltage efficiency of about 85% (65% overall) under practical LEO conditions. Its average voltage at the C/2 discharge rate (based on 100% DOD) is 1.2 V to 60% DOD (cut-off at 1.0V).

It is instructive to compare the specific energies of the Ni-H_2 battery and the true RFC on the single-cell level for a C/2 mission requirement (i.e., all gas stored during charge to 100% degree-of-charge is consumed to a nominal baseline pressure representing container backfill).

The best breakdown to use for this purpose is that described for Ni-H_2 in reference 9. While these cells, in the form of a 14-cell battery of nominal 35 Ah capacity, were not necessarily as optimal as might be desired, they will serve since the comparison with the H_2-O_2 RFC is relative. The system used in an experiment in the Navigation Technology Satellite 2 (NTS-2) vehicle in 1976 was a development of that described in references 10-13. Each single unit consisted of 15 monopolar 38.5 Ah (to 1.0 V at 23°C) bicells each containing two Eagle-Picher electrochemically impregnated aerospace positives in contact (from the inside outwards) with reconstituted asbestos separators, teflon-bonded platinum black hydrogen diffusion electrodes, and plastic gas diffusion screens to allow for gas passage to and from the hydrogen electrodes. The whole system was stacked on a center rod and held in a lightweight Inconel 718 pressure vessel with appropriate mountings, busbars and feedthroughs. Hydrogen pressure varied from 4.1 MPa (41 atm) fully charged to 700 kPa (7 atm) discharged to 1.0 V. The pressure vessel was somewhat over-designed, with a safety factor of 4. Each cell had a total volume of 836 cc, of which

Table 1: Cell Weight Breakdown

Component	Weight (g)	Percent of Total
Nickel Electrodes	348.6	33.9
Hydrogen Electrodes	72.0	7.0
Separators	35.1	3.4
Gas Screens	8.0	0.8
Electrolyte	159.0	15.5
Electrode Stack	622.7	60.6
Center Rod and Insulator	14.3	1.4
Busbars and Tabs	41.4	4.0
Endplates	34.0	3.3
Nut and Washers	4.6	0.4
Terminal Conductors	79.0	7.7
Internal Hardware	173.3	16.8
Pressure Shell	179.0	17.4
Weld and Support Ring	35.0	3.4
Compression Seals	18.4	1.8
Container	232.4	22.6
Cell Total Weight	1028.4	100.00

the internal components were 336 cc. A weight breakdown is given in Table 1. It can be seen that energy density is 44.9 Wh/kg, and volume density is 0.055 Wh/cm^3.

It is easy to compare this with an RFC by replacing the nickel positives with oxygen electrodes, making the necessary volume adjustments to the stack and container, and making provision for electrolyte reservoir plates (ERPS) to store water on discharge (it should be noted that the overall process $NiOOH + 1/2\ H_2 = Ni(OH)_2$ has the advantage of involving no change in electrolyte volume). On this basis, with a total lightweight ERP weight of 35g, and with 72g of electrolyte for a system consuming 12.6 g of water between full discharge and full charge, the stack weight will be 286 g and its volume 190 cc. The container will require 1.5 times the free volume for the Ni-H_2 container to store the hydrogen and oxygen with divided storage (with technology to be decided, since the system described in reference 7 developed cross-leaks). This gives a total system weight of 720.3 g for a volume of 940 cc and the same capacity (in Ah) as the Ni-H_2 system. Since the current density will be the same as that for the latter (with this design), i.e., 22.5 mA/cm^2, performance should be good with the oxygen and hydrogen electrodes now available, i.e., 1.45 V average on charge, 1.0 V (average) on discharge, or 69% overall efficiency. Consequently, on discharge the system will provide 38.5 Wh, giving 53.4 Wh/kg, or 0.041 Wh/cm^2, 19% higher and 25% lower respectively than those for Ni-H_2. In consequence, the attraction of the RFC appears marginal if it is designed for this application.

However, the above is not true if cycle life is considered. For GEO use, Ni-H_2 under normal 60% DOD cycling conditions with standard chemically impregnated electrodes was shown to be capable of more than 2000 cycles in 1976. The failure mode was expansion of the positive as the nickel sinter oxidized and broke up under the internal pressure conditions created. This could be alleviated if a low-loading (69%) of active material was used, when more than 4000 GEO cycles could be achieved (ref. 14). Electrochemically impregnated electrodes (ref. 15) with standard loadings, which have a better distribution of active material in the sinter porosity than chemically impregnated electrodes, gave 4000+ cycles. Finally, 8,000 - 12,000 cycles with low-loading electrochemically impregnated positives can now be routinely demonstrated (ref. 16). If more than 50,000 0.6 h cycles are required for the LEO application, then the Ni-H_2 system must be highly derated to ensure adequate long-term performance, e.g., 50% DOD at C/1.2 or even 40% DOD at C/1.5. In the former case, average discharge potential may be 1.10V, in the latter 1.15 V. Overall real energy densities on the cell level will be 21.1 Wh/kg and 17.7 Wh/kg respectively. The RFC can however be still discharged over many thousands of cycles at 100% DOD, thus delivering around 50 Wh/kg at the higher discharge rates.

The real capability of the fuel cell is however for fast discharge. The power ability of the "stack" within the model RFC considered here is 224 W/kg at 1.67C. This is quite a high figure, since it requires no systems components. For present combination fuel cell-electrolyzer RFCs, the figure will be generally lower. For example, an advanced alkaline fuel cell can deliver 250 W/kg at 1.0 V, 300 mA/cm^2. The complete system, with an advanced electrolyzer operating at 600 mA/cm^2 for 0.9 h charge, the total power system energy density will be 187 W/kg or 112 Wh/kg for the 0.6 h mission requirement. With gases separately stored in Inconel 718 tanks with a safety factor of 4, propellant and tank weight is 5.73 kg/kWh, including a 17% gas reserve (i.e.,

cycling between 4.1 MPa, 41 atm, and 700 kPa, 7 atm). Total system energy density will therefore be 68 Wh/kg. However the system will be capable of pulsed power up to 380 W/kg with only a 10% voltage loss, which is impossible for any type of Ni-H_2 battery delivering only 21 Wh/kg.

Since power system weights are reduced by the use of higher power density systems at equal or similar output voltage, the RFC system can only look better at higher rates. At the 0.6 h rate, the weight of the power system (in the above case, 5.33 kg/kW for nominal output) largely exceeds the weight of the storage system (5.73 kg/kWh, representing 3.44 kg for the mission requirement). However, if long mission requirements (e.g., 8 h) exist, the storage system weight greatly exceeds that of the power system, which results in a total of 6.40 kg/kWh, or 156 Wh/kg. This then exceeds the energy available from any known secondary battery, including sodium-sulfur.

We should also note that at the 0.6 h rate, Ni-H_2 cells have a heat-rejection problem that also limits depth of discharge capability, and the system may require active cooling in advanced compact forms (e.g., bipolar systems), with increase in system weight and complexity. The fuel cell electrolyzer combinations already contain all necessary subsystems.

RFCs: THE FUTURE

Already the RFC based on alkaline technology is capable of 1.0 V, 300 mA/cm^2 in a much lighter, this time bipolar package than that of the Advanced Lightweight Fuel Cell of 1979. In a continuous mode, this system should now be capable of 2 kg/kW at 1.0 V. A lightweight electrolyzer adding 1 kg/kW of output is possible. Similarly, lightweight pressure vessel storage using composite materials and more reasonable safety factors (3 rather than 4) will further lower system weight. Hence, probable relative power system weights of 3 kg/kW with 1.6 kg/kW for a storage system for the 0.6 h mission are possible. This yields 130 wh/kg for a system with 60% overall efficiency, far exceeding the capability of any H_2/X system or of sodium sulfur. In any case, the cycle life capability of the latter has yet to be proven to even 2000 cycles on a systematic basis, and the LEO mission requirement exceeds this by a factor of 30.

Another intriguing possibility is the use of a monolithic, solid oxide fuel cell (SOFC, ref. 17), either alone, or in combination with the lightweight alkaline fuel cell as the electrolyzer unit. As an electrolyzer it will add only 200 g/kW to the fuel cell weight, and it will operate at 1.3 V and 500 mA/cm^2. This approach has the advantage of decreasing system weight, so that in LEO mode 158 Wh/kg can be achieved at the same time increasing system efficiency to 77%. Alternatively, if a lower round-trip efficiency can be tolerated with reduced weight, the monolithic SOFC can be used as a combined electrolyzer-fuel cell, with a stack weight of 200 g/kW (output), and it would operate at 1.3 V (charge) and 0.8 V (discharge) at 500 mA/cm^2, yielding (on paper) 330 Wh/kg in the LEO mode at 62% efficiency. However, systems (heat-rejection) aspects of its use in the exothermic fuel cell mode are presently uncertain, and the technology may not be available before the year 2000.

A more conservative approach is the single-unit low temperature system, either on the lines of the single-cell with pressure vessel approach of

reference 7 (assuming that heat rejection on discharge is acceptable), or in a bipolar mode with a separate advanced storage system. The single cell can use either alkaline or SPE technology. The latter may again have the advantage of lowest weight, whereas the former should have higher efficiency (1.0 V fuel cell, 1.5 V electrolysis, yielding 67% overall). As an example, the SPE system has been recently shown to be capable of 150 g/kW at 0.7 V, 1.75 A/cm^2 using proprietary lightweight stack components, with a low-resistivity 75 micron dry, 113 micron wet Dow Chemical SPE membrane, using data recently obtained by Ballard in Canada (ref. 18). These results show 0.8 V at 500 mA/cm^2, which as a baseline yields 427 g/kW for the stack. Hence total weight, including advanced storage, will be 2 kg/kW for the mission requirement or 300 Wh/kg. The cathode catalyst and bipolar structure will be modified in a proprietary manner to permit electrolysis at 1.50 V, allowing round-trip efficiency of 53%. This can be increased at the expense of weight, if necessary.

The results above are summarized in table 2, which compares the above RFC technologies, Ni-H_2, and a hypothetical long-life 100 Wh/kg Na-S battery for LEO application. The state-of-the-art weight of deployable PV is taken to be 55 W/kg (25 W/lb). All data are reduced to 1 kW output power levels. SOE refers to solid oxide electrolyser. The pacing element is clearly the mass of the PV array, although the weight penalty for the lower efficiency systems is quite small.

Table 2: Total LEO System Reciprocal Power Density Breakdown

Technology	kg/kW	Efficiency	PV (kg/kW)	Total (kg/kW)
Ni/H_2	30.0	78	15.5	45.5
RFC (baseline)	11.0	60	20.2	31.2
RFC (lightweight)	4.6	60	20.2	24.2
Adv. AFC-SOE	3.8	77	15.7	19.5
Regen. SOFC unit	2.0	62	19.5	21.5
Regen. SPE unit	2.0	53	22.6	24.6
Adv. Na-S	6.0	85	14.3	20.3

Finally, it would seem more profitable in future to manufacture H_2/O_2 propellant in space for orbital transfer, since it is energetically more economical to transfer water from earth than to ship the same weight of cryogenic propellant. The fuel cell-electrolyzer combination therefore seems to be a more logical long-term solution to the problem of space energy storage than secondary batteries.

REFERENCES

1. Sheibley, D. W., and McBryar, H., National Fuel Cell Seminary Abstr. 1982, p. 36.

2. McBryar, H., National Fuel Cell Seminar Abstr., 1979, p. 16.

3. Appleby, A. J., and Yeager, E. B., Energy 11, 1986, p. 137.

4. Mullin, J. D., Randolph, L. P., Hudson, W. R., and Ambrus, J. H., Proc. 14th IECEC, 1979, p. 544.

5. Bockris, J. O'M. and Appleby, A. J., Energy 11, 1986, p. 95.

6. Martin, R. E., "Advanced Technology Lightweight Fuel Cell Program," Final Report, CR-169653 FCR-1017, NASA, Washington, D.C., 1979.

7. Klein, M. and Costa, R. L., "Electrolytic Regenerative H_2-O_2 Secondary Fuel Cells," Proc. Space Technology and Heat Transfer Conf., Los Angeles, CA, 1970; American Society of Mechanical Engineers, New York, 1970, 70-Av/SpT-39.

8. Klein, M. Proc. 7th IECEC, 1972, p. 729017.

9. Dunlop, J. D., Van Ommering, G., and Earl, M. W., in "Power Sources 6," D. H. Collins, ed., Academic Press, London, 1977, p. 231.

10. Stockel, J. F., Van Ommering, G., Swette L, and Gaines, L, Proc. 7th IECEC Conf., 1972, p. 729019.

11. Dunlop, J. D., Giner, J, Van Ommering, G., and Stockel, J., U.S. Pat. 3,867,199, 1975.

12. Dunlop, J. D., Stockel, J., and Van Ommering, G., in "Power Sources 5," D. H. Collins, ed., Academic Press, New York, 1974, p. 315.

13. Giner, J., and Dunlop, J. D., J. Electrochem. Soc. 112, 1975, p.4.

14. Appleby, A. J., Final Report, INTELSAT Contract IS-611, 1975.

15. Beauchamp, R., U.S. Pat. 3,653,067, 1972.

16. Van Ommering, G., private communication.

17. Brown, J .T., Energy 11, 1986, p. 209.

18. Srinivasan, S., private communication.

PEROVSKITE OXIDES: OXYGEN ELECTROCATALYSIS AND BULK STRUCTURE

R.E. Carbonio‡, C. Fierro, D. Tryk, D. Scherson, and E. Yeager
Case Western Reserve University
Cleveland, Ohio 44106

Perovskite-type oxides have been considered for use as oxygen reduction and generation electrocatalysts in alkaline electrolytes . This paper is concerned with perovskite stability and electrocatalytic activity, and the possible relationships of the latter with the bulk-solid state properties.

Perovskite oxides have not been found in general to be very active for oxygen reduction, although substantial catalytic activity for hydrogen peroxide decomposition has been found. Instability of some perovkites has been observed over particular potential ranges. In some cases these ranges overlap those in which O_2 reduction occurs.

A series of compounds of the type $LaFe_xNi_{1-x}O_3$ has been used as a model system to gain information on the possible relationships between surface catalytic activity and bulk structure. Hydrogen peroxide decomposition rate constants have been measured for these compounds. **Ex-situ** Mossbauer effect spectroscopy (MES), and magnetic susceptibility measurements have been used to study the solid state properties. X-ray photoelectron spectroscopy (XPS) has been used to examine the surface. MES has indicated the presence of a paramagnetic-to magnetically ordered phase transition for values of x between 0.4 and 0.5. For $0 < x \leq 0.4$ the compounds are paramagnetic, as indicated by the absence of a Zeeman effect in the MES spectra. For $0.5 \leq x \leq 1.0$ the observed Zeeman effect in the MES spectra indicates the presence of a magnetically ordered phase. Complementary magnetic susceptibility measurements indicate that the compounds are antiferromagnetically ordered.

MES also shows that the introduction of Ni into the Fe(III) matrix of $LaFeO_3$ forces some of the Fe(III) into the unusual Fe(IV) state, while part of the Ni(III) is changed to Ni(II), as indicated by XPS.

The hydrogen peroxide decomposition rates have been found to undergo a substantial change in the range $0.25 < x < 0.5$. A correlation has been found between the values of the MES isomer shift and the catalytic activity for peroxide decomposition. Thus, the catalytic activity can be correlated to the d-electron density for the transition metal cations.

INTRODUCTION

Perovskite-type oxides constitute a family of oxides of the type ABO_3 with structures similar to that of the mineral perovskite $CaTiO_3$ (1, 2). Depending on the nature of the A and B cations, the chemical and physical properties can vary over a wide range. An attractive feature is that these

‡ INFIQC, Depto. de Fisico Quimica, Fac. de Ciencias Quimicas, Univ. Nac. de Cordoba. Cordoba. Argentina.

properties can be varied by preparing materials of the type $A_xA'_{1-x}B_yB'_{1-y}O_3$. Their electronic conductivity can vary from insulating to metallic conducting and even superconducting. The magnetic properties can vary from paramagnetic to ferro- or antiferromagnetic. Such compounds are very interesting both from the catalytic and the bulk properties points of view. Mixed oxidation states of both A and B cations are involved. Even if A is not catalytically or electrochemically active, it is possible to control the oxidation state of B by changing the relative amount and nature of the A cation. These materials have been synthesized and studied by several authors (3-6). The objective of this paper is to examine the relationship of the electrochemical properties of these perovskites to their bulk structures.

Since the work of Meadowcroft (7), many workers have examined O_2 reduction and generation on perovskites (8-17). In the more applied work, good performance and stability in long-term operation have been observed for O_2 generation (8, 13). For O_2 reduction, however, good performance is typically observed in short-term operation, but the performance often degrades with time (12).

Matsumoto et al. (8) have examined O_2 generation and reduction on perovskite-type oxides. They were the first to study $LaNiO_3$ as an electrode material for O_2 reduction (8). They used X-ray diffraction to analyze changes in the structure due to exposure to the electrolyte at various potentials. Karlsson (11, 12) has reported that under prolonged cathodic polarization in alkaline solution, $LaNiO_3$ reduces irreversibly to $Ni(OH)_2$ and $La(OH)_3$, thus leading to a gradual loss of performance for O_2 reduction.

Bockris and Otagawa (13, 14) have examined O_2 generation on $LaNiO_3$ as well as a number of other perovskites. They used X-ray photoelectron spectroscopy (XPS) to analyze the surface composition of these perovskites before and after exposure to the electrolyte and proposed that some of the surfaces were different in composition from that of the nominal bulk stoichiometry. The results however should be treated with caution, since it is difficult to use XPS for the quantitative surface analysis of oxides.

Recently in the authors' laboratory (13), it has been shown using Mossbauer effect spectroscopy (MES) that $SrFeO_3$ undergoes an irreversible reduction to $Fe(OH)_2$ in alkaline solution when the potential is set more negative than ca. -0.7 V vs. Hg/HgO, OH^-. These examples point to the possibility that the surface and even the bulk structure of the perovskite can be modified, even irreversibly, under certain potential conditions.

There have been several attempts to relate surface and bulk properties of the perovskites with both O_2 reduction and generation (8, 13, 14). Matsumoto and coworkers (8) have proposed correlations of catalytic activity with the existence of a σ^* band. Bockris and Otagawa (13, 14) have proposed that the catalytic activity for O_2 generation of transition metal-containing perovskites is correlated with the occupancy of the antibonding orbitals of a hydroxylated surface transition metal cation. A variety of bulk physical properties were examined and found not to correlate with the catalytic activity.

While generally speaking it is not valid to correlate bulk properties

with catalytic activity, in selected instances a bulk property can produce an effect upon the surface properties and thus upon the catalysis. In the present work compounds of the type $LaFe_xNi_{1-x}O_3$ have been examined using MES and magnetic susceptibility, which are bulk characterization techniques, and XPS, which is a surface or near-surface (ca. 1-2 nm) technique. A correlation has been found between the catalytic activity for peroxide decomposition and the MES isomer shift.

EXPERIMENTAL

Four preparative methods have been used, the solid state reaction (SSR), nitrate decomposition (ND) and precipitation methods, the latter including the hydroxide precipitation (HP) and inorganic complex precipitation (ICP) methods. In the SSR method a mixture of the oxides of the component elements is ground and then heated at a controlled temperature between 900 and 1100° C. In the ND method (18) a concentrated solution of citric acid is added to a concentrated solution of the metal nitrates so that the molar ratio of citric acid to total metal was 1. The solution was evaporated in a rotary evaporator at 40° C until the precipitate acquired the consistency of a viscous syrup. The residual water was evaporated in a vacuum oven at 110° C for 24 hours. The precursor thus obtained is a fine mixture of the nitrates and citric acid. After being burned at ~200° C, the precursor, which is then black in color, is heated at 900° C in air for 24 hours.

In the HP method a concentrated solution of an organic base (e. g., methylamine) is added to a solution of the metal nitrates. The precipitate is filtered and dried at 110° C in a vaccum oven and then heated in air at a temperature between 600 and 750° C for 24 hours.

In the ICP method a solution of the A ion nitrate [e.g., $La(NO_3)_3$] is added to a solution of a soluble form of the inorganic complex [e.g., $K_3Fe(CN)_6$] and a precipitate of the complex substituted with the A ion is obtained [e.g., $LaFe(CN)_6$]. The precipitate is filtered, dried in a vaccum oven at 110° C for 24 hours and then heated in air at a temperature between 450 and 700° C for 24 hours. Usually the ICP method requires only a very low temperature for the synthesis because of the molecular level mixing of the A and B ions.

Some of the compounds have been examined using X-ray diffraction and found to exhibit no detectable phase impurities. The rest are in progress and the results will be presented in a more detailed report.

XPS measurements were done with a Varian IEE-15 X-ray photoelectron spectrometer equipped with a high-intensity magnesium anode (K_α radiation, 1253.6 eV). The operating parameters were: X-ray power, 640 W (8 kV, 80 mA), analyzer energy, 100 kV, channel width, 0.18 eV. The analyzer pressure was 10^{-6}-10^{-7} torr. An internal standard of Au powder was used in an intimate mixture with the sample to correct for energy shifts caused by surface charging.

The Mossbauer spectra were recorded with a Ranger Scientific MS-900 system, and the statistical analysis performed with the STONE routine (19). The Mossbauer parameters are reported vs. α-iron.

The magnetic susceptibility measurements were performed with a Faraday electrobalance (Cahn RG) with a magnetic field of ~ 10 kG. Ni(ethylenediamine)$_3S_2O_3$ and $Hg[Co(SCN)_4]K_6$ were used as standards for calibration.

For the electrode preparation equal amounts of the catalyst and Shawinigan Black (SB, Gulf Oil Chemicals) (an acetylene black with an approximate surface area of 65 m^2/g) were mixed in water under ultrasonic agitation. A dilute Teflon emulsion (T30B, Dupont) was added to the mixture such that 25 wt.% of the total weight was Teflon. The mixture was then filtered through a fine pore membrane (Nucleopore, polycarbonate membrane, 1.0 μm). The resulting carbon/perovskite/Teflon paste was kneaded until rubbery and then placed on top of a disk of electronically conductive hydrophobic material (Electromedia Corp. Englewood, NJ) containing a nickel screen or carbon fiber in a 1.75 cm diameter die and pressed at 340 kg cm^{-2}. The electrode disk was then trimmed to obtain a rectangle 0.5 x 1.0 cm. A nickel screen was used as the counter electrode and the reference electrode was Hg/HgO, OH^-. The electrochemical experiments were performed either in 0.1 M or 4 M KOH at room temperature.

Hydrogen peroxide decomposition measurements were performed at 22° C using the gasometric method. A small amount of the catalyst (~ 10 to 50 mg) was dispersed in 50 cm^3 of 4 M KOH prepared from distilled water and KOH pellets (Fisher Scientific, Reagent Grade). The initial concentration of HO_2^- was 0.2 M.

RESULTS

A. Bulk Structure

The MES spectra for the different perovskite compositions are shown in Fig. 1. These show for $0 < x \leq 0.4$ the presence of two peaks, which can be attributed formally to Fe^{3+} and Fe^{4+} sites. The existence of Fe^{4+} in perovskites has been reported before for $SrFeO_3$ (4, 20), although in the present case the isomer shift apparently is not as negative as it is in the case of Fe^{4+} in $SrFeO_3$. The site with the less positive isomer shift will be provisionaly assigned to Fe^{4+}. The absence of a six-line splitting in the spectra provides evidence that in the $0 < x \leq 0.4$ compositional region the perovskite is paramagnetic. For $0.5 \leq x \leq 1.0$, however, the spectra yielded six lines, characteristic of a magnetically ordered species. A singlet is also observed, which shows that a paramagnetic phase is still present. This could be explained as follows: statistically, there should be two types of iron atoms for intermediate compositions (i.e. when x ~ 0.5). One type of iron will be mainly surrounded by nickel atoms, and this will lead to the formation of a "paramagnetic site", which will have Fe preferentially in the formal 4+ state. Another type will be surrounded by iron atoms, leading to the formation of an "antiferromagnetic site", which will have Fe preferentially in the 3+ state. The six-line spectra at $x \geq 0.5$ can be attributed to Fe^{3+} and the singlet to Fe^{4+}. This can be supported by the continuity of the isomer shift vs. x curve (Fig. 2), for both types of sites. Two types of iron sites have been observed for $LaFe_xRu_{1-x}O_3$ with MES by Bouchard et al.(3). In that case however both were in the +3 state and were also paramagnetic. Another possible explanation is the existence of two distinct phases for intermediate compositions, one paramagnetic and the other antiferromagnetic, each one with a given isomer

shift which remains relatively constant. The possible existence of two phases must be checked using X-ray diffraction measurements.

A plot of the isomer shift vs. x indicates that the difference in isomer shift between the two types of sites (or phases) reaches a maximum at x = 0.25. Only one type of site (or phase) is present at the two extremes. The composition with x ~ 0 has been assigned using the compound $LaFe_{0.0013}Ni_{0.9987}O_3$, in which all of the iron is ^{57}Fe in order to obtain a good MES signal. Since the isomer shift is a direct measurement of the electron density surrounding the nucleus, it can be concluded that there is a maximum in the difference between the electron densities for the Fe^{3+} and Fe^{4+} sites (or phases) at 25% of iron.

Mossbauer effect spectroscopy has shown that in $LaFe_xNi_{1-x}O_3$, depending on x, Fe is in two oxidation states (i.e. 3+ and 4+). It is interesting to analyze the oxidation states of Ni in the same structure. It is supposed then that, in order to maintain electroneutrality, Ni must be in the 2+ state. (In pure $LaNiO_3$ the normal oxidation state is 3+.) XPS is suitable for checking this possibility if the caveat already mentioned in the introduction is kept in mind.

The $2p_{3/2}$ Ni bands for $LaFe_xNi_{1-x}O_3$ perovskites for different values of x are shown in Fig. 3. One peak is at binding energies between 853 and 855 eV (depending on the composition). As the amount of iron increases, a new peak starts to develop at lower energies, and the original peak is shifted towards higher energies. This is possibly due to a change from good

electronic conduction for low Fe content to semiconducting properties for high Fe content, which will change the surface energy with respect to the Fermi level in the bulk of the semiconductor. At 90 mol% iron, two clearly defined peaks are observed, with the one at lower energies attributed to a Ni^{2+} species. These results are consistent with those obtained from Mossbauer spectroscopy. When Ni is introduced in $LaFeO_3$, part of the original Fe^{3+} is oxidized to Fe^{4+}, and the Ni valence is distributed between the 2+ and 3+ states, so that the formula of the compound can be writen as $LaFe(III)_xFe(IV)_{1-x}Ni(III)_yNi(II)_{1-y}O_3$, where the x and y values depend upon the overall composition. The appearance of Fe^{4+} ions when Ni^{2+} is oxidized to Ni^{3+} has been observed by Corrigan et al.(21) in battery-type nickel hydroxide electrodes doped with iron hydroxide using Mossbauer spectroscopy.

The combination of oxidation sates of B and B' in $LaB_xB'_{1-x}O_3$ regulates the total magnetism of the compound. Thus Fe^{3+} is in a high spin state ($t_{2g}^3\ e_g^2$) in $LaFeO_3$ (22), and this compound is antiferromagnetically ordered. Ni^{3+} is in a low spin state ($t_{2g}^6\ e_g^1$) in $LaNiO_3$ (22), and the compound is a Pauli paramagnet. As was previously mentioned there is a transition from a paramagnetic to a magnetically ordered state in the $0.4 < x < 0.5$ region. The specific assignment of antiferromagnetism for the compounds in the range $x \geq 0.5$ is supported by magnetic susceptibility measurements. The gram magnetic susceptibilities (χ_g) at room temperature are shown in Table I as a function of x. The values of χ_g are to small to be assigned to the ferromagnetic state, for which χ_g should be on the order of 10^{-2}-10^4 emu g^{-1} (23). The χ_g values for paramagnetic or antiferromagnetic compounds should be in the range 0-10^{-4} emu g^{-1}. For these reasons the compounds with $x > 0.5$ are antiferromagnetic, as is $LaFeO_3$ (24).

Perovskites of the type $LaB_xB'_{1-x}O_3$ offer the opportunity to change the distribution of the oxidation states, which can be very useful from the point of view of catalysis. The solid state properties can be changed more or less continuously with composition. For this reason the series of $LaFe_xNi_{1-x}O_3$ perovskites has been chosen as a model system for the examination of electrochemical and catalytic properties.

B. Electrochemical Stability

The voltammograms for $LaFeO_3$ and $LaFe_{0.75}Ni_{0.25}O_3$ are shown in Fig. 4. The electrodes were prepared in the form of a thin porous coating, as described in the experimental section. Over a wide potential range $LaFeO_3$ exhibits no voltammetric peaks. This is consistent with the fact that $LaFeO_3$ is an insulator(1, 22, 24). The introduction of Ni into the $LaFeO_3$ structure increases its conductivity (25), and for $x < 0.2$ the compound is a metallic conductor. As shown in Fig. 4b, the introduction of 25 mol% Ni in $LaFeO_3$ makes it sufficiently conducting to observe redox peaks. Two redox couples are present, one centered at ca. -0.5 V, corresponding to the Fe(III)/Fe(II) couple and the other centered at ca. +0.52 V, corresponding to the Ni(III)/Ni(II) couple. The shapes and positions of the peaks are similar to those for the respective hydrated oxides [$FeOOH/Fe(OH)_2$ and $NiOOH/Ni(OH)_2$] (26). The peak separation for the Fe(III)/Fe(II) redox couple is exaggerated in this case however. A shift in the nickel peaks due to the presence of iron is also observed in this case, as is observed in the Fe/Ni oxyhydroxides(26, 27).

As judged by the integrated charge associated with the voltammetric peaks in the case of $LaFe_{0.75}Ni_{0.25}O_3$ (Fig. 4b), only the surface is involved in the redox processes. (The surface areas of these perovskites are on the order of 1 to 3 m^2/g.) In order to gain additional information concerning the redox processes, in-situ MES was performed with $LaFe_{0.25}Ni_{0.75}O_3$ in 4 M KOH. The ex-situ MES spectrum of the dry electrode and the in-situ MES spectra after polarization at +0.5 , 0.0 and -1.2 V vs. Hg/HgO, OH^- (not shown) are all almost the same. This is consistent with the previously mentioned finding that only a small fraction of the material was involved in the redox process (~ 2 % of the total), which corresponds to material in a thin surface layer.

Since all of the iron in $SrFeO_3$ should be in the 4+ state, it has been used in electrochemical, MES and XPS experiments to provide a reference, even though it is known that the compound is not completely stoichiometric except under special conditions. It is a metallic conductor so that no problems arose due to poor electronic conductivity. The results obtained with cyclic voltammetry are shown in Fig. 5. The anodic and cathodic potential limits were increased in steps. No faradaic current was observed between -0.5 and +0.6 V (Fig. 5a). At +0.6 V anodic current due to O_2 generation was observed. At potentials more negative than -0.5 V, a cathodic peak was observed with a complementary anodic peak in the positive sweep. A voltammogram between the limits -1.3 V and +0.8 V is shown in Fig. 5b. The Fe(III)/Fe(II) redox couple is observed, as in the case of $LaFe_{0.75}Ni_{0.25}O_3$. In this case, however, ca. 100 % of the material takes part in the redox process. In-situ MES performed in this laboratory (28) have shown that $SrFeO_3$ is irreversibly reduced to $Fe(OH)_2$ at potentials more negative than ca. -0.7 V vs. Hg/HgO, OH^- and that, under subsequent anodic polarization at -0.3 V, FeOOH is obtained.

C. Catalytic Activity

In order to examine possible relationships between catalytic activity and bulk structure, the hydrogen peroxide decomposition reaction has been chosen due to its important role in oxygen electrochemistry. Hydrogen peroxide decomposition rate constants have been measured for the $LaFe_xNi_{1-x}O_3$ series using the gasometric method. The rate constants are plotted in Fig. 6 as a function of x. These results should be treated with some caution, however, since they are not normalized to the surface areas.

A maximum is observed at 25% Fe content. This correlates very approximately with the isomer shift variations for Fe^{3+} and Fe^{4+} noted above. The range of x values for which the difference in the electron density for both sites is at a maximum corresponds to that for which the maximum activity for hydrogen peroxide decomposition is observed. It is possible that both the mixed oxidation state for Fe and/or Ni and the unusual presence of Fe^{4+} sites may be factors in promoting the catalytic activity.

This correlation could be considered reasonable in the light of the traditional explanation of hydrogen peroxide decomposition catalysis as proposed by Latimer (29). Any redox couple which falls in the potential range between the O_2/HO_2^- and HO_2^-/OH^- couples can in principle catalyze the disproportionation reaction. If a catalyst simultaneously contains both strongly oxidating and strongly reducing species, the coupled HO_2^- oxidation and reduction might be fast.

REFERENCES

1) Voorhoeve, R. J. H. in "Advanced Materials in Catalysis", Burton, J. J. and Garten, R. L., Eds., Academic Press, New York, 1977, p. 129.

2) Voorhoeve, R. J. H.; Johnson, D. W., Jr.; Remeika, J. P. and Gallagher, P. K.; Science, **195**, 4281 (1977).

3) Bouchard, R. J.; Wehier, J. F. and Gillson, J. L.; J. Solid State Chem., **21**, 135 (1977).

4) Shimony, U. and Knudsen, J. M.; Phys. Rev., **144**, 361 (1966).

5) Obayashi, H.; Kudo, T. and Gejo, T.; Jap. J. Appl. Phys., **13**, 1 (1974).

6) Gibb, T. C.; Greatrex, R.; Greenwood, N. N. and Snowdon, K. G.; J. Solid State Chem., **14**, 193 (1975).

7) Meadowcroft, D. B.; Nature **226**, 847 (1970).

8) Tamura, H.; Yoneyama, H.; and Matsumoto, Y. in "Electrodes of Conductive Metallic Oxides". Elsevier, New York, Amsterdam. (1980-1981). Trasatti, S., Ed.

9) Kobussen, A. G. C.; Van Buren, F. R.; Van Den Belt, T. G. M. and Van Wees, H. J. A.; J. Electroanal. Chem., **96**, 123 (1979).

10) Kobussen, A. G. C.; Willems, H. and Broers, G. H. J.; J. Electroanal. Chem., **142**, 67 (1982).

11) Karlsson, G.; Electrochim. Acta, **30**, 1555 (1985).

12) Karlsson, G.; J. Power Sources, **10**, 319 (1983).

13) Bockris, J. O'M. and Otagawa, T.; J. Electrochem. Soc., **131**, 290, (1983).

14) Bockris, J. O'M.; Otagawa, T. and Young, V.; J. Electroanal. Chem., **150**, 633 (1983).

15) Tseung, A. C. C.; J. Electrochem. Soc., **125**, 1660 (1978).

16) Kudo, T.; Obayashi, H. and Yoshida, M.; J. Electrochem. Soc., **124**, 321 (1977)

17) Calvo, E. J.; Drennan, J.; Kilver, J. A.; Albery, W. J. and Steele, B. C. H.; in McIntyre, J. D. E.; Weaver, M. J. and Yeager, E. B. (Eds.), "The Chemistry and Physics of Electrocatalysis"; The Electrochemical Society, N. J., (1984), pp 489.

18) Tascon, J. M. D.; Mendioroz, S. and Gonzalea Tejuca, L.; Z. Fhys. Chem. N. F., **124 S**, 109 (1981).

19) Dr. M. Darby Dyar from the University of Oregon make available the statistical analysis routine.

20) Shirane, G.; Cox, D. E. and Ruby, S. L.; Phys. Rev., **125**, 1158 (1962).

21) Corrigan, D. A.; Fierro, C. and Scherson D. (to be published).

22) Goodenough, J. B.; in Reiss, H., Ed. "Progress in Solid State Chemistry", Vol. 5. Pergamon Press. Oxford, (1971). pp. 313.

23) Figgis, B. N. and Lewis, J.; in Techniques of Inorg. Chem., Vol. IV, 1965, pp. 137-248. Jonassen, H. B. and Weissberger, A. (Eds.), Wiley-Interscience, New York.

24) Goodenough, J. B. and Longo, J. M.; "Crystallographic and Magnetic Properties of Perovskite and Perovskite Related Compounds", Landolt-Bornstein Tabellen, Neue Serie III/4a, Springer-Verlag, Berlin. (1970).

25) Rao, C. N. R.; Parkash, Om and Ganguly, P.; J. Solid State Chem., **15**, 186 (1975).

26) Cordoba, S. I.; Carbonio, R. E.; Lopez Teijelo, M. and Macagno, V. A., Electrochim. Acta, **10**, 1321 (1986).

27) Corrigan, D. A.; J. Electrochem. Soc., **134**, 377 (1987).

28) C. Fierro, R. E. Carbonio, D. Scherson and E. Yeager. 171st Meeting of the Electrochem. Soc.; Philadelphia. Pennsylvania. May 1987.

29) Latimer, W. M.; Oxidation States of the Elements and their Potentials in Aqueous Solutions, 2nd Edn., Prentice Hall, New Jersey, 1952, p. 44.

TABLE I

Compound	χ_g 10^6/(emu g^{-1})
$LaNiO_3$	5.2
$LaFe_{0.1}Ni_{0.9}O_3$	24.3
$LaFe_{0.25}Ni_{0.75}O_3$	12.6
$LaFe_{0.50}Ni_{0.50}O_3$	15.4
$LaFe_{0.75}Ni_{0.25}O_3$	12.4
$LaFe_{0.90}Ni_{0.10}O_3$	13.2
$LaFeO_3$	9.9

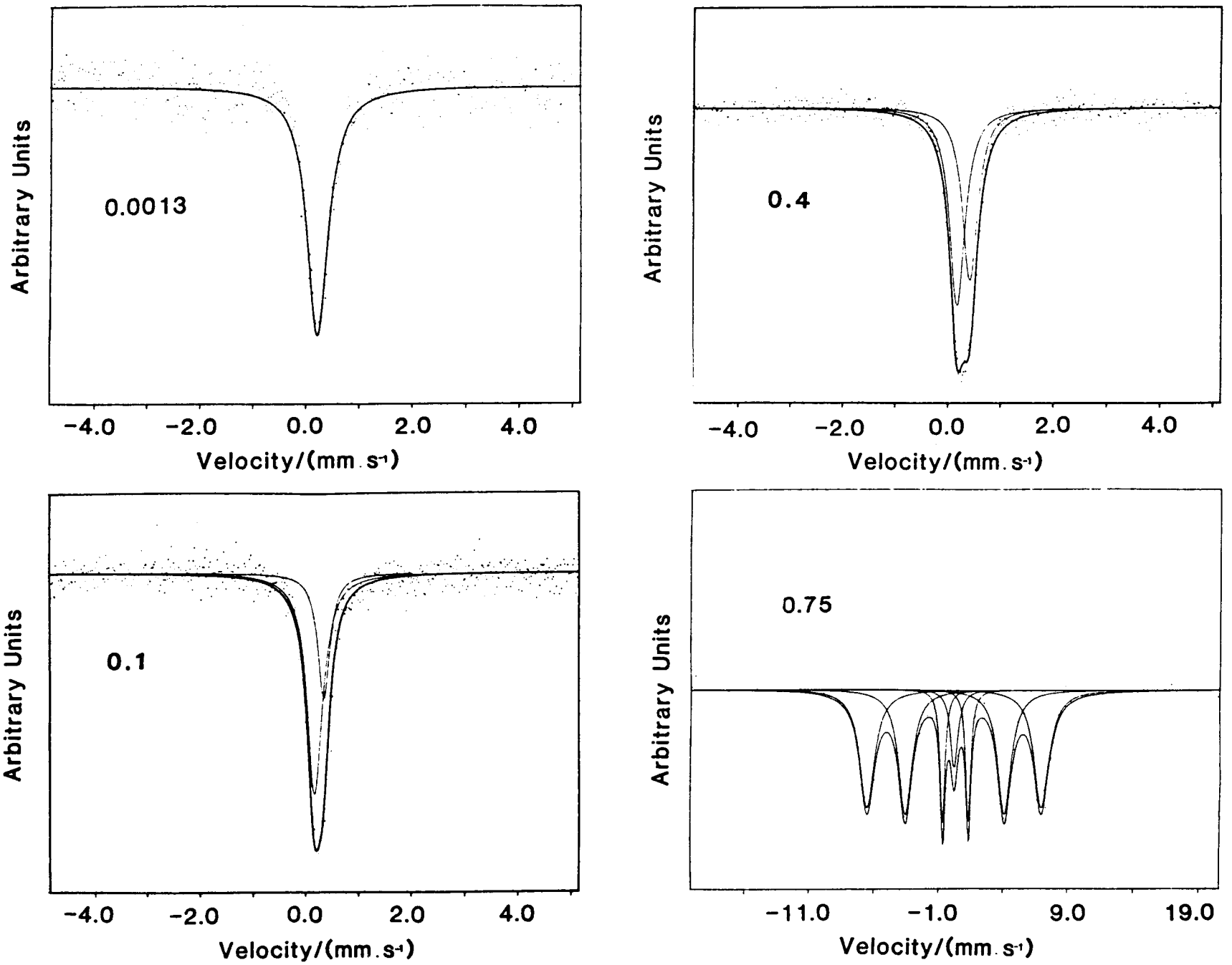

Figure 1: Ex-situ MES for $LaFe_xNi_{1-x}O_3$ for different values of x (the values of x are indicated in the figures).

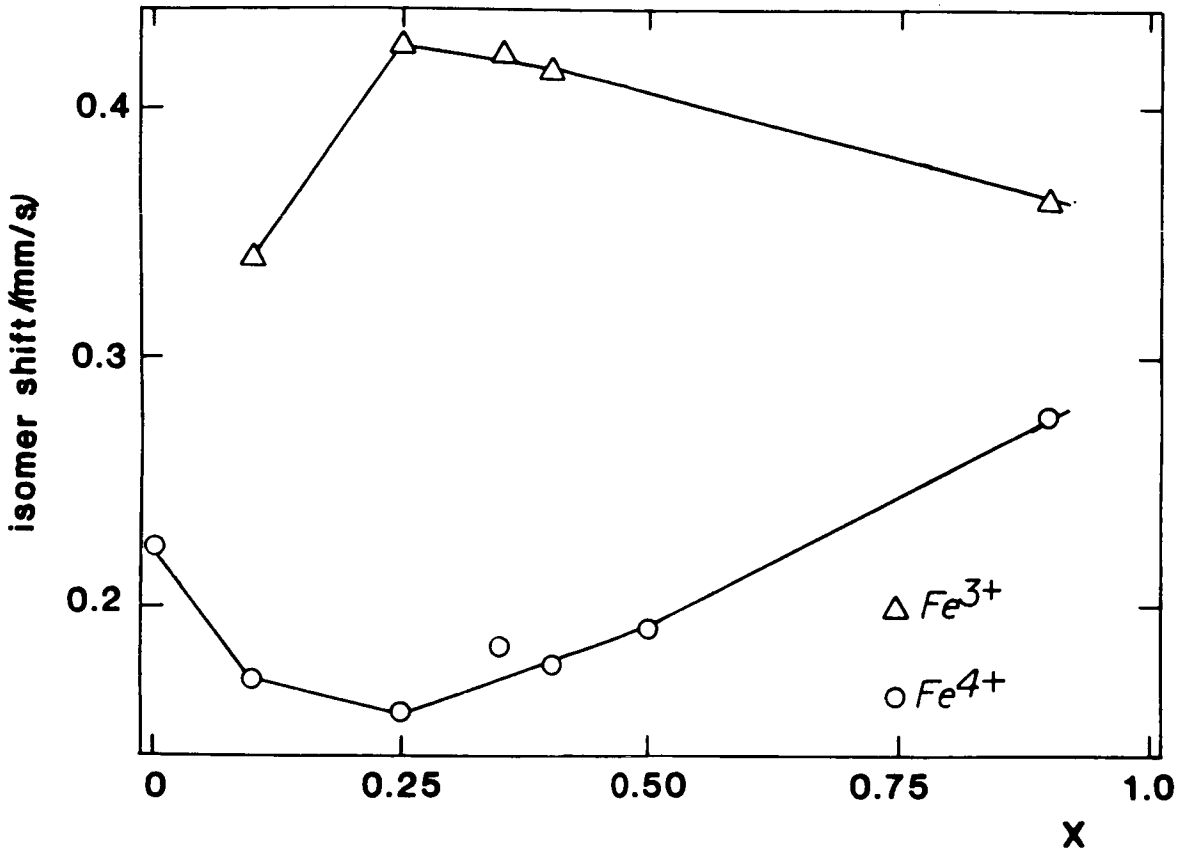

Figure 2: Isomer shift (δ) of Fe^{3+} (δ_1) and Fe^{4+} (δ_2) for $LaFe_xNi_{1-x}O_3$ as a function of x.

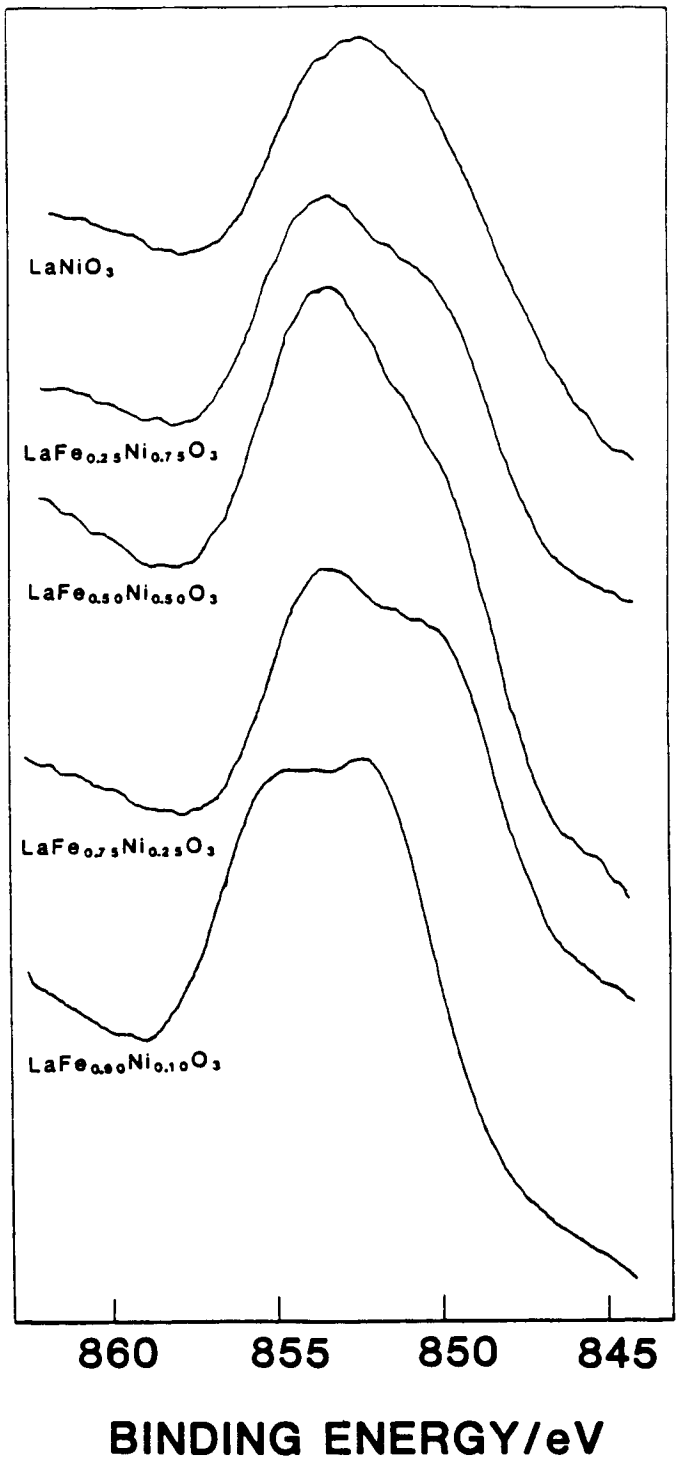

Figure 3: X-ray photoelectron spectra of the Ni $2p^{3/2}$ bands of $LaFe_xNi_{1-x}O_3$ for different values of x.

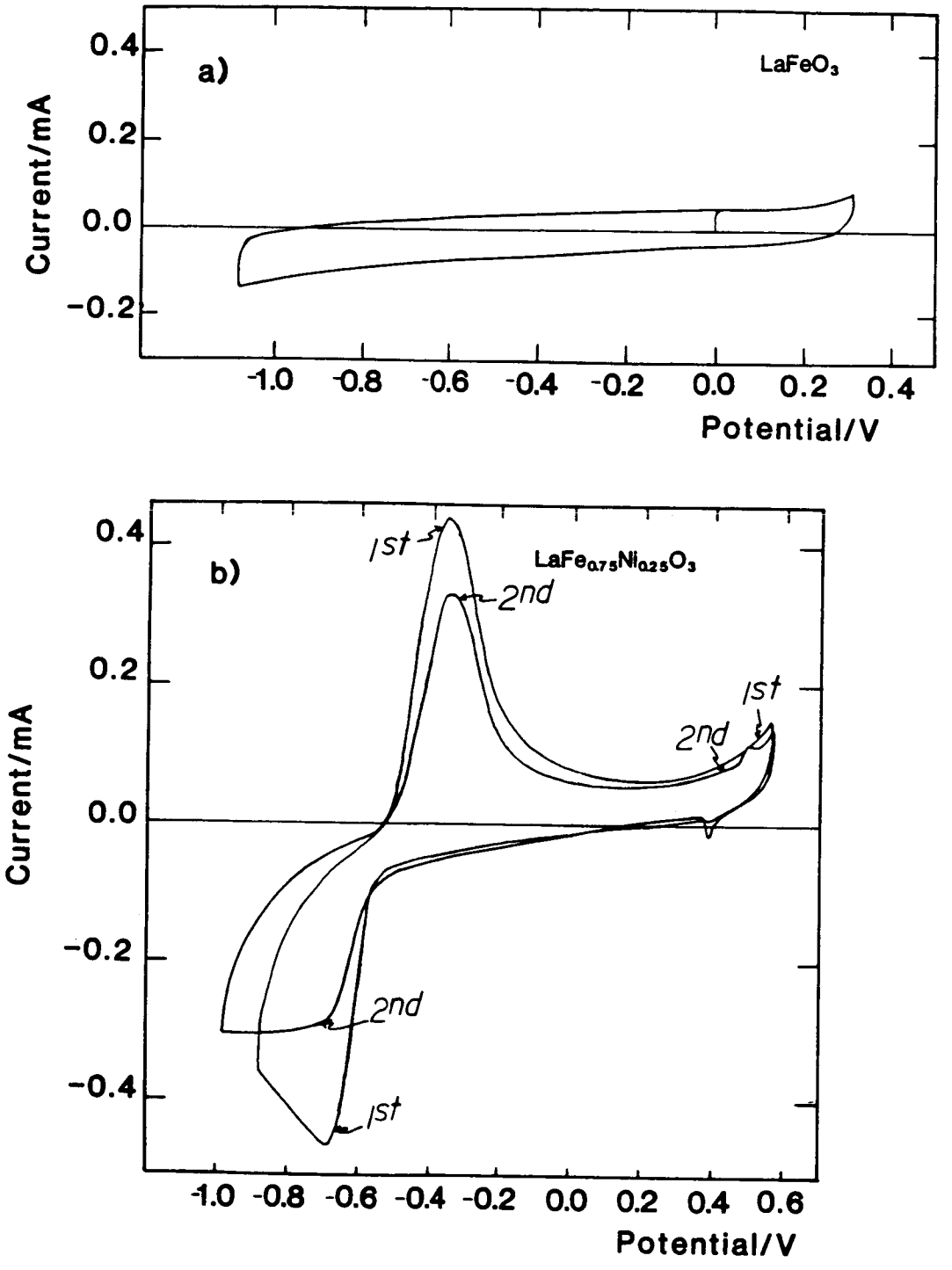

Figure 4: Cyclic voltammograms for thin porous coating electrodes of 50% perovskite in SB carbon on a pyrolytic graphite disk. Electrolyte: 0.1 M KOH, N_2 saturated. Scan rate: 10 mV/s.

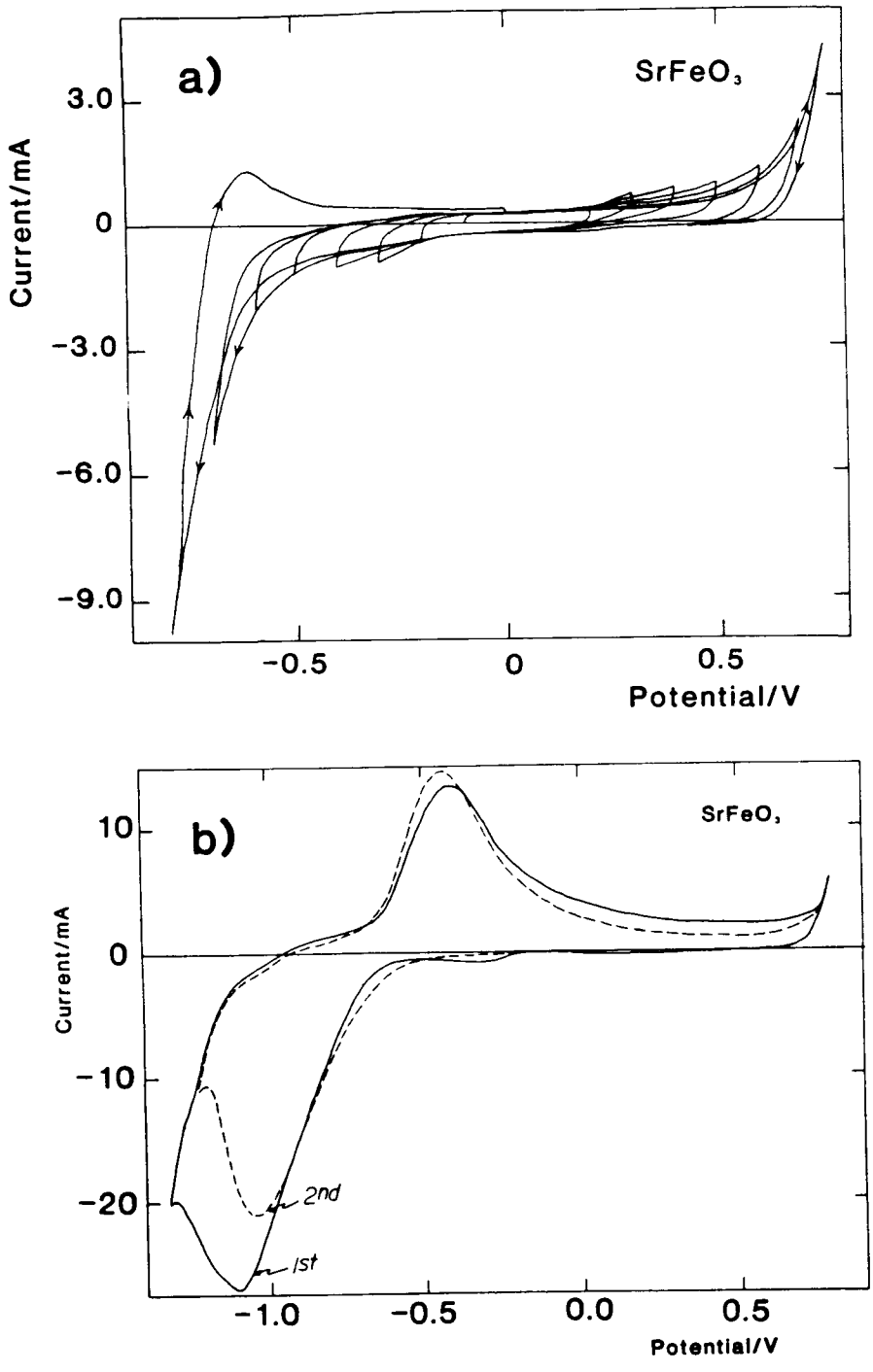

Figure 5: Cyclic voltammograms for floating gas-fed electrodes containing 15 mg cm^{-2} of $SrFeO_3$ plus 15 mg cm^{-2} of SB carbon. Electrolyte: 0.1 M KOH, N_2 saturated. Scan rate: 10 mV/s.

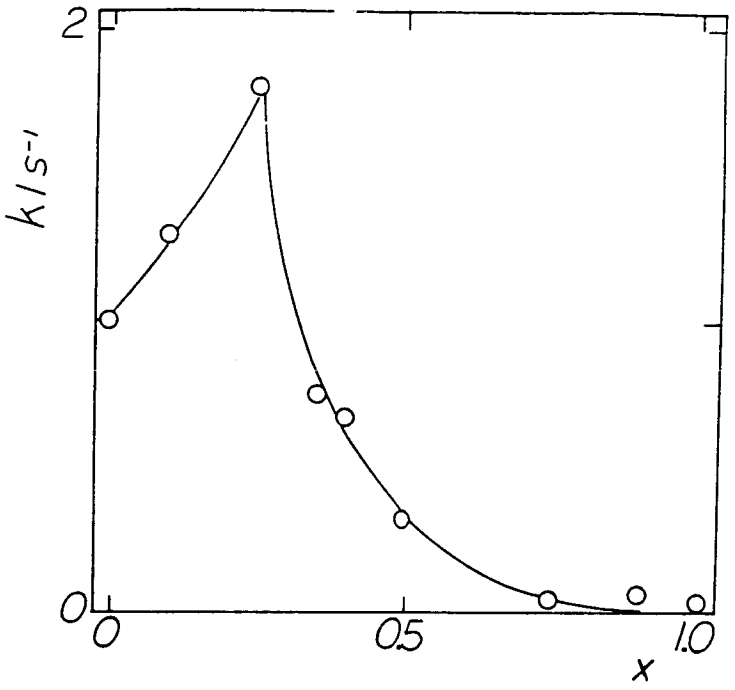

Figure 6: Hydrogen peroxide decomposition rate constants vs. x in $LaFe_xNi_{1-x}O_3$.
The rate constants were measured by the gasometric method in 4 M KOH at 22° C. The initial concentration of peroxide was 0.2 M.

OXYGEN ELECTRODES FOR RECHARGEABLE ALKALINE FUEL CELLS

L. Swette and J. Giner
Giner, Inc.
Waltham, Massachusetts 02254-9147

The primary objective of this program is the investigation and development of electrocatalysts and supports for the positive electrode of moderate temperature single-unit rechargeable alkaline fuel cells. We define the electrocatalyst as the material with a higher activity for the oxygen electrode reaction than the support. Viable candidate materials must meet the following requirements: 1] good electrical conductivity (typically a more demanding requirement for supports than for electrocatalysts), 2] high resistance to chemical corrosion and electrochemical oxidation and/or reduction; 3] electrocatalysts, in addition, must exhibit high bifunctional electrocatalytic activity (O_2 evolution and reduction). Advanced development will require that the materials be prepared in high surface area forms, and may also entail integration of various candidate materials, e.g., one or two electrocatalysts distributed on a less active support material.

At this point in the program eight candidate support materials and seven electrocatalysts have been investigated. Of the eight supports, three materials meet the preliminary requirements in terms of electrical conductivity and stability. Emphasis has now shifted to preparation in high surface area form and testing under more severe corrosion stress conditions. Of the seven electrocatalysts prepared and evaluated, at least five materials remain as potential candidates. The major emphasis remains on preparation, physical characterization and electrochemical performance testing.

For supports, an acceptable conductivity should exceed about 1 ohm-cm^{-1}. This is a difficult initial screening criterion since these materials are being drawn from metal oxides, carbides, nitrides, etc. For catalysts we anticipate that the conductivity can be more than an order of magnitude lower on a high conductivity support. In preliminary corrosion testing, the material is held at 1.4 V versus RHE in 30% KOH at 80°C for 15 to 20 hours. An acceptable anodic current is on the order of a few microamps/mg of material. For more stringent corrosion testing, and for further evaluation of electrocatalysts (which generally show significant O_2 evolution at 1.4 V), samples will be held at 1.6 V or 0.6 V for about 100 hours. The materials and solutions will then be physically and chemically analyzed for signs of degradation.

Determining electrochemical activity for the oxygen electrode reaction requires considerable exploratory electrode preparation and testing, since the measured polarization is highly dependent on surface area and the hydrophobic/hydrophilic balance or "flooded agglomerate" configuration achieved (ref.1). For the experimental materials being studied, a customized electrode fabrication procedure has to be developed for each material. For preliminary testing, catalysts of interest should show $<$ 500 mV polarization (from 1.2 V) in either mode at 200 mA/cm^2. In advanced development we would expect to reduce the polarization to about 300-350 mV.

MATERIALS INVESTIGATED

Supports:

- $LaNiO_3$
- $LaCrO_3$
- $Ba_5Nb_4O_{15-x}$
- TiC
- B_4C
- NbN
- Material A*
- Material B*

Electrocatalysts:

- $PbPdO_2$
- $CdPd_3O_4$
- Bi_2PdO_4
- $Pb_2(Ir_{2-x}Pb_x)O_{7-y}$
- $Pb_2(Ru_{2-x}Pb_x)O_{7-y}$
- $Na_xPt_3O_4$
- CoTMPP (Cobalt tetra-methoxyphenylporphyrin)

Reference materials:

- O_2 reduction
  - 10% Pt/Au (Johnson-Matthey, 11 m^2/g)
  - 10% Pt/Vulcan XC-72 Carbon (Johnson-Matthey,120-140 m^2/g)
- O_2 evolution
  - $Ni_2Co_2O_4$ (Basic Volume, Ltd.)

*patent applications under consideration for these materials

MATERIAL SOURCES

Materials have been acquired both by purchase, where commercially available, and/or by preparation. Initial preparations have tended to follow procedures documented in the literature where available and vary greatly according to reaction requirements, e.g. thermal decomposition of mixed salts ($LaNiO_3$, $LaCrO_3$), high temperature firing of mixed reactant powders or pellets ($Ba_5Nb_4O_{15-x}$, $LaCrO_3$, $Na_xPt_3O_4$, $PbPdO_2$), co-precipitation and heat treatment ($PbPdO_2$, $CdPd_3O_4$, Bi_2PdO_4, $Pb_2Ir_2O_{7-x}$), adsorption/thermal decomposition (CoTMPP on carbon),and gas phase reactions (TiC). The emphasis has been on obtaining materials of verifiable composition and secondarily with desirable electrochemical properties such as high surface area and small particle size. Materials are typically characterized by X-ray diffraction and occasionally in conjunction with thermal gravimetric analysis (ref.2).

EXPERIMENTAL METHODS

Electrical Conductivity

The electrical conductivity of materials is estimated by compressing a small quantity of the powder at about 12000 psi between metal pistons within an insulating cylinder; the resistance of the powder is measured directly with an ohmmeter. If the resistivity thus measured is in the range of a few ohm-cm, the resistance is

determined more accurately by measuring the voltage drop across the powder under the flow of sufficient current to generate easily measured current and voltage signals. When appropriate, a more accurate value can be obtained by a four-point method in which the voltage drop is measured across contacts separate from the current carrying metal pistons.

Corrosion Resistance

For an initial assessment of the stability of candidate support materials and catalysts, the steady-state anodic current is measured in the range of 1.0 to 1.4 V versus RHE in N_2 sparged 30% KOH at 80°C. The powder to be tested is blended with PTFE (DuPont type 30 Teflon suspension) at about 10% by weight and heated to 275°C, to try to achieve a suitable compromise between physical integrity and good electrolyte penetration. A pure gold mesh is used as the current collector and the electrode is suspended vertically in solution to prevent gas bubble occlusion of the surface. If the anodic current observed, after initiation of potentiostatic control, drops to the microamp range, the system is allowed to equilibrate overnight; the steady-state anodic current is then recorded. In a second stage of testing, candidate materials are subjected to higher potential (1.6 V) representative of oxygen evolution conditions, and lower potentials (0.6 V) representative of oxygen reduction conditions. The latter is intended to place stress on the materials used in the oxide form.

The value of residual anodic current measured by these methods is not an unequivocal indicator of electrochemical stability. A low value of anodic current (e.g. a few microamps/mg) is necessary but not sufficient to demonstrate corrosion resistance since the powder may passivate or delaminate from the current collector and exhibit a deceptive value. At the other extreme, a high current may represent the onset of oxygen evolution rather than corrosion, especially in the case of catalytic materials. Finally, the gold current collector always exhibits a base level of anodic current. Consequently the anodic current values measured must be combined with other observations such as weight loss or gain, color changes, and microscopic examination.

MEASUREMENT OF OXYGEN REDUCTION/EVOLUTION PERFORMANCE

For determination of oxygen reduction/evolution performance, materials are tested in a floating electrode cell (ref. 3) in 30% KOH at 80°C. An appropriate electrode is fabricated by blending the powder with PTFE (typically DuPont type 30 TFE suspension, in the range of 15-60% by weight) and heating at temperatures from 300 to 360°C. A gold-plated nickel mesh is used as the current collector. Generally, several iterations of electrode fabrication are necessary to achieve a Teflon-agglomerate structure with a suitable hydrophobic/hydrophilic balance. At this stage, a single structure is not always suitable for both modes of operation.

The polarization characteristics of such electrodes are established by measuring the steady-state current density (compensated for iR loss) at controlled potential steps, using the Dynamic Hydrogen Electrode (DHE, ref. 4), as a reference (typically 2-4 mV negative of Reversible Hydrogen at 1 mA/cm^2). The oxygen evolution measurements can be severely compromised by gas bubble occlusion of the horizontal electrode surface, however. Thus, efforts are currently underway to develop an integral electrolyte membrane suitable for these tests and more representative of a fuel cell operating configuration.

RESULTS AND DISCUSSION

Supports

Of the eight candidate supports evaluated, $LaNiO_3$, Material A and Material B remain as potentially suitable materials. B_4C, $LaCrO_3$, and $Ba_5Nb_4O_{15-x}$ did not exhibit sufficient electrical conductivity to serve as catalyst supports. Boron carbide in stoichiometric form is an insulator. A boron deficient form was reported to be conductive and was used by General Electric investigators as a support for platinum (ref. 5). Such material could not be obtained, but if it derived its conductivity from free carbon it would not be a suitable candidate in any event. Oxygen deficient barium niobate was also anticipated to be conductive. Most materials prepared, however, exhibited resistivities in the range of megohm-cm, or, when significantly lower, showed evidence of residual carbon (used in the preparation). One preparation of $LaCrO_3$, obtained by solid state reaction of La_2O_3 and black Cr_2O_3 (from thermally decomposed chromium oxalate), was considerably more conductive, but still unacceptable at about 1400 ohm-cm.

The remaining candidate support materials all show high conductivity. The conductivities, in increasing order, are ($ohm\text{-}cm^{-1}$): $LaNiO_3$ (5), TiC (50-200), Material B (125), NbN (300), Material A (390). In chemical testing of TiC, NbN, and Material A, after about 5 hours in 45% KOH at 100°C, none of the materials showed any signs of reaction such as gassing or color change, and all retained high conductivity. In electrochemical testing, however, TiC and NbN gave evidence of reactions. A TiC electrode, for example, exhibited a high anodic current even at 1.0 V versus RHE, e.g., about 12 microamps/mg after 22 hours in 30% KOH at 80°C. Post-test examination by scanning electron microscopy showed signs of changes in morphology also. NbN showed a very low anodic current at 1.4 V (0.1 microamps/mg) but higher currents at 1.2 V versus RHE, suggesting passivation (e.g., NbO_2 formation).

$LaNiO_3$, Material A and Material B appear to be stable at anodic potentials in 30% KOH at 80°C. $LaNiO_3$ gave an anodic current of about 0.1 microamps/mg at 1.3 V but showed visible oxygen evolution at 1.4 V, since it is more catalytic than the other materials. At 1.4 V both materials A and B (40 micron powder) show about 0.2 microamps/mg; it should be noted that the bare gold mesh current collector exhibits an anodic current of the same order of magnitude at 1.4 V. For a higher surface area preparation of Material A (1 to 3 micron powder) the anodic current measured was about 1 microamps/mg at 1.4 V versus RHE. This same electrode was then held at 1.5 V for 28 hours. The anodic current was steady at 1.4 mA/cm^2 (70 microamps/mg); the value for 1 cm^2 of bare gold mesh was 1.62 mA. Finally, the electrode was held at 1.6 V for an additional 84 hours. The anodic current was about the same as for bare gold mesh, about 90-100 mA/cm^2. Post-test examination of the electrode showed no weight loss or gain and no visible evidence of change.

ELECTROCATALYSTS

Electrical Conductivity

Good electrical conductivity will be required for electrocatalysts that serve as both catalyst and electrode structure. For materials that may be distributed as small particles on a highly conductive support, a much lower conductivity may be tolerated since each catalyst particle will only need to pass a very small current a short

distance. In anticipation of developing such a structure ultimately, some of the materials included in our present investigation are not highly conductive.

The base-metal/palladium oxides studied are examples of materials of lower conductivity; they exhibit a negative temperature coefficient of resistance characteristic of semiconductors. Lazarev and Shaplygin have reported the following resistivities: 3-15 ohm-cm for $PbPdO_2$ (ref. 6), 300-900 ohm-cm for Bi_2PdO_4 (ref. 7) and 2.1 ohm-cm for $CdPd_3O_4$ (ref.8). $CdPd_3O_4$ and $PbPdO_2$ have been prepared with some success by co-precipitation of the metal salts and heating to about 500°C. Both show broad line XRD patterns for the compounds with traces of the base metal oxide. Bi_2PdO_4 preparations have not been successful to date. The $CdPd_3O_4$ powder has a measured resistivity of 0.5 ohm-cm, consistent with with the range reported for this material. The $PbPdO_2$, however, has shown quite high resistivity (megohm-cm) in most preparation attempts, the best being about 112K ohm-cm.

The measured resistivity of $Na_xPt_3O_4$ powders has also been quite variable. Shannon, *et al.* (refs. 9,10) have reported metallic conductivity for single crystal $Na_{1.0}Pt_3O_4$, e.g. $9x10^{-5}$ ohm-cm. In our earliest attempts to prepare this material, resistivities of the powders (amorphous) were in the megohm range. In subsequent preparations (at x = 1), good conductivities were observed (1.4 to 164 ohm-cm^{-1}) but analysis also showed 15-25% free Pt. (ref.2). In the most recent preparations (x = 0.8, no free Pt), the conductivity is on the order of 50 ohm-cm^{-1}.

Of the two pyrochlores to be studied, only the iridium compound has been prepared. The composition suggested is $Pb_2(Ir_{1.33}Pb_{0.67})O_{7-y}$ (ref.2). The measured conductivity of this powder was about 40 ohm-cm^{-1}.

Corrosion Testing

Most of the corrosion test data for electrocatalysts is considered preliminary because the electrochemical test data is not so readily interpreted for materials that catalyze oxygen evolution.

$Na_xPt_3O_4$ showed visible oxygen evolution above 1250 mV vs. RHE; the anodic current measured after 16 hours at 1250 mV was 2.6 microamps/mg. $CdPd_3O_4$ exhibited oxygen evolution above 1275 mV vs. RHE; the anodic current measured after 15 hours at this potential was about 3.5 microamps/mg. $PbPdO_2$ has too low a conductivity for a practical test of the pure material.

The Pb-Ir pyrochlore showed substantial anodic current at 1.0 V vs. RHE, about 23 μamps/mg after 21 hours in 30% KOH at 80°C. This current level increased slightly at 1200 mV (32 μamps/mg) and at 1300 mV (50 μamps/mg). At 1400 mV, there was visible oxygen evolution at a current density of about 57 mA/cm^2. Subsequently, the electrode was set at 600 mV vs. RHE and held for 112 hours. A low cathodic current was observed during this period (0.5 μamps/mg initially, 1.1 μamps/mg finally) which may be attributed to oxygen impurity in the nitrogen. Subsequent measurement of the anodic current at potentials above 1.0 V showed about an order of magnitude decrease at all potentials. Post-test examination of the electrode sample revealed significant morphological changes, e.g. gross cracking of the catalyst layer, shrinkage and some delamination. These observations may account for the decreased anodic current levels in the final series of measurements.

OXYGEN REDUCTION/EVOLUTION PERFORMANCE

Reference Materials

Three materials were chosen as points of reference for performance: 10% Pt supported on Vulcan XC-72 carbon and 10% Pt/Au for oxygen reduction, and $NiCo_2O_4$ for oxygen evolution. All of these are commercially prepared catalysts. The 10% Pt/C represents Giner,Inc. electrode technology as an internal baseline. The 10% Pt/Au has been used by United Technologies in alkaline fuel cells (ref. 11) and was intended to provide an external reference point; more development was required to achieve satisfactory performance with this material, therefore. The performance of both of these materials as oxygen reduction electrodes is shown in Figure 1.

$NiCo_2O_4$ purchased from Basic Volume LTD. (CheMaterials, U.K.) has, to date, not exhibited performance levels described in the literature for this material as an oxygen evolution catalyst. Some progress has been made, however, and better performance is anticipated. The most recent performance obtained for $NiCo_2O_4$ is shown in Figure 1.

Candidate Catalysts

The $CdPd_3O_4$ preparation was tested for both oxygen reduction and oxygen evolution performance in 30% KOH at 80°C. The results in either mode do not suggest the potential for significant catalytic activity, especially for oxygen reduction, e.g. at a current density of 10 mA/cm² the electrode exhibited a reduction potential of about 0.6V and an oxidation potential of about 1.5V vs. RHE.

The most conductive preparation of $PbPdO_2$ (112K ohm-cm) was still too resistive to make a practical electrode with the pure material. A sample of $PbPdO_2$ supported on carbon (ref.2) was tested as an alternative method of evaluation. This material, as shown in Figure 2, appears to show catalytic activity for oxygen reduction beyond the activity of carbon alone. This catalyst candidate material will be investigated further if it can be deposited successfully on a non-carbon support.

CoTMPP was prepared on carbon supports also, as a method of evaluation. The method described by Scherson, et al (ref.12) was tried using Vulcan XC-72 carbon and a higher surface area carbon, Anthralur KC (Lurgi). The oxygen reduction performance, although better than carbon alone, did not approach the performance reported by Scherson. These results are shown in Figure 2. An early attempt to deposit CoTMPP on a low-surface area non-carbon support, Material A, was at best very non-uniform; X-ray dot mapping for example, did not show evidence of cobalt. This approach will be pursued further with higher surface area non-carbon supports.

$Na_xPt_3O_4$ was prepared by solid state reaction of PtO_2 and Na_2CO_3. The value of x was determined to be about 0.8 (ref. 2). The surface area and particle size, obtained have not yet been determined. The bifunctional oxygen electrode performance, shown in Figure 1, suggests that this material is suitable for further development.

The Pb-Ir pyrochlore preparation was based on a procedure described by Horowitz, et al for $Pb_2(Ru_{1-x}Pb_x)O_{7-y}$ (ref. 13). After firing at 400°C the material was still amorphous. Consequently to determine the structure, a sample was fired at 500°C for 2 hours; X-ray diffraction analysis (ref.2) gave broad lines for the pyrochlore pattern and a lattice parameter of a = 10.396 $\pm$ 6 Å. The composition proposed is

$Pb_2(Ir_{1.33}Pb_{.67})O_{7-y}$. The original material (fired at 400°C) was used to make electrodes for the testing described here. The bifunctional oxygen electrode performance, shown in Figure 1, also suggests promise for further development. The corrosion test results described earlier may indicate some instability, however. Our initial approach will be to try a higher firing temperature, as used for the analytical sample.

ACKNOWLEDGMENT

This work is supported by the NASA-Lewis Research Center under the direction of Dr. William Fielder (Contract No. NAS3-24635).

REFERENCES

1. Giner, J. and Hunter, C.: "The Mechanism of Operation of the Teflon-bonded Gas Diffusion Electrode: A Mathematical Model," *J. Electrochem. Soc.*, vol. 116, 1969, pg. 1124-1130.

2. Chamberland, B.L.: Professor of Chemistry, University of Connecticut. Professor Chamberland has provided materials analysis support as well as guidance in the selection of materials and preparation methods.

3. Giner, J. and Smith, S.: "A Simple Method for Measuring the Polarization of Hydrophobic Gas Diffusion Electrodes," *Electrochem. Technol.*, vol. 5, 1967, pg. 59-61.

4. Giner, J.: "A Practical Reference Electrode," *J. Electrochem. Soc.*, vol. 111, 1964, pg. 376-377.

5. General Electric, "Hydrocarbon-Air Fuel Cells," Technical Summary Report No. 10, USAERDL Contract DA44-009-AMC-479(T), AD649895, pg. 2-7 and 4-10, 1966.

6. Lazarev, V.B. and Shaplygin, I.S.: "Properties and Structure of $PbPdO_2$," *Zh. Neorg. Khim.*, vol. 24, 1979, pg. 885-889.

7. Lazarev, V.B. and Shaplygin, I.S.: "Reactions of Palladium Oxide With Oxides of Group V Elements," *Zh. Neorg. Khim.*, vol. 19, 1974, pg. 2388-2390.

8. Lazarev, V.B. and Shaplygin, I.S.: *Zh. Neorg. Khim.*, vol. 23, 1978, pg. 291.

9. Schwartz, K.B.; Prewitt, C.T.; Shannon, R.D.; Corliss, L.M.; Hastings, J.M.; and Chamberland, B.L.: "Neutron Powder Diffraction Study of Two Sodium Oxides: $Na_{1.0}Pt_3O_4$ and $Na_{0.73}Pt_3O_4$," *Acta Cryst.*, vol. 38, 1982, pg. 363-368.

10. Shannon, R.D; Gier, T.E.; Garcia, P.F.; Bierstedt; Flippen, R.B.; and Vega, A.J.: "Synthesis and Properties of Platinum Metal Oxides of the Type $M_xPt_3O_4$," *Inorg. Chem.*, vol. 21, no. 9, 1982, pg. 3372-3381.

11. Singer, J. and Srinivasin, V.: "Evaluation Parameters for the Alkaline Fuel Cell Oxygen Electrode," NASA Technical Memorandum 87155, November, 1985.

12. Scherson, D.A.; Gupta, S.L.; Fierro, C.; Yeager, E.B.; Kordesch, M.E.; Eldridge, J.; Hoffman, R.W.; and Blue, J.: "Cobalt Tetramethoxyphenyl Porphyrin-Emission Mossbauer Spectroscopy and O_2 Reduction Electrochemical Studies," *Electrochim. Acta*, vol. 28, no. 8, 1983, pg. 1205-1209.

13. Horowitz, H.S.; Longo, J.M. and Lewandoski, J.T.: "Lead Ruthenium oxide, $Pb_2[Ru_{2-x}Pb^{4+}]O_{6.5}$," **Inorganic Syntheses**, McGraw-Hill, New York, pg. 69-72.

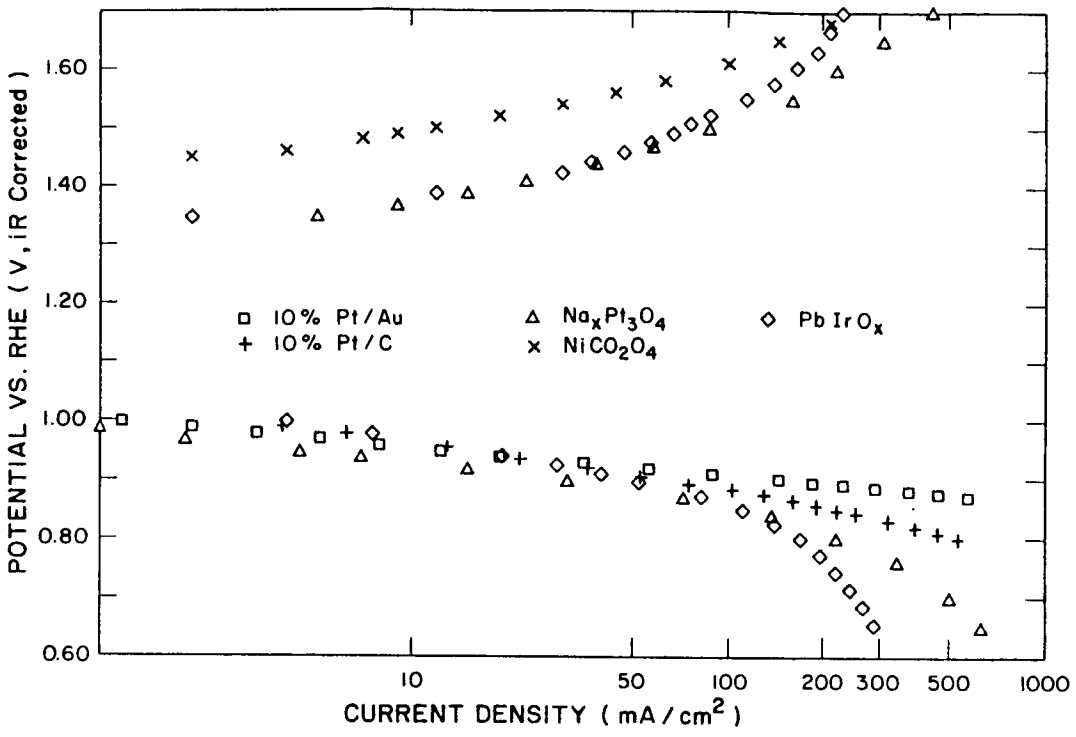

FIGURE 1. OXYGEN REDUCTION / EVOLUTION (30% KOH , 80°C)

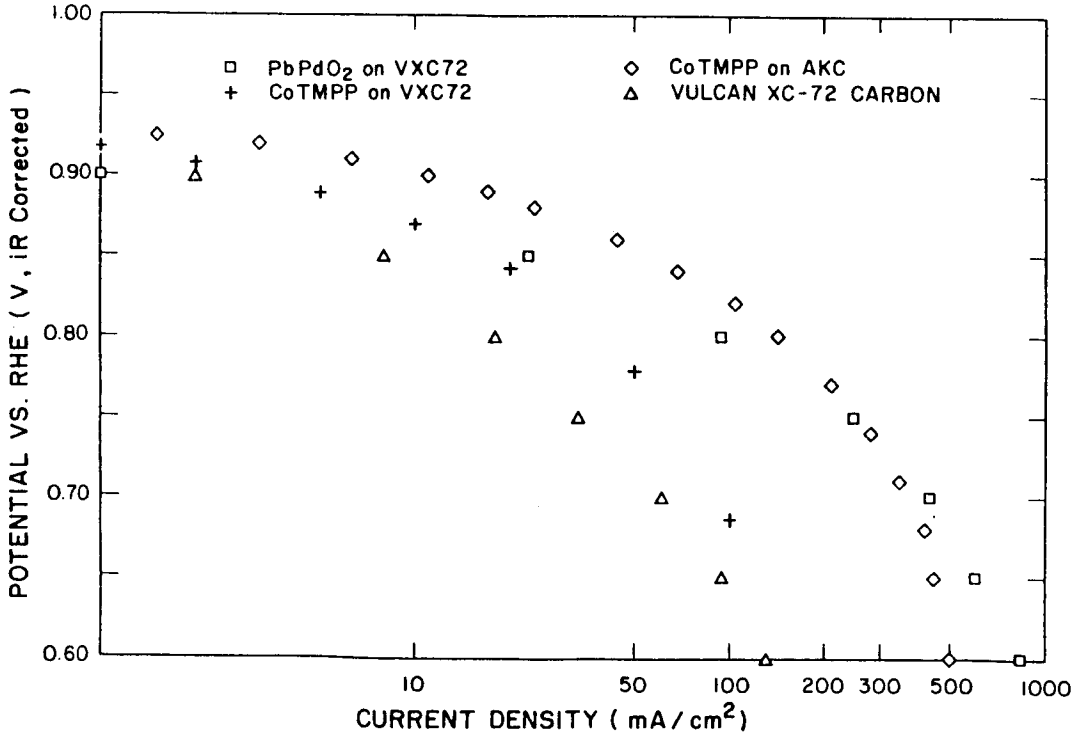

FIGURE 2. OXYGEN REDUCTION (30% KOH , 80°C)

HIGH-SURFACE-AREA, DUAL-FUNCTION OXYGEN ELECTROCATALYSTS FOR SPACE POWER APPLICATIONS

David O. Ham, Gary Moniz, and E. Jennings Taylor
Physical Sciences, Inc.
Andover, Massachusetts 01810

We investigated the processes of hydration/dehydration and carbonation/decarbonation as an approach to provide higher surface area mixed metal oxides that are more active electrochemically. These materials are candidates for use as electrocatalysts and electrocatalyst supports for alkaline electrolyzers and fuel cells. For the case of the perovskite, $LaCoO_3$ we achieved higher surface areas with no change in structure and a more active oxygen electrocatalyst.

INTRODUCTION

An energy storage system to provide energy for the dark side of orbit is required for the space station. One energy storage system concept that has received attention is the dedicated alkaline regenerative fuel cell storage system (ref. 1). This system is based on solar array, alkaline fuel cell, and alkaline water electrolyzer component technologies. The energy storage system operates on a 90-minute cycle, alternately going through dark and light side orbit environments. During the light side of the orbit, the solar array provides electrical power to the satellite module plus excess electrical power used to electrolyze water to produce hydrogen and oxygen. During the dark side of the orbit, the hydrogen and oxygen are reacted in the fuel cell to provide electrical power to the satellite module plus water which is stored for use by the electrolyzer during the light side of the orbit.

An alternative approach is the integrated alkaline regenerative fuel cell storage system (ref. 1). In this system a single electrochemical module operates in both the fuel cell and water electrolysis modes and a substantial reduction in the weight and volume of the regenerative energy storage system is achieved. However, the requirement that the hydrogen and oxygen electrodes operate in the dual function (i.e., reactant consuming, generating) mode presents a materials stability problem, particularly at the oxygen electrode.

During the past several years, numerous workers have investigated mixed metal oxides of the perovskite, spinel, and pyrochlore structures for electrochemical applications. Mixed metal oxides reportedly possess catalytic activity for both oxygen reduction and evolution in alkaline media. Additionally, these materials are attractive as support materials for the gold fuel cell catalysts. Consequently, NASA is interested in mixed metal oxides as: 1) oxygen evolution and/or reduction catalysts for the dedicated regenerative fuel cell/electrolyzer, 2) dual function oxygen electrocatalysts for the integrated regenerative fuel cells, and 3) an electrocatalyst support for high temperature and pressure alkaline fuel cells. One important problem with the mixed metal oxide materials is their relatively low surface area.

The objective of our initial research effort was the demonstration of a new technique for enhancing the surface areas of conventionally prepared mixed metal oxide catalyst materials. We accomplished this surface area enhancement using a pressure hydration/dehydration or carbonation/decarbonation technique. In this approach, we hydrated or carbonated the oxide sample at temperatures up to to 400°C and pressures up to 5000 psi in a stainless steel reactor. This step was followed by dehydration or decarbonation of the oxide sample in a furnace with flowing nitrogen at 400°C. We characterized the results of this process primarily by measuring the surface areas before and after our process using the BET technique. We studied sixteen mixed metal oxide systems using forty-three different process variables and obtained surface area enhancements greater than a factor of two in eleven of these cases. In one case we observed a surface area enhancement of twenty times. For one mixed metal oxide, $LaCoO_3$, we studied the degree of surface area enhancement as a function of the hydration conditions and obtained larger surface areas at lower hydration temperatures.

We characterized the crystal structure of the mixed metal oxide before and after surface area enhancement using Debye-Scherrer, and in two cases diffractometer, x-ray diffraction. In the case of $LaCoO_3$, a potential oxygen electrocatalyst, we observed a surface area enhancement of nearly seven times and no change in peak positions from the x-ray diffraction analysis, indicating that the high surface area material had the same crystal structure as the initial catalyst. In the case of $SrZrO_3$ we obtained increased surface area, but the crystal structure was not retained in a pure form. Using the rotating disc electrode (RDE) technique, we verified increased electrochemical activity for the enhanced surface area $LaCoO_3$ relative to the as received $LaCoO_3$.

Approach to Activity Enhancement

In selecting a catalyst to be electrochemically dual-functional, we are likely to be forced to choose a material with limited specific activity for one reaction in order to optimize overall performances. We have shown in this work that we can achieve increased catalyst activity by increasing the surface area of the catalyst material. Our approach for increasing surface areas has been successfully used for lime type SO_2 sorbent materials. To our knowledge, no similar approach has been used for preparation of any catalyst materials. We have achieved enhancements in surface areas of a variety of mixed metal oxide electrocatalysts using pressure hydration (or carbonation) followed by dehydration (or decarbonation).

The hydration and dehydration processes for one of our successfully expanded catalysts are represented by the reactions:

$$LaCoO_3 + 3H_2O \underset{-1}{\overset{1}{\rightleftharpoons}} LaCo(OH)_6 \quad . \tag{1}$$

Similar carbonation and decarbonation processes of a successful material are

$$SrZrO_3 + 3CO_2 \underset{-2}{\overset{2}{\rightleftharpoons}} SrZr(CO_3)_3 \quad . \tag{2}$$

We have no way of knowing the correct form or stoichiometry of the hydrated or carbonated materials, for instance whether they are mixed or separate metal hydroxides or

carbonates. Based on our experinece with lime type sorbent materials and the catalytic materials studied in this program we expect processes of these types to produce increased surface area materials for any substances that form stable hydroxides or carbonates at achievable conditions. For successful application as catalysts we also require the expanded surface area materials to have the same crystal structure as the low surface area electrocatalysts.

We can predict which mixed metal oxide systems will react with water or carbon dioxide and what conditions are appropriate for the reaction if we have thermochemical data for the mixed metal oxides and hydroxides or carbonates of interest. However, these thermochemical data are available for only a few of the many mixed metal oxides studied as electrocatalysts (ref. 2).

High Surface Area Mixed Metal Oxide Preparation

The surface area enhancement of the mixed metal oxides involved the pressure hydration or carbonation procedure described above. We purchased the mixed metal oxides to be investigated from ChemMaterials Ltd. and Alpha Products Division of Morton Thiokol. One mixed metal pyrochlore, $Pb_2Ru_2O_7$, was prepared as described in the patent literature (ref. 3).

We conducted the pressure hydration or carbonation experiments in a stainless steel reactor manufactured by Parr Instruments Inc. (Model No. 4740). The reactor volume is 71 ml and the maximum allowable pressure is 8500 psi at 350°C. In most experiments we added approximately 0.5 grams of the mixed metal oxide to the reactor and 50 ml of distilled water for the hydration experiment and 900 psi of CO_2 for the carbonation experiment, respectively. The reactor was then heated to temperature (typically 400°C) and held overnight. The reactor was then cooled to room temperature before the reactor was opened to the ambient atmosphere. We also hydrated some samples at ambient conditions. The sample was collected and dried prior to the dehydration or decarbonation step. The dehydration was usually conducted in flowing nitrogen gas at 400°C.

Characterization

We characterized the specific surface areas of the mixed metal oxides using a Micromeretics BET surface area analyzer. The initial surface areas of the mixed metal oxides were determined as received or as prepared. We also characterized the surface areas of the samples in the hydrated or carbonated form and in the dehydrated or decarbonated form.

We characterized the crystal structures of the mixed metal oxides before and after surface area enhancement using Debye-Scherrer powder x-ray diffraction. Two samples were characterized using a powder x-ray diffractometer. The Debye-Scherrer x-ray diffraction analyses were conducted at Eastern Analytical Laboratories and the diffractometer analyses were conducted at NASA Lewis Research Center.

Rotating Electrode Evaluation

When evaluating the electrochemical activity of new or novel oxygen electrocatalyst materials, many researchers prepare gas diffusion electrodes and conduct half cell experiments. One problem with this approach is that the procedure used to prepare gas diffusion electrodes for state-of-the-art electrocatalysts (e.g., unsupported gold) may not result in an optimum electrode structure for the novel electrocatalyst

material. Consequently, the polarization data would contain gas diffusion and reactant transport losses which would mask the desired kinetic polarization behavior. To avoid these problems with gas diffusion electrode preparation, we decided to evaluate the novel electrocatalyst powders using the rotating electrode technique. In the rotating disc electrode (RDE) technique, mass transport corrected kinetic and mechanistic information for the oxygen reduction may be obtained.

This technique is elucidated in a now classic compilation of earlier work (ref. 4) in which the mathematics of fluid dynamics at submerged rotating surfaces was combined with expressions for electrolysis kinetics at electrodes of various geometries. One geometry considered was the disc electrode. The electrode material is mounted on the end as a disc and surrounded by an inert shroud and is rotated while slightly submerged in the electrolyte. By fixing the rotation rate, the transport of reacting species to the electrode surface is constant. The exact relation between the diffusion layer thickness, δ, and electrode rotation, ω, has been derived:

$$\delta = 1.61\ D^{1/3}\ \nu^{1/6}\ \omega^{-1/2} \quad , \tag{3}$$

where ω is the electrode rotation rate (rev/min), ν is the kinematic viscosity, and D is the diffusion coefficient.

Combining equation (3) with Faraday's and Fick's laws, the expression for the limiting disc current is:

$$i_\ell = 0.62\ nFAD^{2/3}\ \nu^{-1/6}\ \omega^{1/2}\ C_b \quad m \tag{4}$$

where F is Faraday's constant, A is the electrode area, and C_b is the bulk reactant concentration. This equation is known as the Levich equation. Good agreement between limiting currents determined experimentally for species with known diffusion coefficients and that predicted by the Levich equation have been reported (ref. 5).

The rotating electrode experiments were conducted in an all Teflon cell using a Pine Instruments Co. Analytical Rotator and a Pine Instruments Bipotentiostat. The data were acquired using an IBM PC with 512 kB of memory and an interface board manufactured by Data Translation Inc. The oxygen reduction experiments were conducted in low concentration NaOH which was saturated with bubbling oxygen gas (99.99 percent purity). The potential was scaned from 1.0 to 0.4V versus RHE at a scan rate of 10 mV/s. The disc current and disc potential data were acquired at a rate of ten points per second or 600 points of data per rotation rate. The rotation rates used were 400 to 4900 rpm. We conducted initial RRDE experiments using smooth platinum in order to verify our technique with those reported in the literature. Several programs were written in Basic to conduct the rotating electrode analysis.

In order to evaluate the electrocatalytic activity of the mixed metal oxide powders, we modified a demountable ring-disc electrode assembly manufactured by Pine Instruments Co. and shown in figure 1. The disc electrode stem was modified to contain a 0.35 mm cavity as shown in figure 2. We applied the electrocatalyst powder to the cavity using Teflon as a binder (ref. 6). After several attempts at preparing the electrocatalyst and binder for the rotating electrode studies, the following procedure was found to be optimum. One hundred milligrams of the electrocatalyst powder was blended with 25 ml of distilled water and enough Teflon (DuPont TFE 30B) to make 20 percent Teflon by weight. The material was mixed to form a suspension and then

vacuum filtered onto a 10μ Millipore Teflon substrate. The filtered material was allowed to air dry overnight and then sintered at 250°C for fifteen minutes. The sintering process resulted in a material with a rubbery consistency. This material was then spread into the disc cavity with a spatula and smoothed using a razor blade. The electrode was then washed in the electrolyte to insure that any surfactant from the Teflon dispersion was removed prior to beginning the rotating electrode experiment.

Specific Surface Area Characterization

The BET specific surface areas of the mixed metal oxides obtained for study in this program are given in Table 1 along with the surface areas achieved by our processing. The highest surface area we measured for materials as received is approximately 30 m^2/g for the lead ruthenium pyrochlore. Most of the measured initial surface areas were 1 to 4 m^2/g. The two lanthanum strontium manganates exhibited surface areas of 7 to 10 m^2/g. These commercially obtained samples were reportedly prepared by the freeze drying of a stoichiometric mixture of the nitrates. Literature sources have reported higher surface areas (typically 15 m^2/g) for mixed metal oxides prepared by this technique. Apparently there is a considerable discrepancy between what is possible in terms of surface area with freeze drying and what is reported.

Surface area data for the mixed metal oxides after dehydration and decarbonation are also presented in Table 1. In general hydration was more successful than carbonation. In only the case of $SrZrO_3$ did carbonation alone enhance the surface area of the mixed metal oxide. In two other cases carbonation as well as hydration resulted in surface area enhancement. For the $SrZrO_3$ mixed metal oxide the thermodynamic calculations indicated a favorable free energy of carbonation and a substantial surface area increase from 3.91 to 50.6 m^2/g was indeed observed. Favorable free energies of reaction were also calculated for hydration and carbonation of $MgTiO_3$ and for carbonation of $SrTiO_3$. The hydration attempt was successful for these substances but the carbonations did not result in surface area enhancement.

We studied the effect of hydration temperature on $LaCoO_3$. We choose this mixed metal oxide because of the moderate degree of success of the initial hydration attempt (i.e., approximately three times surface area enhancement). The initial hydration attempt was at a temperature of 300°C. We also conducted hydrations at 400 and 200°C. The surface area data are presented in figures 3 and 4 as functions of hydration pressure and hydration temperature. For the 400°C hydration, the surface area was increased to only 3.8 m^2/g (from 2.6 m^2/g) while in the case of the 200°C hydration the surface area increased to 18.1 m^2/g. Although the water pressure is decreasing as the reaction temperature is decreasing, we conclude that the equilibrium pressure of the reaction is decreasing faster. This hypothesis is consistent with the general trend of more negative free energies of reaction with decreasing temperature noted for the thermodynamic calculations of various perovskite systems.

One other interesting observation regarding the surface area enhancement is as follows. In the cases where the hydration or carbonation procedure enhanced the surface area, a large fraction of the surface area enhancement was evident after hydration (or carbonation) and prior to dehydration (decarbonation).

X-Ray Diffraction Studies

We used x-ray diffraction to qualitatively study the structure of the mixed metal oxides. We used a Debye-Scherrer camera to measure the d spacings of the mixed metal

oxides before and after the surface area enhancement procedure. We will concentrate our discussion on the $SrZrO_3$ and $LaCoO_3$ results.

The X-ray results for the $SrZrO_3$ exhibit several additional lines in the post decarbonated sample compared to the reference file and the "as received" sample. Although we did not attempt to determine the source of these extraneous lines, we presume they occur from oxides or carbonates of Sr and Zr resulting from the pressure carbonation procedure. An attempt was made to convert the decarbonated sample to the original perovskite sample by passing oxygen over the sample at 400°C for two hours. Some of the extraneous lines are indeed removed. Additionally, the parent perovskite line of d = 1.098 did reappear after oxygen treatment. However, many unaccounted for lines still remain in the pattern. The oxygen treatment only slightly decreased the surface area from 50 to 47 m^2/g. Possibly, further oxygen treatment or decarbonation in flowing oxygen may result in the perovskite structure while maintaining high surface area.

The X-ray diffraction results for the $LaCoO_3$ sample in the "as received" and dehydrated state as well as the reference file are shown in Table 2. This sample was hydrated at 200°C and resulted in a surface area increase from 2.6 to 18 m^2/g. The dehydrated sample X-ray pattern exhibits good qualitative agreement with the "as received" and reference file pattern. Due to the nature of the Debye-Scherrer technique, only qualitative peak positions are determined and limited information regarding peak intensity and shape are available. In order to gain more information regarding these samples, Dr. J. Singer of NASA Lewis Research Center conducted experiments using an x-ray diffractometer.

The diffractometer traces for $LaCoO_3$ "as received" and after dehydration are presented in figures 5 and 6, respectively. The trace in figure 5 for the "as received" sample exhibits well defined peaks predominately corresponding to the perovskite. There is some evidence of lanathum hydroxide in the parent pattern (ref. 7). In the dehydrated diffractometer trace the peaks occur at the same positions as in the parent pattern as was also observed in the Debye-Scherrer patterns. This indicates that no impurity phases were formed during the pressure hydration and dehydration procedures. The diffraction peak in the dehydrated sample also exhibit considerable line broadening and lowering intensity relative to the parent pattern. This most probably results from the smaller crystallite size of the dehydrated sample (ref. 7), consistent with the increase in surface area from 2.6 to 18 m^2/g.

Our presumption for the surface area enhancement mechanism involved the formation of an hydroxide during pressure hydration. This has not been confirmed and other mechanisms for the surface area enhancement may be possible. In order to gain insight into the mechanism, we suggest more extensive characterization of the perovskites at different stages of pressure hydration/dehydration.

Electrochemical Activity Measurement

A set of rotating electrode experiments addressed the change of electrochemical activity with enhanced surface area for the mixed metal oxide $LaCoO_3$. We conducted three rotating electrode experiments using powder disc samples. The electrocatalyst powders were Vulcan XC-72 obtained from Cabot corporation, $LaCoO_3$ "as received" from ChemMaterials, and $LaCoO_3$ hydrated at 200°C and dehydrated at 400°C with the resultant surface area of 18 m^2/g. The disc samples with the perovskite contained 90 percent Vulcan XC-72 and 10 percent $LaCoO_3$ powder plus 20 percent Teflon as a binder.

We present the disc current data for these three electrodes at a rotation rate of 1600 rpm in figure 7. The potential sweep range used did not allow the establishment of a well defined limiting current for the perovskite samples and should have been extended in the cathodic direction. All three samples exhibit a plateau at approximately 0.7V versus RHE which may be attributed to hydrogen peroxide production. The activity of the "as received" perovskite (i.e., 10 percent $LaCoO_3$ and 90 percent Vulcan XC-72) is essentially the same as that of the Vulcan XC-72. However, in the case of the surface area enhanced $LaCoO_3$, the oxygen reduction current is substantially increased over the entire potential range studied. This validates our approach of increasing the activity of mixed metal oxides by increasing their surface area.

REFERENCES

1. Martin, R.E.; Gitlow, B.; and Sheilby, D.W.: Alkaline Regenerative Fuel Cell Energy Storage System for Manned Orbital Satellites. Proceedings of 17th Intersociety Energy Conversion Engineering Conference, Los Angeles, CA, 1982.

2. Barin, I.; Knacke, O.; and Kubaschewski: Thermochemical Properties of Inorganic Substances. Springer-Verlag, 1973; supplement 1977.

3. Horowitz, H.: U.S. Patent 4,129,525, 1978.

4. Levich, V.G.: Physiochemical Hydrodynamics, Prentice Hall, New York, 1962.

5. Greggory, J. and Riddeford, R.: J. Chem. Soc., 3756, 1956.

6. Amadelli, R.: Influence of Metal Ions on Oxygen Reduction on Gold and Platinum. Ph.D. Dissertation, Case Western Reserve University, University Microfilms, Ann Arbor, MI, 1982.

7. Negas, Taki: TransTech, Inc., private communication, 1986.

Table 1. - Surface Area Data for Mixed Metal Oxides
(All Values in m^2/g)

Material	As Received	After Hydration/ Dehydration	After Carbonation/ Decarbonation	Enhancement Factor H_2O/CO_2
La_2CuO_4	0.96	3.23	0.74	3.4/
$La_2O_3 \cdot 2TiO_2$	1.74	2.25	1.84	
$CaTiO_3$	3.36	3.65	3.65	
$MgTiO_3$	3.67	11.33	3.98	3/
$SrTiO_3$	2.32	2.55	2.29	
$SrZrO_3$	3.91	6.64	50.58	/13
$Pb_2Ru_2O_7$	31.2	19.31	34.11	
$SrLaNiO_4$	2.22	11.42	2.56	5/
$La_{0.5}Sr_{0.5}CoO_3$	1.05	1.33	1.28	
$La_{0.7}Sr_{0.3}MnO_3$	7.62	8.63	9.15	
$La_4Ni_3O_{10}$	0.70	4.31	1.92	6/2.7
$LaNiO_3$	0.45	1.11	0.46	2.5/
$LaCoO_3$	2.59	4-18	2.63	1.5-7/
$La_{0.5}Sr_{0.5}MnO_3$	10.1	10.68	9.81	
$CoMn_2O_4$	1.81	2.24	2.68	
$MgO \cdot ZrO_2$	3.61	79.38	35.84	22/10

Table 2. - XRD by the Debye-Scherrer Method for $LaCoO_3$ (hydration 200°C)

Line	File Number 10-268		As Received d(Å) 2.59 m^2/g	Post ($-H_2O$) d(Å) 18.11 m^2/g
	d(Å)	I/Io		
1	3.82	20	3.79	3.87
2			3.43	3.27
3	2.734	100	2.70	2.75
4	2.682	87	2.66	2.69
5	2.281	10	2.23	2.45
6	2.214	24	2.18	2.24
7	1.910	55	1.90	1.90
8	1.566	38	1.57	1.56
9	1.547	17	1.54	1.55
10	1.360	20	1.35	
11	1.344	25	1.34	
12	1.214	20	1.21	
13	1.205	20	1.21	
14	1.109	10	1.11	
15	1.091	4	1.03	
16			1.02	
17			1.02	
18			1.01	

Demountable Rotating Ring Disc Electrode Assembly from Pine Instrument Co.

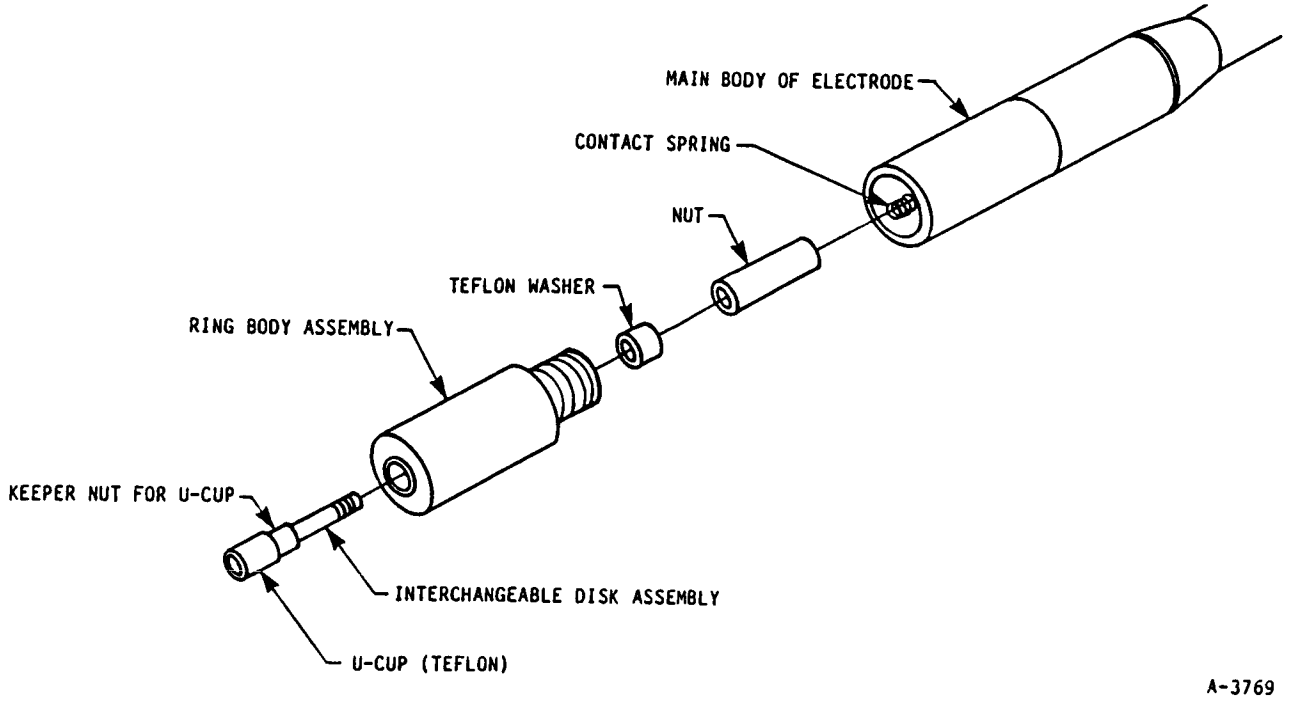

Figure 1.

Stem Containing Cavity for Powder Electrocatalysts Samples

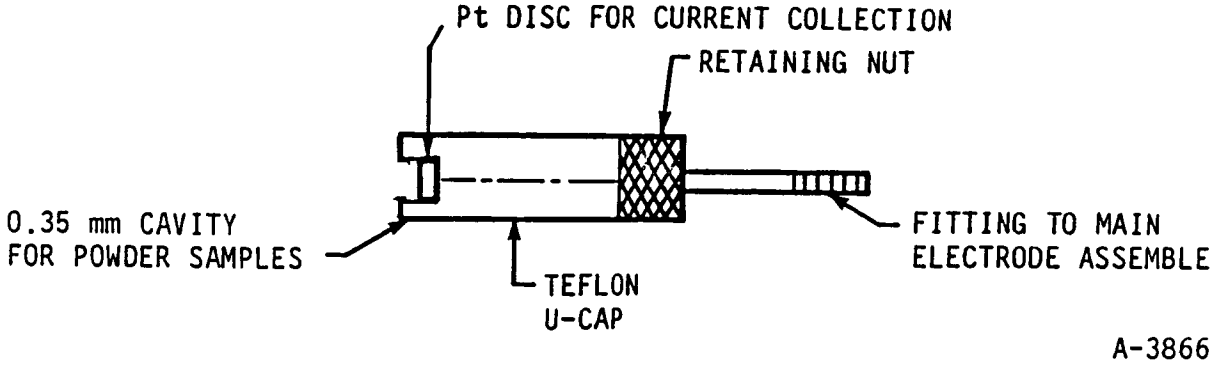

Figure 2.

BET Surface Area of $LaCoO_3$ as a Function of Hydration Pressure

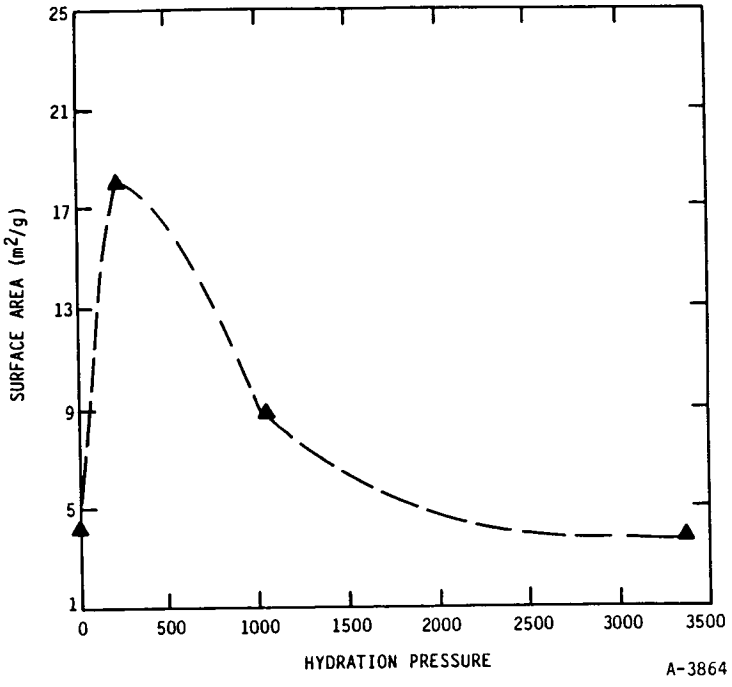

Figure 3.

BET Surface Area of $LaCoO_3$ as a Function of Hydration Temperature

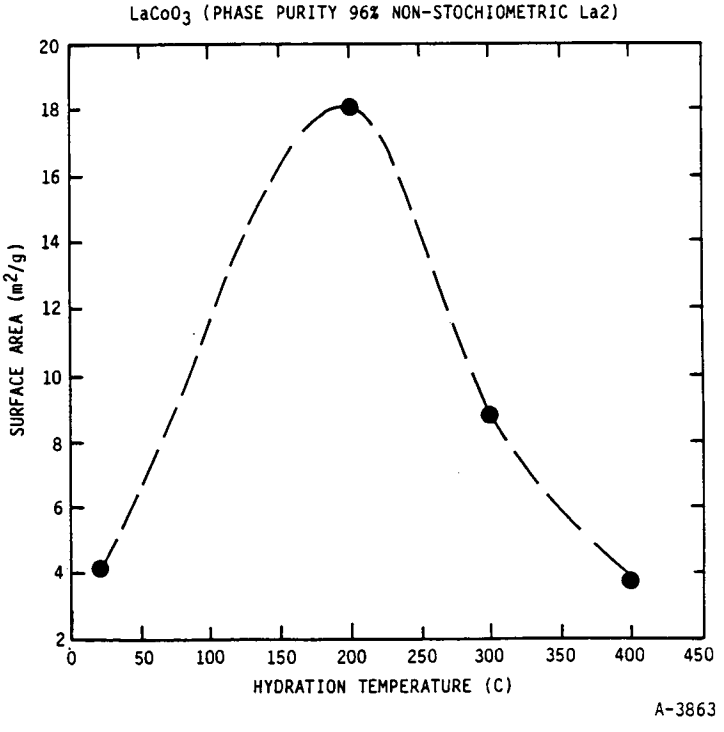

Figure 4.

Diffractogram of $LaCoO_3$ "As Received"

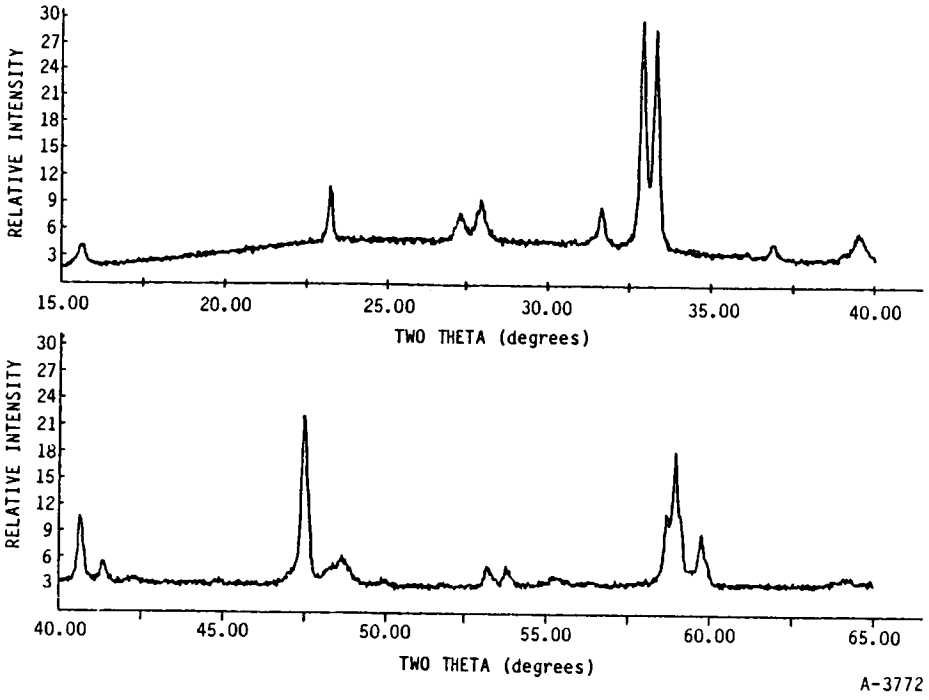

Figure 5.

Diffractogram of Enhanced Surface Area $LaCoO_3$

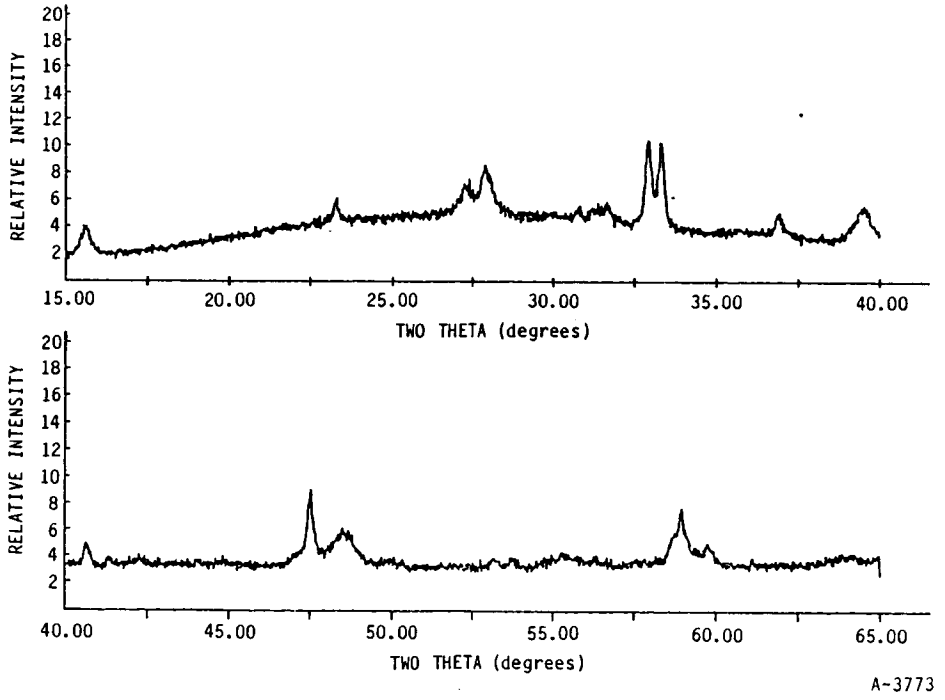

Figure 6.

Oxygen Reduction Current for Vulcan XC-72, 10 Percent LaCoO3 (As Received) + 90 Percent Vulcan XC-72, and 10 Percent $LaCoO_3$ (Expanded) + 90 Percent Vulcan XC-73

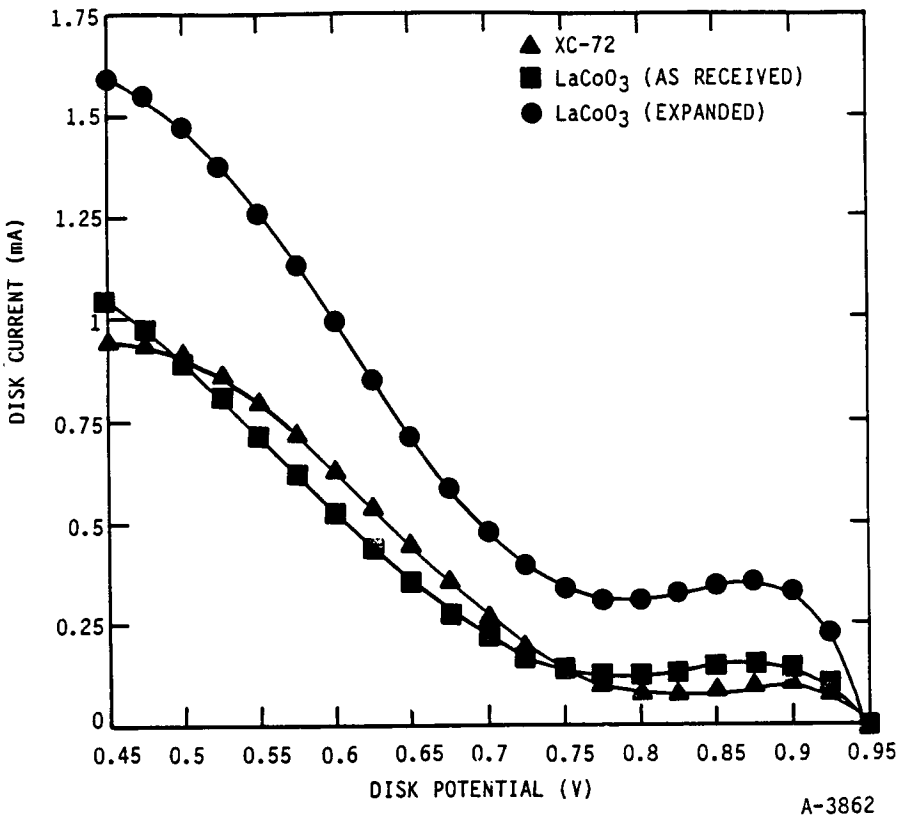

Figure 7.

AC IMPEDANCE STUDY OF DEGRADATION OF POROUS NICKEL BATTERY ELECTRODES

S.J. Lenhart, D.D. Macdonald, and B.G. Pound
SRI International
Menlo Park, California 94025

AC impedance spectra of porous nickel battery electrodes were recorded periodically during charge/discharge cycling in concentrated KOH solution at various temperatures. A transmission line model (TLM) was adopted to represent the impedance of the porous electrodes, and various model parameters were adjusted in a curve fitting routine to reproduce the experimental impedances. Degradation processes were deduced from changes in model parameters with electrode cycling time. In developing the TLM, impedance spectra of planar (non-porous) electrodes were used to represent the pore wall and backing plate interfacial impedances. These data were measured over a range of potentials and temperatures, and an equivalent circuit model was adopted to represent the planar electrode data. Cyclic voltammetry was used to study the characteristics of the oxygen evolution reaction on planar nickel electrodes during charging, since oxygen evolution can affect battery electrode charging efficiency and ultimately electrode cycle life if the overpotential for oxygen evolution is sufficiently low.

Transmission line modeling results suggest that porous rolled and bonded nickel electrodes undergo restructuring during charge/discharge cycling prior to failure. The average pore length and the number of active pores decreases during cycling, while the average solid phase resistivity increases. The average solution phase resistivity remains relatively constant during cycling, and the total porous electrode impedance is relatively insensitive to the solution/backing plate interfacial impedance.

INTRODUCTION

Porous nickel electrodes are used in a number of secondary alkaline battery systems, including nickel-iron, nickel-zinc, nickel-hydrogen and nickel-cadmium cells. Each of these batteries must ultimately meet several performance criteria: high specific power, high specific energy, low cost, and long cycle life. At present, the viability of these batteries is often limited by the degradation of the electrode materials. In some cases, the nickel plate is life-limiting (Ref. 1).

A number of irreversible degradation processes affect the performance of porous nickel battery electrodes. Like all porous electrodes, nickel plates can exhibit electrolyte exhaustion within the pores leading to mass transport and ohmic overpotential losses that reduce cell power. Faradaic efficiency losses from cycle-and temperature-dependent parasitic processes, such as oxygen evolution, can reduce charging efficiency. Also, the structural integrity of porous nickel electrodes frequently is inadequate to endure the mechanical stresses that arise during charge/discharge cycling. Resistive degradation of substrate particle-particle bonds can result from these stresses, and/or the active material may progressively separate from the current collector further reducing the performance of the electrode on cyclic charging and discharging.

In this paper, we report a study of the degradation of porous nickel battery electrodes in alkaline media upon cyclic charging/discharging. AC impedance spectroscopy is used as the principal experimental tool. AC impedance studies of both planar and porous nickel battery electrodes in alkaline solutions have been published previously, but much of this work was restricted to relatively narrow frequency ranges because of limitations with experimental instrumentation (Ref. 2-5). Also, some investigators report impedance data for the total cell rather than the individual electrodes (Ref. 6,7), while other studies have dealt with electrodeposited (thick) oxide films (Ref. 8).

TRANSMISSION LINE MODEL

An understanding of how the properties of porous nickel electrodes are altered during cycling is developed in this study by adopting a transmission line model (Ref. 9,10) for the impedance of the porous mass. The model is adopted from Lenhart, Chao, and Macdonald (Ref. 11) and Park and Macdonald (Ref. 12), and differs from classical TLMs in two ways. First, the model used here recognizes the finite thickness of a practical battery electrode. Accordingly, the electrochemical behavior of the porous mass will be partly determined by processes that occur at the base of the pore between the current collector (backing plate) and the solution (impedance Z', Figure 1), provided that the frequency is sufficiently low that the penetration depth of the AC wave is of the same order as the thickness of the porous mass. Secondly, the model assumes a finite resistance for the active solid phase in order to account for the resistive degradation of particle-particle contacts caused by internal stresses.

As with most porous electrode models developed to date, several simplifying assumptions are made in order to render the mathematics tractable. Thus, the pores are assumed to be parallel right cylinders, and any radial and axial electrolyte concentration gradients within the

pores are neglected. Furthermore, average pore electrolyte and solid phase resistances are used. A uniform layer of active material is assumed to line the walls of the pores, and charge storage processes along the walls are represented by a position-independent interfacial impedance Z. In this work, an equivalent circuit representing the interfacial impedance, Z, and the backing plate impedance, Z', are deduced from planar nickel electrode impedances.

The mathematical details of the modified transmission line model have been described in previous publications (Ref. 11,12) and are discussed only briefly here. The equivalent electrical circuit for a single pore in discretized form is shown in Figure 2, in which R_m and R_s represent the resistance of the solid current-carrying phase per unit pore length (ohm/cm), and the resistance of the solution phase per unit pore length (ohm/cm), respectively. The interfacial impedance, Z, is a specific impedance per unit pore length, (ohm cm^2/cm), so Z/dx has units of ohms. The current collector or backing plate impedance Z' has units of ohms, and is assumed to be independent of pore length.

Current and potential distributions within the porous system, and the total impedance, were derived (Ref. 11,12) by application of circuit analysis equations to a typical discrete unit. The total impedance of n one-dimensional parallel pores was found to be:

$$Z_T = \frac{1}{n}\,\frac{R_m R_s \ell}{R_m + R_s} + \frac{2\gamma^{1/2} R_m R_s + \gamma^{1/2}(R_m^2 + R_s^2)\,C + \delta\, R_s^2 S}{\gamma^{1/2}(R_m + R_s)\,(\gamma^{1/2} S + \delta\, C)} \qquad (1)$$

where

$\gamma = \frac{R_m + R_s}{Z}$, $\delta = \frac{R_m + R_s}{Z'}$, $C = \cosh(\gamma^{1/2}\ell)$, and $S = \sinh(\gamma^{1/2}\ell)$. If A is the total projected area of the porous electrode, and $(1-\Theta)$ is the fraction of that area occupied by pores, then $\Theta A/n$ is the film area per pore, and $(1-\Theta)A/n$ is the average pore area per pore. The solution phase resistance per pore becomes $\rho_s n l/(1-\Theta)A$, and the resistance of the current-carrying solid phase is $\rho_m n l/\Theta A$, where ρ_s and ρ_m are the resistivities (ohm cm) of the solution and solid phases, respectively, and ℓ is the pore length. The resistances R_s and R_m in Figure 2 are therefore

$$R_s = \rho_s\, n/(1-\Theta)A \qquad \text{(ohm/cm)} \qquad (2)$$

$$R_m = \rho_m\, n/\Theta A \qquad \text{(ohm/cm)} \qquad (3)$$

If the specific impedances (ohm cm^2) of the pore wall and pore base are Z and Z', respectively, then the impedance of the pore wall and pore base per pore are $Z_w/2\pi r l$ and $Z_b/\pi r^2$, where r is the average pore

radius. Since the average pore area is $(1-\theta)A/n = \pi r^2$, the average pore radius is given as

$$r = \left(\frac{(1-\theta)\ A}{\pi n}\right)^{1/2} \tag{4}$$

and the per impedance per unit pore length as:

$$Z = \frac{Z_w \ell}{2\pi r \ell} = \frac{Z_w}{2}\left(\frac{n}{\pi\ A\ (1-\theta)}\right)^{1/2} \tag{5}$$

Similarly, the backing plate or current collector impedance Z' per pore is found to be

$$Z' = \frac{Z_b}{\pi r^2} = \frac{Z_b n}{(1-\theta)A} \tag{6}$$

The above expressions for R_m, R_s, Z and Z' are used in Equation 1, which now describes the impedance of a three dimensional porous electrode. The expressions for Z and Z' are determined from planar electrode impedances, as discussed in the Results Section.

EXPERIMENTAL

Test Cell

A three electrode cylindrical PTFE cell was used for all experiments with the working electrode positioned horizontally near the bottom of the cell. A platinum counter electrode and a Hg/HgO reference electrode were positioned over the working electrodes. The cell provided input ports for the electrolyte solution, for high purity argon gas purging, and for a PTFE coated copper/constantan thermocouple. High purity argon purging gas was deoxygenated in two zinc/vanadyl sulfate gas washing bottles. An 8 molal KOH electrolyte solution with 1% LiOH was used for all experiments and was prepared from reagent grade KOH and LiOH in double distilled, deionized water. The small LiOH addition was made to conform with other previously reported battery cycling experiments. Lithium additions are usually regarded as beneficial to porous electrode performance (Ref. 13,14,15,) although recent experiments (Ref. 16) showed little effect on capacity during cycling.

All potentials reported here are relative to the Hg/HgO reference electrode. A paste of Hg/HgO was inserted in a PTFE container above the solution, and contact with the electrolyte was provided by cotton fibers in a PTFE capillary. No liquid junction correction was required with

this arrangement, since the reference and working electrodes were in contact with the same electrolyte. From the reaction

$$HgO + H_2O + 2e^- \rightleftarrows Hg + 2OH^- \quad (7)$$

the potential of the Hg/HgO reference in 8 molal KOH was calculated to be -0.008V (SHE) using the following values for the activity of water and OH^-: $a_{H_2O}(298°K, 8m\ KOH) = 0.5545$, $E° = 0.0984$ V and $a_{OH^-} = (m_{OH^-})\gamma^*_{\pm} = m_{KOH}\gamma_{\pm} = (8molal)(5.902)$ from Pound et al. (Ref. 17).

Three kinds of nickel working electrodes were used: a planar nickel electrode, rolled and bonded porous electrodes, and sintered porous electrodes. The planar nickel specimen was cut from a rod of 99.5% nickel. It was polished to a 0.05 micron alumina powder finish and was rinsed with distilled water. Typically less than 10 minutes elapsed between polishing and polarizing the sample, and only a few seconds elapsed between solution contact and polarization.

The porous electrodes used in this study were prepared by commercial electrode fabricators. The active material in the rolled and bonded electrodes was supported by a PTFE "web" making up 1 w/o of the total electrode material; the remainder being 30% graphite, 1% cobalt hydroxide, and hydrated nickel hydroxide. The graphite served as the current carrier to the backing plate, and the cobalt was added to increase capacity during cycling (Ref. 18). A capacity of 0.29 A hr/gm was reported based on a one electron transfer from nickel hydroxide to nickel oxyhydroxide. The structural features of the sintered electrodes were very different from the rolled and bonded electrodes. For the former, nickel powder was sintered to a nickel wire mesh, and NiOOH was chemically deposited in the pores. The sintered nickel metal (and not graphite) carried the current to/from the wire mesh, which served as a backing plate. The capacity was 0.015 A hr/cm^2 projected (flat) area.

Experiments were performed at temperatures ranging from 0 to 100°C. The temperature was controlled to within ± 2°C as indicated by a thermocouple inside the test cell.

Cyclic Voltammetry

Only planar nickel electrodes were studied by cyclic voltammetry. Freshly polished nickel electrodes were inserted into the cell and, on contact with the electrolyte, were polarized to -850 mV. The solution and cell were then heated or cooled to the desired temperature. After temperature stabilization, a triangular potential/time perturbation was applied to the cell via a coupled function generator and potentiostat.

Various sweep rates from 1 to 100 mV/s were employed, and the potential was swept from below the hydrogen evolution potential to well

above the oxygen evolution potential before reversing the sweep direction. At a given temperature, E/I traces were first recorded at 100 mV/s, then at progressively lower sweep rates. After the lowest sweep rate voltammogram was recorded, E/I traces were recorded at consecutively higher sweep rates up to 100 mV/s. The voltammograms reported here were reproducible to within ± 3 mV and ± 0.5 mA/cm^2 on the potential and current scales, respectively.

AC Impedance Spectroscopy

Impedance data were recorded with either a Solartron 1172 or 1250 Frequency Response Analyzer. For all impedance measurements, the Solartron sine wave output was superimposed on an applied DC bias from a Princeton Applied Research Model 173 potentiostat. Solartron potential and current input leads were taken directly from the cell and not from the potentiostat electrometer and current output jacks. A unity gain voltage follower based on an AD 521J operational amplifier was placed between the cell and the potential input of the Solartron to avoid polarizing the reference electrode. The amplifier had a differential input impedance of 3×10^8 ohms, and a flat frequency response (± 1%) at unity gain to 75 kHz. The voltage follower was accurate to 0.1 mV DC relative to a digital voltmeter.

Planar electrode impedance spectra were recorded over a range of DC potentials. Impedances were usually measured sequentially without repolishing the electrode between measurements. Electrodes were first polarized for two hours at the lowest potential of a given measurement sequence (typically -150 mV). The impedance spectrum was recorded, followed by a potential step (usually 100 mV) to the next highest potential. After one hour at the higher potential, another impedance spectrum was recorded. This procedure was normally repeated up to about 500 or 600 mV.

Porous electrode impedances were recorded in the fully discharged condition (0 mV). They were recorded periodically after selected numbers of charge/discharge cycles. The cycling process is described below, and one hour elapsed at constant potential (0 mV) before impedance spectra were recorded.

Charge/Discharge Cycling

Porous electrodes were cycled at constant current using an ECO Model 545 Galvanostat/Electrometer. Various charging currents were used, but the electrodes were always discharged at twice the charge rate. They were usually charged to 100% of rated capacity, and were fully discharged (100% DOD) on each cycle. Four or five "conditioning" cycles were completed before impedance data were recorded.

The galvanostat provided for automatic current reversal at selected potentials by presetting front panel potentiometers. However, in most cases, it was necessary to use constant charging and discharging

times. Two timers were used to control switches connected to charge and discharge trigger inputs on the galvanostat. When charging efficiency was less than 100%, it was necessary to stop the discharging current before the end of the set discharge time. A voltage comparator based on an LM 311 amplifier was constructed and included in the timer circuitry to stop the discharging current prematurely at any selected potential until the next charging cycle started.

RESULTS AND DISCUSSION

Planar Electrodes - Cyclic Voltammetry

Cyclic voltammetry was used to determine the extent of oxygen evolution during nickel hydroxide oxidation. Oxygen evolution is a parasitic reaction during charging of nickel battery electrodes, and oxygen gas bubble formation may contribute to electrode degradation by generating internal stresses within the electrode pores. The large KOH concentration and elevated temperatures used in this study serve to enhance oxygen evolution by decreasing the overpotential.

For most cycling experiments, only one anodic oxidation peak, appearing at about 500mV, was recorded prior to oxygen evolution. Similarly, only one oxyhydroxide reduction peak at about 300mV was observed on the reverse sweep. Similar voltammograms have been reported for nickel in various alkaline solutions (Ref. 14,19).

At the highest sweep rate of 100mV/s, no steady state voltammogram was observed even after cycling continuously for over 19 hours (Figure 3). Both the anodic peak currents and anodic charge were found to increase steadily with time, but at a decreasing rate. Cathodic peak currents and the associated cathodic charge were difficult to determine since the cathodic current base line was obscured by the oxygen evolution current. However, minimum and maximum values for the cathodic parameters were estimated. For the first few tens of cycles, results indicate that more charge is consumed during hydroxide formation on the cathodic sweep than is liberated during oxyhydroxide formation on the preceding anodic sweep ($q_c > q_a$). This is possible if oxygen becomes trapped within the film or does not desorb from the film/electrolyte surface rapidly, and is reduced during the subsequent cathodic sweep (Ref. 20). After several additional cycles, the anodic charge becomes larger than the cathodic charge ($q_a > q_c$). This suggests that athe nickel substrate oxidizes during cycling and possibly that some film dissolution occurs.

Cycling time at 100 mV/s had only a minor effect on the proximity of the hydroxide oxidation peak to the oxygen evolution line at ambient temperature. The anodic peak potentials initially decreased and then increased with cycling time, but overall the changes were small, as indicated in Figure 3.

Anodic peak potentials were closer to oxygen evolution curves at higher temperatures. Figure 4 shows voltammograms at 0, 45, and 100°C after 10 cycles at 100 mV/s. Nickel hydroxide oxidation and oxygen evolution are within about 100 mV at 100°C compared with more than 200 mV at 0°C. The separation decreases primarily because of the shift in the equilibrium potential for oxygen evolution to more negative values and a decrease in the overpotential for this reaction. Furthermore, at higher temperatures, the anodic peak shifts closer to the oxygen evolution line with increasing cycle time (Figure 5). In a relatively short time, the anodic peak disappears completely from the voltammogram trace (Figure 6), although the presence of the cathodic peak indicates that nickel hydroxide oxidation occurs simultaneously with oxygen evolution. At 100°C, anodic peak shifting is even more rapid, while at 0°C virtually no peak shifting with cycle time is observed.

As noted by Macdonald and Owen (Ref. 21) and by McKubre and Macdonald (Ref. 19), the reversible potential for oxygen evolution is more negative than that for $Ni(OH)_2/NiOOH$ at all temperatures of interest. The appearance of the nickel hydroxide oxidation peak on the voltammograms is due to a high overpotential for oxygen evolution. However, as the temperature is increased, the overpotential is reduced, such that at 80°C and after extensive cycling a distinct oxidation peak is no longer observed. This phenomenon may have serious consequences for porous nickel electrode performance in concentrated alkali solutions at elevated temperatures, because oxygen evolution in the pores will occur simultaneously with charging. As noted previously, gas formation within the pores may contribute significantly to internal tensile stresses that can rupture particle-particle ohmic contacts within the active mass. Also, oxygen evolution represents a significant parasitic process that will lower the coulombic efficiency of the porous electrode over a charge/discharge cycle.

The anodic charge and peak current associated with nickel hydroxide oxidation increase considerably at higher temperatures, suggesting that more active material is present on the electrode surface. If film thickness is assumed to be proportional to anodic charge, then thicker films are formed at higher temperatures in a given number of cycles. A proportionality between charge and film thickness is supported by the work of McKubre and Macdonald (Ref. 19) where no evidence of film dissolution in rotating ring disc experiments is reported. This indicates that an increased battery electrode capacity might be anticipated if battery electrodes are operated at higher temperatures, but of course any advantage may be offset by the decrease in the oxygen evolution overpotential noted above.

Planar Nickel Electrodes - AC Impedance Spectroscopy

The transmission line model requires a knowledge of the interfacial electrolye/pore wall and electrolyte/backing plate impedances. It is assumed in this work that these impedances can be described by the impedance of a planar electrode in the same electrolyte. This

assumption can be supported by several arguments. First, neglecting pore wall curvature, the basic structure of the sintered battery electrode at the electrolyte/pore wall interface, consisting of the metal, film, and electrolyte, should be similar to that for a planar electrode. The structure of the rolled and bonded porous electrodes deviates somewhat from this geometry but it is similar if the graphite is regarded as a substitute for the metal phase. Second, a concentrated electrolyte was selected for this study, so electrolyte depletion within the pores of the porous electrode should be minimal, particularly after one hour at constant DC bias prior to the measurement of the AC impedance spectra. The electrolyte concentration at the pore wall should be approximately the same as that at the film/electrolyte interface for a planar electrode.

In this study, an equivalent circuit for planar electro-oxidized (thin) film electrode impedances is used as the interfacial impedance input to the transmission line model. It can be argued that planar thick film electrode impedances should be used, since the active material in nickel battery electrodes is typically chemically or electrochemically deposited to a relatively large thickness within the pores. However, thick films themselves can be porous. Electro-oxidized thin films have comparatively smooth surfaces and are more suitable for use as interfacial impedances in the transmission line model.

Impedance spectra were recorded in sequences of increasing applied DC bias. Figures 7 and 8 show a typical sequence of ambient temperature Bode plots of log $|Z|$ vs. log ω, and phase angle vs. log ω, respectively, where $|Z|$ is the impedance magnitude, ω is the angular frequency ($2\pi f$), and the phase angle is the arc tangent of the ratio of the imaginary and real parts of the measured impedance. Impedance magnitudes are found to decrease with increasing potential, and a large decrease is observed when the nickel oxyhydroxide phase is formed at 500 mV. Phase angles generally show two maxima within the frequency range studied. The high frequency maximum shifts sharply to lower frequencies at 500 mV corresponding to the film transformation from nickel hydroxide to oxyhydroxide. However, both the magnitudes and the phase angles exhibit similar features above and below the nickel hydroxide/oxyhydroxide transition.

Impedance data were relatively unaffected by the potential step increments used in the DC bias sequences. In one test sequence, an electrode was polarized at 0 mV for one hour prior to an impedance spectrum measurement, then was cycled potentiodynamically between -800 mV and 600 mV at 100 mV/sec for 90 minutes. Following this, the impedance spectrum was again recorded at 0 mV after a one hour polarization at this potential. Both impedance spectra were virtually identical indicating that prior polarization to higher potentials does not significantly affect the planar electrode impedance spectra. It also suggests that charge/discharge cycling in of itself will not significantly affect the solution/pore wall impedance in the transmission line model.

Planar electrode impedance spectra were also recorded at other temperatures (Figures 9 and 10). Spectra were similar at all temperatures from 23°C to 100°C. However, at 0°C the high frequency relaxation shifted markedly to lower frequencies, and only the beginning of the low frequency relaxation is observable at the minimum frequency employed (6 mHz). At higher temperatures, higher minimum frequencies were used to avoid data scattering from noise, and again only the beginning of the lower frequency relaxation is observable. Despite the restricted view of the low frequency relaxation, the features of the elevated temperature data appear very similar to the ambient temperature spectra discussed above.

The planar electrode impedance spectra described above were modeled with the equivalent circuit shown in Figure 11. Mathematical impedance expressions derived from this circuit were used in the transmission line model, together with best fit component values (ie. capacitances, resistances and Warburg coefficients) obtained from a curve fitting technique.

An (infinite thickness) Warburg diffusion impedance was used in the equivalent circuit because previous results by Chao, Lin, and Macdonald (Ref. 22), Liang et al (Ref. 23), Madou and McKubre (Ref. 8), and Zimmerman et al. (Ref. 7) indicated that a diffusion impedance dominated the low frequency spectra over a wide potential range. Best fit component impedance values in each of the equivalent circuits were determined by minimizing the weighted sum of squares differences between the experimental and calculated impedance data. An example of fitted data using the circuit shown in Figure 11 and a spectrum recorded at 0 mV DC bias is shown in Figure 12. Clearly the essential features of the experimental data are reproduced by the model. Table 1 lists the best fit equivalent circuit parameter values at several potentials.

Porous Battery Electrode Impedances

The transmission line model (TLM) contains eight independent variables. Two of these variables are the pore wall and backing plate interfacial impedances that are taken as planar nickel electrode impedances in this study. Planar electrode impedances are each described by four component impedance elements that may be frequency and DC bias dependent, as described in the previous section. A total of 16 independent variables are used to describe the impedance of porous nickel battery electrodes.

The TLM is used in this section to model porous electrode degradation processes. Each of the 16 variables in the model were first determined as accurately as possible in separate experiments. Impedance spectra were then calculated from the model and were compared to porous nickel electrode impedance spectra. Adjustments to key parameters allow the calculated spectra to progressively follow experimental impedances during degradation induced by galvanostatic cycling at various

temperatures. The TLM clearly showed cycle dependent trends in several variables, and these trends are consistent with experimental observations, as described below.

Initial estimates of transmission line model parameters for rolled and bonded electrodes were selected as follows:

1. Pore wall and backing plate impedances, Z and Z', can be represented by planar electrode frequency dispersions from either experimental data or best fit calculated data derived from the equivalent circuits shown in Figure 11. The circuit shown in Figure 11 and its best fit component values (Table 1) at 0 mV DC bias were selected for this work.

2. Scanning electron microscope examination of rolled and bonded electrodes indicated that about 15000 pores were visible (at 100X) on electrodes of area 1.27 cm^2 given two "conditioning" charge/discharge cycles to their rated capacity. The smallest pores on the electrode surface could not readily be resolved at 100X and were not counted.

3. The initial average pore length, ℓ, was approximated as the thickness of the electrodes (0.11 cm).

4. The projected electrode area was 1.27 cm^2 for rolled and bonded electrodes.

5. The total surface area of a rolled and bonded electrode after two conditioning cycles was found to comprise approximately 33% pores.

6. The KOH concentration in the pores was assumed to be constant along the length and radius of the pores since a high KOH concentration was used. While this assumption may not be strictly obeyed, the KOH/H_2O conductivity data of Lown and Thirsk (Ref. 22) shows that a 60% increase in conductivity is realized by halving the KOH concentration from 8 molar to 4 molar. This is within a factor of two. Therefore, the solution resistivity was approximated as a constant of 3.1 ohm cm for an 8 molar solution from the Lown and Thirsk data.

7. The solid phase resistivity, ρ_m, was difficult to estimate. The rolled and bonded electrodes contain principally graphite and nickel hydroxide. Graphite has a resistivity of about 0.0014 ohm cm (Ref. 25) while the resistivity of nickel hydroxide can be as much as ten or twelve orders of magnitude larger at 0 mV as indicated by planar electrode impedances. In this work, the

graphite was assumed to determine the solid phase resistivity, so an initial estimate of ρ_m was taken as 10 ohm cm.

Bode plots calculated by direct substitution of the above parameters in the TLM were compared with impedances for a rolled and bonded electrode cycled twice at 23°C, with 40 minutes charging to rated capacity, and 20 minutes for 100% depth of discharge (DOD). The experimental impedance spectrum was measured after the electrode was held in the fully discharged condition at 0 mV for one hour. The features of the experimental impedance spectrum were present in the calculated spectrum. However, the fit of the calculated curve was relatively poor. Parameter value assignments were adjusted with a design optimization software package (OPTDES) written at Brigham Young University. OPTDES uses a set of design variables to minimize or maximize one or more objective functions defined by the user in a user-supplied Fortran subroutine. Four optimization algorithms were used in succession for each curve fitting.

OPTDES was used to minimize the sum of squares residuals (in the Nyquist plane) defined as the objective function in the Fortran subroutine. In a typical optimization sequence, interfacial and backing plate impedances for 0 mV applied DC bias plus the electrode area were first held constant, while the remaining variables were optimized. Then some or all of the component impedances in the interfacial and backing plate impedance expressions were allowed to vary along with the other design variables.

Curve fitting procedures indicated that small adjustments to several parameters significantly reduced the sum of squares error between the experimental and calculated impedance spectra (Figures 13 and 14). These parameter adjustments from the initial value assignments are discussed below.

1. The pore length, ℓ, required for the "best" fit of the experimental data is about three times the electrode thickness (0.35 cm compared with 0.11 cm thickness). This suggests that tortuosity along the pores increases the active pore length by this amount.

2. The best fit number of pores is about 23000, whereas about 15000 pores could be resolved in a 100X SEM photomicrograph. This may indicate that smaller pores (not counted in the photomicrograph) are not inactivated by their relatively larger solution resistance, $\rho_s l/a$, where a represents the cross sectional area of a pore.

3. The optimized surface coverage of pores ($1-\theta$) was 0.33. This is in good agreement with the initial estimate of 0.3.

4. From Equation 4, the average pore radius can be calculated from the optimized number of pores and the surface coverage fraction of pores given above. The calculated average radius is 24 μm, which agrees well with the pore sizes observed in the SEM photomicrographs.

5. The optimized resistivities of the solid and solution phases were 9.3 and 4.5 ohm cm, respectively. Predicted values were 10 and 3.1 ohm cm, again in reasonable agreement.

6. The pore wall impedance, Z, required a small change to improve the fit with experimental data. Specifically, the smaller (high frequency) capacitance was decreased to about 7 μF from 43 μF at 0 mV DC bias. The latter number was obtained from the 0 mV, 23°C planar electrode impedance spectra as described in the previous section. Smaller capacitances (around 29 μF) were obtained in a similar manner for planar electrode impedances at lower potentials (-150 mV). Therefore, the smaller capacitnce required to fit the porous electrode data at 0 mV may be due to the potential drop across the porous electrode. The pore wall impedance input to the TLM represents an interfacial impedance averaged along the pore wall. If a potential drop occurs along the pore, then the pore wall impedance expression is selected at the average potential. The decreased (optimized) capacitance suggests that the average potential is lower than 0 mV, and therefore, that a potential drop exists across the electrode. Experimentally, the porous electrode is polarized anodically at 0 mV, so the sign of the potential drop predicted by the TLM is in agreement with that imposed on the electrode in the cell.

7. The backing plate impedance, Z', had little effect on the shape of the calculated impedance spectra. This result supports the previous findings of a large pore length, and a large number of pores. Both of these parameters are proportional to the average solution resistance per pore ($\rho_s n\ell/(1-\theta)A$) and when large cause a redirection of current to the solid phase (away from the solution/backing plate interface.)

8. The remaining variables in the pore wall interfacial impedance (specifically the resistance, R, capacitance, C_1, and Warburg coefficient in Figure 12 were not optimized. Attempts to optimize these variables always resulted in slightly smaller sum of squares error, but with simultaneous distortions of the calculated

spectrum. The optimization software found pathways to reduce the sum of squares error by skewing the features of the calculated spectrum. This may indicate that the best fit curves shown in Figures 13 and 14 represent only localized sum of squares minima and that a better fit might be found. More likely, it shows only that the optimization software can, in some cases, reduce sum of squares residuals on curves with complex shapes by unrealistic (albeit creative) manipulation of a large number of variables. In this study, the reproduction of the essential features of the experimental impedance spectrum is considered more important than a smaller sum of squares error.

Cycle Dependence

Impedance spectra for rolled and bonded electrodes at ambient temperature are shown in Figures 15 and 16 after 2, 12, and 27 galvanostatic charge/discharge cycles. Impedance magnitudes increase with cycle number at intermediate frequencies, while phase angle maxima decrease at low frequencies and increase at high frequencies. This behavior can be modeled by optimizing TLM parameters to minimize the sum of squares error between experimental and calculated impedance data. Parameter adjustments are discussed below:

1. The optimized active pore length decreased from 0.35 to 0.28 to 0.20 cm after cycles 2, 12, and 27, respectively. A considerable amount of the active material had spalled from the electrode by the end of 27 cycles, and was found scattered throughout the test cell. This could account for the decreased pore length. However, the electrode also swelled during the test, and after 27 cycles, the net thickness at the center of the electrode was actually larger than the original thickness. The active material remaining on the surface of the electrode was easily flaked off, suggesting that the solid phase particles farthest from the backing plate were not active. The solid phase resistivity between these outer particles may have been so large that they did not participate in the electrochemical processes, and the pore length effectively decreased.

2. Cycle dependent adjustments to the solid phase resistivity, ρ_m, supports the above assertion that the outer particles were not active. The average solid phase resistivity changed from 8.9 to 13.2 to 12.4 ohm cm after 2, 12, and 27 cycles. The increase from the initial value is readily explained by particle-particle bond damage or breakage during the swelling process. Sloughing of the outer particles suggests that a

resistivity gradient developed across the electrode, with the highest resistivity at the outer particles.

3. Optimized solution resistivities, ρ_s, remained virtually constant throughout the cycling process. Resistivities after 2, 12, and 27 cycles were 4.5, 4.9, and 4.0 ohm cm, respectively. Cycle independence was predicted since the KOH concentration was large making electrolyte depletion or exhaustion within the pores unlikely.

4. TLM modeling showed that the number of active pores, n, decreased from 23000 to 8500 to 3300 during this cycling sequence. A reduced number of active pores with cycling might be explained by "restructuring" and solid phase particle-particle bond breakage which inactivates many of the pores.

5. The optimized pore coverage fraction, $(1-\Theta)$, decreased slightly during cycling, from 0.33 to 0.27, and 0.25 after 2, 12, and 27 cycles. This is also consistent with the gradual inactivation of pores during cycling.

6. According to the TLM, the potential drop across the porous electrode diminished somewhat with increasing cycle number. The optimized smaller capacitance in the pore wall interfacial impedance increased from 7 uF after cycle 2, to 34 uF after cycle 27. This indication of a cycle dependent decreasing potential drop is also readily explained. The resistance of the solid and solution phases per pore ($\rho_m n l/\Theta A$ and $\rho_s n\ell/(1-\Theta)A$, respectively) can be regarded as indicators of the potential drop across the porous electrode at a given DC bias. Both resistances decrease with increasing cycle number principally because of the decreasing pore length and number of pores, and the potential drop decreases accordingly.

Temperature Dependence

AC impedance spectra for rolled and bonded electrodes at 0 mV were measured at 0 and 40°C during their cycle life. The data had the same features as those at ambient temperature, suggesting that electrode degradation processes are similar at these temperatures.

No rolled and bonded impedance spectra were successfully recorded at 60°C or at 100°C. Electrodes failed in less than one or two cycles, and each test was terminated before impedance spectra were recorded. Failure was associated with severe spalling of the active material and the inability of the electrode to carry the imposed galvanostatic current within the output voltage range provided by the galvanostat.

The cyclic voltammetric results presented earlier show that oxygen evolution occurs rapidly during nickel hydroxide oxidation at 60°C and higher temperatures. Oxygen evolution and the associated bubble pressures within the pores are apparently major contributors to the rapid electrode degradation at higher temperatures. Slow swelling and sloughing at lower temperatures may also be related to the relatively slower oxygen evolution reaction rate.

Porous Sintered Electrode Impedances

Sintered electrodes behaved quite differently from rolled and bonded electrodes. At all temperatures between 0 and 60°C, impedance spectra were independent of cycle number and galvanostatic cycling current. However, sintered electrodes failed abruptly. The only indication of an impending failure was a slight wavering of the electrode potential versus time curve recorded during the galvanostatic cycles just preceding failure. Even after failure, no sloughing or swelling was observed. Generally, the performance of the sintered electrodes rated in terms of cycle life were far superior to rolled and bonded electrodes. However, breakdown also occurred rapidly at 100°C, presumeably due to oxygen evolution within the pores.

SUMMARY AND CONCLUSIONS

Transmission line modeling results indicate a set of parameter changes with cycle number that are consistent with experimental observations. Initial estimates and measurements of individual parameter values compare favorably with parameter values determined by curve fitting to real rolled and bonded electrode impedances at 0 mV and at 23°C. Rolled and bonded electrode impedances measured at 0 and 40°C behave similarly to those at ambient temperature, and similar parameter changes with cycle number are indicated.

Specific changes with cycle number at 23C are:

1. The average pore length decreases with cycle number, but always remains larger than the thickness of the electrode.

2. The average solid phase resistivity increases with cycle number.

3. The solution resistivity within the pores remains virtually unchanged during the cycle life of the electrodes.

4. The number of active pores decreases during cycling.

5. The average resistance per pore of the solution and solid phases decreases during cycling, and the potential drop across the electrode decreases accordingly.

6. The total porous electrode impedance is relativley insensitive to the solution/backing plate interfacial impedance. This indicates that little current flows along the entire pore length in the solution.

Rolled and bonded electrodes break down rapidly when cycled at 60 and 100°C. Cyclic voltammetric results at elevated temperatures show that the oxygen evolution reaction proceeds at a significant rate concurrent with the electrode charging reaction after the first few voltammetric cycles. Rapid rolled and bonded electrode breakdown during galvanostatic cycling at elevated temperatures is probably due to parasitic oxygen evolution processes.

Conversely, sintered electrode impedances do not change during galvanostatic cycling, and failures occur abruptly after a relatively large number of cycles. However, breakdown also occurred rapidly at 100°C, indicating that oxygen evolution processes may also affect sintered electrode cycle life.

ACKNOWLEDGMENTS

The work reported in this paper was carried out at The Ohio State University in partial fulfillment of the requirements for a Ph.D. degree in Metallurgical Engineering by S. Lenhart. The authors gratefully acknowledge the financial support of this work by The U.S. Dept. of Energy through LBL under Contract No. 712955.

REFERENCES

1. Katz, M. H., McLarnon, F. R., Cairns, E. J., in Battery Division Extended Abstracts, The Electrochem. Soc., Fall Meeting, Oct. 17-21, 1982, p. 24.

2. Silverman, D. C., Corrosion , Vol. 37, No. 9, Sept. 1981, pp. 546-548.

3. Glarum, S. H., Marshall, J. H., J. Electrochem. Soc., Vol. 129. No. 3, March 1982, pp. 535-541.

4. Weininger, J. L., Breiter, M. W., J. Electrochem. Soc., Vol. 111, No. 6,June 1964, pp. 707-712.

5. Sathyanarayana, S., Venugopalan, S., Gopikanth, M. L., J. Applied Electrochemistry, Vol. 9, 1979, pp. 125-139.

6. Zimmerman, A. H., Janecki, M. G., in "Proceedings of the Symposium on The Nickel Electrode," Gunther, R. G., and Gross, S. eds., JES, Vol. 82-4, 1982, pp. 199-215.

7. Zimmerman, A. H., et al., J. Electrochem. Soc., Vol. 129, No. 2, Feb. 1982, pp. 289-293.

8. Madou, M. J., McKubre, M.C.H., J. Electrochem. Soc., Vol. 130, No. 5, May 1983, pp. 1056-1061.

9. De Levie, R., Electrochimica Acta, Vol. 8, 1963, pp. 751-780.

10. De Levie, R., in "Advances in Electrochem. and Electrochem. Eng.," P. Delahy, ed., Vol. 6, Interscience, New York, 1969, pp. 329-398.

11. Lenhart, S. J., Chao, C. Y., Macdonald, D. D., in "Proceedings 16th Intersociety Energy Conversion Engineering Conference, ASME, New York, Aug. 9-14, 1981, pp. 663-666.

12. Park, J. R., Macdonald, D. D., Corrosion Science, Vol. 12, No. 4, 1983, pp. 295-315.

13. Tuomi, D., J. Electrochem. Soc., Vol. 112, No. 1, Jan. 1965, pp. 1-12.

14. Weininger, J. L., in "Proceedings of the Symposium on the Nickel Electrode," Gunther, R. G. and Gross, S. eds., J. Electrochem. Soc., Vol. 82-4, 1982, pp. 1-18.

15. Takehara, Z., Kato, M., Yoshizawa, S., Electrochimica Acta, Vol. 16, 1971, pp. 833-843.

16. Maskalick, N. J., Buzzelli, E. S., in Battery Division Abstracts, The Electrochem. Soc., Fall Meeting, Oct. 17-21, 1982, p. 24.

17. Pound B. G., Singh, R. P., Macdonald, D. D., J. Power Sources, Vol. 18, p. 1 1986.

18. Pickett, D. F., U.S. Air Force Technical Report AFAPL-TR-75-34, Part I, Oct. 1975.

19. McKubre, M.C.H., Macdonald, D. D., J. Energy, Vol. 5, 1981, p. 368.

20. Sattar, M. A., Conway, B. E., Electrochemical Acta, vol. 14, 1969, pp. 695-710.

21. Macdonald D. D., Owen D., "The Electrochemistry of Nickel Metal in Lithium Hydroxide Solutions at 22, 170, and 250°C." High Temperature High Pressure Electrocemistry in Aqueous Solutions,

Eds. R. W. Staehle, D. deG. Jones, and J. E. Slater, National Association of Corrosion Engineers, Houston, 1976.

22. Chao, C-Y, Lin, L.F., Macdonald, D. D., J. Electrochem. Soc., Vol. 129, 1982, 1874.

23. Liang, R., Pound, B., Macdonald, D. D., Electrochem. Soc., Ext. Abstr., 84-2, 1984, 356

24. Lown O. A., Thirsk H. R., Trans. Farad. Soc., Vol. 67. No. 1, 1971, p. 132.

25. Handbook of Chemistry and Physics, Weast R. C. ed., CRC Press Inc., 1974, p. F 159.

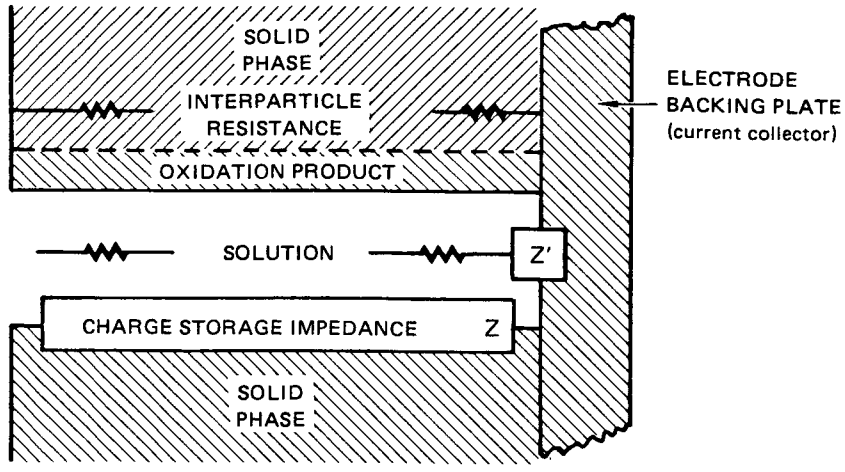

FIGURE 1 RIGHT CYLINDRICAL MODEL OF IDEAL SINGLE PORE

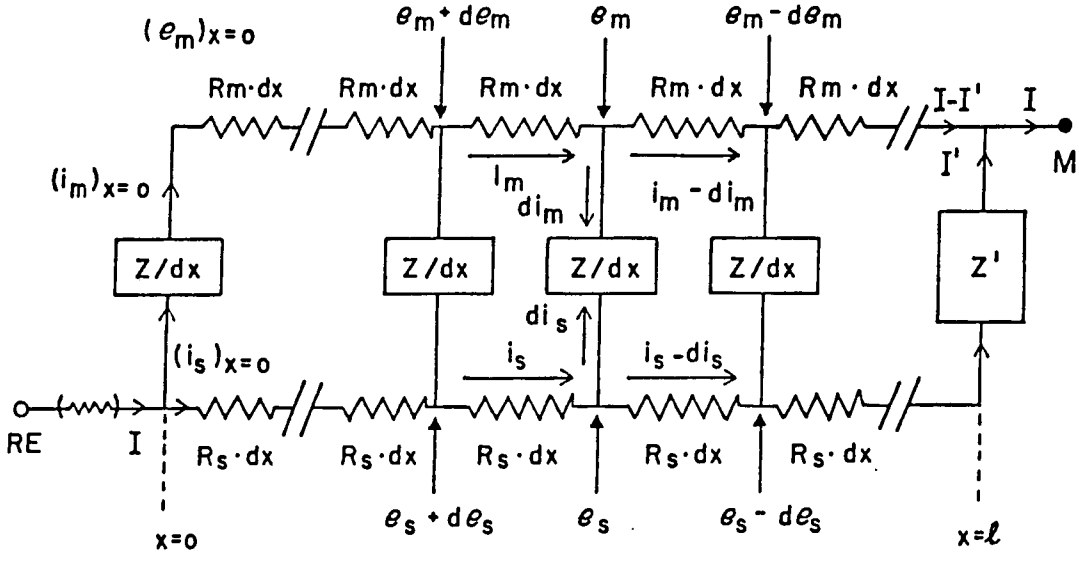

FIGURE 2 DISCRETIZED FORM OF TRANSMISSION LINE MODEL FOR A POROUS BATTERY ELECTRODE OF FINITE THICKNESS

e_m and e_s are potentials in the metal and solution phases respectively.
i_m and i_s are currents in the metal and solution phases, respectively.
I and I' are the total current and the current flowing across the electrode backing plate/solution interface at the base of the pore, respectively.
RE and M designate the reference electrode and current collector locations respectively.

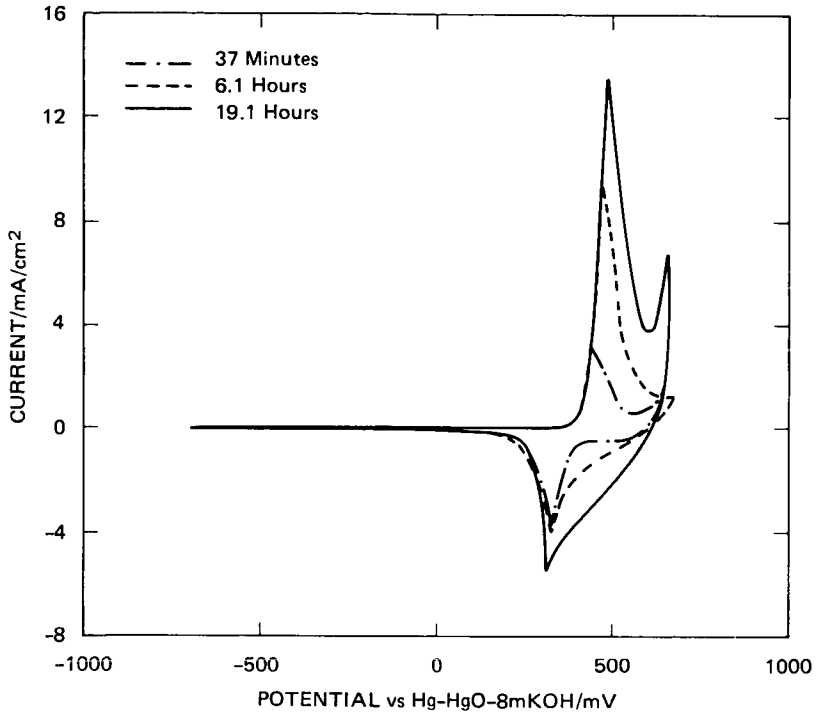

FIGURE 3 VOLTAMMOGRAMS FOR PLANAR Ni ELECTRODE IN 8 m KOH + 1% LiOH AT 23°C AS A FUNCTION OF CYCLING TIME. VOLTAGE SWEEP RATE = 100 mV/s

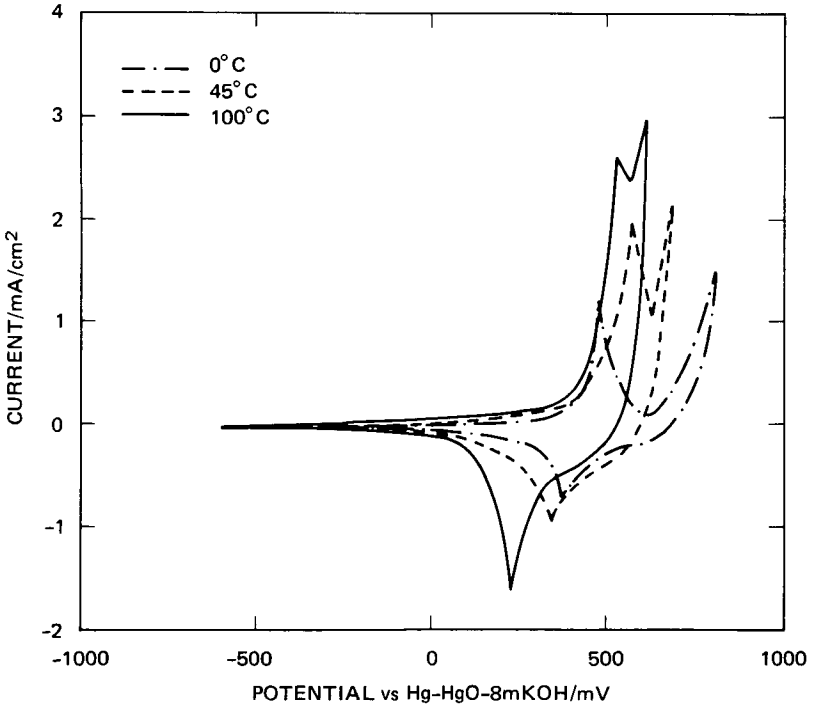

FIGURE 4 VOLTAMMOGRAMS FOR PLANAR Ni IN 8 m KOH + 1% LiOH AT VARIOUS TEMPERATURES AFTER 10 CYCLES AT 100 mV/s

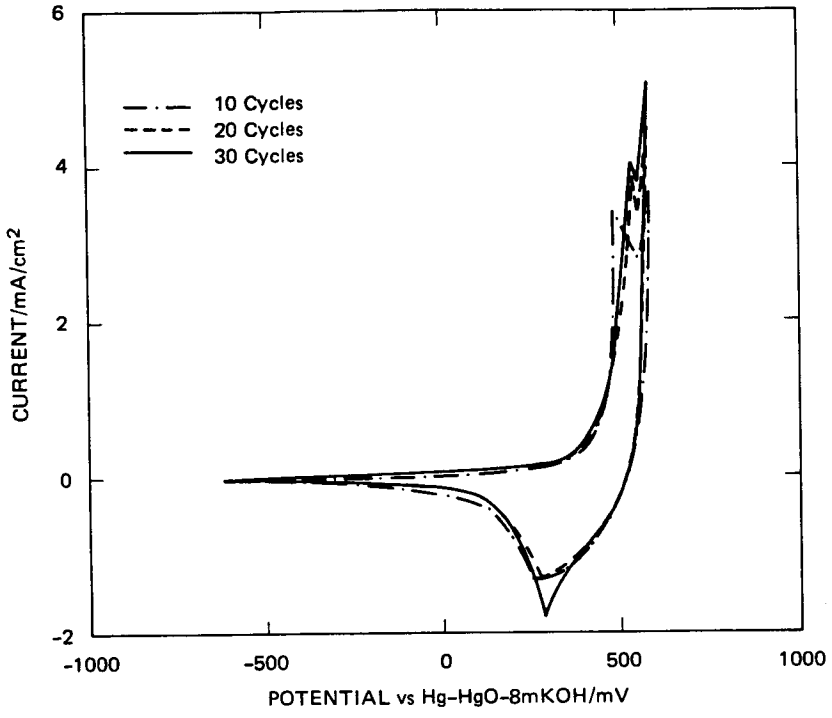

FIGURE 5 VOLTAMMOGRAMS FOR PLANAR Ni IN 8 m KOH + 1% LiOH AT 80°C, 100 mV/s AND 10, 20 AND 30 CYCLES

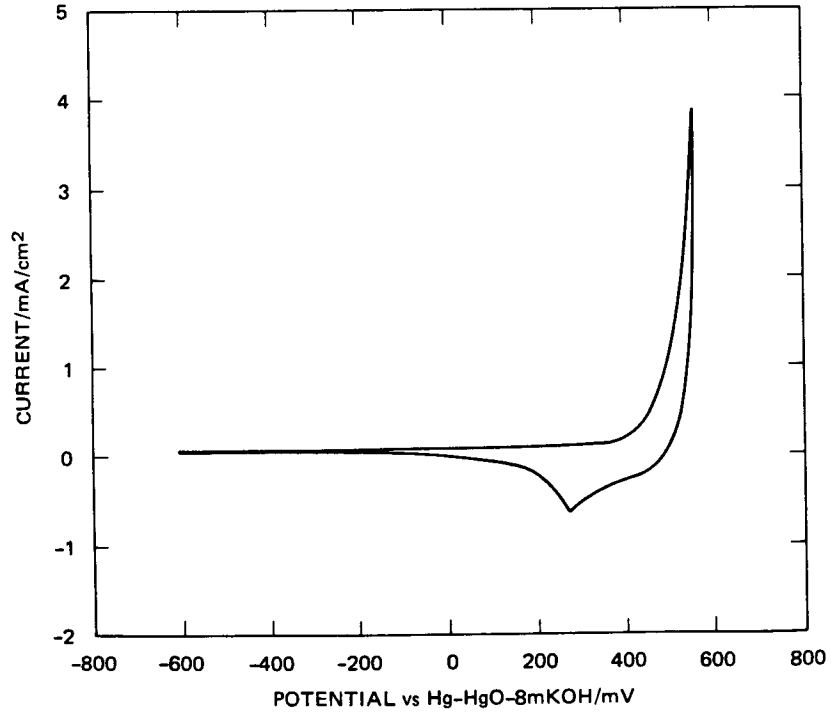

FIGURE 6 VOLTAMMOGRAM FOR PLANAR Ni in 8 m KOH + 1% LiOH AT 80°C, 20 mV/s, CYCLE 81

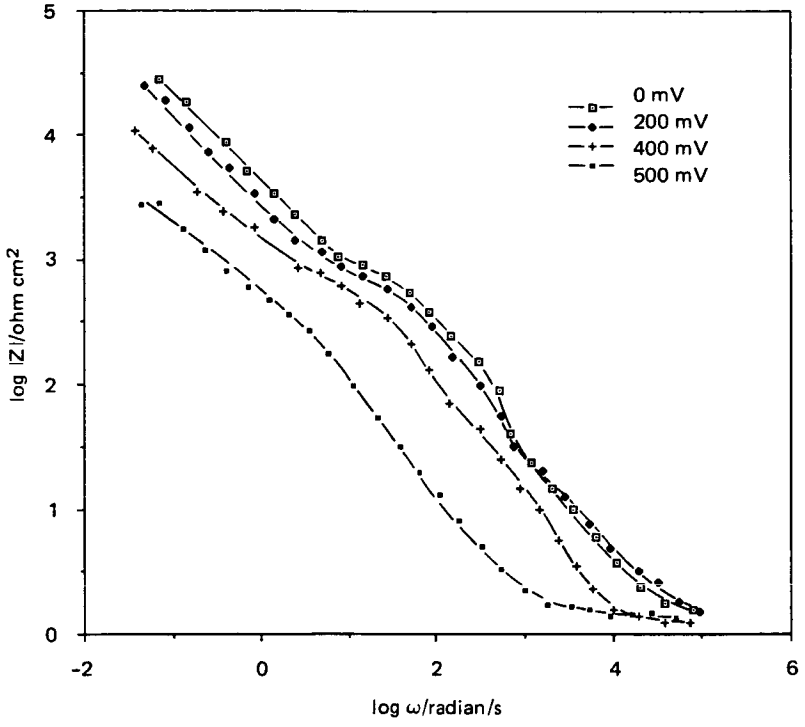

FIGURE 7 AMBIENT TEMPERATURE log |Z| vs log ω DATA FOR PLANAR Ni ELECTRODES IN 8 m KOH + 1% LiOH OVER A RANGE OF APPLIED DC BIAS

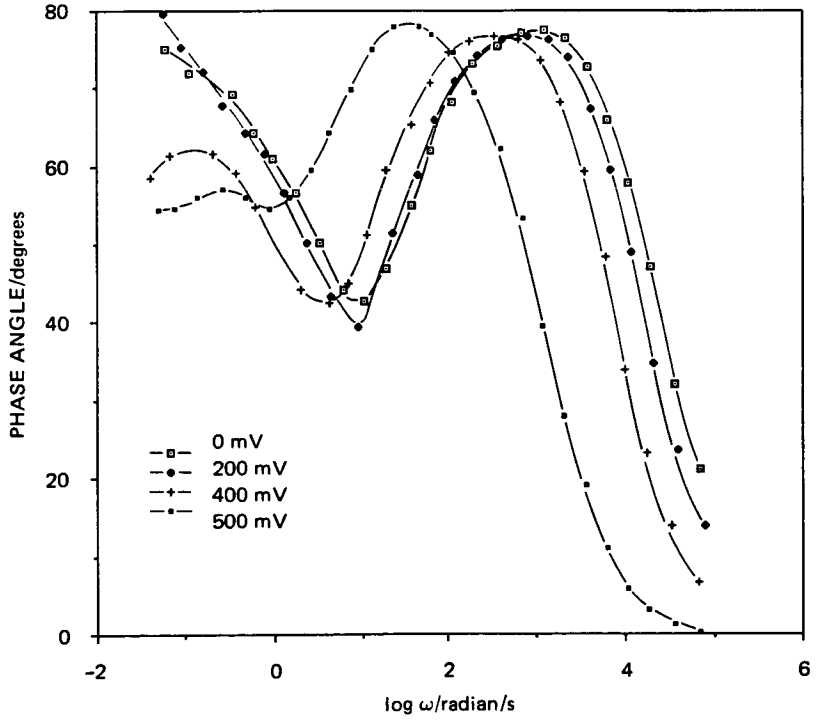

FIGURE 8 PHASE ANGLES CORRESPONDING TO DATA IN FIGURE 7

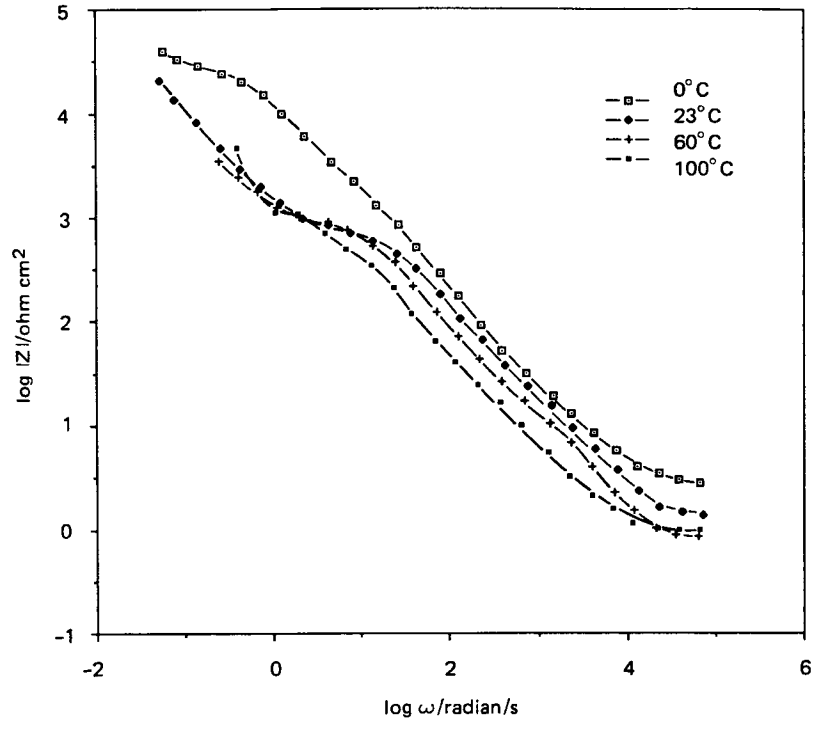

FIGURE 9 IMPEDANCE SPECTRA AT VARIOUS TEMPERATURES FOR A PLANAR Ni ELECTRODE IN 8 m KOH + 1% LiOH AT 200 mV

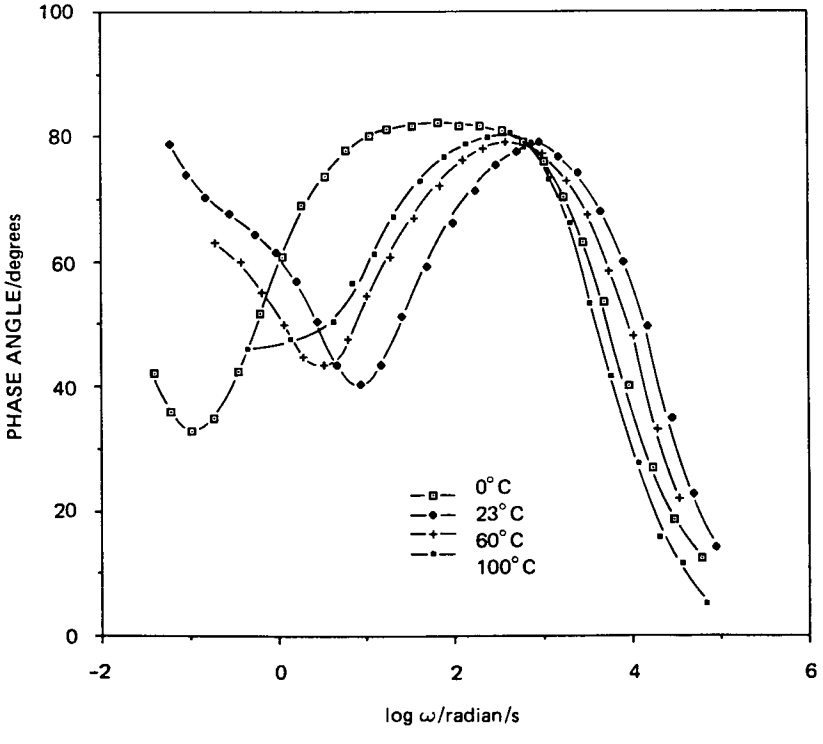

FIGURE 10 PHASE ANGLES CORRESPONDING TO DATA IN FIGURE 9

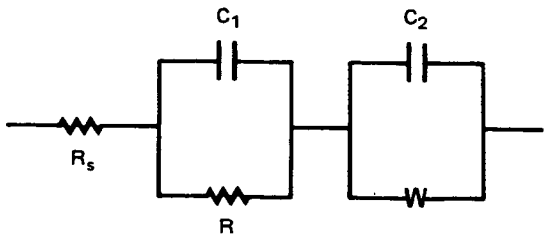

FIGURE 11 AN EQUIVALENT CIRCUIT FOR PLANAR NICKEL ELECTRODE IMPEDANCES IN 8 m KOH + 1% LiOH

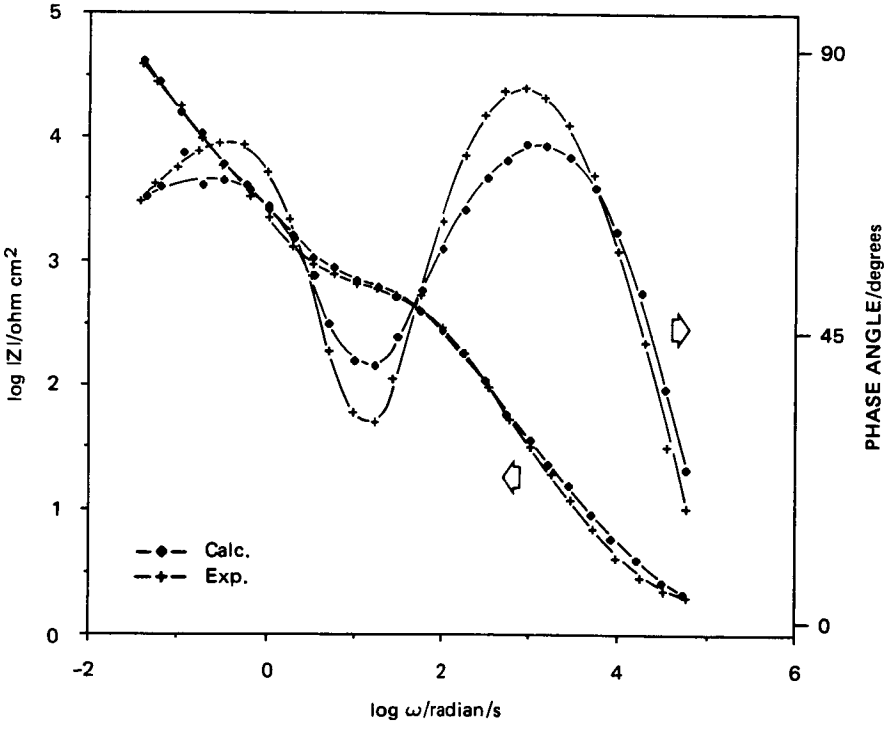

FIGURE 12 EXPERIMENTAL AND CALCULATED IMPEDANCE SPECTRA AT 0 mV APPLIED DC BIAS USING THE EQUIVALENT CIRCUIT IN FIGURE 11 FOR IMPEDANCE CALCULATIONS. (23°C)

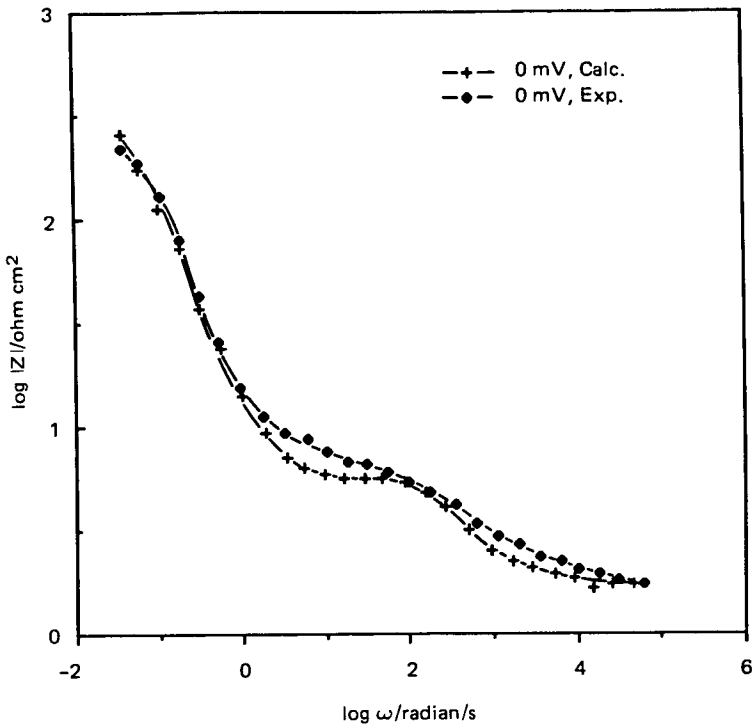

FIGURE 13 EXPERIMENTAL AND CALCULATED log |Z| vs log ω DATA AT 0 mV AND 23°C FOR A ROLLED AND BONDED POROUS ELECTRODE CYCLED TWICE. (40 min CHG TO CAPACITY AND 20 min TO 100% DOD.) CALCULATED SPECTRUM DETERMINED FROM OPTIMIZED TLM PARAMETERS DESCRIBED IN TEXT.

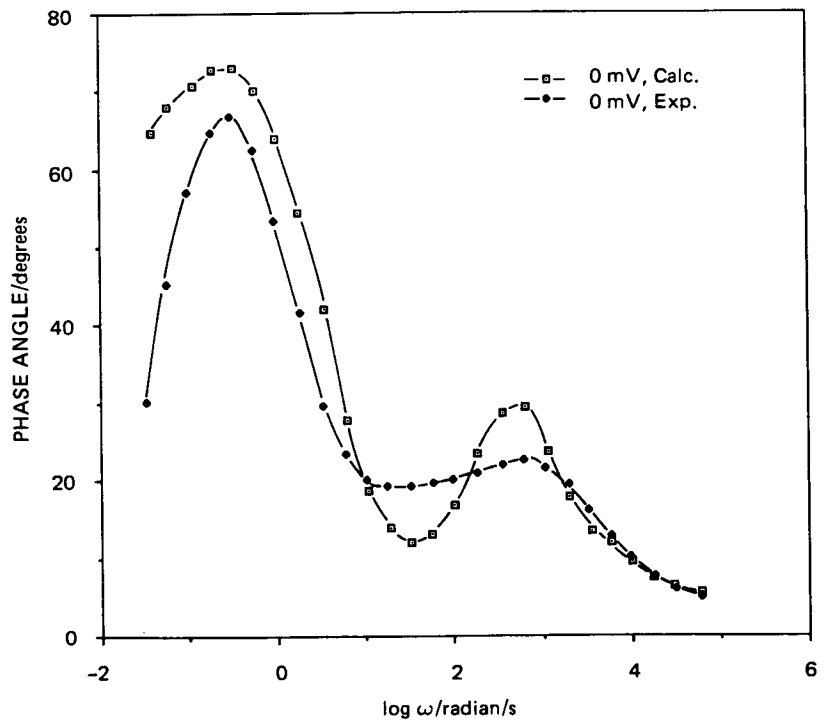

FIGURE 14 PHASE ANGLES CORRESPONDING TO DATA SHOWN IN FIGURE 13

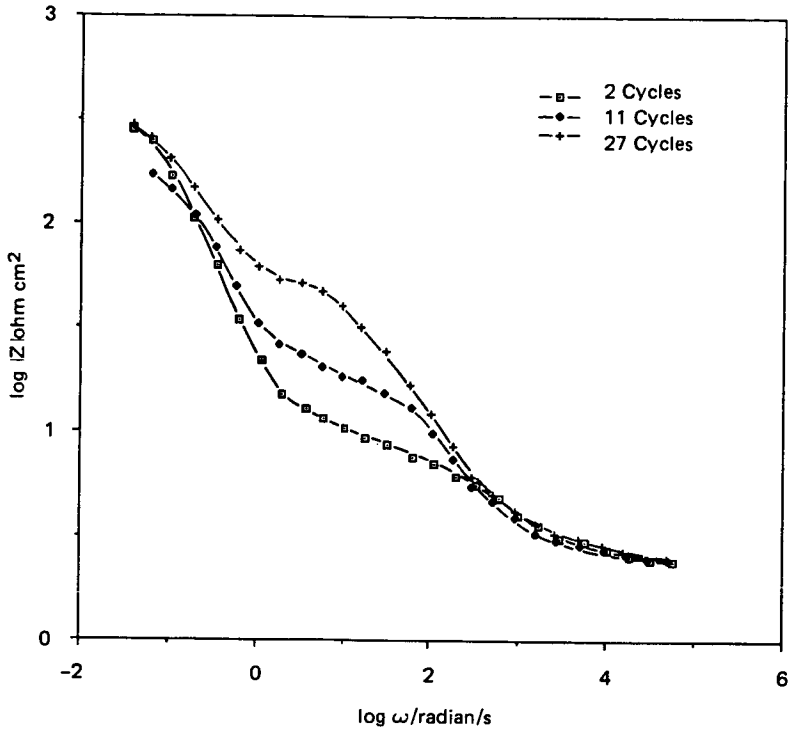

FIGURE 15 EXPERIMENTAL log |Z| vs log ω DATA FOR A ROLLED AND BONDED POROUS ELECTRODE AT 0 mV AND 23°C AFTER VARIOUS CYCLES. (40 min CHG TO CAPACITY AND 20 min TO 100% DOD.)

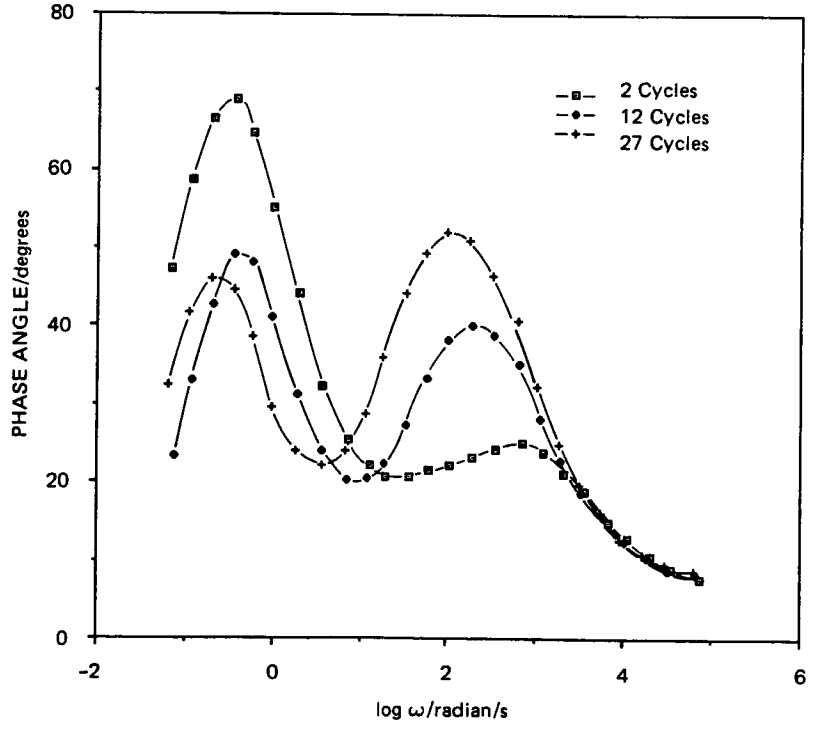

FIGURE 16 PHASE ANGLES CORRESPONDING TO DATA SHOWN IN FIGURE 17

ELECTROCHEMICAL IMPREGNATION OF NICKEL HYDROXIDE IN POROUS ELECTRODES

Kuo-Chuan Ho and Jacob Jorné
The University of Rochester
Rochester, New York 14627

The electrochemical impregnation of nickel hydroxide in porous electrode has been investigated both experimentally and theoretically. The loading level and plaque expansion were the most important parameters to be considered. The effects of applied current density, stirring, ratio of solution to electrode volume and pH have been identified. A novel flow–through electrochemical impregnation is proposed in which the electrolyte is forced through the porous nickel plaque. The thickening of the plaque can be reduced while maintaining high loading capacity. A mathematical model is presented which describes the transport of the nitrate, nickel and hydroxyl ions and the consecutive heterogeneous electrochemical reduction of nitrate and the homogeneous precipitation reaction of nickel hydroxide. The distributions of precipitation rate and active material within the porous electrode are obtained. A semi–empirical model is also proposed which takes into account the plugging of the pores.

INTRODUCTION

Early in the research and development of nickel hydroxide electrodes, effort was focused on achieving high loading of active material into sintered plaques in order to increase the specific energy of battery systems. Higher specific energies were obtained by increasing the sinter porosity, varying the powder type, addition of lightweight inert filler material, and increasing the impregnation rate by raising the solution temperature up to its boiling point. However, higher porosity results in a structurally weak material which cannot endure the stresses involved in impregnation and cycling. In addition, Seiger et. al. [1] have shown that as the plaque becomes more porous, the tendency to blister and shed increases which leads to a decrease in utilization efficiency, i.e., the amount of active material that is electrochemically available during discharge (the measured capacity) divided by the amount of active material impregnated into the porous sintered plaque (the theoretical capacity). They experimentally found that the utilization efficiency linearly depends upon sinter porosity over a wide range of practical porosities used. Ford and Baer [2] have also shown that utilization efficiency begins to decrease markedly at a loading of 2.1 g/cm^3.

In recent years the trend has been to somewhat sacrifice loading in order to achieve longer design life. Lim [3] found that increasing the loading level of the nickel electrode could result in a better initial performance, which is not necessarily an indication of good life performance. This is because several physical changes occur inside the porous structures during cycling, especially at high loading, and adversely shorten the cycle life. These structural changes can be related to the dimensional expansion of the electrode. One may therefore infer that there must exist an optimum loading level for a long nickel electrode cycle life. Indeed, Lim [3]

has shown that the loading level of the active material affects the cycle life of the nickel electrodes, and reported an optimum loading of 1.6 g/cm^3 using the sintered nickel plaque of 82 % porosity and 29 *mils* thickness. At this loading level, only about 40 % of the void volume is actually filled with active material.

With conventional chemical impregnation, it is difficult to deposit the active material inside the pores of the plaque without precipitation in the bulk solution and on the outside of the plaque surface. Studies on cathodic electrochemical impregnation have probably been an impetus of the trend to reduce loading level, since electrodes fabricated by electrochemical impregnation exhibit improved utilization with reduced loading. Nevertheless, with cathodic electrochemical impregnation, it is well known that thickening of plaques usually occurs even after the electrode was freshly manufactured [1, 4, 5, 6]. This is especially true at high impregnation current densities. It has been shown that to some extent agitation does retard the formation of nickel hydroxide on the surface. It may therefore be expected that an electrode impregnated under flow–through conditions would suppress surface loading by sacrificing process efficency. In this study, cathodic electrochemical impregnation has been conducted under various flow configurations. The effect of flow rate on loading level and thickening of nickel electrodes has also been studied.

EXPERIMENTAL

One of the motivating factors in the present approach was to identify the effect of flow on the loading and thickening of nickel electrodes. These topics are important in designing and processing plaques into positive electrodes with higher energy densities and longer cycle life.

Porous sintered nickel plaques supplied by General Electric were used in the flow–through electrochemical impregnation studies. The wettability of the plaques was also tested. Both tube and rectangular–type modified cells were used for the experiments. The only design change has been the connection of the external conduits to the cell ends so that the electrolyte can flow through the cathode. A reservoir containing 100 *ml* of 3.0M $Ni(NO_3)_2$ solution was used in order to provide sufficient electrolyte and regulate the flow. In the tube–type cell, the nickel plaque was screwed in, clamped and tightly sealed with 0–rings between two glass tubes. This procedure frequently caused cracking and damage to the plaque. Later, this problem was solved by using a rectangular–type cell. Another advantage of the rectangular–type cell over the tube–type cell is that the former can operate at a very low flow rate (0.06 $cm^3/cm^2 \cdot min$), using gravity feeding. The tube–type and the rectangular–type cells with the counterelectrode placed in a downstream position are shown in Figures 1 and 2, respectively. By reversing the flow direction, both tube–type and rectangular–type cells can operate with upstream counterelectrode placement. Electrodes were visually inspected after impregnation. Electrode thickness and weight gain were measured in order to characterize the electrodes. The electrode separations in the tube–type and rectangular–type cells were 8.5 *cm* and 4.0 *cm*, respectively. Initially, the *pH* of solution was adjusted to 3.0 or 4.5, depending on the purpose of each run.

Auxiliary experiments have been carried out in a thicker electrode which consists of two nickel electrodes with a counterelectrode placed in the upstream position. The second electrode is made electrochemically inert by winding Teflon tape

around the edges, thus, any $Ni(OH)_2$ particles escaping from the first electrode were collected subsequently by the second electrode, which acts as a filter.

In order to have better utilization of the porous electrode, two–side impregnation was performed under stagnant and flow–through conditions. Figure 3 shows the electrodes and flow configurations. Figure 3(a) represents a stagnant, two–side impregnation where each side was separately impregnated for equal period of time. Figure 3(b) represents a flow–through electrode in an upstream counterelectrode configuration with gravity fed electrolyte. Once again, the impregnation time of each side was the same and the current and flow were always in the same direction.

Finally, experiments were also conducted for two–side impregnation where both sides were impregnated simultaneously. Figure 4 shows the electrode and flow configurations for simultaneous two–side impregnation. Figure 4(a) represents a stagnant, two–side impregnation, while Figure 4(b) represents a flow–through two–side impregnation where the flow was periodically reversed. Thus, each side was alternately exposed to an upstream and downstream positioning of the counter electrode.

RESULTS AND DISCUSSION

Figure 5 compares the loading level under stagnant and flow conditions in a tube–type cell with the counterelectrode placed in the downstream position. In both cases, limiting loading levels were approached, however, lower loading was obtained under flow through conditions ($V_x = 0.30\ cm/min$). Figure 6 shows a similar plot for a stagnant and flow–through impregnation carried out in a rectangular–type cell. Two velocities ($V_x = 0.06\ cm/min$ and $0.30\ cm/min$) were studied and the loading data suggest that the higher the flow velocity, the lower the loading level. The loading curve under flow conditions is characterized by two plateaus. The first plateau is obtained under flow–through conditions, while the second one appears to be reached after the electrode is plugged and can be regarded as a stagnant electrode. The transition region defines the onset time for electrode plugging. The electrode was plugged after 75 *min* operation, as can be seen from Figure 6. This was observed experimentally when the electrolyte overflowed from one compartment to the other. Figure 7 presents the plaque expansion vs. loading level for the three loading curves shown in Figure 6. The experimental results show that a very small flow rate ($V_x = 0.06\ cm/min$) can retard the formation of nickel hydroxide on the surface. Under carefully controlled flow conditions, one might expect to obtain a uniformly distributed $Ni(OH)_2$ precipitation without surface deposit. However, under flow–through conditions the loading level is substantially lower, due to the removal of the newly–formed $Ni(OH)_2$ by convection. Therefore, it is expected that an optimal flow–through velocity exists such that a longer cycle life is achieved by sacrificing loading and by eliminating surface precipitation. It is also expected that the distribution of $Ni(OH)_2$ is more uniform in a flow–through configuration.

Figure 8 presents loading curves for stagnant and flow–through impregnation conducted in a rectangular–type cell with the counterelectrode placed in the upstream position. The shape of the curves is similar to those shown in Figure 6 for a downstream positioning of the counterelectrode. Once again, the overflow of electrolyte was observed. However, in a flow–through operation, an upstream place-

ment of the counterelectrode reached stagnant behavior faster than a downstream placement, 45 *min* for upstream placement as compared to 75 *min* for downstream placement. This is because of the nonuniformity of precipitation and an earlier plugging of the pores. The corresponding plot for plaque expansion vs. loading level is shown in Figure 9. A visual examination of the electrodes after impregnation shows that when the electrolyte flows in the same direction as the current (upstream counterelectrode), a more uniform distribution of active material inside the plaque is obtained as compared to a downstream placement of the counterelectrode in which the electrolyte and current flow in opposite directions. When the counterelectrode is placed in the upstream position, the ohmic potential drop favors precipitation at the front while mass transfer of hydroxyl ions favors precipitation at the back resulting in fairly uniform distribution of active material.

Figure 10 shows the same loading experiment to that in Figure 8 except under a lower initial pH value ($pH_o = 3.0$ vs. 4.5). The experimental data show that the pH_o has little or no effect on the loading level. A plot of plaque expansion vs. loading level with $pH_o = 3.0$, as shown in Figure 11, exhibits a very similar trend as that of $pH_o = 4.5$. This is because the internal pH (inside the pores) does not vary with the external pH (in the bulk), and it is the pH value inside the pores which determines the loading characteristics of the process.

Experimentally, it is interesting to notice that there was always a loss of active material when impregnation was carried out in the flow–through conditions, regardless of the electrode placement. The loss of $Ni(OH)_2$ reaches as high as 50 % compared to the stagnant case, especially before the pores were plugged. The colloidal form of $Ni(OH)_2$ was carried away and precipitated at the bottom of the cell and in the reservoir. Later, the lost active material was collected by an additional porous nickel electrode with insulated edges attached to the working electrode. The flow rate was 0.06 $cm^3/cm^2.min$, and the counterelectrode was placed in the upstream position. It was observed that some of the escaping $Ni(OH)_2$, in powder form of light green color, was presented in the gap between the two electrodes. Agglomerations of this powder, which apparently had escaped from the first electrode, was found randomly distributed over the surface of the second electrode. Weight gain analysis of the first electrode was consistent with the loading data obtained in Figure 8 under the same flow condition. However, the weight gain of the second inert electrode revealed that a significant amount of $Ni(OH)_2$ was hydrodynamically washed out. The weight gain of the two electrodes under flow–through conditions is shown in Figure 12 and compared with the data for stagnant and flow–through operations with a single electrode. The loading with double electrodes under flow–through conditions is higher for the stagnant electrode, apparently because of the continuous supply of $Ni(NO_3)_2$ to the porous electrode in the flow–through case.

Figures 13 and 14 show the loading level and plaque expansion with two–side impregnation for stagnant and flow–through conditions. The data indicated by the blank triangles represents two–side impregnation with time equally divided for each side, while the data with black triangles represent two–side impregnation, where each side receives cathodic impregnation periodically for 2.5 *min*. The trends are similar to the earlier results with one–side impregnation. The electrode becomes plugged after a 45 *min* operation. However, a comparision of Figure 9 with Figure 14 reveals that, regardless of flow conditions, a better electrode can be obtained with two–side impregnation in terms of plaque thickening. At the same loading

level, plaque expansion is reduced by nearly 50 % in two–side impregnation both for stagnant and flow–through conditions. This is because a better utilization of the electrode is achieved in two–side impregnation.

The loading level and plaque expansion for simultaneous two–side impregnation are shown in Figures 15 and 16, respectively. It can be seen that, with a combination of upstream and downstream counterelectrode and a small flow rate ($V_x = 0.06\ cm/min$) can reduce surface loading without significantly sacrificing process efficiency, as shown in Figure 15. However, a close examination after electrochemical impregnation reveals that a moderate plaque thickening does exist even with flow–through operation. This is because stagnant behavior is reached in a very short time (less than 15 min) as a result of pore–plugging and, therefore, further loading of the surface is preferred.

MATHEMATICAL MODEL

Electrochemical impregnation is by nature an unsteady state process owing to structure variation as the process proceeds. The complexity of the problem involving structural change as well as escape of $Ni(OH)_2$ has made a quantitative description difficult. However, pseudo–steady state is a good assumption for porous electrodes under flow–through conditions [7, 8]. In this section, a model of flow–through porous electrode suitable for electrochemical impregnation is presented and the distributions of active material and loading capacity are derived. Finally, a critical, pore plugging time, is analytically calculated at which the porosity at the front of electrode reaches half of its initial value [9]. The predicted plugging time is compared with experimental data. This pore–plugging process is very similar to the one mentioned in the recovery of copper ions [9].

Figure 17 represents flow–through electrochemical impregnation with the counterelectrode placed downstream. $x = 0$ represents the flow inlet and $x = L$ represents the outlet. No precipitation occurs within region I ($0 \leq x \leq \delta_o$), where δ_o is the position of the onset of the precipitation reaction. Precipitation occurs within region II.

The following equations for region I and II can be written as:

$$\frac{\partial(\epsilon C_1)}{\partial t} = \epsilon D_1 \frac{\partial^2 C_1}{\partial x^2} - V_x \frac{\partial C_1}{\partial x} + \epsilon D_1 \frac{\partial}{\partial x}(C_1 \frac{\partial \xi}{\partial x}) - A j_{1n} \tag{1}$$

$$\frac{\partial(\epsilon C_2)}{\partial t} = \epsilon D_2 \frac{\partial^2 C_2}{\partial x^2} - V_x \frac{\partial C_2}{\partial x} - 2\epsilon D_2 \frac{\partial}{\partial x}(C_2 \frac{\partial \xi}{\partial x}) - R_{ppt} U(x - \delta_o) \tag{2}$$

$$\frac{\partial(\epsilon C_3)}{\partial t} = \epsilon D_3 \frac{\partial^2 C_3}{\partial x^2} - V_x \frac{\partial C_3}{\partial x} + \epsilon D_3 \frac{\partial}{\partial x}(C_3 \frac{\partial \xi}{\partial x}) - 2R_{ppt} U(x - \delta_o) + 9A j_{1n} \tag{3}$$

$$-C_1 + 2C_2 - C_3 = 0 \tag{4}$$

$$j_{1n} = \frac{S_1}{nF} i_o [e^{(1-\beta)n\xi} - e^{-\beta n \xi}] \tag{5}$$

$$[\kappa^{-1} + \sigma^{-1}]^{-1} \frac{\partial^2 \xi}{\partial x^2} = \frac{nF^2}{S_1 RT} A j_{1n} \tag{6}$$

In addition, the following equations are also valid in the precipitation region II:

$$C_2 C_3^2 = K_{sp} \tag{7}$$

$$\frac{\partial \epsilon}{\partial t} = -M_j \rho_j^{-1} R_{ppt} \tag{8}$$

where subscripts 1, 2 and 3 corresponding to NO_3^-, Ni^{+2} and OH^-, respectively. $U(x-\delta_o)$ is the unit step function. Eqs. (1), (2) and (3) represent the mass balance equations for NO_3^-, Ni^{+2} and OH^-, respectively. Eq. (4) is the electroneutrality condition. Eq. (5) expresses the flux of reacting nitrate in terms of the Butler–Volmer equation. Eq. (6) is the potential equation inside the porous electrode. Eq. (7) is the fast equilibrium condition between Ni^{+2} and OH^-. Eq. (8) is the mass balance equation for $Ni(OH)_2$. For the case of pseudo–steady state operation, $C_i \frac{\partial \epsilon}{\partial t} \gg \epsilon \frac{\partial C_i}{\partial t}$, or $C_i(x,t) \simeq C_i(x)$ $(i = 1,2,3)$. Combining Eq. (8) with the assumption that $C_j \gg C_i$ $(i = 1,2,3)$, Eqs. (1), (2) and (3) become

$$\epsilon D_1 \frac{d^2 C_1}{dx^2} - V_x \frac{dC_1}{dx} + \epsilon D_1 \frac{d}{dx}(C_1 \frac{\partial \xi}{\partial x}) - A j_{1n} = 0 \tag{9}$$

$$\epsilon D_2 \frac{d^2 C_2}{dx^2} - V_x \frac{dC_2}{dx} - 2\epsilon D_2 \frac{\partial}{\partial x}(C_2 \frac{\partial \xi}{\partial x}) - R_{ppt} U(x-\delta_o) = 0 \tag{10}$$

$$\epsilon D_3 \frac{d^2 C_3}{dx^2} - V_x \frac{dC_3}{dx} + \epsilon D_3 \frac{\partial}{\partial x}(C_3 \frac{\partial \xi}{\partial x}) - 2R_{ppt} U(x-\delta_o) + 9 A j_{1n} = 0 \tag{11}$$

The dimensionless overpotential distribution can be obtained under the case of low irreversibility, therefore, the concentration profile of nitrate can be calculated. The concentration distributions of nickel and hydroxyl ions in region II can be obtained by eliminating the rate of precipitation and using the equilibrium condition, Eq. (7). The following section shows the analysis of flow–through electrochemical impregnation during early stages of operation.

ANALYSIS

Analytical solution can only be obtained with the assumptions that linear kinetics and constant specific surface area and porosity are obeyed. It can be shown that the approximate concentration profiles for this systems are [10]

$$C_1^{I\&II} \simeq C_{1o} - p_1 a_1^{-1} \sinh(mx) \tag{12}$$

$$C_2^I \simeq C_2|_{\delta_o} \simeq C_{2o} \tag{13}$$

$$C_2^{II} \simeq C_2|_{\delta_o} - (9/2) p_1 a_1^{-1} m (x-\delta_o) \tag{14}$$

$$C_3^I \simeq C_{3o} - p_3 a_3^{-1} \sinh(mx) \tag{15}$$

$$C_3^{II} \simeq K_{sp}^{1/2} [C_2|_{\delta_o} - (9/2) p_1 a_1^{-1} m (x-\delta_o)]^{-1/2} \tag{16}$$

where $a_1 = V_x/\epsilon D_1$, $a_3 = V_x/\epsilon D_3$, $p_1 = iS_1/nF\epsilon D_1 sinh(mL)$, $p_3 = -9iS_1/nF\epsilon D_3 sinh(mL)$. For typical impregnation conditions in an acidic solution ($pH = 3-6$), $C_{3o} = 10^{-14}-10^{-11}$ $mole/cm^3$, $C_{2o} = 3\times10^{-3} mole/cm^3$, $T = 90^oC$, however, $C_3|_{\delta_o} \simeq (K_{sp}C_{2o}^{-1})^{1/2} = 1.24\times10^{-9}$ $mole/cm^3$, therefore, $C_{3o} \ll C_3|_{\delta_o}$. According to Eq. (15)

$$C_3|_{\delta_o} = -p_3 a_3^{-1}\sinh(m\delta_o) \simeq -p_3 a_3^{-1} m\delta_o = \frac{9iS_1 m\delta_o}{nFV_x \sinh(mL)} \tag{17}$$

in the case when $mL \leq 0.5$, $\sinh(mL) \simeq mL$, Eq. (17) gives

$$(\frac{\delta_o}{L}) = \frac{nFV_x C_3|_{\delta_o}}{9iS_1} \tag{18}$$

assuming that $i = -100$ mA/cm^2, $V_x = 0.06$ cm/min, $C_3|_{\delta_o} = 2.1\times10^{-9}$ $mole/cm^3$, the calculated value of (δ_o/L) is on the order of 10^{-6}, which practically means that the pH of the solution inside the pores is always high enough to cause precipitation within the whole electrode. It is clear that for a constant inlet concentration of nickel ions ($C_{2o} = const.$), the higher the flow velocity, the higher the value of δ_o. On the other hand, for a constant flow velocity and constant inlet concentration of nickel ion, the higher the applied current density, the lower the value of δ_o. At constant current density and flow velocity, increasing C_{2o} will decrease $C_3|_{\delta_o}$ and, hence, decrease δ_o. The expressions for rate of precipitation, distribution of nickel hydroxide, porosity and loading are presented below.

· Rate of Precipitation:

The rate of precipitation can be obtained from Eqs. (10) and (14) by neglecting diffusion and migration

$$R_{ppt} = -V_x\frac{dC_2}{dx} = -V_x[-(9/2)p_1 a_1^{-1} m] \tag{19}$$

or

$$R_{ppt} = (1/2)V_x C_3|_{\delta_o}\delta_o^{-1} = (9/2)(\frac{iS_1}{nFL}) \tag{20}$$

In fact, Eq. (20) expresses the rate of precipitation in the limit when $t \to 0$, i.e., $R_{ppt}(x, t = 0)$. By differentiating Eq. (10) with respect to time and using Eq. (8), one obtains

$$R_{ppt}(x,t) = R_{ppt}(x,t=0)e^{-g(x)t} \tag{21}$$

where

$$g^{-1}(x) \equiv \frac{C_j}{[D_2\frac{d^2C_2}{dx^2} - 2D_2\frac{d}{dx}(C_2\frac{d\xi}{dx})]} \tag{22}$$

$g^{-1}(x)$ is the local characteristic time of the system if diffusion and migration are the mechanisms for the transport process. After substituting the expressions for C_2 and ξ, one gets

$$g(x) = C_j^{-1}(-2D_2/L^2)(FiL/\kappa RT)(C_{2o} - 9p_1 a_1^{-1} mx) \tag{23}$$

Typical operating conditions and physical parameters are: $C_{2o} = 3 \times 10^{-3}$ $mole/cm^3$, $i = -100$ mA/cm^2, $T = 90°C$, $D_2 = 0.72 \times 10^{-5}$ cm^2/s, $\kappa = 0.4$ mho/cm, $L = 0.1$ cm, $C_j = 4.15/92.72$ $mole/cm^3$. Therefore, 10^6 $sec \leq g^{-1}(x) \leq 10^7$ sec. This confirms the fact that for porous electrodes operating under flow–through conditions, the convective term is dominant. Thus, the real impregnation time is much shorter than the characteristic time

$$t/g^{-1}(x) \ll 1 \tag{24}$$

An examination of the expression for the rate of precipitation under flow–through conditions (Eq. (21)) reveals the existence of a time–invariant reaction rate

$$R_{ppt}(x,t) = R_{ppt}(x,t=0) \tag{25}$$

However, according to Eq. (20), the initial rate of precipitation is space–invariant. Finally, one concludes that under flow–through conditions, the rate of precipitation is time and space–invariant, as compared to the relatively nonuniform rate for static operation. With knowledge of the rate of precipitation, one can calculate the distribution of nickel hydroxide, the loading level and the porosity distribution.

· **Distribution of Nickel Hydroxide:**

The concentration of precipitated nickel hydroxide is given by

$$C_{ppt}(x,t) = \int_o^t R_{ppt}(x,t)dt = (1/2)V_x C_3|_{\delta_o}\delta_o^{-1}\frac{1}{g(x)}[1 - e^{-g(x)t}] \tag{26}$$

In the case when $g(x) \to 0$, Eq. (26) takes the form

$$C_{ppt} = R_{ppt}t = (1/2)V_x C_3|_{\delta_o}\delta_o^{-1}t = (9/2)(iS_1/nFL)t \tag{27}$$

· **Loading Level:**

The local loading is given by integrating the rate of precipitation over time

$$W_g(x,t) = \int_o^t R_{ppt}(x,t)M_j\epsilon_o^{-1}dt = M_j\epsilon_o^{-1}C_{ppt}(x,t) \tag{28}$$

and the average loading is given by

$$\bar{W}_g(t) = M_j\epsilon_o^{-1}R_{ppt}t \tag{29}$$

The rate of precipitation is obtained from Eq. (20). Therefore, Eq. (29) becomes

$$\bar{W}_g(t) = -M_j(\epsilon_o L)^{-1}(9i/16F)t = S_F t \tag{30}$$

where

$$S_F = -M_j(\epsilon_o L)^{-1}(9i/16F) \tag{31}$$

Equation (30) relates the theoretical loading capacity to the applied current density by Faraday's law during the early stages of the process, regardless of flow conditions. However, with a flow–through single electrode, the real loading rate is only about 50 % of its theoretical value even in the early stages. The loss in capacity is believed to be caused by hydrodynamic flow which carries away some of the $Ni(OH)_2$. The recovery of Faraday's behavior by using a flow through double electrode with the second electrode serving as a filter and the agreement with Faraday's slope confirm this finding (Figure 12).

The loading characteristics of a flow–through double electrodes can be represented by a semi–empirical equation where the rate of precipitation is proportional to the fraction of maximum loading which is available for further precipitation

$$\frac{d\bar{W}_g(t)}{dt} = S_F(1 - \bar{W}_g/\bar{W}_{g,max}) \tag{32}$$

By integraion one obtains

$$\bar{W}_g(t) = \bar{W}_{g,max}(1 - e^{-S_F t/\bar{W}_{g,max}}) \tag{33}$$

where $\bar{W}_{g,max}$ is the maximum loading capacity under flow–through conditions, and can be estimated from the density of nickel hydroxide, ρ_j, i.e.,

$$\bar{W}_{g,max} = \rho_j \tag{34}$$

· **Porosity Distribution:**

By integrating Eq. (8), one may obtain the porosity distribution

$$\epsilon(x,t) = \epsilon_o - C_j^{-1} R_{ppt}(x,t=0)[\frac{1}{g(x)}(1 - e^{-g(x)t})] \tag{35}$$

In the limit when $g(x) \to 0$, Eq. (25) becomes

$$\epsilon(x,t) = \epsilon_o - C_j^{-1} R_{ppt}(x,t=0)t \tag{36}$$

A critical pore plugging time (t_p), can be defined for which $\epsilon(x=L,t_p) = \epsilon_o/2$

$$t_p = \frac{\rho_j \epsilon_o}{2M_j R_{ppt}(x=L,t=0)} \tag{37}$$

where $R_{ppt}(x=L,t=0)$ represents the initial rate of precipitation at the front of the electrode and is also equal to the rate at pseudo–steady state because the rate of precipitation is time and space invariant. Equation (29) indicates that from the

slope of the loading curve, one may calculate the real rate of precipitation, which is an important and practical quantity under flow–through operation. Hence

$$R_{ppt}(x,t) = R_{ppt} = M_j^{-1}\epsilon_o S_f \tag{38}$$

where S_f represents the initial slope of the loading curve under flow– through conditions. Substitution of Eq. (38) into Eq. (37) gives

$$t_p = \rho_j / 2S_f \tag{39}$$

The loading curve in Figures 6 and 8 gives S_f a value of 2×10^{-2} $g/cm^3.min$ and 2.7×10^{-2} $g/cm^3.min$ for downstream and upstream counterelectrode placement, respectively. The predicted pore plugging time for downstream and upstream counterelectrode placement are 100 min and 75 min, respectively. This is in reasonable agreement with the experimental onset time of plugging, which can be identified from Figures 6 and 8 as 75 min and 45 min for downstream and upstream counterelectrode placement, respectively. Furthermore, escape of nickel hydroxide carried away by the flow may result in earlier plugging.

CONCLUSIONS AND SUMMARY

It has been experimentally shown that the thickening of plaques during electrochemical impregnation of nickel hydroxide electrodes can be reduced by using a flow–through porous cathode. The effects of flow rate, flow direction, initial pH as well as electrode configuration on loading level and plaque expansion have been identified.

In the case of an electrode impregnated on one side, flow–through of electrolyte reduces the formation of surface deposit, but at the same time it also reduces the loading level. The cause of the decrease in loading has been identified to be the escape of $Ni(OH)_2$, as the newly formed active material was continuously exposed to flow. A flow rate on the order of 0.06 $cm^3/cm^2.min$ may cause such a loss. Visually, a cell configuration in which the electrolyte flows in the same direction as the current (upstream counterelectrode) gives uniform distribution of $Ni(OH)_2$ and reduces the plaque thickening. A cell configuration in which the porous nickel plaque is sandwiched between two anodes with an upstream position for the active anode gives the best electrode characteristics.

A pseudo–steady state model suitable for electrochemical impregnation under flow–through condition has been developed and analyzed. The analysis allows us to predict theoretically the onset time for plugging. The predicted pore plugging time is in reasonable agreement with the experimental results.

The experimental results provide an insight to the loading capacity and thickening of electrode during electrochemical impregnation under stagnant and flow–through conditions. It is suggested that by a careful selection of the flow rate, flow direction and electrode configuration, optimum conditions for the fabrication of nickel hydroxide electrodes can be achieved.

REFERENCES

[1] H. N. Seiger, V. J. Puglisi, P. F. Ritterman, and D. F. Pickett, "High Energy Density Sintered Plate Type Sealed Nickel Cadmium Battery Cells. Part I. The Positive Electrode/Plaque Relationships, "Proceedings of the 9th IECEC, 868, San Francisco, CA (1974).

[2] F. E. Ford and D. A. Baer, "Design and Manufacturing Changes Incorporated in the Nickel–Cadmium Space Cell during the Past Decade, "Proceedings of the Symposium of Battery Design and Optimization, vol. 79–1, pp.114–127, The Electrochemical Society, Pennington, NJ (1979).

[3] H. S. Lim, "Long Life Nickel Electrodes for Nickel–Hydrogen Cells, "NASA CR–174815 (1984).

[4] V. J. Puglisi, H. N. Seiger, and D. F. Pickett, "High Energy Density Sintered Plate Type Nickel–Cadmium Battery Cells. Part II. Electrochemical Impregnation Methods to Produce Nickel Oxide Electrodes, "Proceedings of the 9th IECEC, 873, San Francisco, CA (1974).

[5] P. K. Ng and E. W. Schneider, "Distribution of Nickel Hydroxide in Sintered Nickel Plaque Measured by Radiotracer Method during Electroimpregnation, "*J. Electrochem. Soc.*, **133**, 17 (1986).

[6] H. N. Seiger, Comments, *J. Electrochem. Soc.*, **133**, 1524 (1986).

[7] R. C. Alkire, E. A. Grens II, and C. W. Tobias, "A Theory for Porous Electrodes Undergoing Structural Change by Anodic Dissolution, "*J. Electrochem. Soc.*, **116**, 1328 (1969).

[8] K. C. Ho and J. Jorné, "A Pseudo–Steady State Theory for Flow–Through Porous Electrodes Undergoing Structural Change, "Ext. Abs. # 63, The Electrochem. Soc., Meeting, Las Vegas, Nevada (1985).

[9] D. N. Bennion and J. Newman, "Electrochemical Removal of Copper Ions from Very Dilute Solutions, "*J. Appl. Electrochem.*, **2**, 113 (1972).

[10] K. C. Ho, "Electrochemical Impregnation of Nickel Hydroxide in Porous Electrodes, "Ph. D. Dissertation, The University of Rochester, NY (1987).

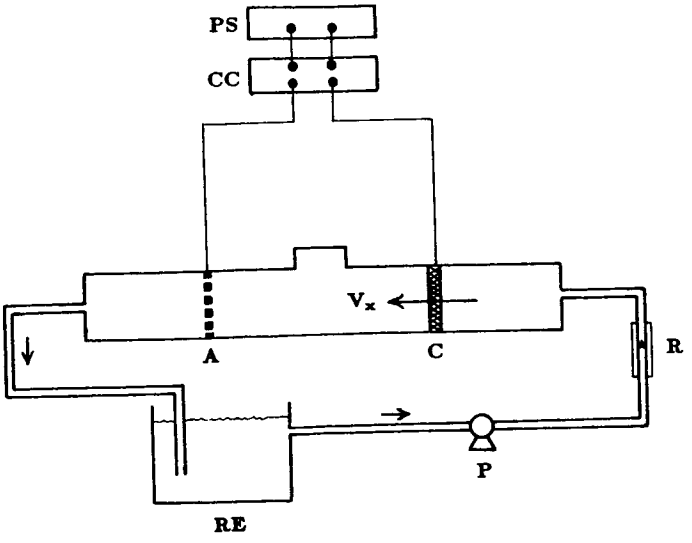

Figure 1. The Flow Tube–Type Cell with Anode Placed in Downstream (A: Anode, C: Cathode, CC: Current Controller, P: Micropump, PS: Power Supply, R: Rotameter, RE: Reservoir).

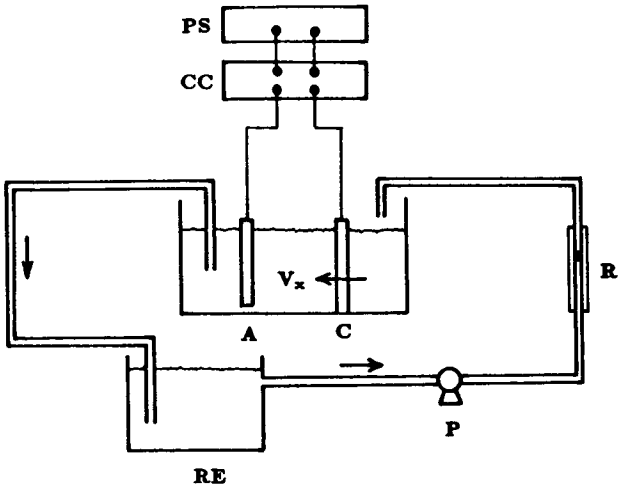

Figure 2. The Flow Rectangular–Type Cell with Anode Placed in Downstream (A: Anode, C: Cathode, CC: Current Controller, P: Micropump, PS: Power Supply, R: Rotameter, RE: Reservoir).

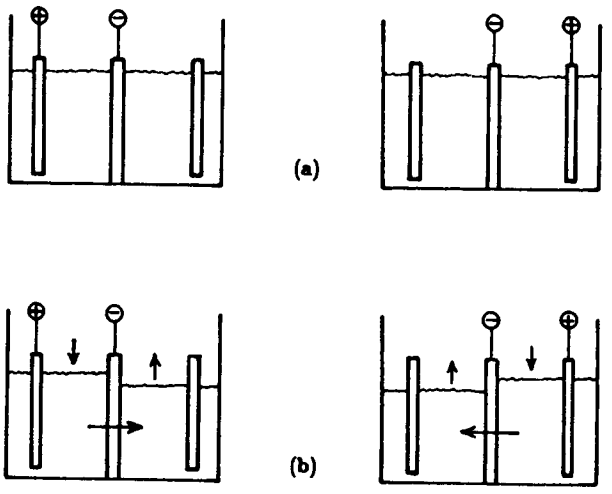

Figure 3. Electrode and Flow Configurations with Two-side Impregnation for (a) Stagnant, and (b) Flow-Through Upstream Counter.

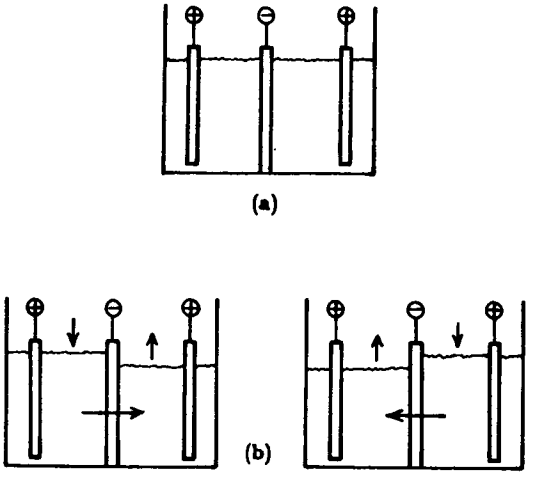

Figure 4. Electrode and Flow Configurations with Simultaneous Two-side Impregnation (a) Stagnant, and (b) Flow-Through under Alternating Upstream-Downstream Counterelectrode.

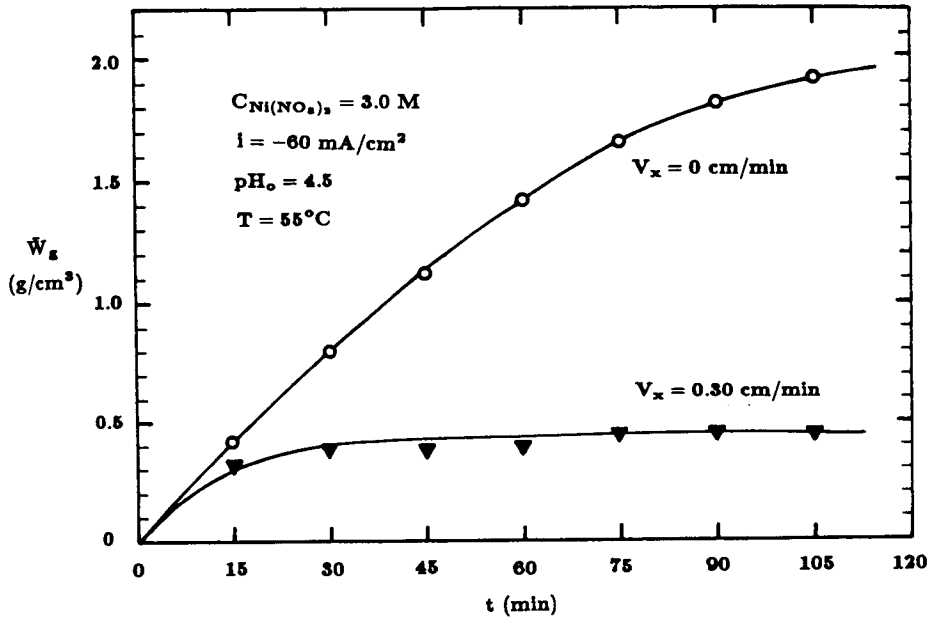

Figure 5. Loading Level vs. Impregnation Time for Stagnant and Flow–Through Conditions in a Tube–Type Cell (Downstream Counter, $V_s/V_p = 2 \times 10^2$).

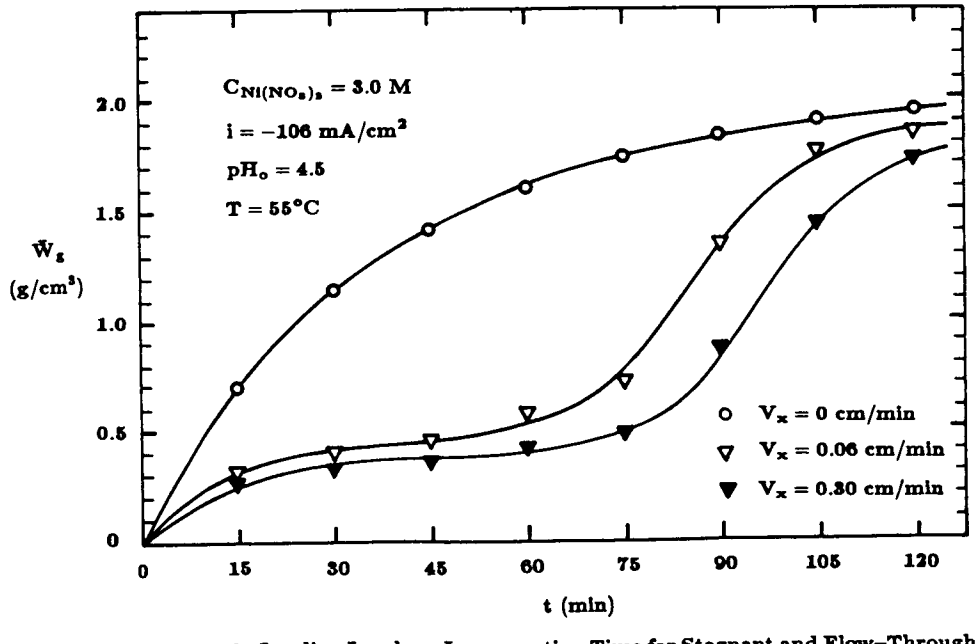

Figure 6. Loading Level vs. Impregnation Time for Stagnant and Flow–Through Conditions in a Rectangular–Type Cell at pH_o = 4.5 (Downstream Counter).

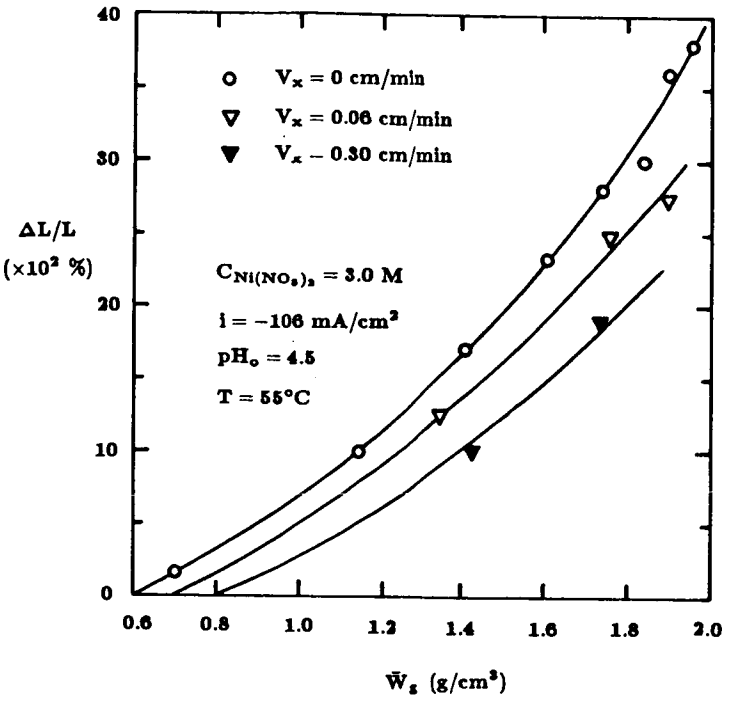

Figure 7. Plaque Expansion vs. Loading Level for Stagnant and Flow Conditions in a Rectangular–Type Cell at $pH_o = 4.5$ (Downstream Counter).

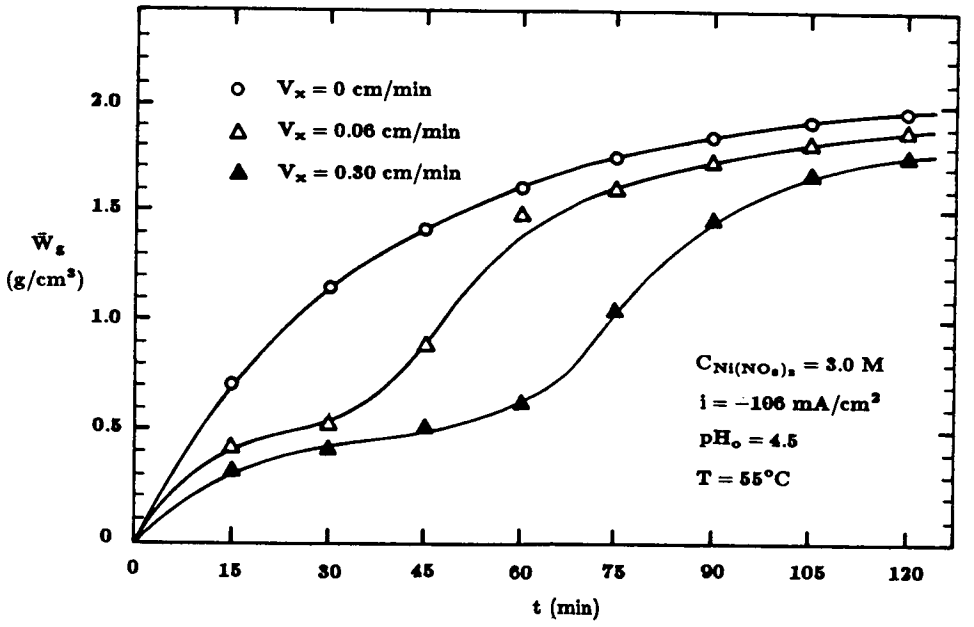

Figure 8. Loading Level vs. Impregnation Time for Stagnant and Flow–Through Conditions in a Rectangular–Type Cell at $pH_o = 4.5$ (Upstream Counter).

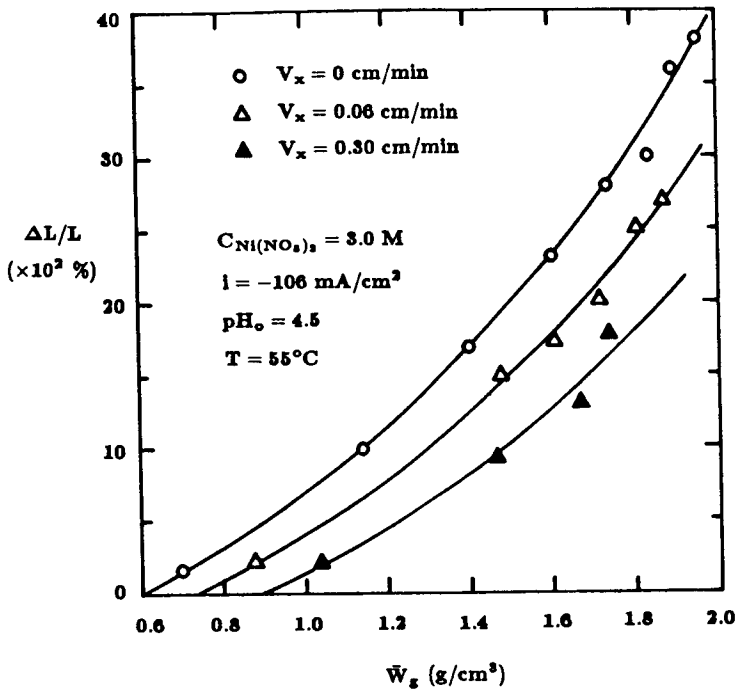

Figure 9. Plaque Expansion vs. Loading Level for Stagnant and Flow-Through Conditions in a Rectangular-Type Cell at $pH_o = 4.5$ (Upstream Counter).

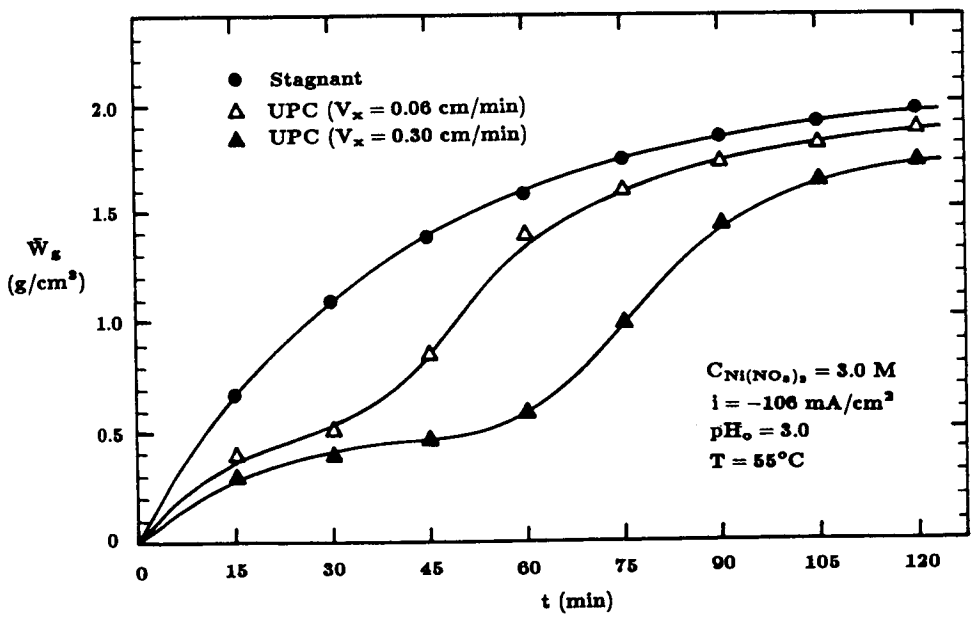

Figure 10. Loading Level vs. Impregnation Time for Stagnant and Flow-Through Conditions in a Rectangular-Type Cell at $pH_o = 3.0$ (Upstream Counter).

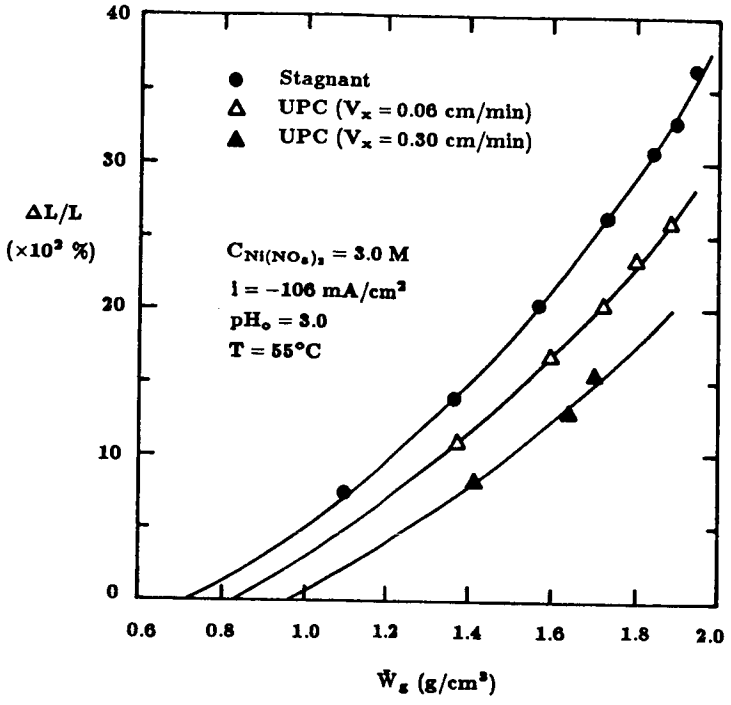

Figure 11. Plaque Expansion vs. Loading Level for Stagnant and Flow–Through Conditions in a Rectangular–Type Cell at pH_o = 3.0 (Upstream Counter).

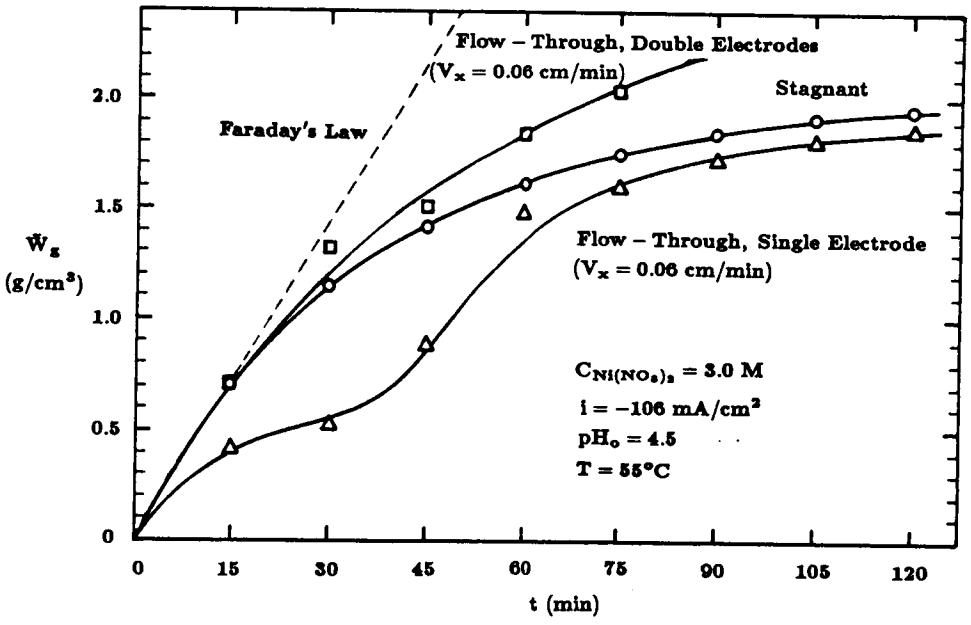

Figure 12. Loading Level vs. Impregnation Time for Stagnant, Flow–Through Single Electrode, and Flow–Through Double Electrodes in a Rectangular–Type Cell at pH_o = 4.5 (Upstream Counter).

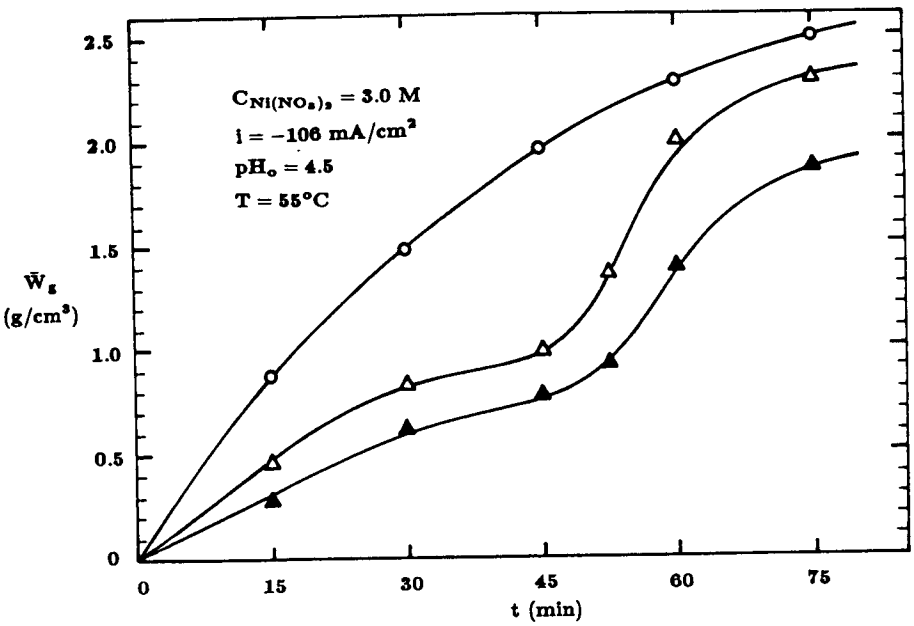

Figure 13. Loading Level vs. Impregnation Time for Stagnant and Flow–Through Conditions (Upstream Counter) with Two–side Impregnation in a Rectangular–Type Cell at pH_o = 4.5.

○ Stagnant: each side impregnated with equal time.

△ Flow–Through: V_x = 0.06 cm/min, each side impregnated with equal time.

▲ Flow–Through: V_x = 0.06 cm/min, each side impregnated periodically for 2.5 min .

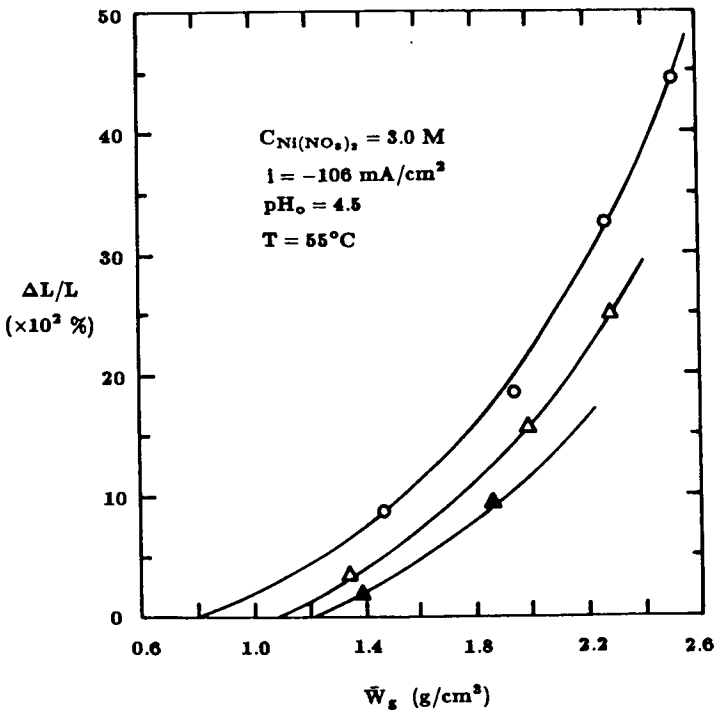

Figure 14. Plaque Expansion vs. Loading Level for Stagnant and Flow–Through Conditions (Upstream Counter) with Two–side Impregnation in a Rectangular–Type Cell at pH_o = 4.5 (Captions Are the Same as in Figure 5–13).

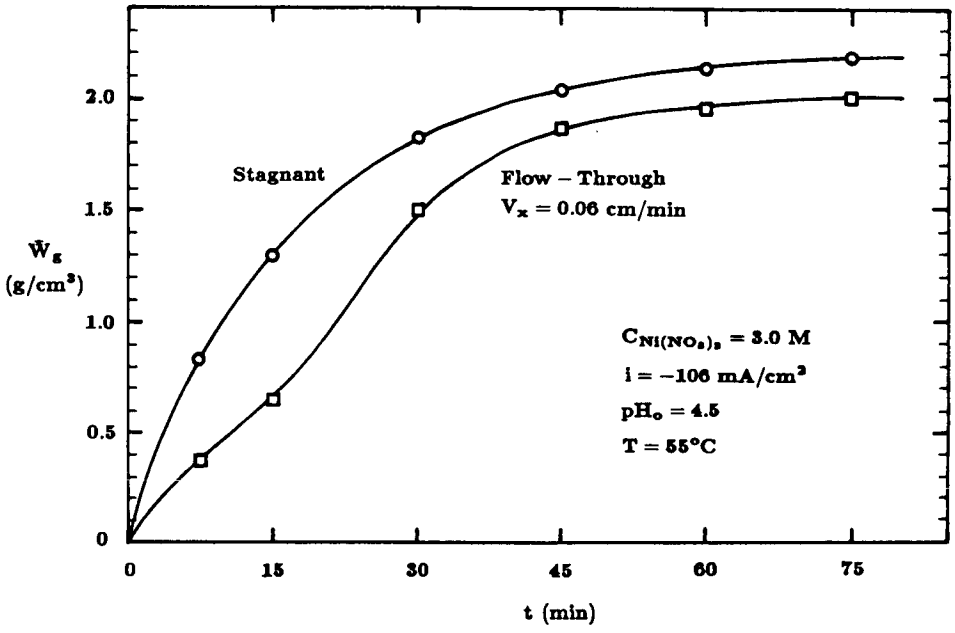

Figure 15. Loading Level vs. Impregnation Time for Stagnant and Flow–Through Conditions with Simultaneous Two–side Impregnation in a Rectangular–Type Cell at $pH_o = 4.5$.

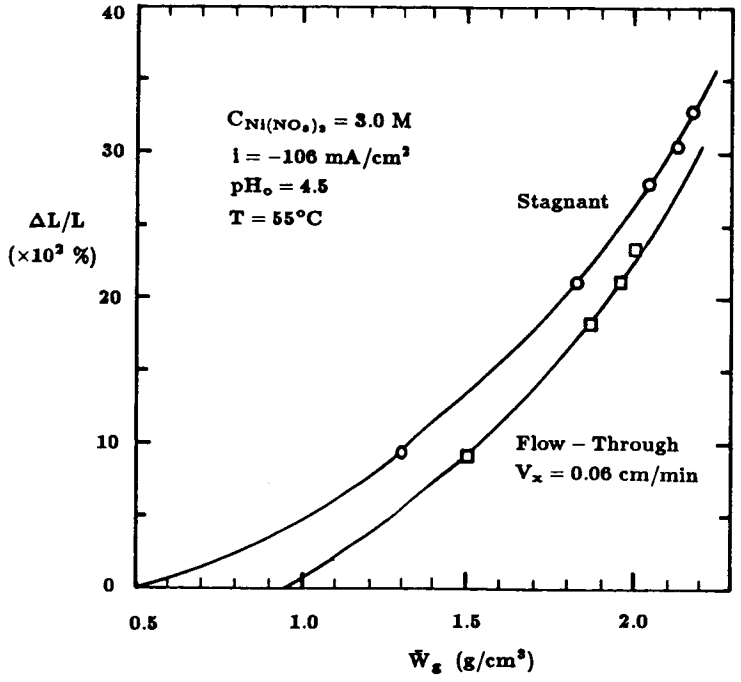

Figure 16. Plaque Expansion vs. Loading Level for Stagnant and Flow–Through Conditions with Simultaneous Two–side Impregnation in a Rectangular–Type Cell at $pH_o = 4.5$.

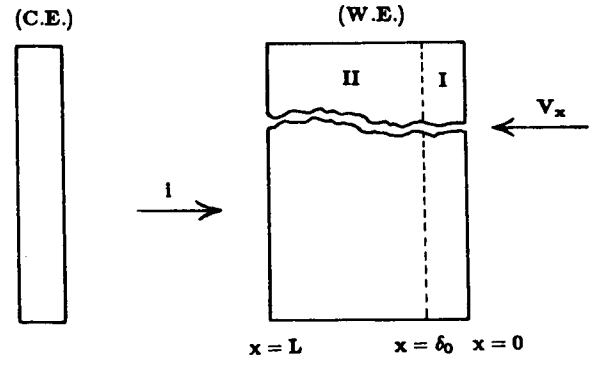

Figure 17. Schematic Representation of Electrochemical Precipitation within a Flow-Through Porous Electrode.

EFFECT OF STRUCTURE ON CURRENT AND POTENTIAL DISTRIBUTIONS IN POROUS ELECTRODE*

Oscar Lanzi and Uziel Landau
Case Western Reserve University
Cleveland, Ohio 44106

Porous electrodes generally contain constricted macropores and localized micropores. We have studied the effects of the macropore constrictions on the resistance of a capillary and have developed an analytical model for predicting the current distribution in a constricted macropore which directly includes constriction effects and does not require an empirical tortuosity parameter. We have also investigated the current and concentration distributions in localized micropores and have shown that the microporous area is fully accessible to charge and mass transfer processes. From these analyses we conclude that the micropores primarily affect the kinetics of the interfacial processes by contributing to the interfacial area, while the macropores impose ohmic and mass transport limitations through the volume of the porous electrode.

INTRODUCTION

Porous electrodes are often used in electrochemical reactors because they potentially allow electrochemical reactions, which are heterogeneous, to be carried out in three dimensions. For example, porous nickel oxide electrodes have been used in nickel-hydrogen and nickel-cadmium batteries (in the latter, the cadmium electrode is also porous), because the charge and discharge reactions may be made to take place throughout the volume of the electrode, thus allowing larger capacities in a given cell volume.

Euler and Nonnemacher [ref.1] followed by Newman and Tobias [ref. 2] developed a model to determine the current and concentration distributions within porous electrodes under Tafel kinetics, both with and without mass transfer limitations. These authors treated the pore structure as a superposition of continuous phases without regard to the structural details within the electrode. This approach has been been adapted by many workers in models for specific porous electrodes, such as nickel oxide electrodes [refs. 3, 4], gas-fed electrodes [refs. 5, 6], and halogen electrodes for zinc-halogen batteries [refs. 7-9]. These constitute only a few more recent examples; a more extensive review is provided by Newman and Tiedemann [ref 10].

The authors cited above followed the precedent of [refs. 1 and 2] by assuming the electrode to be a superposition of continuous phases. They did not attempt to relate the model parameters, particularly the tortuosity and specific area, to the structural characteristics of the pores. A numerical study based on a random-network

*The research was supported by a NASA Lewis grant. We acknowledge helpful discussions with Dr. Paul Kang.

model by Kramer and Tomkiewicz [ref. 11] suggests that such relations can be found, since their results were found to agree qualitatively with those of a single-pore model. The objective of this study is to determine, using both analytical and numerical modeling, the significance to the tortuosity and the interfacial area parameters of simple one-dimensional models and to relate them to pore structure.

We will develop a model for prediction of the effect of pore constrictions on conduction and diffusion within a non-cylindrical pore geometry, thereby allowing the "tortuosity" parameter to be interpreted in terms of such constrictions. The predictions will be compared to a numerical two-dimensional model applied to specific constricted pore structures. We also will model current and concentration distributions in a micropore embedded in a macropore to demonstrate that the microporous interfacial area can readily be penetrated and thus the electrochemically active area should include it, even when the micropores are quite small. These results have important effects on the design of porous electrodes for optimum performance.

SYMBOLS

Latin

a	Interfacial area/Total pore volume, cm^2/cm^3
a_M	Interfacial area/Macropore volume, cm^2/cm^3
b	Tafel parameter, V
$c(z)$	Local concentration in micropore, mol/cm^3
$\bar{c}(z)$	Local concentration in macropore, mol/cm^3
C_1	Integration constant, V/cm
D	Diffusivity, cm^2/s
F	Faraday constant, C/eq
$i(z)$	Interfacial current density, A/cm^2
i_{avg}	Average interfacial current density, A/cm^2
$I'(z)$	Total current along pore axis, A
L	Length of pore, cm
R	Gas constant, 8.3144 J/mol•K
$S(z)$	Local cross-sectional area, cm^2

T	Temperature, K
z	Distance into pore from electrode-electrolyte interface, cm

Greek

α	Transfer coefficient, dimensionless
Λ	Dimensionless average interfacial current density
ζ	Integration variable in Eq. [2], cm.
η	Overpotential, V
κ	Electrolyte conductivity, mho/cm
λ	Local averaging distance, cm
ϕ	Potential, V
τ_c	Constriction factor, dimensionless

CONSTRICTED PORE STRUCTURES

Fig. 1 depicts a schematic model of the structure generally found in porous electrodes. There are two scales of pore size: the macropores, which generally extend through the volume of the porous electrode structure, and the micropores, which are much smaller than the macropores and tend to be confined to localized regions such as individual particles. For example, in nickel oxide electrodes pore size distribution data [ref. 12] show clearly the existence of 1-μm radius macropores and 0.004 to 0.01-μm micropores. We show later that the microporous structure is important in determining the active electrochemical area, at least in flooded electrodes where the reactants are distributed throughout the volume of the electrolyte phase. This section is devoted to the macroporous structure.

An important feature of the macropore structure is the presence of constrictions in the capillary, as can be seen in Fig. 1. An idealized representation of these constrictions, on which our study of the constriction effects is based, is given in Fig. 2. Such constrictions lead to addditional mass transfer and ohmic resistance inside the porous structure. We now pursue a model to describe this constriction effect and use it to predict the overall pore resistance.

Prediction of Pore Resistance

Following Sides and Tobias [ref. 13] and Lanzi and Savinell [ref. 14], who examined constriction effects in the electrolyte phase in bubble layers on gas evolving electrodes, we assume that the current in the pore is directed primarily in one dimension along the pore axis, and is uniformly distributed in the pore cross-section at any point along the axis. We also assume that the microstructure can be represented by a segment of length λ which is much less than the pore length L. The model is shown in Fig. 3. With the assumption of a uniform current distribution throughout the cross-section S(z), the potential balance takes a simple form that is independent of the, pore geometry:

$$d\phi/dz = -I'/S(z)\kappa \tag{1}$$

To integrate this equation it is convenient to introduce the following:

$$\langle f \rangle \equiv (1/\lambda) \int_z^{z+\lambda} f(\zeta)\, d\zeta \tag{2}$$

The averaged value $\langle f \rangle$ is essentially the same as f itself if the averaging length λ is sufficiently small compared to the pore length L. However, derivatives of f and $\langle f \rangle$ with respect to position may differ because of the position-dependent cross-sectional area.

With Eq. (2), Eq. (1) may be averaged over λ to give:

$$d\langle\phi\rangle/dz = -\langle I'/S\rangle/\kappa \tag{3}$$

Since the averaging length is assumed to be much less than the pore length L, I' may be taken as constant, so that (3) becomes:

$$d\langle\phi\rangle/dz = (-I'/\kappa)\langle 1/S\rangle \tag{4}$$

For the prediction of pore resistance Eq. (4) is multiplied by $\lambda\langle S\rangle/\langle S\rangle$ to obtain:

$$\phi(z+\lambda)-\phi(z) = [-I'\lambda/\kappa\langle S\rangle]\langle S\rangle\langle 1/S\rangle \tag{5}$$

The term in brackets represents the resistance of a cylindrical pore segment whose length and volume are identical to those of the real pore segment. The additional factor $\langle S\rangle\langle 1/S\rangle$ arises specifically from the constrictions in the pore structure and hence is a constriction factor. This constriction factor is always greater than 1 in noncylindrical pores and thus contributes to the observed "tortuosity" factor. The same constriction effect applies also to diffusion, so that Eq. (5) implies a similar equation for the effect of constrictions on diffusion:

$$\bar{c}(z+\lambda)-\bar{c}(z) = [-I'\lambda/nFD\langle S\rangle]\langle S\rangle\langle 1/S\rangle \tag{6}$$

We will discuss further the significance of the constriction factor and how it relates to pore resistance after showing that this development can be used to determine current distributions inside constricted pore structures. Only secondary current distributions are modeled, but the analogy between Eqs. (5) and (6) shows that this approach works equally well with mass transfer limitations, provided that the mass transfer is by diffusion.

Current Distributions in a Constricted Pore

Kessler and Alkire [ref. 15] have modeled the secondary and tertiary current distribution in through-holes under Tafel kinetics. For constricted pore structures, the development of [ref. 15] must be modified to include the constriction effects. The current balance for this case is as follows:

$$[I'(z+\lambda)-I'(z)]/\lambda = dI'/dz = a_M\langle S\rangle i(z) \tag{7}$$

in which the assumption that I' is constant over the length λ (see Eq. (4)) has been used. Here the quantity a_M represents the interfacial area pre unit of macropore volume because we are concentrating on the macropores, which traverse the entire electrode length. Combining this with Eq. (4) gives:

$$d^2\langle\phi\rangle/dz^2 = [(-1/\kappa)a_M i(z)]\langle S\rangle\langle 1/S\rangle \qquad (8)$$

in which one can observe the presence of the constriction factor already noted in Eq. (4). This must be combined with a kinetic equation. For Tafel kinetics:

$$d\eta/di = -d\phi/di = -d\langle\phi\rangle/di = \pm b/i \qquad (9)$$

in which the Tafel parameter b is $RT/\alpha F$, and the equivalence between ϕ and $\langle\phi\rangle$ embodies the assumption that λ is much less than L. The $\pm$ sign is positive for anodic kinetics, negative for cathodic kinetics. As a boundary condition, we assume that I' = 0 at the current collector z = L. This is valid if the electrode phase is a good conductor. Not all porous electrode materials are good conductors, of course, but the conductivity of this phase can be improved by, for example, using a sintered plate design. With this condition, Eqs. (8) and (9) may be solved analytically to give:

$$|i| = (C_1^2\kappa b/4a_M L\tau_c)\ \sec^2[C_1(L-z)/2b] \qquad (10)$$

in which τ_c is the constriction factor $\langle S\rangle\langle 1/S\rangle$. The integration constant C_1 can be determined from the average current density:

$$(C_1 L/2b)\ \tan\ (C_1 L/2b) = \tau_c \Delta \qquad (11)$$

where

$$\Delta = a_M |i_{avg}| L^2/b\kappa \qquad (12)$$

The quantity Δ represents a dimensionless current density analogous to the parameter used by Kessler and Alkire [ref. 15] to describe through-hole plating. It is the presence of τ_c which differentiates this model from that for cylindrical pores.

We compared this analytical prediction to the results of a two-dimensional finite-difference model [ref. 16] which was applied to the constricted capillary shapes shown in Figs. 4 and 5. For both geometries the constriction factor is 1.8. We investigated the range $0.3<\Delta<1.7$. For a 0.05 cm long macropore in 31% KOH electrolyte (κ = 0.64 mho/cm [ref. 17]), with α taken as 0.6 (3), this corresponds to $a_M|i_{avg}|$ ranging from about 3 to 18 A/cm^3 macropore volume. This range is of interest because it is here that a significant nonuniformity develops, as will shortly be seen. It also corresponds to discharge rates which are likely to be used in a nickel oxide electrode (the results, however, are applicable to other electrodes for similar values of Δ.) For the geometry in Fig. 4, the comparison of the two-dimensional numerical and one-dimensional analytical results shows good agreement even for a nonuniform current distribution; for the largest value of Δ the current

density ratio i(0)/i(L) is about 3 and is predicted to within 7%. Numerical current and potential distributions for some values of Λ are shown in Figs. 6 and 7. Similarly, Table 2 and Figs. 8 and 9 show comparisons and distributions for the geometry in Fig. 5. Table 2 reveals greater discrepancies than Table 1, and the differences are in the opposite direction. The difference between the geometries in Figs. 4 and 5 arises from the fact that in these models λ is not much less than L, as it would likely be in a real porous electrode; thus there are "end effects" at the electrode-electrolyte interface because in Fig. 5 more current must pass through the constrictions than in Fig. 4. Since the end effects are much smaller in real porous electrodes than in the constricted structures in Figs. 4 and 5, they may be averaged out, and this leads to an error of about 7% when i(0)/i(L) is about 3. It can be seen that the simple model for pore resistance given by Eq. (4) gives a useful relation between the pore resistance and the constriction effects without the need for an empirical tortuosity parameter.

The significance of the constriction factor, then, is that it measures the contributions of constrictions within the capillary to the pore resistance. In the above comparisons, τ_c could be equated directly to the tortuosity factor. In reality, the situation is more complicated. One such effect is suggested by Eq. (7), in which the specific area is introduced on the basis of macropore volume. This is because it is the macropores that transport mass and charge throughout the porous electrode structure; the micropores, as we will see, serve to increase the interfacial area but cannot be expected to contribute to the global transport throughout the electrode. Thus, the pore-size distribution data in [ref. 12] suggest that half of the total pore volume consists of macropores in a typical porous electrode; only this fraction can be expected to distribute reactants through the electrode.

Another effect is that of differing pore orientations at various points in the electrode. This can be accounted for by using more sophisticated structural models than those applied here. One approach is suggested by the random network model of Kramer amd Tomkiewicz [ref. 7]. Another is to assume an isotropic cross-linked structure whose orientation can be randomized without altering the predicted tortuosity.

MICROPORE PENETRATION

In the previous development, attention was focused on the resistance or tortuosity of the capillary. This section is concerned with the microporous component of Fig. 1. The ability of the current and reactant to penetrate these micropores is important because this determines what interfacial area is actually effective in bring about the electrochemical reaction and, therefore, should be used in the specific area parameter employed in porous electrode models.

We examined the current, potential, and concentration distributions in two simple micron-size features shown in Figs. 10 and 11. Each contains a micropore of equivalent radius 0.1 μm. Micropores may be much smaller than this, but it will be seen that this will not affect the results obtained.

Electrolyte properties employed for the finite-difference calculations correspond to the 31% KOH electrolyte used with nickel oxide electrodes. The conductivity is 0.64 mho/cm [ref. 17], the transference number of hydroxide ion is 0.78 [ref. 17], and these data and activity coefficient calculations by Akerlof and

Bender [ref. 18] lead to an electrolyte diffusivity of 2.4×10^{-5} cm^2/s. The interfacial current density was taken to be +2.4 A/cm^3 total pore volume (compare to the previous section where current densities were based on macropore volume). The concentration distributions obtained from the finite difference algorithm of [ref. 16] are shown in Figs. 12 and 13, where $\bar{c}$ refers to the average concentration in the portion of the pore shown in each structure. It can be seen that there is very little concentration variation inside the micropore. The same holds for potential and current density, for which variations could not be resolved even with four significant figures (the concentration variations occur in the fifth place). The small concentration nonuniformities that are observed in the graphs arise not from micropore depletion, but from the gradient imposed by the macropore to which the micropore is connected in each case. The results apply directly to micropores of 0.1 μm equivalent radius, whereas they are an order of magnitude smaller in actual nickel oxide electrodes. However, if the micropore in Fig. 10 or 11 is made 10 times smaller to simulate the pore size to be expected in the actual electrode, the voltage, current density, and concentration variations within the interior of the micropore (excluding the macropore coupling noted above) would only be increased by a factor of 10 and would remain insignificant. It follows that nonuniformities do not develop in the microporous structure and that the microporous area must be included with the electrochemically active area. For example, observed interfacial areas in a nickel oxide electrode [ref. 3] are generally two orders of magnitude greater than would be expected on the basis of the macropore structure alone. The physical reason for this is that the micropores, being much smaller than the macropores, do not carry reactant over the length of the electrode. Rather, they distribute it locally, on the micron scale, and the diffusion and conduction path in the micropore is two to three orders of magnitude smaller than in the macropore. This overrides the difference in the radii of the individual pores. By the same token, however, these micropores do not contribute to the distribution of the reaction throughout the electrode, so that when macropore transport limitations set in, the micropores will not increase the electrode capacity or the current that can be delivered. In addition, the microporous paths are far more numerous: even though the micropores are individually about seven orders of magnitude smaller in volume, in aggregate they occupy about the same volume as the macropores.

CONCLUSIONS

Three important conclusions can be drawn from this study concerning the nickel oxide electrode and porous electrodes in general. First, the details of the macroporous structure are important in determining the ohmic and mass transfer resistance within the macropores. In particular, constrictions within the micropore structure contribute to the apparent "tortuosity" of the capillaries and this contribution can be predicted with good accuracy given a reasonable pore model. Second, the macropores alone determine the ohmic and mass transfer limitations in the porous structure. These effects are negligible in micropores because these are too localized. Third, the interfacial processes occur throughout the microporous area, which is thus included in the effective surface area of the pore. Therefore, the micropores affect primarily the kinetics of the electrochemical reaction and other interfacial processes. Whenever increasing the micropore volume and area fails to improve cell delivery or capacity, it is because the limitations are associated with macropore ohmic or transport resistance, not with micropore inaccessibility.

REFERENCES

(1) J. Euler and W. Nonnenmacher, *Electrochim. Acta* 2, **268** (1960).

(2) J. Newman and C. W. Tobias, *J. Electrochem. Soc.* **109**, 1183 (1962).

(3) K. Micka and I. Rousar, *Electrochim. Acta* **25**, 1085 (1980).

(4) K. Micka, *Ibid.* **27**, 765 (1982).

(5) G. Wilemski, *J. Electrochem. Soc.* **130**, 117 (1983).

(6) R. E. White, M. A. Nicholson, L. G. Kline, J. Van Zee and R. Darby, *Ibid.* **131**, 2368 (1984).

(7) J. Van Zee and R. E. White, *Ibid.* **130**, 2003 (1983).

(8) E. Royaie and J. Jorne, *Ibid.* **131**, 1237 (1984).

(9) K. C. Ho nd J. Jorne, *Ibid.* **133**, 1394 (1986).

(10) J. Newman and W. Tiedemann, *A.I.Ch.E. J.* **21**, 25 (1975).

(11) M. Kramer and M. Tomkiewicz, *J. Electrochem. Soc.* **131**, 1283 (1984).

(12) H. S. Lim, *Long Life Nickel Electrodes for Nickel--Hydrogen Cells*, NASA CR-174815, December 1984, pp.106ff.

(13) P. Sides and C. W. Tobias, *J. Electrochem. Soc.* **129**, 2715 (1982).

(14) O. Lanzi and R. F. Savinell, *Ibid.* **130**, 799 (1983).

(15) T. Kessler and R. Alkire, *Ibid.* **123**, 990 (1976).

(16) M. Menon and U. Landau, accepted for publication in *J. Electrochem. Soc.*, July 1986.

(17) G. W. D. Briggs, E. Jones and W. F. K. Wynne-Jones, *Trans. Faraday Soc.* **51**, 1433 (1983).

(18) G. C. Akerlof and P. Bender, *J. Amer. Chem. Soc.* **70**, 2366 (1948).

Table 1. Comparison of one-dimensional analytical predictions (1-dim.) of currrent nonuniformity to two-dimensional finite difference results (2-dim.) in pore geometry shown in Fig. 4.

Δ	i(0)/i(L) [1-dim.]	i(0)/i(L) [2-dim.]
1.657	3.286	3.002
1.226	2.532	2.370
0.828	1.938	1.858
0.538	1.565	1.532
0.339	1.336	1.320

Table 2. Comparison of one-dimensional analtyical predictions (1-dim.) of current nonuniformity to two-dimensional finite difference results (2-dim.) in pore geometry shown in Fig. 5.

Δ	i(0)/i(L) [1-dim.]	i(0)/i(L) [2-dim.]
1.425	2.867	3.579
1.043	2.247	2.655
0.731	1.808	2.037
0.492	1.510	1.638
0.317	1.313	1.381

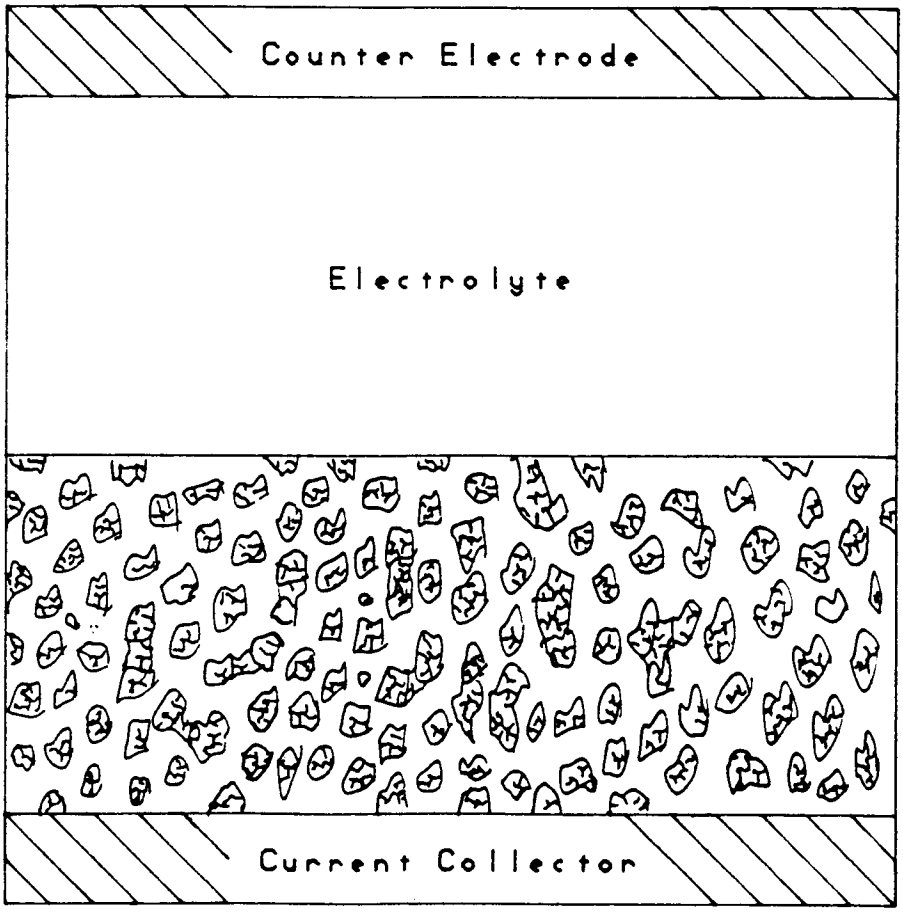

Figure 1. Structure of particulate porous electrodes showing macropores and localized micropores.

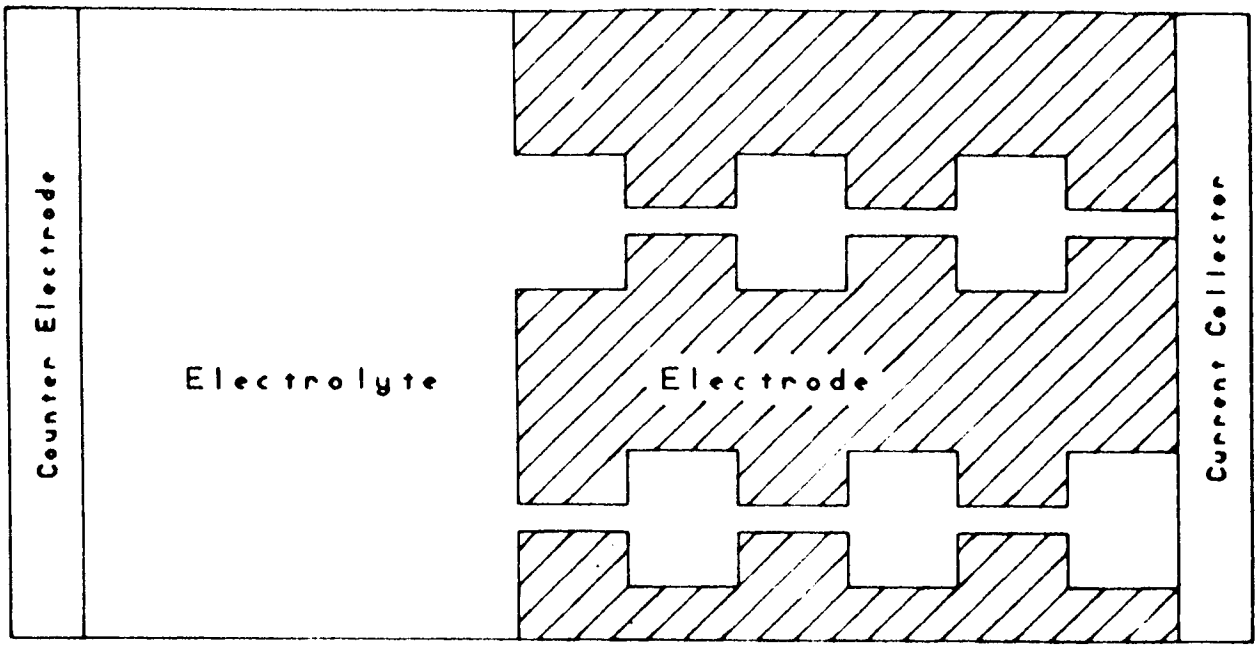

Figure 2. Idealized representation of constricted pore structure.

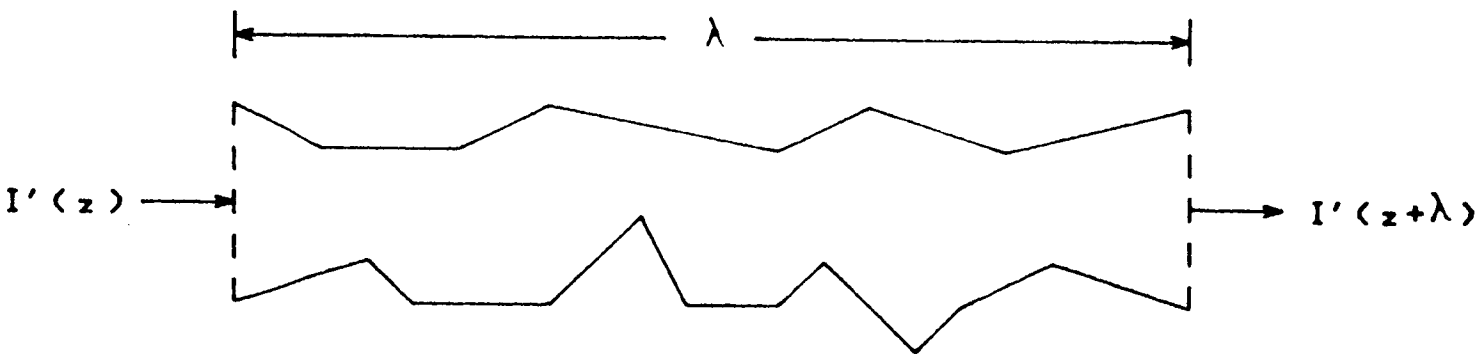

Figure 3. Constricted pore geometry showing assumed one-dimensional current flow.

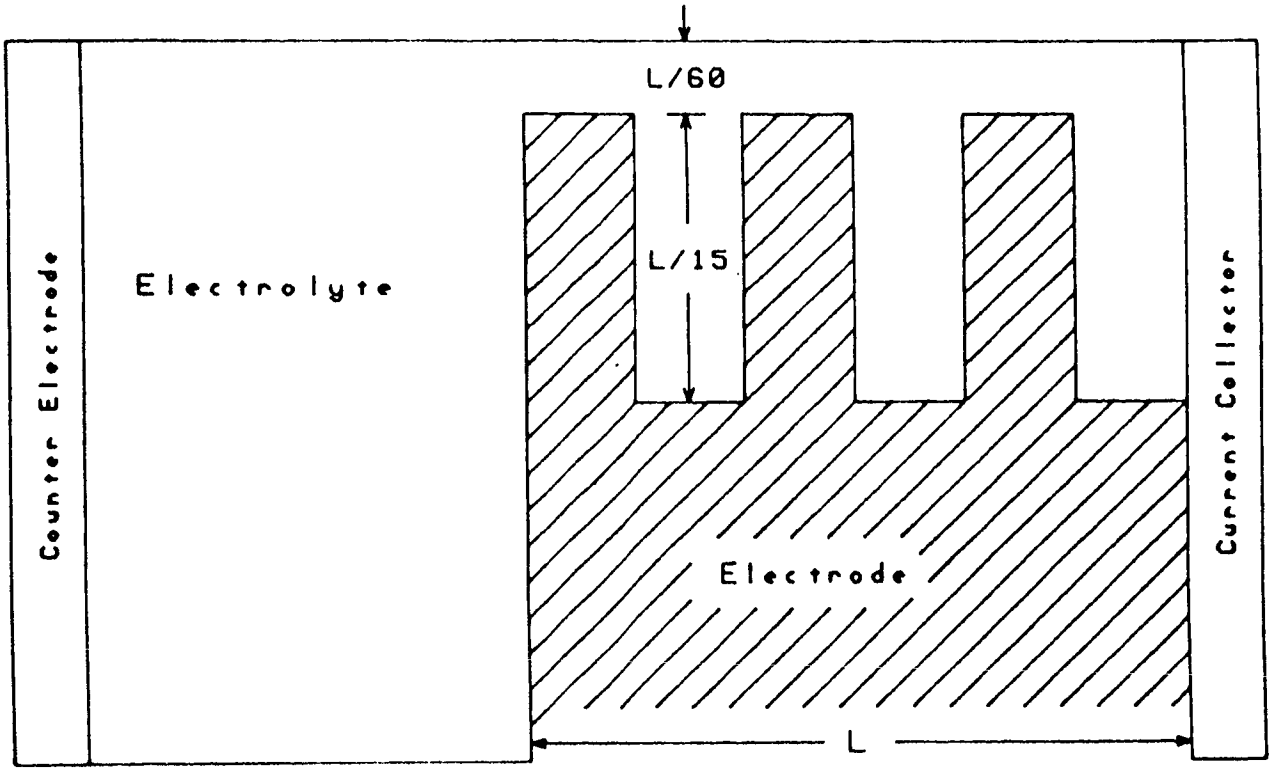

Figure 4. Pore geometry for constriction effect analysis.

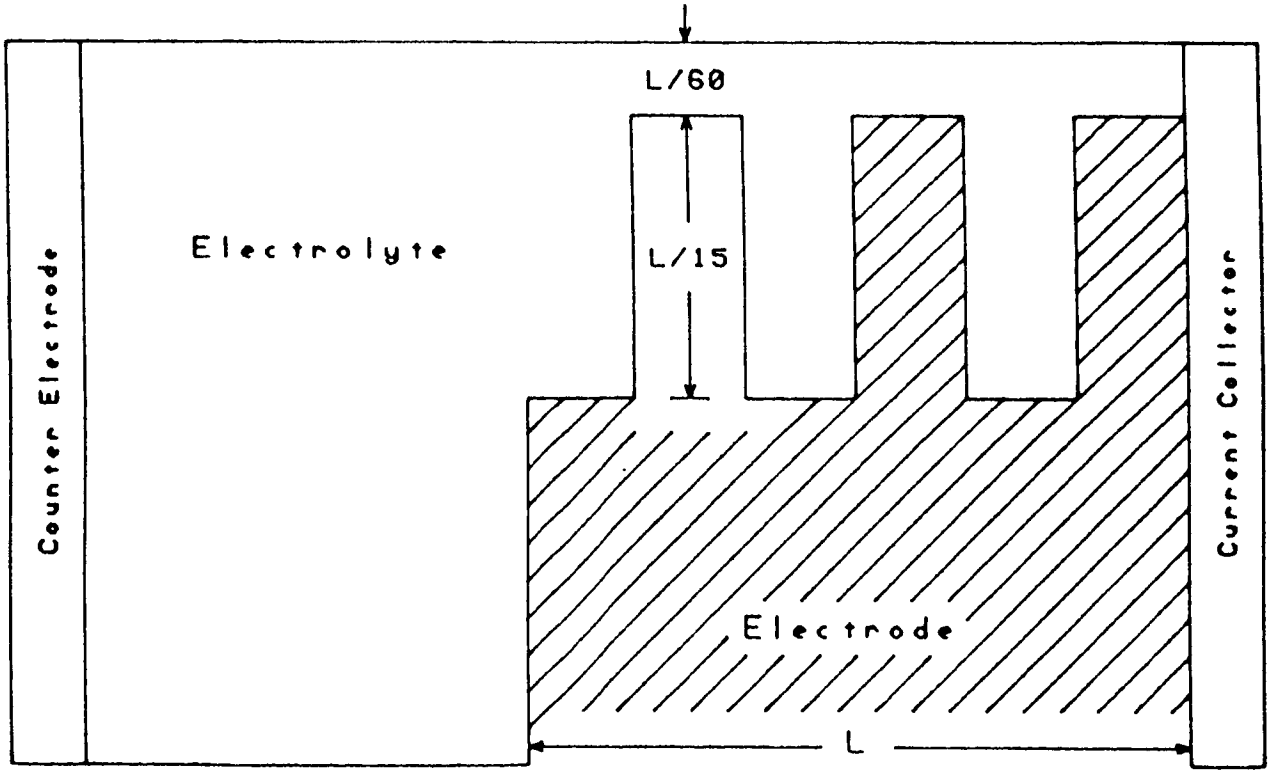

Figure 5. Pore geometry for constriction effect analysis. This geometry differs from Figure 4 because it has a constriction at the electrode-electrolyte interface.

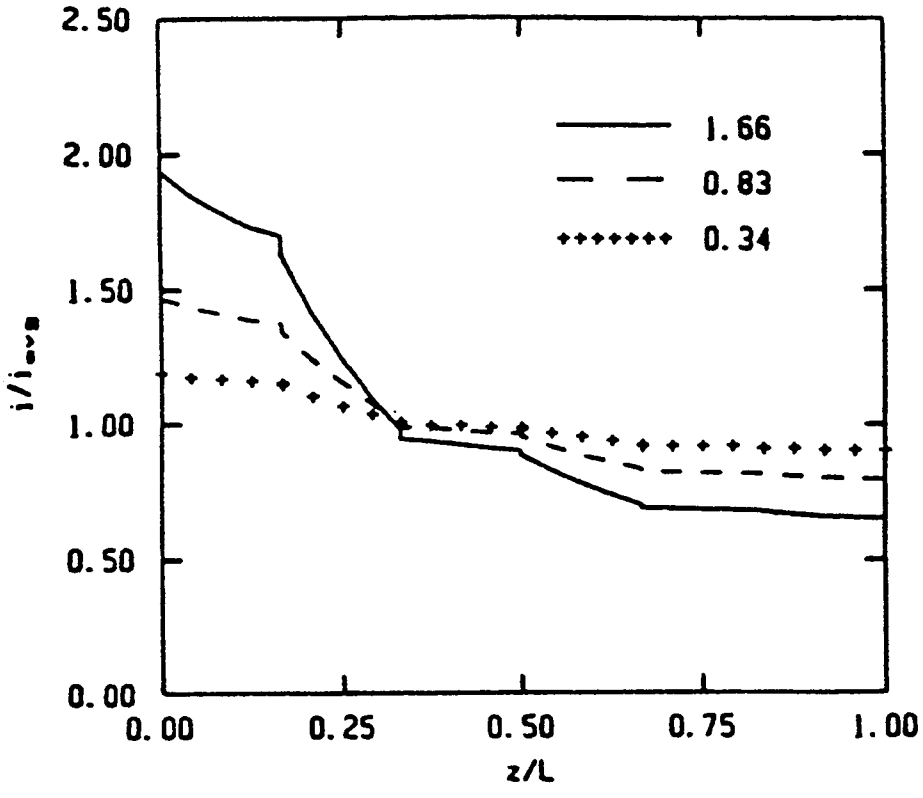

Figure 6. Numerically determined current distributions in the pore geometry shown in Figure 4. Numerical values represent $\Delta = a_M |i_{avg}| L^2 b/\kappa$.

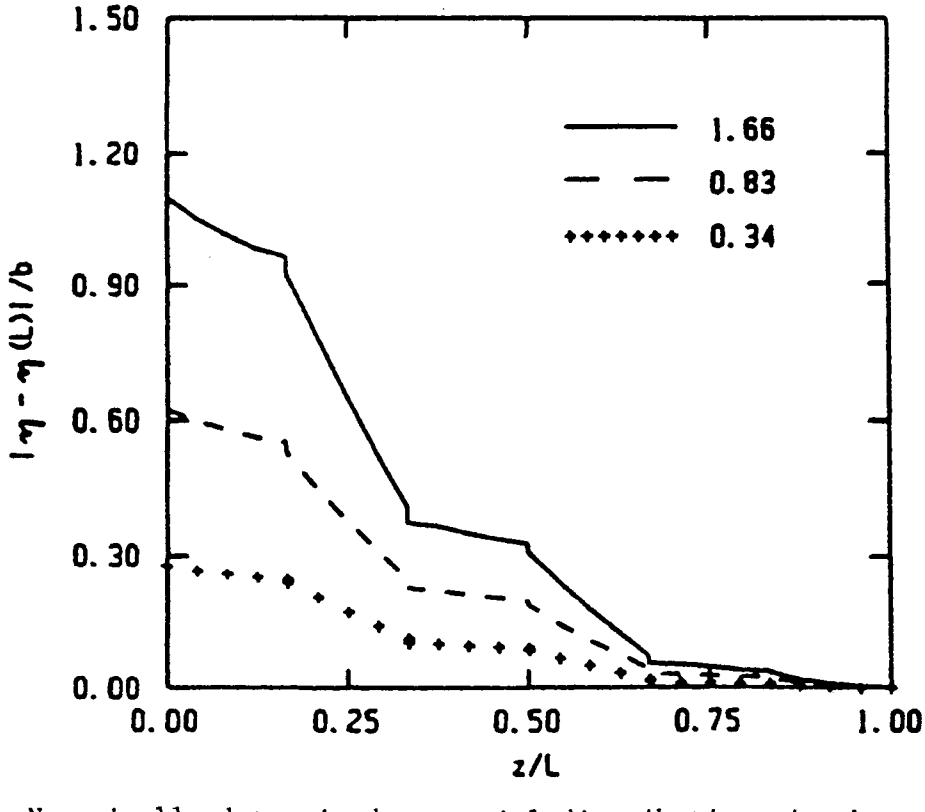

Figure 7. Numerically determined potential distributions in the pore geometry shown in Figure 4. Numerical values represent Δ.

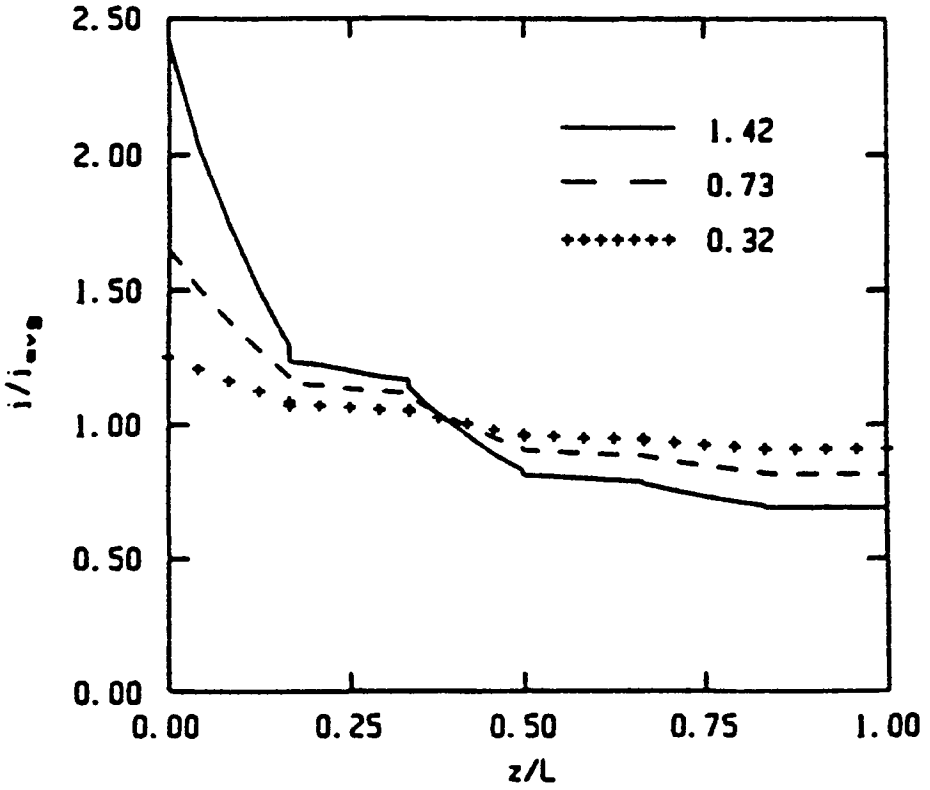

Figure 8. Numerically determined current distributions in the pore geometry shown in Figure 5. Numerical values represent Δ.

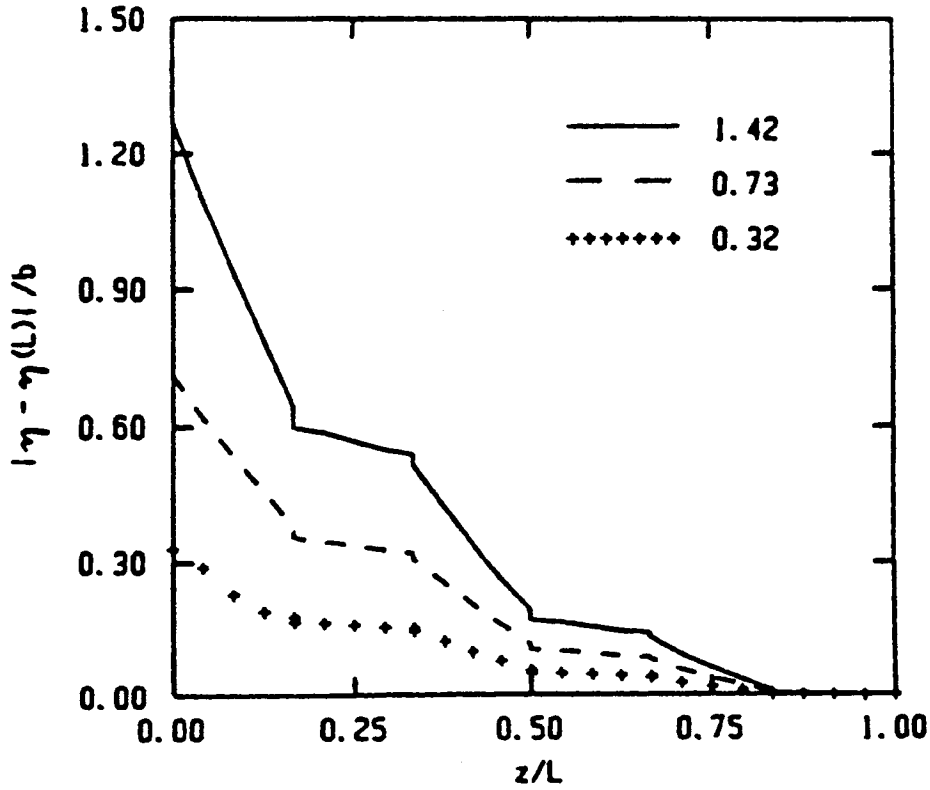

Figure 9. Numerically determined potential distributions in the pore geometry shown in Figure 5. Numerical values represent Δ.

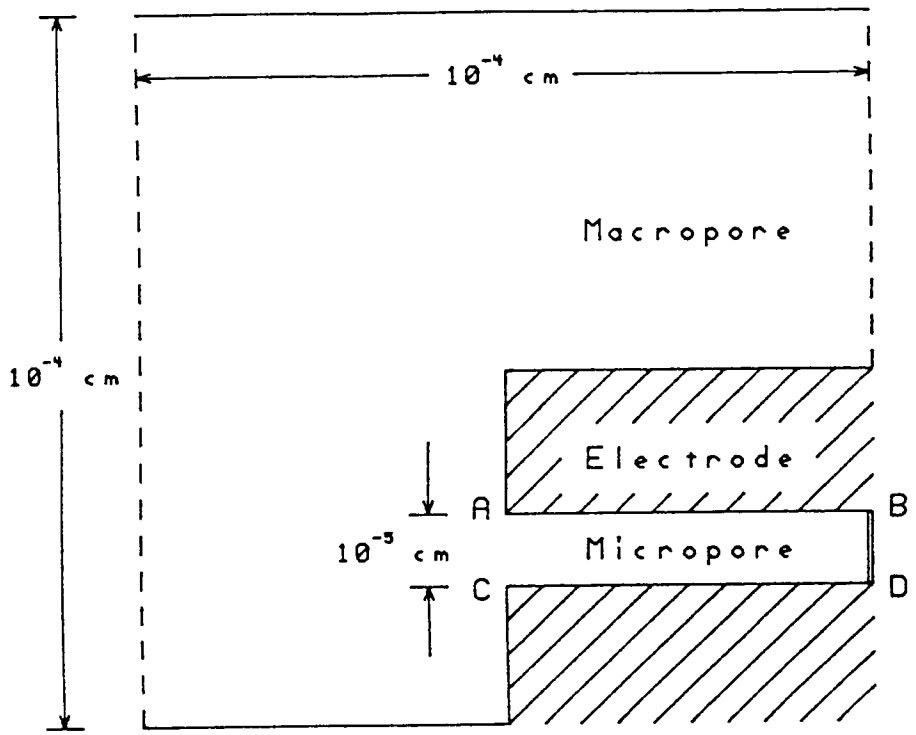

Figure 10. Macropore-micropore structure with micropore parallel to macropore axis. Dotted lines represent cross-sectional planes; solid boundaries represent interfacial area.

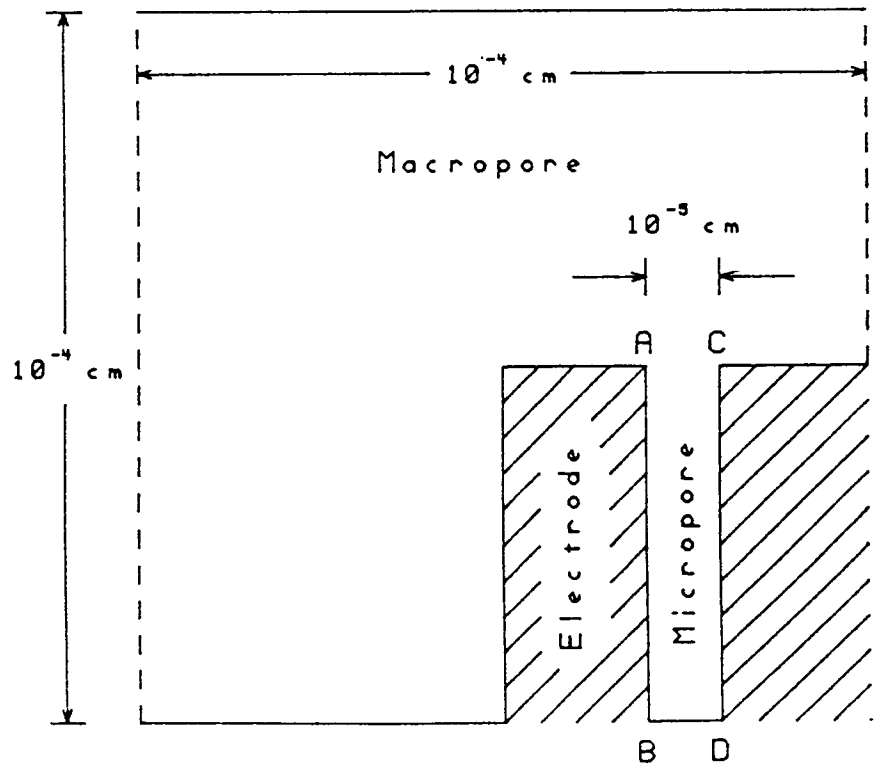

Figure 11. Macropore-micropore structure with micropore perpendicular to macropore axis.

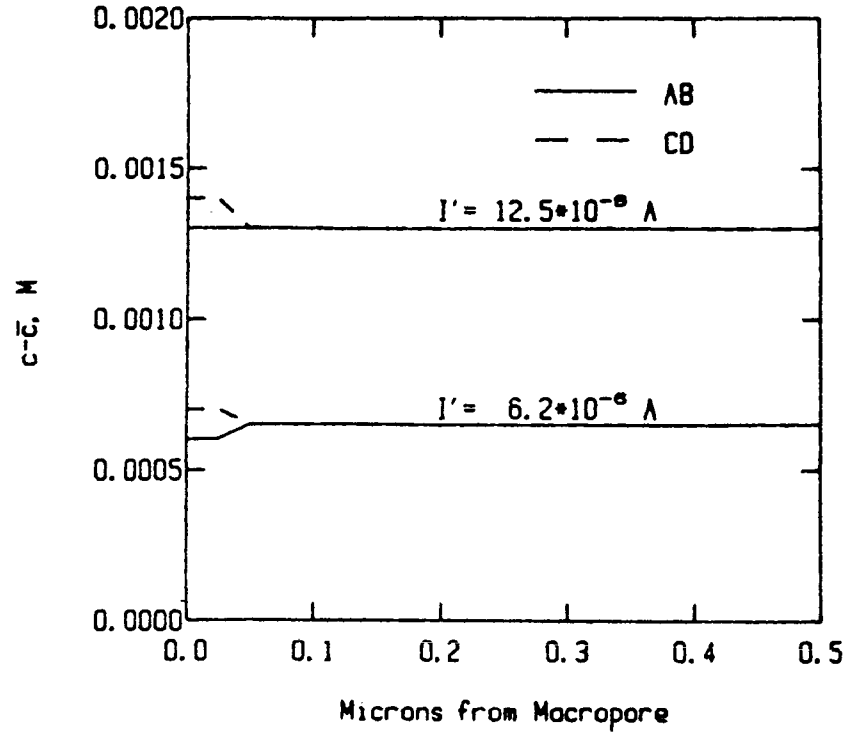

Figure 12. Concentration variations in the micropore in Figure 10. The average concentration in the macropore-micropore structure is $\bar{c}$; the variation is seen to be quite small.

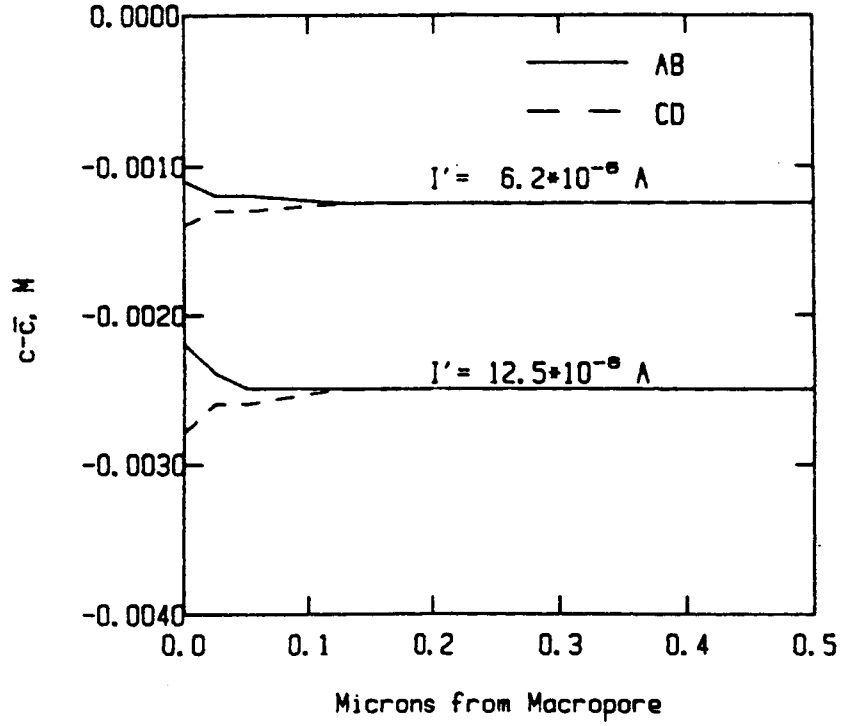

Figure 13. Concentration variations in the micropore in Figure 11.

THEORETICAL PERFORMANCE OF HYDROGEN-BROMINE RECHARGEABLE SPE FUEL CELL*

R.F. Savinell and S.D. Fritts
Case Western Reserve University
Cleveland, Ohio 44106

A mathematical model was formulated to describe the performance of a hydrogen-bromine fuel cell. Porous electrode theory was applied to the carbon felt flow-by electrode and was coupled to theory describing the SPE system. Parametric studies using the numerical solution to this model have been performed to determine the effect of kinetic, mass transfer, and design parameters on the performance of the fuel cell. The results indicate that the cell performance is most sensitive to the transport properties of the SPE membrane. The model was also shown to be a useful tool for scale-up studies.

INTRODUCTION

Hydrogen-bromine fuel cells are of interest as both primary and regenerative energy storage systems. The fuel cell system can be coupled with solar cell arrays to provide the power necessary to charge the system. The regenerative capability of hydrogen-bromine fuel cell systems, along with their high energy densities, make them excellent candidates for space power applications.

The electrochemical reactions for the hydrogen-bromine system are nearly reversible, and the use of solid polymer electrolytes has eliminated cell gaps. Consequently, good energy storage efficiencies can be obtained even at high current density operation.

High current density operation requires reactor designs which enhance mass transfer rates. A flow system is used to improve mass transfer and to aid in thermal management.

A promising design for a hydrogen-bromine device is one having a negative half-cell with only a gas phase which is separated by a solid polymer ionic conducting membrane from a positive half-cell with a flowing aqueous electrolyte. The hydrogen and bromine are stored external to the cell, the hydrogen in the form of a metal hydride. This configuration warrants theoretical treatment for further development and scale-up. Therefore, this work has focused on the development of a theoretical model capable of predicting overall cell performance.

In this paper, a theoretical model of a hydrogen-bromine fuel cell is described. The model equations were solved by numerical techniques. The parametric studies with this model elucidate the effects of catalyst activity, mass and ion transport, and cell scale-up on single cell performance. A discussion is presented on the results of these studies.

*This Research was supported by NASA Contract NAG 3-500 and NSF award CPE-8351849

SYMBOLS

A_t = characteristic area of an SPE consisting of exposed and unexposed membrane, cm^2

a = specific electrode area (i.e. the active area per unit electrode volume), cm^{-1}

$a'^{\delta}_{Br_2}$ = surface bromine activity

$a^{f\,\delta}_{Br_2}$ = bromine activity of reactor feed

C^{δ}_{Br-} = local bulk bromide concentration, mol/l

C'^{δ}_{Br-} = surface bromide concentration, mol/l

C^{β}_{H+} = bulk β-phase concentration of protons in equilibrium with the δ-phase, mol/l

C'^{β}_{H+} = proton concentration in the β-phase at the electrode surface, mol/l

$C^{f\delta}_{Br-}$ = cell feed concentration of bromic acid, mol/l

D^{δ}_{Br} = diffusion coefficient of bromide ion in solution, mol/l

D^{β}_{H+} = effective proton diffusion coefficient in the membrane, mol/l

F = Faraday's constant, 96, 487 A-s/equil

f = fraction of SPE not in contact with the current collector

k_m = mass transfer coefficient, cm/sec

I = total current from a characteristics area (A_t), A

i = current density in the porous electrode based on the true electrode area, A/cm^2

$i_{o,ref}$ = bromine reaction exchange current density evaluated for a bromine reference electrode at cell inlet concentrations, A/cm^2

i' = hydrogen side current density, (based on membrane area) A/cm^2

$i'_{o,ref}$ = exchange current density (based on membrane area) evaluated at unit proton activity and hydrogen pressure, A/cm^2

L, L' = length and width of SPE section not in contact with current collector, cm

n = number of electrons transferred in reaction, equiv/mol

$p_{H_2}^{\alpha}$ = hydrogen partial pressure, atm.

R_s = effective membrane area resistivity, ohm-cm^2

t = porous electrode thickness, cm.

t_β = membrane thickness, cm.

t_+ = transport number for protons in the membrane

U = equilibrium cell potential, volts

v_y = plug flow solution velocity through the porous electrode, cm/sec

α_a, α_c = anodic and cathodic transfer coefficients, respectively, and usually reported as both being 1/2

δ_e = thickness of platinum catalyst layer on SPE, cm

ϵ = void fraction of bromine electrode

ϵ' = volume fraction of membrane material between platinum catalyst particles

κ = effective electrolyte conductivity, mho/cm

ρ_e = effective resistivity of platinum catalyst, ρ_e^o of solid platinum, ohm-cm

ϕ_1, ϕ_2 = bromine side metal and solution phase quasielectrostatic potentials versus a bromine reference electrode at feed concentrations, V

ϕ_1', ϕ_2' = hydrogen half cell quasielectrostatic potentials relative to a normal hydrogen electrode of the metal phase and the β-phase respectively, V

THEORY

The description of a single hydrogen-bromine cell is shown in figure 1. The hydrogen electrode is treated as a planar electrode having a current carrying bus network. The bromine electrode is a porous carbon felt.

The planar hydrogen electrode, (α-phase), is in direct contact with the solid polymer electrolyte denoted as the β-phase. The kinetic expression for the hydrogen reaction can be written according to the nomenclature and analysis of Trainham and Newman [ref. 1] as

$$i' = i'_{o,ref}\left[\left[\frac{p^{\alpha}_{H_2}}{1\ atm}\right]^{1/2} \exp\left\{\frac{\alpha_a F}{RT}(\phi'_1-\phi'_2)\right\} - \frac{C'^{\beta}_{H+}}{1\ mol/l} \exp\left\{\frac{-\alpha_c F}{RT}(\phi'_1-\phi'_2)\right\}\right] \quad (1)$$

where the nomenclature is presented above.

The partial pressure of hydrogen at the catalyst surface is assumed to be equal to that of the bulk. The kinetic expression also requires specification of the concentration of the protons at the surface of the platinum particles. The Nafion membrane is believed to be composed of clusters of hydrophilic sites in a hydrophobic matrix [ref. 2]. Protons are associated with the fixed functional sulfonate groups and with the free water phase. For our model we assumed that the protons involved with the surface reaction come from the free acid phase. Protons are then transported across the membrane through a diffusion/migration mechanism. The interfacial mass transfer can be expressed as:

$$i' = \frac{-nFD^{\beta}_{H+}}{(1-t_+)t_{\beta}} [C^{\beta}_{H+} - C'^{\beta}_{H+}] \times 10^{-3} \quad (2)$$

The concentration of protons in the membrane at the side opposite the hydrogen electrode is assumed to be in equilibrium with the adjacent HBr solution. This concentration was estimated by using a curve fit of the data given by Yeo and Chin [ref. 3], which is expressed as:

$$C^{\beta}_{H+} = -0.458 + 0.80067C^{\delta}_{Br-} + 0.023843C^{\delta\ 2}_{Br-} \quad (3)$$

We have recently begun work to examine the role of the protons associated with the fixed ions on the kinetics and to examine the proton diffusion mechanisms in Nafion membranes.

The metal phase potential, ϕ'_2, is taken to be uniform. A conductive bipolar plate feeds the current to the platinum catalyst. Although current must flow through a thin platinum layer to the bipolar plate contact point, the potential drop is estimated to be small. A simple model which justifies this assumption is described in the Appendix.

The bromine electrode performance is described by macroscopic homogeneous porous electrode theory [ref. 4,5]. The necessary descriptive equations are now summarized. The charge balance, can be written as

$$\frac{d^2\phi_2}{dx^2} = -\frac{ai}{\kappa} \quad (4)$$

with boundary conditions

$$x = 0, \quad \frac{d\phi_2}{dx} = 0 \tag{5}$$

$$x = t, \quad \phi_2 = \phi_2' + U - i'R_s \tag{6}$$

where R_s is the membrane resistivity. After neglecting diffusion in the axial direction, the conservation of mass of the bromide ion is written as

$$v_y \frac{\partial C^{\delta}_{Br-}}{\partial y} = \epsilon D^{\delta}_{Br-} \frac{\partial^2 C_{Br-}}{\partial x^2} - \frac{ai}{nF} \times 10^3 \tag{7}$$

with boundary conditions of

$$x = 0, \ t \quad \frac{dC^{\delta}_{Br-}}{dx} = 0 \tag{8}$$

$$y = 0, \quad C^{\delta}_{Br-} = C^{f\ \delta}_{Br-} \tag{9}$$

The surface concentration is related to the bulk concentration through the mass transfer coefficient, k_m, by the following expression.

$$i = nFk_m [C^{\delta}_{Br-} - C'^{\delta}_{Br-}] \times 10^{-3} \tag{10}$$

The kinetics of this reaction can be expressed by

$$i = i_{o.ref} \left[\frac{C'^{\delta}_{Br-}}{C^{f\ \delta}_{Br-}} \exp\left\{ \frac{\alpha_a F}{RT} (\phi_1 - \phi_2) \right\} - \left[\frac{a'^{\delta}_{Br_2}}{a^{f}_{Br_2}} \right]^{1/2} \exp\left\{ \frac{-\alpha_c F}{RT} (\phi_1 - \phi_2) \right\} \right] \tag{11}$$

In these calculations, the ratio of the bromine activities is taken to be unity and the carbon phase potential, ϕ_1, is assumed to be uniform.

At the membrane-porous electrode interface, the membrane current density, i', is related to the porous electrode current density, i, by the following expression:

$$\kappa \frac{d\phi_2}{dx} \Bigg|_{x=t} = i' = -a \int_0^t i \, dx \tag{12}$$

The equations of this model were combined, made dimensionless, linearized, and then solved using an implicit numerical technique. The dimensionless equations are listed in Table 1, with the corresponding dimensionless groups given in Table 2.

The numerical technique used here was that developed by Newman [ref. 6]. The nonlinear equations (B) and (D) of Table 1 were linearized by a first order Taylor

series expansion. Then the derivatives were written in second order finite difference form. The boundary at the bromine electrode-membrane interface was taken into account by two methods. In the first method (Equation (E)), the gradient of the potential in the solution phase is equated to the membrane current density. At the electrode entrance, the distributions are calculated using the boundary conditions and Equations (B) through (E). A step is made in the axial direction, and Equations (A) through (E), along with the appropriate boundary conditions are solved using the Crank-Nicholson symmetric form. All the equations are solved implicitly with C_1 - C_6 unknown variables. The iterative technique was carried out until convergence with the Taylor series expansions taken about the solution of the previous iteration.

An alternate method of handling the bromine electrode-membrane interface involved using equation (E') instead of equation (E). The integration was carried out using the trapezoidal method. Since C_4 and C_6 are only needed at the membrane position, these variable were used as dummy variables for storing the summation terms of the integration across the porous electrode. This eliminated extra variables, and allowed the integration to be performed implicitly.

The results of the numerical calculations were checked by comparing the results at the boundary conditions and by verifying intermediate calculations. The step sizes across the porous electrode and along the axial direction were varied to be sure that they did not have a significant effect on the results. The convergence criterion was increased from a relative error of 5 E-6 to 5 E-8. This had no effect on the calculated results.

The calculations using equation (E) took ~7 iterations at the first position and about ~3 iterations at subsequent axial positions for the base case. We devised the second method (use of equation (E')) because it was thought to be more stable since high current-densities and consequently steep gradients were expected with this system. However, the number of iterations to convergence and computational times were about the same. Even when comparing the two methods with high overpotentials, the second method required a few more iterations and slightly more computer time. Therefore, any advantages offered by the second method were not recognized and the method did not appear to justify the added programming complexities which were necessary to implement it.

RESULTS AND DISCUSSION

Model calculations were first done on a base case of parameters which represent reasonable values for a small single cell. The values for these parameters are listed in Table 3. The feed bromide concentration corresponds to approximately a 17% state of charge of an initial solution concentration of 48% HBr. The membrane resistivity was estimated from data for a 24% HBr solution [ref. 3]. The effective solution conductivity was calculated from the conductivity of the electrolyte by [ref. 1].

$$\kappa = \kappa_o \epsilon^{1.5}$$

where $\kappa_o = 0.8\Omega^{-1}cm^{-1}$ [9] and ϵ was estimated by knowing the density of carbon felt [10] and the density of graphite [7]. The dimensionless axial length for the base case was chosen to be Y = 0.0282656. This length corresponds to a cell length to

velocity ratio of 77.5 s (or a 15.5 cm long cell operating with a solution velocity of 0.2 cm/s).

The open circuit potential, OCV, of a prototype SPE hydrogen-bromine cell was measured experimentally. The details of this study were reported elsewhere [ref. 11] and only a summary of the findings will be given here. In figure 2 the mean experimental values of the OCV and the corresponding 95% confidence interval are shown as a function of state of charge. The OCV's for solutions with a charge capacity of 48 wt% HBr (i.e. initial uncharged solution) are lower than the OCV's for a system with a charge capacity of 35 wt%. This indicates that a trade-off exists between the OCV and the charge capacity of the system.

The experimentally measured OCV's of this work were compared to the semi-empirical correlation reported by Yeo and Chin [ref. 3]. Their correlation was derived from experimental data assuming a unit activity of bromine. The correlation predicts somewhat greater open circuit voltages than those found in our experimental work at the lower states of charge. At the highest state of charge, the OCV predicted by the Yeo and Chin correlation was somewhat less than that found experimentally, even though the solubility of bromine in the experimental solution was exceeded (i.e. the bromine activity was unity). The differences could be due to the differences in tribromide and pentabromide concentrations. Overall, though, the comparison between our experimental data and the correlation of Yeo and Chin [ref. 3] was good; See figure 3. Therefore, in this simulation study the correlation of Yeo and Chin [ref. 3] was employed for estimating the OCV of a hydrogen-bromine fuel cell.

Base Case Calculations

Some calculation results for base case conditions are given in figures 4 and 5. The calculations were done for a charging mode of operation with a 200 mV applied polarization. Figure 4 shows the distribution of local current density across the bromine electrode. Under these conditions, only half of the electrode appears to be active. A larger current density occurs near the cell entrance. In figure 5 the distribution of bromide ion across the bromine electrode is shown. At the cell entrance, the bromide concentration is constant as established by the boundary condition. However, a significant concentration variation across the bromine electrode is noted when moving up the cell in the axial direction. Also, one can even note the drop in bromide concentration near the current collector. This, of course, is due to a net consumption of bromide ions. The significance of these calculations will become clear when variations on the base case are discussed.

Bromide Ion Mass Transport

The mass transfer coefficient associated with the bromine electrode for the base case was calculated from the Bird correlation (12) using a velocity of 1 cm/s, and assuming a cylindrical geometry for the fibers of the porous carbon electrode. The calculations show that there is very little effect on cell performance if the magnitude of the product ak_m is lowered by one order of magnitude or increased by two orders of magnitude. Mass transfer of the bromide species to the carbon fibers does not appear to be a problem in this system.

Kinetic Effects

The model calculations are useful for assessing the effectiveness of electrode catalyst. For the base case solution composition , the exchange current density was estimated [ref. 13] using data given by Mastragastino and Gramellini [ref. 14] for a smooth vitreous carbon electrode. As shown in figure 6 , an increase in the exchange current density will only have nominal impact on cell performance. For the hydrogen electrode, the base case exchange current density was estimated by assuming that the ratio of true platinum area to membrane area is 300:1 (i.e. an exchange current density of 0.3 A/cm^2). As shown in figure 7, a further increase in platinum loading or enhancement of surface area will not significantly improve cell performance. However, a loss in platinum activity could severely compromise the performance of the cell. This could occur, for example, if bromine species are transported across the membrane so that they adsorb on the platinum and thus poison the active area.

Membrane Effects

The model calculations demonstrate that the membrane transport properties have the most dramatic impact on cell performance. To demonstrate this, charge and discharge polarization curves are shown in figure 8. The performance is enhanced significantly when the membrane resistivity is lowered by an order of magnitude (psi/10). In this figure, a limiting current density is approached when in the charging mode. This effect is caused by a limit in the diffusion rate of protons across the membrane. The diffusion coefficient of protons was calculated by using the Nernst-Einstein relation and membrane conductivity data. If transport is restricted to only migration of protons associated with fixed ions, then a concentration gradient would not exist. However, since there is a significant amount of free acid in the membrane under these conditions [ref. 3], the transport number for proton does not necessarily equal unity. Thus, a concentration gradient can be established. Actually, the transport mechanism is likely to be more complicated since protons are moved by simple diffusion and migration in the free acid and by migration only along the fixed ion sites. Therefore, the effective transport number is probably not constant with current density. These results indicate that further detailed studies of membrane transport under these conditions are necessary.

Another aspect of the membrane effect deals with the local acid concentration in the solution phase adjacent to the membrane being much lower than the inlet acid concentration. This was shown earlier in figure 5. The computer calculations were modified to account for this effect. The result is shown in figure 9 where the membrane current density along the axial direction is reported. Under these conditions, the changing acid concentration is shown to have a large effect on cell performance.

Scale-up Effects

Some scale-up considerations were examined using the model developed here. For example, increasing the length of the cell in the axial direction results in a lower overall cell current. This is shown in figure 9. Another question which often surfaces when designing a cell deals with ascertaining the optimum thickness of a porous electrode. The effect on cell performance of electrode thickness when the electrolyte velocity is maintained constant is shown in figure 10. As can be seen in this figure, under these conditions an electrode thickness greater than ~1.8 mm only provides marginal improvement in cell performance. As the electrode thickness is increased though, a large volumetric flowrate of electrolyte passes through the cell and consequently, the conversion per pass decreases.

On the other hand, if the volumetric flowrate is maintained constant when examining the effect of electrode thickness, the current density decreases as the electrode thickness increases. This is shown in figure 11. In this case, as the electrode thickness increases, the linear velocity decreases which also decreases the convective transport of mass. As a consequence of this, the concentration of bromic acid drop considerably which causes slower kinetics and thus lower current density.

CONCLUDING REMARKS

A mathematical model was formulated for evaluating design and operating parameters of a hydrogen-bromine fuel cell. The model coupled porous electrode theory applied to the bromine electrode with membrane transport and a planar treatment of the hydrogen electrode.

The parametric studies demonstrate that both the bromine and hydrogen electrode specific surface area and kinetic parameters influence cell performance. However, the magnitude of performance enhancement decreases as catalytic and surface area effects increase. Mass transfer does not seem to be a significant limitation in the bromine electrode.

The calculations indicate that the transport properties of the membrane are the most influential factor in controlling cell performance. Further research appears to be necessary to characterize the proton transport mechanisms in the membrane material.

Finally, the model developed here was demonstrated to be a useful tool for studying cell scale-up effects.

LITERATURE CITED

1. Trainham, J. A. and J. Newman, J. Electrochem. Soc., 130, 533 (1977).

2. Hsu, W.Y. and T.D. Gierke, J. Membrane Sci., 13, 307, (1983).

3. Yeo, R. S., and D-T. Chin, J. Electrochem. Soc., 127, 549 (1980).

4. Newman, J. and C. W. Tobias, J. Electrochem. Soc., 109, 1183, (1962).

5. Newman, J. and W. Tiedemann, A.I.Ch.E. J., 21, 25, (1975).

6. John Newman, Electrochemical Systems, (Prentice-Hall Inc., Englewood, Cliffs, NJ) 1973.

7. CRC Handbook of Chemistry and Physics, R. C. Weast, editor, 59th Edition, (Chemical Rubber Company, West Palm Beach, FL), 1975, a.p F62, b.p.F171.

8. Fedkiw, P. S., and R.K. Watts, J. Electrochem. Soc., 131, 701, (1984).

9. Haase, J., Sauermann, P.F. and K.H. Ducker, Zeit. Phys. Chem., 47, 227 (1965).

10. Jalen, V., Morriseau, B., and L. Swette, NASA Contract DEN 3-198, Giner Inc., 1982.

11. Fritts, S.D., M.S. Thesis, The University of Akron, 1986.

12. Bird, R. B., Stewart, W. E., and E. N. Lightfoot, Transport Phenomena, John Wiley and Sons, New York, 1960.

13. White, R.E., Lorimar, S.E. and R. Darby, J. Electrochem. Soc., 130, 1123, (1983).

14. Mastragostino, M. and C. Gramellini, Electrochimica Acta, 30, 373 (1985).

15. Lanzi, O. and R.F. Savinell, J. Applied Electrochem, 14, 425 (1984).

APPENDIX

Justification of the Equipotential Hydrogen Electrode Assumption

An enlarged view of the porous platinum electrode with a current collector is shown in figure A1. The electronic current must be conducted through the platinum layer to the current collector. The closer the current collector contacts are to each other, the lower the voltage drop will be within the electrode. However, many contact points will block the platinum surface and thus will cause higher overpotentials. This trade-off will now be examined.

Assuming an approximate uniform current distribution, a voltage balance gives [ref. 15]

$$\Delta\phi_1' = \frac{I}{LL'} \rho_e \frac{L^2}{8\delta_e}$$

where L' is the width of the electrode section, and δ_e is the thickness of the platinum layer. In this expression, $\Delta\phi_1'$ is the potential drop in the platinum layer over the distance L/2. If f is the fraction of electrode area exposed to the gas phase, then for a symmetrical current collector system

$$A_t f = LL' \quad (A-2)$$

where A_t is the total area of the membrane. The apparent current density can be written as

$$i' = \frac{I}{A_t} = \frac{f\ I}{LL'} \quad (A-3)$$

Therefore, equation (A-1) becomes

$$\Delta\phi_1' = \frac{i'}{f}\frac{\rho_e}{\delta_e}\frac{L^2}{8} \qquad (A\text{-}4)$$

Of course, as f approaches unity, the contact area between the current collector and the platinum electrode diminishes and the contact resistance may become substantial. This effect, however, is negliected in this analysis.

Assuming the platinum layer consists of a close packing of spherical particles, the Bruggeman equation can be used to relate the effective metal phase resistivity, ρ_e, to the resistivity of solid platinum, ρ_e^o:

$$\rho_e = \rho_e^o(1-\epsilon')^{-3/2}$$

In this expression, ϵ' is the void volume fraction between the platinum particles.

A summary of calculations of the potential drop is shown below. These results indicate that the potential drop along the platinum electrode is small. Therefore, the assumption in the model of an equipotential electrode is justified in most instances.

Calculation of $\Delta\phi_1'$ Summary

$\epsilon' = 0.3$ $\quad \rho_e = 1.81 \times 10^{-5}$ ohm-cm (ref. 7b)

$\delta_e = 30$ μm $\quad i' = 1000$ mA/cm^2

f	L, mm	δ_e, μm	$\Delta\phi_1'$, mV
0.2	2	5	0.9
		10	0.45
	5	5	5.65
		10	2.82
0.5	2	5	0.36
		10	0.18
	5	5	2.26
		10	1.13

Table 1. Dimensionless Model and Boundary Conditions.

$$\frac{\partial C_1}{\partial Y} = \frac{\partial^2 C_1}{\partial X^2} - \Omega\,(C_1 - C_2) \tag{A}$$

$$\beta C_f(C_1 - C_2) = C_2\exp\{\phi - C_3\} - \exp\{C_3 - \phi\} \tag{B}$$

$$\frac{d^2 C_3}{dX^2} = -\gamma C_f(C_1 - C_2) \tag{C}$$

$$-\lambda(C_6 - C_4) = P^{1/2}\exp\{\sigma - C_5\} - C_4\exp\{C_5 - \sigma\} \tag{D}$$

$$\eta(C_4 - C_6) = \frac{dC_3}{dX} \tag{E}$$

$$C_6 - C_4 = \chi C_f \int_0^1 (C_1 - C_2)dX \tag{E'}$$

Boundary conditions:

$$X = 0 \qquad \frac{dC_1}{dX} = 0 \tag{F}$$

$$\frac{dC_3}{dX} = 0 \tag{G}$$

$$X = 1 \qquad C_3 = C_5 + \theta + \psi(C_6 - C_4) \tag{H}$$

$$\frac{dC_1}{dX} = 0 \tag{I}$$

$$Y = 0 \qquad C_1 = 1 \tag{J}$$

Table 2. Definition of Dimensionless Variables and Parameters.

Variables

$$C_1 = \frac{C_{Br-}^{\delta}}{C_{Br-}^{f\ \delta}}, \qquad C_2 = \frac{C_{Br-}^{\prime\ \delta}}{C_{Br-}^{f\ \delta}}, \qquad C_3 = \frac{\alpha F \phi_2}{RT} \qquad C_4 = \frac{C_{H+}^{\beta}}{1\ \text{mol/l}}, \quad C_5 = \frac{\alpha F \phi_2}{RT},$$

$$C_6 = \frac{C_{H+}^{\beta}}{1\ \text{mol/l}}, \qquad X = x/t, \qquad Y = \frac{\epsilon D_{Br-}}{v_y t^2}$$

Parameters

$$\phi = \frac{\alpha \phi_1 F}{RT}, \qquad \theta = \frac{\alpha U F}{RT}, \qquad \sigma = \frac{\alpha \phi_1' F}{RT}, \qquad C_f = \frac{C_{Br-}^{f\ \delta}}{1\ \text{mol/l}},$$

$$\beta = \frac{nFk_m(0.001\ \text{mol/cc})}{i_{o,ref}},$$

$$\gamma = \frac{anF^2\alpha t^2 k_m(0.001\ \text{mol/cc})}{\kappa RT}, \qquad \Omega = \frac{ak_m t^2}{\epsilon D_{Br-}^{\delta}},$$

$$\lambda = \frac{nFD_{H+}^{\beta}(0.001\ \text{mol/cc})}{t_\beta i'_{o,ref}(1-t_+)}, \qquad P = \frac{p_{H_2}^{\alpha}}{1\ \text{atm}},$$

$$\psi = \frac{\alpha nF^2 D_{H+}^{\beta} R_s(0.001\ \text{mol/cc})}{t_\beta RT\ (1-t_+)}, \qquad \chi = \frac{ak_m t t_\beta (1-t_+)}{D_{H+}^{\beta}},$$

$$\eta = \frac{(0.001\ \text{mol/cc})\alpha F^2 n t D_{H+}^{\beta}}{\kappa RT\ (1 - t^+)}$$

Table 3. Base case values used in parametric studies.

$p_{H_2}^{\alpha}$ = 10 atm. $C_{Br^-}^{f,\delta}$ = 7.45 mole/liter t = 0.3175 cm.

t_β = 0.025 cm. [ref. 3] $D_{H^+}^{\beta} = 9.49\times10^{-7}$ [ref. 3] $D_{Br^-}^{\delta} = 3.87\times10^{-5}$ [ref. 7a]

R_s = 0.255 Ω-cm^2 [ref. 3] κ = 0.74 Ω^{-1}cm^{-1} [ref.8,9] a = 280 cm^{-1} [ref. 8]

ρ = 1.49 g/cc μ = 1 g/cm-sec k_m = 0.0866 cm/sec,

$i_{o,ref}$ = 39.7 mA/cm^2 $i'_{o,ref}$ = 300 mA/cm^2 U = 0.816 V [ref. 3]

ϕ_1 = 1.016 V ϵ = 0.95 t_+ = 0.975

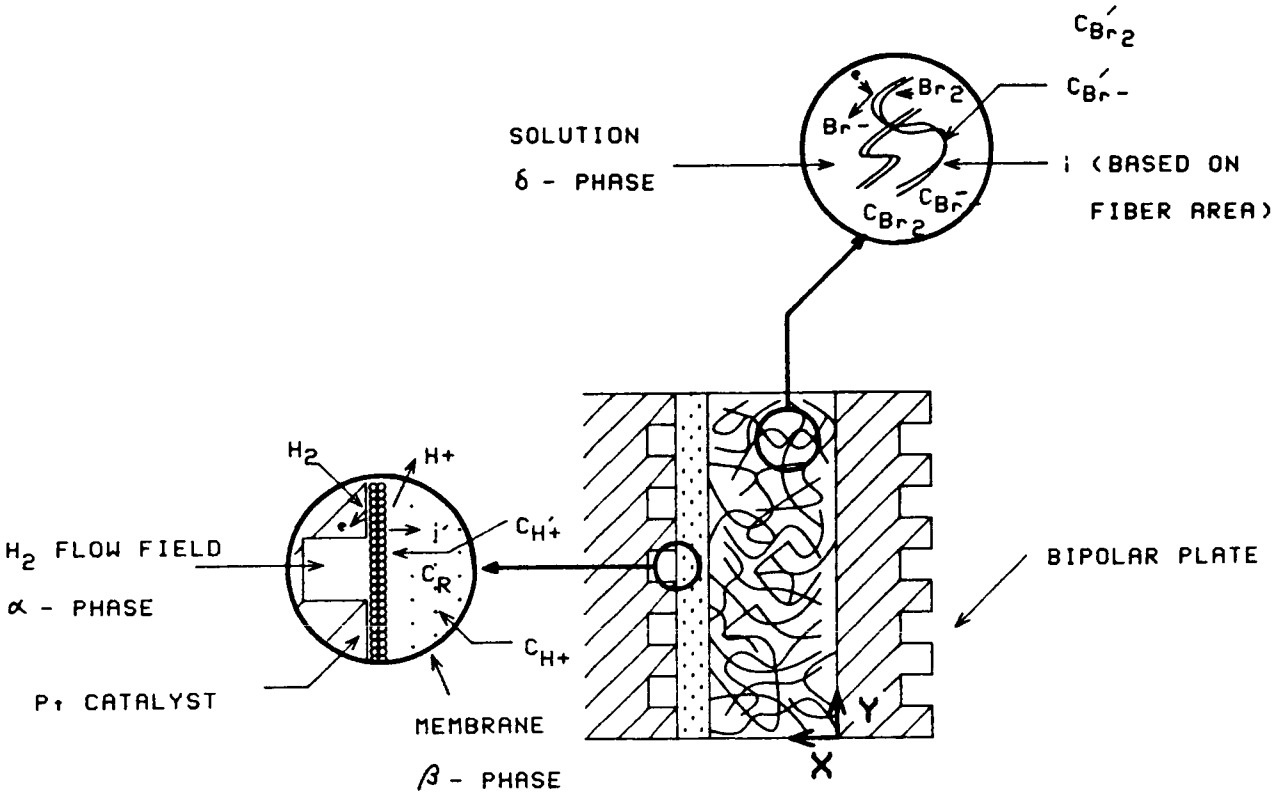

Figure 1: Diagram of H_2-Br_2 fuel cell details for mathematical modeling.

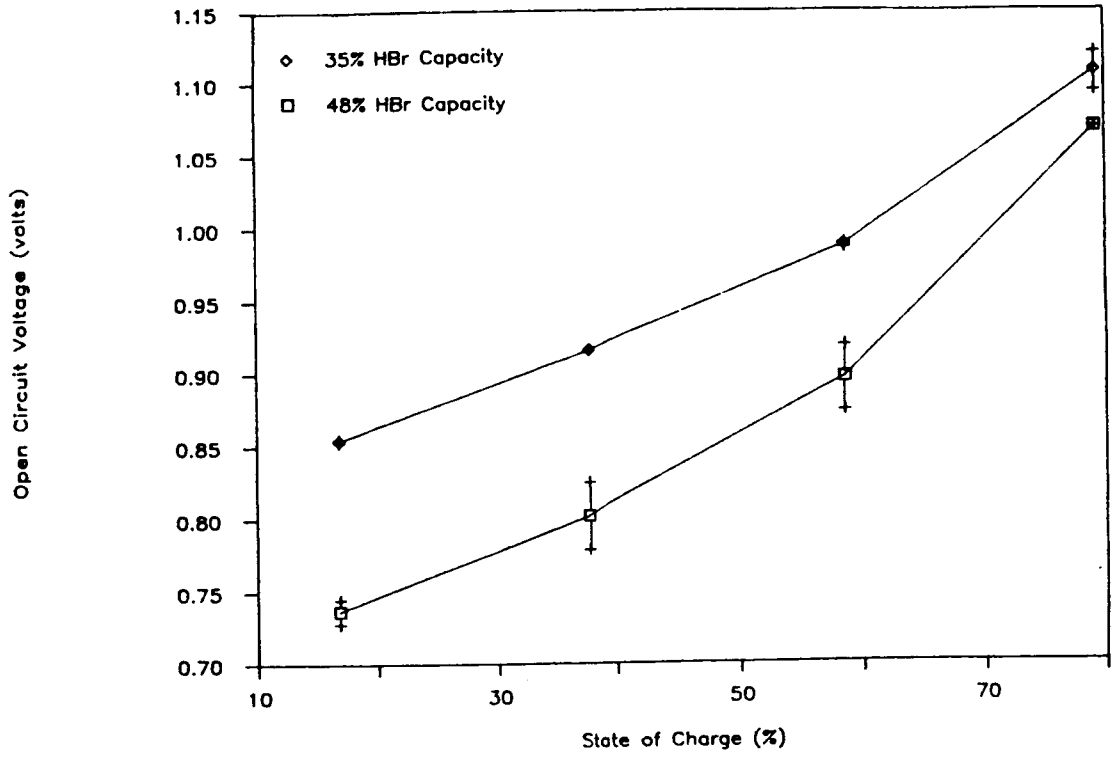

Figure 2: Mean open circuit voltages of H_2-Br_2 cell.

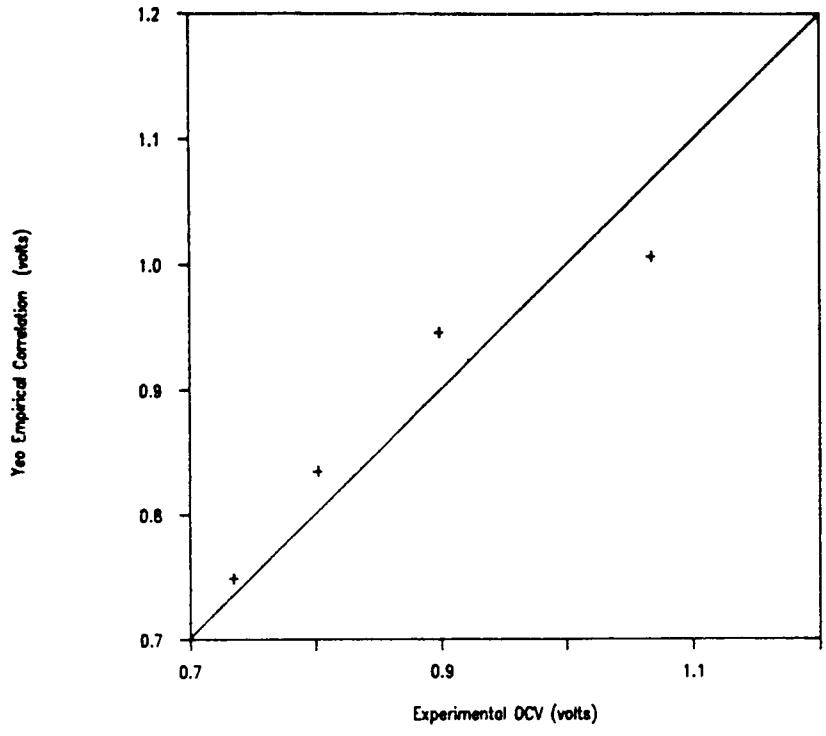

Figure 3: Comparison of experimental open circuit voltages for solutions with 48% HBr charge capacity to open circuit voltages predicted by correlation of Yeo and Chin.

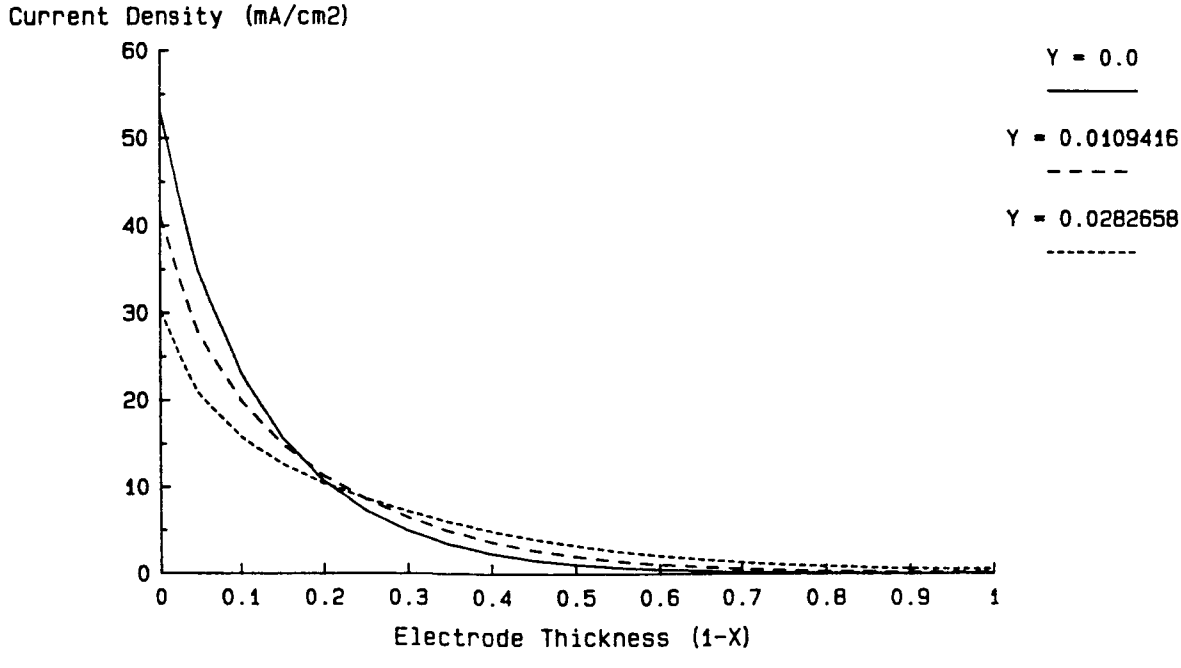

Figure 4: Local current density distribution in porous bromine electrode.

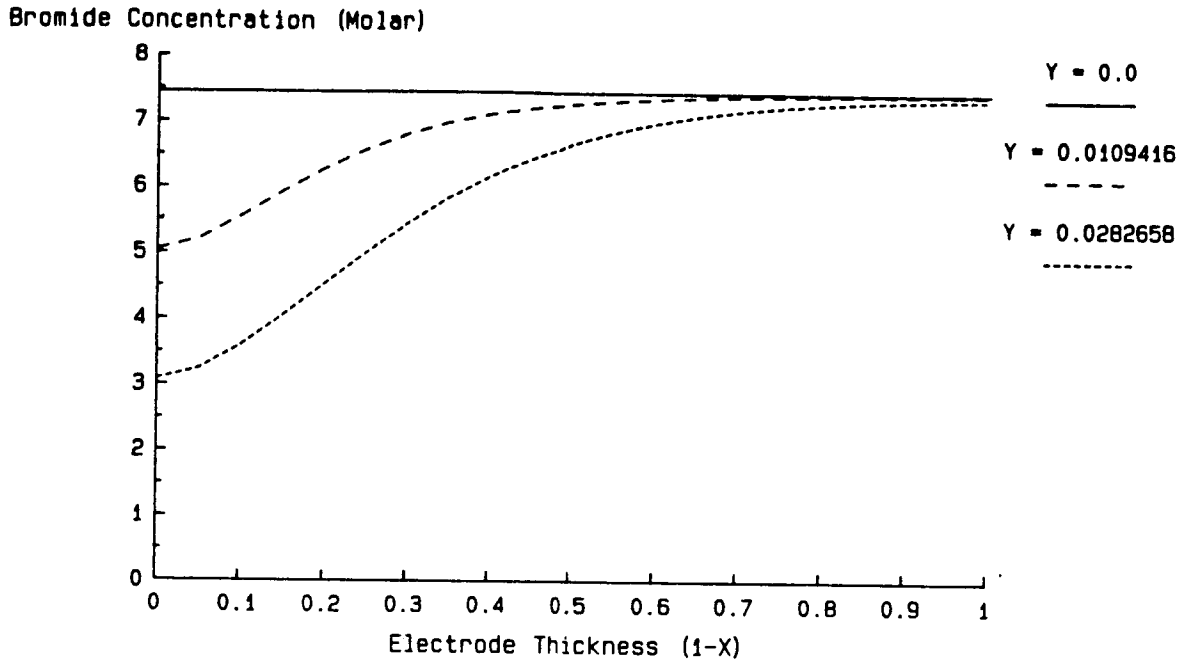

Figure 5: Local bromide ion distribution in porous bromine electrode.

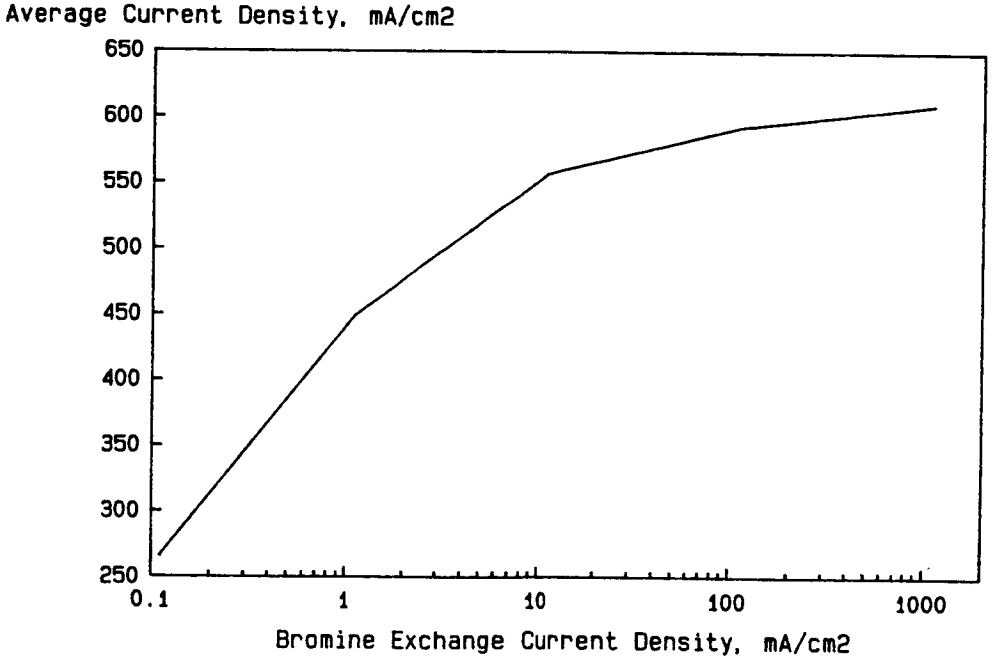

Figure 6: The effect of bromine electrode activity on average cell current density.

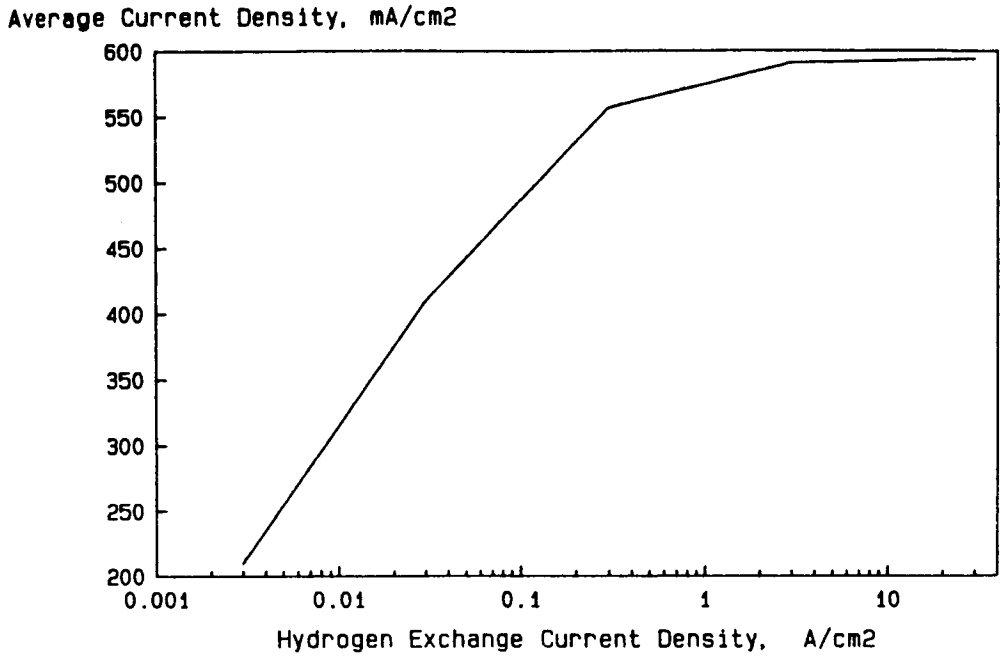

Figure 7: The effect of hydrogen electrode activity on average cell current density.

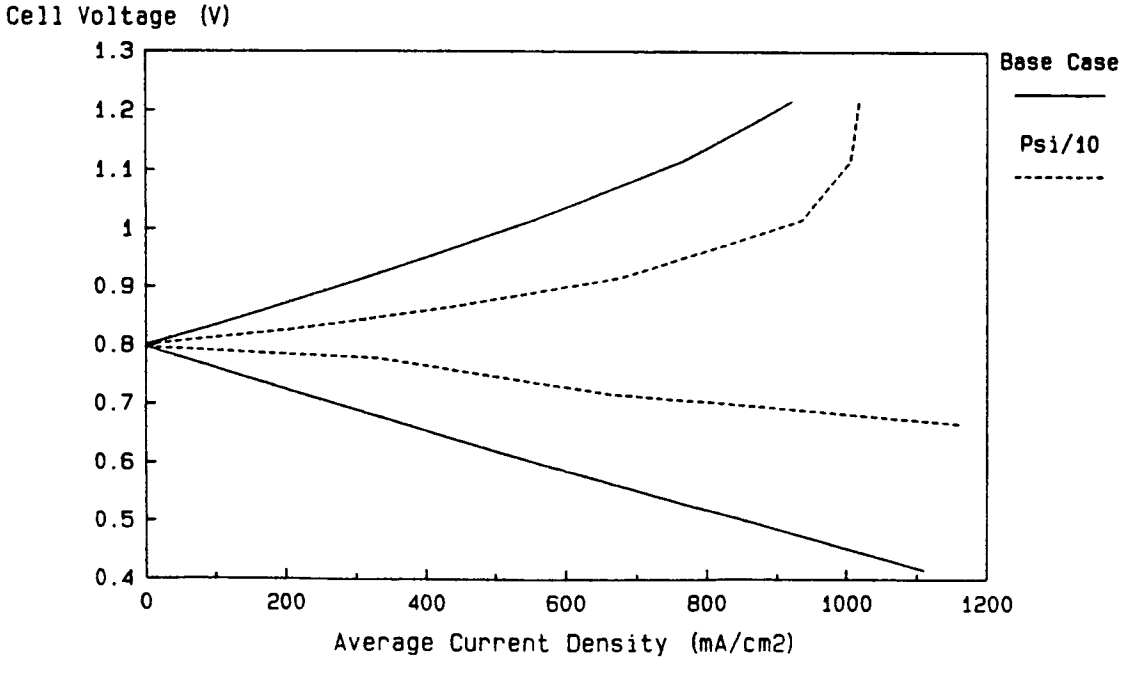

Figure 8: Predicted cell polarization curves.

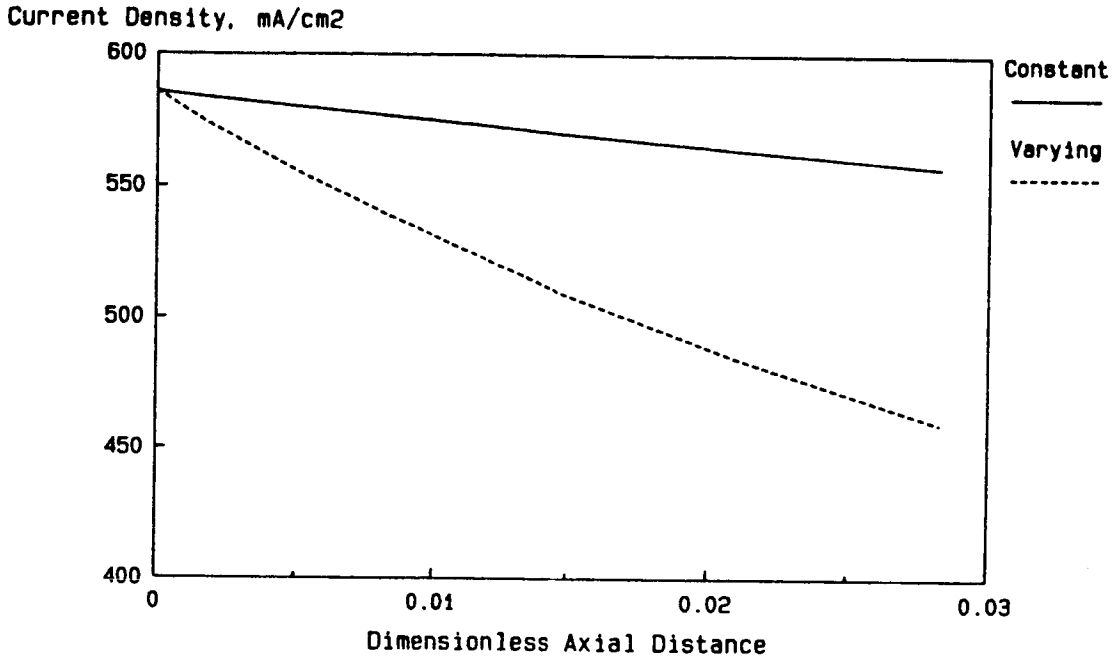

Figure 9: The effect of membrane proton concentration on membrane current density.

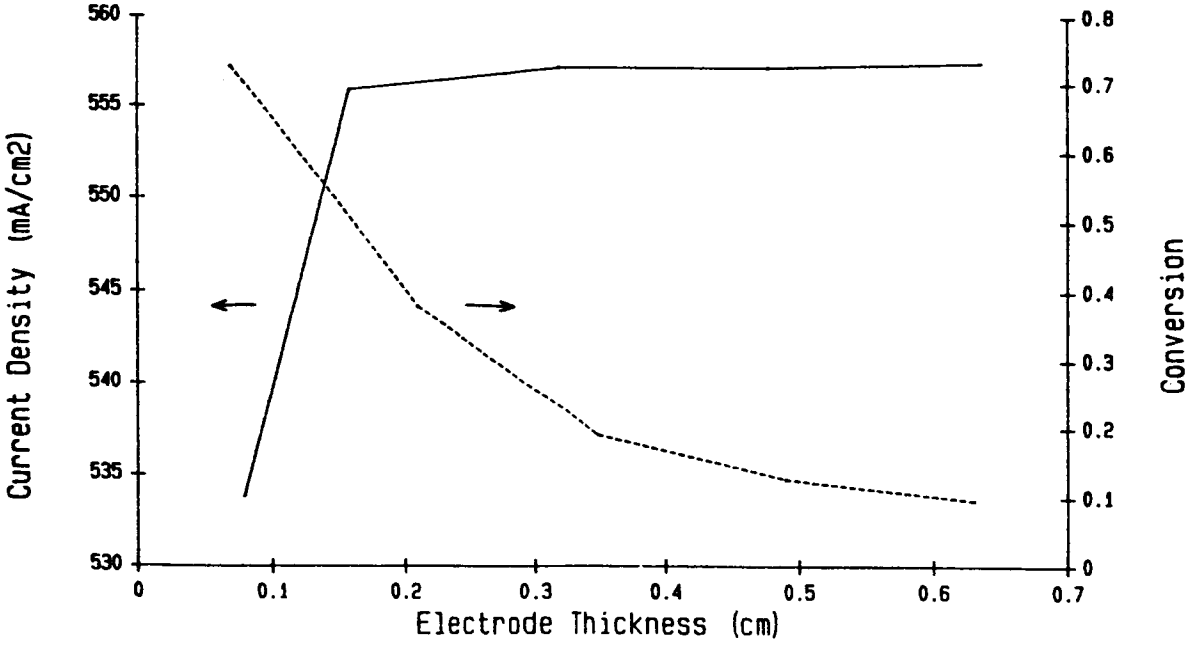

Figure 10: The effect of electrode thickness on cell performance with constant solution velocity.

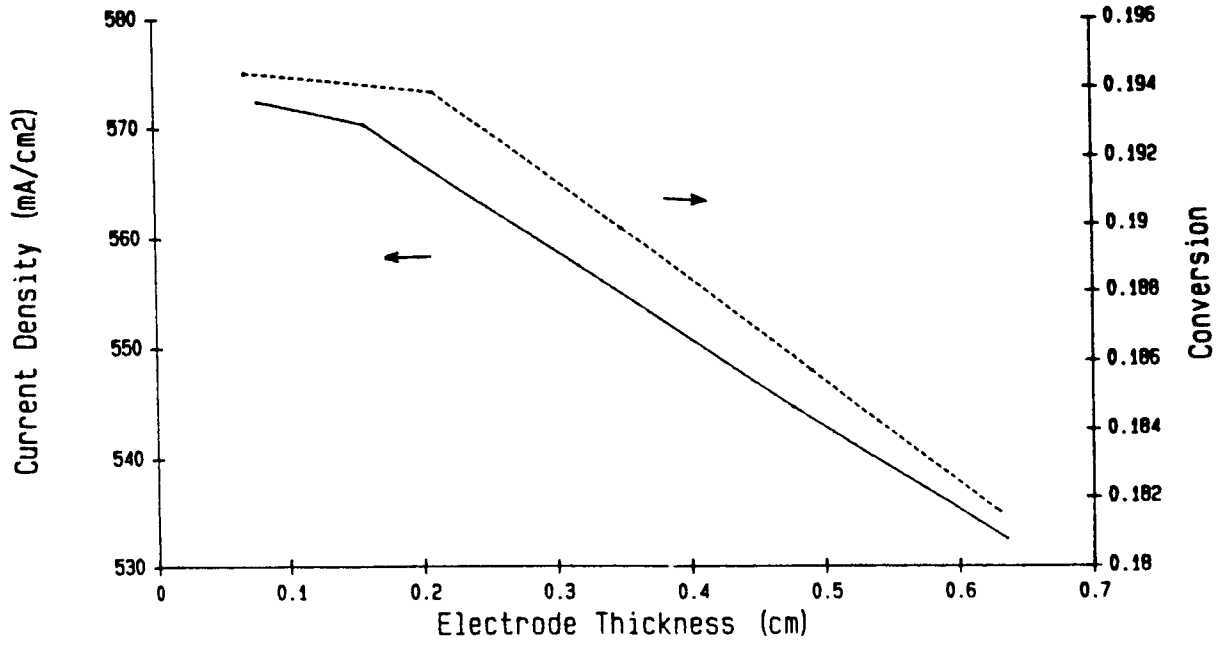

Figure 11: The effect of electrode thickness of cell performance with constant solution volumetric flow rate.

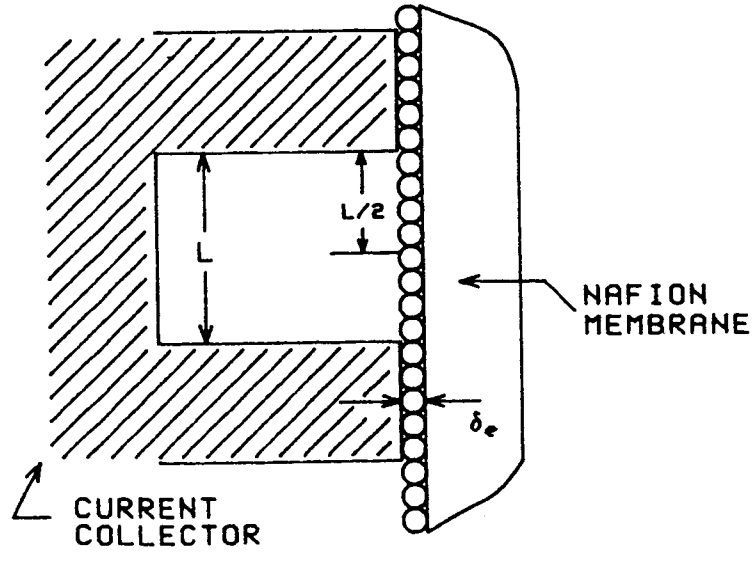

Figure A1: Expanded view with dimensions of a hydrogen electrode of a hydrogen-bromine SPE cell.

ADVANCED RECHARGEABLES WORKSHOP

Gerald Halpert
Jet Propulsion Laboratory
Pasadena, California 91109

The approach in the advanced rechargeables workshop was threefold: (1) review the applications, (2) look at the goals for the technology to meet those applications, and (3) list all the electrochemical systems to be considered in meeting those applications. We selected several technologies that we felt would be available in the next 10 yr for consideration on NASA flights, although not specifically flight qualified. The list includes older as well as present technologies:

(1) Nickel-hydrogen
(2) Sodium-sulfur
(3) Advanced nickel-cadmium
(4) Zinc-bromine
(5) Secondary lithium
(6) Nickel-zinc
(7) Low-temperature sodium - beta alumina
(8) Lithium alloy - iron sulfide and lithium - titanium sulfide
(9) Zinc-oxygen
(10) Aluminum-oxygen
(11) Silver-hydrogen
(12) Silver-zinc
(13) Regenerative hydrogen-oxygen fuel cells
(14) Bipolar

Applications

For low-Earth-orbit (LEO) applications we selected a 100-min duty cycle with a 10-yr goal of 50 000 cycles, 25 W-hr/kg of usable energy, 80 percent efficiency, and a temperature range of -10 to 30 °C. The broad temperature range was selected to avoid the penalties of closely controlling the temperature. The thermal containment system would be on the outside of the battery pack.

Discussions of geosynchronous-Earth-orbit (GEO) applications raised the new concept of using the batteries to maintain electric propulsion. The typical GEO mission goes through two dark periods a year and remains in the Sun the rest of the time (100 cycles/yr). We considered a 20-yr mission that would experience 1 cycle/day. The usable energy would be 100 W-hr/kg and the temperature range would again be broad (-10 to 30 °C). These are old goals that we wanted to speak to when we looked at individual electrochemical systems. Three kinds of applications were considered for load leveling. A powerplant on the Moon or Mars would entail a large battery system that would be used in load leveling. During a planetary comet mission equipment would be operated constantly and charged once a day or so - a kind of load leveling. In a rover a

radioisotope thermoelectric generator (RTG) would provide the main power and a battery would provide the load-leveling power for the peak performance areas (e.g., going over hills). All these applications would require limited cycles, long active shelf life, again 100 W-hr/kg of energy, and obviously 10 yr of intermittent use.

Another application was deep-discharge power if the rover contained only a battery and not an RTG for reasons such as safety or cost. The battery would be the main source of power. An orbit transfer vehicle, which uses a large amount of energy, needs a deep discharge and then a full recharge in some period of time. Again the goals are limited cycles, 100 W-hr/kg of energy, and 80-percent depth-of-discharge (DOD) capability.

Pulse power applications are similar to the rover application. Digging holes into a planet requires a short application of high pulse power. Also, the inertial upper stage or other transfer vehicle would need a large amount of energy to get moving. Thereafter it could be controlled with electropropulsion. These applications require a hybrid battery to supply the pulse power.

On the basis of these requirements we narrowed down the candidates to what we thought would be available in 10 yr. The list includes nickel-hydrogen batteries, regenerative fuel cells, advanced nickel-cadmium batteries, sodium-sulfur batteries (both high and moderate temperatures), zinc-bromine batteries, lithium-TiS_2 batteries, and possibly bipolar batteries of various kinds.

Prime Candidates

In looking at the applications it became clear that even for a single application (e.g., LEO) two levels of power are required. A typical science mission requires a small (1 kW) power system. The space station will require enormous amounts of power. We would want to select the cells and batteries for an electrochemical system that can meet both requirements. Because what is good for the small system might not be good for the large one, and vice versa, we narrowed down the candidates further. These candidates are in no priority order although some might be ready before others for the large systems like space station. For each system we listed what we know that would be helpful in making the selection.

Nickel-hydrogen battery. - The nickel-hydrogen battery has demonstrated $20x10^3$ cycles with a usable energy of 15 W-hr/kg and has greater than 80 percent efficiency. The temperature is in the range 5 °C î 5 deg. Although the nickel-hydrogen battery can supply 750 W or more, obviously much higher power will be required for the space station. A disadvantage of the nickel-hydrogen battery is its volume energy density. To reach the goal of 60 W-hr/l, a common pressure vessel or hydride storage may be needed to reduce the volume. Achieving 25 W-hr/kg of usable energy requires new plate technology; and, as the DOD increases, greater temperature dissipation capability will be needed. Obviously, pulling out in a LEO orbit (a repetitive, relatively short-term orbit) requires high DOD. The higher the DOD, the more energy is taken out of the battery and therefore more heat must be dissipated in a shorter time. Temperature then becomes the more serious issue.

Regenerative fuel cell. - Regenerative fuel cells have the advantage of stable electrode morphology. In the single system concept for large static applications the electrodes are reversed on charge, making the system simpler. The problems are low efficiency and the need for a catalyst for the oxygen electrode as well as the problem of rechargeability.

High-temperature sodium-sulfur battery. - High temperature sodium-sulfur batteries appear possible within the next 10 yr with high specific energy (100 W-hr/kg) and thermal containment. As reported by Douglas Allen, 6300 cycles have been demonstrated at 40 percent DOD - applicable to large systems. The disadvantages are limited cycle life and a 50-50 chance of solving the materials problems at the high temperatures.

For applications smaller than space station two systems look promising - nickel-cadmium and lithium rechargeable batteries.

Nickel-cadmium battery. - The nickel-cadmium system, which of course has been in use for some time, is intended for LEO applications. A number of changes have helped it demonstrate 43 000 cycles at 40 percent DOD. The boilerplate cell has a usable specific energy of 20 W-hr/kg (80 W-hr/l). One disadvantage, the lack of a data base, is easily solvable. The main problem with the nickel-cadmium system is the limited growth potential in terms of specific energy density. A nickel-cadmium battery has a finite specific energy. However, that does not mean that nickel-cadmium batteries are not going to be flown after the next 10 yr. There may be many of these systems; there will be applications requiring them. Let me emphasize that we are not looking to replace one electrochemical system with another. There are enough niches in the NASA program for the various kinds of specialized batteries. We do not want to just say that the sodium-sulfur battery is the best, stop there, and throw out everything else. Obviously there are going to be different applications requiring different systems. We intend to continue work on nickel-cadmium systems.

Lithium rechargeable battery. - The second small system is the lithium rechargeable battery. The advantage of using this system is that a specific energy of 100 W-hr/kg can be projected. Several experimental cells have demonstrated 12 GEO seasons, and these batteries can operate at ambient temperatures.

Some of the disadvantages of the lithium rechargeable battery are that the system is rate limited by the use of nonaqueous electrolyte at ambient temperatures. Safety issues and capacity degradation still need to be resolved. All of these disadvantages are being looked at, and in 10 yr there should be some answers.

Candidates for GEO Missions

Two other systems should be considered for GEO because of their shorter cycle life and longer charge period: the lithium rechargeable battery, which has previously been discussed, and the zinc-bromine battery.

The zinc-bromine system is similar in specific energy to the nickel-hydrogen systems and has demonstrated 5000 cycles at 100 percent DOD for

terrestrial applications. There are obviously zero-g issues, questions of pumping system reliability, and materials problems associated with electrode warping.

Load-Leveling and Propulsion Candidates

Because the workshop was running out of time, for the next few systems we did not go into as much detail. The load-leveling and propulsion candidates for the large systems were sodium-sulfur batteries and fuel cells; for the small systems, rechargeable lithium batteries and low-temperature sodium - beta alumina batteries. Other systems considered were bipolar lead-acid batteries and nickel-cadmium batteries. We were looking into the future for some new systems for these missions. The workshop felt that we could not decide which would be ready in 10 yr.

Pulse Power Candidates

The pulse power candidates are being driven at present mainly by the Strategic Defense Initiative (SDI) activities, but NASA missions also require pulse power, as mentioned. A number of possibilities are being looked at for pulse power: bipolar batteries, thin-film batteries, capacitors, noninductive strip-line cells, superconducting rings, and fuel cells. We were not able to discuss them in detail.

Generic Questions

The following questions were to be considered during the workshop:

Q. Which projected NASA missions would benefit from successful development of these systems?

A. We felt that all the missions were divided by class and they would all benefit.

Q. Are these systems enabling or enhancing with regard to projected missions?

A. Certainly no mission I can think of would not get off the ground if we did not have any of these improvements. Some missions in NASA's long-term future will require a nuclear system like the SP-100. Researchers are working on very high-power technology that would enable some primary systems that we did not discuss.

Q. What are the advantages and disadvantages of these systems relative to the state of the art?

A. These have been addressed in discussing the specific systems.

Q. What are the critical technology barriers keeping the systems from achieving their projected potentials?

A. Again these have been addressed for each system.

Q. Is surmounting these technology barriers a high-, moderate-, or low-risk undertaking?

A. We did not quantize them. Some may be less difficult (though not simpler) than others, but we were not able to pick those. Time will tell which systems will be the solvable ones.

Q. In what timeframe can these technology barriers be reasonably expected to be surmounted?

A. We selected 10 yr as the time when these particular systems should be available.

Questions from Audience

Q. You talked about a low-temperature sodium - beta alumina system. What is that?

A. By low temperature we mean a system that operates somewhere near 100 to 150 °C, and there are three or four on the market.

C. I think you were talking about systems such as sodium - iron chloride, sodium salt protector chloride, and sodium - aluminum chlorosulfate. Most of them use sodium-tetrachloroaluminate as a molten salt to contain or to contact the positive electrode material with the sodium - beta alumina. They operate at moderate temperature, 150 to 200 °C.

C. An EIC battery in a prepilot stage of development that was sponsored by NASA operated with sodium - aluminum chloride molten salt at 180 °C for 500 cycles without any damage. The depth of discharge was shallow, about 20 percent, but the battery was projected to operate at 50 W-hr/lb.

Q. Regarding the lithium cells that demonstrated 12 GEO seasons, was that the lithium rechargeable system or the lithium - titanium disulfide system? Do you perceive that system as lasting 20 seasons in the near future?

A. Lithium - titanium disulfide. Rockwell tested a series of five cells at 0.5 or 1 A-hr. JPL provided the cells; Mr. Subbarao showed the data in his presentation.

Q. Why did you not discuss flywheels?

A. We do not think they will be available in 10 yr.

C. Looking at the LEO mission goals, you have chosen 80 percent efficiency and 25 W-hr/kg, which will work out to about 30 kg/kW for the particular mission. This would require about 15 kg of photovoltaic array. And if we go instead to a lightweight fuel cell configuration, say at only 60 percent efficiency, only 5 kg/kW would be required. That would mean only 5 kg more for the array. We should be looking at the total sum of the whole unit, the array plus the storage system rather than just the storage system, in determining the total weight requirements and the overall efficiency requirements.

A. That is a very appropriate comment. We started to take that into consideration but then realized that it would be very difficult to do. Therefore we decided to consider the battery including the thermal system as a separate plug-in unit. But obviously it was appropriate that we consider the system, not only the battery. The charge control is an essential issue because, with the expense of the photovoltaic array and the larger sizes, in the last few missions people have tended to reduce the amount of solar array and therefore are running into problems charging the batteries. So yes, system concepts are extremely essential.

ADVANCED CONCEPTS WORKSHOP

Ralph Brodd
Gould, Inc.
Eastlake, Ohio 44094

There is a certain amount of overlap between an advanced rechargeable and an advanced concept. We also discussed some of the same systems. Considerable improvements are possible in these technologies, and to stop working on them would be a mistake for the longer term.

We were getting bogged down with details of LEO and GEO and finally decided just to talk about large and small electrochemical systems. We will let NASA sort out which systems are better. We discussed the advantages and disadvantages of the various systems and then tried to rank them in order of promise. Keep in mind that this is somewhat subjective and that systems ranked close together may actually be equally promising. We made some estimate of the development time. If you only worked on one particular system, how long would it take to reach fruition? We were a little naive in this assumption, and the development time and the timeframes for system availability may not be accurate for each system we discussed. Clearly there is a need for supporting research. Fluctuations in funding create a problem, particularly with advanced concepts, because you need continuity of process and effort to achieve goals. If a researcher is forced to discontinue work after, for example, 5 yr, all that time is lost even if research is resumed again later. We feel strongly that there is a need for continuing funding, particularly in basic research, and not just in small business and innovative research (SBIR) contracts, which tend to be goal orientated.

In my opinion the Japanese have been approaching battery system research and development differently from the way we have in the United States. The Japanese government generally has picked a system, or group of systems, and then demonstrated its use in a specific application. Our programs tend to go by fits and starts. And if we are not careful, we are going to be importing technology from Japan for many critical programs. In the primary battery field many advanced systems are already being imported from Japan, and many of the technologies are being purchased.

Mobile Applications

We spent a fair amount of time talking about small systems for mobile applications, journeys to and from a central station or location.

Sodium-sulfur battery. - Sodium-sulfur batteries have some significant ceramics problems. The preparation of the ceramic and the failure mode are critical. The number of cycles, particularly in outer space, is a problem that needs to be addressed. Sodium-sulfur systems for mobile applications will probably be available in 5 to 10 yr.

Flywheel. - The flywheel has a long shelf life, but it cannot be activated in orbit because it has poor shock and vibration resistance at launch. However, it does have control, a fast recharge for high-power applications, long cycle life, and good steady charge indication. The flywheel is probably nearer term than the sodium-sulfur battery for mobile applications and certainly should be considered.

Lithium - iron sulfide battery. - The lithium - iron sulfide battery has a slightly lower energy density than the sodium-sulfur battery. Perhaps with a new electrolyte, its performance can be improved in the nearer term. It will be 5 yr before a decision can be made on that particular system.

Fuel cells. - Fuel cells, particularly the solid polymer electrolyte (SPE) and the solid oxide, are good candidates in our estimation. The alkaline cell has already flown. The SPE cell has also flown and it has been shown to be a reliable system. New catalysts and new membranes would be necessary to improve its performance. SPE was judged to be worthy of an advanced concept development. The ceramic monolithic structure especially would be useful in mobile applications. Lifetime could be a problem as long as these ceramic compositions are being used. It is not clear whether low power is a problem for some fuel cells. A general question that we might ask ourselves about fuel cells is, Is your design for high power or low power? Is there a problem area there? Here the gas pressure indicates the state of charge, and this is a useful application for most battery systems. SPE systems can be somewhat inefficient, so the system efficiency needs to be addressed. Long shelf life with average power is certainly a possibility.

Rechargeable lithium systems. - The next grouping of mobile applications includes rechargeable lithium systems that, by and large, are room temperature. These systems are lithium - titanium disulfide, lithium - molybdenum disulfide, lithium - sulfur dioxide, lithium intercalation, hydrogen-chlorine, hydrogen-bromine, sodium - iron chloride, and lithium - aluminum disulfide. Lithium - aluminum disulfide and lithium titanium disulfide have in a sense been demonstrated in small units. They do not have the reliability desired for long missions. The lithium - sulfur dioxide system, in particular, is capable of 150 W-hr/kg and 5 W-hr/in.^{3} and can satisfy many current missions requirements. Its progress, however, is somewhat suspect in that there was no real support except in private industry. And right now private industry seems to be discontinuing this work. These lithium systems can be organic or they can be polyethylene oxide (PEO) based. Although PEO is not a subject of intense research development in the United States, it is part of the solvent electrolyte complex phenomenon and needs to be addressed. So what we are really looking at is new organic electrolytes, whether they are solid or liquid. Also, there is a possibility of using lithium alloys. The Japanese have demonstrated long cycle life with woods metal alloy in lithium systems. Alloys have been used in the lithium - iron sulfide system, but they have not been looked at strongly in the smaller units here in the United States. Alloy work certainly is needed.

Hydrogen-chlorine and hydrogen-bromine batteries. - The hydrogen-chlorine and hydrogen-bromine systems are less advanced. They have slightly lower energy density than the hydrogen-oxygen system but higher efficiency, which may be important for some longer missions.

Sodium - iron chloride battery. - Environmental control would be an application for the sodium - iron chloride system. The system is somewhat interesting as a rechargeable system. It would open up possibilities if alloying could be done on sodium as it is on lithium. There are many ways to get around the need for large aluminum separators or new separator concepts. This is exciting research.

Sodium heat engine. - A sodium heat engine has liquid sodium and sodium vapor on either side of a large aluminum membrane. The concentration difference in the sodium produces an electromotive force. This system has some potential.

Lithium hydride, lithium-hydrogen, and lithium - hydrogen peroxide systems. - Lithium hydride, lithium-hydrogen, and lithium - hydrogen peroxide are also possibilities for longer missions. Lithium-hydrogen as a thermal rechargeable system might be interesting not just for mobile applications but also for central station power.

Central Station Power

Even though the central station power system might be a nuclear reactor, we felt there was a need to consider load-leveling characteristics, particularly in view of some problems experienced on terrestrial systems. Large systems (300 kW, 4 to 10 MW-hr, and a minimum of 5000 cycles) present long term load-leveling problems.

Regenerative fuel cell. - Here the regenerative fuel cell appears to be very promising. It could be an SPE, alkaline, or solid oxide, so it might be useful for mobile as well as the central station power. Hydrogen and oxygen would serve as the environment or for the environmental control aspects of the central station.

Flywheel. - The flywheel is certainly a viable candidate for central station power. Larger flywheels are perhaps less advanced than those for mobile systems but still should be considered for longer space applications. Often the electrochemical community feels that batteries are the only answer to power system considerations. In fact, many times the mechanical aspects of flywheels and Stirling engines must also be considered. The fact that they are not used today, in part, is because people making the decisions tend to choose electrochemical systems. Many times the mechanical systems have equal or greater opportunities for development than many electrochemical systems.

Sodium-sulfur battery. - The sodium-sulfur battery is another possibility for central station power. Certainly the lifetime of the ceramic membrane is a real consideration and is not yet as long or reliable as needed.

Hydrogen-bromine and hydrogen-chlorine regenerative fuel cells. - Hydrogen-bromine and hydrogen-chlorine regenerative fuel cells would be applicable for central station power - particularly with the necessary environmental control.

Sodium heat engine. - The sodium heat engine, particularly with a thermal nuclear reactor or other nuclear heat source, would become a viable candidate.

Critical Materials Through Electrolysis

Another category that we spent some time discussing is making critical materials by electrolysis. Away from the Earth, you have to generate oxygen (refer to the paper by Anthony Sammels on generating oxygen from lunar materials). Once you have oxygen you can use lithium in electrochemical cells such as lithium - hydrogen oxygen. Lithium - hydrogen peroxide, or lithium-water. Perhaps we ought to take a broader view and think in terms of making the materials to build a space station.

Research Needs

We need to look longer term and take a global view, looking not just at the power source, or the environmental control, or at the sewage problem, but looking at the entire project and developing a strategy. The Space Studies Institute at Princeton was doing some of these studies in 1982, and I am sure that NASA is continuing these kinds of studies. The global view is something that very few people are willing to spend any time on. If we are serious about going out there 20 yr from now, we are going to have to do much more than we are presently doing. For instance, if we are interested in lithium-fluorine systems, we need to do work on fluorine. One of the reasons that developments in superconductivity have come so rapidly is that superconductivity researchers had some ideas about it. If you are not working on fluorine or other systems of that category, you are never going to have that breakthrough needed to achieve the higher energy density system. The fact that you are not working on higher energy density systems guarantees that you are not going to have a new one when it is needed.

We need some continuity of effort - ongoing funding for fundamental research. What is needed is a small amount of seed money, $50 000 to $100 000 contracts - maybe $50 000 from several sources. You must seed projects and keep them going so that you will have an opportunity to recognize that critical breakthrough. Most of those in this room have the energy and the serendipity that are called creativity. You have to have the opportunity to let that creativity go. In exploratory work looking at materials and processes, systems, and constructions should be about 10 percent of your total budget. Systems includes not just electrochemical systems but also mechanical systems such as the flywheel and the Stirling engine.

Ceramics is another area that needs support because of the beta aluminum material and the solid oxide fuel cell. A deliberate program in separators would certainly be very much worthwhile.

Questions from Audience

Q. Many of the proposed battery systems have been researched under Development of Energy (DOE) programs. Probably several hundred million dollars have been spent on these systems here and in other countries. I believe we can learn quite a bit from what has been done so far. DOE must have supported at least 10 programs, and now it has come down to only one or two. Can we not narrow the list considerably from all the experiences in our research and development programs?

A. The DOE programs are directed toward a specific short-term goal. For instance, the lithium - iron sulfide program has in effect been discontinued by DOE, although Paul Brown is doing some work. That system did not reach fruition during the program. The good cycle life for the lithium-sulfide did not occur until after the storage program had come to an end. So that development could have gone on and there could have been improvements in that particular system. Therefore you cannot say that the DOE program is going to produce a system that we need for our space program. First, they are looking for different things, and second, they have a tendency to look for large advances and not see the effect on other systems. That is why I made the comment about the Japanese programs. Today if you want to find out how the DOE battery systems (sodium-sulfur, zinc-bromine, the Redox system, zinc-chlorine) really work, you go to Japan and look at them. That is where the main emphasis is now. Yes, the DOE program provides a valuable baseline to help us judge systems and to identify problems. But that does not mean that if they have stopped work on a system, we should consider that system finished. That is a mistake.

Q. Most of the workshop addressed rechargeable batteries. Did you consider new concepts for primary batteries, and if so, would not the lithium-chlorine be a good candidate in that category?

A. We did not spend much time talking about primary batteries. We were looking at systems that could be put into space and used again and again - not used and then thrown away. Perhaps that was short sighted. Certainly some advanced primary systems would be viable. Lithium-chlorine may be such a system, but I would tend to consider thionyl chloride and sulfuryl chloride and perhaps extend work to a next logical system from thionyl chloride.

C. By way of clarification the lithium - iron sulfide systems are not totally dead. They were abandoned to some extent, but they have been picked up again. The Electric Power Research Institute (EPRI) and DOE hope next year to have a vehicle powered by the iron sulfide system.

C. As a matter of fact, Gould Ocean Systems Division is the prime contractor on that, and the Tennessee Valley Authority (TVA) is both the prime and the subcontractor depending on whether you are looking at EPRI or DOE efforts. The iron disulfide system is also making advances and some of those advances, are being transferred to the iron sulfide - lest we bury that system too quickly.

C. That is in part what I was saying earlier. Sometimes work on a program is stopped for the wrong reasons. Although it may not be viable in the short term, it is worth consideration in the longer term. That is the philosophy I was trying to convey. We have a proliferation of systems and do not know which to choose.

Q. You looked at major applications, higher loads, and lighter loads. The environment must also be considered. How will the system work on Mars, Venus, etc.? What type of system is needed, higher pressure or lower pressure?

A. We talked some about the environment. For instance, we talked about the -95 °C and -5 °C top and bottom temperatures on Mars and what batteries to use for mobile and central station power. You have to be concerned about the temperature of liability. In that sense the flywheel was a good choice because as a mechanical system it has less temperature variation associated with it. That was part of the reason we put the flywheel higher on the list. A sodium alloy - nickel bronze system might have better low-temperature characteristics than the high-temperature sodium systems. However, we did not spend much time considering the kind of environment these systems would be in. We did discuss the environment in the central station area, and we recognized then the need to consider all aspects of the environment.

C. The charge release time is 20 yr.

C. Here again the flywheel looked very good from an active standpoint. It could be stored for long times without damage. Not many battery systems can be stored for 10 yr before they are used. We did consider storing a discharged battery system and then charging rather than using a battery system that was stored charged for 10 yr. We did not go into details but only recognized the problem.

Q. The flywheel is sensitive to shock and vibration, but you are listing it for mobile applications. What happens if the rover drops into a pothole?

A. When we talked about the shock and vibration problem, it was with regard to currently designed flywheels and approximately a 2-g loading both radially and axially. Further research could improve the capabilities of the flywheel, and it was not clear what problems the weight penalty would cause. I think that the weight penalty would not be extremely severe, but we did not go into much detail.

C. The problem of vibration clearly limits the flywheel, and with the 17 to 20 g's at vehicle launch it looks as though the weight would be an extreme penalty.

One comment on using electrolysis to produce oxygen - To the extent that iron oxides, zinc oxides, and manganese oxides are available locally, iron, zinc, and manganese can be produced rather easily by electrolysis as a byproduct of construction, and that could eventually become a major factor.

C. We have a relatively high-temperature system that might work well on Venus, although we are not going to tackle that at present. We have ambient temperature varieties, but Mars is going to require some temperature varying, perhaps to -70 °C. An advanced cryogenic battery that would work at -70 °C is especially appropriate with superconductivity and the oxides being considered. We are going to spend a long time on Mars if we are to build a station there. Although the concept of a cryogenic battery sounds weird right now, it may not be too far off.

A. I would hope that you got the idea that the NASA program or the NASA Lewis program, which we did not really discuss in detail, focuses mainly on understanding and extending the life of the nickel electrode as well as developing advanced catalysts for new kinds of fuel cell systems. So we are critically aware of these kinds of material issues, which are the problem areas in electrochemistry.

CRITICAL PHYSICAL AND ELECTROCHEMICAL ISSUES WORKSHOP

Douglas N. Bennion
Brigham Young University
Provo, Utah 84601

The workshop spent most of its time trying to decide on the critical issues. We came up with this list:

(1) Long-term considerations
  (a) New system concepts
  (b) New materials concepts
  (c) Alloys

(2) Electrode-electrolyte interface
  (a) Catalyst: what - where - form - time
  (b) Catalyst morphology
  (c) Reaction paths
  (d) Surface in situ examinations
  (e) Impedance measurements
  (f) Supports
  (g) Three-dimensional catalysis
  (g) Electrode morphology
  (i) Access to catalyst

(3) Bulk properties (subsurface)
  (a) Oxide structure (Ni)
  (b) Catalyst
  (c) In situ

(4) Electrolytes
  (a) New electrolytes (nonaqueous (aprotic) and polymers)
  (b) Membrane structures and function
  (c) Solid electrolytes

(5) Failure mode analysis
  (a) Accelerated testing
  (b) Modeling

(6) Reactant storage
  (a) Hydrides
  (b) Oxidants
  (c) Alloys
  (d) Amorphous - H_2 storage

Long-Term Considerations

Long-term commitment was mentioned more in private discussions than in the general discussions. Ralph Brodd made the point that we need to continue

research programs, to be committed to coming up with new ideas, and to maintain funding in a way that allows continuous creativity. Its been my observation that often a great push comes during a crisis. Necessity may be the mother of invention and it does drive certain creative processes, but often during a crisis the creativity winds up more in the engineering and creative minds cease coming up with wholly new ideas. There has to be a continuing commitment to look at the fundamentals and to explore new ideas so that when the need comes there is something there to push forward with.

Although we did not discuss it in the workshop, I believe there is a 50-50 chance that the battery systems NASA is applying in 15 yr will not be the systems we have discussed. New system concepts must be continuously looked at and supported although not at a high level of funding. If you put too much money into a system, the bright people become managers and quit being creative. The funding must be kept at just the right level. Certainly many of the ideas that we are trying to create are limited by the need for new materials. I agree that we should work more on alloys. There are other items that could be added to our long-time operations list, but those were three that came out.

Electrode-Electrolyte Interface

Catalyst. - A large part of our discussions revolved around the electrode-electrolyte interface, for electrochemists, particularly fundamental electrochemists, I think that is natural. NASA is interested in gas electrodes, particularly the oxygen electrode, where catalysis is immensely important. The questions we need to consider are, What catalysts are you going to use? What are the materials? Where are they located - on the surface or in the porous electrode or in relationship to the other parts of the electrode that they are catalyzing? What form are they in? What is the morphological state? How do they alter as the device is operating or as the electrode is fabricated? Do they change during cycles?

Catalyst morphology. - We need fundamental studies on catalysis morphology. What is the structure they they are lying on, what do they look like, and what is their physical form?

Reaction paths. - We need to know more about reaction paths. What step is it that we are catalyzing? Charles Tobias, my thesis director of 20 years ago, used to be dismayed at the endless arguments about the elementary steps of a particular reaction. There seems to be so much conflicting evidence about any particular reaction path. It is a very difficult subject. It causes debates that should be more scientific and less emotional. It certainly must be understood if we are going to understand what the catalysis is trying to do.

Surface in situ examinations. - Surface in situ examination was emphasized. This relates to some of the comments that I just made. That is, what do you measure in one situation? It always reminds me of the slightly inebriated person looking for his billfold under the streetlight although he lost it in the field because that is where he can see. We often look at catalysis or a surface under one condition when it is actually operating in another. We should at least take a look at this situation and learn something about it.

Impedance measurements. - Another person suggested that we ought to circle back and take a greater look at impedance measurements. Although I am not sure we can interpret them properly, much can be exhumed from pulses and looking at impedance measurements.

Supports. - We also need to look at supports. Michelle Badall emphasized 20 yr ago the interaction between the catalyst and the surface on which it lies and the support and how it relates to it. Apparently, the answers are not yet known and we need to look more at it.

Three-dimensional catalysis. - Although this was not discussed in the workshop, we should also consider the concept of three-dimensional catalysis: how things happen in depths and in sequences. In biological catalysis different sites are specific to a certain reaction. The molecule goes from one site to the next; at each site specific changes occur. In three-dimensional catalysis the catalysis also could take place in a series of steps. We should be concerned about that and how the sites relate geometrically to one another.

Electrode morphology. - Electrode morphology is different than catalysis morphology in that is refers to larger scale structures. We need to know the overall structure of the electrode and how it relates to catalysis or where the catalyst is placed.

Access to catalyst. - We should also consider how materials get to the catalyst and away from it. And that gets to an exciting area, problems associated with the fundamentals of mass transfer. We need to apply good sound theoretical ideas. We need to take what the pure fundamental theorist is doing and relate that to our catalyst development in a meaningful way. Too often the applied-catalysis person relies on serendipity. Although we cannot predict exactly how a catalyst is going to work, thinking through the theory can point to what to try next.

Bulk Properties

If we understood the oxides, the different phases they may form, how they interrelate and how different materials affect their chemical and physical properties, we might be able to arrange the electrodes so that they work better. It is also important to understand why you cannot do something. Understanding the detailed structures of the oxides, particularly nickel oxide, would indicate that there are many other important oxides, both in terms of catalysis and in terms of new electrodes, that we might be able to understand and make work better.

Many of the comments made about surfaces also apply to the in situ measurements of bulk properties.

Electrolytes

We need fundamental measurements on electrolytes. It is generally agreed that we need new electrolytes. New batteries will evolve from new electrolytes and from new ideas on how to make and use electrolytes. We should consider inorganic, organic, and organometallic materials as well as polymers. Polymers

should also be considered for separators. Polymers can give better ion control and thus better control of the transference number. We need to understand membrane structures and functions better. How does a membrane work and how do you then create membranes to provide the functions that you want? For solid electrolytes we were thinking in terms of lower temperature materials than the zirconium oxides, entirely different materials that do roughly the same thing at 400 or 500 °C rather than several thousand degrees, where we are presently working.

Failure Mode Analysis

Why do things fail? How do you do accelerated testing? The key problem here is that in an accelerated test the system frequently fails from a mechanism or cause entirely different than the long-term cause. How do you understand that? How do you understand what the long-term failure mechanism is going to be? This is particularly important to NASA in reaching 20-yr system life. We cannot wait 20 yr to decide whether to launch a particular system. The answer that many of us discussed and agreed with is to do a careful, thorough job of modeling. That does not mean putting the whole system together in one giant model. What you have to be able to do, and this takes a great deal of skill on the part of the investigator, is perceive what the key critical failure mechanism process is and model it carefully. You may have many different models related to many different possibilities. Analyze each one carefully and thoroughly and then run tests to see if your model is correct. Once your model is validated you can begin to say with confidence that because of that particular problem this system will last only so long.

Reactant Storage

Hydrides. - Reactant storage is another area that may become important. At least two storage concepts were discussed under hydrides. One was some sort of a hydride that would work like an alloy as part of the electrode. The other was a hydride where the hydrogen is stored external to the electrode and the gas is hydrogen or the hydrogen in some form transfers from the electrode to the storage site. You could even circulate the liquid itself through the electrode, if you were clever enough.

Oxidants. - We need to find new and better oxidants. The reducing agents we are using seem to be a fairly limited number: zinc, cadmium, lithium, sodium, calcium, hydrogen, etc. However, many oxidants are being considered. It seems likely that the oxidizing agent that will be used in batteries 20 yr from now has not yet been found. We may know the general idea, but we do not know the exact form and how it will be incorporated in a battery.

Alloys and amorphous materials. - Amorphous materials and other alloys can be used for hydrogen storage. Oxygen can be stored as a peroxide, as a chlorine, or as just a higher oxide. Or pure oxygen can be stored by dissolving it. Those were the critical issues we discussed. Then we asked, How would we apply those to different systems?

Systems

The systems we considered somewhat in the order of what the group seemed to think was their importance, were as follows: nickel-hydrogen, hydrogen-oxygen, hydrogen-bromine, sodium-sulfur, sodium (general), lithium (general), rechargeable metal oxides, and general halogen electrodes.

Nickel-hydrogen systems. - Regarding nickel-hydrogen batteries, we need to understand and model the failure analysis and apply the concepts mentioned earlier. We need to understand the second plateau, how it comes in, and how it affects the long-term function of this battery system.

Plaque failure is apparently related to corrosion. The morphology of and chemical changes within nickel electrodes need to be understood better. We need to understand how to control and reduce oxygen overvoltage to make battery systems last longer and to get more storage. We need to investigate the hydride storage of hydrogen.

Hydrogen-oxygen systems. - In considering the hydrogen-oxygen system we first discussed aqueous-based hydrogen-oxygen, the bifunctional electrode. Can you go back and forth with the oxygen electrode? What are the limitations? What does it support? What catalyst should we use? We considered gold, iridium, and various oxides. Porous electrode structures of Teflon and Fluon were mentioned. Teflon inside the porous electrodes seems to be a problem. We need to pay more attention to there the Teflon goes and how to wetproof the liquid-gas interface.

Many different ideas are appearing on how to construct a membrane to fill particular functions. Some interesting ideas were brought up in the workshop, and there are many others we should consider, for example, membranes that control water transport in the hydrogen-oxygen fuel cell and membranes that allow only proton transport. We would like to make them perfect. Beta alumina is an example of a membrane that has essentially a transference number of 1 for a particular ion. We are looking for membranes that would do that for other ions. On the other hand, we need to understand, control, and live with leakage. Trying to get membranes that have transference numbers of 1 may not always be best, but we discussed how to do that. Ways to modify existing membranes were suggested by a number of workshop attendees, as well as ways to make them work better and, of course, ways to build the catalyst and the electrode into the membrane. This whole field of solid oxide membranes, alternatives to zirconium oxide, and electrodes that go on the oxide may break out and become very productive. NASA may want to consider it.

Hydrogen-bromine systems. - We did not spend much time on the hydrogen-bromine fuel cell. Others have already talked about it. Many of those fundamental ideas can be applied there.

Sodium systems. - We briefly discussed the sodium-sulfur battery. One of the more critical issues was the failure of the beta alumina where it connects to the glass. The weakness caused by the interaction of the materials needs to be considered. We discussed sodium batteries in general, not just sodium-sulfur, but sodium-chlorine, sodium - beta alumina, and sodium - iron chloride.

We also discussed storing chlorine by putting it on iron and changing the valence state of the iron, storing it as a liquid, or storing it in oil or another absorbent that would maintain the vapor pressure of the chlorine.

Lithium systems. - We generally applied the fundamentals to new types of lithium batteries. We already mentioned new solvents, better lithium alloys, and new electrode systems. Here we talked primarily about the positive electrode, new cathode materials, and putting the whole system together. Some think we should reinvestigate the rechargeable metal oxides or take a look at some new ones. It is surprising that no one has tried to develop a zinc-oxygen battery. It looks like it could be done and would have good energy density. After all, we have a nickel-hydrogen battery. Why not create a nickel-oxygen battery to store the oxygen at high pressure. For the same pressure twice the number of coulombs can be stored in a oxygen container as in a hydrogen container. Metal deposition and integration of the oxygen electrodes would be the major problems.

We also looked at the fundamentals related to halogen electrodes.

Questions from Audience

Q. Why not take a new look at thermally regenerative systems? There may be many systems that have not been considered for a thermally regenerative battery, for instance, lithium-hydrogen in the form of a hydride system. Some of these systems may be identified as very appropriate for use with solar dynamic basic power systems. NASA was a leader in this field 25 years ago. Maybe it is time to bring it back. There have been some hints of it, for example, the beta alumina system.

The pioneer in zinc-oxygen systems was Marty Kline and the Energy Research Corporation. It did not catch on because of all the problems with shape change in the zinc electrodes. Also at high rates it had a tendency to dry out and could explode. The zinc would react rapidly with the oxygen. Perhaps it is time to reconsider zinc-oxygen.

C. The zinc electrode problem can be solved, in principle, the same way the lithium electrode problem was solved, if you happen to be fortunate enough to find a useful zinc alloy. But can you get zinc to move as fast as lithium in an alloy?

C. I have a comment to add about the zinc-oxygen system because Lewis supported work then with McDonnell Douglas, which was the predecessor of the laboratory where sulfur work is now going on. The devices would explode because the catalyst on the oxygen electrode would dissolve during recharging and plate onto the zinc. It became difficult to charge the zinc electrode, which was covered with platinum. The battery would mainly generate hydrogen on recharge.

I think Union Carbide also worked on rechargeable zinc-oxygen batteries.

MODELING WORKSHOP

Sid Gross
The Boeing Company
Seattle, Washington 98124

To summarize, it is quite clear from the experience of all the people in our workshop and, I think, most of the people at this conference that modeling is an extremely valuable tool. NASA and all of us should make much more use of modeling. It adds another degree of freedom to research into batteries and fuel cell systems and particularly to understanding what is happening with these technologies. Modeling has a number of specific advantages. It considerably reduces the number of costly experiments. Of particular importance is the better understanding that we get by comparing a model with observations. We can then apply this knowledge to design cells that give better performance. In the long run this will save time and money. We concluded that NASA, which has been doing some modeling, should be active in expanding this work, particularly to emphasize the life and reliability of existing systems as well as to aid in the development of advanced systems.

Benefits of Modeling

We categorized the benefits of modeling in three areas - missions, technology, and fundamentals:

(1) Missions
- (a) Enables tradeoffs of competing systems
- (b) Enables power system studies
- (c) Identifies energy storage requirements
- (d) Provides basis for autonomous operation and expert systems

(2) Technology
- (a) Reduces weight
- (b) Increases reliability
- (c) Shortens development time
- (d) Predicts performance

(3) Fundamentals
- (a) Improves electrode design by clarifying molecular and microscopic structure
- (b) Identifies problem areas
- (c) Guides conduct of experiments
- (d) Identifies interactions that affect life or performance

Missions. - Evaluating competing systems for mission applications requires a good understanding of all systems. That understanding can be achieved by establishing a good model of each system. For example, in recent work for the space station system NASA put together a good analytical model of a regenerative fuel cell system. The model allowed that system to be evaluated and compared with other systems for durability. Energy storage systems must be

compared for vehicle missions at the power system level. Therefore the energy storage system model should be developed as part of the overall system studies because only when the evaluations are made at the power system level can you be sure that a particular energy storage system is the right choice. Also in establishing the requirements for a particular battery or fuel cell application, you must go back to the vehicle that the system is going to be used in. Modeling, or more accurately system studies, is necessary to establish the requirements before you begin work in an area. There may be a need in some future systems for autonomous operation and expert systems. To identify that need, you again must go back to basic system studies.

Technology

Now, modeling clearly has great potential benefits in technology. The major objectives are the trinity of low weight, reliable life, and performance. Achieving these objectives depends primarily on technology.

Fundamentals

Modeling has very direct application to understanding the fundamentals of energy storage systems at the macroscopic and particularly the microscopic levels. For example clarifying molecular and microscopic structure will help identify the problems in electrode design modeling. It will guide you in preparing experiments, and it can be useful in determining the identifying interactions.

Modeling Efforts Required

System level modeling. - System level modeling must include power systems. There is also a need to analyze reliability effects and subsystem interactions and to identify the requirements for the batteries in fuel cells.

Microscopic level modeling. - In microscopic level modeling there is always a need to look more carefully at electrode design, pore size and distribution, the effects of aging on the structure, the optimization of these structures, the kinetics involved, and the transport of mass and heat into and out of these structures.

Cell test modeling. - In cell test modeling it is important to predict the effects of aging. Although understanding aging requires a lot of supporting research, ultimately it would be desirable to have models that depict the effects of aging under normal and accelerated conditions. That may allow the development of realistic accelerated tests, tests that will cause cells to fail by the same mechanisms as under normal conditions. Modeling could be particularly valuable in that area.

Documentation of existing modeling. - There is a gap in the use of modeling technology or modeling in general between the university researchers and the users. One way to make modeling technology more available to users is to document the existing models and to identify the modeling work already being done. This would assist in the development of new models and would also make some

parts of other work accessible. Although we are not sure how best to address the problem of bringing modeling down into the user community, there is a need to do this. NASA could play an important role in solving this problem.

Aging models. - Returning to the subject of aging, the need to predict the effects of cycling and storage supports the comments made on aging models. We need models specifically identified as aging models; such modeling is in fact being done. Almost every major space program tries to predict how performance will degrade over time. Most aerospace companies have models to do this, but some are primitive. A better model could be developed even today on a macroscopic level from the information available. For example, the models that are used typically are of two types: statistical models and total cell models.

Most of the models are statistical models in which data have been fitted to polynomial equations. Better models are available that are based on modifications of Sheppard's equation. Although Sheppard's equation is not as good as it might be, it is still quite good. There is a need to develop a more precise Sheppard's equation that allows better use of available data. NASA could play a major role in developing a general-purpose model to help predict and correlate the degradation of current batteries. Modeling of extreme-value statistics would help predict worse-case situations. Often you want to know when the first cells or the first few cells of a battery might fail or the extreme conditions at which all the cells in the battery are not going to operate identically. Extreme-value modeling has been used in the corrosion field to find out when the first pit corrosion occurs and where the first pit penetrates - similar to the needs in the battery field.

Total cell modeling. - Total cell modeling at the macroscopic level would aid in designing cells and also in predicting cell performance at steady-state, transient, and extreme conditions. Because the thermal behavior of batteries and cells goes hand in hand with the electrochemical performance, it is necessary to have good thermal models of energy storage systems.

Molecular and structural level modeling. - Additional molecular and structural level modeling is needed particularly to understand new material. Many advances in batteries and fuel cells will probably take place through the development of new catalysis and separator materials. Although we understand electrochemistry fairly well, the new material are probably the key to new and better battery systems. It would be useful to be able to identify whether a particular group of candidate materials would be electrochemically active or whether they would be likely to cycle as secondary systems or be discharged once for primary systems. It has been possible to do this theoretically for intercalation materials, but the problems are going to be quite difficult for many other materials. We concluded that there probably would be some materials whose performance could be predicted by modeling and others where that would be unlikely. Molecular/structural modeling could also be used to detect the initiation of failure. Failures start as tiny flaws in the cells. For example, beta alumina starts to fail with a microcrack or a small insurgence of sodium into a void. Then there is always need to do work in kinetics.

Expert systems. - Most of the discussion of expert, or autonomous, energy storage systems has been through the military. However, these systems should be considered for NASA applications. For planetary missions the time to transmit data from the spacecraft to the Earth could be so long that it could

be too late for the ground to take action. Some automatic autonomous system must detect the problem and take corrective action. Now an expert system in general takes the best knowledge of true experts in an area and supplements it with other information that makes clear exactly what is happening even though the experts are no longer available. NASA might explore expert systems in connection with the nickel-hydrogen battery for the space station. Another possibility would be for planetary missions.

Questions from Audience

C. Models that do not work are typically rejected and not well documented. Therefore the reasons for rejecting a model have to be discussed continually. The same is true for accelerated testing. Some means should be devised to collect and organize information on failed models and tests so that money is not wasted in repeating the work.

A. That is a good point. If NASA documented the attributes and weaknesses of existing and rejected models, it would provide guidance for future use.

C. A researcher often needs fundamental rather than specific data, for example, the exchange current density based on real area not on porous electrode area and the dimensions of capillaries. Such data are lacking because industry researchers look for microscopic data for a particular system. University researchers, pure chemists, like to work with pure systems that are well characterized. We need data that are typical to working systems but fundamental in nature to plug into the models, and those data are not available.

A. That is a good point. Although I failed to mention it here, we did discuss it at the workshop. One of the values of models is that they force a person to deal with data, to make an assumption based on the model, to find what the numbers are. If numbers are not available, the logical thinking is to run experiments to get the numbers. however, until you have identified the need for a particular value, you might never run that experiment. For example, in modeling the lithium - thionyl chloride battery, one of the important parameters is the precipitation of the reaction (discharge) products. It is important to the overall efficiency of the system whether the discharge products occur within the pores, where they would block further actions, or whether they end up in the electrolyte. The National Battery Advisory Committee (to DOE) needed data on battery systems and it just was not available. Fundamental information about transport properties and electrolytes was generated only when it was recognized in reports through the modeling work. Another example strengthens the need for fundamental work. Exchange currents for battery reactions, in particular zinc, used to be available in the literature and or through conversations with university researchers. For lithium batteries and other new systems the experts are located in private companies and consider much information to be proprietary. Thus, the information is generally not available. We need to address that situation. Also it may be 20 yr between the start of work and the production of important results. Few people are available from the beginning to the end of this period. People move in and out of the technology, and it is necessary to have things written down and identified.

ATTENDEES
SPACE ELECTROCHEMICAL RESEARCH
AND
TECHNOLOGY CONFERENCE

NASA LEWIS RESEARCH CENTER
APRIL 14 - 16, 1987

Allen, Douglas
AFWAL/POOS-2
WPAFB/ Oh. 45433
(513) 255-7770

Acevedo, Julio
NASA HQ
Code RP
Washington, DC 20546
(202) 453-2861

Appleby, John
Texas A&M University
Chemical Engineering Dept.
College Station, TX 77843-3577
(409) 845-5571

Attia, Alan
Jet Propulsion Laboratory
4800 Oak Grove Drive M.S. 277-212
Pasadena, CA 91109
(818) 354-0965

Auborn, James
AT&T Bell Labs.
600 Mountain Ave., Room 6F-211
Murray Hill, NJ 07974-2070
(201) 582-4263

Badcock, Charles
Aerospace Corporation
P.O. Box 92957, MS M2/275
Los Angeles, CA 90009
(213) 336-5180

Baldwin, Richard
NASA Lewis Research Center
21000 Brookpark Road, M.S. 301-3
Cleveland, OH 44135
(216) 433-6156

Beninga, Kelly
Science Applications International Corp.
10401 Roselle Street
San Diego, CA 92121
(619) 458-3760

Bennion, Douglas
Brigham Young University
Dept. of Chemical Engineering
Provo, UT 84602
(801) 378-2393

Bittner, Harlan
Aerospace Corporation
P.O. Box 92957, M.S. M2/275
Los Angeles, CA 90009
(213) 336-1525

Brandhorst, Henry
NASA Lewis Research Center
21000 Brookpark Road, M.S. 301-3
Cleveland, OH 44135
(216) 433-6149

Britton, Doris
NASA Lewis Research Center
21000 Brookpark Road, M.S. 309-1
Cleveland, OH 44135
(216) 433-5246

Brodd, Ralph
Gould Inc.
Foil Division
35129 Curtis Blvd.
Eastlake, OH 44094
(216) 953-5065

Brown, J.
Westinghouse Electric Corp.
1310 Beulah Road
Pittsburgh, PA 15235
(412) 256-1950

Carbonio, Raul
Case Western Reserve University
Department of Chemistry
Cleveland, OH 44106
(216) 368-3736

Cataldo, Robert
NASA Lewis Research Center
21000 Brookpark Road, M.S. 309-1
Cleveland, OH
44135
(216) 433-5254

Charleston, Jo Ann
NASA Lewis Research Center
21000 Brookpark Road, M.S. 309-1
Cleveland, OH 44135
(216) 433-5247

Cornilsen, Bahne
Michigan Technological University
Dept. of Chemistry and Chemical Eng.
Houghton, MI 49931
(906) 487-2295

Dyer, Chris
Bell Communication Research Labs.
435 South St. MRE-2L-149
Morristown, NJ 07960-1961
(201) 829-4941

Dymek, Chester
Seiler Research Labs.
USAF Academy
Colorado Springs, CO 80840-6528
(303) 472-3148

Feduska, W.
Westinghouse Electric Co.
Pittsburgh, Pa.

Fielder, William
NASA Lewis Research Center
21000 Brookpark Road, M.S. 309-1
Cleveland, OH 44135
(216) 433-5258

Fordyce, Stuart
NASA Lewis Research Center
21000 Brookpark Road, M.S. 3-5
Cleveland, OH 44135
(216) 433-2962

Fuhr, Kenneth
Martin Marietta Aerospace
P.O. Box 179
Denver, CO 80201
(303) 977-4495

Gabris, Edward
NASA HQ
Code RP
Washington, DC 20546
(202) 453-2847

Gahn, Randall
NASA Lewis Research Center
21000 Brookpark Road, M.S. 301-3
Cleveland, OH 44135
(216) 433-6158

Gentry, William
Johnson Controls Inc.
5757 North Greenbay Ave.
Milwaulkee, WI 53201
(414) 961-6578

Giner, Jose
Giner Inc.
14 Spring St.
Waltham, MA 02254-9147
(617) 899-7270

Gosciniak, Jeffrey
Eveready Battery Company
25225 Detroit Road
P.O. Box 45035
Westlake, OH 44145
(216) 835-7719

C-5

Gosciniak, Kathleen
Eveready Battery Company
25225 Detroit Road
P.O. Box 45035
Westlake, OH 44145
(216) 835-7660

Grimes, Pat
Exxon Research and Engineering Co.
Route 22 East
Annandale, NJ 08801
(201) 730-2420

Gross, Sid
Boeing Aerospace Co.
P.O. Box 3999, MS 81-16
Seattle, WA 98124
(206) 773-5744

Hagedorn, Norman
NASA Lewis Research Center
21000 Brookpark Road, M.S. 301-3
Cleveland, OH 44135
(216) 433-6157

Hall, Arnold
Yardney Corporation
82 Mechanic Street
Pawcatuck, CT 02891
(203) 599-1100

Halpert, Gerald
Jet Propulsion Laboratory
4800 Oak Grove Drive, MS 277-102
Pasadena, CA 91109
(818) 354-5474

Ham, David
Physical Sciences Inc.
P. O. Box 3100
Andover, MA 01810
(617) 475-9030

Harney, David
Eltech Systems Corporation
625 East Street
Fairport Harbor, OH 44077
(216) 357-4044

Huggins, Robert
Stanford University
Dept. of Materials Science
& Engineering
Stanford, CA 94305
(415) 723-4110

Jalan, Vinod
ElectroChem, Inc.
499 W. Cummings Park
Woburn, MA 01801
(617) 932-3383

Jorne, Jacob
University of Rochester
Dept. of Chemical Eng.
Rochester, NY 14607
(716) 275-4584

Kang, Paul
NASA Lewis Research Center
21000 Brookpark Road, MS 301-3
Cleveland, OH 44135
(216) 433-5263

Kennedy, John
Yardney Corporation
82 Mechanic Street
Pawcatuck, CT 02891
(203) 599-1100 Ext. 321

Kirk, James
University of Maryland
Mechanical Engineering Dept.
College Park, MD. 20742
(301) 454-8864

Juda, Walter
Prototech
70 Jaconnet
Newton, Ma. 02161

Kolecki, Joseph
NASA HQ
Code MTS
Washington, DC 20546
(202) 453-1881

Kosek, Jack
Giner, Inc.
14 Spring Street
Waltham, MA. 02254-9147
(617) 899-7270

LaConti, Anthony
Giner, Inc.
14 Spring Street
Waltham, MA. 02254-9147
(617) 899-7270

Landau, Uziel
Case Western Reserve University
Chemical Engineering Dept.
Cleveland, OH 44106
(216) 368-4132

Leddy, Johna
Queens College
Chemistry Department
Flushing, NY 11367
(718) 520-7688

Leibecki, Harold
NASA Lewis Research Center MS 301-3
21000 Brookpark Road
Cleveland, OH 44135
(216) 433-6172

Lenhart, Stephen
SRI
333 Ravenswood Ave.
Menlo Park, CA 94025
(415) 326-6200

Lim, Hong
Hughes Research Labs.
3011 Malibu Canyon Rd.
MS-RL70
Malibu, CA 90265
(213) 317-5379

Manzo, Michelle
NASA Lewis Research Center MS 309-1
21000 Brookpark Road
Cleveland, OH 44135
(216) 433-5261

Maurer, Dean
AT & T Bell Labs.
600 Mountain Ave., Room 1E-207
Murray Hill, NJ 07974-2070
(201) 582-3237

Maurer, Dorian
RCA-Astro Electronics Div.
MS> 410-2-C19
P. O. Box 800
Princeton, NJ 08540
(609) 426-3837

McBreen, James
Brookhaven National Lab.
Dept. of Applied Science
Upton, NY 11973
(516) 282-4513

McElroy, James
Hamilton Standard
Division of UTC
MS 1A-2-6
Windsor Lock, CT 06096
(203) 654-6000

Mehandru, S.
Case Western Reserve University
Chemistry Department
Cleveland, OH 44106
(216) 368-2608

Mercanti, Enrico
NASA Goddard Space Flight Center
Code 402
Greenbelt, MD 20771
(301) 286-8108

Miller, Lee
Eagle-Pitcher Industries
P. O. Box 47
Joplin, MO 64802
(417) 623-8000 Ext. 390

Miller, Tom
NASA Lewis Research Center M.S. 501-1
21000 Brookpark Road
Cleveland, OH 44135
(216) 433-6300

Niksa, Marilyn
Eltech Systems Corp.
625 East Street
Fairport Harbor, OH 44077
(216) 357-4096

O'Donnell, Patricia
NASA Lewis Research Center
21000 Brookpark Road MS 309-1
Cleveland, OH 44135
(216) 433-5248

Olszewski, Mitchell
Oak Ridge National Laboratory
P. O. Box Y
Oak Ridge, TN 37821
(615) 574-0770

Owens, Boone
University of Minnesota
Dept. of Chemical Engineering
Minneapolis, MN 55455
(612) 645-2514

Pawlik, Eugene
Jet Propulsion Laboratory
M.S. 168-327
Pasadena, CA 91109
(818) 354-0086

Pickett, David F.
Hughes Aircraft Company
P.O. Box 92919
(541/A315)
Airport Station
Los Angeles, CA 90009
(213) 648-2128

Powers, Robert
Case Western Reserve University
Edison Sensor Tech Center
Cleveland, OH 44106
(216) 368-6119

Puglisi, Vince
Gates Energy Products
P. O. Box 114
Gainesville, FL 32602
(904) 462-3911

Reed, James
Atlanta University
Chemistry Dept.
223 Brawely Drive SW
Atlanta, GA 30314
(404) 681-0251 Ext. 354

Reid, Margaret
NASA Lewis Research Center
21000 Brookpark Road MS 309-1
Cleveland, OH 44135
(216) 433-5253

Ross, Paul
Lawrence Berkeley Lab.
University of California, Bldg. 62-203
Berkeley, CA 94720
(415) 486-6226

Rosso, Matthew
Ergenic Power Systems
681 Lawlins Road
Wyckoff, NJ 07481
(201) 891-9103

Sammells, Anthony
Eltron Research, Inc.
4260 Westbrook Dr.
Aurora, IL 60504
(312) 898-1583

Sanabria, Olga
NASA Lewis Research Center
21000 Brookpark Road MS 309-1
Cleveland, OH 44135
(216) 433-5252

Savinell, Robert
Case Western Reserve University
Dept. of Chemical Engineering
Cleveland, OH 44106
(216) 368-2728

Schnyer, Arnold .
NASA HQ
Code R
Washington, DC 20546
(202) 453-2843

Scott, William
Miami University
Paper Science and Engineering Dept.
229 Gaskill Hall
Oxford, OH 45056
(513) 529-2200

Sheibley, Dean
NASA Lewis Research Center
21000 Brookpark Road, MS 501/17
Cleveland, Ohio 44135
(216) 433-5378

Sindorf, Jack F.
Johnson Controls, Inc
5757 N. Green Bay Ave.
Milwaukee, WI 53201
(414) 228-1200

Singer, Joseph
NASA Lewis Research Center
21000 Brookpark Road, MS 309-1
Cleveland, OH 44135
(216) 433-5251

Smithrick, John
NASA Lewis Research Center
21000 Brookpark Road, MS 309-1
Cleveland, OH 44135
(216) 433-5255

Srinivasan, Supramaniam
Los Alamos National Laboratory
M. S. D429
Los Alamos, NM 87545
(505) 667-0196

Stedman, Jay
International Fuel Cell
P. O. Box 109
South Windsor, CT 06074
(203) 727-2211

Stockel, Joseph
Centeral Intelligence Agency
Washington, DC 20505
(703) 351-2065

Subbarao, Rao
Jet Propulsion Laboratory
4800 Oak Grove Drive M.S. 277-102
Pasadena, Ca 91109
(818) 354-0352

Swette, Larry
Giner, Inc.
14 Spring Street
Waltham, MA 02254-9147
(617) 899-7270

Taylor, E. Jennings
Physical Sciences Inc.
P. O. Box 3100
Andover, MA 01810
(617) 475-9030

Thaller, Lawrence
NASA Lewis Research Center
21000 Brookpark Road, MS 301-3
Cleveland, OH 44135
(216) 433-6146

Thierfelder, Helmut
G. E. Space Systems Div.
P. O. Box 8555
Bldg. 100 RM. M2508
Philadelphia, PA 19101
(215) 354-2027

Trumbore, Forrest
AT & T. Bell Labs.
600 Mountain Ave., Rm 1E-217
Murray Hill, NJ 07974-2070
(201) 582-2793

Vaidyanathan, Hari
COMSAT Labs.
22300 Comsat Drive
Clarksburg. MD 20871-9475
(301) 428-4507

Viswanathan, S.
Energy Research Corp.
3 Great Pasture Road
Danbury, CT 06813
(203) 792-1460 ext. 281

Wasel, Robert
NASA HQ
Code RP
Washington, DC 20546
(202) 453-2855

Weaver, Robert D.
Electric Power Research Institute
3412 Hillview Ave.
Palo Alto, CA 94304
(415) 855-8947

Yeager, Ernest
Case Western Reserve University
Chemistry Department
Cleveland, OH 44106
(216) 368-3626

Yi, Thomas
NASA Goddard Space Flight Center
Code 711
Greenbelt, MD 20771
(301) 286-3051

NASA
National Aeronautics and Space Administration

Report Documentation Page

1. Report No.	2. Government Accession No.	3. Recipient's Catalog No.
NASA CP-2484		

4. Title and Subtitle	5. Report Date
Space Electrochemical Research and Technology (SERT)	September 1987
	6. Performing Organization Code: 506-41-21
7. Author(s)	8. Performing Organization Report No.: E-3506
	10. Work Unit No.
9. Performing Organization Name and Address: National Aeronautics and Space Administration, Lewis Research Center, Cleveland, Ohio 44135	11. Contract or Grant No.
	13. Type of Report and Period Covered: Conference Publication
12. Sponsoring Agency Name and Address: National Aeronautics and Space Administration, Washington, D.C. 20546	14. Sponsoring Agency Code

15. Supplementary Notes

16. Abstract

This document contains the proceedings of NASA'S first Space Electrochemical Research and Technology Conference, held at the Lewis Research Center on April 14-16, 1987. The conference provided a forum to assess critical needs and technologies for the NASA electrochemical energy conversion and storage program. It was aimed at providing guidance to NASA on the appropriate direction and emphasis of that program. A series of related overviews were presented in the areas of NASA advanced mission models (space station, low- and geosynchronous-Earth-orbit missions, planetary missions, and space transportation). Papers were presented and workshops conducted in a variety of technical areas, including advanced rechargeables, advanced concepts, critical physical electrochemical issues, and modeling. This document contains the overviews, the technical papers, and summaries of the technical workshops.

17. Key Words (Suggested by Author(s))	18. Distribution Statement
Electrochemistry; Advanced rechargeables; Modeling; Fuel cells; Batteries; Catalyst; Advanced concepts	Unclassified - unlimited Subject Category 44

19. Security Classif. (of this report)	20. Security Classif. (of this page)	21. No of pages	22. Price*
Unclassified	Unclassified	372	A16

NASA FORM 1626 OCT 86

*For sale by the National Technical Information Service, Springfield, Virginia 22161

NASA-Langley, 1987